L'érosion et l'altération en Himalaya et leur évolution depuis le tardi-pléistocène : analyse des processus d'érosion à partir de sédiments de rivière actuels et passés au Népal central

Guillaume Morin

L'Érosion et l'Alteration en Himalaya et leur Évolution depuis le tardi-Pleistocene : Analyse des Processus d'Érosion a partir de Sediments de Riviere actuels et passes au Nepal central

These

Présentée pour l'obtention du titre de
Docteur de l'Université de Lorraine
Spécialité Géosciences

par Guillaume Morin
soutenance prévue le 9 Décembre 2015

Composition du jury :

Rapporteurs	
François Chabaux	Professeur, LHyGeS, Strasbourg, FR
Jérôme Gaillardet	Professeur, IPGP, Paris, FR
Examinateurs	
Albert Galy	Professeur, CRPG, Nancy, FR
Pascale Huyghe	Maître de conférence, ISTerre, Grenoble, FR
Invité	
Rajiv Sinha	Professor, IITK, Kanpur, IN
Directeurs de thèse	
Christian France-Lanord	DR, CRPG, Nancy, FR
Jérôme Lavé	DR, CRPG, Nancy, FR

Résumé

L'altération chimique et l'érosion physique de la croûte continentale mobilisent de grandes quantités de matière sous formes solide et dissoute. Première productrice de sédiments sur le globe, la chaîne Himalayenne délivre ~1 Gt/a de sédiments aux océans. L'importance des différents facteurs qui contrôlent les flux érodés et celle des processus d'érosion (glaciers, glissements de terrain, sols) sont pourtant encore mal définies. Il en va ainsi des facteurs climatiques, en particulier de leur impact au cours des transitions climatiques. Afin de répondre à ces questions, ce travail s'attache à comparer la composition géochimique des produits de l'érosion à celles des sédiments actuels de rivière et des archives sédimentaires de la plaine du Gange.

Un premier bilan des processus d'érosion a été établi petite échelle dans le bassin Haut-Himalayan de la Khudi. L'érosion actuelle conséquente de ce bassin de ~3 mm/a se produit lors de la mousson, correspond pour l'essentiel à l'érosion des sols et surtout à l'intense activité d'une zone de glissement de terrain. Grâce au développement d'une nouvelle méthode de destruction de la matière organique, la mesure de l'hydratation des silicates a pu être utilisée comme traceur inédit des sols. Sur cette base, l'inversion des compositions des sédiments de la rivière démontre que l'érosion physique est dominée à ~80% par le glissement de terrain, l'érosion de sols étant mineure et comparable aux taux d'érosion des autres bassins alentours. L'érosion chimique qui conduit à un flux d'éléments dissous de 7.9 kt/a (soit une érosion équivalente de 0.02 mm/a) semble dériver de l'altération profonde du substrat rocheux. Néanmoins les flux d'éléments dissous dessinent également une relation marquée avec les flux particulaires durant la mousson, suggérant une altération additionnelle des sédiments au cours du transport fluvial.

Une approche similaire a ensuite été menée à l'échelle plus vaste du bassin de la Narayani drainant l'ensemble du Népal central. Grâce à des mesures de courant par ADCP

combinées à l'échantillonnage de sédiments en profondeur, un modèle de transport sédimentaire a été utilisé pour intégrer les flux sédimentaires en profondeur et ainsi réviser le taux d'érosion moyen sur le bassin versant à une valeur de ~1.7 mm/a, proche des taux d'érosion long-terme. Un système géochimique associant la mesure du δD des silicates associée aux concentrations en carbonate s'est révélé un traceur diagnostique de l'érosion glaciaire dans le Nord du bassin, tandis que la teneur en matière organique du sédiment a pu être utilisée comme traceur des sols. L'analyse temporelle des flux de sédiments, de leur composition et du signal granulométrique, a ainsi permis d'établir que seule une faible fraction des sédiments (<20%) provenait de l'érosion par les glaciers et les sols. À l'échelle du Népal central, l'érosion physique semble donc également dominée par les glissements déclenchés lors de la période de mousson.

Le grand cône alluvial de la Narayani-Gandak, situé au débouché de cette rivière dans la plaine du Ganges, a enregistré l'histoire récente de l'érosion du Népal central. Trois forages réalisés dans ce méga-cône permettent ainsi d'étudier l'évolution de l'altération et de l'érosion en Himalaya au cours du tardi-Pléistocène. Ces dépôts sédimentaires révèlent une étonnante stabilité depuis ~45 ka de la géochimie, des provenances et du degré d'altération des sédiments. Seule l'intensité de l'érosion mesurée par isotopes cosmogéniques semble augmenter au cours de l'Holocène.

Par contraste, l'évolution très récente de la distribution de l'érosion dans la chaîne est marquée par un accroissement (×3) de la proportion de matériel des régions basses et plus peuplées de l'Himalaya, montrant que les activités anthropiques, via notamment une forte croissance du réseau routier durant la dernière décennie, ont eu un impact beaucoup plus marqué sur l'érosion que la dernière transition climatique Pléisto-Holocène.

Abstract

Chemical weathering and physical erosion of the continental crust mobilise huge amounts of both solid and dissolved material. As the first sediment generator on the Earth, the Himalayan range releases around 1 Gt/y of sediment into the ocean. The relative influence of the different factors that control the eroded fluxes and the importance of the erosion processes (such as landslides, glaciers, soils) are as yet poorly understood. The same is true of the climatic factors, especially regarding their impact during climatic transition periods. In order to address those questions, this work focuses on comparing the geochemical composition of erosion products to the composition of present river sediment and of sedimentary records in the Ganga Plain.

A first budget of the erosion processes was done on a small scale in the Khudi catchment of Higher Himalaya. The total present-day erosion is considerable, at around 3 mm/y and takes place during the monsoon. It is mainly linked to the soils erosion and more importantly to the intense activity of a landsliding area. The development of a new method for the destruction of organic matter enabled the use of silicates hydration as a tracer for soils. Based on this method, a mathematical inversion of the sediment compositions was performed. It highlights that the landslide is responsible for ~80% of the overall physical erosion. The soil erosion is minor and is comparable to the erosion rates measured in the neighbouring catchments. The chemical erosion leads to a dissolved flux of 7.9 kt/y (corresponding to an erosion rate of 0.02 mm/y) and seems to come from the bedrock deep weathering. Nevertheless, the dissolved fluxes also appear to be linked with the particles fluxes during the monsoon. This suggests an additional weathering of the sediment during the fluvial transport.

A similar approach was used on a larger scale in the Narayani catchment that drains the whole of Central Nepal. Through ADCP-based current measurements combined with

deep sediment sampling, a model for sedimentary transport was used to integrate the deep sediment fluxes. The average catchment-scale erosion rate was then corrected to a value of ~1.7 mm/y, close to the long-term erosion rates. A geochemical system that combines the measurement of the δD of silicates and the concentrations of carbonates was found to be a diagnosis tracer for glacial erosion in the northern part of the catchment. The organic matter ratio was used as a tracer for soils. The temporal analysis of sediment fluxes, as well as the sediment composition and granulometry showed that only a small fraction ($< 20\%$) of the sediment comes from glacial and soils erosion. Over the whole Central Nepal, the physical erosion seems also to be dominated by the landslides that are triggered during the monsoon.

The large Narayani-Gandak alluvial fan is located at the river mouth and can be used as a record of the recent history of Central Nepal erosion. Three drillings were done in this fan to enable the study of the evolution of Himalayan weathering and erosion during the Late Pleistocene. The sedimentary deposits display a surprising stability in their geochemistry, their sources and their weathering stage for the last ~45 ky. The erosion intensity derived from cosmogenic nuclides is the only feature that seems to have risen during Holocene. However, the very recent evolution of the erosion distribution in the range is characterised by an increase ($\times 3$) of the proportion of products coming from the lower, more densely populated areas. This shows that the anthropogenic activities have had a larger impact on the erosion than the last Pleistocene-Holocene transition, especially through the rapid growth of the road network during the last decade.

Remerciements

Je tiens tout d'abord à remercier mes deux directeurs de thèse, Christian France-Lanord et Jérôme Lavé. Merci à Christian de m'avoir poussé à m'engager sur de nombreuses voies, parfois même sur des rivières en crue, grâce à lui j'ai progressé au delà de ce que j'imaginais. Merci à Jérôme de m'avoir apporté sa vision rigoureuse, son point de vue lumineux face aux difficultés que les résultats dressaient sur mon chemin, ainsi que de m'avoir aidé et soutenu lorsque j'ai souhaité aborder d'autres disciplines.

Tous mes remerciements vont à François Chabaux et Jérôme Gaillardet pour avoir accepté de rapporter ce manuscrit ainsi qu'aux autres membres du jury, Albert Galy, Pascale Huyghe et Rajiv Sinha de s'être intéressés à mon travail.

Au CRPG, je remercie Caroline pour m'avoir accueilli aux « stables » devant les lignes et les spectros avec sourire et patience, et surtout Thomas pour avoir pris son relai, m'avoir aidé à gérer les séances d'analyses, avoir débloqué de nombreux soucis de machine, et ce, 7 jours sur 7. Je remercie également Laurie, Catherine, Aimeryc et Christiane pour la bonne humeur dans la salle blanche et les mesures de Sr et Nd, ainsi que toute l'équipe du SARM pour avoir (parfois en urgence) produit une grande quantité de données que j'ai utilisées dans ce travail. Merci aussi à Nathalie pour son soutient et son enthousiasme qui m'ont accompagnés depuis mes premiers pas en recherche.

Je tiens aussi à remercier Cati, Aurélie et Isabelle pour la gestion des missions et papiers, et bien sûr le service général : Bruno, Nordine et Yannick. Merci au STEVAL, Bob, Fred, Jean-Marie pour les coups de main et pour la bonne humeur des TP.

Un grand merci à Harka, Bhairab et à tous les porteurs, sur le terrain. Merci aussi à Ananta pour toute l'aide à Kathmandu et pour la quantité de travail sur les échantillons.

Un grand merci aussi à l'équipe de l'IIT Kanpur, en particulier au Pr Sinha et à Gaurav pour le temps passé en Inde entre la campagne électrique, l'ADCP et au campus de Kanpur. Merci à Valier d'avoir partagé son temps et son énergie sur le dirt-burner pendant la semaine à Woods Hole.

Un grand merci aux « collègues » du CRPG qui font de ce lieux un endroit de vie, merci pour les bols et bulles d'air ainsi que les embruns à PH, Yves, Julien C, Lydé, Marianne, David, Pierre, Yannick, Tix, Delphine et merci à François qui n'a jamais refusé une pause ni une mauvaise blague et à Gaston pour le commerce amical des fruits de saison.
Mes pensées vont à Pete et à Romain.

Merci au bureau 210 pour l'essentiel du temps passé au « travail » : Flo, merci pour les coups de mains, corrections de fin, les bouffées d'oxygène et les longues discussions ici ou ailleurs ; Te-Fang, merci pour les discussions philosophiques et cet optimisme inaltérable.

Merci aux amis et « compagnons de galère » avec qui j'ai partagé la traversée : Maïa pour son soutient et sa présence pendant une grande partie du chemin, Flo et Jo (que dire, 7 ans que votre porte est chaleureusement et immanquablement ouverte...), Camille et Martin (merci pour vos sourires et présences inoxydables), Antonio pour les breaks « out of the vortex » (un grande abbraccio), Sarah (quand tu veux pour un dimanche marché/thé), Laurette et Julien (Aligato !). Merci aux thèsards et post-docs plus anciens : Maayt, Bid, Mag, Tutu, Marie, Puch, Julien A., Evelyn ; moins anciens : Gaëlle, Romain, Léa, Julien H., Léo, Guillaume, Dimitri, Précilia, Clio, bien entendu bon courage à Jesse (You'll make it my friend !). Je dédie une chanson pour l'Auvergnat à Émilie, Nastasia et Jérémy pour la sortie de l'hiver, de même à Rosine et Abilio pour un accueil plus que familial dans leur havre vosgien, ainsi qu'à Yves et Anne lors des derniers milles décisifs à revisiter « je ponce donc je suis ».
Je remercie aussi tous mes amis en Lorraine qui m'ont permis de relativiser et qui ont su mettre de la couleur dans une vie de thésard : Marko, Pierre B., Mathilde, Sam et Sandra, l'AMAP de la MJC Vandœuvre, ainsi qu'Hélène et Matthias. À tous ceux que j'oublie ici...

Enfin, je tiens à remercier mes parents Brigitte et Thierry ainsi que mon frère Julien, qui m'ont accompagné et soutenu de près, et ce depuis toujours.

Table des matières

Table des figures

Liste des tableaux

Organisation du manuscrit

Ce manuscrit s'organise autour de 6 chapitres. Les chapitres 1, 2 et 3 sont dédiés à la présentation du contexte scientifique général de ce travail, des lieux d'études et des méthodes utilisées.
Le chapitre 1 s'articule autour d'un état de l'art des études concernant l'érosion, l'altération et leurs intéractions avec la tectonique et le climat. Un accent particulier est mis sur les chaînes de montagne qui ont constituées le principal terrain d'étude de ce travail.
Le chapitre 2 présente le contexte général de cette étude : la chaîne Himalayenne. Il décrit le cadre tectonique, hydrologique et climatique de l'Himalaya, qui constituent les principaux facteurs contrôle de l'érosion. Une partie de cette thèse est axée sur l'étude des enregistrements sédimentaires récents de la plaine de la Narayani-Gandak. Aussi, nous présentons brièvement les bassins d'avant-pays himalayens de la plaine du Ganges dans ce chapitre.
Le chapitre 3 est dédié à la présentation des méthodes d'analyses qui ont été utilisées pour mener à bien cette étude. Dans ce chapitre sont présentés : 1- les méthodes de prélèvement et de traitement des échantillons, 2- les méthodes d'acquisitions géophysiques qui ont permis la caractérisation de la stratigraphie de sub-surface de la plaine de la Gandak, ainsi que celles qui ont permis les mesures du courant par ADCP associées aux prélèvements de sédiments de rivière en profondeur, 3- les méthodes d'analyses géochimiques et isotopiques du carbone, des hydroxyles d'hydratation des sédiments et des pré-traitements associés.
Le chapitre 4 s'articule autour d'un article de conférence et d'un manuscrit d'article scientifique portant sur l'analyse de l'érosion physique et chimique dans un bassin typique du flanc sud himalayen : le bassin de la Khudi Khola situé dans le massif du Lamjung au Sud-Est des Annapurnas. Cette étude présente une première analyse des sédiments produits

par les différents processus d'érosion dans la chaîne, et en particulier les glissements de terrains et l'érosion des sols. Elle met en regard les bilans d'érosion physique et d'érosion chimique et propose un premier cadre interprétatif de l'utilisation de la géochimie des sédiments pour tracer les processus d'érosion.
Le chapitre 5 s'articule autour d'un manuscrit d'article scientifique portant sur l'étude temporelle des flux de sédiments exportés par la Narayani, rivière qui draîne l'ensemble du Népal central. Un modèle de transport sédimentaire a été proposé, il a été basé sur les échantillonnages en profondeur et les mesures de courants par ADCP qui y ont été menées. Ce modèle permet de réévaluer les taux d'érosion au Népal central, les approchant des taux de dénudation long-terme précédemment publiés. De l'analyse du cycle hydrologique, des flux sédimentaires et de l'évolution des caractéristiques des sédiments au cours d'une année, cette étude appuie le fort impact des glissements de terrain dans le budget de la dénudation du Népal central, relayant les rôles des glaciers et de l'érosion des sols à un ordre inférieur.

Le chapitre 6 présente l'interprétation de l'évolution de l'altération et de la dénudation du Népal central depuis la fin du Pléistocène, basée sur l'étude de forages de la plaine de la Narayani-Gandak. Cette partie s'attache à décrire la structure ainsi que la stratigraphie du mégafan de la Gandak, cette dernière ayant fait l'objet d'un article issu de nos collaborations avec les équipes de l'IIT Kanpur (Inde) qui est placé en annexe du manuscrit. L'évolution de l'altération et de la dénudation de la chaîne depuis le tardi-Pléistocène y est interprétée à partir de l'analyse de la géochimie des archives sédimentaires. La comparaison de l'érosion passée et de l'érosion très récente y fait aussi l'objet d'un manuscrit d'article scientifique dans lequel nous observons le fort impact que les activités humaines ont eu sur l'érosion de la chaîne depuis une dizaine d'années.

I

Chapitre 1

Introduction

La matière est extraite de la roche par l'action de l'eau de ruissellement et de l'eau d'infiltration, des fleuves et des rivières, des mouvements de terrains, des glaciers ou encore du vent, qui la transportent « ailleurs ». Ce transport est appelé « érosion » (*erosion*). Lorsqu'il a lieu sous forme dissoute, on parle d*'« érosion chimique »* (*chemical erosion*) alors qu'on emploie le terme « érosion physique » lorsqu'il a lieu sous forme solide. De façon complémentaire, les modifications physiques ou chimiques des propriétés initiales d'une roche sous l'action de l'eau, de la température, des gaz atmosphériques et des acides, des organismes biologiques, des variations thermiques ou des cycles gel-dégel, constituent l'« altération » (*weathering*). L'altération concerne les modifications de l'« état » de la roche. Comme l'érosion, l'altération se divise en deux champs : l'« altération chimique » (*chemical weathering*) et l'« altération physique » (*physical weathering*). La distinction entre l'érosion chimique et l'altération chimique n'est pas exclusive : l'altération chimique concerne l'étude de la matière résiduelle et implique le départ d'éléments solubles ; elle dépend donc d'un transport. La somme de l'altération et de l'érosion correspond à la « dénudation » (*denudation*). Par abus de langage et sauf si précisé, nous utiliserons par la suite le terme d'« érosion » à sa place.

Chaque agent, ou processus, impliqué dans l'érosion et l'altération constitue une « pièce du moteur » responsable de la séparation de la matière entre les grands réservoirs à la surface de la Terre. Les rivières et fleuves, en particulier, font le lien entre les réservoirs continentaux et océaniques, et de ce fait, participent à de nombreux cycles bio-géochimiques de la surface terrestre. L'érosion chimique et l'érosion physique estimées dans les bassins

versants des plus grands fleuves du globe démontrent d'une part la domination globale de l'érosion physique sur l'érosion chimique de plusieurs ordres de grandeur, et d'autre part la diversité du ratio entre érosion chimique et physique qui existe en différents endroits du monde (cf. 1.0.1). Cette diversité s'explique par de nombreux facteurs comme l'âge des terrains, les lithologies drainées, la topographie ou encore le climat dont il est difficile d'appréhender les influences respectives car ils sont souvent inter-dépendants.

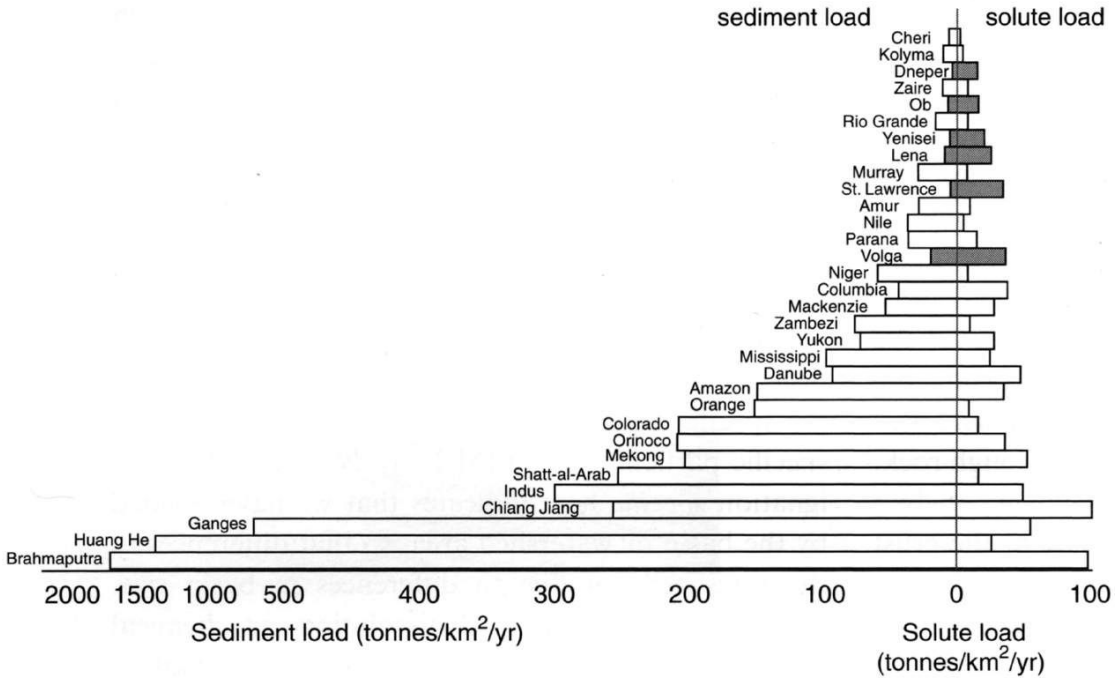

FIGURE 1.0.1 – Flux solides et dissous des principaux fleuves du monde. D'après [Anderson 10]

Parmi tous les environnements rencontrés à la surface de la Terre, les orogènes actuels sont les lieux des plus intenses taux de dénudation mesurés, et les processus géologiques impliqués s'y déroulent de manière démonstrative et souvent quantifiable. Les jeunes chaînes de montagnes actives résultent d'un épaississement de la croûte continentale produit par la tectonique. La tectonique donne ainsi naissance aux topographies montagneuses définies par de fortes élévations et d'importants reliefs. Le climat, lui, agit sur les processus de l'érosion et de l'altération qui amincissent la croûte continentale, diminuent l'élévation et sculptent les reliefs (cf. figure 1.0.2).

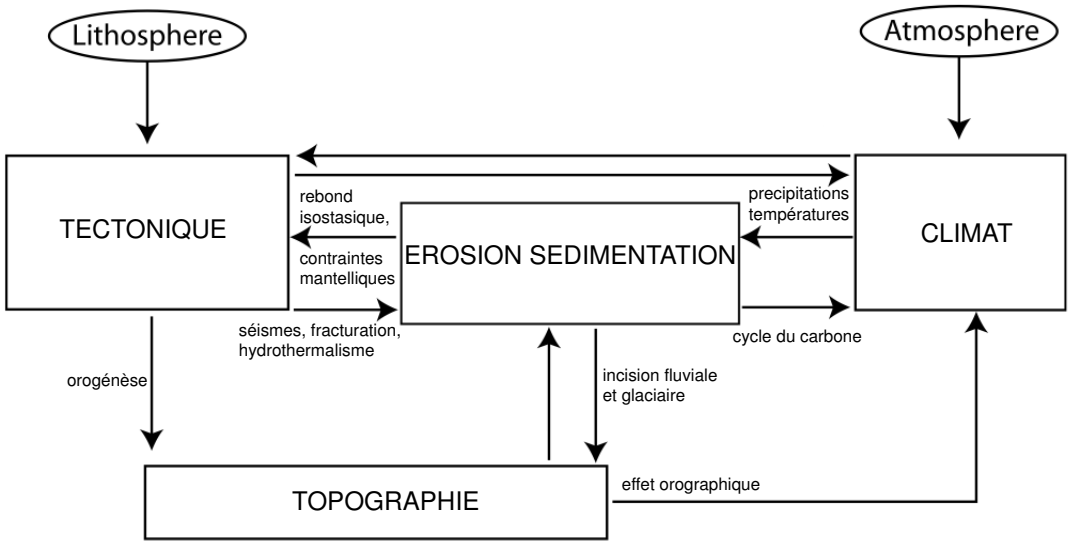

FIGURE 1.0.2 – Schéma des interactions entre Érosion - Tectonique - Climat. Modifié d'après [Champagnac 12]

Cette vision simplifiée explique pourquoi les orogènes actifs, environnements où la tectonique et le climat sont très intenses et contrastés, sont les laboratoires privilégiés de l'étude des interactions entre l'érosion, la tectonique et le climat. Concernant l'érosion, il a été proposé que les flux de sédiments sont inversement corrélés à la taille des bassins versants mais positivement corrélés à la topographie et à l'activité tectonique et volcanique [Milliman 92, Milliman 11]. Ne représentant pourtant qu'une faible partie des surfaces continentales (~10%), les chaînes de montagnes, et en particulier les petits bassins montagneux, auraient un rôle prépondérant et bien plus important que les plaines en totalisant plus de 50% de la dénudation globale et 30% de l'érosion chimique [Larsen 14a].

C'est dans ce contexte actuellement très débattu entre, d'une part l'importance des chaînes de montagnes dans la dénudation globale [Willenbring 13, Kirchner 13, Warrick 14, Willenbring 14, Larsen 14a] et d'autre part la compréhension des contrôles de l'érosion par la tectonique [Whipple 99a, Burbank 03, Huyghe 05, Godard 14, Scherler 14] ou par le climat [Dadson 03, Reiners 03, Grujic 04, Huyghe 05, Grujic 06, Thomson 10, Deeken 11, Andermann 12b, Herman 13] que s'inscrit ce sujet de thèse. En étudiant l'érosion et l'altération dans le bassin de la Narayani-Gandak qui draine la chaîne himalayenne du Népal

central, ce travail s'est attaché à apporter quelques éléments de réponse au traçage des agents érosifs (glaciers, sols, glissements de terrain) à partir de l'analyse des sédiments de rivières actuels.

De plus, alors qu'un refroidissement global et une modification des taux d'érosion sont observables au cours du Cénozoïque, les modalités des changements d'érosion observés sont mal connues et ne permettent pas d'interpréter ces modifications parfois contradictoires de l'érosion [Molnar 04]. En analysant les archives sédimentaires du Népal central déposées dans la plaine de la Narayani-Gandak correspondant à la période du tardi-Pléistocène à aujourd'hui, la deuxième partie de ce travail s'est attaché à comprendre quelle influence le dernier grand changement climatique a eu sur la distribution et l'intensité de l'érosion, ainsi que sur la modification de la dynamique des processus et agents érosifs actifs dans la chaîne himalayenne.

1.1 Érosion, tectonique et climat

1.1.1 Interactions entre tectonique et érosion

1.1.1.1 Influence de la tectonique sur l'érosion

La formation et l'évolution des chaînes de montagnes sont le résultat d'une compétition entre la géodynamique qui crée la topographie et l'érosion qui la détruit [Molnar 03]. La tectonique au travers des grandes collisions et subductions provoque la surrection de la croûte continentale, l'élévation de la topographie et donne naissance aux chaînes de montagnes actuelles. Lors de l'orogénèse, l'érosion va résulter de l'augmentation des reliefs, des gradients et des pentes par augmentation de l'incision produite par les rivières, le déclenchement de glissements de terrains, et l'apparition éventuelle d'une érosion glaciaire. Les corrélations entre le relief, les pentes moyennes et l'érosion ont déjà été démontrées au sein des orogènes [Vance 03] ainsi qu'à l'échelle du globe [Milliman 92, von Blanckenburg 05, Syvitski 07, Portenga 11, Milliman 11, Champagnac 12, Willenbring 13]. En effet, de nombreuses études montrent qu'il y a un couplage direct entre le forçage tectonique et l'érosion des versants par l'incision produite par les rivières [Burbank 96a, Whipple 99b, Lavé 01, Larsen 12, Mueller 13], ou par le déclenchement de glissements de terrain au delà d'une pente limite [Burbank 96a]. Ces glissements sont d'ailleurs cités comme le

principal agent de l'érosion des versants dans les bassins de montagnes non englacés (e.g. [Hovius 97, Shroder 98a, Shroder 98b, Hovius 00, Struck 15]). La structure et la fragilisation du bâti rocheux par fracturation, souvent lié à une activité sismique et au développement de failles tectoniques, sont aussi évoquées comme facteur favorisant les ruptures de pentes [Larsen 10]. Enfin, l'influence active des séismes sur le déclenchement des glissements de terrains et de l'érosion des orogènes a été démontrée à Taïwan [Dadson 04].

1.1.1.2 Influence de l'érosion sur la tectonique

La rétroaction de l'érosion sur la tectonique est moins intuitive. Le transfert des masses depuis l'orogène vers les bassins sédimentaires diminue la masse continentale au niveau de l'orogène et induit une modification de l'équilibre de la croûte et du manteau qui conduit à l'*uplift* [Avouac 96]. L'érosion déforme le champ de contraintes du manteau et provoque sa remontée entraînant la croûte sus-jacente par « rebond isostasique » [Molnar 90, Champagnac 07]. Paradoxalement, sous l'effet du rebond isostatique et du fait que la dénudation se produit principalement au niveau des thalwegs des vallées (incision fluviatile ou ablation glaciaire), l'altitude des pics et crêtes des chaînes de montagnes augmente sous l'effet de l'érosion, alors que l'altitude moyenne ne change pas [Molnar 90, Champagnac 07]. Cette réponse mantellique peut être très rapide et a été observée à l'échelle de quelque dizaines de milliers d'années dans les Alpes européennes [Champagnac 07]. Elle est souvent asymétrique car les précipitations orographiques, et l'érosion qui en dérive, ne concernent souvent qu'un seul flanc de l'orogène. Compte tenu des grandes échelles de temps impliquées, ces réponses ont été testées par la construction de simulations couplant structure, tectonique et processus de surface [Willett 99, Zeitler 01, Beaumont 01]. Récemment, [Whipple 09] ont montré que les modifications des champs de contraintes de la lithosphère résultant d'une érosion asymétrique de ce type pouvaient reproduire les taux de surrection et exhumation mesurés dans les Alpes européennes [Koons 90] et expliquer les topographies asymétriques de chaînes de montagnes (cf. figure 1.1.1).

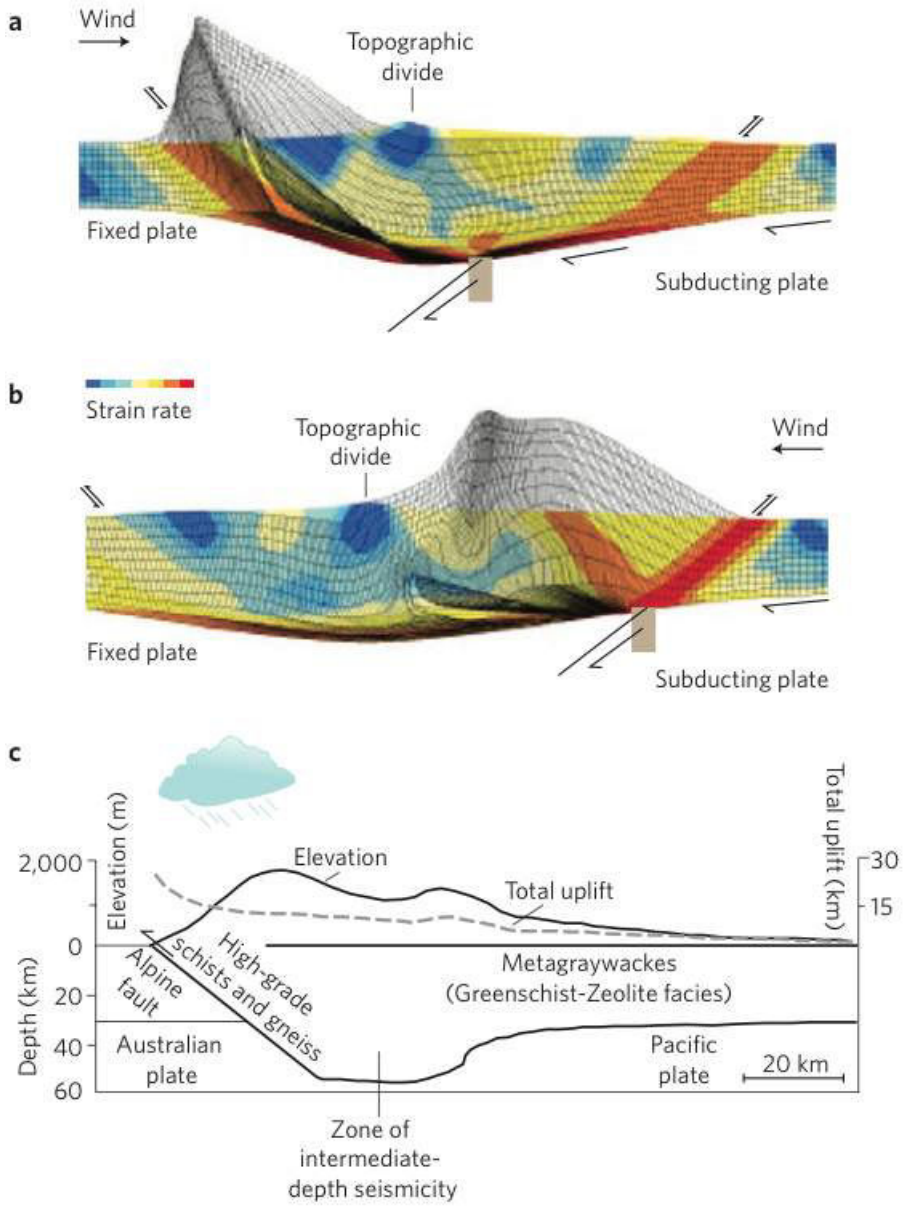

FIGURE 1.1.1 – Asymétrie de l'évolution tectonique et structurale d'un orogène soumis à un régime de précipitations orographiques [Whipple 09].
En a), les flux d'Ouest induisent la concentration des contraintes, de la surrection et de l'exhumation le long de la faille en orange élevant la partie occidentale de l'orogène. En b), le flux d'Est provoque l'inverse. En c), l'architecture des Alpes européennes proposée par [Koons 90] est reproduite par le modèle numérique de [Whipple 09].

1.1.2 Interactions entre l'érosion et le climat

Dans le cadre du projet ANR blanche « CALIMÉRO » (anagramme de CLIMAt et ÉROsion), ce travail de thèse s'est plus particulièrement porté sur les interactions entre l'érosion et le climat (cf. figure 1.0.2). Les paragraphes suivants tentent de faire un état de l'art des problématiques scientifiques qui y sont associées.

1.1.2.1 Influence du climat sur l'érosion

L'influence du climat est souvent invoquée pour expliquer les « grandes formes » de l'érosion observées dans les chaînes de montagnes.

Les températures

Comme évoqué précédemment, les températures basses favorisent l'apparition des glaciers, puissants agents érosifs qui, par ablation, sont responsables de la formation de larges vallées glaciaires [Valla 10, Iverson 12, Sternai 13, Pedersen 13]. L'influence de l'érosion glaciaire a été proposée comme le principal contrôle de l'élévation des chaînes de montagnes à long-terme, par effet de rabotage ou *buzz-saw* des sommets situés au dessus des « Lignes d'équilibre des Neiges Éternelles » (*ELA)* [Egholm 09] (cf. figure 1.1.2 A, B). Par une étude extensive des taux d'exhumation à travers le monde, [Herman 13] concluent que l'augmentation globale de l'érosion des chaînes de montagnes serait liée aux glaciations du Plio-Pléistocène, démontrant que les glaciers seraient le principal agent de dénudation des orogènes à long terme. Cependant, l'asymétrie observée dans la topographie des Andes patagoniennes semble indiquer que l'érosion subie au cours du Cénozoïque a été contrôlée par le contraste d'extension des glaciers entre le Nord et le Sud : largement étendus au Sud, ils auraient protégé de l'érosion, alors que plus localisés dans le Nord, ils auraient participé à l'érosion de l'orogène [Thomson 10]. Ces résultats ont récemment été précisés par [Koppes 15] qui montrent que l'extension glaciaire, les vitesses de fluage et les flux de glaces ne jouent qu'un rôle secondaire dans l'érosion glaciaire des Andes. Ce sont le climat et les régimes thermiques des glaciers qui contrôleraient l'érosion glaciaire : à semelles liquides, les glaciers sont très érosifs dans le Nord et à semelles englacées, ils protègent de l'érosion dans le Sud. Ces résultats, bien que variables, semblent néanmoins renforcer l'hypothèse d'un rôle majeur des glaciers dans la dénudation des orogènes.

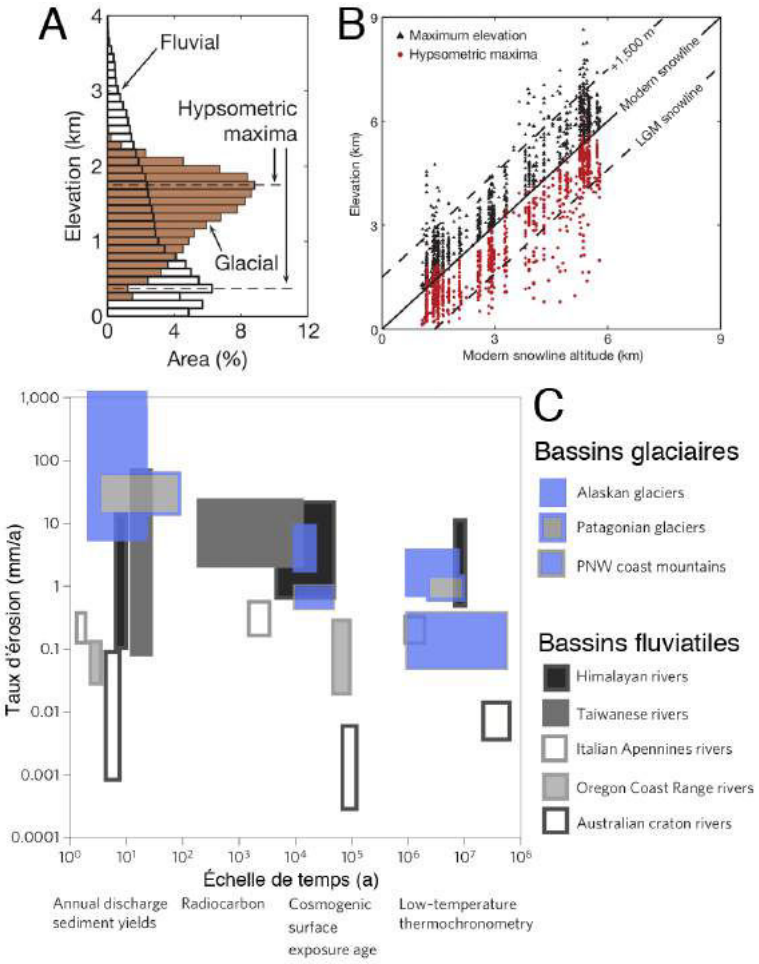

FIGURE 1.1.2 – Influence de l'érosion glaciaire sur la dénudation globale. L'extension glaciaire et l'érosion glaciaire contrôlent l'élévation des chaînes de montagnes (A.) par effet *buzz-saw* (B.) qui, parce que localisée sur les sommets, limitent les altitudes maximales lors des variations d'altitude des *ELA* (Ligne d'Équilibre des Neiges Éternelles) [Egholm 09]. C. Comparaison de taux d'érosion glaciaires et fluviatiles sur plusieurs échelles de temps et plusieurs endroits du monde [Koppes 09]. L'érosion glaciaire ne semble pas plus efficace que l'érosion fluviale à long-terme.

Les glaciers ne semblent cependant pas avoir la faveur générale dans le contrôle de l'érosion des chaînes de montagnes car ils ne seraient pas plus efficaces que l'incision fluviatile à long terme [Koppes 09] (cf. figure 1.1.2 C).

Au contraire, les températures élevées favorisent la dénudation [Portenga 11] et en particulier l'altération chimique à travers le développement des sols. Les influences du climat et de la température ont été approchées par l'étude des rivières et des éléments dissous. En étudiant des bassins versants aux conditions climatiques variées, [White 95] démontrent que les flux de Na et de SiO_2 sont dépendants de la température alors qu'elle ne semble avoir qu'un effet mineur sur les flux de K et nul sur les flux de Ca et Mg [White 99]. Cette observation a aussi clairement été démontrée par la corrélation des flux de SiO_2 et cations issus des silicates aux températures moyennes de petits bassins versants en plusieurs endroits du monde [West 05], bien que ces auteurs voient une nette diminution de cette influence aux plus fortes températures. Observant une franche diminution de l'altération chimique avec l'altitude en milieux montagneux, [Riebe 04b] ont aussi démontré l'importance de premier ordre des températures sur l'altération chimique. À plus grande échelle, les températures élevées ne semblent pas forcément se traduire par des taux d'altération chimique élevés. Si la relation est conservée pour de nombreux fleuves, elle ne semble plus valable pour un nombre important de très grands fleuves [Gaillardet 99b] (cf. figure 1.1.3).

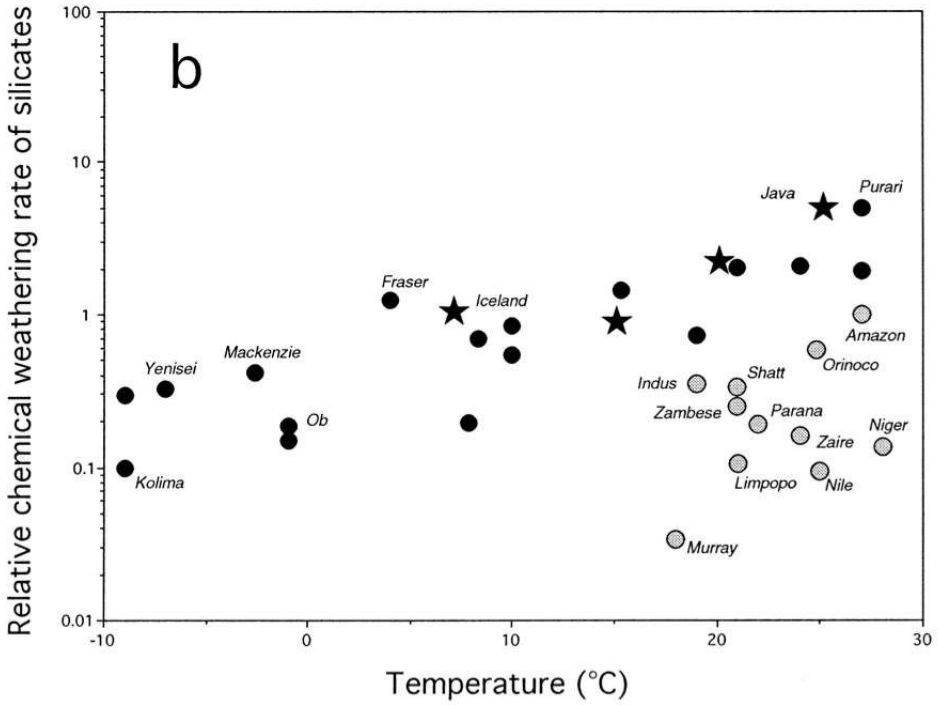

FIGURE 1.1.3 – Altération des silicates normalisée à l'Amazone en fonction de la température moyenne du bassin versant. D'après [Gaillardet 99b].
La relation de l'altération des silicates à la température n'est pas valable pour de nombreux grands fleuves (en gris dans le graphique).

L'altération chimique ne dérive cependant pas totalement de l'altération « superficielle » et/ou du développement des sols. L'altération chimique se produit aussi en profondeur dans les aquifères. Dans ces réservoirs, l'altération chimique est grandement modifiée par rapport à la surface parce que les temps de réaction sont beaucoup plus longs et que les rapports Eau : Roche sont moins importants et plus favorables aux saturations et à la cristallisations de minéraux secondaires (e.g. [Garrels 67, Crerar 81, Meredith 13]).

Dans le bassin versant de la Liwu à Taïwan, où les pentes sont importantes et les précipitations associées aux typhons sont très intenses, [Calmels 11] suggèrent que les charges dissoutes des rivières dérivent de 3 composants : le flux dérivé des aquifères qui représente 16 ± 3% du flux total, le flux d'écoulement superficiel « rapide » qui totalise 63 ± 5% et le flux d'écoulement superficiel « lent » plus modeste avec 21 ± 5%. Bien que modeste au niveau de l'érosion chimique totale, ce composant souterrain (dérivés des aquifères) de l'érosion chimique représente 1/3 de l'érosion chimique totale des silicates. Au

Népal en particulier, les études de [Tipper 06a, Tipper 06b, Tipper 06c] montrent aussi que l'altération souterraine favorise l'altération des silicates : les compositions isotopiques du Ca et du Mg témoignent des processus de sub-surface qui fractionnent ces éléments dans des réservoirs spécifiques [Tipper 06a]. Enfin, au Népal, les flux d'érosion chimique superficielle calculés dans les rivières doivent aussi être corrigés des flux hydrothermaux associés au métamorphisme qui peuvent représenter jusqu'à 35% de l'alkalinité des rivières [Evans 01, Evans 04].

L'influence des températures moyennes sur l'altération chimique semble toutefois être confirmée par la modification des signaux d'altération générée par les changements climatiques, et ceci, à différentes échelles de temps. À très court terme, grâce à l'enregistrement de 43 années consécutives, l'augmentation significative de l'altération détectée dans des bassins islandais a été attribuée à l'élévation des températures moyennes de 3 à 5°C au cours des dernières décennies [Gislason 09]. Dans le bassin du Ganges, l'intensification continue de l'altération chimique des sédiments dans la plaine a été détectée dans les dépôts marins du Cône du Bengale *(Bengal fan),* et attribuée au réchauffement climatique récent de l'Holocène [Lupker 13]. À plus long-terme, par analyse des cortèges argileux des séries Siwaliks, [Huyghe 05] montrent que les régimes d'altération dans la plaine du Gange étaient plus importants lors des périodes plus « chaudes » du Cénozoïque.

Les plaines continentales actuelles, par leurs faibles élévations, leurs températures plus élevées que les chaînes de montagnes, et leur très grandes capacités de stockage des sédiments pendant de longues périodes de temps, semblent constituer les réacteurs privilégiés de l'altération chimique à la surface du globe [West 02, Lupker 12b, Bouchez 12, Dellinger 14]. La proportion de sédiment qui va y être altéré chimiquement est variable. Par l'analyse des isotopes du Lithium dans les bassins de l'Amazone, de la Mackenzie et du Gange-Brahmapoutre, [Dellinger 14] montrent que seulement 35 % des sédiments exportés par ces bassins relèvent d'une altération récente, le reste étant dérivé du cannibalisme de sédiments déjà altérés, par exemple de roches sédimentaires.

D'autres environnements comme par exemple les plaines côtières et les estuaires, dont les températures sont importantes et régulières, ont récemment été proposés comme « réacteurs » alternatifs de l'altération des silicates [Gislason 06, Oelkers 11, Oelkers 12, Jones 12, Pearce 13, Jones 14, Morin 15] pour tenter de comprendre le déséquilibre actuel observé dans le calcul des bilans entre les flux élémentaires arrivant aux océans (ri-

vières, hydrothermalisme aux dorsales, atmosphériques etc.) et la composition chimique des océans [Vance 09, Tréguer 13]. Il n'en reste pas moins qu'à l'échelle du globe et à très long terme, l'augmentation des températures implique un contrôle sur la production des sols et des régimes d'altération chimique accrus.

Les précipitations

Les précipitations constituent l'autre paramètre principal du climat et sont un facteur de contrôle incontournable de l'érosion. Même s'il parait trivial de le rappeler, les eaux météoriques vont : participer à l'érosion superficielle en ruisselant à la surface de la terre ; servir de solvant aux molécules et acides (CO_2, acides humiques) susceptibles d'altérer les minéraux à la surface ou en profondeur ; alimenter la végétation ; provoquer le déclenchement de mouvements gravitaires (glissements de terrains etc.) ; ou encore alimenter les glaciers et le cours des rivières qui incisent les roches.

Le contrôle direct de l'érosion des chaînes de montagnes par les précipitations semble nettement s'exprimer dans les Cascades Mountains à l'Ouest des USA où [Reiners 03] ont mesuré un fort couplage entre les précipitations orographiques contrastées d'Est en Ouest, et des variations des taux d'exhumation (érosion) de près d'un ordre de grandeur. Comme précédemment évoquée (§1.1.1.1), la dissymétrie de certains orogènes tels que les St Elias en Alaska, les Alpes européennes, les Andes et les Alpes Néo-Zélandaises semble résulter de ce contrôle [Whipple 09]. Dans les Andes comme dans les Alpes néo-zélandaises, les flux d'Ouest apportant les précipitations provoquent d'intenses taux d'érosion sur les flancs occidentaux de ces orogènes en favorisant l'érosion glaciaire [Thomson 10, Herman 15] ou les glissements de terrain [Hovius 97]. À Taïwan, les précipitations intenses dues aux typhons sont le facteur déclencheur des glissements de terrain permettant d'expliquer les taux d'érosion très intenses de l'île [Hovius 00, Dadson 03, Hilton 08]. Le rôle des glissements de terrain dans l'érosion des chaînes de montagnes semble majeur [Shroder 98b, Shroder 98a] et leur déclenchement contrôlé par les précipitations [Iverson 00, Gabet 04a, Gallo 14a, Gallo 14b]. En Himalaya, les mouvements de pentes déclenchés par les précipitations de mousson [Bookhagen 10] sont décrits comme étant le processus dominant dans le bilan de l'érosion de la chaîne [Andermann 12b]. Des résultats de modélisation récents concluent même que l'alternance entre incision fluviatile et érosion par les glissements seraient en mesure de contrôler la durée de vie des orogènes

[Egholm 13]. Ce contrôle de l'érosion par les précipitations reste cependant encore débattu car la relation semble par endroit découplée [Burbank 03, Finnegan 08].

L'effet des précipitations sur l'altération et l'érosion chimique est toutefois plus clairement démontré, et ce, à de nombreuses échelles. Les flux de cations et de silice semblent être linéairement corrélés aux précipitations ou à l'écoulement spécifique dans de nombreux petits bassins à travers le monde [Bluth 94, Stewart 01, West 05] et cette relation reste valable à l'échelle de grands bassins versants [Gaillardet 99b]. [White 95] proposent même que certains flux (SiO_2, K) soient modélisés par une relation linéaire aux précipitations et par une relation de type Arrhénius à la température.

1.1.2.2 Influence de l'érosion sur le climat

La dénudation exerce en retour un contrôle important sur le climat global de la Terre à l'échelle des temps géologiques par piégeage du CO_2 atmosphérique [Berner 83]. L'acidification des eaux terrestres due au CO_2 atmosphérique, à la dissolution de sulfures, à la respiration racinaire ou encore aux acides humiques, provoque l'altération chimique et la dissolution des minéraux. Les roches libèrent sous formes dissoutes des éléments tels que Na^+, K^+, Ca^{2+}, Mg^{2+}, $Si(OH)^{4-}$, HCO_3^-, SO_4^{2-}, PO_5^{2-}, NO_3^{2-} etc. Parmi ces éléments, le Ca et le Mg dissous alimentent les micro-organismes composant la faune planctonique des océans qui construisent leurs squelettes ou « tests » en précipitant du carbonate selon la réaction ci-dessous, piégeant par la même occasion le CO_2 atmosphérique :

$$(Ca, Mg)^{2+} + 2HCO_3^- \rightarrow (Ca, Mg)CO_3 + CO_2 + H_2O$$

Ce net bilan de précipitation du CO_2 dans les calcaires et dolomites marins (1 mole de CO_2 séquestrée pour une mole de Ca^{2+} ou Mg^{2+} arrivant aux Océans) n'est valable que pour l'altération de roches silicatées. L'altération des roches carbonatées, en libérant du CO_2 lors de leur dissolution ne participe pas à long terme à cet effet :

$$(Ca, Mg)CO_3 + 2H_3O^+ \rightarrow (Ca, Mg)^{2+} + CO_2 + 3H_2O$$

Seul les flux de Ca et Mg dérivés des roches silicatées conduisent à une capture nette du CO_2 en libérant Ca ou Mg sans émettre de CO_2 comme le montre par exemple l'hydrolyse totale de l'anorthite :

$$CaAl_2Si_2O_8 + 8H^+ \rightarrow Ca^{2+} + 2Al^{3+} + 2SiO_2(aq) + 4H_2O$$

La rétroaction de la tectonique et de l'érosion sur le climat a été très tôt abordée en proposant que les périodes de refroidissement qu'a connu le Cénozoïque résulteraient de la surrection des chaînes de montagnes [Chamberlin 99].

Cette hypothèse a été réintroduite par [Raymo 88, Raymo 92]. Ces auteurs ont proposé que la surrection de l'Himalaya aux alentours de 40-50 Ma [Patriat 84] aurait été responsable du refroidissement global enregistré entre l'Éocène et l'Oligocène. Leur hypothèse reposait d'une part sur les enregistrements des compositions isotopiques ^{13}C et ^{18}O marins qui montrent un refroidissement global au cours du Cénozoïque, et d'autre part sur la forte augmentation de la composition isotopique en $^{87}Sr/^{86}Sr$ des océans à partir de 40 Ma qui aurait dérivé de l'accroissement des flux d'altération continentale silicatée (plus radiogéniques) issus de la surrection de reliefs, notamment de l'Himalaya. L'accroissement de l'altération aurait ainsi conduit à la diminution du taux de CO_2 atmosphérique et induit le refroidissement par diminution de l'effet de serre.

Or de nombreuses études ont démontré par la suite que les flux de Sr dérivés de l'altération de l'Himalaya sont très radiogéniques [Edmond 92, Derry 96, Quade 97, Blum 98, Galy 99c, Bickle 01] découplant le signal isotopique de Sr de l'altération silicatée et concluant que l'enregistrement du Sr océanique renseignerait plus sur l'exhumation des unités Himalayennes que l'augmentation réelle de l'altération.

L'autre puits de carbone associé à l'érosion est issu de l'association des sédiments avec la matière organique, l'enfouissement du carbone organique C_{org} dans les structures sédimentaires côtières et océaniques pouvant se révéler être un puits majeur de carbone. [Broecker 70, Shackleton 85, Hedges 95, Hayes 99, Aller 04, Aller 08]. L'érosion de l'Himalaya en particulier, s'est révélée être un puissant moteur de cette capture à long-terme dépassant largement l'altération des silicates [France-Lanord 97, Galy 07c].

Le débat a été récemment réouvert par l'utilisation de nouveaux traceurs et notamment les isotopes du Li. L'augmentation du rapport $^{7}Li/^{6}Li$ des océans observée au cours du Cénozoïque a conduit [Misra 12, Froelich 14] à proposer le même type d'interprétation. Selon ces auteurs, le refroidissement du Cénozoïque dériverait de l'augmentation des vitesses d'altération chimique provoquée par l'exposition de roches « fraiches » à la surface des continents due la surrection des chaînes de montagnes. Cette accélération étant alors à l'origine d'une capture du CO_2 atmosphérique et du refroidissement global. Ce signal a

récemment été réinterprété en attribuant cette variation à la diminution du stockage du Li dans les profils de sols (argiles) alors que le climat de la Terre se refroidissait, laissant le flux d'altération apporté par les rivières et riche en ^{7}Li provoquer l'augmentation de la composition δ^7Li des océans [Vigier 15].

1.1.3 Couplages entre érosion physique et érosion chimique

Le paradigme selon lequel une érosion physique accrue induit une augmentation de l'érosion chimique repose sur le fait que l'érosion physique débarrasse les surfaces continentales de la chape des profils de sols trop développés qui la recouvre et la protège, amène des minéraux frais à la surface où ils ne sont que métastables, provoque l'augmentation des surfaces réactives totales en fragmentant les roches, et apporte des masses sans cesse renouvelées de minéraux « frais » susceptibles d'être altérés dans les grands « réacteurs chimiques » que sont les plaines ou les environnements côtiers.

L'étude de nombreux bassins versants à travers le monde semblent démontrer que l'érosion chimique procède d'une relation à l'érosion physique de type puissance 2/3 [Millot 02] (cf. figure 1.1.4), d'une relation affine [Riebe 04a] alors que d'autres ne relaient cette relation qu'à un second ordre comparé à d'autres facteurs [White 95]. Ce type de relation reste délicat tant l'influence des autres facteurs est difficile à déconvoluer.

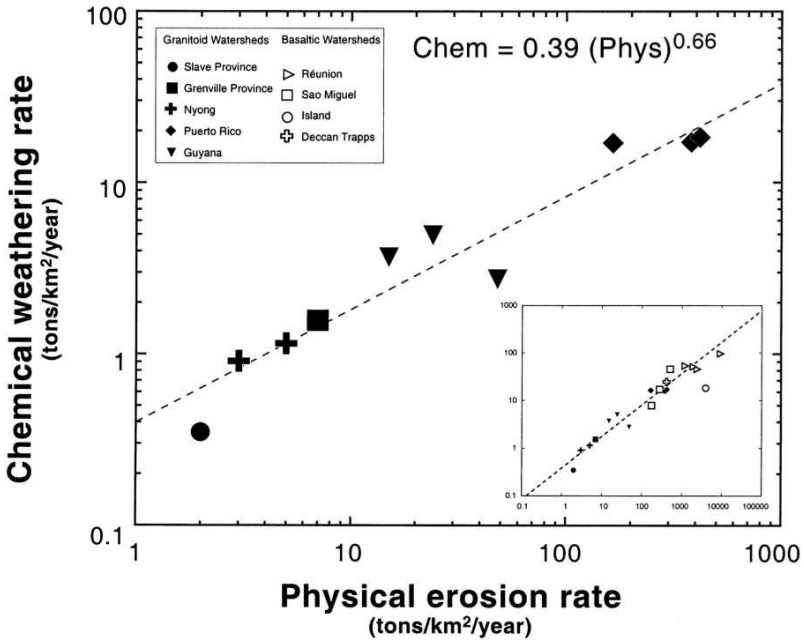

FIGURE 1.1.4 – Relation de puissance 2/3 entre érosion chimique et érosion physique. D'après [Millot 02].

Dans les contextes érosifs comme les chaînes de montagnes, les liens et couplages entre altération et érosion physique semblent cependant procéder de relations non-linéaires distinguant deux cas : le cas *transport-limited* et le cas *kinetically-limited* [Riebe 04a, West 05, Gabet 07, Gabet 09, Hilley 10] :

— le cas *transport-limited* correspond aux systèmes où la capacité d'érosion et de transport est inférieure aux vitesses de production des sols dans ces environnements. Il en résulte un épaississement du *regolith*, des profils de sols qui vont protéger la roche sous-jacente et limiter l'érosion chimique (e.g. [Dixon 09a, Dixon 09b]).

— le cas *kinetically-limited* : les taux d'érosion dépassent très largement la capacité de production de sols, débarrassant le paysage de sa couverture de sol, ne laissant plus la possibilité à l'altération chimique d'avoir lieu. Il en résulte des paysages ou seul le substrat rocheux affleure [Heimsath 12].

Les seuils limites de taux de production de sols qui étaient jusqu'alors proposés autour de 1 à 1.5 mm/a [Gabet 09, Heimsath 12] viennent d'être repoussés [Larsen 14b], ce qui ouvre le champ à de nouvelles perspectives concernant l'altération chimique des milieux montagneux. [Larsen 14b] démontrent par cette découverte deux choses cruciales : que les

taux de production des sols ~2.5 mm/a dans le Sud des Alpes néo-zélandaises sont bien supérieurs aux limites qui étaient jusqu'alors proposées, et que le taux de production de sol est lié par une relation linéaire aux taux de dénudation (cf. 1.1.5).

Ces résultats relancent complètement l'importance de l'étude de l'altération dans les milieux montagneux. Ils suggèrent de nouvelles perspectives quant aux temps de réponse et d'adaptation des chaînes de montagnes aux changements climatiques de fréquences élevés comme ceux observés depuis le Pléistocène [Zachos 01]. De plus, cela replace les chaînes de montagnes en concurrence avec les plaines considérées comme *loci* privilégié de l'altération.

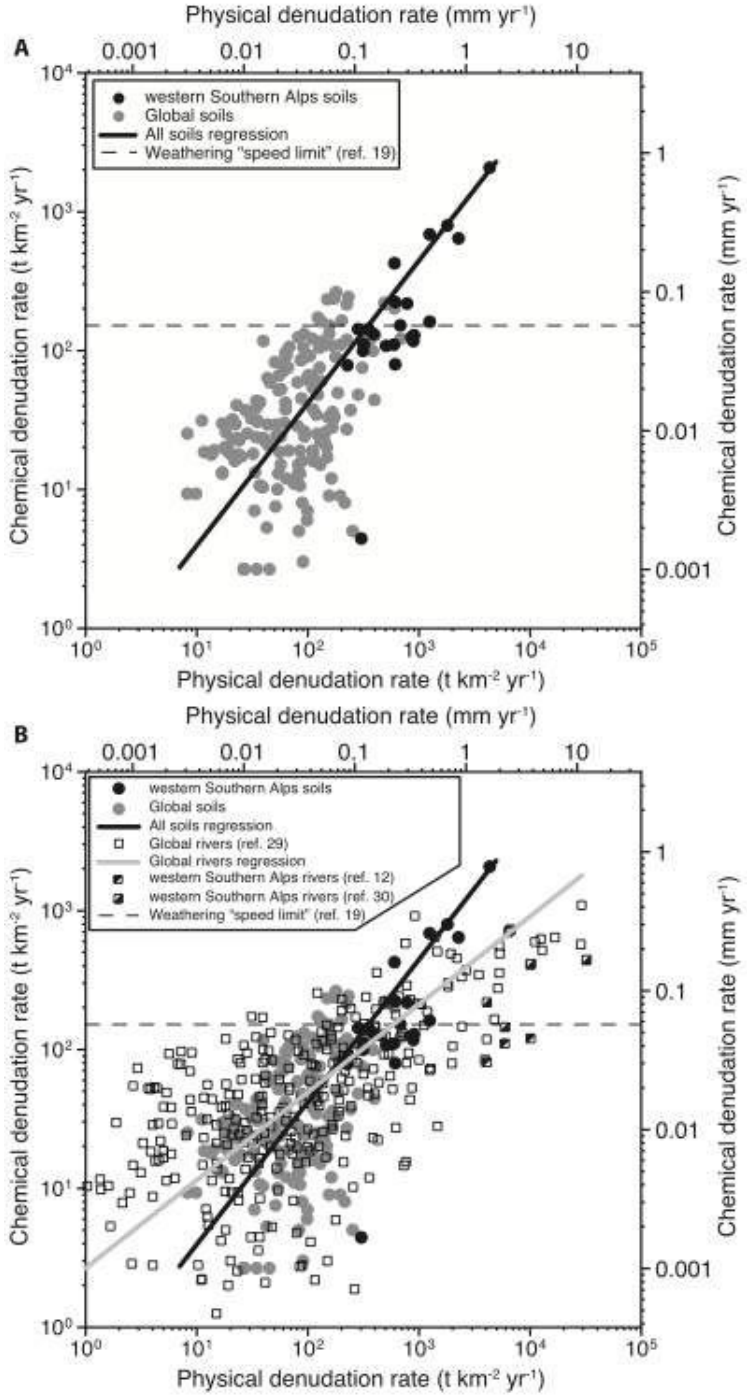

FIGURE 1.1.5 – Relation entre l'érosion physique et taux de productions de sols in-situ ainsi que l'érosion chimique dérivée des rivières. D'après [Larsen 14b]

En haut, la relation linéaire entre taux de production des sols et la dénudation (en noir, les taux exceptionnels mesurés dans les Alpes Néo-Zélandaises). En bas, comparaison avec les rivières du globe, il est à noter que les rivières Néo-Zélandaises montrent des taux de dénudation comparables aux sols.

1.2 Problématique et cadre de l'étude.

Ce travail de thèse s'est intégré dans le cadre du projet ANR Blanche « Caliméro » qui porte sur l'étude des interactions entre l'érosion et le climat.

L'orogène himalayen présente la particularité d'être l'une des zones de convergence continentale des plus élevées au monde et de subir une activité sismique très importante (comme en ont témoigné les séismes du printemps 2015). De surcroît, elle se situe à une latitude qui lui confère un climat tropical humide dont le fort contraste saisonnier entre hiver et été est marqué par le phénomène de mousson. Elle représente ainsi l'un des cadres privilégiés de l'étude des interactions entre tectonique, climat et érosion.

Le sujet de thèse s'articule autour de l'analyse des sédiments de rivières et des processus d'érosion qui affectent les pentes du Népal central, en particulier dans le bassin de la Narayani-Gandak. Héritant d'une collection importante d'échantillons de roches sources et de sédiments de rivières himalayennes, ce travail s'est principalement axé sur la recherche dans les sédiments de rivières de signatures « visibles » relevant des agents d'érosion physique que sont les glissements de terrain et les glaciers, et des agents d'altération chimique que sont les sols.

Dans le cadre de cette problématique, plusieurs questions se posent :

— Peut-on tracer les processus majeurs de l'érosion d'une chaîne de montagnes par l'analyse de la composition géochimique des sédiments des rivières actuelles ? Peut-on les quantifier ? Quels en sont les traceurs pertinents ?

— Si l'on s'intéresse aux plus petites « cellules » de ces systèmes : les petits bassins versants de la chaîne, quels bilans peut-on établir en terme d'érosion physique et érosion chimique ?

— Plus largement, quels sont les processus qui dominent les bilans d'érosion actuelle de la chaîne du Népal central ? De quelle dynamique procèdent-ils, notamment en réponse au phénomène climatique et cyclique annuel que constitue la mousson ?

— Par analogie avec les sédiments des rivières actuelles, que nous apprennent les archives sédimentaires de la fin du Quaternaire sur l'évolution de l'érosion de la chaîne lors du passage de l'époque glaciaire de la fin du Pléistocène à l'interglaciaire actuel ? Quelle a été la réponse de la chaîne en terme d'altération ou de dénudation à

ce dernier grand changement climatique ?

L'échantillonnage a été dimensionné en ce sens et à différentes échelles : des profils de sols, aux glissements de terrains et aux sédiments glaciaires, des petits bassins versants aux rivières trans-himalayennes jusqu'à l'exutoire du bassin de la Narayani drainant l'ensemble du Népal central. De même, des séries temporelles regroupant une centaine d'échantillons ont été collectées afin de documenter l'évolution du signal sédimentaire sur une mousson, et ce, pour caractériser la dynamique des processus érosifs au cours des cycles saisonniers. Ces échantillonnages ont été réalisés grâce à la collaboration de Ananta P. Gajurel de l'Université Tribhuvan à Kathmandou au Népal. Enfin, par la réalisation de forages dans la plaine de la Narayani-Gandak, nos résultats sur la chaîne actuelle devaient permettre la lecture des archives sédimentaires du bassin d'avant-pays. Ces forages ont été réalisés avec la collaboration du Pr Rajiv Sinha de l'IIT Kanpur en Inde.

Tourné vers l'analyse des sédiments solides, ce travail s'est appuyé sur des méthodes mises en place au laboratoire « isotopes stables » du CRPG pour la mesure des signatures d'altération des sédiments : la concentration en hydroxiles d'hydratation des silicates et leurs compositions isotopiques en hydrogène. Cette méthode avait précédemment été utilisée dans l'évaluation de l'altération actuelle et passée dans la plaine du Gange [Lupker 12b, Lupker 13]. L'objectif était de tracer les provenances glaciaires. On sait qu'altérés par les précipitations très négatives d'altitude (distillation de Rayleigh provoqué par l'effet orographique), les sédiments glaciaires présentent des compositions isotopiques en oxygène et hydrogène plus négatives en altitude [Garzione 00, Garzione 08]. De plus, il convenait aussi d'adapter la méthode au traçage des sols dont l'hydratation est très marquée, afin d'en évaluer les bilan érosifs actuels à l'échelle du Népal. Une méthode de prétraitement a été montée et calibrée avec succès pour effectuer ces analyses.

Dans le souci de tracer les provenances des sédiments actuels et anciens, ce travail a aussi bénéficié de nombreux outils analytiques comme : la mesure des concentrations et compositions isotopiques des carbonates ou la mesure de matière organique totale disponibles au laboratoire des isotopes stables du CRPG. Ces analyses ont été réalisées grâce à l'aide précieuse de Caroline Guillemette puis de Thomas Rigaudier.

De même, pour le traçage des sources de sédiments, j'ai pu profité des infrastructures d'analyse isotopique du Sr et Nd du CRPG, grâce au concours de Laurie Reisberg,

Christiane Parmentier de Catherine Zimmerman. Concernant les éléments majeurs, la plateforme du SARM au CRPG a fourni la grande majorité des analyses qui ont servi à ce travail.

Les mesures par [^{10}Be] cosmogénique des taux d'érosion passés dans les forages ont été réalisés à l'unité de traitement des isotopes cosmogéniques du CRPG, et les analyses ont été effectuées au CEREGE par l'équipe ASTER à Aix-en-Provence.

Afin d'établir la chronostratigraphie des forages, nous avons bénéficié de la collaboration avec Valier Galy du WHOI aux États-Unis pour les datations ^{14}C des fractions de C_{org} extraites par « *dirt-burner* », et de la collaboration avec Pierre Valla et Fréderic Herman de l'Université de Lausanne en Suisse pour les datations OSL *single-grain* .

II

Chapitre 2

Objets

2.1 L'orogène Himalayen

L'Himalaya est la plus grande et la plus haute chaîne de montagnes sur Terre. Elle forme un arc d'axe O-NO/E-SE qui s'étire sur près de 2500 km de long depuis le Nanga Parbat au Pakistan à l'ouest, au Namche Barwa à l'est au Tibet et atteint parfois 400 km de large. Elle culmine à 8810 m ASL avec le Mont Everest et borde le Sud du plateau Tibétain d'une altitude moyenne de 5000 m ASL (au dessus du niveau de la mer) [Fielding 94]. La plaine Indo-Gangétique représente la surface plane la plus vaste au monde avec une superficie de 2.55 Millions de km^2et une altitude comprise entre 0 et 300 m ASL. Elle est constituée des deux bassins versants de L'Indus à l'Est et du Gange à l'Ouest séparés par des reliefs de 300 m ASL appelés « Delhi ridge », qui constituent la limite de partage des eaux.

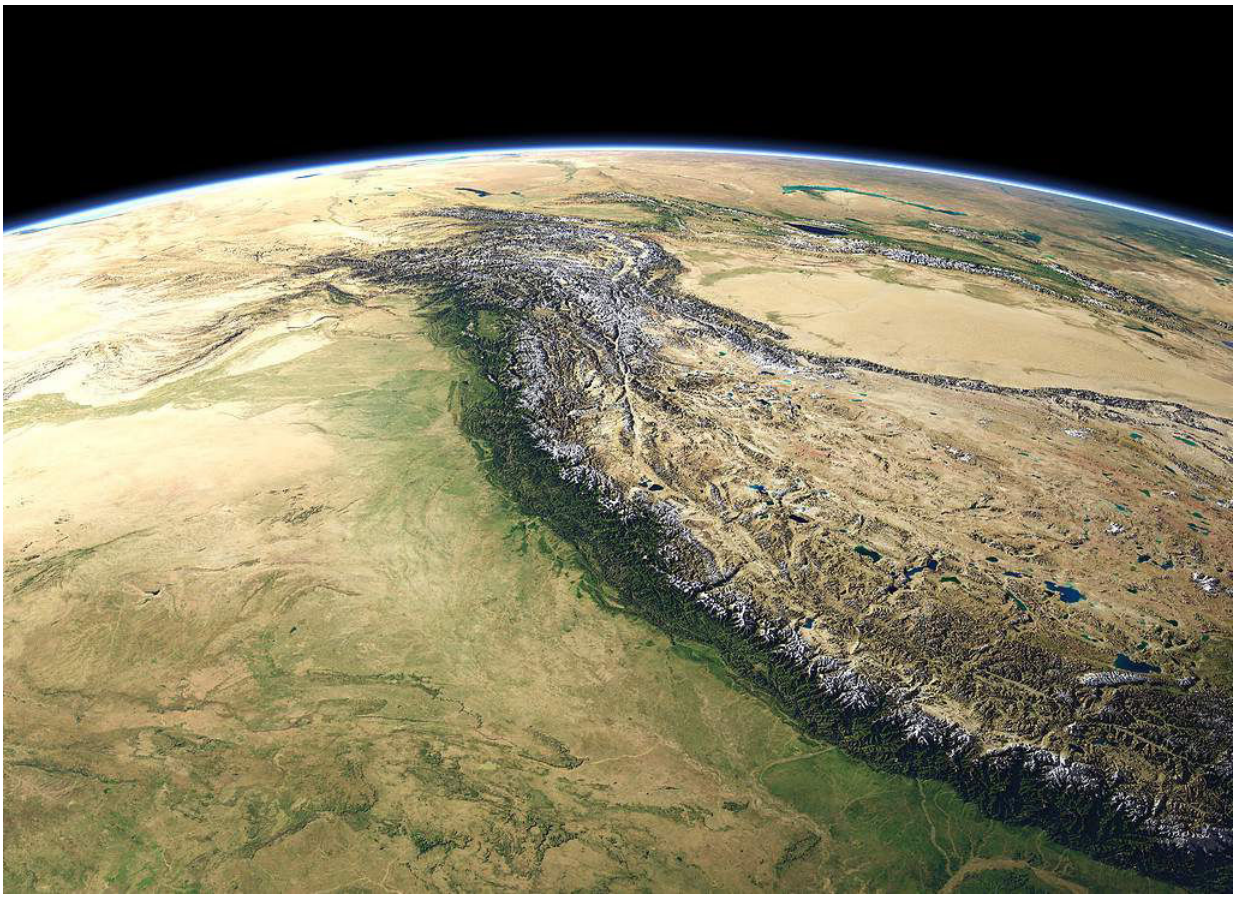

FIGURE 2.1.1 – Chaîne de l'Himalaya et de la plaine du Gange.
La perspective est orientée vers le NW et le Nanga Parbath. À gauche le craton indien, à droite le plateau du Tibet. Le Népal se situe au tiers inférieur des reliefs visibles. (picture Views of the Earth, copyright Christoff Hormann earth.imagico.de)

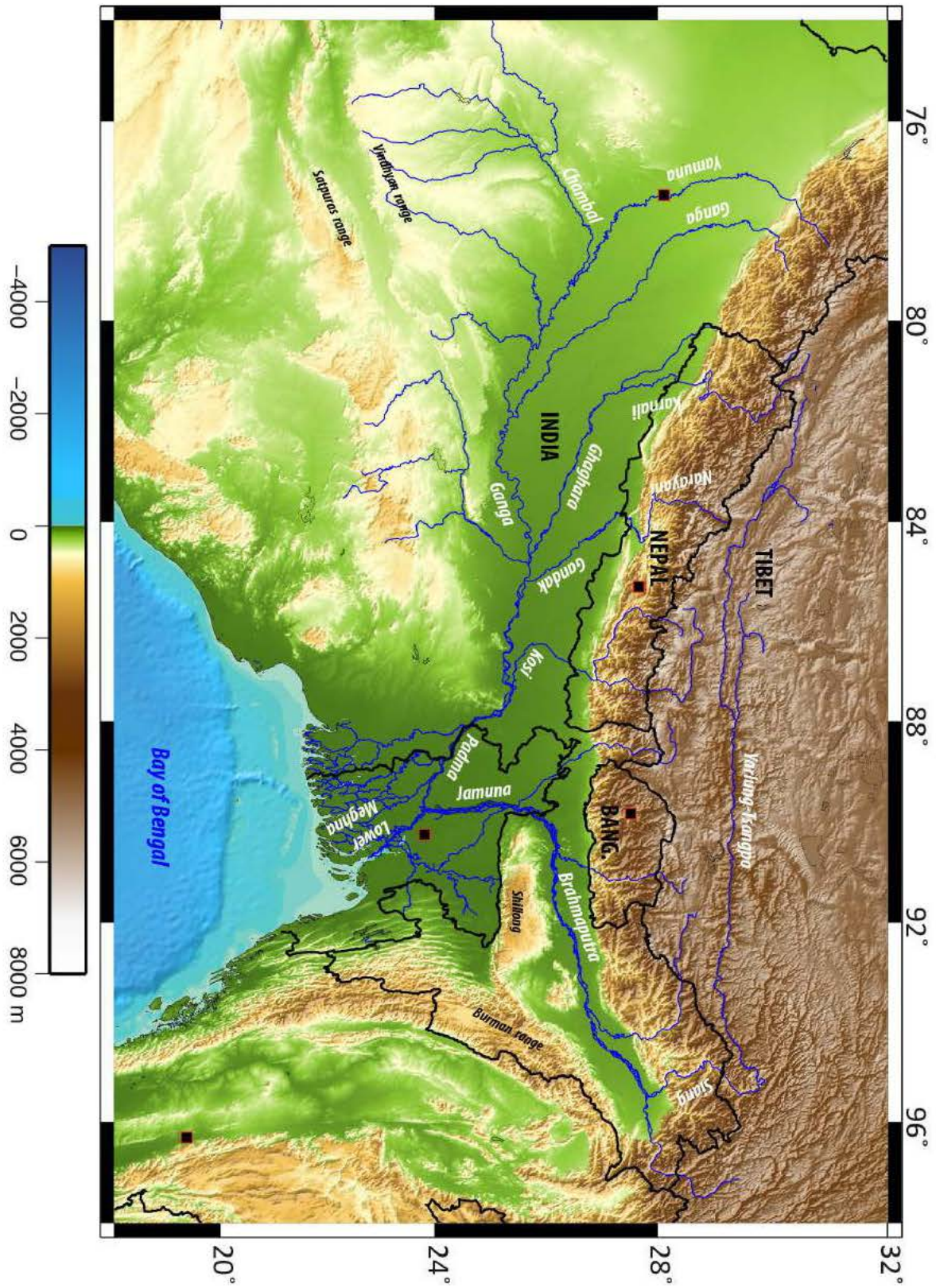

FIGURE 2.1.2 – Topographie et réseau hydrographique du système Gange-Brahmapoutre. *(Données GEOTOP30, USGS, courtesy M.Lupker).*

L'orogène Himalayen est né de la collision entre la plaque Indienne et la plaque Eurasiatique qui a eu lieu il y a 50~55 Ma [Patriat 84]. De nombreux modèles de convergence ont été proposés, et la reconstitution de la paléogéographie fait toujours l'objet de travaux. Cependant, les auteurs s'accordent pour dire que la collision des deux marges débute vraisemblablement vers 52 Ma dans la majeure partie de la zone de collision [Patriat 84, Rowley 96, Najman 01]. La fin à la suture et les derniers événements auraient eu lieu il y a 50 Ma [van Hinsbergen 12].

Ces différences induisent des variations latérales des unités géologiques à l'échelle de l'arc qui demandent de prendre certaines précautions dans l'interprétation des séries sédimentaires, notamment celle des cônes océaniques.

La chaîne himalayenne moderne est une jeune chaîne de montagne active, qui accommode la convergence continue, estimée à 36 à 38 mm de raccourcissement par an, entre les plaques continentales indienne et eurasienne [Wang 01]. L'illustration la plus parlante de la cinématique d'éjection de la croûte depuis l'arc fût proposée par les modèles analogiques d'indentation de l'Eurasie par l'Inde [Tapponnier 82]. Ils expliquent la structure de cet arc et l'éjection vers l'Est de la croûte Sud-asiatique qui a été confirmée par la suite par les mesures de déplacements relatifs par GPS [Larson 99].

2.1.1 Physiographie et géologie.

De cette collision entre les plaques Inde et Eurasie, l'Himalaya hérite sa structure géologique actuelle. Généralement, la structure de l'Himalaya est divisée en quatre zones tectonostratigraphiques (cf. figure 2.1.3). Les unités décrites sont du Nord au Sud : les séries sédimentaires Téthysiennes du Tibet, de degré métamorphique faible qui sont délimitées au sud par le STDZ : « South Tibetan Detachment Zone », les séparant des roches ignées et de haut-degré métamorphiques du Haut Himalaya. Ces dernières recouvrent les métapélites de bas degré métamorphique du Bas Himalaya qui elles-mêmes chevauchent les sédiments Siwaliks et les sédiments quaternaires de la plaine actuelle du Gange.

Du Nord au Sud la chaîne se compose donc successivement de :

1. la zone sud-tibétaine ou thétysienne présente une zone de plateau à plus de 5000 m d'altitude qui s'étend jusqu'aux versants nord des hauts reliefs himalayens. Elle est

constituée par des séries sédimentaires marines épaisses (parfois 10 km d'épaisseur) d'âges Paléocène à Eocène. Ces séries épicontinentales de la marge passive Nord indienne ont enregistré les phases tectoniques de l'orogénèse.

2. le Haut Himalaya (High Himalayan Cristalline ou HHC) est la zone de forts reliefs de la chaîne et des plus hauts sommets dont l'Everest. Essentiellement constitué de la dalle du Tibet, le HHC se compose de métasédiments et orthogneiss d'âges protérozoïques de haut degré métamorphique [Brouand 89, Barbey 96] , dans lesquels ont intrudé les leucogranites du HH (HHL) [Le Fort 75, Deniel 87, Le Fort 87, France-Lanord 88, Barbey 96]. L'épaisseur de la dalle varie entre 5 km au centre Népal et 30 km dans l'Est du Népal [Le Fort 75, Pecher 78]et implique que l'extension en surface de cette formation est très variable selon les bassins versants.
3. le Bas-Himalaya (Lesser Himalaya LH) présente des reliefs plus atténués avec des altitudes comprises entre 200 et 3000 m. Il se compose de nappes autochtones de métasédiments précambriens à paléozoïques, et de klippes et nappes charriées de matériel allochtone de la dalle, des séries thétysiennes ou d'unités latitudinalement intermédiaires. Les nappes inférieures peu métamorphisées pourraient atteindre 10 km d'épaisseur.
4. les Siwaliks, d'altitudes comprises entre 0 et 1000 m représentent les plissements les plus frontaux de la zone de déformation active. Ces plis correspondent à de la tectonique de couverture qui reprennent les sédiments issus de l'érosion de la Haute Chaîne déposés dans la plaine du Ganges. L'épaisseur des séries ainsi plissées atteint entre 4000 et 6000 m [Delcaillau 92].
5. Le bassin d'avant pays de la plaine du Gange se situe entre 0 et 200 m d'altitude. Il résulte du fléchissement de la lithosphère indienne sous le poids des reliefs himalayens et se comporte comme un vaste réceptacle des produits de l'érosion et de l'incision de la Haute Chaîne, où ont sédimenté plusieurs kilomètres de remplissage molassique. Cependant la majorité des produits d'érosion de la chaîne (>80% [Métivier 99b]) ne fait que transiter par le bassin d'avant- chaîne et va se déposer dans le cône du Bengale ou celui de l'Indus pour la partie Ouest de la chaîne. Des contacts tectoniques majeurs, pour la plupart des chevauchements, délimitent les grandes zones définies précédemment. La zone chevauchante la plus septentrionale correspond à la zone de collision initiale entre l'Inde et l'Asie, c'est à dire à la suture

de l'Indus-Tsangpo [Yin 00].

L'orogène himalayen est bordé au sud par les dépôts alluviaux du piémont de la plaine du Teraï qui annoncent la grande plaine du Gange.

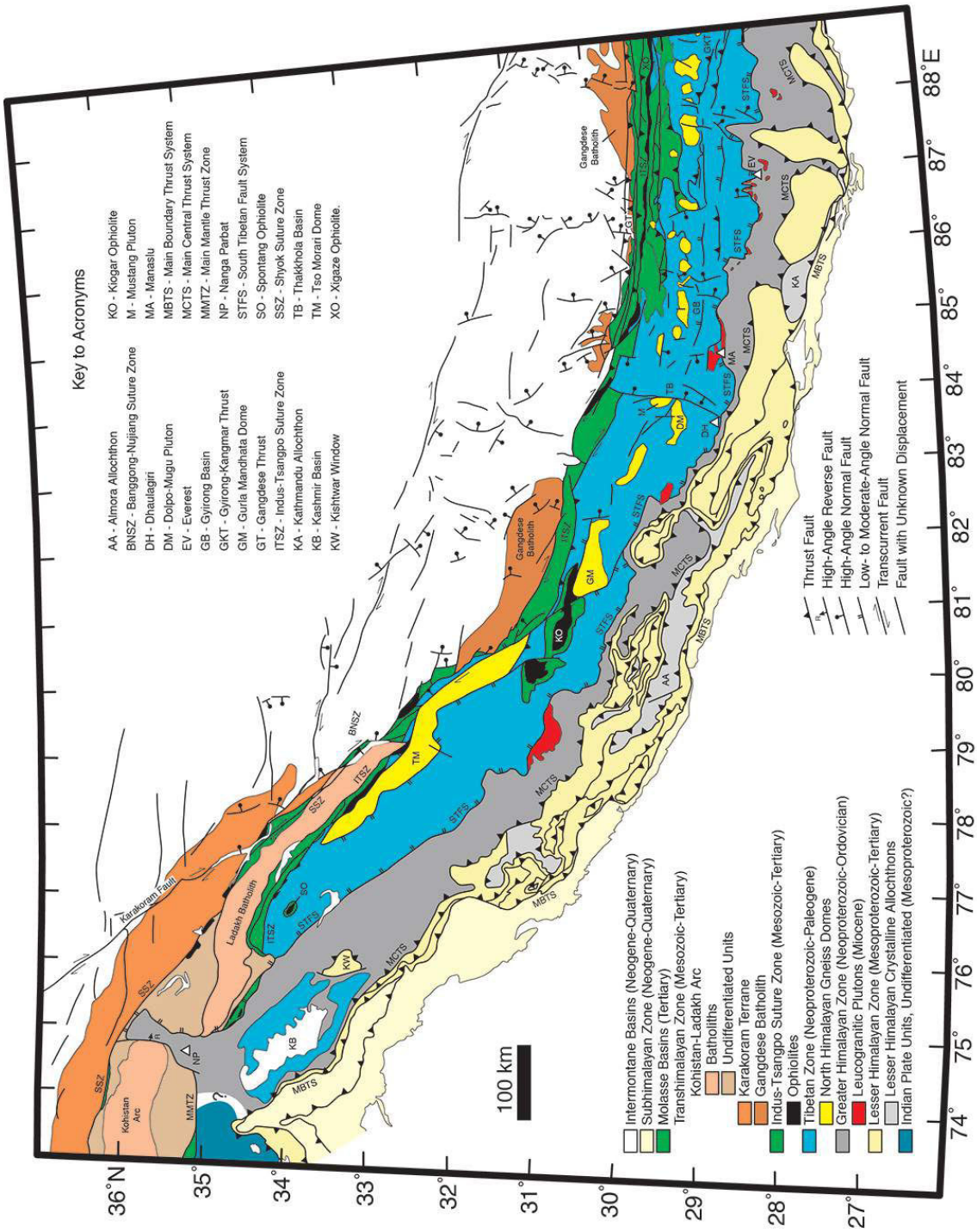

FIGURE 2.1.3 – Synthèse structurale et géologique de la chaîne himalayenne (d'après [Hodges 00])

2.1.2 Tectonique, structure, et sismicité.

Les contraintes tectoniques et le type de collision continentale confèrent à l'Himalaya sa structure actuelle « en rampe », et sont responsables de son élévation et de ses reliefs très importants. Les unités géologiques décrites précédemment sont formées d'écailles qui se chevauchent du Nord vers le Sud le long des rampes formées par les grands accidents tectoniques qui les séparent. Tous ces accidents rejoignent un grand plan de rampe de chevauchement, le MHT (*Main Himalayan Thrust*) à pendage Nord, situé au niveau supérieur de la croûte.

L' activité sismique du Népal central est concentrée sur le MHT (*Main Himalayan Thrust*). Il a été proposé que l'accommodation est essentiellement effectuée par cette zone de détachement unique auxquelles sont connectées les failles de surfaces [Pandey 88, Pandey 95, Sapkota 12]. C'est le long du MHT et au niveau du Haut-Himalaya, qu'ont eu lieu les grands séismes du 25/04/2015 à 06 :11 :25 (UTC) de M7.8, épicentre 36 km à l'E de Khudi, dans le Lamjung et du 12/05/2015 07 :05 :19 (UTC) de M7.3, épicentre 19 km au SE de Kodari qui ont si durement touché le Népal central.

L'activité microsismique himalayenne est principalement localisée au niveau du flanc sud du Haut Himalaya à une profondeur entre 10 et 20 km de profondeur, sur le plan de la rampe crustale du MHT sous les séries HHC [Pandey 95, Bettinelli 08] (cf. figure 2.1.4). La co-localisation de la sismicité et des taux d'*uplift* s'explique par la géométrie de cette rampe et de la croûte supérieure de la chaîne.

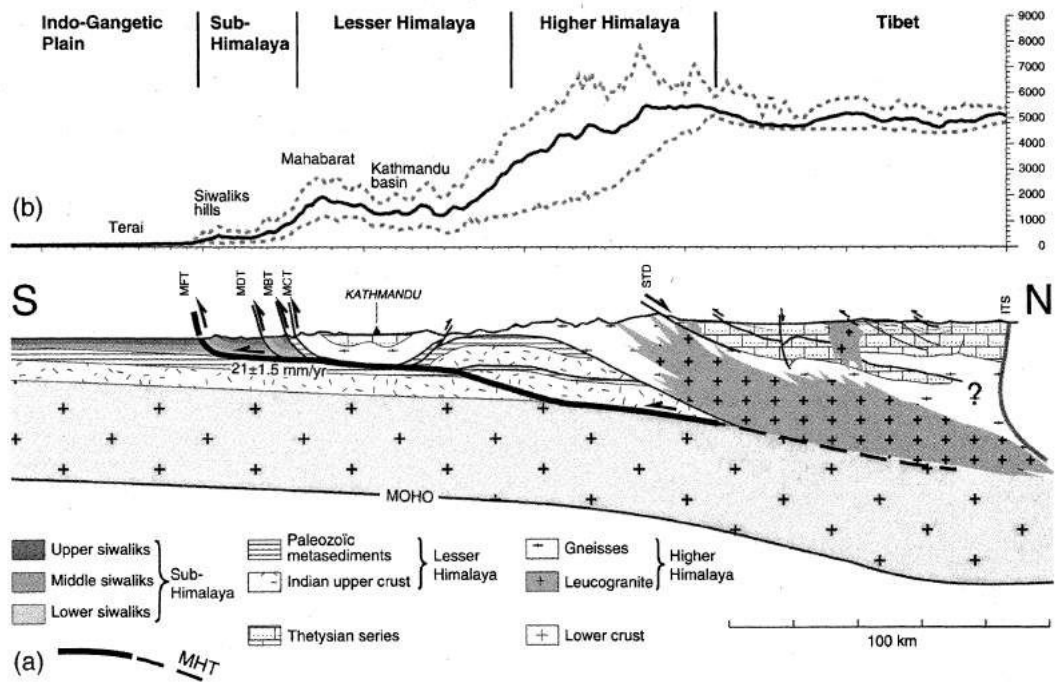

FIGURE 2.1.4 – Topographie et coupe structurale de l'Himalaya. (D'après [Lavé 01])

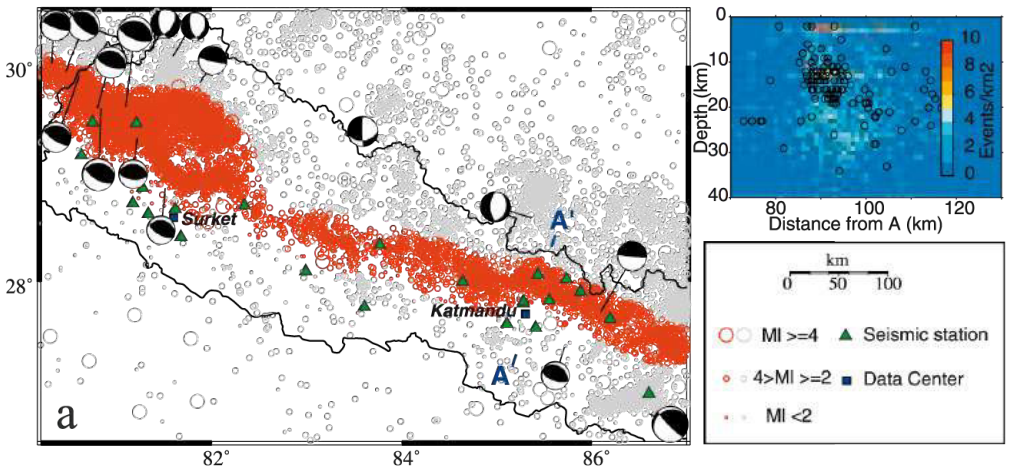

FIGURE 2.1.5 – Projection en surface de la microsismicité enregistrée au Népal entre 1995 et 2000. (D'après [Bollinger 07])

L'activité sismique moderne était restée modérée en Himalaya, aucun événement sis-

mique majeur n'était survenu depuis le séisme de Mw 8.0 - 8.2 de 1934, mais les prévisions d'accumulation des contraintes proposaient une rupture au niveau de la rampe du MHT et en surface au MFT [Pandey 88, Pandey 95].

Ces séismes majeurs ont provoqués de nombreux glissements de terrains dont les cartographies sont en cours [Bilham 15] et ont probablement impacté de manière sensible le réseau hydrographique.

2.1.3 Le climat

Le cadre climatique de la chaîne présente les particularités remarquables de saisonnalité et d'intensité liées à la situation tropicale, aux très forts reliefs de l'Himalaya, et au phénomène annuel cyclique de la mousson. Le climat constitue un forçage principal de l'érosion.

2.1.3.1 la mousson Sud-asiatique

La mousson Sud-asiatique est un phénomène annuel saisonnier cyclique provoqué par la remontée de l'*Inter-Tropical Convergence Zone* (ITCZ) dans l'hémisphère Nord. La remontée de l'ITZC résulte de la différence d'insolation entre les mois d'hivers et d'été générée par l'inclinaison de l'axe terrestre. Cette zone de basses pressions qui entoure la Terre au niveau de l'Equateur est formée par la convergence de masses d'air chaud et humide des tropiques transportées par les alizés et reste circonscrite au niveau des tropiques. La variation d'insolation saisonnière induit un décalage de la cellule de Hadley et provoque un contraste saisonnier très marqué avec des hivers secs, et des étés aux précipitations abondantes. En début de mousson, la ITZC se déplace vers le nord, ce qui entraîne la migration de la circulation d'air océanique chaud et humide en provenance du Golfe du Bengale vers le nord et le nord-ouest (cf. figure 2.1.6).

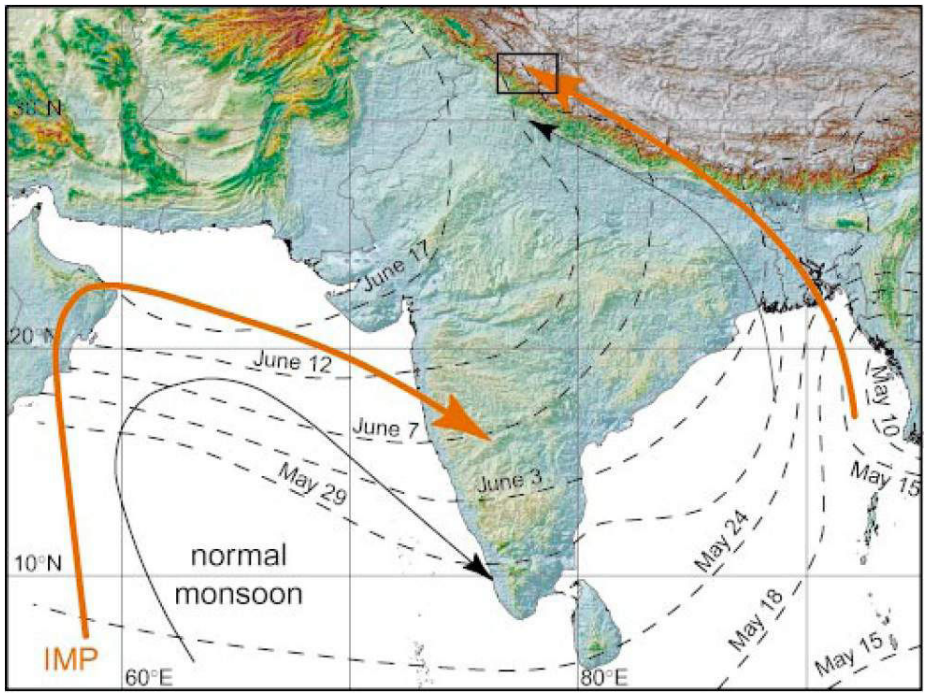

FIGURE 2.1.6 – Dynamique actuelle de la Mousson et ses variations d'intensité. Les circulations atmosphériques dominantes (flèches noires) impliquent des entrées S-SE d'air océaniques au cours de la mousson (progression données par les date indiquées sur les lignes pointillées). Ces circulation sont remplacées par des circulations plus pénétrantes (flèches oranges) lors périodes d'intensité accrue. (d'après [Bookhagen 05b])

Cette masse d'air traverse facilement la plaine du Gange pour aller se heurter aux reliefs de l'Himalaya qui agissent comme une barrière physique, ce qui induit le soulèvement et le refroidissement des masses d'air chargées d'humidité. Cela provoque des précipitations intenses sur la chaîne par effet orographique (cf. § suivant 2.1.3.2).

Le phénomène de mousson a longtemps été expliqué par l'aspiration de l'air océanique chaud et humide généré à la surface de l'Océan indien par la dépression créée au niveau du plateau Tibétain. La dépression provoquée par l'échauffement de l'atmosphère au niveau du plateau tibétain en période printano-estivale, était considérée comme le « moteur » principal de cette circulation atmosphérique. Cependant, les études récentes proposent que l'effet du plateau agissant comme source de chaleur active n'en serait pas le moteur principal, mais plutôt que la barrière topographique de l'Himalaya aurait un rôle de pre-

mier ordre en bloquant les flux d'air froid en provenance du Nord (*jet-stream*). De fait, les remontées d'air chaud et humide en provenance du SE ne seraient plus contrebalancées, et la mousson indienne développerait ainsi une ampleur sans comparaison à l'échelle du globe (cf. [Molnar 10] pour une revue détaillée). Il a été démontré que l'intensité de la mousson pouvait varier fortement d'une année sur l'autre[Shrestha 00, Gadgil 04, Bookhagen 05a] et des périodes de fortes intensités ont été rapportées à la fin du Pléistocène (29–24 ka) et de l'Holocène (10–4 ka) [Bookhagen 05b]. Cela a eu un impact important sur le climat (précipitations) avec comme conséquence d'intenses périodes d'érosion dans les parties Nord et intérieures de la chaîne [Bookhagen 05a, Clift 08]. La compréhension des variations d'intensité de ce phénomène climatique extraordinaire, et de son couplage aux autres phénomènes intenses comme El Nino/La Nina dans le Pacifique [Shrestha 00, Gadgil 04] apportent de nombreuses perspectives pour interpoler l'impact d'un réchauffement climatique dans les décennies à venir. La découverte récente d'une mousson active et marquée à l'Eocene (il y a 55–34 Ma) [Licht 14], période pendant laquelle la teneur en CO_2 atmosphérique était forte et le plateau tibétain peu développé, implique que les forçages climatiques de la mousson (modification des gradients de pressions atmosphériques continents-océans) sont certainement aussi importants que les modèles basés sur la surrection de l'Himalaya-Tibet.

2.1.3.2 Topographie et climat

La répartition des précipitations sur la chaîne himalayenne répond à la topographie et aux flux atmosphériques liés au phénomène de mousson.
L'air se charge d'humidité dans le Golfe du Bengale et est ensuite poussé par les vents de Sud-Est de mousson au contact de la chaîne. Les masses d'air s'élèvent au contact des reliefs et subissent alors une décompression adiabatique dont la conséquence est la chute de la température et la condensation de gouttelettes d'eau par passage sous le point de rosée. Cela provoque les précipitations, ce phénomène est appelé effet orographique. En conséquence, la chaîne himalayenne subit de fortes précipitations en flanc Sud alors que le flanc Nord et le plateau Tibétain ne reçoivent que la faible partie d'air humide ayant réussi à passer les reliefs du Haut Himalaya et, de fait, n'observent que de faibles taux de précipitations. (cf. figure 2.1.7).

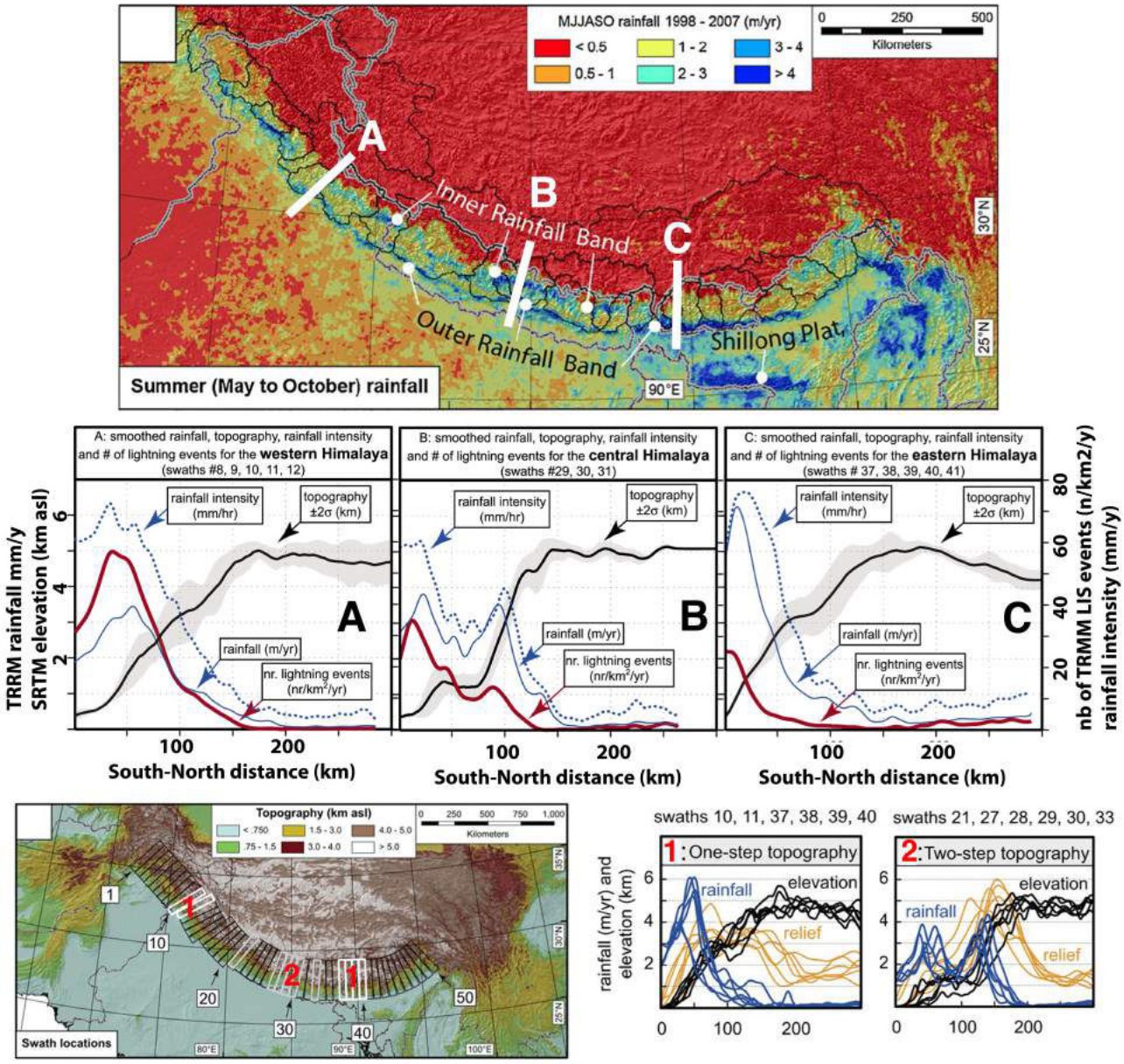

FIGURE 2.1.7 – Effet orographique et répartition des précipitations de mousson liée à la topographie de la chaîne Himalayenne.
En haut, les images issues du *Tropical Rainfall Measuring Mission* satellite TRMM des précipitations en période de mousson montrent le contraste entre faibles précipitations du plateau comparé à la chaîne, et le contraste entre l'Est et l'Ouest de la plaine du Gange. Les transects A, B, et C montrent la répartition Sud-Nord des précipitations et l'effet orographique produit par les reliefs. La répartition bi-modale des précipitations du Népal central est liée aux deux sauts topographiques qu'on y rencontre, et explique que l'intérieur de la chaîne y est plus arrosée qu'à l'Ouest et l'Est de la chaîne. (d'après [Anders 06, Bookhagen 10])

La combinaison du phénomène de mousson et de l'effet orographique provoque un contraste climatique saisonnier et géographique marqué.

Comme en témoignent les données satellites TRMM (cf. figure 2.1.7), la répartition des précipitations est marquée par de forts contrastes Sud - Nord : 1 - la chaîne himalayenne reçoit de fortes précipitations, entre 1 et plus de 4 m/a (Népal central, Bhoutan) lorsque le plateau en reçoit moins de 0.5 m/a ; 2 - L'Est de la plaine du Gange est bien plus arrosée et reçoit en moyenne 2 à 4 m/a de précipitations alors que l'Ouest n'en reçoit que 0.5 à 1 m/a. [Bookhagen 06, Bookhagen 10, Anders 06]

2.1.4 Hydrologie

La topographie de la chaîne divise le réseau hydrographique en deux espaces où les précipitations, par effet orographique, sont très contrastées. Cela a pour conséquence un développement très différent du réseau de drainage entre le flanc Nord et le plateau tibétain d'une part, et le flanc Sud d'autre part (cf. 2.1.8).

Ainsi, les bassins versants du plateau tibétain, à l'exception de ceux de l'Indus et du Tsangpo, sont principalement endoréiques, les rivières finissent leurs courses sur le plateau sans atteindre le réseau de drainage des grands fleuves. Les bassins versants du flanc Nord font partie des réseaux de l'Indus à l'Ouest et du Tsangpo à l'Est. L'hydrologie de l'Himalaya est principalement contrôlée par le phénomène de mousson puisque près de 70 à 80 % des précipitations tombent de juin à septembre [Barros 00, Putkonen 04, Bookhagen 10, Andermann 11] comme en témoignent les hydrographes annuels de la Tista (cf. figure 2.1.9). La contribution des eaux de fonte glaciaire n'atteint au maximum que 25% de la décharge et ceci seulement lors de la saison de pré-mousson. Leurs débits sont ensuite complètement dépassés par les eaux provenant des précipitations de mousson qui composent la quasi totalité des débits spécifiques de Mai à Octobre. De fait, les eaux de fonte glaciaire ne contribuent qu'entre 2 et 10% au total des eaux exportées au cours de l'année [Bookhagen 10, Andermann 12c]. L'effet de l'évapotranspiration (E-T) reste mineur et limité à quelques pour-cents. Enfin, l'infiltration dans les reliefs Himalayen est très important et a été estimé entre 75% et 85% du total des débits [Bookhagen 10, Andermann 12c]. Les eaux souterraines impactent ainsi sensiblement les débits des rivières. Cela s'explique par les fortes perméabilités des réservoirs souterrains, certainement dues aux réseaux de

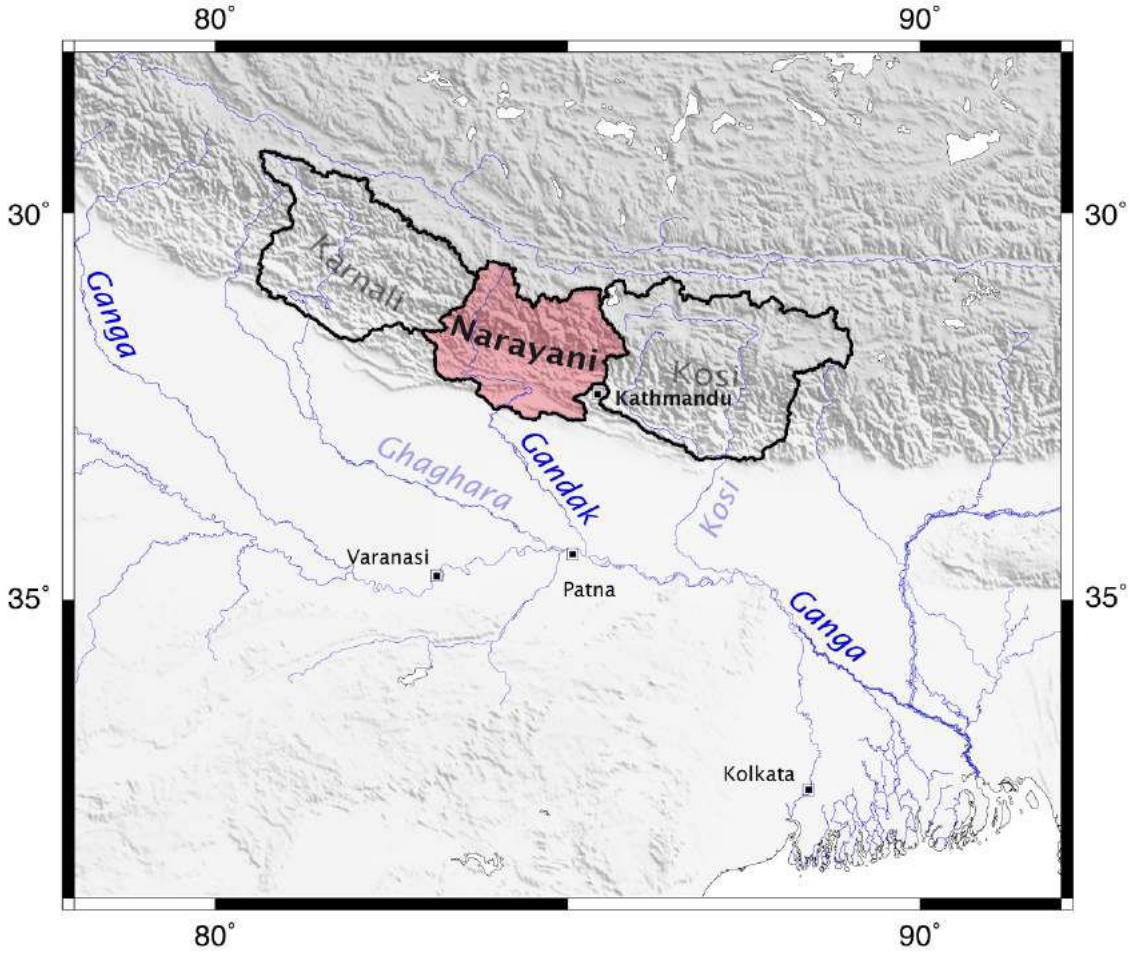

FIGURE 2.1.8 – Situation du bassin de la Narayani dans le système hydrographique du Gange-Brahmapoutre. (Données GEOTOPO30, USGS)

Le bassin versant draîne une superficie de 32000 km^2 et constitue l'un des trois bassins versants principaux draînant le Népal avec les bassins de la Karnali-Ghaghara à l'Ouest, et de la Kosi à l'Est.

fractures des versants dont la capacité de stockage transitoire est estimée à 28 km^3 pour l'ensemble des 3 bassins du Népal central[Andermann 12c]. Les forts taux d'infiltration et la grande perméabilité des nappes en montagne impliquent une vidange rapide des nappes avec un temps de résidence évalué à 45 jours[Andermann 12c]. Ceci explique pourquoi les débits d'étiages hors mousson sont atteints rapidement après la fin des précipitations de mousson, et pourquoi ils sont essentiellement dus à la fonte glaciaire.
Malgré leur participation mineure au débit total, les glaciers jouent un rôle important dans l'approvisionnement en eau au cours de la saison sèche. A ce titre, le changement climatique, qui implique le recul des glaciers, diminue la capacité de stockage de l'eau en hivers sous forme de neige, et diminuent les débits d'eau douce issus de la fonte glaciaire en été. Cela amoindrit d'autant l'approvisionnement en eau douce de la plaine pendant la saison sèche. Comme la proportion de l'eau apportée au sous-continent Indien provient à ~50% de l'Himalaya [Sinha 12], on comprend l'ampleur de l'aléas que génère la modification des cycles hydrologiques de ces bassins sur les populations en aval.

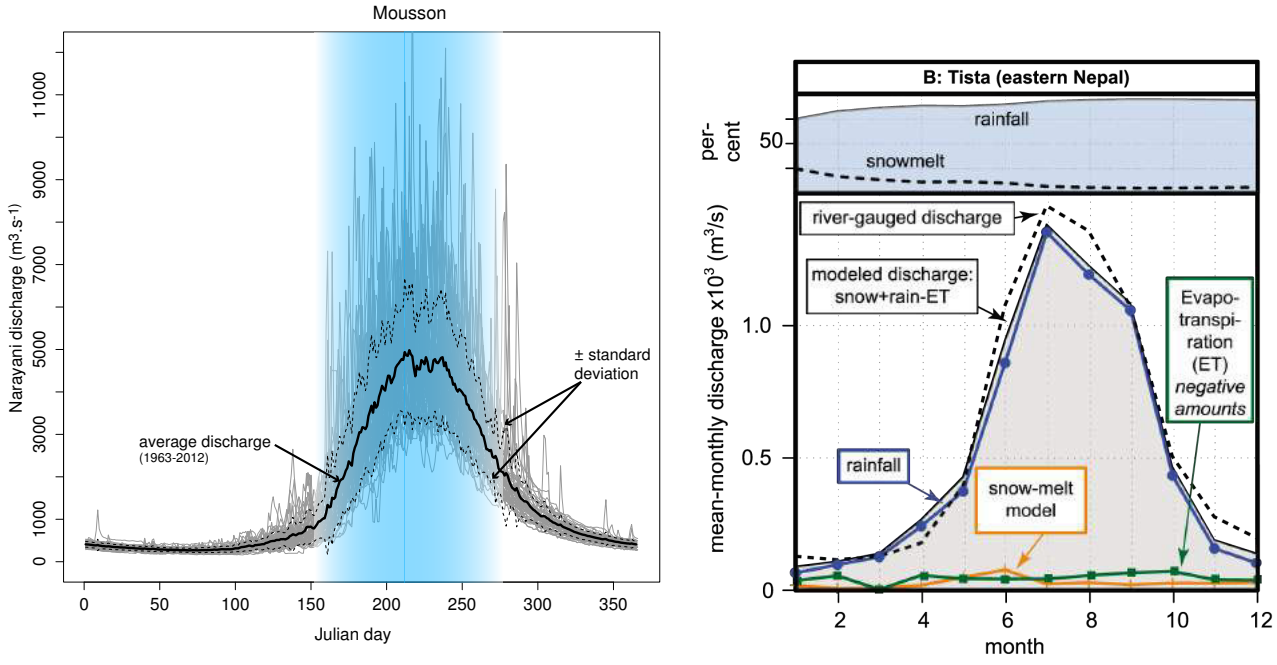

FIGURE 2.1.9 – Hydrographe annuel de la Narayani au Népal central (à gauche, drainage 32000 km^2) et de la Tista à l'Est du Népal (à droite, drainage 20000 km^2). (Narayani, données DHM, Tista d'après [Bookhagen 10])

Les hydrographes de la Narayani couvrent la période 1963-2012, les débits majeurs sont principalement observés pendant la période de mousson.
Pour le bassin de la Tista, les précipitations (ligne bleue) ont lieu principalement entre juin et septembre et représentent la quasi-totalité du débit enregistré des rivières (lignes tiretées et encart supérieur). La contribution des eaux de fonte glaciaire reste très faible atteignant au maximum 25% lors de la pré-Mousson.

2.1.5 Érosion.

Les flux sédimentaires exportés par les deux bassins drainant l'Himalaya : l'Indus et le Gange-Brahmapoutre, sont respectivement de 250 Mt/a et de 0.9 à 1.1 Gt/a [RSP 96, Meybeck 96, Métivier 99a, Syvitski 03, Lupker 11b]. Par conséquent, le système Gange-Brahmapoutre occupe le premier rang global en terme de flux sédimentaires délivrés aux océans. Ces flux colossaux sont restés stables depuis 2 Millions d'années[Métivier 99a] et sont à l'origine de gigantesques bassins sédimentaires qui s'étirent sur toute l'Asie du Sud [Métivier 99b]. L'étude de la production des sédiments en Himalaya apporte donc des

informations sur un système géologique qui a un impact global.

Les chaînes de montagnes et les petits bassins versants montagneux sont connus depuis longtemps pour être les plus intenses producteurs de sédiments au monde [Milliman 83]. Sous l'influence de leurs climats humides et tropicaux, les jeunes chaînes de montagnes d'Asie du Sud montrent les plus grands taux d'érosion du globe [Milliman 92, Milliman 11]. L'étude de l'érosion qui a cours au sein de l'Himalaya à l'échelle de bassins de taille modeste présente donc un intérêt de premier plan car ils contrôlent une grande part des flux sédimentaires qui nourrissent les bassins sédimentaires continentaux et marins, et les cycles bio-géo-chimiques océaniques.

La distribution de l'érosion en Himalaya et la recherche des facteurs qui la contrôlent sont à l'origine d'une littérature fournie. Certaines études montrent l'impact prépondérant de la tectonique sur l'érosion à long terme.[Burbank 96a, Burbank 03, Godard 14]. Les liens avec l'érosion sont ténus puisque l'uplift est à l'origine de la topographie qui provoque l'incision de la roche-mère (*bedrock*) par les rivières [Whipple 99b, Scheingross 14]. Cela implique un couplage spatial entre l'uplift et l'incision démontré en Himalaya par les modèles numériques couplés aux mesures d'incision et datations des terrasses fluviatiles [Lavé 01, Finnegan 08], ainsi que par les taux de dénudation calculés par isotopes cosmogéniques [Vance 03]. Les modèles d'incision placent les plus forts taux d'incision et d'uplift à l'endroit où s'élèvent les pentes du Haut-Himalaya [Lavé 01] (c.f. figure 2.1.10). Les taux d'érosion calculés pour l'ensemble du bassin sont de l'ordre de ~1.5 mm /a [Andermann 12b] (par mesures de la charge en suspension) à ~1.7 mm/a [Lupker 12a] (par analyse des isotopes cosmogéniques). Les taux d'érosion varient sensiblement du Nord au Sud, le plateau connaît des taux de l'ordre de ~1.2 mm/a [Vance 03], ils sont les plus élevés dans Haut-Himalaya où ils atteignent 2.5-3.5 mm/a [Vance 03, Garzanti 07, Gabet 08, Godard 12, Godard 14], puis ils chutent à ~0.8 mm/a et <0.6 mm /a dans le Bas-Himalaya où la topographie est modérée [Vance 03].

Dans ce contexte d'érosion massive, l'étude de chacun des processus d'érosion en lien avec les facteurs qui les déclenchent peut apporter de nombreuses clés sur la réponse de la chaîne face au changement climatique. Pour appuyer ce contrôle climatique sur l'érosion, certains avancent une cohérence spatiale entre les précipitations et l'érosion [Gabet 08, Deeken 11]. L'étude de la dynamique des glissements de terrains et leurs

déclenchements par les précipitations a aussi été proposé pour expliquer l'érosion intense des chaînes de montagnes actives (e.g. [Hovius 97, Dadson 03, Gabet 04a, Korup 10, Gallo 14b, Struck 15]).

L'érosion glaciaire est plus difficile à estimer, et reste limitée à l'extension spatiale des glaciers. Mais il a été montré qu'au Népal, elle n'est pas négligeable dans le bilan des grandes rivières et peut même atteindre localement des taux d'érosion de l'ordre de ~5 mm/a [Godard 12].

C'est dans ce contexte que cette étude s'est attachée à rechercher les traces des agents érosifs dans les sédiments de rivières.

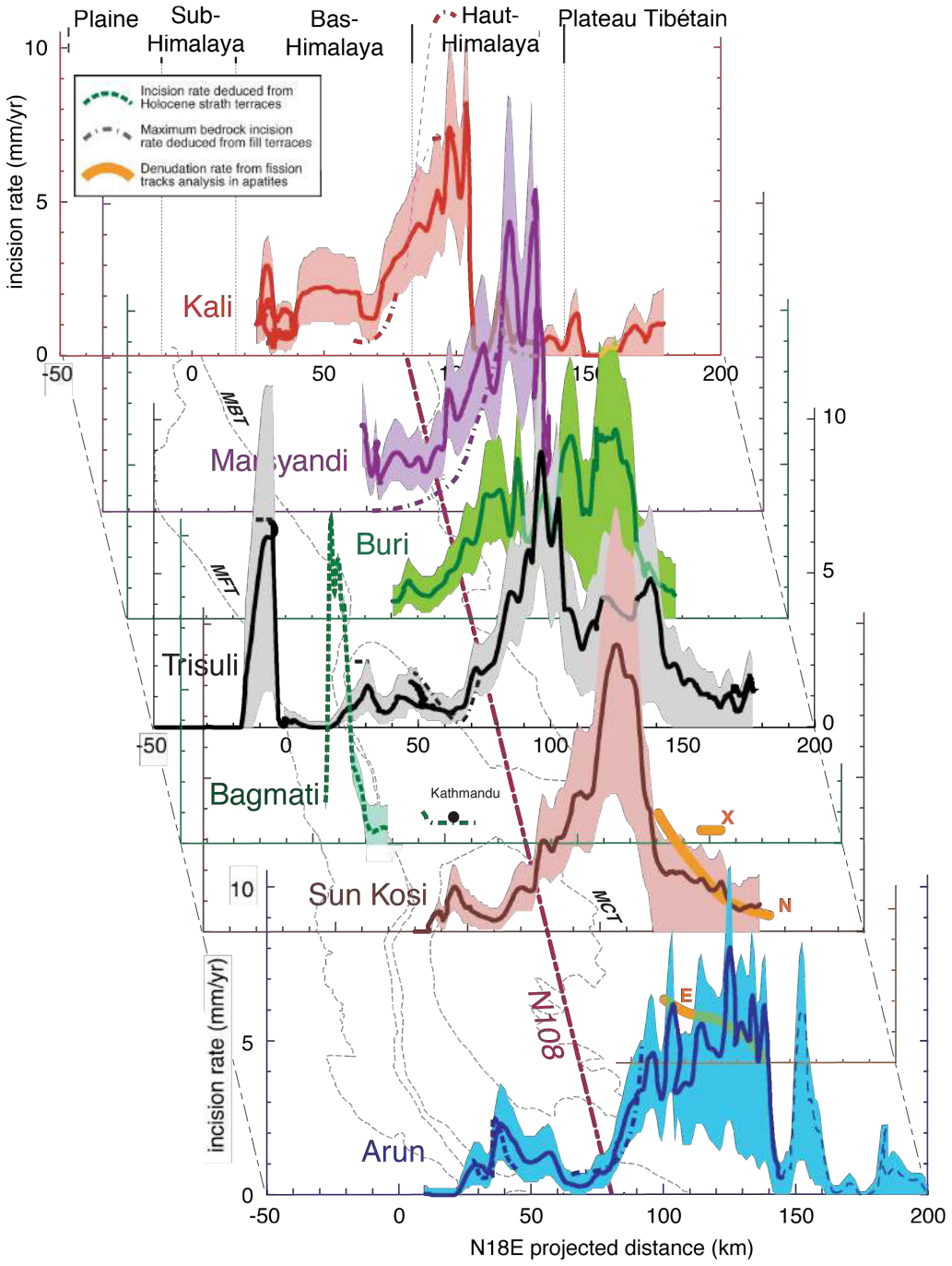

FIGURE 2.1.10 – Vitesses d'incision calculées par les modèles d'incision et datations des terrasses démontrant le couplage entre uplift et incision/érosion au Népal. (D'après [Lavé 01])

2.2 Les terrains d'études.

2.2.1 Khudi : bassin typique du flanc Sud, Massif du Lamjung, Annapurnas.

La Khudi Khola est un affluent de la Marsyandi située en flanc Sud au niveau du massif du Lamjung à l'Est des Annapurnas. Le bassin présente une superficie de 138 km^2 et un fort gradient topographique, avec des altitudes variant de 800 m à 5000 m ASL en quelques 20 km (2558 m en moyenne).

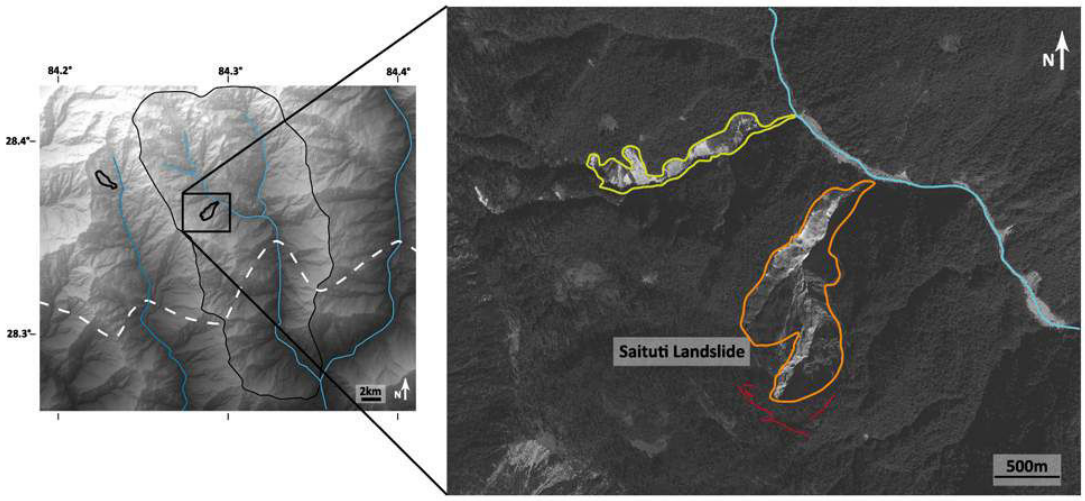

FIGURE 2.2.1 – Topographie du bassin de la Khudi Khola, Massif du Lamjung et extension des zones de glissements de terrain qu'il présente [Gallo 14a].
A gauche, les tirets blancs représente le MCT qui délimite les gneiss du HHC au N et les métapélites du LH au Sud. Ce bassin versant présente deux glissements de terrain dont le glissement de Saituti se révèle être actif depuis au moins 40-50 ans (matérialisé en orange ici). Les fractures en couronne de glissement sont matérialisées en rouge. Les relevés datent d'Octobre 2011.

Ce bassin est représentatif d'un bassin typique du flanc sud : les pentes y sont importantes, la végétation y est fortement développée et les précipitations y sont intenses, atteignant à certains endroits jusqu'à 5000 mm/a [Putkonen 04]. Le bassin ne présente actuellement pas de glaciers, et semble n'avoir subi qu'une érosion glaciaire passée limitée. Les morphologies glaciaires vestigiales n'ont été retrouvées qu'au Nord du bassin et

la déglaciation datée à 14.1 ka [Pratt-Sitaula 11].

Ce bassin présente aussi une zone de glissement très active depuis au moins 50 ans [Gallo 14a]. Les taux d'érosion moyens qui y ont été mesurés sont parmi les plus importants de cette région puisqu'ils ont été estimés entre 2.5 et 3 mm/an par mesure de la charge de suspension dans la rivière [Gabet 08, Gallo 14b], entre 2 et 4.5 mm/an par isotopes cosmogéniques [Niemi 05, Godard 12, Puchol 14, Gallo 14b], et entre 2 à 4 mm/an pendant le Quaternaire par les mesures de taux d'exhumation thermo-chronométriques [Blythe 07, Whipp 07]. Le bassin draîne essentiellement les gneiss du HHC, ainsi la diversité des lithologies rencontrées est assez limitée pour qu'une étude comparative des processus d'altération et d'érosion à l'échelle du bassin puisse avoir lieu.

FIGURE 2.2.2 – Vue en contre-plongée du glissement de terrain de Saituti en Novembre 2012.

D'un point de vue technique, ce bassin présente aussi l'avantage de posséder une station hydro-électrique exploitée par la société Khudi Hydro Power. La station ne détourne

qu'une faible partie du flux de la rivière, le captage de l'eau est réalisé à 2 km en amont des turbines et nous a permis de mettre en place nos instruments.

FIGURE 2.2.3 – Station de captage d'eau de la station hydroélectrique située à 4,5 km en amont de la confluence avec la Marsyandi.

Par son contexte climatique, géologique, érosif, et géomorphologique, ce bassin constitue un laboratoire idéal de l'étude comparée de l'érosion des sols et de l'érosion par les glissements de terrains. Les sédiments, les sols et les eaux collectés dans le bassins ont fait l'objet de l'étude qui est présentée en partie 4 de ce manuscrit.

2.2.2 Le bassin de la Narayani

La Narayani est la rivière majeure qui draîne la chaîne du Népal central (cf. figure 2.2.4). Son bassin versant draîne une superficie de 32000km^{2}depuis le Nord et le plateau tibétain par les bassins de la Kali Gandaki et de la Trisuli, jusqu'aux reliefs du Mahabarrat et le flanc Nord des collines Siwaliks. Il présente ainsi toute la variété des zones altitudinales rencontrées en Himalaya, depuis les collines à forêts denses, humides et climat sub-tropical du bas Himalaya, aux environnements sub-alpins et alpins du Haut

Himalaya où se développent les glaciers.

Il est le bassin le plus arrosé du Népal avec près de 1.4 m/a, par endroit plus de 4 m/a [Putkonen 04, Bookhagen 10], et présente des zones particulièrement touchées par les orages de mousson, notamment au niveau du massif des Annapurnas [Bookhagen 10, Andermann 12c]. 80 % de ces précipitations tombent pendant la mousson [Bookhagen 10, Andermann 12c, Barros 03, Barros 00] mais une fraction significative tombe sous forme de précipitations nivales. La superficie couverte par les glaciers est d'environ 10 % du bassin versant (données GLIMS, [Andermann 12b]), il est donc le plus englacé du Népal. Cette particularité s'explique par le fait que 37% du bassin s'élève à des altitudes supérieures à 4000 m, et comprend de nombreux massifs très élevés : Manaslu, Annapurnas, Manaslu, Lirung. Les principaux affluents de la Narayani sont d'Ouest en Est : La Kali Gandaki, la Séti, la Marsyandi, la Bhuri Gandaki et la Trisuli. La Kali et la Trisuli sont des bassins dit « trans-himalayens » puisqu'une partie de leur superficie ~40% draine le plateau tibétain.

La géologie du Népal central présente, à l'image de la chaîne himalayenne, cette organisation en bandes Ouest-Est des unités géologiques héritées de la collision Indo-Eurasienne. Ces unités géologiques recouvre une superficie du bassin représentant 33% pour les TSS, 23% pour le HHC et 40% pour le LH et moins de 5 % pour les Siwaliks (cf. figure 2.2.4). Les conditions de précipitations et de températures respectent aussi globalement ce schéma en bandes Ouest-Est. Cette coïncidence spatiale du climat avec la géologie s'est révélée très utile pour cette étude. En traçant les provenances géologiques des sédiments nous avions déjà une information sur l'importance relative des « zones climatiques » dans le bilan de l'érosion.

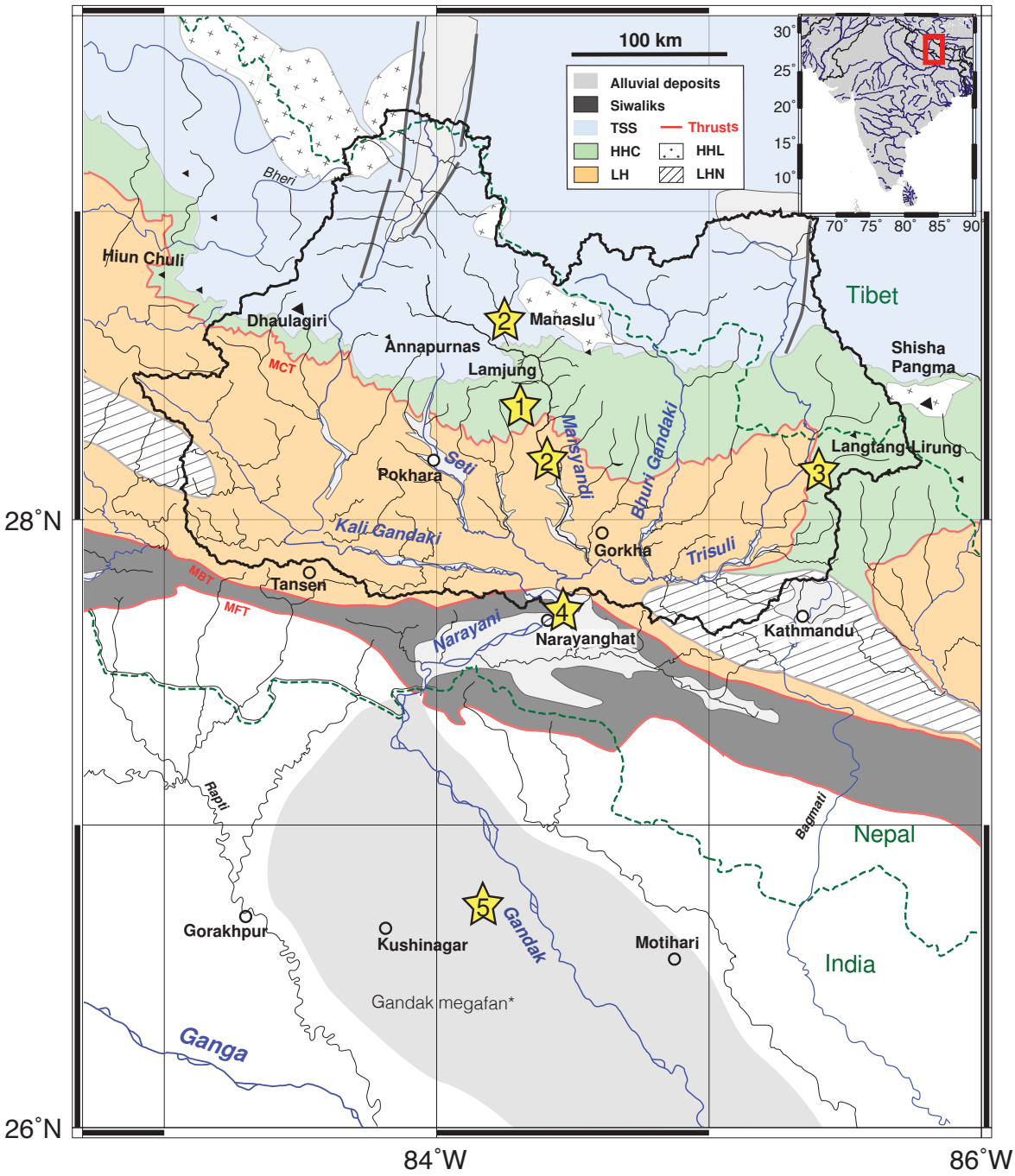

FIGURE 2.2.4 – Bassin versant de la Narayani-Gandak.
Les limites des unités géologiques sont issues de [Colchen 86], et les limites du mégafan de [Mohindra 92]. La topographie et le réseau hydrographique sont issus des données SRTM. Les zones d'études : 1 : Bassin de la Khudi, 2 : Bassin de la Marsyandi, 3 : Bassin du Langtang, 4 : Bassin de la Narayani à l'exutoire, 5 : Bassin d'avant-pays et plaine de la Narayani-Gandak.

Population et impact anthropique

Le bassin compte environ 3,3 millions d'habitants avec une densité moyenne de 122 per/km^2(Nepalese Population Survey). Les villes de Narayanghat-Barathpur, Pokhara et Gorkha concentrent la majeure partie de la population actuelle avec des densités atteignant 320 per/km^2, population urbaine qui a fortement augmenté suite à l'exode rurale et l'essort de l'activité touristique [Banister 81].

Sa répartition est très contrastée, la population du bassin est essentiellement concentrée dans les districts du Sud et dans le Lesser Himalaya où les densités sont de l'ordre de 200 à 250 pers/km^2, alors que dans le Haut Himalaya les densités tombent sous les 50 pers/km^2, parfois même inférieure à 3.8 pers/km^2. (cf. figure 2.2.5).

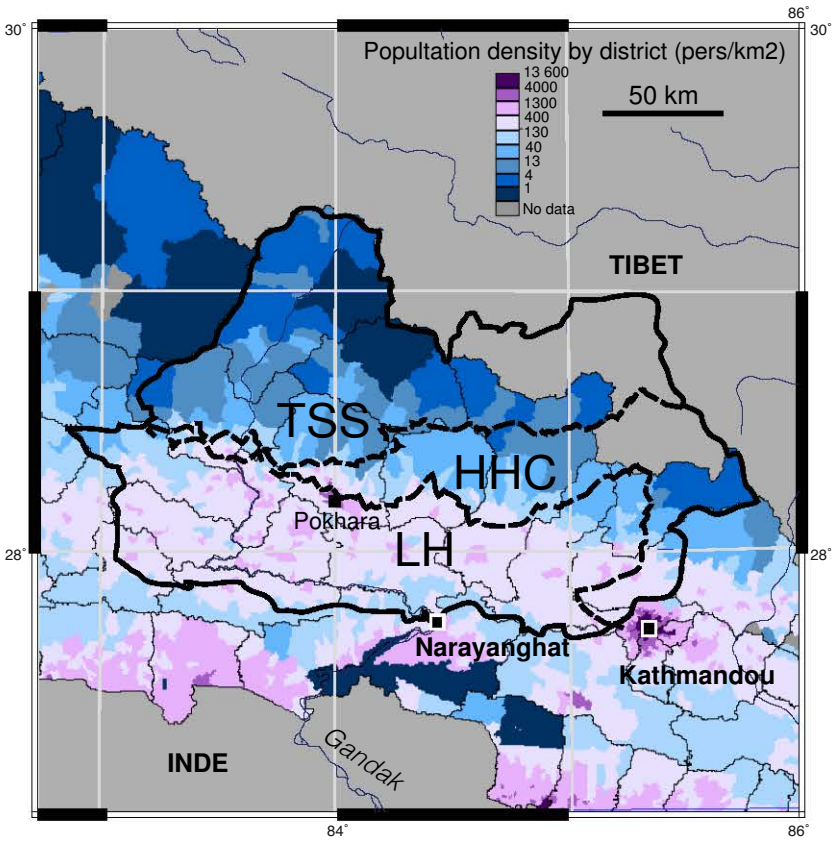

FIGURE 2.2.5 – Carte de répartition de la densité de population par district (Nepalese Population Survey).

L'occupation du Nord est augmentée lors de la saison estivale par les activités agro-pastorales et touristiques. L'impact environnemental du tourisme dans les régions protégées est aujourd'hui discuté [Nepal 00]. De plus, depuis la fin de la monarchie en 2007 et la période d'insurrection maoïste, l'essort économique et l'intérêt que ses géants voisins, 'Inde et la Chine portent au pays, se traduisent par une modification de l'utilisation des terrains (e.g. [Rao 01, Semwal 04]), un développement accéléré des infrastructures, des réseaux de communications et des routes [Thapa 13].

Ces activités anthropiques, souvent mal dimensionnées, sont à l'origine de nombreuses instabilités des terrains notamment dans le Lesser Himalaya où la densité de population est forte [Ghimire 06, Ghimire 13b, Ghimire 13a], et ont un impact sensible sur le réseau

hydrographique [Ghimire 90, Fort 10, Devkota 12, Regmi 14]. Ces observations au Népal font écho aux autres pays d'Asie du Sud où les impacts environnementaux du développement des routes et la mauvaise gestion de l'environnement montagneux sont de plus en plus mis en évidence [Sidle 06, Sidle 11, Sidle 12].

2.2.3 La plaine de la Narayani-Gandak et le bassin Gangétique.

L'érosion de la chaîne et du plateau tibétain a donné naissance à de grands bassins sédimentaires continentaux situés aux piémonts Sud et Est de la chaîne avec les bassins de la plaine Indo-gangétique et de l'Asie du Sud-Est [Métivier 99a]. La pile sédimentaire continentale peut atteindre jusqu'à 4 à 5 km d'épaisseur au dessus du socle protérozoïque dans certaines parties du bassin, notamment à l'Est de la plaine au niveau des rivières Kosi et Teesta (e.g. [Burbank 92, Hetényi 06]). Elle est essentiellement contrôlée par le bombement flexural de la plaque indienne provoqué par la subduction sous la plaque eurasienne et le poids de la charge sédimentaire qui s'y accumule [Lyon-Caen 85].

L'espace d'accommodation du bassin d'avant-pays reste limité par les taux de subsidences. Compte tenu des flux sédimentaires du Gange-Brahmapoutre estimés à 1 - 1.2 Gt/a, les masses de sédiments arrivant aux domaines océaniques sont colossales puisque seul 10% semblent être stockés dans la plaine [Lupker 11b]. L'érosion himalayenne a ainsi donné naissance aux grands cônes sédimentaires océaniques au cône de l'Indus à l'Ouest et au cône du Bengale à l'Est pour le système Gange-Brahmapoutre, qui constituent parmi les plus grands structures sédimentaires connues à la surface de la Terre.

Les âges des dépôts de la plaine sont vraisemblablement Miocène à Pléistocène et sont estimés par les séries Siwaliks. Les Siwaliks correspondent aux sédiments de couverture et paléodépots de la plaine qui ont été tectonisés sous forme de plis et d'écailles chevauchantes, et mobilisés par la progression du MFT vers le Sud [Delcaillau 92].

Les dépôts fluviatiles actuels de la plaine du Gange accommodent la subsidence du bassin et montrent des taux de sédimentation variables de l'ordre de 0.05 à 1.5 mm/an [Sinha 96, Chandra 07, Rahaman 09, Srivastava 10, Rahaman 10]. Les flux sédimentaires très importants provenant des bassins népalais en flanc Sud ont aussi provoqués la formation de structures sédimentaires remarquables appelées mégafan [Sinha 12].

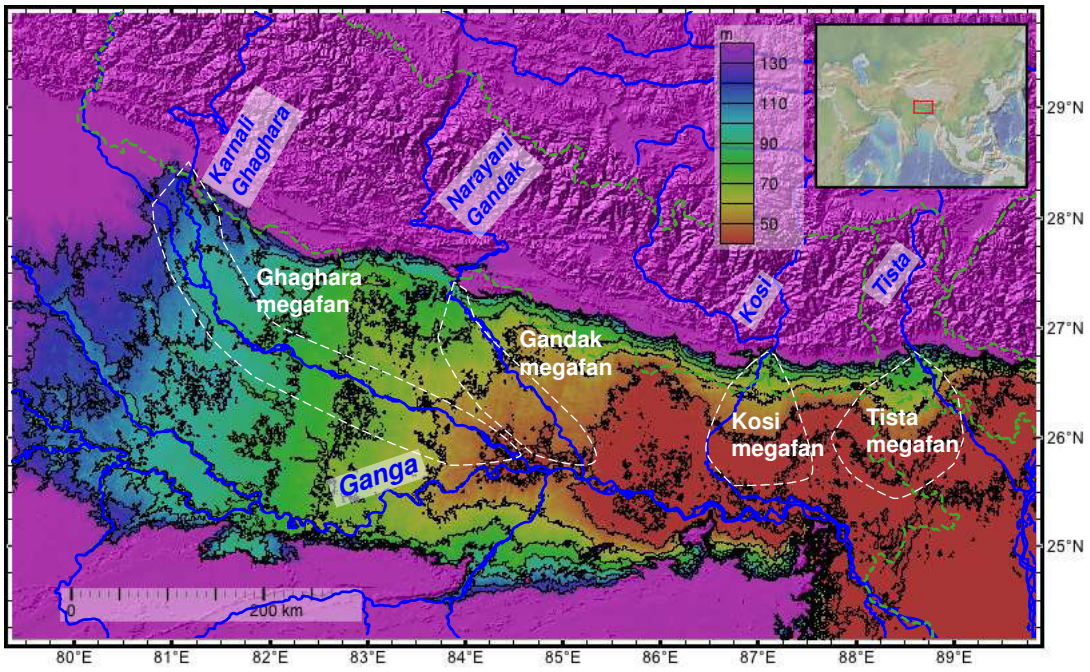

FIGURE 2.2.6 – Topographie de la plaine du Gange illustrant les mégafans des rivières du flanc Sud.
Les lignes de niveau correspondent à 15 m d'altitude. *(Données issues du SRTM)*

Ces cônes sédimentaires continentaux sont formés par l'accumulation rapide des sédiments apportés par les affluents majeurs drainant l'Himalaya à leur entrée dans la plaine Gangétique. D' Ouest en Est, ces formations correspondent aux bassins de la : Ghagara, Gandak [Mohindra 92, Sinha 14], Kosi [Chakraborty 10b], et Tista [Chakraborty 10a] (cf. figure 2.2.6). La géométrie des systèmes fluviatiles est certainement issue de la déviation des rivières himalayennes par la formation des reliefs Siwaliks au front, et de leurs captures latérales par les 4 rivières majeures que sont La Karnali, la Narayani, la Kosi et la Tista [Gupta 97]. Ces captures latérales ou *anabranching*, connaissant les débits sédimentaires de chacune de ces rivières, ont donc considérablement augmenté le flux sédimentaire des seules rivières traversant le front. Dépassant largement la capacité d'accommodation de la plaine à ces exutoires, ces captures ont probablement conduit à la construction des ces cônes sédimentaires continentaux remarquables.

Dans le cadre de notre étude, l'intérêt principal de ces structures réside dans le fait qu'ils enregistrent les modifications des flux sédimentaires et de provenance de la chaîne en lien

avec les changements climatiques passés. Compte tenu de leurs taux d'accumulation élevés, ces enregistrements sédimentaires présentent une résolution temporelle élevée [Sinha 12, Sinha 14]. De surcroît, ils présentent l'avantage de n'avoir subi qu'un transport dans la plaine limité, contrairement aux enregistrements sédimentaires précédemment étudiés dans la plaine du Gange [Rahaman 09, Rahaman 10, Srivastava 10]. Ils témoignent ainsi directement des processus d'érosion qui ont eu lieu dans la chaîne, et non pas ceux qui ont lieu dans la plaine où les sédiments sont remaniés et altérés pendant leur transport [Bouchez 11b, Lupker 12b, Dellinger 14].

III

Chapitre 3

Méthodes

Dans ce chapitre, nous avons souhaité développer les méthodes d'échantillonnage et de préparation des échantillons, les méthodes d'acquisition des données géophysiques (sondages électriques et mesures de courant par ADCP), et la méthode de destruction de la matière organique (MO) qui a été développée pendant cette thèse afin d'effectuer la mesure d'hydratation des silicates. Pour de plus amples détails, nous vous invitons à vous reporter aux parties méthodes des chapitres suivants.

3.1 Echantillonnage

Cette partie présente les principales campagnes de terrain pendant lesquelles ont été collectés les échantillons utilisés dans cette thèse. Nous y présentons la stratégie d'échantillonnage et les méthodes de préparation / caractérisation des échantillons que nous avons utilisés avant d'effectuer les analyses.

3.1.1 Échantillonnage des processus d'érosion et des sédiments de rivière

3.1.1.1 Missions d'échantillonnage au Népal central

Les données présentées dans ce manuscrit sont issues d'analyses d'échantillons prélevés en Himalaya par les équipes du CRPG depuis les années 1970. Les échantillons de roches prélevées de 1970 à 1990 ont été collectés par P. Le Fort, A. Pêcher, C. France-Lanord,

S. Guillot et M. Brouand. Cette collection de roches sources a été complétée par de très nombreux échantillons de rivières himalayennes et gangétiques prélevés par C. France-Lanord, J. Lavé, A. Galy, A.C. Pierson-Wickmann, V. Galy, M. Lupker.

Les missions d'échantillonnage reportées ici sont celles qui ont permis de prélever les échantillons nécessaires à cette étude.

1. Novembre 2009, [E. Dambrine, C. France-Lanord, A. P. Gajurel, J. Lavé, M. Lupker, N. Puchol] Cette première mission « CALIMERO » a permis de prélever les profils de sols, les produits des glissements de terrain et les sédiments de rivière de la Khudi, destinés à documenter la production de sol, les caractéristiques des produits des glissements de terrain, et leurs proportions dans les sédiments de rivière de bassin du Haut-Himalaya.
2. Novembre 2010, [A. P. Gajurel, F. Gallo, J. Lavé, G. Morin, N. Puchol] (1 mois) Cette mission a été divisée en 4 semaines : 1 - Relevés d'érosion dans la Bakeya au MFT, 2 - Echantillonnage dans la vallée de la Khudi, 3 - Echantillonnage dans la vallée du Langtang, 4 - Echantillonnage dans la vallée de la Dudh.

   a) Les mesures de micro-érosion effectuées dans la Bakeya ont complété la base de données des vitesses d'incision que constitue J. Lavé depuis une dizaine d'années au niveau du MFT [Lavé 00, Lavé 01].

   b) Dans le bassin de la Khudi, une collecte complémentaire à la mission 2009 des échantillons de sol et de glissements de terrain a été réalisée, ainsi que l'échantillonnage de bassins versants d'ordres inférieurs.

   c) Pour évaluer l'impact du climat sur les caractéristiques géochimiques des sols et leur érosion, nous souhaitions étudier un bassin de taille semblable à la Khudi, présentant une lithologie comparable mais dont le régime des précipitations était inférieur à celui de la Khudi. Alors que la moyenne des précipitations est de 3000-4000 mm/an dans la vallée de la Khudi située dans le massif des Annapurnas [Putkonen 04], les précipitations sont inférieures de l'ordre de 1000 mm/a dans la vallée de la Langtang qui se situe dans la haute Trisuli, massif du Langtang-Lirung. Cette vallée orientée E-W est située dans le Haut-Himalaya, les lithologies y sont dominées par les gneiss de la Dalle du Tibet [Macfarlane 93]. Des échantillons de sols, de glissements de terrains, des sédiments de rivières ainsi que des petits tributaires ont été prélevés le long du cours de la Langtang et dans

la vallée. Nous avons aussi échantillonné le très grand glissement de terrain du Tsergo Ri (Vol = 10^{10} m^3) décrit comme résultant d'un effondrement en masse d'une partie du massif [Korup 10].

d) S'agissant des produits glaciaires, nous avons collecté les sédiments dans les ruisseaux de fonte, les lacs pro-glaciaires et les moraines actuelles des glaciers des vallées du Langtang (bassin de la Trisuli) et de la Dudh (bassin de la Maryandi).

3. Août 2011, [C. France-Lanord, A. P. Gajurel, G. Kumar, G. Morin, R. Sinha] (1 mois) Cette mission a été organisée en deux parties, 1 - une partie dédiée à compléter l'échantillonnage des sols HHC de la Khudi, et à prélever les eaux de ruissellement des petits bassins versants pour mesurer les éléments dissous en période de mousson 2 - une seconde partie axée sur les mesures de courants par ADCP de la Narayani et de la Kosi à la sortie de la chaîne, associé à l'échantillonnage simultané des sédiments en profondeur. Ce travail de terrain a été réalisé en collaboration et grâce au matériel de l'équipe de F. Métivier IPG Paris, France, et du Pr R. Sinha de l'IIT Kanpur, Inde.
4. Octobre 2011, [G. Morin] (3 semaines) Cette mission a permis de réaliser des profils géophysiques par sondages électriques verticaux (VES) dans le but de caractériser les sédiments de subsurface de la plaine d'inondation de la Gandak. Ces relevés devaient orienter le choix de la localisation des forages de la plaine de la Gandak. Une semaine a aussi été consacrée à l'échantillonnage de la Gandak, en amont de sa confluence avec le Gange à Patna, et en aval de son entrée dans la plaine à Tribeni. pour documenter l'évolution du sédiment actuel à l'entrée de la plaine.
5. Juillet-Août 2013, [C. France-Lanord, Maarten Lupker, Romain Michel] Cette mission a été dédiée au suivi à très haute résolution temporelle de la Khudi Khola en période de mousson. Les flux d'éléments dissous et de sédiments ont été mesurés grâce à l'utilisation d'une sonde de turbidité associée à un échantillonnage journalier et horaire de la rivière. De plus, les échantillonnages couplés des matières en suspension en surface et en profondeur ont permis de documenter le gradient des concentrations de MES dans la colonne d'eau, et ainsi de préciser les flux de sédiments exportés.
6. Octobre 2013, [C. Bosia, C. France-Lanord et Q. Soraruff] Cette mission complémentaire était dédiée à l'échantillonnage des sables et MES de la Khudi en profondeur,

et de réaliser un échantillonnage systématique de la Marsyandi et de ses affluents. Les objectifs concernaient deux points particuliers :

a) Documenter la variabilité de la charge sédimentaire MES de la Khudi avec une forte résolution temporelle, et préciser les variations hydrologiques journalières de la Khudi. Ces échantillons ont été prélevés par un système d'échantillonnage en profondeur qui a été adapté sur le mur de l'intake par C. France-Lanord et P. Baillot en mai 2012. Ce système est constitué d'une bouteille de type « Niskin » maintenue à l'horizontale et fixée sur un rack coulissant permettant son introduction à la profondeur souhaitée, sans risquer l'emport de la bouteille par le puissant courant de la rivière.

b) Tracer les processus glaciaires par le prélèvement des sédiments de rivières tout au long du cours principal de la Marsyandi, ainsi que de tous ses affluents, et en particulier les bassins drainant des morphologies glaciaires. L'objectif étant de tester l'impact de l'érosion glaciaire sur la géochimie des sédiments d'une rivière himalayenne majeure.

3.1.1.2 Echantillonnage des sédiments de rivières

Echantillonnage des MES de la mousson 2010

Afin de documenter les variations du signal sédimentaire des rivières himalayennes au cours de la mousson, un échantillonnage quotidien de MES prélevées pendant toute la mousson 2010 a été effectué sur les deux sites du Khudi Dam (bassin de la Khudi) et du Pont de Narayanghat à l'exutoire du bassin de la Narayani

Les deux séries d'échantillons : SKD (Sediment Khudi Dam) et SNG (Sediment NarayanGhat) ont été échantillonnés par les personnels de l'usine hydro-électrique ou *powerhouse* exploitée par la société « Khudi Hydro Power » dans la Khudi, d'un habitant de Narayanghat qui avait été préalablement entraîné, et d' A. Gajurel qui supervisait les échantillonnages et a assuré les filtrations et pesées des échantillons à Kathmandu. Ces échantillons sont constitués de prélèvements de surface dans la Khudi (SKD) au niveau de l'*intake* (endroit de dérivation du flux de la rivière pour alimenter l'usine hydro-électrique) de l'usine hydro-électrique, et de la Narayani prélevés depuis le pont de Narayanghat (SNG) . Les prélèvements ont été effectués par deux prélèvements d'un litre. Les échantillons d'eau non filtrés ont été transférés et stockés dans des bouteilles

Nalgene. Concernant les échantillons SKD (Khudi) les bouteilles ont été ramenées à Kathmandu une fois par mois pour être filtrées. Les échantillons SNG (Narayani) ont quant à eux ont été directement filtrés sur place.

« Gros » échantillons de 100L

Deux échantillons de 100L de matières en suspension de surface ont été prélevés, un de la Khudi khola à la sortie du bassin de la Khudi au niveau de la *powerhouse* , un autre sur la Narayani à Narayanghat depuis le pont. La méthode d'échantillonnage est assez simple et consiste à prélever à l'aide d'un simple seau de 10 L attaché à une corde des échantillons successifs de matière en suspension de surface. Il est nécessaire de faire « franchement » plonger le seau et de le remonter quasi instantanément pour éviter qu'il soit emporté par la rivière, et permettre que la prise soit la plus représentative possible.

Échantillonnage en profondeur

Il est indispensable de prendre en compte de nombreuses précautions lors de l'évaluation des bilans sédimentaires des sédiments de rivières. Des méthodes ont été développées afin de prendre en compte les variabilités verticales et latérales des concentrations de sédiments par les équipes de l'IPG Paris en collaboration avec le CRPG afin d'échantillonner les sédiments en profondeur et de les associer aux mesures de vitesse du courant et de débit sur une section complète de la rivière [Galy 07c, Galy 08, Lupker 11b, Bouchez 11b, Bouchez 11a]. Effectué à différents régimes hydrologiques, le couplage de ces deux manipulations permet la modélisation du transport sédimentaire, et son extrapolation sur l'ensemble de l'année.

Les principes de l'échantillonnage en profondeur ont été précédemment décrits [Lupker 11b], nous souhaitons ici rappeler ces techniques que nous avons appliquées à la Narayani et la Kosi en précisant les quelques « aménagements » nécessaires compte tenu des très fortes vitesses de courant.

L'échantillonneur utilisé en 2011 est une bouteille de type « Niskin » d'une capacité de 5L constituée d'un tube de 40 cm et 14 cm de diamètre (cf. figure 3.1.1). L'échantillonneur est équipé d'une jauge de pression et lesté par un plomb de 20 kg. L'échantillonneur est maintenu ouvert et plongé progressivement jusqu'à ce que la profondeur souhaitée soit atteinte. Le bateau est maintenu à la dérive au centre du chenal et reste donc immobile

par rapport à l'eau. Lors de cette phase d'immersion, l'eau et les sédiments circulent librement et ne s'accumulent pas dans la bouteille. La prise de l'échantillon s'effectue par déclenchement pneumatique des pistons qui libèrent les clapets de fermeture. Ces derniers capturent instantanément l'eau et le sédiment dans la bouteille grâce à l'action de puissants ressors. La prise est déclenchée au moment où la zone d'échantillonnage est atteinte et la position GPS exacte est notée. Après la remontée, le bateau est amené à la berge et la prise est transférée dans des poches plastiques stériles, hermétiques et opaques. Le bateau peut ensuite remonter la rivière et se replacer en amont du point d'échantillonnage. Les conditions de courants (U~35 km/h au centre du chenal) nous ont contraints à procéder au transfert des échantillons à terre et à remonter le courant le long des berges à très faible vitesse. Les profils effectués sur la Narayani en 2011 sont constitués de 3 à 4 prises. La réalisation d'un « profil » complet demande donc beaucoup de temps.

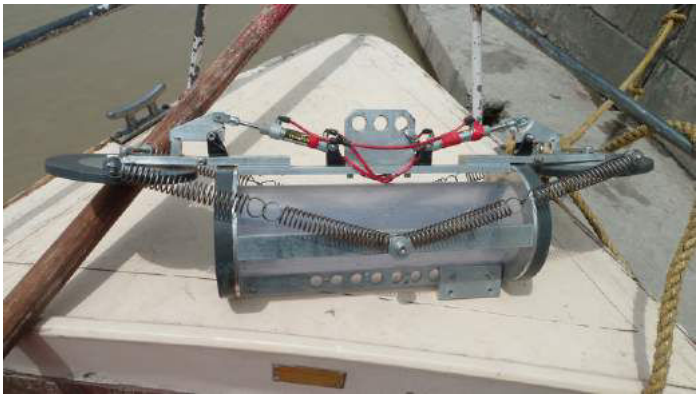

FIGURE 3.1.1 – L'échantillonneur en profondeur de type « niskin » du CRPG (capacité = 5L).
À droite, la bouteille contient un échantillon et le bateau est amené à la berge pour effectuer le transfert dans de bonnes conditions.

Echantillonnages de la charge de fond et des galets

La mesure et l'échantillonnage de la charge de fond *(bedload)* transportée par une rivière sont toujours très difficiles à réaliser. De nombreuses techniques existent pour effectuer son échantillonnage et en déterminer les flux : pesées par bascules, dragage, prélèvements en période d'étiage, cycle de purge des barrages hydroélectriques etc.

Les plus précises sont les pesées par bascule qui échantillonne le flux de fond en continu, mais ces techniques nécessitent une section calibrée par une installation bâtie, et des conditions hydrologiques moins dynamiques. À défaut, les charges de fond sont généralement calculées, et leur échantillonnage se fait par dragage ou lors de l'étiage sur les bancs.

En pleine mousson, le dragage sur les rivières himalayennes depuis une embarcation « légère » a été rendu difficile par plusieurs facteurs : 1 - le courant est souvent très fort, ce qui rend les manœuvres à bord délicates, et limite le temps disponible pour effectuer les prélèvements, 2 - les concentrations au fond et la taille des galets sont importantes ce qui rend impossible la bonne pénétration de l'échantillonneur dans la charge de fond et entraîne parfois la perte du matériel (été 2011).

A contrario, pendant la période d'étiage, si le centre du chenal qui abrite le cours permanent reste ennoyé, les rives sont généralement accessibles et composées des sables et bancs de galets déposés à la dernière crue majeure. L'échantillonnage selon cette méthode accessible et sûr s'est révélé être le seul possible à mettre en œuvre au Népal. Afin d'être le plus représentatif possible, l'échantillonnage est effectué le long d'un axe matérialisé par un ruban de plusieurs dizaines de mètres de long, et tous les galets de même taille situés sur cet axe sont systématiquement collectés. Cela représente des échantillons d'environ 100 galets.

3 séries d'échantillons de galets ont été prélevées :

1. Les galets de la Khudi khola au niveau d'un guet en aval de l'*intake* des bassins de siltation de la station hydroélectrique (par F. Gallo)
2. Les galets de l'exutoire du glissement de Saituti dans la vallée de la Khudi (par J. Lavé)
3. Les galets de la Narayani sur les berges proches de Narayanghat (par C. France-Lanord)

FIGURE 3.1.2 – Bancs de galets du chenal de la Narayani en amont de Devghat.

3.1.1.3 Méthode de filtration

Les unités de filtration utilisées pour séparer les sédiments et l'eau sont des tubes d'acier recouverts par du téflon, auxquels sont adaptés des porte-filtres permettant d'utiliser des filtres en PES (polyéthersulfone) de 90 mm de diamètre (cf. figure 3.1.3). Le bas des unités est fermé par le porte-filtre. Les échantillons d'eau de rivière contenant les MES sont chargées par le haut des unités. Lorsqu'elles sont remplies, le haut est fermé hermétiquement par le couvercle où arrive le tuyau d'air comprimé, puis l'air intérieur du tube est mis sous pression (2 à 4 bars) en utilisant une pompe. Après filtration, les MES ont été stockées directement avec les filtres dans des sacs à échantillons qui n'ont été ouverts qu'au laboratoire. Au laboratoire, les filtres et échantillons ont été congelés et lyophilisés. Cette technique, comparée au simple séchage dans une étuve, permet de ne pas altérer les phases sensibles à la température comme les composés organiques, les hydroxydes, et les phases secondaires mal cristallisées. Les filtres sont en PES, un polymère dont le maillage fin (0.2 µm) ne permet que le passage des particules dont la taille est inférieure aux colloïdes (cf. figure 3.1.3). Ces filtres présentent deux avantages supplémentaires : 1- une faible rétention des MES, ce qui rend plus aisée la récupération totale des particules les plus fines, 2- une bonne résistance, ils ne se désagrègent pas facilement et évitent de contaminer les échantillons avec des microparticules de plastique.

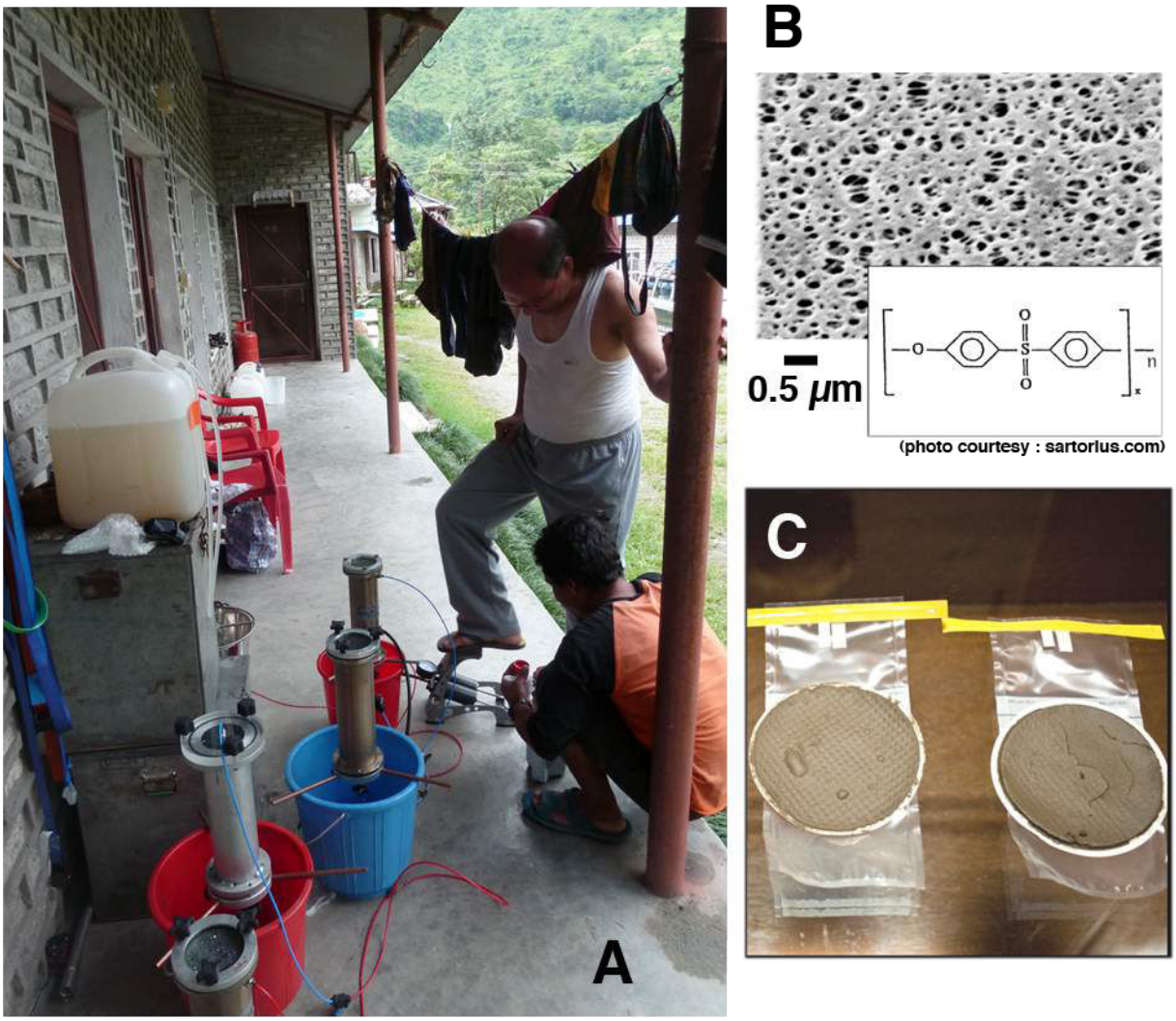

FIGURE 3.1.3 – Filtration des MES
En A, atelier de filtration au Khudi Power House présentant 4 unités de filtration pressurisées à l'aide d'une pompe. En B, image au MEB d'une membrane de PES et sa formule semi-développée. *(photo courtesy http ://www.sartorius-france.fr)*. En C, MES sur filtres après filtration.

3.1.2 Logging et échantillonnage des carottes de forages

Nous n'avons pas participé aux campagnes de forage a proprement parlé. Ces opérations ont eu lieux en février 2013 et ont été supervisées par l'équipe du Pr Sinha de l'IIT Kanpur. Nous avons cependant participé aux étapes d'ouverture, de *logging* et d'échantillonnage

des carottes lors de deux missions.

1. Avril 2012 [C. France-Lanord, G. Morin] (3 semaines) Cette mission a essentiellement été dédiée à la découpe, au logging et à l'échantillonnage des carottes de forages. Ce travail a été rendu possible grâce aux infrastructures de l'unité de stockage des carottes du département d'Ingénierie civile à l'IIT Kanpur et à la collaboration avec le Pr. R. Sinha.
2. Février 2013 [G. Morin] (2 semaines) Cette deuxième mission de prélèvement dédiée aux forages a permis le prélèvement des échantillons destinés aux datations par Luminescence OSL-IRSL, et a permis simultanément de compléter l'échantillonnage de « gros » échantillons destinées à l'études des isotopes cosmogéniques.

3.1.3 Préparation et caractérisation des échantillons

3.1.3.1 Séparations granulométriques

Tamisages

Les deux types de tamisages ne permettent pas d'obtenir le même résultat et n'imposent pas les mêmes contraintes.

Les tamisages ont principalement été effectués en voie sèche pour éviter l'entrainement des particules fines par l'eau et un temps de décantation/récupération des matières fines <63µm généralement long.

Les sols ont tous été tamisés à 2 mm car les produits de sols sont définis par convention par une granulométrie inférieure à 2 mm.

Les sables de berges de rivière (*banks*) ont tous été tamisés à 2 mm afin de pouvoir être comparés aux sols. Les refus, peu fréquents, représentaient tout au plus quelques % de la masse initiale.

Séparations d'argiles

La séparation des argiles à partir du sédiment total a été effectuée sur 6 échantillons par simple technique de sédimentation.

Principe

Selon la loi de Stokes, les produits de granulométries [1] différentes peuvent être séparés selon leurs vitesses de sédimentation car ces dernières sont proportionnelles à la taille des grains pour des particules d'aspect sphérique :

$$v = \frac{2r^2 g \Delta(\rho)}{9\eta}$$

avec : v, vitesse limite de chute (en m/s) ; r, rayon de la sphère (en m) ; g, accélération de la pesanteur (en m/s^2) ; $\Delta(\rho)$=ρ_{solide}-ρ_{fluide}, différence de masse volumique entre la particule et le fluide (en kg/m^3) ; η, viscosité dynamique du fluide (en Pa.s).

Cette méthode est imparfaite pour la séparation d'éléments grossiers. Les densités et les facteurs de forme différents selon les minéraux peuvent influencer grandement la vitesse de chute et conduire à des mélanges poly-minéraux de granulométries différentes.

Cependant, elle reste valable pour les argiles qui sont < 2 µm par définition, et dont la vitesse de chute ne dépend plus de la densité car l'effet du facteur de forme prime sur l'effet de la masse à ces tailles.

Protocole de séparation par colonnes

Le sédiment est placé dans un flacon complété par un volume d'eau distillée (~600 mL) tel que le rapport Eau/Roche W/S ~ 20, puis placé en agitation circulaire pendant 48h. Le mélange est alors décanté dans des éprouvettes graduées (1L) après avoir été complété par de l'eau distillée. Le temps de décantation est calculé à partir de la distance de chute (surface - profondeur de prélèvement) et la vitesse de chute variable selon la température calculée pour des particules de 2 µm. La décantation est répétée jusqu'à obtention d'un surnageant sans matière en suspension apparente. Le surnageant est siphonné en évitant au maximum les remises en suspension, puis est ensuite centrifugé à grande vitesse. Après centrifugation, l'eau est siphonnée et le résidu solide placé en congélation pour ensuite être lyophilisé. Les temps de traitement très longs nous ont conduits à abandonner cette voie. Cependant, quelques échantillons ont été produits avec succès par cette méthode.

1. NB : Le terme granulométrie pour définir la taille des grains est un usage abusif courant, le terme adéquat serait granularité. Nous avons cependant préféré utiliser granulométrie.

3.1.3.2 Caractérisation de la granulométrie des échantillons

Distributions granulométriques

La mesure des spectres granulométriques des sédiments est possible grâce à plusieurs méthodes. Les plus courantes reposent sur la pesée des refus de tamis. Les méthodes récentes d'optique et les applications du laser ont permis de grandes avancées sur les techniques de détection des particules. Depuis quelque temps les méthodes de détermination de la tailles des grains par diffraction sont de plus en plus performantes.

Principe de granulométrie laser

Les granulomètres laser mesurent la diffraction d'un rayon de lumière produite par la matière fragmentée pour en déterminer la distribution granulométrique. Le principe est simple : l'échantillon est mis en suspension dans un liquide (de l'eau distillée dans notre cas) et constamment agité. Cette « pulpe » (échantillons + eau) est mise en circulation et passe par une cellule où est établi un flux laminaire entre deux plaques d'acier disposant de fenêtres de quartz. Un laser tire en continu au centre de ces cellules, la lumière diffractée est refocalisée à l'aide de lentilles et est ensuite analysée par une cellule à détecteurs concentriques.

Les spectres complexes issus de la superposition des anneaux de diffractions par les particules, et les interférences résultantes sont analysées et permettent le calcul de la répartition granulométrique de l'échantillon. L'intervalle de mesure dépend des détecteurs mais aussi des lentilles de focalisation.

Nous avons effectué les mesures grâce à un granulomètre laser Symantec HELOS/BF équipé d'une cellule SUCELL au LIEC, Nancy, France. Équipé de 2 lentilles de focalisation, ce matériel permet l'analyse de 0.1 à 875 µm dans deux intervalles différents : 0 - 50 µm et 4.5 - 875 µm.

Précaution d'usage

Les échantillons d'une même rivière ont généralement été passés dans la même série. A chaque début de série, des tests ont été nécessaires pour calibrer le temps d'ultrasonification (US) des échantillons et les temps de mesures. Pour ce faire plusieurs répliquats de mesure du même échantillon avec des temps d'US croissants ont permis de déterminer un

temps caractéristique de désagrégation des agrégats (flocs) d'argiles correspondant à 30 s dans le cas de nos échantillons himalayens. Des temps d'US longs sont nécessaires pour les échantillons contenant beaucoup d'argiles, et les échantillons de séparations d'argiles démontrent très bien cet effet avec des temps d'US nécessaires au minimum d'1 min. La mesure de sédiments de rivière contenant de nombreux micas grossiers est parfois rendue difficile par la création d'artefacts. L'appareil considère ces grains comme dépassant la taille maximale de mesure et délivre des résultats erronés. Il convient alors de procéder à un temps d'acquisition plus court (10 s) ou de re-tamiser les échantillons.

3.2 Campagnes de mesures géophysiques

3.2.1 Mesures des vitesses de courant par ADCP

L'échantillonnage en profondeur permet de documenter la distribution des concentrations des sédiments en profondeur. Cependant, si la répartition des vitesses de courant en profondeur n'est pas mesurée, il n'est pas possible de calculer les flux de sédiments avec précision. La détermination des vitesses de courant est couramment faite par des mesures au moulinet (hélice ou électromagnétique) réparties en plusieurs points de la section du chenal. Plus récemment, l'arrivée des *Accoustic Doppler Current Profilers* (ADCP) ont considérablement facilité ces mesures, rendant possible l'estimation de débits sur les grandes rivières comme la Narayani. Ce matériel a été utilisé durant la mousson 2011 dans les bassins de la Narayani et de la Kosi et couplé par l'échantillonnage de sédiments en profondeur. Pour plus d'informations sur le fonctionnement des ADCPs, nous conseillons les lecteurs de se reporter aux rapports de [Simpson 90, Adler 01, Muste 04, Oberg 02, Teledyne 14].

Principes

La mesure de courant par ADCP repose sur la mesure du temps de retour d'ondes acoustiques. Le signal directionnel émis par l'ADCP est réfléchi sur les particules de la colonne d'eau avec un déphasage par « effet Doppler ». La mesure du déphasage des fréquences permet le calcul de la vitesse des particules (cf. figure 3.2.1) selon la formule suivante : $\nu r = 2 \cdot \nu e \cdot \frac{Up}{C} \cdot \cos(\theta)$, avec νr fréquence des ondes retour, νe fréquence des

ondes émises, Up vitesse des particules et C célérité des ondes dans le milieu (1450 m/s dans l'eau), θ l'angle entre la direction des ondes et la vitesses des particules.

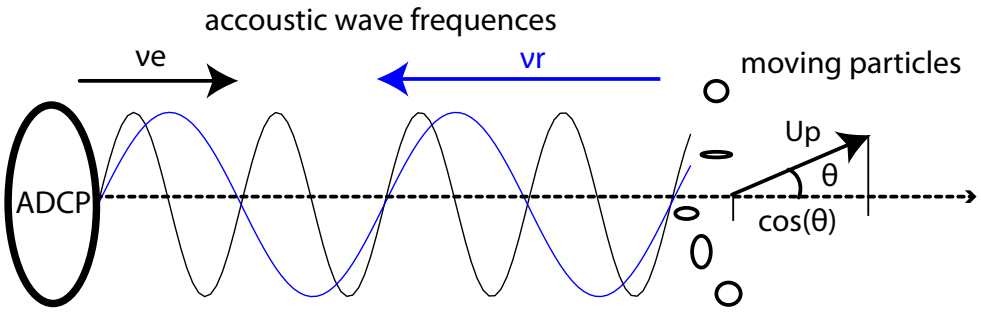

FIGURE 3.2.1 – Schéma de principe de la mesure de vitesse de courant par ADCP.

Nous avons utilisé un ADCP de modèle Rio Grande 1200 kHz (Teledyne) qui appartient à l'équipe de F. Métivier de l'IPG Paris. Il est composé de 4 *transducers* qui chacun émet et reçoit le signal. La vitesse des particules est calculée à partir de trois *transducers*, le quatrième vérifie la cohérence du signal. L'angle d'émission entre 2 transducers est de 20°, ainsi le volume sondé par un *ping* (une émission) est dépendant de la profondeur et peut représenter une surface équivalente d'une dizaine de mètres carrés au fond (cf. figure 3.2.2).

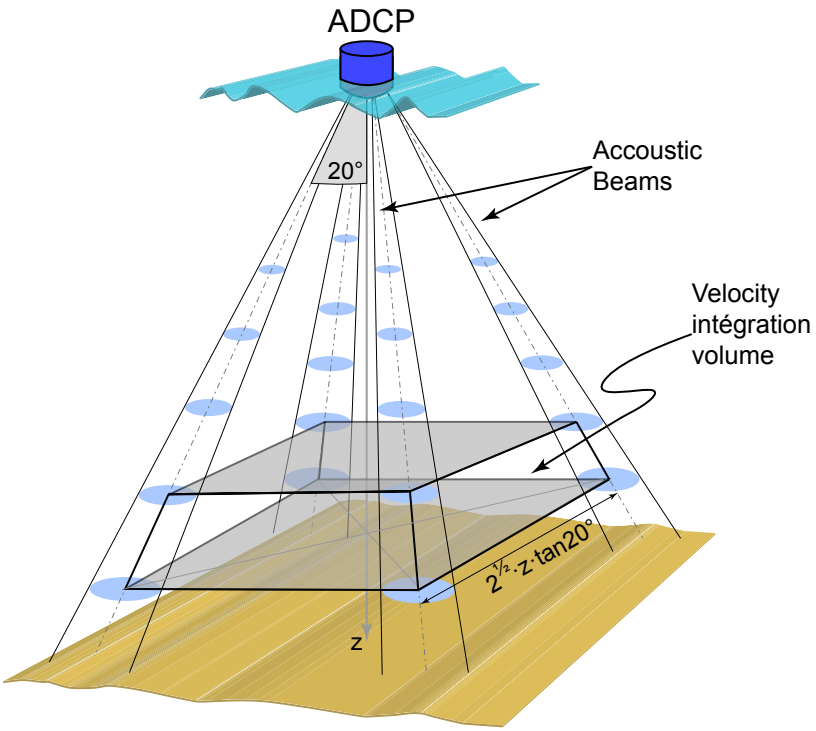

FIGURE 3.2.2 – Volumes sondés par l'ADCP lors d'un *ping*. D'après [Lupker 11a]

Pratique

L'ADCP a été adapté à la structure souple du zodiac de l'IIT Kanpur grâce à un cadre de tubes en acier, qui permettait de relever l'ADCP en dehors des mesures. L'ADCP n'était immergé que lors des mesures afin d'éviter sa détérioration par contact avec le fond et pour permettre de remonter le courant en annulant la trainée qu'il génère. Les mesures de débit ont été effectuées en traversant la rivière de part en part en essayant de maintenir une trajectoire la plus rectiligne possible. L'exercice s'est révélé assez difficile mais les résultats étaient exploitables. Sur la Narayani, l'ADCP était couplé à un GPS et un écho-sondeur de type Tritech-PA200. Le GPS a permis à l'ADCP de calculer les vitesses et les positions selon un référentiel terrestre. L'écho-sondeur a permis de détecter avec une grande précision le fond (angle solide 12° et résolution 1 mm). Ces deux instruments généralement accessoires se sont révélés indispensables. La détection du fond par l'ADCP était rendue impossible par les conditions fortes de courant, l'ADCP a donc utilisé le référentiel GPS pour calculer les vitesses de l'eau et les données de l'écho-sondeur pour

la détection du fond. L'utilisation de l'écho-sondeur n'a pas empêcher des erreurs de détection du fond qui nous ont obligé à re-traiter les données.

FIGURE 3.2.3 – Adaptation de l'ADCP sur le bateau.
À gauche, l'ADCP, ici remonté, est fixé à une structure adaptée au bateau par le tube en acier. À droite, embarcation équipée du matériel : le cadre qui supporte l'ADCP (centre du zodiac) et l'échantillonneur (proue du zodiac).

Traitement des données

L'ADCP est fourni avec un logiciel d'interface facile d'utilisation qui permet l'acquisition et le traitement des données. Ce logiciel, comme ceux de ses concurrents, fonctionne grâce à une bibliothèque de routines algorithmiques communes. Dans la plupart des cas, les données ainsi traitées suffisent pour obtenir le calcul du débit de la rivière. Dans notre cas, des erreurs de détection du fond ont provoqué de nombreux « vides » dans le relevé des vitesses des sections (cf. figure 3.2.4). Ces mesures n'avaient pas été effectuées avec de telles vitesses de courant (> 7 m/s) à notre connaissance. Ces données ont été corrigées et les débits recalculés à partir de la modélisation des vitesses. La cohérence de l'estimation des débits mesurés par ADCP et des débits calculés à partir de la hauteur d'eau et de la courbe de tarage à la station DHM renforce la validité des deux approches. Pour de plus amples détails nous vous invitons à vous reporter au chapitre 5.

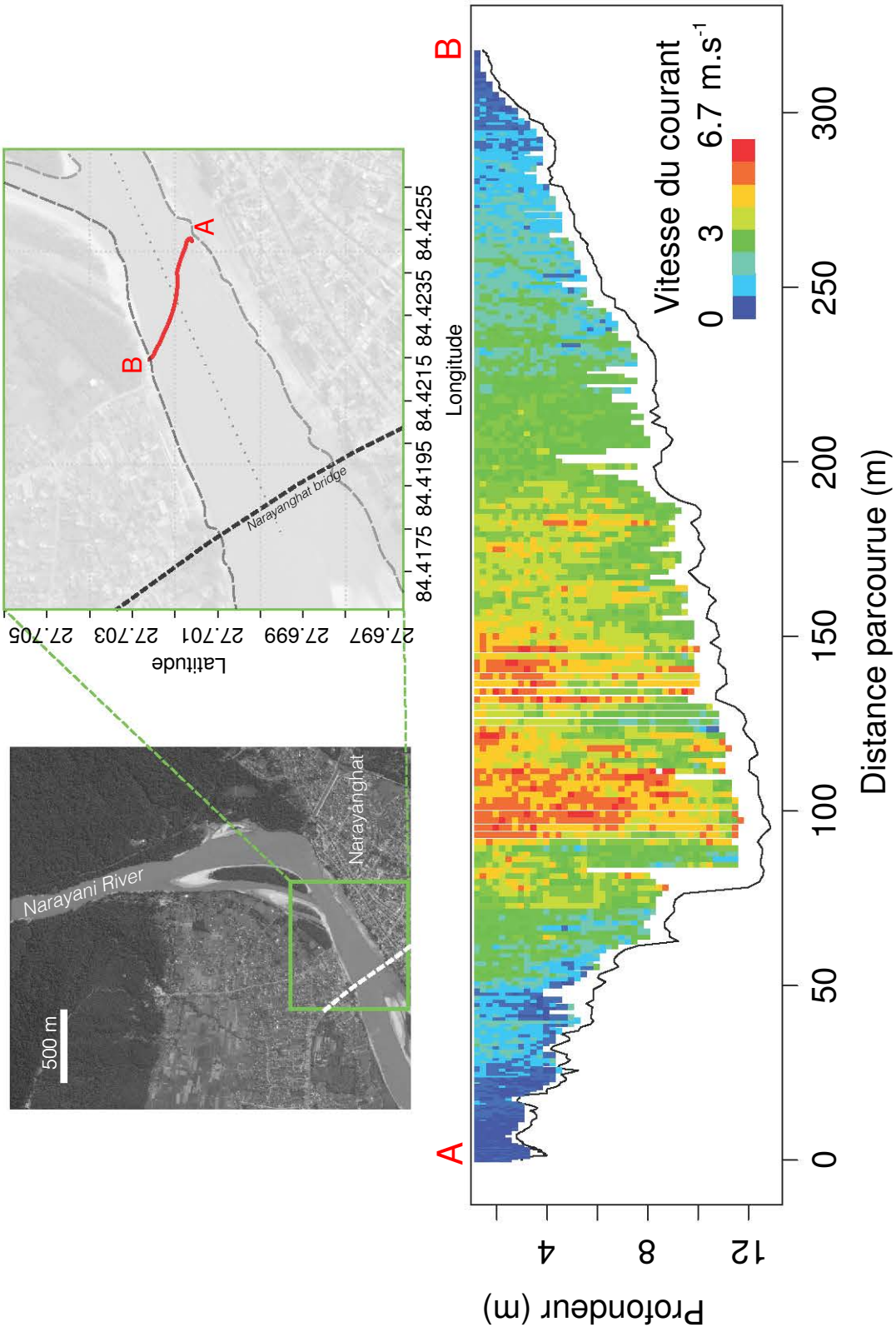

FIGURE 3.2.4 – Mesure de courant par ADCP sur la Narayani à Narayanghat lors de la mousson 2011 (débit mesuré : 5450 m^3/s par ADCP, 5300 m^3/s par la station DHM)

3.2.2 Sondages électriques verticaux (VES) de la plaine du Gange.

En Octobre 2011 sur une période d'un mois, j'ai participé aux relevés géophysiques des sondages électriques verticaux visant à caractériser les dépôts sédimentaires de sub-surface de la Gandak et de la Kosi.

Le sondage électrique vertical est utilisé depuis longtemps pour la détection et la caractérisation des aquifères, la prospection des minéralisations d'intérêt économique [Loke 99], ou encore la détection de constructions enfouies lors de fouilles archéologiques [Balkaya 08, Sinha 13b]. Cependant il n'avait été que peu appliqué dans ce type d'environnement alluvial, où les résistivités des couches lithologiques sont très proches [Loke 99]. Cette technique est souvent associée à d'autres techniques comme l'ESRI pour accéder à la lithostratigraphie (e.g. [Bersezio 07]). Le sondage électrique vertical a été précédemment utilisé en Inde pour caractériser la géométrie des alluvions de sub-surface de la plaine du Gange [Yadav 10, Sinha 10, Sinha 13b]. Notre objectif était d'établir les caractéristiques des sédiments de sub-surface (0 à 100 m de profondeur) et ainsi nous permettre de guider le choix de la localisation des forages de la plaine de la Gandak. Deux préoccupations majeures le justifiaient :

1. Éviter les barres de galets présentes au piémont de la chaîne qui peuvent être retrouvées à 15-20 km du MFT [Dubille 15], qui auraient rendu impossible la poursuite du forage carotté plus profond. Ce cas a été rencontré sur la Kosi et a arrêté les forages sur la partie proximale du mégafan.
2. S'assurer de la présence de paléochenaux en profondeur correspondant à la Gandak, afin de documenter l'érosion passée du Népal central et son évolution.

FIGURE 3.2.5 – Dispositif de sondage électrique vertical utilisé pour la détermination des dépôts sédimentaires de sub-surface.
Le dispositif utilisé exploite la méthode Schlumberger. Il est ici installé dans un champ de riz fraîchement fauché près de Bettiah dans la plaine de la Gandak, Nord Bihar, Inde.

Principe de fonctionnement du sondage électrique vertical.

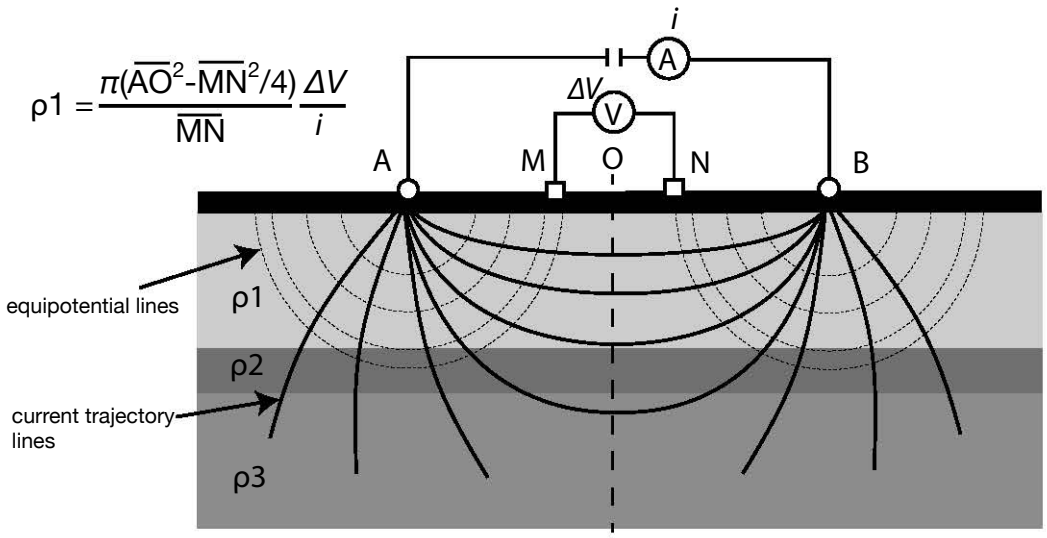

FIGURE 3.2.6 – Schéma de principe de la méthode de sondage électrique Schlumberger.

Le sondage électrique vertical par méthode Schlumberger permet de calculer la résistivité des couches lithologiques en profondeur et leurs épaisseurs grâce à l'inversion des courants mesurés aux électrodes à différentes distances d'écartement (cf. figure 3.2.6). Par écartement progressif des électrodes, la profondeur des terrains sondés augmente, permettant ainsi de sonder les couches de plus en plus profondes. La propagation en profondeur maximale correspond à environ 1/3 de la distance entre électrode d'injection et de réception, soit dans notre cas environ 100 m (écartement de 400 m des électrodes). Les différences de potentiels et courants mesurés en surface permettent de calculer la résistivité de la couche sous-jacente (cf. figure 3.2.6). Les gammes de résistivités des lithologies sont connues et de nombreux abaques existent (cf. figure 3.2.7).

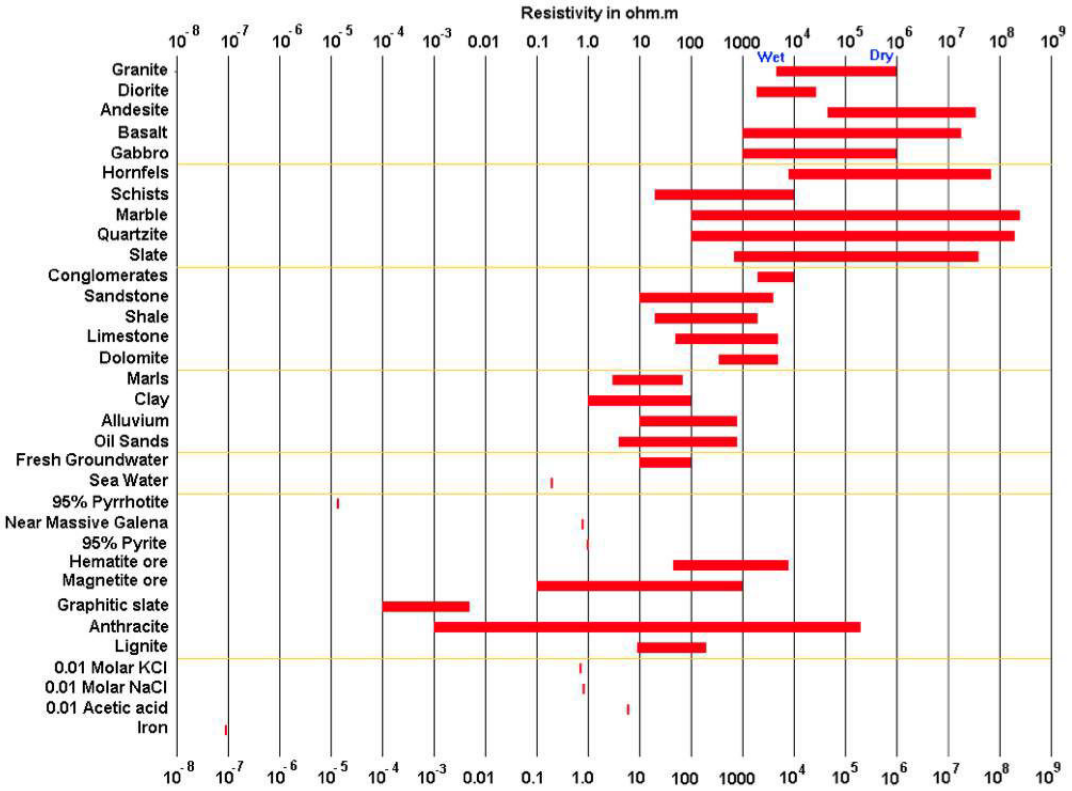

FIGURE 3.2.7 – Gamme de résistivités des différentes lithologies. Extrait de [Loke 99]

Cela se complexifie en profondeur puisque la résistivité inversée dépend des multiples couches traversées. Des algorithmes permettent d'inverser les courbes de résistivités en fonction de la profondeur, et de nombreux logiciels proposent même de déterminer automatiquement le modèle et le nombre de couches pour obtenir la meilleur adéquation par méthode des moindres carrés. Nous disposions de relevés de forages hydrogéologiques proches des sondages, ce qui a permis de calibrer empiriquement les données de résistivités (cf. figure 3.2.8). Grâce à ces comparaisons, des modèles sédimentologiques des alluvions ont été proposés (cf. [Sinha 14] en annexe de ce manuscrit).

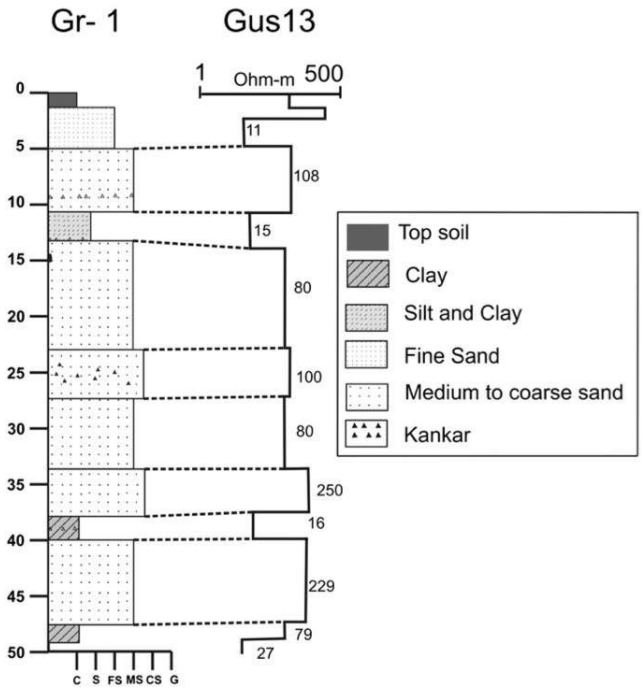

FIGURE 3.2.8 – Calibration empirique des résistivités des différentes lithologies de subsurface de la plaine de la Gandak. D'après [Sinha 14]

3.3 Méthodes analytiques

Toutes les méthodes utilisées pour ce travail ne seront pas présentées ici. Celles-ci sont décrites dans les parties méthodes dans les chapitres suivants. Nous présenterons ici les analyses des isotopes stables et la méthode de destruction de la MO par plasma préalable à l'analyse des hydroxyles (OH) d'hydratation des silicates.

3.3.1 Analyses des carbonates

Une partie des analyses des carbonates dans les sédiments a été obtenue par méthode conventionnelle sur ligne d'extraction en verre sous vide : les concentrations ont été mesurées par mesure manométrique du CO_2 issu de la calcite de la dissolution par de l'acide phosphorique à 50°C pendant 3h, puis du CO_2 issu de la dolomite en poursuivant la réaction à 25°c selon [Sheppard 70, Galy 99a]. Les mesures isotopiques au spectromètre de masse à VG-602 modifié à introduction gazeuse du laboratoire des isotopes stables du

CRPG
La majorité des mesures ont été acquises par dissolution par de l'acide phosphorique à 70°C dans un passeur automatique de type *gasbench*, et l'analyse du CO_2 par un spectromètre de masse MAT253 après correction des fractionnements analytiques [Sheppard 70]. Ces analyses donnent les concentrations et compositions isotopiques des carbonates totaux, sans possibilité de séparation de la calcite et de la dolomite. L'incertitude de mesure est de $\pm$ 1.5% pour les concentrations en carbonates, et inférieure à $\pm$ 0.2 ‰ pour la composition isotopique δ^{13}C du carbone.

3.3.2 Analyses élémentaires : isotopie du Carbone organique C_{org}, et des Hydroxyles d'hydratation H_2O+

Les mesures des concentrations et compositions isotopiques du C et de l'H ont été effectuées par TC/EA *High Temperature Conversion Elemental Analyser* (de type EuroVector) couplé à un spectromètre de masse IRMS *Isotope Ratio Mass Spectrometer* (de type Isoprime).

Principe

Le principe de l'analyse élémentaire est résumé en figure3.3.1. Les échantillons sont pesés dans leur capsule d'étain et introduits dans les passeurs qui ont été modifiés afin de maintenir les échantillons dans une atmosphère d'He et d'éviter les contacts avec l'air et l'humidité ambiante. Successivement, chaque échantillon tombe dans le réacteur où il subit une pyrolyse flash ce qui produit des mélanges gazeux : CO_2, H_2O etc. dans le cas de l'analyse du C, et H_2, CO etc. dans le cas de l'analyse de l'H. Les gaz produits sont entraînés par le gaz vecteur (He) et séparés selon leurs masses moléculaires par chromatographie en phase gazeuse, *Gaz Chromatography* (GC). Les temps d'arrivée des cortèges gazeux sont calibrés au préalable et seuls les spectres du CO_2 ou du H_2 de l'échantillon sont enregistrés. Les gaz sont ionisés dans la source du spectromètre et séparés par l'aimant selon leurs rapports « masse sur charge » (m/z), ce qui permet de mesurer l'intensité de chacun des isotopes sur chacune des deux cages de Faraday : dans le cas du C : $^{12}CO_2$ (m=44) contre $^{13}CO_2$ (m=45) ; dans le cas de l'H : H_2 (m=2) contre H-D (m=3). Les aires des masses principales (44 pour CO_2 ou 2 pour H_2) sont intégrées pour calculer les concentrations. La concentration en carbone organique totale (TOC) est communément exprimée

en % poids. La concentration en OH est notée H_2O+ et est exprimée en % poids. La méthode nécessite un *dual-inlet* : ces intensités sont comparées aux intensités mesurées avant chaque échantillon d'un gaz standard de composition isotopique connue, ce qui permet de s'affranchir des fractionnements instrumentaux. La méthode de mesure n'est donc pas absolue mais relative, les abondances isotopiques sont déterminées par le calcul du rapport des intensités mesurées dans l'échantillon sur celles du gaz standard. La mesure de l'H_2 nécessite une correction de la production des ions H_3^+dans la source, linéairement dépendante de l'intensité ; et calibrée avant analyse à partir du gaz standard. Les mesures sont effectuées entre 10 et 13 nA, l'influence du blanc est négligeable à ces intensités. Afin de s'affranchir du fractionnement dans l'étape de pyrolyse, les échantillons sont passés avec des standards internes (dans le cas du carbone : sable du Brahmapoutre « BFSd », sucre blanc industriel « sucre Daddy », sédiment de la Baie du Bengale « ODP-129-802A » ; dans le cas de l'hydrogène : muscovite « MuscD65 », phlogopite « Mica-Mg », sédiment de la Baie du Bengale « SO188 ») qui avaient été calibrés avec des standards internationaux (dans le cas du carbone : sols NIST SRM2711, IGCE GSS-1, USGS GX-R-2, sédiment de rivière IGCE GSD-12 et shale USGS Sco-1, polyéthylène IAEA CH7) ; dans le cas de l'hydrogène : IAEA huile NBS22, biotite NBS30, et polyéthylène CH7, et une argile USGS Wyoming Na-Montmorillonite SWy-2) d'après [Galy 2007] et [Lupker 12b]. Les standards internationaux sont régulièrement analysés afin de confirmer l'homogénéité des standards internes. Les compositions isotopiques de carbone et OH sont exprimées en unités δ notées δ^{13}C et δD. La notation δ correspond à :

$$\delta X = 1000 \times \left(\frac{Rsample - Rstandard}{Rstandard}\right)$$

où le rapport $R = \frac{Isotope\,lourd}{Isotope\,léger}$ avec isotope lourd sur léger :^{13}C/^{12}C ou D/H.

Les incertitudes de mesures sont TOC ± 0.03 %, δ^{13}C ± 0.05 ‰, H_2O+ ± 0.1%, δD ± 2‰.

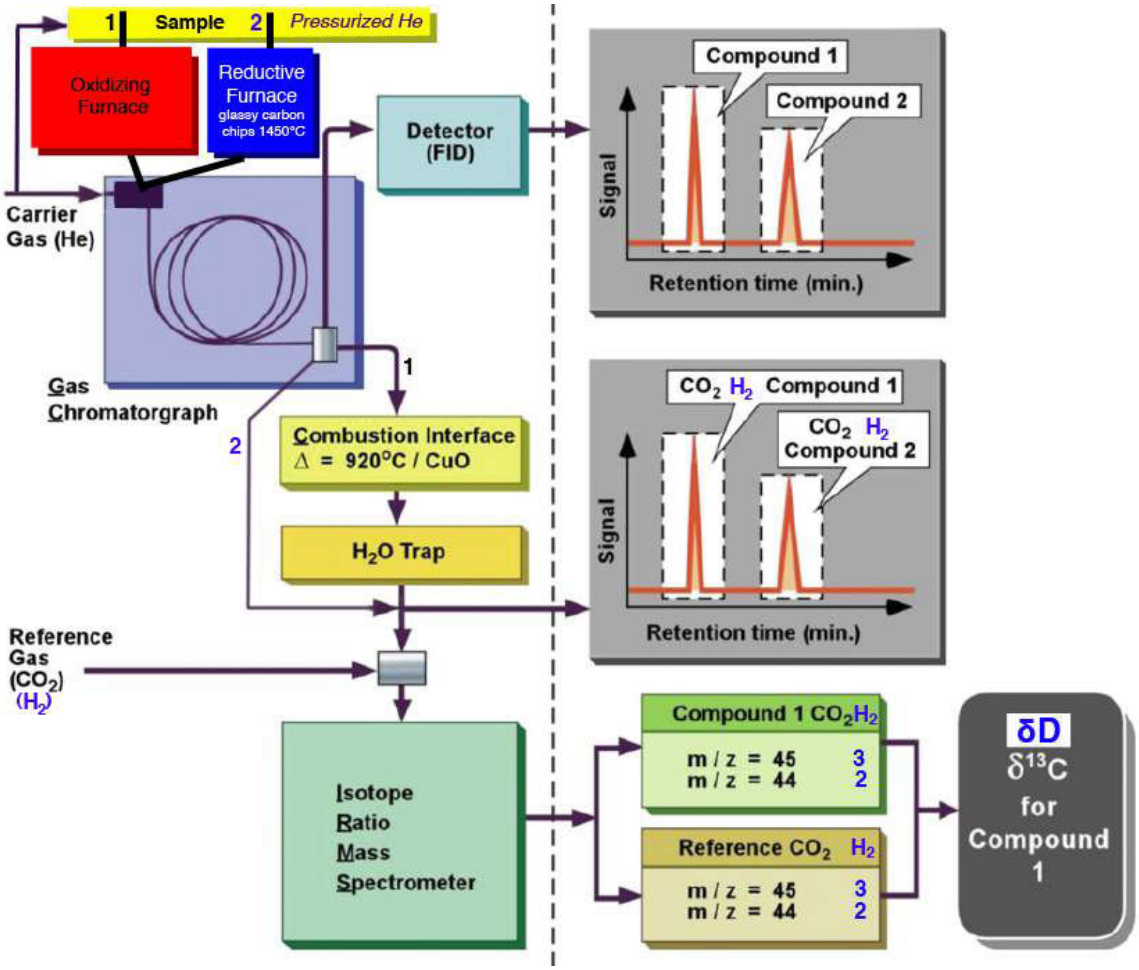

FIGURE 3.3.1 – Schéma analytique de la mesure isotopique du carbone (circuit 1) et de l'hydrogène (circuit 2) par EA-IRMS.

Prétraitements

Des étapes de prétraitements sont nécessaires dans les deux types d'analyses.
Avant la mesure du carbone organique, les sédiments des rivières himalayennes sont débarrassés de leur contenu en carbonates par dissolution à l'acide chlorhydrique HCl (4% poids) à 80°C pendant 45 min selon [Galy 2007].
Dans le cas de la mesure de l'hydrogène, le prétraitement est plus long. En effet, une partie des OH contenus dans l'échantillon est issue de l'eau adsorbée à la surface des minéraux ou de l'eau interfoliaire qui sont connues pour rapidement s'équilibrer isotopiquement avec l'environnement [Savin 70]. Une pré-étape de déshydratation est donc nécessaire afin de re-

tirer les molécules d'eau « non-liées ». Les temps et températures de déshydratation ne font pas consensus dans la littérature : les temps varient de 2-3h à 20 jours et les températures de 70°C à 450°C [Savin 70, Girard 96, Gilg 96, Yapp 97, Gilg 00, Gong 07, Garzione 08]. [Lupker 12b] proposent une déshydratation pendant 48h à 120°C sous vide pour les sédiments himalayens afin de pouvoir être comparés aux roches sources et sédiments himalayens précédemment analysés [France-Lanord 87, Lupker 12b]. Nous avons scrupuleusement suivi ce protocole dans les analyses présentées dans ce manuscrit. Après pesée, les échantillons sont déshydratés et ensuite introduits dans le passeur hermétique dans une boîte à gants ou l'hygrométrie est maintenue à moins de 3%. Le passeur est ensuite immédiatement adapté sur le TC/EA et pompé avant d'être placé sous atmosphère d'He. Ces étapes contraignantes doivent être rigoureusement suivies car la réhydratation par adsorption d'eau atmosphérique peut survenir en quelques minutes et provoquer le shift vers des compositions isotopiques plus négatives de -15‰ [Bauer 14].

3.3.3 Isotopie de l'hydrogène et altération

Lors de l'altération, l'hydratation des phases primaires (par exemple la vermiculitisation des biotites) et l'intégration des OH dans le réseau cristallin des phases néoformées sont hérités des conditions d'altération et des compositions de l'eau environnementale. La composition isotopique d'altération est donc enregistrée moyennant un fractionnement isotopique dépendant de la température [Savin 70, Savin 98]. Les isotopes de l'hydrogène et de l'oxygène mesurés dans les phases d'altération ont permis ainsi de remonter aux conditions de températures et compositions de l'eau environnementale, i.e. aux conditions d'altérations dans les sols et les sédiments marins (e.g. [Lawrence 72, France-Lanord 88, Girard 97, Gilg 00, Melchiorre 11, Lupker 13]). Dans le bassin du Gange, les isotopes de l'H et de l'O permettent donc de remonter aux conditions d'altération et potentiellement de tracer les provenances des sédiments. Le contraste des compositions isotopiques des précipitations et de l'eau des rivières observé entre le Nord (δD de -138‰) et le Sud (δD de ~ -65‰ pour les rivières du front) du bassin himalayen [Gajurel 06] permet théoriquement de tracer les provenances des phases d'altération. Ainsi, le traçage des conditions d'altérations et des provenances peut être envisagé à partir des analyses des OH silicatés des sédiments de rivière. Nous avons travaillé sur sédiment total pour quantifier les provenances dans les sédiments.

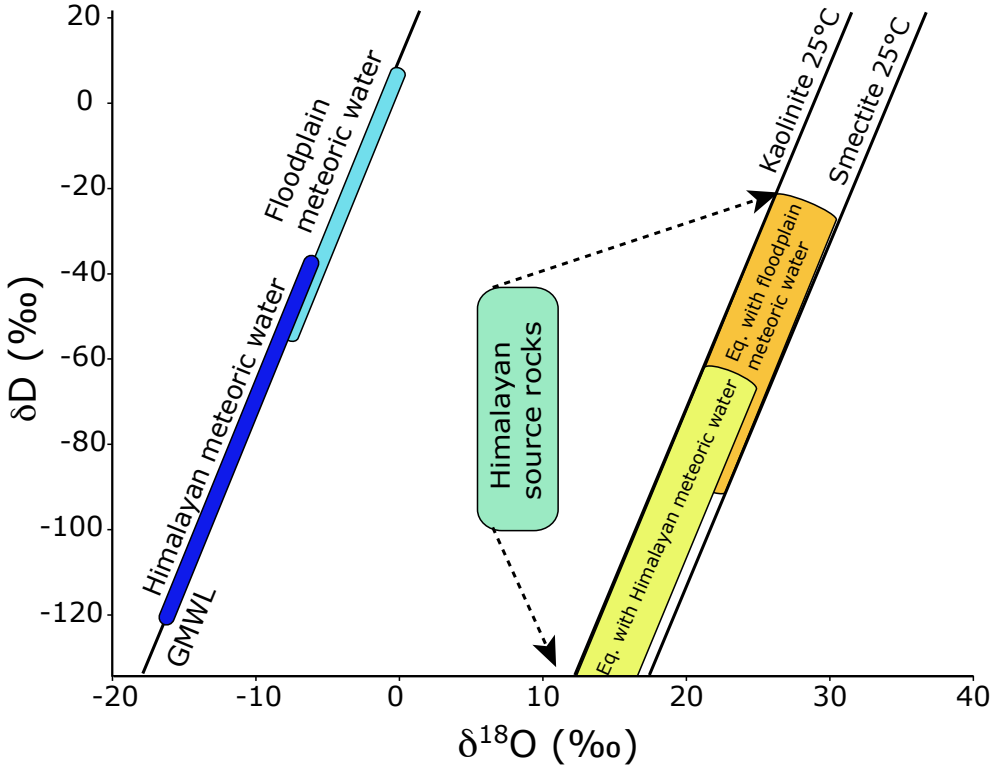

FIGURE 3.3.2 – δD et δ^{18}O des roches sources himalayennes [France-Lanord 87] comparées aux argiles secondaires : smectites et kaolinites en équilibre avec les précipitations du système himalayen. Extrait de [Lupker 11a] modifié d'après [Bouquillon 90].
Compositions des argiles d'après [Lawrence 72, Yeh 76, Yeh 80], des eaux météoriques de la chaîne d'après [Garzione 00, Gajurel 06].

3.3.4 Méthode de destruction de la MO (MO) par plasma-ashing.

Dans les sols, la mesure d'hydratation et des isotopes des OH des silicates est rendue difficile par la présence de MO car elle contient de grande quantité d'hydrogène. En effet, la concentration de carbone organique dans les sols peut atteindre plusieurs dizaines de % lorsque l'hydratation des silicates ne dépasse que rarement les quelques %. Les quantités d'hydrogène lié à la MO varient selon les composés, les rapports H/C des composés dans les sols de 0.5 à 2 [Rice 91] (cf. figure 3.3.3).

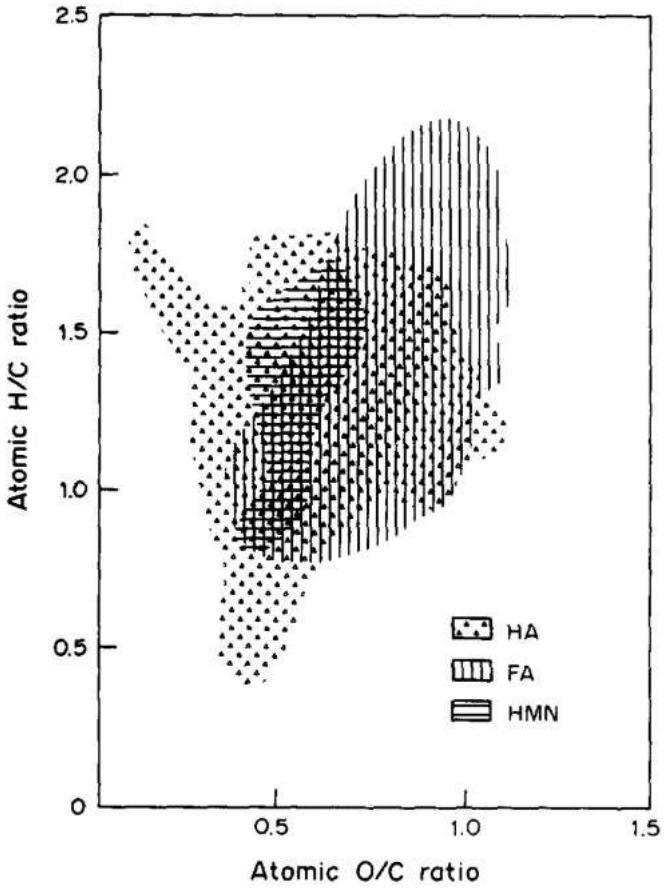

FIGURE 3.3.3 – Rapports élémentaires H/C et O/C dans les composés organiques de sol (n=650)[Rice 91]
HA : acides humiques (n=410), Fa : acides fulviques (n=214), HMN : humines (n=26).

Classiquement, la MO des sols est oxydées en solution aqueuse contenant du H_2O_2 ou du NaOCl à température ambiante. Nous souhaitions éviter ce type de traitements agressifs pour les phases d'altération (néo-formées) mal cristallisées . De plus nous avons été convaincus que ces méthodes souffraient parfois de rendements faibles avec seulement 30%-70% de destruction [Mikutta 05], probablement dus à des effets de protection de la MO par les phases minérales [Mikutta 06, Mikutta 11].

La méthode de destruction de la MO par plasma à oxygène basse température ou *plasma-ashing* a donc été envisagée. Cette technique a été récemment comparée aux méthodes classiques par destruction chimique [Lebeau 14]. Ces auteurs ont utilisé des mélanges de roches et de masses variables de levures utilisées comme substitut de MO, et ont

mesuré l'effet de la technique sur la composition isotopique la sidérite pédogénique des échantillons. Leurs conclusions sur les rendements de destruction de la MO recommandent cette méthode. Pour nos applications, nous devions au préalable vérifier l'efficacité avec de la véritable litière organique de sol, et surtout vérifier l'effet de la méthode sur les concentrations H_2O+ et compositions isotopiques δD des OH liés.

Principe

Le *plasma-ashing* est une méthode utilisée pour stériliser les instruments de chirurgie. Un flux faible d'oxygène est envoyé dans un tube en verre pompé sous vide et un plasma y est généré par générateur Haute-Fréquence 3.3.4.

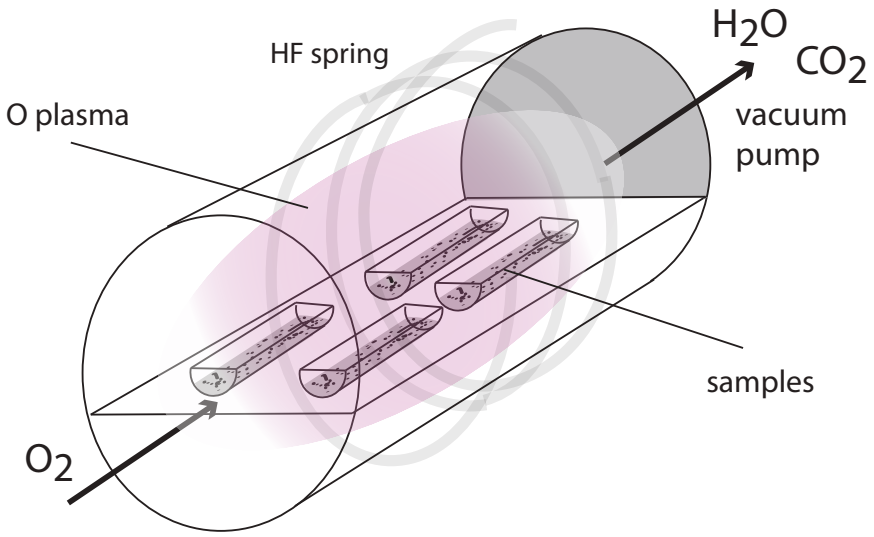

FIGURE 3.3.4 – Schéma de principe du *plasma-asher*.

Le plasma est constitué des noyaux et électrons libres des atomes d'oxygène. Les noyaux très oxydants viennent oxyder les composés organiques qui sont alors pompés sous forme de gaz H_2O, CO_2, SO_2, NO_2 etc. Les OH intra-cristallins des silicates ne sont pas affectés par cette oxydation et la température en surface reste relativement faible <100°c. Les échantillons sont placés dans des nacelles semi-tubulaires en silice qui reposent sur une plaque en verre afin de les placer de manière optimale au centre du plasma.

Protocoles

Nous avons choisi de réaliser 3 séries (*batch*) de tests afin de mesurer : l'efficacité de la méthode sur la destruction de la MO, et son innocuité sur les concentrations et compositions isotopiques :

1. Le premier *batch*, comporte des sols du Haut-Himalaya (bassins de la Khudi et du Langtang) dont les TOC varient de 0.4% à 19%. Les nacelles ont été remplies sur toute la longueur sur une épaisseur de 3 mm. Les échantillons ont été remués toutes les 12 h avec une spatule en inox préalablement nettoyée avec de l'acétone. La durée de cette expérience exploratoire a été limitée à 160 h.
2. Le second *batch* comporte des sols du Haut-Himalaya comparables au *batch* 1 dont les TOC varient de 0.2% à 9.7%. Cette fois, les nacelles n'ont été remplies que sur 1 mm d'épaisseur et remuées seulement aux moments des prélèvements des échantillons. La durée de cette expérience a été poussée à 1300 h. L'objectif était de déterminer l'effet de remuer régulièrement sur la vitesse de dégradation et les limites de dégradation pour des temps d'expérience très longs.
3. Le troisième *batch* comporte une smectite industrielle standard SWy-2, deux matières en suspension de la Narayani et un sédiment issu de glacier. L'objectif était de tester la nécessité de procéder à cette dégradation sur les sédiments de rivière, et de vérifier l'impact de la technique sur la composition isotopique d'un standard et d'un sédiment glaciaire, dont la composition isotopique est très différente de la roche source dont il est issu. La durée de l'expérience a été poussée à 973 h.

Résultats

Les résultats du protocole 1 sont reportés dans le tableau 3.1 et présentés en figure 3.3.5.

Sample #	Pf	type	Exp. Time	aliquot	**TOC**	**δ13Corg**	TOC/TOC0	δ13C-δ13C0	**H2O+Sil**	**δD**	H2O+/H2O+0	δD-δD0
	[%]		[Hours]		**[%]**	**[‰]**			**[%]**	**[‰]**		
CA907_155_175	11.85	soil	0	1PO2-I-0	**0.44**	**-22.2**	1.00	0.0	**8.84**	**-82.9**	1.00	0.0
			24	1PO2-I-1	**0.44**	**-23.8**	1.00	-1.6	**9.26**	**-84.5**	1.05	-1.6
			48	1PO2-I-2	**0.35**	**-23.5**	0.79	-1.3	**9.02**	**-85.4**	1.02	-2.5
			93	1PO2-I-3	**0.29**	**-24.7**	0.66	-2.4	**9.22**	**-86.1**	1.04	-3.2
			122	1PO2-I-4	**0.43**	**-26.8**	0.96	-4.6	**8.65**	**-90.7**	0.98	-7.8
			161	1PO2-I-5	**0.44**	**-22.1**	1.00	0.1	**7.74**	**-84.3**	0.88	-1.4
CA907_90_110	9.45	soil	0	1PO2-II-0	**1.19**	**-21.9**	1.00	0.0	**6.18**	**-87.3**	1.00	0.0
			24	1PO2-II-1	**1.12**	**-22.0**	0.93	-0.1	**6.21**	**-86.4**	1.00	0.9
			48	1PO2-II-2	**1.00**	**-22.0**	0.84	-0.1	**6.00**	**-86.9**	0.97	0.5
			93	1PO2-II-3	**0.80**	**-21.9**	0.67	0.1	**6.31**	**-86.1**	1.02	1.2
			122	1PO2-II-4	**0.82**	**-22.3**	0.69	-0.4	**6.37**	**-91.9**	1.03	-4.5
			161	1PO2-II-5	**0.69**	**-27.0**	0.58	-5.1	**5.71**	**-93.7**	0.92	-6.3
CA926_40_60	8.28	soil	0	1PO2-III-0	**1.29**	**-28.2**	1.00	0.0	**3.28**	**-105.8**	1.00	0.0
			24	1PO2-III-1	**1.13**	**-28.8**	0.88	-0.5	**3.11**	**-100.9**	0.95	4.9
			48	1PO2-III-2	**0.98**	**-29.3**	0.76	-1.1	**2.96**	**-93.1**	0.90	12.7
			93	1PO2-III-3	**1.59**	**-30.3**	1.24	-2.1	**2.70**	**-98.8**	0.82	7.1
			122	1PO2-III-4	**1.15**	**-29.8**	0.89	-1.6	**2.47**	**-105.1**	0.75	0.7
			161	1PO2-III-5	**0.68**	**-30.4**	0.53	-2.2	**2.22**	**-104.1**	0.68	1.8
CA929_10_15	18.94	soil	0	1PO2-IV-0	**7.10**	**-24.3**	1.00	0.0	**6.73**	**-120.2**	1.00	0.0
			24	1PO2-IV-1	**5.32**		0.75		**5.49**	**-110.9**	0.82	9.2
			48	1PO2-IV-2	**4.87**	**-23.7**	0.69	0.6	**4.80**	**-109.6**	0.71	10.6
			93	1PO2-IV-3	**3.85**	**-23.8**	0.54	0.5	**3.79**	**-89.4**	0.56	30.8
			122	1PO2-IV-4	**3.45**	**-24.4**	0.49	-0.1	**3.52**	**-115.4**	0.52	4.8
			161	1PO2-IV-5	**2.13**	**-24.2**	0.30	0.1	**2.68**	**-116.2**	0.40	4.0
CA916_30_40	22.99	soil	0	1PO2-V-0	**8.12**	**-26.4**	1.00	0.0	**9.99**	**-90.0**	1.00	0.0
			24	1PO2-V-1	**6.35**	**-26.3**	0.78	0.1	**8.29**	**-81.0**	0.83	9.0
			48	1PO2-V-2	**5.00**	**-26.1**	0.62	0.3	**6.99**	**-79.7**	0.70	10.3
			93	1PO2-V-3	**3.68**	**-26.2**	0.45	0.2	**5.76**	**-86.5**	0.58	3.5
			122	1PO2-V-4	**2.31**	**-25.9**	0.28	0.5	**4.60**	**-92.3**	0.46	-2.3
			161	1PO2-V-5	**1.45**	**-26.5**	0.18	-0.1	**3.44**	**-88.5**	0.34	1.5
CA10158B	18.33	soil	0	1PO2-VI-0	**7.00**	**-25.6**	1.00	0.0	**6.93**	**-89.7**	1.00	0.0
			24	1PO2-VI-1	**4.90**	**-25.7**	0.70	0.0	**5.20**	**-82.1**	0.75	7.6
			48	1PO2-VI-2	**3.05**	**-25.7**	0.43	0.0	**4.06**	**-78.4**	0.59	11.2
			93	1PO2-VI-3	**1.51**	**-25.4**	0.22	0.2	**4.77**	**-89.4**	0.69	0.3
			122	1PO2-VI-4	**1.56**	**-27.4**	0.22	-1.8	**2.60**	**-101.0**	0.37	-11.3
CA10158A	24.42	soil	0	1PO2-VII-0	**9.99**	**-26.7**	1.00	0.0	**9.66**	**-92.7**	1.00	0.0
			24	1PO2-VII-1	**7.19**	**-26.6**	0.72	0.0	**7.01**	**-86.7**	0.73	6.0
			48	1PO2-VII-2	**3.85**	**-26.3**	0.39	0.4	**4.78**	**-87.9**	0.49	4.8
			93	1PO2-VII-3	**2.64**	**-26.6**	0.26	0.0	**3.48**	**-88.9**	0.36	3.9
CA10159A	44.52	soil	0	1PO2-VIII-0	**19.48**	**-28.5**	1.00	0.0	**13.78**	**-96.2**	1.00	0.0
			24	1PO2-VIII-1	**14.25**	**-28.1**	0.73	0.3	**12.68**	**-89.1**	0.92	7.1
			48	1PO2-VIII-2	**9.35**	**-27.9**	0.48	0.5	**7.83**	**-90.2**	0.57	6.0
			93	1PO2-VIII-3	**5.84**	**-27.6**	0.30	0.8	**5.70**	**-98.1**	0.41	-1.9
			122	1PO2-VIII-4	**2.68**	**-27.2**	0.14	1.2	**3.42**	**-86.7**	0.25	9.5

TABLE 3.1 – Résultats du test de destruction de la MO dans les sols suivant le protocole 1.

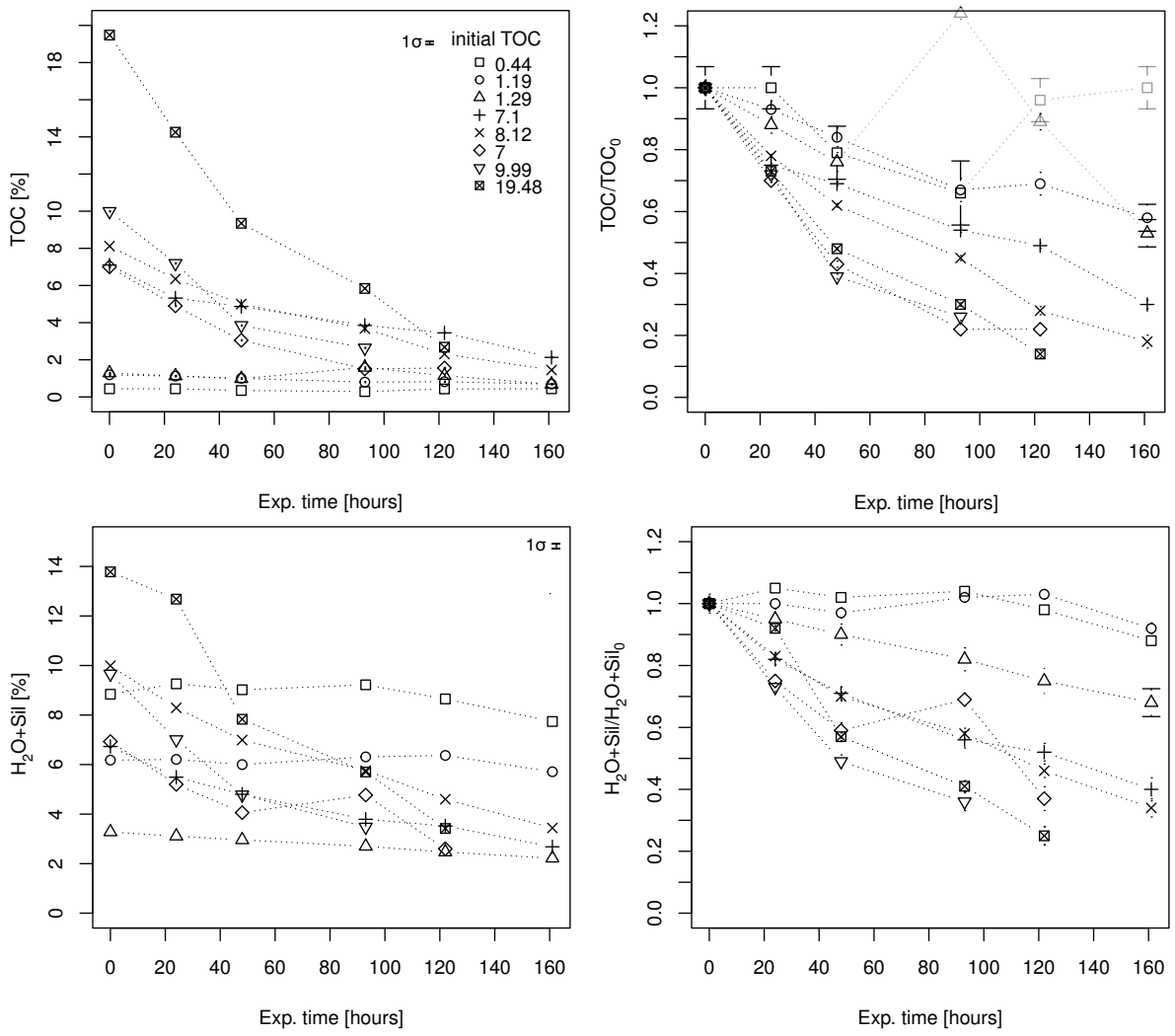

FIGURE 3.3.5 – Effet de la destruction de la MO dans les sols par plasma-ashing (suivant le protocole 1).

Sur les 160 h d'expériences, les TOC et H_2O+ des échantillons de sols diminuent continuellement. Les rendements de dégradation de la MO varient entre 14 % et 58 % pour des valeurs TOC initiales de 1.2 % à 19.5%. La dégradation semble plus complète pour les valeurs de TOC >1.3 %. Les valeurs finales et les vitesses de dégradation dépendent des valeurs TOC initiales. Les échantillons montrant une augmentation des TOC en fin d'expériences sont des échantillons contenant de faibles concentrations en MO. Ils ont certainement été contaminés lors des manipulations et ne sont pas pris en compte dans les

résultats. Parallèlement, les valeurs d'H_2O+ décroissent de manière similaire. Les échantillons présentant des concentrationsTOC initiales < 1.3 % observent une perte en H_2O+ de 8% à 32%, alors que les échantillons plus riches TOC de 7.1 à 19.5 % montrent des diminutions respectives de 60% à 75%. La méthode semble efficace pour les échantillons aux TOC > 1% et la perte en H_2O+ qui est observée pour ces échantillons semble correspondre à de l'hydrogène constitutif de la MO.

Les résultats du protocole 2 sont reportés dans le tableau 3.2 et présentés en figure 3.3.6.

Sample #	Pf [%]	type	Exp. Time [Hours]	aliquot	**TOC [%]**	**δ13Corg [‰]**	TOC/TOC0	δ13C-δ13C0	**H2O+Sil [%]**	**δD [‰]**	H2O+/H2O+0	δD-δD0
CA10158D	4.77	soil	0	2PO2-I-0	**0.21**	**-24.1**	1.00	0.0	**2.85**	**-97.1**	1.00	0.0
			26	2PO2-I-1	**0.17**	**-24.7**	0.81	-0.6	**2.85**	**-92.3**	1.00	4.9
			195	2PO2-I-2	**0.11**	**-24.7**	0.50	-0.7	**2.78**	**-97.7**	0.98	-0.5
			1300	2PO2-I-3	**0.06**	**-22.8**	0.26	1.2	**2.63**	**-97.1**	0.92	0.1
CA10157B	5.58	soil	0	2PO2-II-0	**0.77**	**-25.2**	1.00	0.0	**2.42**	**-89.9**	1.00	0.0
			26	2PO2-II-1	**0.64**	**-25.4**	0.84	-0.2	**2.47**	**-90.6**	1.02	-0.7
			195	2PO2-II-2	**0.38**	**-24.7**	0.49	0.5	**2.21**	**-87.7**	0.91	2.2
			1300	2PO2-II-3	**0.10**	**-24.2**	0.14	1.0	**1.95**	**-88.1**	0.81	1.8
CA10105E	12.29	soil	0	2PO2-III-0	**1.88**	**-25.2**	1.00	0.0	**4.35**	**-101.5**	1.00	0.0
			26	2PO2-III-1	**2.00**	**-25.8**	1.07	-0.6	**4.40**	**-90.4**	1.01	11.1
			195	2PO2-III-2	**1.21**	**-24.9**	0.65	0.3	**4.39**	**-93.8**	1.01	7.6
			1300	2PO2-III-3	**0.61**	**-24.7**	0.32	0.5	**3.93**	**-96.3**	0.90	5.2
CA10157A	12.22	soil	0	2PO2-IV-0	**3.78**	**-26.2**	1.00	0.0	**4.66**	**-96.1**	1.00	0.0
			26	2PO2-IV-1	**3.16**	**-26.0**	0.84	0.2	**4.04**	**-88.7**	0.87	7.4
			195	2PO2-IV-2	**2.34**	**-26.0**	0.62	0.2	**3.41**	**-87.7**	0.73	8.4
			1300	2PO2-IV-3	**0.79**	**-25.8**	0.21	0.4	**2.81**	**-88.9**	0.60	7.2
CA10155A	17.34	soil	0	2PO2-V-0	**6.97**	**-21.8**	1.00	0.0	**7.18**	**-97.1**	1.00	0.0
			26	2PO2-V-1	**6.30**	**-22.0**	0.90	-0.3	**6.65**	**-92.4**	0.93	4.7
			195	2PO2-V-2	**5.07**	**-22.3**			**5.14**	**-89.1**	0.72	8.1
			1300	2PO2-V-3	**2.16**	**-21.3**			**3.02**	**-85.7**	0.42	11.4
CA9290.05	18.42	soil	0	2PO2-VI-0	**8.98**	**-24.8**	1.00	0.0	**9.24**	**-116.4**	1.00	0.0
			26	2PO2-VI-1	**6.80**	**-25.1**	0.76	-0.2	**7.02**	**-110.8**	0.76	5.6
			195	2PO2-VI-2	**4.08**	**-24.6**	0.45	0.2	**4.93**	**-109.7**	0.53	6.7
			1300	2PO2-VI-3	**1.19**	**-24.5**	0.13	0.3	**2.06**	**-97.6**	0.22	18.8
CA10158A	24.42	soil	0	2PO2-VII-0	**9.73**	**-26.9**	1.00	0.0	**9.41**	**-93.6**	1.00	0.0
			26	2PO2-VII-1	**8.34**	**-26.8**	0.86	0.1	**8.25**	**-89.6**	0.88	4.0
			195	2PO2-VII-2	**5.49**	**-26.6**	0.56	0.3		**-68.6**		25.1
			1300	2PO2-VII-3	**1.55**	**-25.9**	0.16	1.0	**2.03**	**-90.4**	0.22	3.2

TABLE 3.2 – Résultats du test de destruction de la MO dans les sols suivant le protocole 2.

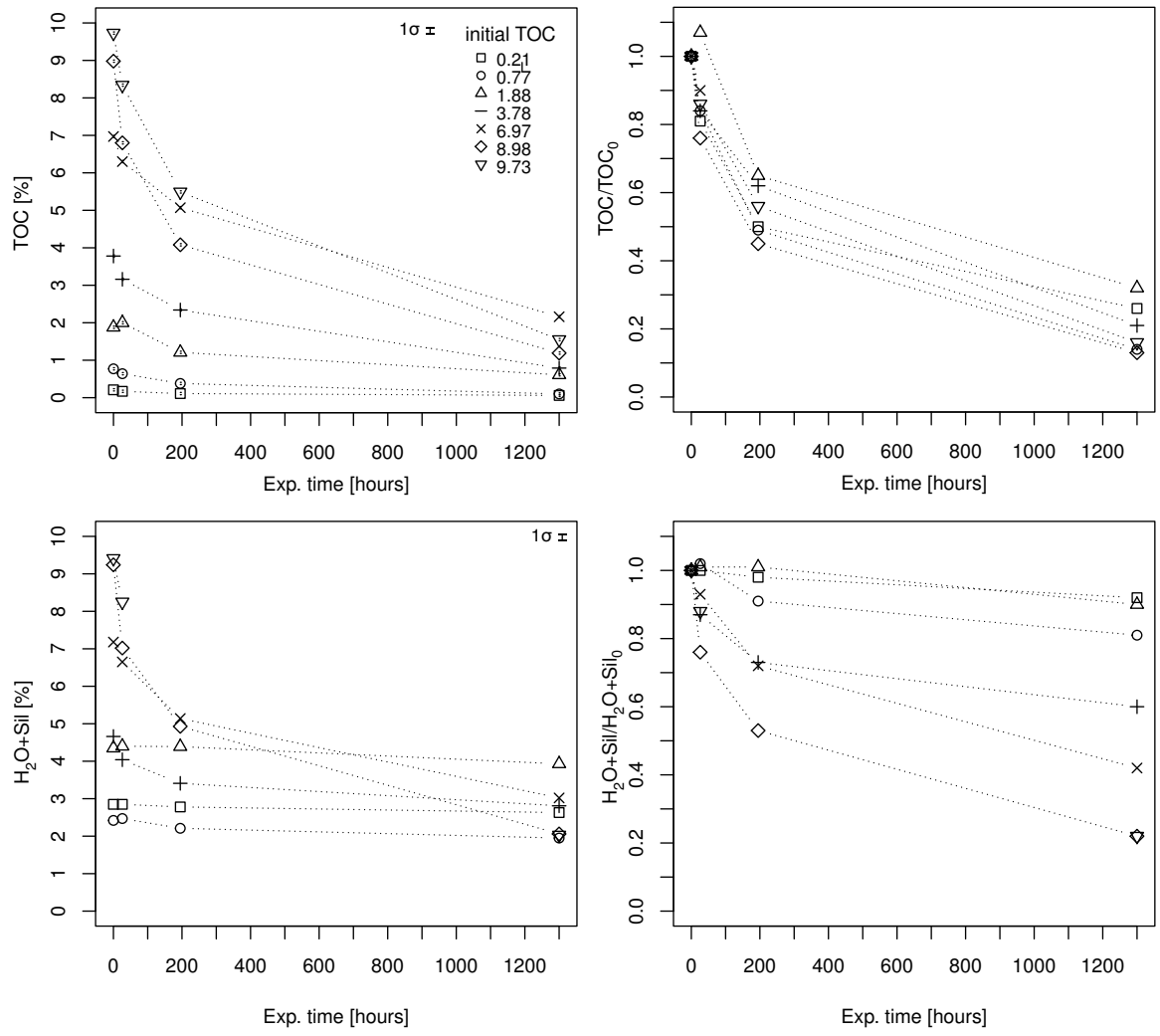

FIGURE 3.3.6 – Effet de la destruction de la MO dans les sols par plasma-ashing (suivant le protocole 2).

Sur les 1300 h d'expériences, les TOC et H_2O+ des échantillons de sols diminuent exponentiellement. Les valeurs de TOC finales sont beaucoup plus comparables entre elles que celles obtenues avec le protocole 1. Les valeurs de TOC finales ne semblent plus dépendre des valeurs initiales et les rendements varient entre 68 % et 86 %. Les vitesses de dégradation ne semblent plus dépendre des valeurs initiales de TOC. Parallèlement, les valeurs d'H_2O+ décroissent de manière similaire. Les échantillons CA10158D et CA10157B présentant des TOC initiaux faibles 0.2-0.8% n'observent des pertes en H_2O+ que très

limitées de 8% à 19% ; alors que les échantillons plus riches TOC de 1.9 à 9.7 % montrent des rendements de 10% à 78% respectivement. Les très faibles pertes en H_2O+ pour les TOC faibles démontrent que le stock d'hydrogène de ces échantillons est en majorité associé à la matière minérale. La destruction pour les TOC élevés semble très similaire au protocole 1.

La comparaison des résultats des protocoles 1 et 2 permet d'optimiser le protocole et renseigne sur les limites de la technique :

— Une limite de destruction avec des rendements autour de 80-90% semble être atteinte même pour des temps très longs (cf. figure 3.3.7). Le carbone résiduel est certainement pétrogénique et ne porte pas d'hydrogène. La bonne dégradation du carbone pétrogénique est illustrée par les échantillons CA10158D et CA10157B (protocole 2). Le carbone de ces échantillons est faiblement porteur d'hydrogène. Il est dégradé avec des rendements similaires aux échantillons dont le carbone est porteur d'hydrogène (litière organique CA10159A 19% TOC) ce qui indique que la méthode dégrade aussi efficacement tous les composés. Même si le carbone résiduel n'est pas entièrement détruit, ce carbone ne comporte que très peu d'hydrogène susceptible de biaiser la mesure de l'hydratation.

— les différentes vitesses obtenues entre les échantillons avec le protocole 1 sont attribuées à un effet de rapport de la surface exposée au plasma sur volume total dans la nacelle. L'oxydation étant un processus de surface, le volume de l'échantillon protège la MO de la dégradation. Le fait d'avoir limité l'épaisseur à 1 mm a effacé cet effet lors du protocole 2 dont tous les échantillons présentent des vitesses identiques. Ainsi, il convient de limiter l'épaisseur de poudre à 1 mm lors de la dégradation.

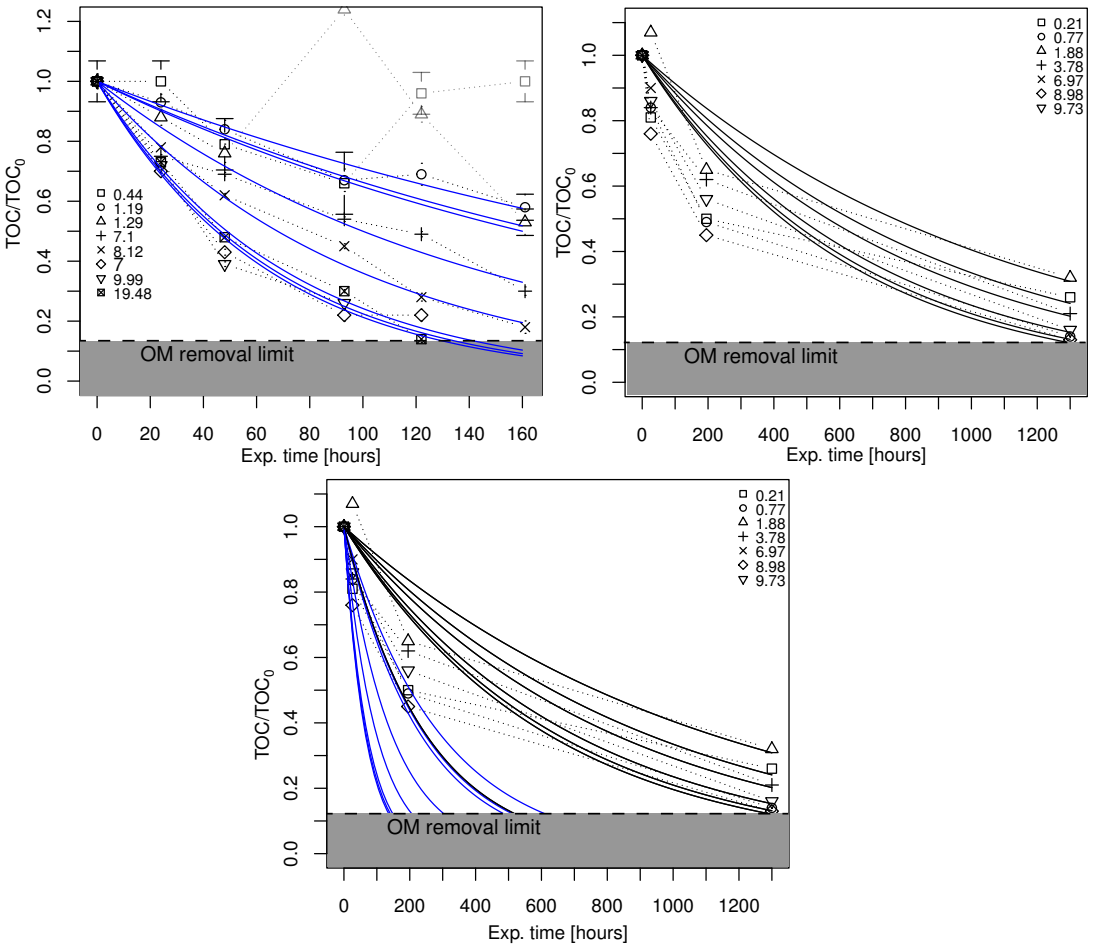

FIGURE 3.3.7 – Modélisation des résultats de destruction de la MO dans les sols (protocoles 1 et 2).

— Les constantes de vitesse de destruction peuvent être déterminées par l'équation : $TOC(t) = TOC(0) \cdot \exp(-\lambda \cdot t)$ avec TOC(t) le TOC en fonction du temps d'expérience t, TOC(0) le TOC initial, λ la constante de vitesse de dégradation. Les résultats sont présentés dans le tableau 3.3 et la figure 3.3.8.

Batch 1 (stirred)	TOC_0[%]	0.44	1.19	1.29	7.1	8.12	7	9.99	19.48
	$\lambda \cdot 10^3$	4.333	3.446	4.113	6.934	10.214	14.183	15.470	14.940
Batch 2 (unstirred)	TOC_0[%]	0.21	0.77	1.88	3.78	8.98			
	$\lambda \cdot 10^3$	1.094	1.562	0.904	1.230	1.628			

TABLE 3.3 – Résumé des vitesses de destruction suivant les protocoles 1 et 2.

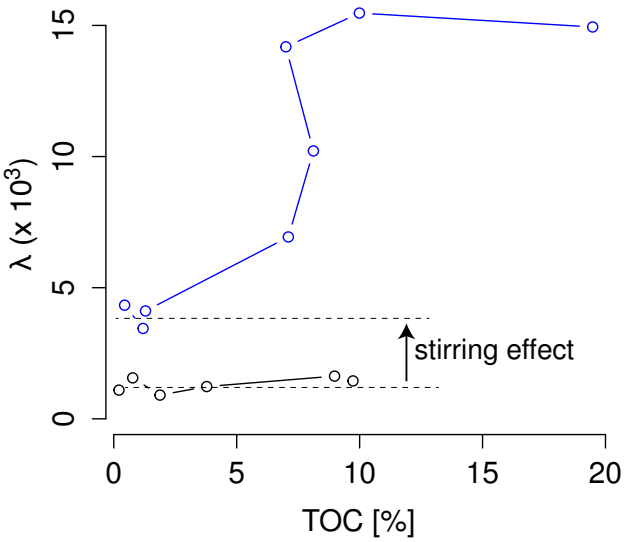

FIGURE 3.3.8 – Comparaison des vitesses de destruction selon les protocoles 1 (en bleu) et 2 (en noir).

Les constantes de vitesses de destruction obtenues pour des TOC initiaux équivalents démontrent que remuer les échantillons toutes les 12h augmente les vitesses de dégradation d'un facteur $\times 4$ à $\times 6$. Selon ces modèles, le temps maximal nécessaire pour la dégradation est de 600h en remuant les échantillons toutes les 12h, contre plus du double sans remuer.

Les résultats du protocole 3 sont reportés dans le tableau 3.4 et présentés en figure 3.3.9.

Sample #	type	Exp. Time [Hours]	aliquot	**TOC [%]**	**δ13Corg [‰]**	TOC/TOC0	δ13C-δ13C0	**H2O+Sil [%]**	**δD [‰]**	H2O+/H2O+0	δD-δD0
SWY2	standard	0	SWY2					**4.60**	**-133.3**	1.00	0.0
		113	3PO2-I-1b					**4.48**	**-133.7**	0.97	-0.4
		157	3PO2-I-2					**4.54**	**-133.9**	0.99	-0.6
		203	3PO2-I-3					**4.65**	**-134.1**	1.01	-0.8
		277	3PO2-I-4					**4.67**	**-133.1**	1.01	0.2
		349	3PO2-I-5					**4.63**	**-130.1**	1.01	3.2
		973	3PO2-I-6					**4.55**	**-131.0**	0.99	2.3
SNG25	river	0	SNG25	**0.46**	**-25.2**	1.00	0.0	**2.10**	**-89.6**	1.00	0.0
		113	3PO2-VI-1	**0.19**	**-25.7**	0.41	-0.6	**2.15**	**-92.5**	1.02	-2.9
		157	3PO2-VI-2	**0.26**	**-26.7**	0.56	-1.5	**2.32**	**-89.7**	1.10	-0.1
		203	3PO2-VI-3	**0.17**	**-26.9**	0.37	-1.7	**1.95**	**-88.3**	0.93	1.3
		277	3PO2-VI-4	**0.14**	**-26.7**	0.31	-1.5	**2.27**		1.08	
		349	3PO2-VI-5	**0.14**	**-26.9**	0.30	-1.7	**2.19**	**-82.5**	1.04	7.1
		973	3PO2-VI-6	**0.07**	**-27.4**	0.16	-2.2	**2.37**	**-88.1**	1.13	1.5
SNG63	river	0	SNG63	**0.32**	**-25.0**	1.00	0.0	**1.97**	**-91.1**	1.00	0.0
		113	3PO2-VII-1	**0.21**	**-26.2**	0.68	-1.1	**1.92**	**-91.4**	0.97	-0.3
		157	3PO2-VII-2	**0.21**	**-26.7**	0.65	-1.7	**1.77**	**-86.0**	0.90	5.1
		203	3PO2-VII-3	**0.17**	**-26.4**	0.55	-1.4				
		277	3PO2-VII-4	**0.22**	**-27.3**	0.69	-2.3	**1.79**	**-88.8**	0.91	2.3
		349	3PO2-VII-5	**0.11**	**-26.8**	0.34	-1.8	**1.77**	**-90.9**	0.90	0.2
		973	3PO2-VII-6	**0.10**	**-26.9**	0.30	-1.9	**1.93**	**-87.2**	0.98	3.9
CA10133	glacier	0	CA10133t0	**0.06**	**-18.5**	1.00	0.0	**0.78**	**-133.1**	1.00	0.0
		113	CA10133t11	**0.04**	**-17.8**	0.66	0.7	**0.77**	**-132.5**	0.99	0.6
		157	CA10133t15	**0.05**	**-19.9**	0.93	-1.4	**0.77**	**-129.8**	0.98	3.3
		203	CA10133t20	**0.05**	**-19.7**	0.99	-1.1	**0.78**	**-129.6**	1.01	3.5
		277	CA10133t27	**0.04**	**-18.7**	0.81	-0.1	**0.78**	**-129.9**	1.00	3.3
		349	CA10133t34	**0.05**	**-18.2**	0.86	0.3	**0.84**	**-127.6**	1.07	5.5
		973	CA10133t97	**0.03**	**-15.0**	0.60	3.5	**0.80**	**-129.5**	1.02	3.6

TABLE 3.4 – Résultats de destruction de la MO dans les sédiments de rivière suivant le protocole 1.

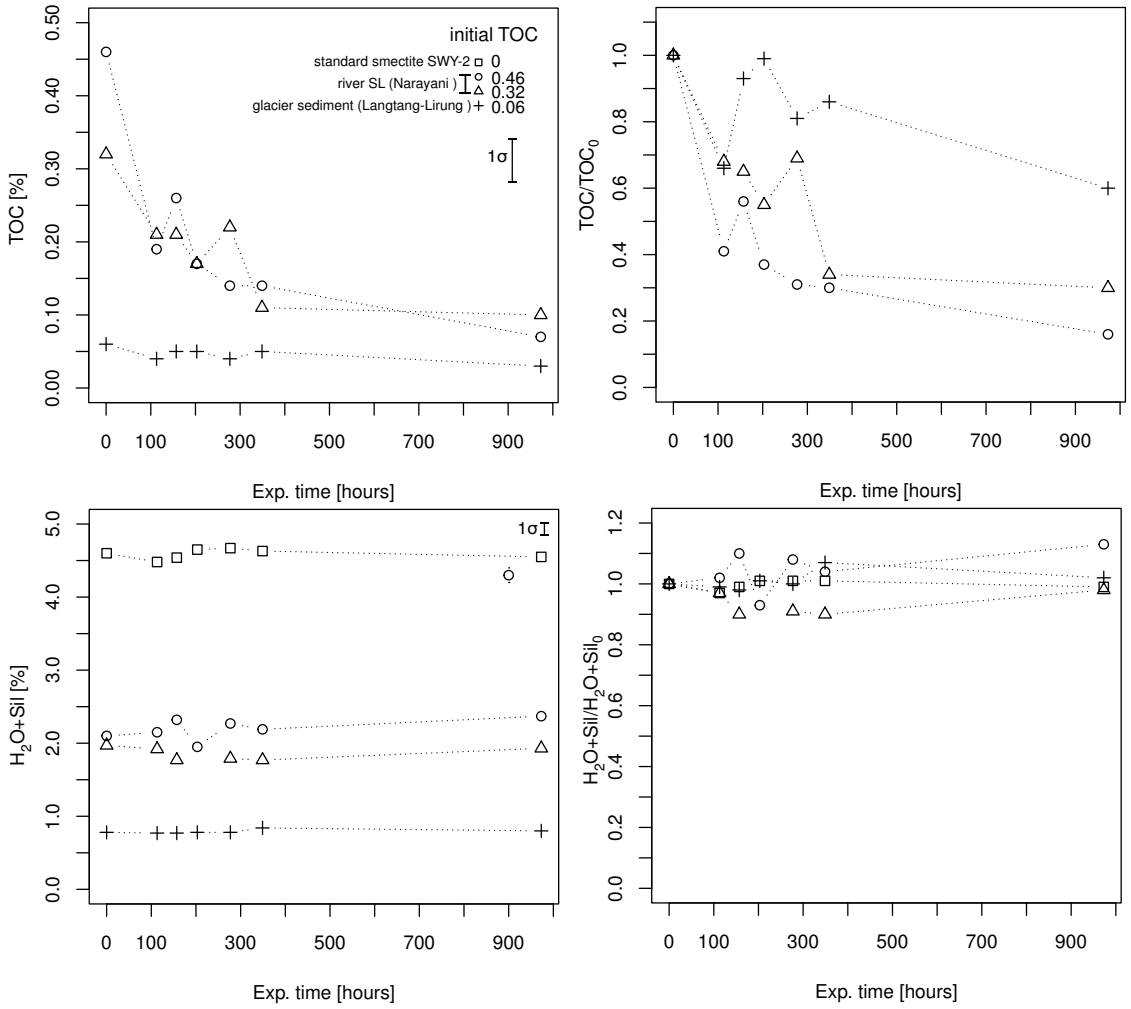

FIGURE 3.3.9 – Effet de la destruction de la MO sur un standard SWy-2, dans les sédiments de rivière et glaciaires au cours du temps (suivant le protocole 3).

Ce test a été poussé à 973 h d'expérience ce qui correspond à 1.5 fois le temps recommandé par les résultats des tests précédents.

Les résultats sont sans équivoque :

1. Les concentrations et compositions isotopiques de la smectite SWy-2 et du sédiment glaciaire CA10133 sont restées constantes et dans les gammes d'incertitudes de l'analyse à l'EA-IRMS : 4.5% ± 0.1 H_2O+ et -133‰ ±3 δD ; et 0.7% ± 0.1 H_2O+

-130 ± 3 δD (cf. tableau 3.4). Nous avons choisi deux échantillons dont les hydratations sont très différentes : SWy-2 d'hydratation élevée (4.5%) afin d'observer si la technique a un effet sensible sur H_2O+, CA10133 d'hydratation faible (0.7%) avec afin d'observer sensiblement si la technique avait un effet sur la composition δD (le leucogranite sur lequel se développe ce glacier a des compositions de -90‰). Cela permet de conclure avec confiance à l'innocuité de la méthode envers le signal d'hydratation des OH liés et de leurs compositions isotopiques.

2. La destruction de la matière organique des sédiments de rivière et de glacier est notable avec des rendements respectifs de 70-84% et 40%. L'absence de variation d'H_2O+ indique que ce carbone n'est pas porteur d'hydrogène, il est certainement pétrogénique (graphite). Il n'est donc pas nécessaire de procéder à cette étape de destruction de la MO dans les sédiments de rivière.

La figure 3.3.10 résume les résultats en présentant l'évolution des H_2O+ et TOC au cours des expériences de dégradation. Il illustre clairement la différence de composition de la MO entre les sols dont le TOC est $> 1\%$ et ceux de TOC plus faibles $< 1\%$. La pente H/C observée avec les échantillons de sols dont TOC $> 1\%$ est de 1.9 ($H_2O+/TOC = 0.95$) ce qui est compatible avec des composés de types humines et acides fulviques présents dans les sols [Rice 91].

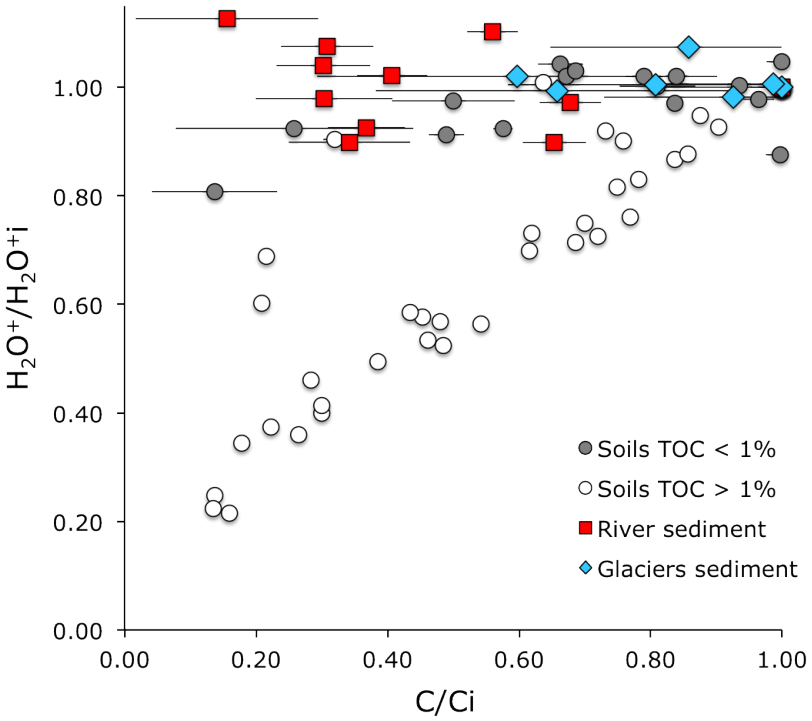

FIGURE 3.3.10 – Évolution de l'H_2O+ [weight %] en fonction du TOC [weight %] lors des test de destruction de la MO au plasma.

Conclusion

La méthode de destruction de la MO par *plasma-ashing* s'est révélée très efficace dans le prétraitement des sols. Cette méthode semble présenter tous les avantages nécessaires à la mesure des OH d'hydratation des silicates :

— aucune déshydratation des OH liés n'est provoquée par la méthode, même avec des temps longs (1000 h).

— ainsi qu'aucun fractionnement isotopique n'est provoqué même pour des échantillons très faiblement hydratés ($< 1\%$ H_2O+).

Les sédiments de rivières et de glacier de l'Himalaya présentant des TOC faibles n'ont pas besoin d'être prétraités avant analyse des OH des silicates.

Nous recommandons le protocole suivant :

— bien répartir les poudres d'échantillons dans les récipients sans dépasser 1 mm de hauteur pour maximiser l'effet de réaction de surface.

— remuer les échantillons au minimum toutes les 12h en prenant un soin tout particulier au nettoyage de l'outil utilisé.
— le temps de traitement maximal recommandé est de à 600h en suivant les recommandations précédentes.

Tous les résultats d'hydratation des sols de ce manuscrit sont issus d'un traitement préalable suivant les recommandations ci-dessus.

IV

Chapitre 4

Processus d'érosion dans la chaîne himalayenne par analyse des sédiments de rivières actuelles.

Ce chapitre est divisé en deux parties qui sont liées l'une à l'autre :

La première est constituée d'un article de conférence étudiant les liens entre l'érosion physique et l'érosion physique dans la Khudi Khola. La problématique de l'étude était de préciser les flux en éléments solubles et de sédiments dans le bassin de la Khudi en échantillonnant la rivière à haute résolution temporelle, afin d'évaluer l'impact des cycles diurnes des précipitations qui sont observés dans la chaîne [Barros 00, Barros 03].

La seconde partie est constituée d'un manuscrit d'article scientifique en préparation qui porte plus particulièrement sur les bilans d'érosion physiques et chimiques du bassin de la Khudi. Par l'étude fine des compositions chimiques des sédiments collectés dans le bassin, nous avons cherché à déterminer l'impact de l'érosion des sols et des grands glissements de terrain actifs sur le bilan de l'érosion physique. Par comparaison avec les sédiments d'autres bassins himalayens équivalents de la région, nous proposons une évaluation de l'érosion physique qui a lieu dans ce type de bassins en terme de processus érosifs. De plus, par analyse des éléments dissous, nous évaluons l'érosion chimique dans le bassin de la Khudi, puis nous la comparons à l'érosion physique, et discutons du fonctionnement du bassin de la Khudi en le comparant aux données d'autres bassins du Népal et dans le monde.

4.1 *High K and Ca chemical erosion triggered by physical erosion in a watershed of the High Himalaya of Nepal* [Morin 14]

Available online at www.sciencedirect.com

ScienceDirect

Procedia Earth and Planetary Science 10 (2014) 292 – 296

Procedia Earth and Planetary Science

Geochemistry of the Earth's Surface meeting, GES-10

High K and Ca chemical erosion triggered by physical erosion in a watershed of the High Himalaya of Nepal

Guillaume Morin[a*], Christian France-Lanord[a], Ananta Gajurel[ab], Florian Gallo[a], and Jérôme Lavé[a]

*

[a]*CRPG, CNRS-Université de Lorraine, BP 20, Vandœuvre les Nancy 54501, France*
[b]*Dep. of Geology, Tribhuvan University, Kathmandu, Nepal*

Abstract

The Khudi river in Nepal is an example of a basin undergoing intense physical erosion by landslide under very wet monsoonal conditions. Although under such a regime, dissolved element concentrations are expected to during the monsoon, we observe marked increases in dissolved K and Ca during flood events. These peaks in K and Ca concentrations are well correlated with increases of suspended load by an order of magnitude. The data suggest that release of K and Ca is enhanced by physical erosion and rock disaggregation events during sediment transfer.

Peer-review under responsibility of the Scientific Committee of GES-10

Keywords: weathering; sediment transport; landslide; monsoon

1. Introduction

The influence that physical erosion exerts on chemical erosion by enhancing the reactive surface between mineral and surface water is an intuitive relationship because the increase of fresh mineral surface in contact with surface

* Corresponding author. Tel.: +33 38359 4220; fax: +33 38351 1798.
E-mail address: morin@crpg.cnrs-nancy.fr

Peer-review under responsibility of the Scientific Committee of GES-10
doi:10.1016/j.proeps.2014.08.067

water leads to a potential increase of total weathering flux. Thus, it has been invoked that at the continental scale, orogenic phases that boost physical erosion could trigger global cooling[1]. There are clear examples of direct correlations between physical and chemical erosion approximated by sediment and solute exports of river[2]. However, West et al.[3] showed that when physical erosion become very high, weathering might be kinetically limited. Through a modeling approach, Gabet & Mudd[4] proposed that where erosion rates are greater than 100 t/km^2/yr ($\approx$ 0.04 mm/yr), increase in erosion rate leads to progressive decrease in weathering rate because maximum production rate of regolith is overtopped by physical erosion. These approaches are however hampered by the difficulty to define the effective soil thickness and to take into account weathering occurring outside of the soil zone such as weathering in fractured bedrock or in landslide areas[5].

The Khudi khola (river) in Central Nepal Himalaya is one example where physical erosion exceeds 2 mm/yr, where physical erosion appears to be much higher than chemical erosion, and where chemical erosion should be kinetically limited. However, in this study we present a daily survey of both physical and chemical erosion of the Khudi river during monsoon 2010 showing that dissolved fluxes of K and Ca are triggered by very high physical erosion events. These data are compared with earlier record of the river in 2002 by Wolf-Boenish et al.[6] when physical erosion was weaker. Additional sampling from July 2013 is also considered.

2. Study area and sampling

The Khudi khola is a 150 km^2 watershed draining the south flank of the Lamjung massive in Central Nepal. Elevation ranges between 800 and 4900m and no glacier is present. The watershed is exposed to heavy rainfall, up to 4 m during the three months of the monsoon[7]. The basin is undergoing intense physical erosion estimated around 1.5 to 3 mm/yr by suspended load x discharge measurements[8]. Recent survey of the basin reveals that most of the sediment flux originates from 2 active landslides present in the higher part of the basin and which show almost continuous sediment supply during the monsoon[9].

During 2010 monsoon, daily water and sediment sampling was performed from a bank of the intake station from the Khudi hydropower plant. Daily, two litres of water were sampled. Samples were then filtered so that sediments concentrations and dissolved element concentrations could be measured. Since 2012, the basin has been equipped with turbidity and conductivity probes. Rain gauges in different locations of the basin also provide an estimate of rainfall. In addition, suspended sediment and water sampling was performed using a one litre horizontal double opening bottle. Because of the high velocity and turbulence of the stream, the sampler was operated on a vertical rail installed on the wall of the intake station from a hydropower installation. This system allowed sampling in reproducible conditions and at the surface and ca. 40 cm above riverbed. Discharge was estimated using a theoretical rating curve, i.e. the relation between water stage and discharge at the Intake river section, using the HEC-RAS model (1D hydraulic model). In 2010, we use the limnimetric record of the power station and in 2012 the pressure gage record. We controlled the computed total discharge integrated over the year to be roughly equal to the annual precipitation falling upstream minus the mean yearly evapotranspiration.

3. Monsoon 2010 data.

Data are presented in figure 1. From the onset of the monsoon in June to its climax at the end of July, discharge increased from $\approx$3 to 15-30 m^3/s and gradually decreased at the end of the monsoon. Daily rainfall events generally occurring over night generated daily discharge peaks which increased the base discharge by a factor 2 to 10. Discharge and suspended sediment concentrations were clearly related. Sediment concentrations varied from 0.5 to 5 g/l under steady conditions and reached values higher than 50 g/l during peak discharge.

Major dissolved element species displayed contrasted evolutions. Na and Si both progressively decreased throughout the monsoon corresponding well to a "dilution" effect due to the increase of rainfall and direct runoff. [Na^+] reduced from 90 to 50 µmol/l and [Si] from 150 to 100 µmol/l. On the contrary, [K^+] and [Ca^{++}] showed an overall increase during the monsoon and displayed sharp variations. [K^+] base level stayed stable around 70 µmol/l

and peaked up to 250 µmol/l during some flood events. [Ca^{++}] base level decreased from 280 to 180 µmol/l and peaked up to 600 µmol/l. [Mg^{++}] overall decreased during the monsoon but also displayed moderate peaks correlated with K^+ and Ca^{++} fluctuations. K^+ and Ca^{++} peaks were well correlated and also corresponded to peak discharge and suspended sediment concentrations (Fig. 2).

4. Discussion

Such high K^+ and Ca^{++} rich waters were not observed before in Nepal rivers[10] nor during the first survey of the Khudi river in 2002[6]. However, physical erosion of the Khudi river was notably lower during that period. As a matter of fact, 2002 Khudi waters were significantly less concentrated in K^+ than 2010 waters: 40-55 μmol/l during 2002 compared to 55-85 μmol/l for 2010 base values.

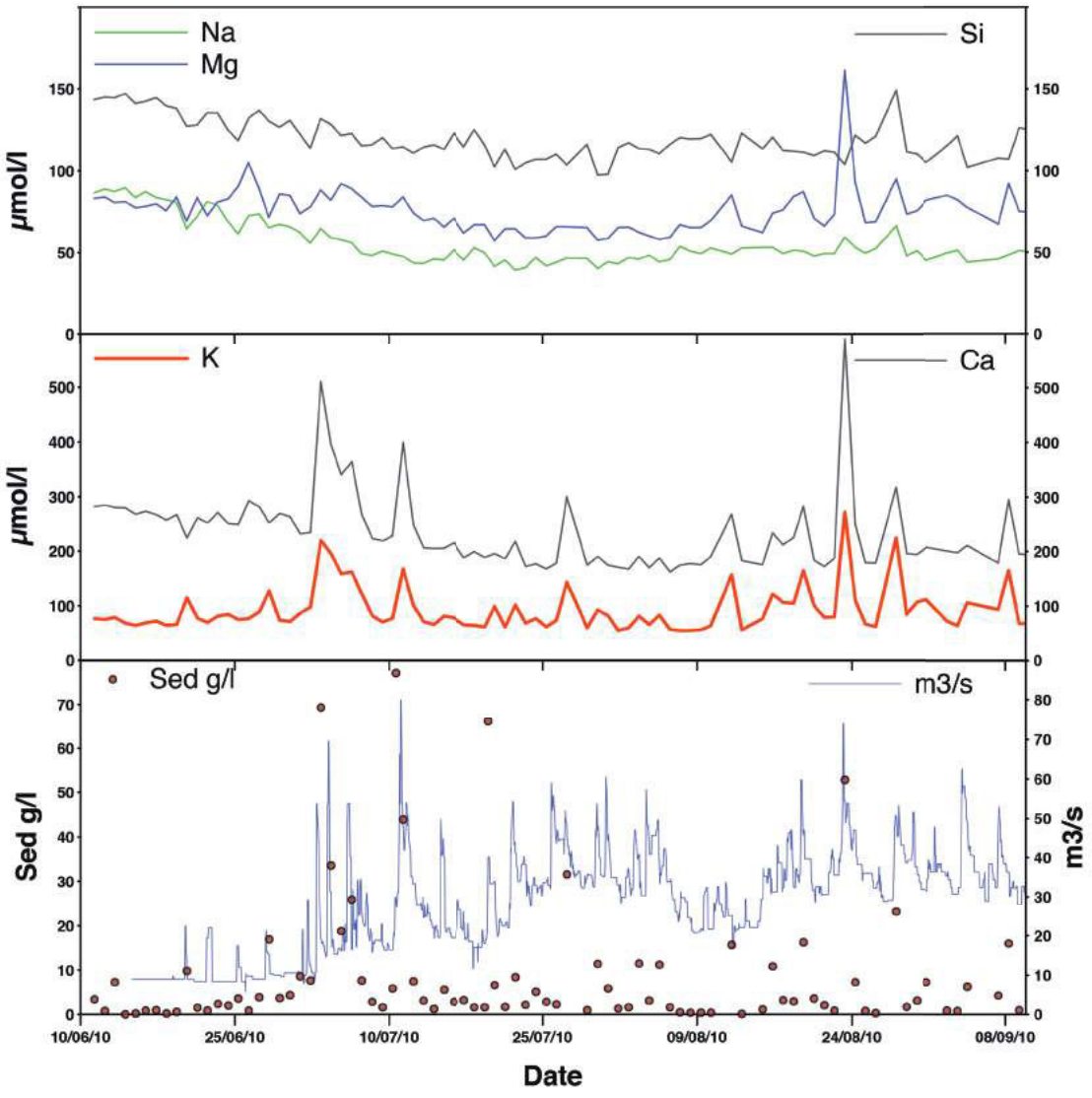

Fig. 1. Khudi record during monsoon 2010 for: discharge & suspended sediment concentration (bottom); dissolved K & Ca (middle); dissolved Na, Mg & Si (top). Suspended sediment and dissolved element concentration were determined from the same samples taken daily at 08h00.

Because peak concentrations in K^+ and Ca^{++} correlate with suspended sediment concentrations, we initially suspected that post sampling exchange or weathering of the sediment load could have occurred because samples taken in 2010 were stored for variable time before filtration. However subsequent sampling in 2013 performed with immediate filtration during a large flood event replicated the same observation (Fig. 2). We are therefore confident that these data reflect real variations in K^+ and Ca^{++}. In addition, combined conductivity measurements and discharge in 2012 and 2013 show flood events accompanied by conductivity increase, although this relationship is not systematic.

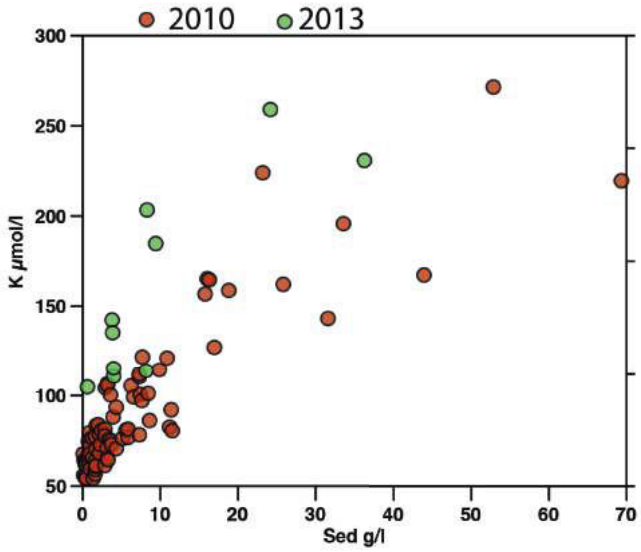

Fig. 2. Relationship between suspended sediment concentration and dissolved K+ concentration in 2010 and 2013 samples.

Flood events are usually correlated with decreases of the dissolved load due to dilution by direct runoff. In some cases, release of leachable element stock in soils can lead to initial increase of dissolved load. But such effects are unlikely in the case of intra-monsoon flood event as the upper soil reservoirs are saturated and thoroughly leached. One sample of soil water taken in July 2011 showed lower concentrations than any of those recorded in the river. None of the other known sources of dissolved elements seem to fit with a combined increase of K and Ca. Hydrothermal springs are characterised by high Na concentration and are likely diluted during the monsoon. Groundwaters sampled from springs during dry season in the upper basin reveal no composition compatible with those observed during floods of the Khudi river. Therefore the main implication is that the release of dissolved K and Ca is associated to physical erosion processes. High sediment fluxes in the present Khudi river are associated to continuous creeping in the active landslide area that delivers sediments to the river (Gallo et al., submitted). As a consequence, the average suspended sediment concentration recorded in 2010 was 8 g/l, whereas it was 1.5 g/l during the 2002 monsoon season[8]. The processes and reactions associating K and Ca release with peaks in sediment discharge are matter for discussion. The more direct sources of K and Ca are biotite and calcite respectively. Biotite is very abundant in the gneisses and shows traces of transformation to vermiculite. Calcite is present in very small proportion ($\approx 0.1\%$) in the gneisses. Processes that deliver cations to the river require high dissolution kinetic (e.g. calcite dissolution) or leaching of exchangeable cations. Fresh exposure of mineral surfaces by rock crushing during the flood event may trigger the release of these cations. Partially ground landslide material is stored in deposits at the outlet of the landslide area and undergoes weathering for days until it is flushed during the next flood event. Overall this process appears as a significant source of dissolved K and Ca to the river. Although the relationship between discharge and dissolved load is not straightforward when we observe time-series, if we consider a base concentration of 70μmol/l for K and 180μmol/l for Ca, we can estimate that at least 50 to 75% of dissolved K and 35 to 70% of dissolved Ca in the river are due to this prompt process during major flood events.

Acknowledgements

This study was supported by the ANR project #ANR-09-BLAN-0221 “Calimero”. We thank Mr. M.P. Pradhan and the staff of Khudi hydropower plant for material support and help during sampling of the Khudi river.

References

1. Raymo ME, Ruddiman WF. Tectonic forcing of late Cenozoic climate. *Nature* 1992; **359**(6391):117–22
2. Millot R, Gaillardet J, Dupre B, Allegre CJ. The global control of silicate weathering rates and the coupling with physical erosion: new insights from rivers of the Canadian Shield. Earth and Planetary Science Letters 2002; 196(1-2):83–98
3. West A, Galy A, Bickle M. Tectonic and climatic controls on silicate weathering. *Earth and Planetary Science Letters.* 2005; **235**:211–28
4. Gabet EJ, Mudd SM. A theoretical model coupling chemical weathering rates with denudation rates. *Geology* 2009; **37**:151–54
5. West AJ. 2012. Thickness of the chemical weathering zone and implications for erosional and climatic drivers of weathering and for carbon-cycle feedbacks. *Geology* 2012; **40**: 811–14
6. Wolff-Boenisch D, Gabet EJ, Burbank DW, Langner H, Putkonen J.. Spatial variations in chemical weathering and CO2. Geochimica et Cosmochimica Acta 2009; 73:3148–70
7. Putkonen JK. Continuous snow and rain data at 500 to 4400 m altitude near Annapurna, Nepal, 1999-2001. *Arctic, Antarctic, and Alpine Research* 2004; **36**:244–48
8. Gabet E, Burbank D, Prattsitaula B, Putkonen J, Bookhagen B. Modern erosion rates in the High Himalayas of Nepal. *Earth and Planetary Science Letters* 2008; **267**:482–94
9. Gallo F, Lavé J. Evolution of a large landslide in the High Himalaya of central Nepal during the last half-century. *Geomorphology*; in press.
10. Galy A, France-Lanord C. Weathering processes in the Ganges–Brahmaputra basin and the riverine alkalinity budget. *Chemical Geology* 1999; **159**:31–60

4.2 *Deep landslides erosion in actively eroding basins affects physical and chemical erosion of High Himalayan basins.*

Deep landslides erosion in actively eroding basins affects physical and chemical erosion of High Himalayan basins.

(In preparation)

Morin G. P.[1*], France-Lanord C.[1], Lavé J.[1], Rigaudier T.[1], Lupker M.[2], Gallo F.[3], Gajurel A. P.[4]

1- Centre de Recherche Pétrographique et Géochimique (CRPG) CNRS UMR 7358, Université de Lorraine, 15 rue Notre Dame des Pauvres, F-54500 Vandoeuvre-lès-Nancy, France ; 2- ETH Zürich, Institute of Geochemistry and Petrology, Clausiusstrasse 25, NW, CH-8092 Zürich, Switzerland ; 3- Met Office, Exeter, UK ; 4-Department of Geology, Tribhuvan University, Ghantaghar, Kathmandu, Nepal

4.2.1 Introduction

Chemical and physical erosion processes and fluxes are largely studied through various approaches on modern basins at different space and time scales, and rely on a variety of hydrological, geomorphological, and geochemical approaches (e.g. [Milliman 83, Gaillardet 99b, Kirchner 06]). Exploring past erosion requires utilizing detrital sedimentary records that can document eroded sources from mineralogical and geochemical tracers, and erosion rates using geochronologial or accumulation rate approaches. Deciphering chemical erosion is more tentative as dissolved riverine fluxes are rarely recorded except through their global impact on ocean chemistry (e.g.[Krishnaswami 92]). At basin scale, the geochemical characteristics of sediments can be used to decipher the weathering associated to erosion processes and fluxes using either major and trace element geochemistry (e.g. [Gaillardet 99a, Lupker 13]), isotopic tracers of weathering (e.g. [Dellinger 14]). Applying these approaches is however frequently relying on hypotheses on the composition of the source rock exposed to erosion. In large scale basins, where there is a large variety

of upper crustal rocks, this generally limits the capacity to interpret the sedimentary record. On the Himalayan basin, [Lupker 12b] compared weathering fluxes derived from a detailed dataset of suspended river sediments with fluxes of river dissolved elements. This showed that while there is a rough correspondence between both approaches, there is also large uncertainties linked to source rock that hamper estimates of certain elements. Understanding the link between erosion processes and fluxes, and the composition of eroded sediments is therefore a key element for the interpretation of past erosion from sedimentary archive.

With the general goal of documenting how erosion processes translates into river sediments characteristics, our study focuses on the initial stage of erosion in a head Himalayan basin. We compare geochemical signatures of sediments collected from soils and active landslides, to those of river sediments and to the fluxes of dissolved elements. The approach focuses principally on the Khudi khola valley, which is a well studied watershed typical of the south Himalayan flank, exposed to heavy precipitation and undergoing intense physical and chemical erosion [Gabet 08, Wolff-Boenisch 09] . It is also a basin where a large landslide is active [Gallo 14a] allowing studying the imprint of this process. We also compare these sediments to those of the Dordi and Chepe basins, which are equivalent but less exposed to landslides than the Khudi one. In order to assess weathering occurring on hillslopes, we compare rivers sediments to a dataset of rock samples from the LH and HHC formations, collected from 1970 to present day. We propose a descriptive budget in terms of physical erosion and relative roles of erosive agents through their geochemical signatures and comparison with river sediment. We also analyzed stream waters to assess chemical erosion flux, and clearly establish both spatial and intensity discrepancy between chemical and physical erosion in such highly erosive environments.

The study relies on an effort to assess the composition of sediment as representatively as possible. This includes daily sampling of suspended load and river water during one full monsoon season that reveal the variability of sediment and dissolved load of the river.

4.2.2 Settings

This study mainly focuses on the Khudi khola (river) basin, a N-E oriented valley situated in the south flank of the central part of the Himalayan range (c.f. figure 4.2.1).

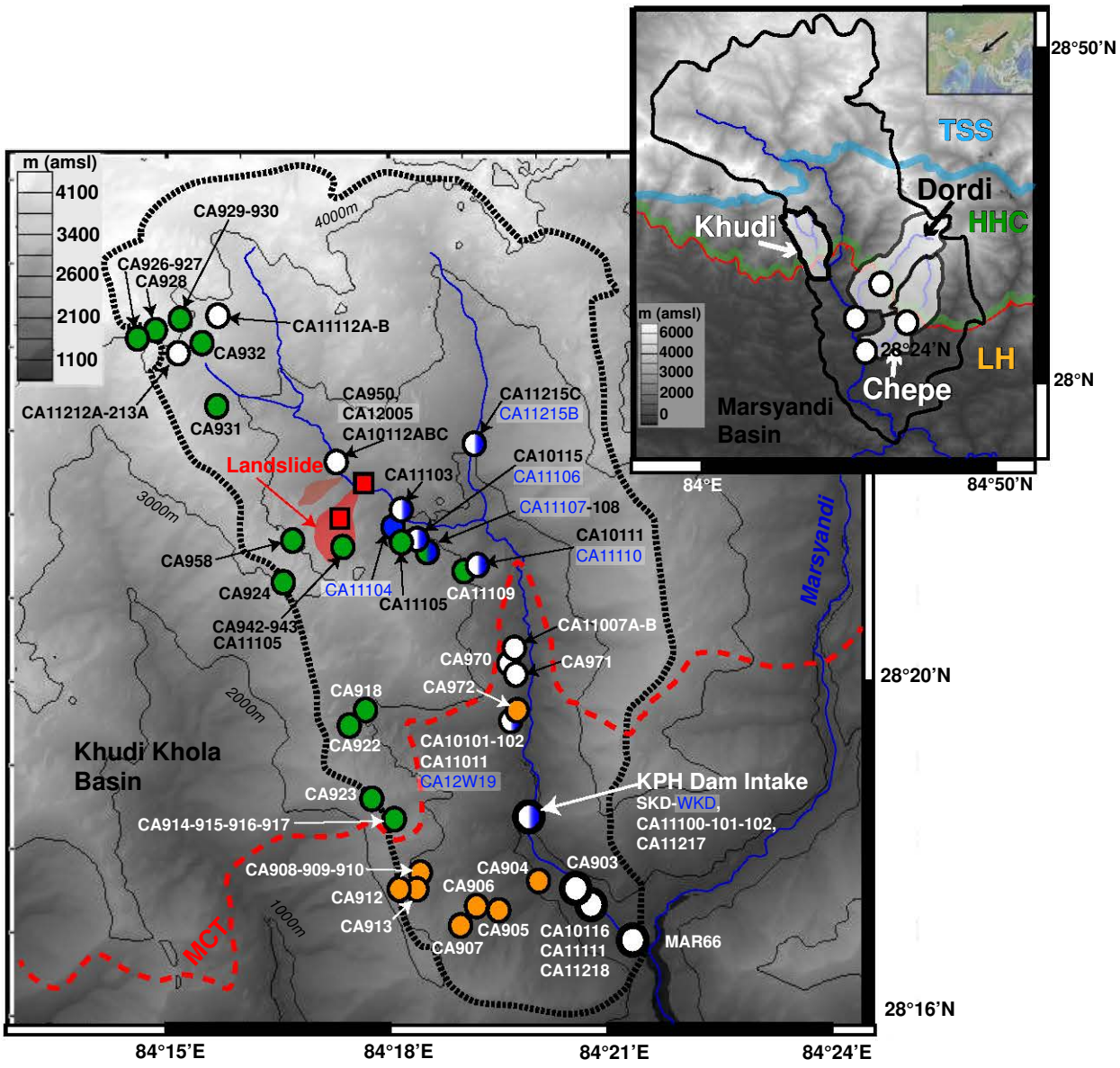

FIGURE 4.2.1 – Locations of the Khudi Khola, Dordi and Chepe basins in the Marsyandi basin, Central Nepal.
Detailled sampling locations in the Khudi basin, red areas show the active landslide areas, and dashed red line the MCT position. Samples color-code is as follow : white dots for river sediments, blue dots for waters, green dots for HHC soils, orange dots for LH soils and red for landslide debris. This color-code is the same in all following captions.

The basin drains 146 km^2 in the Lamjung massive, the southeast of the Annapurna

massive in central Nepal. It collects intense precipitation that is amongst the highest in Nepal. Annual precipitations are 2.6 m/yr at 800 m at Khudi village, and as high as 4.2 m/yr at 3200 m, of which 65% fall during summer monsoon [Putkonen 04]. This induces very high specific discharge of 3.54 m/y [Gabet 08]. This climatic setting is also similar for the nearby basins of Dordi and Chepe. Overall, monsoon rainfall distribution and their amount in total annual precipitations is observed at regional scale in the Narayani basin account for >70% of annual precipitations between May and October, while snowmelt contribution is <25% [Bookhagen 10]. Khudi basin elevation ranges from 800 m up to 4930 m, nevertheless there is no modern glaciers nor permanent snow cover in the higher areas of the basin although snow water equivalent precipitation was measured around 1 m/yr on crests at 4400 m [Putkonen 04]. Moreover, this basin has been non glaciated during the Holocene, as demonstrated by the very limited periglacial and glacial deposits in the North of the basin and dated at 14.1 ka [Niemi 05, Pratt-Sitaula 11]. Climatic and tectonic settings of the basin lead to erosion rates between ∼2 and 3.5 mm/y as measured by terrestrial cosmogenic nuclides TCN [Niemi 05, Godard 12, Puchol 13, Godard 14] or suspended load (SL) fluxes measurements [Gabet 08, Gallo 14b]. This is about double of the regional erosion rate in the Narayani basin (e.g. [Andermann 12b, Lupker 12a]). Two active landslide areas present in the NW part of the basin on the HHC series have been found to be active for at least 40 years and represent important erosion areas [Gabet 08, Gallo 14b, Gallo 14a, Puchol 14].

Comparatively, in Chepe and Dordi basins, no active landslide were reported [Gallo 14b]. Chepe is non glacierized like the Khudi, and Dordi glaciers extent is limited to 5.1 km^2, that is ∼1.5% of total basin area. Erosion rates derived from TCN are significantly lower than for the Khudi and are around 0.5 mm/y for the Chepe and 1 mm/y for the Dordi [Godard 12, Godard 14] in agreement with erosion rates of other High Himalayan basins of the Marsyandi basin [Gabet 08].

Geologically, the Khudi basin drains the MCT (Main Central Thrust) zone, the exact position of MCT is not well defined but is in the area of Probi village. Below the MCT, the lower valley lithology is composed of medium to high grade metapelites of the Lesser Himalaya (LH) formation. It comprises micashist, quartzite and dolomitic limestone. Above the MCT, the upper and northern part of the valley is composed of paragneisses of the High Himalaya Cristalline (HHC). This is Formation 1 as describled by [Colchen 86].

The metamorphism degree encountered has been mapped as intermediate to high-grade because of the presence of biotites, garnet, kyanite and sillimanite. Khudi, Dordi and Chepe basin drain mainly the HHC. The area draining LH is $\sim$ 25 % of total basin area at the outlet of the Khudi, and $\sim$13 % at the Khudi HydroPower (KHP) intake station where daily monsoon samples SKD and WKD were taken. Chepe and Dordi basins drain higher extents in LH representing 40 % and 33% of total basins areas respectively, but sediment samples of these rivers were also taken at the MCT where upstream geological unit is exclusively HHC.

The vegetation is mainly composed of deciduous forest on hillslopes under 3500 m, and shrubby to barren-alpine vegetation on the upper valley above this elevation. Vegetation cover is divided into two main altitudinal zones with a transition from humid forest in the lower valley slopes and thalweg, to alpine landscapes in the very upper valleys and on the crests.

Finally, the population density in the valleys is low and only present in the southern and low-relief parts of the basins. Anthropogenic impact on the natural systems is therefore considered negligible despite summer pasturing and growing activities in the upper valley.

4.2.3 Sampling strategy

All samples locations are detailed in figure 4.2.1. Sampling strategy was designed to document geochemical composition of sources and eroded material. This includes : 1 - soils developed on slopes and crests, 2 - sediments of landslides, 3 – discrete river sediment and waters from Khudi tributaries in various locations of the basin, 4 - Khudi river sediments and water at one downstream station where daily sampling was performed during monsoon season, and 5 - pebbles sampling to document average bedrock compositions. Dordi and Chepe samples were taken at the basins outlets, and also upstream at the limits between LH and HHC so that only HHC areas outcrop upstream.

4.2.3.1 Soils sampling

Soils samples were collected along depth-profiles dug down to 1 to 5 m depth in different part of the Khudi basin. We mainly sampled the western part of the valley on the western hillslope. We sampled every recognizable pedogenic horizons and designed our sampling

to document most geomorphological environments present in the basin : crests, barren hillslopes and forested hillslopes. Samples were collected at elevations ranging from 1000 m to 4100 m. Soils of the Khudi valley developed on forested hillslopes and barren crests were identified as type 1 - alfisols / podzols (spodosols). Higher crests and in the northern and elevated parts of the basin have type 2 soils - inceptisols / entisols and rankers. Type 1 soils have already been described in toposequence studies in other parts of Himalaya in Likkhu Khola [Right 86, Gardner 96], in Salme district [Right 86] or in Bhutan [Baillie 04, Caspari 06]. They are generally developed on siliceous rocks in Alpine to sub-Alpine humid mountainous regions. Type 2 soils are young to embryonic soils with negligible degree of soil formation to intermediate and immature state of development, and are generally encountered in Alpine and mountainous environments. We noted the presence of clastic fragments in the depth-profiles, which appear exogenous compared to the embedding soil structure. These clasts remain competent and unweathered, and are indications of solifluction and rockfall along the hillslopes. They are evidence for polygenic origin of soil material in some hillslopes.

4.2.3.2 Landslide debris sampling

Inner landslide debris were both sampled in the landslide and on the edges. Coarse sieving were done on the field, and after drying at laboratory for fine fractions. Grain-size fractions collected ranges from sand (< 2 mm) to very coarse pebbles (2-5 cm). Sands from the stream draining the landslide were collected at different years to evaluate temporal variability. Although all samples originate from a relatively narrow area, there is high apparent petrographic contrast between migmatitic gneiss displaying coarse grain minerals, and more homogeneous gneisses displaying finner grains that are typical for Formation 1. Rocks often present rusty colors coating, implying apparent variable degree of alteration, but this alteration is limited to the surface and is mostly due to iron oxides coating.

4.2.3.3 Small stream and Khudi tributary sampling

Sampling locations were designed to document the sediment composition of sub-catchment order and include :

— the Thulo cascade (CA10101-102,CA11011), a small Khudi tributary draining a

sub basin of 13 km^2 (9.4% of Khudi basin area) dominantly draining LH series. - 2 streams draining densely forested sub-order basins in the HHC and located between Probi village and the Saituti landslide (CA10111-115).

— 2 streams of upper western branch situated in elevated parts of the basin (CA11112A-B, CA11212A-213A).

— the western branch of the Khudi Khola ∼1.5 km downstream the Saituti landslide (CA11103 c.f. A1 fig. 4.3.1) which drain an area of 36 km^2 in the HHC (26.1% of Khudi basin area), and the western Khudi branch upstream the two landslides (CA950,CA10112A-B-C,CA12005) that only carries no suspended sediment and minor proportions of sand (c.f. A1 fig. 4.3.1)

— the northern branch of the Khudi Khola (CA11215C) that drain 28 km^2 (20.3% of Khudi basin area) exclusively in the HHC.

Samples are all composed of sand and gravels taken in the beds of little streams. No suspended sediment were observed in streams and tributaries, even during the monsoon (c.f. A1 fig. 4.3.1, 4.3.2 and 4.3.3). We attribute the absence of suspended matter to the lack of permanent erosion in these sub-basin and to the role of filter that vegetation cover and forest litter have on runoff waters. It may retain particules on slopes. Small streams samples were sieved at 2 mm to be compared to Khudi river sediment of same grain-size.

Water samples were taken in small streams, catchment springs, landslide spring, soil water, and Khudi khola river in various part of the basin. The aim was to document the diversity of runoff waters in the basin and to compare them to the Khudi khola river waters. Samples include therefore :

— the Thulo cascade (CA12W9).

— 4 small streams draining densely forested sub-order basins in the HHC and located between Probi and the Saituti landslide (CA11104-106-107-110).

— the western branch of the Khudi Khola ∼1.5 km downstream the Saituti landslide (CA11104).

— the northern branch of the Khudi Khola (CA11215B).

4.2.3.4 Downstream Khudi sediment and water sampling.

During the 2010 monsoon season, the hydropower intake station agent sampled daily surface of river water and SL. The basin area drain by the Khudi Khola at the KPH Intake station totalizes 119 km^2 of which 86% outcrops the HHC FI paragneisses. SL were manually taken along a concrete wall of the intake station with an open bottle sampler. Two bottles of one liter were taken successively around 8 AM each day. Samples were filtrated either on site or in Kathmandu using pressurized filtration device coated with teflon.

4.2.3.5 Khudi Khola river and Saituti landslide pebbles sampling

An average pebble sample of the Khudi at KHP intake station river has been sampled in order to asset the coarsest part of bedload transported by the river. Approximately 200 pebbles between 5 and 20 cm were sampled and separated by their distinct lithologies at the laboratory, each fractions were weighted and powder-crushed to be analyzed. The same sampling was done for Saituti landslide debris at the outlet. Nearly 100 pebbles of 5 cm were sampled ; we processed to the same separation and preparation at the laboratory as followed for river pebbles.

4.2.3.6 Other HHC basins sampling, Dordi and Chepe.

For comparison with watershed presenting similar geological and climatic characteristics but less impacted by landslide, we sampled bank and SL sediments of the Dordi and Chepe rivers. Samples of bank and SL were taken at the outlet of Chepe and Dordi and upstream in the MCT area where upstream basins drain HHC gneisses exclusively.

4.2.4 Analytical methods

4.2.4.1 Sediment sample analysis

Sediment treatment

Soils samples were freeze-dried and sieved at 2 mm, we retained fraction < 2 mm for analysis and defined this fraction as soil. Landslide debris samples were freeze-dried and we treated differently two types of samples : debris sieved on the field were kept

as clasts fractions, whereas landslide stream sands were sieved at 2 mm and the < 2 mm fractions were kept for analysis. River sediments collected from springs and rivers we filtrated through 0.45 µm PES membranes on field the day of sampling, with a pressurized filtration unit coated with teflon. We stored sediments and filters ceiled in sample bags until their treatment at the laboratory. 2010 monsoon time series samples of Khudi khola river (SKD) were collected at the intake of Khudi hydropower station by trained plant-workers and stored in 2L containers. SKD samples containing water and sediments were stored ceiled and protected from light until their monthly collection and their filtration at Tribhuvan University of Kathmandu. We applied the same treatment procedure to streams sediments and Khudi khola sediments than soils and landslides samples. After sieving, < 2 mm fractions of sediments samples were divided using a riffle-splitter to obtain representative fractions for grain-size and geochemical analysis. Special care was taken to avoid any loss of material during all steps.

Major and trace elements analysis

After freeze-drying, soils and sediments were powdered in agate mortar. Major elements concentrations were measured by ICP-AES and trace elements by quad-ICP-MS at "Service d'Analyse des Roches et des Minéraux" (SARM–CRPG, Nancy-France), after lithium metaborate fusion on bulk aliquots >100 mg of powder following [Govindaraju 87, Carignan 01] . Overall uncertainty in major elements is less than 2%.

Organic carbon analysis

TOC and $\delta^{13}C$ of bulk C_{org} were measured by EA-IRMS on a modified Euro Vector EuroEA3028-HT coupled with a GV Isoprime. The overall 2σ uncertainties associated with TOC and $\delta^{13}C$ of bulk C_{org} determination are 0.03% and 0.2‰ respectively.

Hydroxyls concentration and δD isotopic compositions

Hydroxyls concentrations [H_2O+] and D/H stable isotopic compositions were analysed by an Elemental Analyzer (EA) coupled to a VG Isoprime Isotope Ratio Mass Spectrometer (IRMS) following the procedure developped for sediments by [Lupker 12b] (analytical procedures detailed therein). Because hydrogen beared by organic matter compounds can represent a significant part of the total hydrogen content in samples, we proceeded to

organic matter removal by an oxidizing pre-treatment by low-temperature oxygen-plasma ashing system. This method was successfully tested to measure pedogenic siderites and shows better yields and more accurate isotopic results than classical chemical oxidation using aqueous solutions of NaOCl or H_2O_2 [Lebeau 14]. We tested the effect of the method on δD determination using standards smectites SWY2 and low C_{org} content natural samples, corresponding to deep-soils and glaciers sediments. Results demonstrate that method of plasma-ashing does not induce any modification of D/H isotopic compositions in these samples and efficiently remove hydrogen-bearing organic matter. Between 2 and 8 mg of powdered sample previously treated by plasma-asher were used for hydration content determination.

4.2.4.2 Dissolved load analysis

Water samples

We filtrated bulk water samples collected from springs, Khudi khola river and its tributaries through 0.45 µm PES membranes on field the day of sampling, with a pressurized filtration unit coated with teflon. We stored them in ceiled nalgene containers protected from light. 2010 monsoon time series samples of Khudi khola river (WKD) were collected at the intake of Khudi hydropower station by trained plant-workers and stored in 2L containers. WKD samples containing water and sediments were stored ceiled and protected from light until their monthly collection and their filtration at Tribhuvan University of Kathmandu, as described above.

Cations and anions analysis

Major cations were analyzed at SARM, CRPG Nancy on ICP-OES. Major elements uncertainties are less than 5%. Anions were analyzed by ion chromatography at LIEC, Nancy.

4.2.5 Results

Comparing bedrock, soil, and landslide material with river sediment imply to take into account mineral sorting related to river transport (e.g. [Bouchez 11b, Lupker 11a]). Mineral sorting by hydrological processes can be stretched in geochemical diagrams presenting

elemental compositions vs. Al/Si. This elemental ratio reflects sorting of quartz opposed to phyllosilicates and is generally well correlated to grain size as coarse grains are dominated by quartz, while fine grain sediments are enriched in micaceous and clays minerals., In order to assess weathering in our samples, we chose to present mobile elements compositions normalized to Al that is considered as an immobile element in most environments as soils [Gardner 96] or rivers sediments [France-Lanord 97, Viers 09, Bouchez 12, Dellinger 14].

4.2.5.1 Bedrock characterization

Bedrock is indeed difficult to document because in such large crustal segment there is an important variability of lithologies. Bedrocks from the Khudi basin are all metasediments but with variable lithologies and compositions ranging from sandstones to pelites, and from pure silicate rocks to marbles [Pecher 78, Colchen 86]. While there is a high variability in the Lesser Himalaya series, Formation 1 paragneisses are less diverse. Nevertheless partial melting processes lead to strong differentiation for Na, K, Fe, Mg in migmatitic gneisses [Brouand 89, Barbey 96]. We use a geochemical database that has been constructed using geochemical sampling performed in Central Nepal during geological expeditions leaded by Patrick Le Fort and Arnaud Pêcher from 1970 to 1990. Samples selected on field were chosen moving aside any rocks showing traces of weathering, this pool composes therefore the best pristine parental bedrock signature available. The sampling area lies between the Kali Gandaki and the Trisuli rivers, which is much larger than the Khudi basin but formations remain quite similar all-over central Nepal. The data are listed in supplementary Table S1 and S2 and represented in figure 4.2.2. For the Lesser Himalaya, most data are derived from [Pecher 78]. We selected carbonate-free lithologies. For HHC Formation 1, we excluded samples for which there are extreme signatures of migmatisation, which are characterized by major iron depletion as described in [Barbey 96].

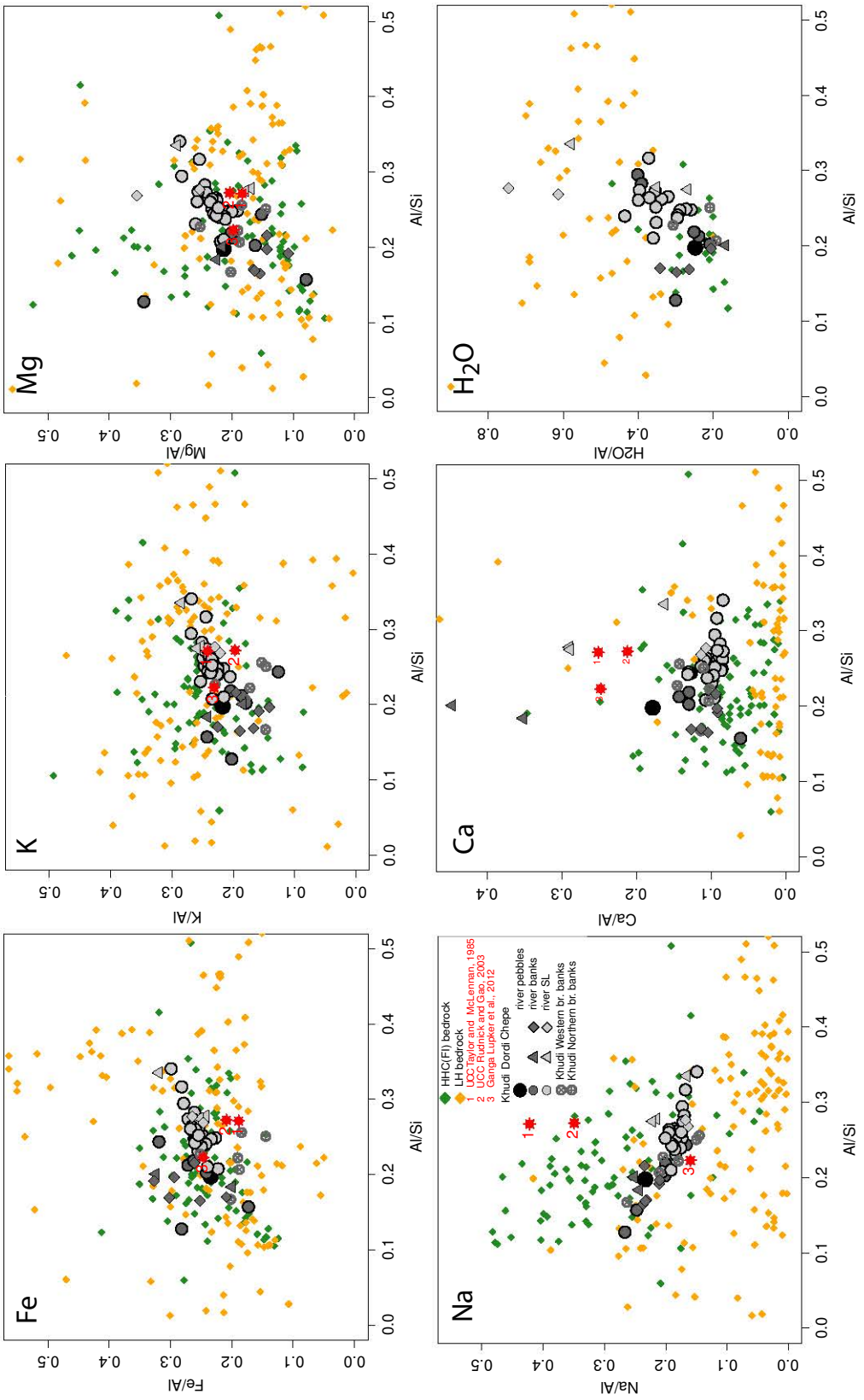

FIGURE 4.2.2 – Major elements compositions and hydration content of Khudi Khola river sediments compared to HHC and LH protoliths.

LH and HCC lithologies show quite undistinct composition in Fe/Al, K/Al and Mg/Al diagrams despite the fact that HHC show less variability than LH (c.f. figure 4.2.2). On the opposite, HHC and LH show clear differences on Na, Ca concentrations and [H_2O+] contents. Na/Al and Ca/Al vs. Al/Si diagrams illustrate that Na and Ca concentrations are 3 to 4 times higher in the HHC than in the LH, which reflects that HHC metasediment are less mature or less recycled than those of the LH. For a limited set of these bedrock samples, we performed additional hydration [H_2O+] analysis. Hydration appears contrasted amongst the two formations, HHC show significantly lower [H_2O+] than LH, reflecting higher degree of metamorphism close to granulitic conditions.

Defining average composition of HCC or LH is indeed tentative given the dispersion of data and the range of Al/Si ratios inherited from the sedimentary protoliths. UCC estimates range between 0.26 and 0.30. Based on observation and modelling of sediments exported by the Ganga and large Himalayan rivers, [Lupker 11a, Lupker 12b] estimated the average Al/Si of Himalayan crust to 0.23. This is more silicic than UCC but more usual for upper crustal dominantly detrital sediment. While Fe, K, and Mg compositions of our bedrock database are comparable to UCC, Na and Ca are significantly lower reflecting their preferential leaching during successive erosional cycling.

4.2.5.2 Khudi khola sediment composition

Suspended sediments

Bank and suspended sediments compositions data are presented in table 4.1 and figure 4.2.2.

Ech.#	River	Locality	Elevation	Type	Charge [g/L]	North	East	Julian day	Date	SiO2 weight%	Al2O3	Fe2O3	MnO	MgO	CaO	Na2O	K2O	TiO2	P2O5	Pf	Total
CA11201A	Khudi khola	Khudi dam	967	Pebbles - Fl unweath. / slightly weath.	33%wt	28.2959539	84.3383613	308	05/11/11	74.59	10.63	4.36	0.07	2.02	2.35	1.74	1.94	0.58	0.14	1.09	99.51
CA11201B	Khudi khola	Khudi dam	967	Pebbles - Fl moderately weath.	27%wt	28.2959539	84.3383613	308	05/11/11	71.31	12.83	5.04	0.08	1.89	1.52	1.96	2.49	0.62	0.14	1.20	99.08
CA11201C	Khudi khola	Khudi dam	967	Pebbles - Fl weath. / very weath.	25%wt	28.2959539	84.3383613	308	05/11/11	70.68	14.67	5.48	0.10	1.53	0.83	1.86	3.23	0.67	0.10	1.34	100.49
CA11201D	Khudi khola	Khudi dam	967	Pebbles - LH quartzish	2%wt	28.2959539	84.3383613	308	05/11/11	86.12	6.18	2.13	0.11	0.39	3.04	0.47	0.16	0.33	0.10	0.50	99.53
CA11201E	Khudi khola	Khudi dam	967	Pebbles - LH schists	8%wt	28.2959539	84.3383613	308	05/11/11	66.73	9.14	2.04	0.03	3.11	4.56	0.69	2.86	0.36	0.20	8.80	98.50
CA11201F	Khudi khola	Khudi dam	967	Pebbles - Fl quartzish	5%wt	28.2959539	84.3383613	308	05/11/11	68.60	10.80	3.48	0.06	2.55	5.47	1.67	1.69	0.40	0.09	3.97	98.76
Weight. aver. pebl	Khudi khola	Khudi dam	967	Av. Pebbles	-	28.2959539	84.3383613	308	05/11/11	72.02	12.02	4.54	0.08	1.94	2.11	1.71	2.43	0.58	0.13	1.95	99.52
MAR66	Khudi khola	Basin outlet	800	Bank	-	28.28063	84.356726			79.79	10.63	2.88	0.05	0.66	0.71	1.60	2.38	0.40	0.07	1.60	100.78
CA10116	Khudi khola	Power house	846	Bank	-	28.28797	84.34507	319	16/11/10	71.33	12.85	5.47	0.13	2.02	2.02	1.53	2.21	0.53	0.19	2.08	100.36
CA11218 <2mm	Khudi khola	Power house	846	Bank/Gravels	-	28.2871537	84.3472593	318	15/11/11	71.26	13.21	5.43	0.11	2.10	1.88	1.61	2.49	0.57	0.17	1.58	100.41
CA903	Khudi khola	Khudi dam	920	Bank	-	28.29605	84.3382	307	04/11/09	69.36	14.34	7.16	0.26	1.72	2.00	1.46	1.68	0.42	0.16	0.62	99.17
CA11217	Khudi khola	Khudi dam	967	Bank/Gravels	-	28.3055873	84.3300991	318	15/11/11	73.42	12.60	4.77	0.11	1.62	1.80	1.55	2.09	0.45	0.13	1.27	99.79
CA11111	Khudi khola	Power house	846	SL	-	28.28851	84.34518	209	29/07/11	66.58	14.26	5.68	0.08	2.50	1.78	1.74	3.09	0.70	0.15	1.99	98.55
LO1004	Khudi khola	Khudi dam	967	SL	-	28.3055873	84.3300991			68.04	14.54	5.65	0.08	2.63	1.52	1.54	3.32	0.73	0.11	1.73	99.89
SKD10	Khudi Khola	Khudi dam	967	SL	9.75	28.3055873	84.3300991	170	20/06/10	58.64	16.95	7.94	0.08	3.82	1.57	1.54	4.20	0.96	0.17	4.11	99.98
SKD14	Khudi Khola	Khudi dam	967	SL	2.00	28.3055873	84.3300991	174	24/06/10	62.71	15.67	6.84	0.06	3.49	1.64	1.65	3.89	0.87	0.15	3.17	100.14
SKD20	Khudi Khola	Khudi dam	967	SL	4.32	28.3055873	84.3300991	180	30/06/10	71.58	12.62	4.40	0.04	2.18	1.49	1.58	2.73	0.57	0.10	1.92	99.21
SKD21	Khudi Khola	Khudi dam	967	SL	8.53	28.3055873	84.3300991	181	01/07/10	64.11	15.38	6.29	0.07	2.97	1.49	1.59	3.57	0.79	0.14	3.25	99.65
SKD22	Khudi Khola	Khudi dam	967	SL	7.55	28.3055873	84.3300991	182	02/07/10	68.49	13.42	5.36	0.06	2.75	1.46	1.50	3.14	0.70	0.10	2.34	99.32
SKD23	Khudi Khola	Khudi dam	967	SL	64.84	28.3055873	84.3300991	183	03/07/10	68.26	14.36	5.88	0.10	2.34	1.59	1.61	2.86	0.66	0.14	1.72	99.52
SKD24	Khudi Khola	Khudi dam	967	SL	32.45	28.3055873	84.3300991	184	04/07/10	66.37	14.94	6.02	0.07	2.67	1.46	1.68	3.37	0.76	0.14	2.15	99.63
SKD25	Khudi Khola	Khudi dam	967	SL	18.47	28.3055873	84.3300991	185	05/07/10	66.19	14.72	5.85	0.06	2.61	1.37	1.62	3.39	0.75	0.14	2.33	99.03
SKD29	Khudi Khola	Khudi dam	967	SL	1.67	28.3055873	84.3300991	189	09/07/10	64.95	15.03	6.16	0.07	2.87	1.39	1.56	3.44	0.78	0.13	3.40	99.78
SKD30	Khudi Khola	Khudi dam	967	SL	5.79	28.3055873	84.3300991	190	10/07/10	70.74	12.62	4.74	0.08	2.13	1.33	1.47	2.51	0.55	0.09	2.36	98.62
SKD31	Khudi Khola	Khudi dam	967	SL	42.10	28.3055873	84.3300991	191	11/07/10	69.07	14.58	5.18	0.07	2.20	1.37	1.66	3.03	0.66	0.11	1.39	99.32
SKD32	Khudi Khola	Khudi dam	967	SL	7.35	28.3055873	84.3300991	192	12/07/10	69.09	14.49	5.30	0.07	2.29	1.38	1.69	3.01	0.68	0.11	1.41	99.52
SKD34	Khudi Khola	Khudi dam	967	SL	1.27	28.3055873	84.3300991	194	14/07/10	64.64	15.03	6.39	0.07	3.03	1.52	1.57	3.37	0.79	0.14	2.83	99.38
SKD39F	Khudi Khola	Khudi dam	967	SL	62.02	28.3055873	84.3300991	199	19/07/10	67.29	14.36	5.71	0.07	2.64	1.50	1.61	3.19	0.71	0.13	2.55	99.76
SKD43	Khudi Khola	Khudi dam	967	SL	2.15	28.3055873	84.3300991	203	23/07/10	65.65	14.70	6.11	0.07	2.70	1.73	1.74	3.25	0.77	0.16	2.63	99.51
SKD51	Khudi Khola	Khudi dam	967	SL	1.31	28.3055873	84.3300991	212	01/08/10	68.61	13.94	5.34	0.07	2.42	1.52	1.49	2.91	0.67	0.12	2.14	99.23
SKD63	Khudi Khola	Khudi dam	967	SL	1.20	28.3055873	84.3300991	226	15/08/10	60.44	16.24	7.17	0.07	3.25	1.65	1.66	3.67	0.89	0.18	4.05	99.27
SKD70	Khudi Khola	Khudi dam	967	SL	0.89	28.3055873	84.3300991	233	22/08/10	65.75	14.51	5.90	0.07	2.70	1.73	1.72	3.13	0.76	0.16	2.65	99.08
SKD71	Khudi Khola	Khudi dam	967	SL	50.18	28.3055873	84.3300991	234	23/08/10	68.95	14.08	5.35	0.08	2.36	1.50	1.60	2.94	0.67	0.12	1.97	99.62
SKD79	Khudi Khola	Khudi dam	967	SL	0.91	28.3055873	84.3300991	244	02/09/10	69.16	13.92	5.45	0.10	2.32	1.61	1.57	2.64	0.62	0.11	1.78	99.28
SKD84	Khudi Khola	Khudi dam	967	SL	0.94	28.3055873	84.3300991	251	09/09/10	65.51	14.49	6.07	0.08	2.94	1.74	1.54	3.15	0.75	0.14	3.47	99.88
CA11100	Khudi Khola	Khudi dam	967	SL	0.30	28.30551	84.32998	209	29/07/11	67.77	14.06	5.74	0.08	2.55	2.00	1.62	3.13	0.69	0.19	1.95	99.78
CA11101	Khudi Khola	Khudi dam	967	SL	-	28.30551	84.32998	209	29/07/11	66.42	13.81	5.56	0.08	2.45	1.98	1.60	3.00	0.67	0.19	4.42	100.17
CA11102	Khudi Khola	Khudi dam	967	SL	-	28.30551	84.32998	209	29/07/11	68.40	14.05	5.73	0.09	2.51	2.03	1.62	3.07	0.68	0.18	2.25	100.60
CA11215C	Khudi Khola	Northern branch	2019	Bank/Gravels		28.3174547	84.3564019	317	14/11/11	70.39	14.98	5.36	0.17	1.72	1.82	1.37	2.03	0.48	0.12	0.88	99.29
CA950	Khudi Khola	Western branch	2365	Bank		28.37559	84.28865	314	11/11/09	73.40	13.85	4.57	0.09	2.08	1.55	1.51	2.21	0.48	0.11	1.05	100.90
CA12005<2mm	Khudi Khola	Western branch	2377	Bank		28.37175	84.286666	121	01/05/12	73.07	12.82	4.31	0.07	1.90	1.46	1.64	2.14	0.46	0.10	1.15	99.12
CA10112A	Khudi Khola	Western branch	1962	Bank		28.36517	84.30536	318	15/11/10	69.12	13.33	5.30	0.08	2.65	2.13	1.66	2.83	0.62	0.15	2.60	100.46
CA10112B	Khudi Khola	Western branch	1962	Bank		28.36517	84.30536	318	15/11/10	76.66	10.87	3.67	0.07	1.73	1.36	1.74	1.48	0.41	0.09	1.99	100.07
CA10112C	Khudi Khola	Western branch	1962	Bank		28.36517	84.30536	318	15/11/10	67.40	14.64	7.33	0.21	2.13	2.29	1.29	2.08	0.52	0.23	1.82	99.96
CA11103	Khudi Khola	Western branch	1962	SL		28.36516667	84.30515	211	31/07/11	64.40	14.87	6.62	0.08	3.41	1.98	1.40	3.59	0.82	0.19	2.93	100.28
CA13014	Dordi	Basin outlet Chiti	659	Bank	-	28.19213	84.45468	159	09/06/13	70.96	11.06	3.46	0.05	1.97	4.28	1.64	2.47	0.42	0.08	2.78	99.18
CA13015	Dordi	Basin outlet Chiti	659	SL	0.007	28.192	84.45484	159	09/06/13	55.69	15.85	7.93	0.10	3.63	2.83	1.60	4.18	0.97	0.14	NA	92.90
CA13103	Dordi	HHC basin, Kirtipur	573	SL	-	28.25169	84.48745			60.37	14.25	5.43	0.07	1.91	4.54	1.86	3.33	0.70	0.13	NA	92.58
CA13104	Dordi	HHC basin, Kirtipur	573	SL	-	28.25169	84.48745	200	20/07/13	61.76	14.41	5.69	0.08	2.03	4.58	1.94	3.46	0.77	0.14	NA	94.85
CA13108	Dordi	HHC basin, Kirtipur	577	Bank	-	28.25169	84.48745	201	21/07/13	66.83	11.39	5.78	0.19	1.94	5.59	1.75	1.94	0.73	0.23	2.44	98.80
MAR-26	Chepe	Basin outlet	509	Bank	-	28.11199	84.42655			74.20	12.39	5.71	0.18	1.40	1.25	1.58	1.62	0.48	0.20	0.82	99.83
Sed112	Chepe Khola	Basin outlet	453	Bank	-	28.11199	84.42655	311	08/11/06	76.79	10.75	4.24	0.11	1.31	1.24	1.55	1.88	0.44	0.09	1.98	100.38
CA13016	Chepe	Basin outlet	453	Bank	-	28.05659	84.48038	159	09/06/13	75.01	10.84	3.55	0.05	1.41	1.35	1.53	2.26	0.45	0.10	2.27	98.81
CA13182	Chepe Khola	HHC basin, Selitar I	651	SL	-	28.3043833	84.3869167	212.8	01/08/13	62.20	14.17	5.47	0.07	3.97	1.77	1.41	2.89	0.65	0.14	8.48	101.23
CA13184	Chepe Khola	HHC basin, Selitar I	653	SL	-	28.3043833	84.3869167	212.8	01/08/13	62.36	14.65	6.07	0.08	2.93	1.73	1.50	3.12	0.73	0.15	7.07	100.39
CA13199	Chepe Khola	HHC basin, Selitar I	668	Bank	-	28.3043833	84.3869167	213.4	02/08/13	75.68	10.84	5.13	0.15	1.40	1.51	1.54	1.67	0.56	0.22	1.45	100.15
MO 50	Chepe	Source	3250	Bank	-	28.29546	84.64759	125	06/05/97	72.56	11.79	6.04	0.27	1.01	1.18	1.51	1.73	0.42	0.11	1.55	98.17
MO 59	Chepe	Source	3250	Bank	-	28.29546	84.64759	126	07/05/97	71.52	13.10	5.36	0.19	1.48	1.35	1.87	2.37	0.47	0.16	2.08	99.95

TABLE 4.1 – Geochemical compositions of Khudi Khola, Chepe and Dordi sediments.

Ech.#	Fe/Al mol:mol	Na/Al	K/Al	Ca/Al	Mg/Al	Al/Si	Si/Al	TOC [%]	δ^{13}Corg [‰]	H2O+ [%]	δD [‰]	H_2O+/Al	$^{87}Sr/^{86}Sr$ Sil	±2σ 1.E-06	$^{143}Nd/^{144}Nd$ Sil	±2σ 1.E-06	εNd_0 Sil	Carb. Cont. [%]
CA11201A	0.2620	0.2684	0.1970	0.2010	0.2398	0.1680	5.9528			0.86	-87.0	0.2292						
CA11201B	0.2510	0.2518	0.2104	0.1077	0.1862	0.2120	4.7172			1.07	-85.7	0.2363						
CA11201C	0.2384	0.2089	0.2383	0.0515	0.1321	0.2446	4.0876			1.33	-87.1	0.2568						
CA11201D	0.0000	0.1251	0.0284	0.4479	0.0797	0.0846	11.8272			0.22	-90.5	0.1009						
CA11201E	0.1423	0.1241	0.3385	0.4536	0.4309	0.1614	6.1975			1.34	-78.9	0.4155						
CA11201F	0.2054	0.2537	0.1696	0.4605	0.2990	0.1855	5.3911			0.69	-88.9	0.1811						
Weight. aver. pebl	0.2347	0.2334	0.2173	0.1782	0.2136	0.1976	5.2714			1.05	-86.2	0.2478						
MAR66	0.1729	0.2476	0.2428	0.0606	0.0790	0.1570	6.3678											
CA10116	0.2716	0.1955	0.1864	0.1428	0.1990	0.2123	4.7097	0.07	-25.1	1.08	-90.9	0.2381	0.76147	11	0.51187	3	-15.0	
CA11218 <2mm	0.2625	0.2003	0.2043	0.1296	0.2013	0.2184	4.5790			1.17	-89.9	0.2510						
CA903	0.3188	0.1670	0.1266	0.1267	0.1518	0.2437	4.1037											
CA11217	0.2414	0.2018	0.1793	0.1297	0.1623	0.2023	4.9431			0.93	-89.8	0.2091						
CA11111	0.2544	0.2009	0.2346	0.1133	0.2220	0.2524	3.9621						0.76300	17	0.51186	3	-15.2	
LO1004	0.2477	0.1739	0.2475	0.0951	0.2292	0.2519	3.9696											
SKD10	0.2990	0.1495	0.2683	0.0842	0.2852	0.3406	2.9358	0.32	-24.0									
SKD14	0.2786	0.1732	0.2688	0.0951	0.2819	0.2945	3.3960	0.23	-23.7	2.22	-90.7	0.4015						
SKD20	0.2225	0.2060	0.2342	0.1073	0.2186	0.2078	4.8131	0.07	-23.6									0.04
SKD21	0.2610	0.1701	0.2513	0.0881	0.2444	0.2827	3.5372	0.19	-23.1	2.12	-90.1	0.3912						
SKD22	0.2549	0.1839	0.2534	0.0989	0.2593	0.2309	4.3308	0.05	-24.0	1.67	-91.8	0.3518						
SKD23	0.2614	0.1845	0.2157	0.1007	0.2062	0.2479	4.0337	0.10	-23.0	1.31	-92.3	0.2590						0.07
SKD24	0.2572	0.1850	0.2442	0.0888	0.2262	0.2653	3.7698	0.15	-22.9	1.69	-91.2	0.3205						0.03
SKD25	0.2537	0.1811	0.2494	0.0846	0.2244	0.2621	3.8158	0.16	-23.3	1.75	-89.1	0.3374						0.09
SKD29	0.2616	0.1708	0.2478	0.0841	0.2417	0.2727	3.6670	0.27	-24.0	1.88	-93.2	0.3547						
SKD30	0.2397	0.1916	0.2154	0.0958	0.2136	0.2102	4.7567	0.07	-25.8	1.60	-109.9	0.3601						0.09
SKD31	0.2268	0.1873	0.2250	0.0854	0.1910	0.2488	4.0200	0.14	-23.2	1.40	-87.0	0.2727						0.09
SKD32	0.2335	0.1919	0.2249	0.0866	0.2000	0.2471	4.0462	0.17	-23.8	1.48	-88.7	0.2884						
SKD34	0.2714	0.1718	0.2428	0.0919	0.2551	0.2740	3.6495	0.28	-23.8	2.10	-94.9	0.3967						
SKD39F	0.2538	0.1845	0.2405	0.0950	0.2327	0.2515	3.9764	0.15	-23.2	1.79	-93.4	0.3533						0.04
SKD43	0.2653	0.1947	0.2394	0.1070	0.2324	0.2639	3.7898	0.26	-23.9	1.92	-94.8	0.3698						
SKD51	0.2445	0.1758	0.2260	0.0991	0.2197	0.2394	4.1766	0.21	-24.9	2.14	-94.8	0.4357						
SKD63	0.2818	0.1682	0.2447	0.0924	0.2533	0.3166	3.1582	0.42	-23.7	2.13	-95.6	0.3719						
SKD70	0.2595	0.1950	0.2336	0.1084	0.2355	0.2601	3.8452	0.32	-24.5									0.04
SKD71	0.2425	0.1870	0.2261	0.0968	0.2121	0.2406	4.1555	0.12	-23.6	1.46	-95.3	0.2948	0.76270	11	0.51189	3	-14.5	
SKD79	0.2499	0.1856	0.2054	0.1051	0.2109	0.2372	4.2161	0.19	-24.3	1.45	-95.6	0.2955						0.14
SKD84	0.2674	0.1748	0.2354	0.1092	0.2568	0.2607	3.8365	0.21	-24.2	2.04	-95.0	0.3996						
CA11100	0.2605	0.1896	0.2412	0.1290	0.2297	0.2445	4.0902	0.20	-24.4									
CA11101	0.2570	0.1908	0.2353	0.1303	0.2242	0.2450	4.0813											
CA11102	0.2605	0.1902	0.2368	0.1313	0.2256	0.2421	4.1312											
CA11215C	0.2285	0.1502	0.1467	0.1103	0.1449	0.2507	3.9888			0.78	-96.7	0.2091	0.75502	10	0.51187	3	-15.0	
CA950	0.2104	0.1796	0.1730	0.1020	0.1904	0.2223	4.4981											
CA12005<2mm	0.2147	0.2108	0.1803	0.1032	0.1876	0.2068	4.8359			0.87	-87.3	0.1922						
CA10112A	0.2537	0.2045	0.2295	0.1454	0.2518	0.2272	4.4008	0.13	-23.5	1.45	-90.3	0.3074	0.75758	8	0.51189	2	-14.5	
CA10112B	0.2157	0.2635	0.1474	0.1138	0.2019	0.1671	5.9857											
CA10112C	0.3195	0.1454	0.1540	0.1424	0.1844	0.2560	3.9067											
CA11103	0.2841	0.1549	0.2612	0.1210	0.2903	0.2722	3.6744											
CA13014	0.1999	0.2442	0.2417	0.3519	0.2252	0.1837	5.4430			0.98	-97.0							
CA13015	0.3193	0.1663	0.2853	0.1624	0.2895	0.3354	2.9819			3.24	-105.8	0.5789						
CA13103	0.2431	0.2150	0.2528	0.2899	0.1697	0.2781	3.5963			1.76	-105.0	0.3509						
CA13104	0.2522	0.2216	0.2600	0.2891	0.1783	0.2749	3.6382			1.36	-101.2	0.2681						
CA13108	0.3238	0.2523	0.1844	0.4466	0.2158	0.2008	4.9812			0.67	-93.8	0.1670						
MAR-26	0.2942	0.2098	0.1416	0.0917	0.1430	0.1968	5.0819			0.90	-91.3	0.2060	0.75440	-	0.51182	-	-15.9	
Sed112	0.2520	0.2374	0.1896	0.1044	0.1546	0.1650	6.0617			1.13	-91.8	0.2972						
CA13016	0.2091	0.2316	0.2257	0.1132	0.1649	0.1703	5.8731			1.31	-90.3	0.3426						
CA13182	0.2464	0.1639	0.2211	0.1136	0.3548	0.2685	3.7241											
CA13184	0.2644	0.1682	0.2307	0.1071	0.2532	0.2768	3.6126											
CA13199	0.3020	0.2334	0.1667	0.1269	0.1629	0.1688	5.9244			1.01	-99.7	0.2642						
MO 50	0.3270	0.2107	0.1589	0.0910	0.1084	0.1915	5.2225	0.18	-24.2									
MO 59	0.2612	0.2348	0.1959	0.0937	0.1430	0.2158	4.6329											

Table 4.1 (continue)

In comparison with bedrock, major elements compositions of banks and SL of the Khudi river show much lower dispersion with Fe, K, Na, Ca and Mg being well correlated to Al/Si ratio, which relates to mineral sorting processes that principally segregate quartz from phyllosilicates.

As observed on larger rivers, Al/Si is correlated with grain size (e.g. D50,) but in the case of the Khudi river the range of variation is much narrower (0.21 to 0.34) than for large rivers of the Himalayan basin (0.10 to 0.35 ; Lupker et al. 2012). This results from the lower degree of sorting of the Khudi due to high turbulent regime. From integration of grain size data that are available for 139 samples from 2010 and 2012 of surface SL, the

average D50 is around 170 µm which corresponds to an Al/Si ratio of 0.25, which places an upper limit for the Al/Si of the eroded parent rock. Total organic carbon (TOC) is around 0.5 wt%, notably higher that HHC bedrocks. $\delta^{13}C$ of TOC are -22 and -26‰ with an average of -24‰. This is higher than HHC bedrock data [Galy 07c, Galy 08] and lower than most of soils analyses (see bellow).

Positive correlations of Fe, K and Mg relative to Al/Si ratios are explained by the mixing between coarse quartz rich sand (low Al/Si ratios) and fine fraction rich in phyllosilicate. Fe, K and Mg are principally carried by biotites whose proportion is higher in fine grain fractions. In contrast with Fe, Mg and K, Na/Al ratios show negative correlation to Al/Si, which can be explained either by a dilution effect by Al-bearing minerals such as micas in fine sediment, or increased proportions in finer sediments of clays that contain no Na, as observed on larger floodplains rivers [Garzanti 10, Garzanti 11, Lupker 11a, Bouchez 12].

Compared to bedrock compositions, Na and Ca concentrations of the river sediment display values incompatible with the HHC of LH bedrock. While river sediment stands in the lower part of HHC rocks and higher part of LH rocks in a Na diagram, Ca compositions are amongst the highest observed for both geological units. Although this basin contain minor LH marbles formations, there is no notable concentration of carbonate in the sediment. Relatively high concentrations in Ca therefore relates to protolith differences. Finally, hydration [H_2O+] of SL span a relatively narrow range that is in the higher range of the HHC and lower than for the LH formations.

Sr and Nd isotopic compositions of sediments of the Khudi sediment were analyzed in order to assess the proportion of material derived from LH compared to HHC. These geological formations have contrasted isotopic signatures related to differences in their crustal ages [Hodges 00, Najman 05]. Data are presented in Figure 4.2.3 and Table 4.1 and Table 4.2.

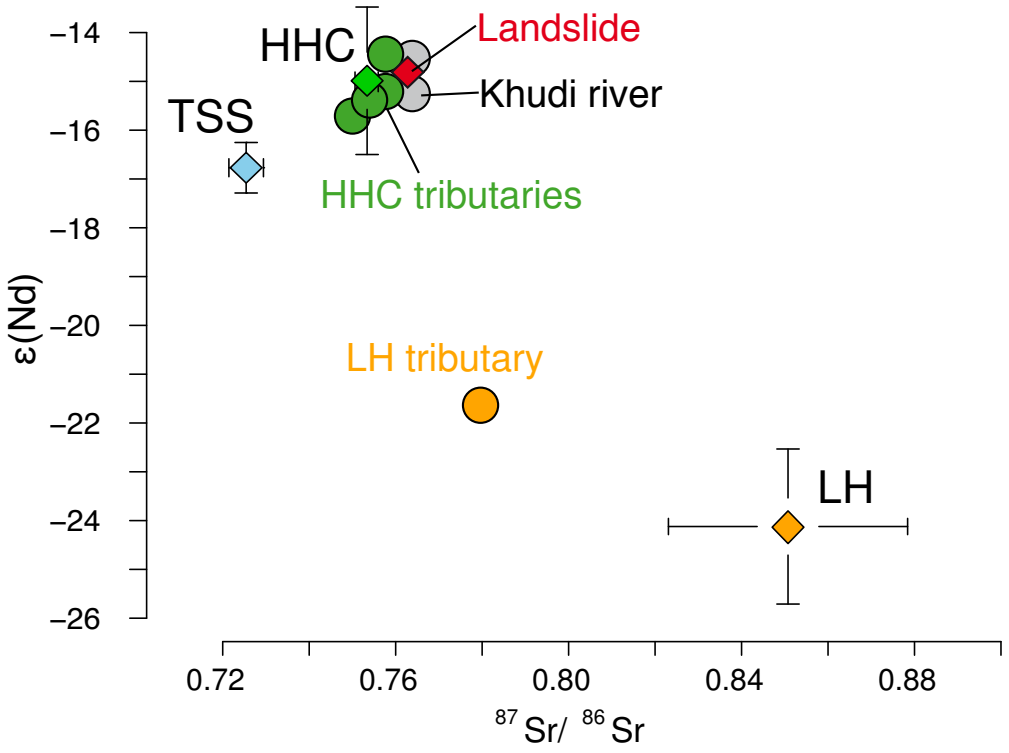

FIGURE 4.2.3 – Sr and Nd isotopic compositions of Khudi khola river sediments, its HHC, LH tributaries and the upper Northern and Western branches of the basin. Composition of the Khudi are grouped on HHC Sr and Nd isotopic compositions and demonstrate that river sediments derive quite exclusively from the basin area where HHC units outcrop. Sr and Nd isotopic compositions are from [Singh 02, Galy 10] and [Morin et al., submit].

To the exception of one tributary sample draining LH formations, all data are very homogeneous and fall in the field of HHC formations as defined in Morin et al. (submit). Because there is no difference between Khudi sediments at the Intake station and from sediments sampled in the HHC, it can be stated that more than 95% of the sediments exported by the Khudi river are derived from the HHC.

Chepe and Dordi rivers sediments compositions are very comparable to those of the Khudi river exepted for Ca of Dordi due to the presence of carbonates. Hence, Dordi CaO compositions range from 2.8 % to 5.6 % while Chepe and Khudi range from 1.2 % to maximum 2%.

Bed sediments and Pebbles

Bank sediments and pebbles are generally less altered than SL and provide alternative information on bedrock composition. Average compositions of unaltered pebbles were determined from ca. 121 and 54 samples for LH and HHC units respectively. The weighted average pebble composition has Al/Si = 0.20, that places a lower limit for bedrock compostion (figure 4.2.2). This value is also comparable to the average of bank sediments and coarse surface sediments SL. While averaged pebbles and banks compositions appear similar to SL sediments in Fe, K, Mg, Na and hydration, pebbles and some banks samples display significantly higher Ca concentration (Ca/Al = 0.16), likely attributed to the fact that pebbles are more pristine than the SL.

Upper Khudi

Bank sediments sampled in the Western and Northern branches samples have compositions in Mg, Ca, Na, H_2O very comparable to the Khudi Khola banks sampled at intake but display lower K/Al and Fe/Al. It may relate to a different protolith that would contain lower amount of micas and especially biotite or to sorting effect as these are not suspended sediments.. As observed in the river at these sites (c.f. A1 pictures 4.3.2 and 4.3.3), SL concentrations are very low so sediment proportions coming from these parts of the basin are equally low, and likely have a minor impact on the sediment transported by the Khudi river.

Tributary sediments

Compositions of sub-order tributaries sediments are presented in table 4.2 and figure 4.2.4.

Ech.#	Locality	Elevation	Type	North	East	Julian day	Date	SiO2 weight%	Al2O3	Fe2O3	MnO	MgO	CaO	Na2O	K2O	TiO2	P2O5	Pf	Total
Landslide																			
CA13201 intermediary	Out. Landslide	2290	33 % weight	28.37177	84.29403			69.67	13.44	5.55	0.08	2.55	1.51	2.02	2.89	0.71	0.22	1.01	99.65
CA13201 fine grain FI	Out. Landslide	2290	9 % weight	28.37177	84.29403			69.66	12.55	5.51	0.09	2.86	2.87	1.77	2.40	0.68	0.23	0.97	99.56
CA13201 migmatitic	Out. Landslide	2290	61 % weight	28.37177	84.29403			67.08	15.81	5.46	0.07	1.73	1.15	2.01	3.12	0.67	0.15	1.37	98.61
Weight aver. pebbles	Out. Landslide	2290	*Av. Pebbles*	*28.37177*	*84.29403*			*68.14*	*14.77*	*5.49*	*0.07*	*2.09*	*1.42*	*1.99*	*2.98*	*0.68*	*0.18*	*1.22*	*99.03*
CA953	Out. Landslide	2290	Bank	28.37177	84.29403	314	11/11/09	68.80	14.43	5.59	0.09	2.13	1.43	1.40	3.00	0.63	0.12	1.70	99.32
CA954	Out. Landslide	2290	Bank	28.37177	84.29403	314	11/11/09	68.11	14.76	5.94	0.10	2.54	1.70	1.54	3.07	0.68	0.15	1.70	100.28
CA955	Out. Landslide	2290	Bank	28.37177	84.29403	314	11/11/09	69.28	14.09	5.25	0.07	1.71	2.81	2.09	2.23	0.64	0.43	1.75	100.35
CA11003	Inner Landslide	2643	Bank	28.35	84.28333	339	05/12/11	71.87	11.89	5.12	0.09	2.77	1.76	1.31	2.83	0.63	0.11	2.68	101.05
CA11207<2mm	Inner Landslide	2756	Sand/Gravels	28.36248	84.28762	311	08/11/11	69.67	13.52	5.00	0.07	2.16	1.33	1.43	3.19	0.65	0.11	2.90	100.01
CA12002<2mm	Out. Landslide	2397	Bank	28.37153	84.29366	120	30/04/12	70.82	13.86	5.24	0.07	1.77	1.61	1.46	2.53	0.54	0.16	1.90	99.96
CA12004<2mm	Outlet, N. Landslide	2377	Bank	28.37175	84.28667	120	30/04/12	72.32	12.39	4.97	0.11	2.14	1.95	1.54	2.33	0.51	0.15	1.25	99.65
Tributaries																			
CA970		1380	Bank	28.34044	84.3283	316	13/11/09	72.01	11.45	4.716	0.057	2.942	1.305	1.562	1.985	0.607	0.121	3.386	100.1
CA971		1305	Bank	28.33811	84.33086	316	13/11/09	78.28	9.463	2.938	0.033	1.649	1.064	1.666	1.233	0.392	0.088	2	98.81
CA10101	Dhadu	1090	Bank	28.32525	84.33199	314	11/11/10	76.74	9.615	4.001	0.065	1.657	1.908	1.351	2	0.39	0.1	2.14	99.97
CA10102	Probi	1090	Bank	28.32525	84.33199	314	11/11/10	75.51	9.148	5.112	0.066	1.845	1.671	1.02	2.399	0.436	0.11	2.53	99.84
CA10111		1976	Bank	28.35442	84.31812	318	15/11/10	71.7	13.39	5.428	0.157	1.568	1.954	1.425	1.804	0.413	0.13	1.45	99.41
CA10113		1967	Bank	28.36476	84.30473	318	15/11/10	76.56	11.35	3.804	0.068	2.016	1.533	1.795	1.778	0.439	0.11	1.64	101.1
CA10115		1984	Bank	28.36198	84.30741	318	15/11/10	81.01	8.86	2.516	0.025	1.507	1.119	1.885	1.198	0.346	0.09	1.49	100.1
CA11007A		1399	Bank	28.33333	84.31667			72.01	13.63	5.561	0.141	2.075	1.263	1.593	1.737	0.529	0.09	1.79	100.4
CA11007B		1399	Bank	28.33333	84.31667			72.98	7.859	2.587	0.061	1.785	5.62	1.273	1.66	0.289	0.08	5.18	99.38
CA11011		1114	Bank	28.32525	84.33199			76.02	9.458	3.748	0.042	1.939	1.68	1.438	2.204	0.386	0.11	2.65	99.67
CA11212A<2mm	Upper NW basin	3675	Sand/Gravels	28.40531	84.26293	313	10/11/11	73.94	11.51	3.798	0.055	1.774	1.862	1.901	2.032	0.431	0.13	2.49	99.92
CA11213A<2mm	Upper NW basin	3530	Sand/Gravels	28.395	84.25574	313	10/11/11	74.49	13.39	3.695	0.067	1.53	1.522	1.492	1.824	0.4	0.07	1.37	99.85

TABLE 4.2 – Geochemical compositions of HHC, LH tributaries and the upper Northern and Western branches of the basin.

Ech.#	Fe/Al mol:mol	Na/Al	K/Al	Ca/Al	Mg/Al	Al/Si	Si/Al	TOC [%]	δ^{13}Corg [‰]	H2O+ [%]	δD [‰]	H_2O+/Al	$^{87}Sr/^{86}Sr$ Sil	±2σ 1.E-06	$^{143}Nd/^{144}Nd$ Sil	±2σ 1.E-06	εNd_0 Sil
Landslide																	
CA13201 intermediary	0.2637	0.2470	0.2330	0.1023	0.2399	0.2274	4.3982										
CA13201 fine grain FI	0.2802	0.2314	0.2070	0.2077	0.2882	0.2122	4.7117										
CA13201 migmatitic	0.2204	0.2089	0.2134	0.0661	0.1386	0.2778	3.5998										
Weight aver. pebbles	*0.2374*	*0.2217*	*0.2186*	*0.0872*	*0.1792*	*0.2554*	*3.9152*										
CA953	0.2473	0.1591	0.2248	0.0901	0.1867	0.2472	4.0453	0.15	-24.6	1.53	-87.3	0.2998					
CA954	0.2566	0.1718	0.2254	0.1045	0.2175	0.2554	3.9147	0.15	-22.6	1.61	-89.0	0.3094	0.76186	7	0.511880	2	-14.8
CA955	0.2378	0.2438	0.1715	0.1814	0.1538	0.2397	4.1726	0.11	-25.6	1.31	-95.0	0.2626					
CA11003	0.2747	0.1813	0.2582	0.1348	0.2944	0.1949	5.1315	0.11	-21.6	1.56	-92.7	0.4071					
CA11207<2mm	0.2362	0.1736	0.2552	0.0895	0.2019	0.2286	4.3741	0.20	-23.0	1.31	-90.6	0.2741					
CA12002<2mm	0.2412	0.1736	0.1975	0.1053	0.1616	0.2307	4.3347										
CA12004<2mm	0.2558	0.2041	0.2033	0.1427	0.2188	0.2019	4.9524										
Tributaries																	
CA970	0.2630	0.2245	0.1878	0.1036	0.3253	0.1873	5.3387										
CA971	0.1982	0.2896	0.1411	0.1022	0.2205	0.1425	7.0200										
CA10101	0.2656	0.2312	0.2252	0.1804	0.2181	0.1476	6.7728						0.77830	16	0.511530	3	-21.6
CA10102	0.3567	0.1834	0.2840	0.1661	0.2552	0.1428	7.0044										
CA10111	0.2587	0.1751	0.1459	0.1326	0.1482	0.2201	4.5433										
CA10113	0.2140	0.2602	0.1697	0.1228	0.2248	0.1747	5.7250						0.75655	7	0.511862	4	-15.1
CA10115	0.1813	0.3500	0.1464	0.1148	0.2153	0.1289	7.7589										
CA11007A	0.2604	0.1922	0.1380	0.0842	0.1926	0.2231	4.4826										
CA11007B	0.2101	0.2665	0.2287	0.6501	0.2874	0.1269	7.8801										
CA11011	0.2529	0.2501	0.2523	0.1615	0.2594	0.1466	6.8206										
CA11212A<2mm	0.2106	0.2717	0.1912	0.1471	0.1950	0.1834	5.4513						0.74840	11	0.511835	3	-15.7
CA11213A<2mm	0.1761	0.1833	0.1475	0.1033	0.1446	0.2119	4.7194										

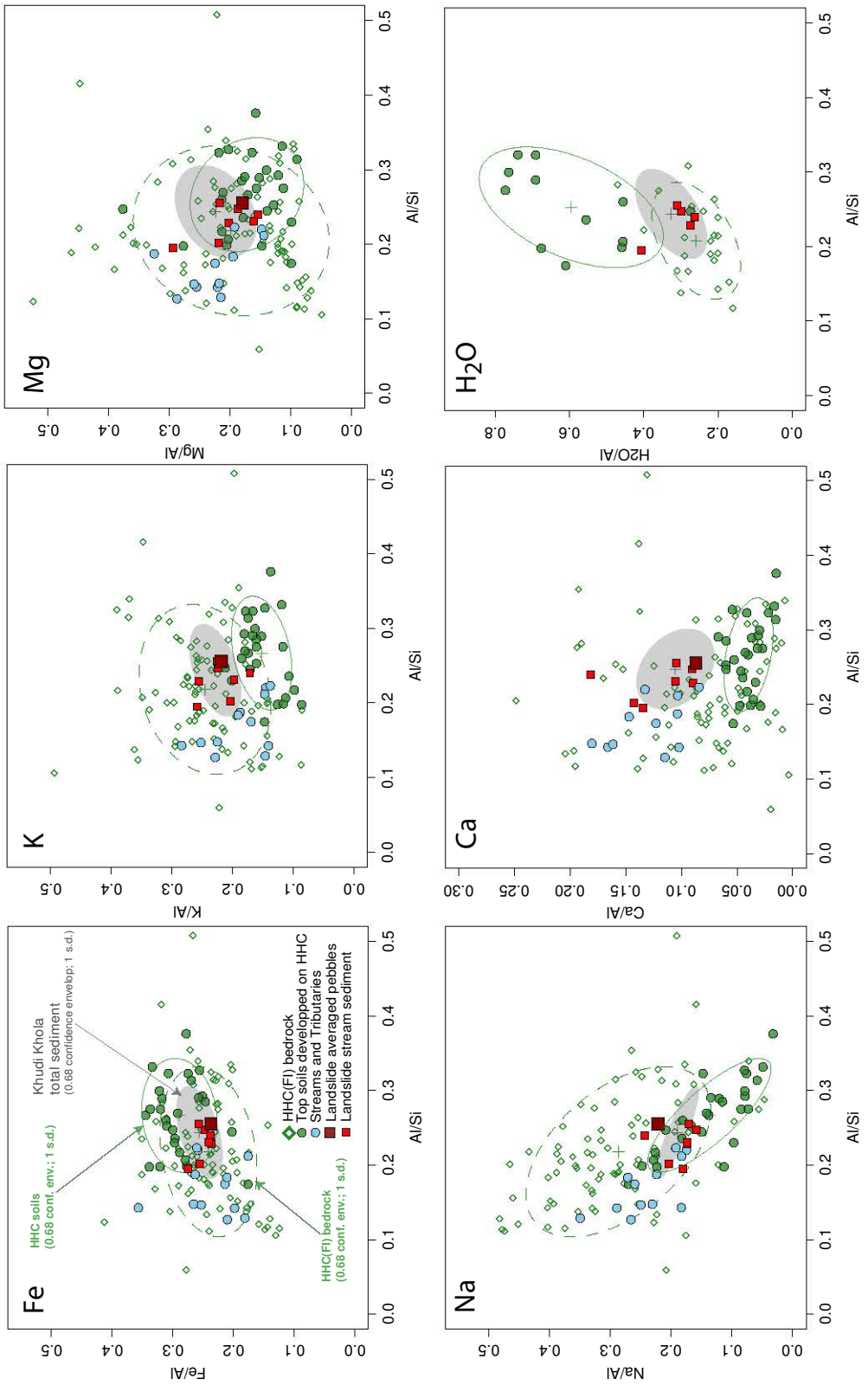

FIGURE 4.2.4 – Weathering signatures of soils and landslide sediments, small tream and tributaries and Khudi khola river sediments by chemical compositions in major elements and hydration content compared to HHC protolith. Ellipses display 1 standard deviation (68% confidence interval).

Averaged sands and gravels compositions have more silicic compositions compared to Khudi river sediment (grey ellipse in figure 4.2.4), with an average Al/Si = 0.17. Their compositions spread very large range for most elements. This may derive from local lithological heterogeneity or differential mineral sorting that can induce placers in such small streams. Their composition in Na/Al, Mg/Al, Ca/Al show apparent anti correlation with Al/Si and higher values than river sediment. We interpret these apparent pristine signatures as a combined result of transport and resistance to weathering. Indeed, sediment collected in these streams results from runoff erosion of surface of hillslopes. Only unweathered and competent minerals, mixed gravels and pebbles and quartzites that have resisted to weathering are susceptible to be stored in these stream-beds for long time as fine particules are easily flushed and transported with the washload. The fact that observations during monsoon that washload is quasi-inexistent in these streams is an argument suggesting low erosion fluxes. Finally, given their compositions, it seems very difficult to imagine high fluxes coming from these slopes to explain Khudi river sediment composition, which agree with low erosion rates ~ 0.14 mm/y calculated from TCN in these sub-order basins [Niemi 05]. It must be underlined however that our sampling is only based on sand and gravels sampled in the bed of these streams principally during the dry season. Such sampling therefore does not comprise episodic events of SL transport linked to local failure or small and surficial landslide.

Compared to parental material that is mainly HHC Formation I, Khudi Chepe and Dordi khola rivers sediment river sediment appears richer in Ca, analog in Fe, Mg and [H_2O+], slightly poorer in K and sensibly poorer in Na c.f. figure 4.2.2. Na and K compositions of the river sediment could either correspond to a loss during weathering on hillslopes, known to account around 60 to 65 % of the silicate alkalinity flux across the Himalayan part of Ganga basin [Galy 99b], or the fact HHCFI rocks give an overestimated composition in Na and K compared to the Khudi crust. Ca composition of the river sediments remain problematic because seem enriched in Ca, standing in the highest values of HHC FI bedrock, and even well above this value for Dordi sediments This particularity may be explained by the presence of carbonates in trace in the HHC formation I. We detected traces of carbonates in the Khudi khola sediment : measured carbonates content ranges between 0.03 to 0.14 % with an average of 0.07% (cf. table 4.1). It represents Ca ~ 0.0007 mol /100g which compare to an average value of Ca ~ 0.0272 mol/100g in Khudi

sediment, therefore less than 3% the Ca composition in the river. Such minor contents are not sufficient to explain the high Ca observed in Khudi and Chepe sediments compared to the HHC FI, which contains very little Ca. Except this particular element, Dordi, Chepe and Khudi river sediment compositions are remarquably comparable to Fe, K, Mg, Na compositions of Ganga basin crust estimated by [Lupker 11b, Lupker 12b].

4.2.5.3 Soils compositions

Classically, chemical compositions of soils display a loss of mobile elements with depth, from the parental bedrock and saprolite to the topsoil that relates to chemical weathering of primary minerals (e.g. [Kump 00, Brantley 11, White 14] . Weathering in soils was already described on comparable parental material HHC gneisses in tributaries of Trisuli basin : by chemical compositions analysis in the Likkhu khola basin [Gardner 96], and by determination of clay and silts composition soils profiles in the Salankhu khola basin, on Salme slope [Lorphelin 85, Right 86]. Results of both studies describe weathering trend from the bedrock material toward the surface topsoils marked by a progressive loss of mobile cations K and Na, loss of Na, K, Mg [Gardner 96] and associated changes in mineralogy : dissolution of chlorite, vermiculitisation of micas, weathering to goethite and weathering of feldspars into smectite [Right 86].

Geochemical compositions of soils profiles of the Khudi are presented in figure 4.2.4 and data are listed in table 4.3

Ech.#	Elevation [m] (asl)	Depth [m]	North	East	SiO2	Al2O3	Fe2O3	MnO	MgO	CaO	Na2O	K2O	TiO2	P2O5	Pf
					weight%										
LH soils															
CA904	1040	0.15	28.29351	84.33225	63.36	12.47	5.61	0.10	5.01	0.70	0.24	2.19	0.50	0.27	8.97
CA904	1040	1.1	28.29351	84.33225	62.61	12.90	6.11	0.09	5.26	0.58	0.17	2.14	0.51	0.42	8.88
CA904	1040	2.3	28.29351	84.33225	63.29	13.46	6.20	0.09	5.36	0.51	0.14	2.16	0.54	0.39	8.12
CA905	1575	0.1	28.28948	84.32068	60.81	16.29	5.57	0.06	3.22	0.52	0.35	3.30	0.58	0.17	8.32
CA905	1575	0.8	28.28948	84.32068	60.43	19.64	6.02	0.02	3.53	1.07	0.37	3.87	0.61	0.09	5.30
CA906	1720	0.6	28.29037	84.31641	54.99	19.58	7.61	0.13	2.98	0.44	0.18	2.49	0.65	0.11	10.83
CA907	2120	0.75	28.28717	84.31229	62.15	16.13	4.91	0.04	3.49	0.10	0.10	3.25	0.65	0.10	8.70
CA907	2120	1.05	28.28717	84.31229	59.14	18.87	5.94	0.09	2.88	0.32	0.20	2.69	0.64	0.11	9.45
CA907	2120	1.65	28.28717	84.31229	49.79	22.96	7.75	0.24	4.06	0.55	0.11	1.95	0.65	0.11	11.85
CA907	2120	2.5	28.28717	84.31229	61.28	18.41	6.24	0.05	3.69	0.88	0.32	2.66	0.53	0.06	6.85
CA908	2145	0.6	28.2979	84.30232	62.29	16.97	7.28	0.06	2.67	NA	0.12	5.67	0.70	NA	4.25
CA908	2145	1.5	28.2979	84.30232	64.94	14.60	7.47	0.13	2.81	NA	0.09	4.88	0.60	0.07	4.01
CA909	2145	0.5	28.2979	84.30232	55.76	19.71	7.34	0.14	2.99	0.04	0.21	8.28	0.82	0.06	4.59
CA910	2145	0	28.2979	84.30232	68.14	13.25	5.51	0.04	2.59	0.13	0.97	4.24	0.57	0.08	4.74
CA912	2155	0.05	28.29574	84.29911	57.57	15.18	6.34	0.10	2.66	0.18	0.74	3.73	0.66	0.20	12.85
CA912	2155	0.6	28.29574	84.29911	61.23	16.23	6.86	0.10	2.43	0.13	2.13	4.41	0.63	0.11	6.23
CA912	2155	0.7	28.29574	84.29911	59.85	17.23	7.09	0.08	3.10	0.33	2.65	5.20	0.69	0.12	4.15
CA913	2210	0.05	28.29592	84.30104	55.75	15.58	6.80	0.08	2.11	0.18	0.34	2.61	0.81	0.21	15.73
CA913	2210	0.4	28.29592	84.30104	57.78	17.51	7.93	0.13	2.42	0.17	0.27	2.68	0.95	0.13	10.73
CA913	2210	1	28.29592	84.30104	58.06	17.41	8.35	0.09	2.69	0.08	0.56	4.54	0.71	0.08	6.72
CA913	2210	1.45	28.29592	84.30104	60.67	18.05	7.95	0.07	1.95	0.05	0.57	6.09	0.74	0.07	4.44
CA913	2210	2.25	28.29592	84.30104	61.18	17.60	5.52	0.05	2.50	0.09	1.11	6.00	0.67	0.09	4.46
CA972	1110	0	28.32528	84.33286	60.97	16.16	4.88	0.02	3.09	1.28	1.06	3.49	0.62	0.34	7.71
HHC soils															
CA914	2382	0.25	28.30948	84.2984	55.16	14.42	7.10	0.04	1.44	0.41	0.49	1.57	0.90	0.15	18.23
CA914	2382	0.85	28.30948	84.2984	54.39	17.71	7.66	0.12	2.28	0.28	0.35	2.41	0.92	0.12	12.72
CA914	2382	1.95	28.30948	84.2984	56.85	18.20	8.09	0.12	2.55	0.48	1.15	2.41	0.77	0.15	8.15
CA914	2382	2.6	28.30948	84.2984	70.80	12.49	6.06	0.07	2.19	0.32	1.14	1.63	0.82	0.11	4.90
CA915	2382	0.25	28.30948	84.2984	52.39	14.75	7.71	0.04	1.33	0.27	0.44	1.62	0.91	0.21	19.89
CA915	2382	0.55	28.30948	84.2984	55.01	17.55	7.64	0.10	2.19	0.29	0.35	2.23	0.96	0.13	13.00
CA915	2382	1.75	28.30948	84.2984	68.19	14.25	5.87	0.05	2.13	0.44	1.16	1.39	0.72	0.11	6.04
CA916	2500	0.05	28.30948	84.2984	63.78	10.71	5.39	0.04	1.25	0.56	0.74	1.25	0.68	0.15	16.38
CA916	2500	0.35	28.30948	84.2984	54.06	12.62	6.33	0.03	1.12	0.38	0.56	1.37	0.83	0.21	22.99
CA916	2500	0.95	28.30948	84.2984	56.89	16.76	7.89	0.08	2.28	0.43	0.41	2.14	0.86	0.11	12.16
CA916	2500	1.75	28.30948	84.2984	73.27	11.71	4.90	0.05	1.91	0.85	0.78	0.88	0.67	0.13	5.47
CA916	2500	4.25	28.30948	84.2984	74.45	11.12	4.48	0.07	2.15	1.17	0.88	1.84	0.65	0.15	3.67
CA917	2500	2.35	28.31379	84.29287	69.65	12.69	4.76	0.02	3.41	0.74	1.01	1.99	0.62	0.06	4.88
CA918	2245	0.1	28.33045	84.29181	64.56	11.90	5.38	0.07	2.01	0.54	1.64	1.08	0.66	0.35	12.05
CA918	2245	0.35	28.33045	84.29181	70.17	11.84	5.14	0.11	1.92	0.49	1.79	1.27	0.68	0.43	6.35
CA918	2245	0.55	28.33045	84.29181	70.15	12.30	5.38	0.11	1.98	0.48	1.71	1.29	0.69	0.42	6.12
CA918	2245	0.75	28.33045	84.29181	69.44	12.03	5.84	0.07	1.90	0.44	1.74	1.24	0.74	0.36	6.21
CA922	2365	0.35	28.32828	84.28743	64.16	12.83	5.96	0.07	1.81	0.63	1.42	1.27	0.75	0.26	10.90
CA924	3200	0.05	28.35564	84.27526	57.10	11.14	5.18	0.02	0.87	0.41	0.66	2.07	0.79	0.22	21.70
CA924	3200	0.85	28.35564	84.27526	58.46	16.66	7.50	0.07	2.04	0.39	0.69	2.63	0.92	0.18	10.09
CA924	3200	1.6	28.35564	84.27526	61.47	18.77	6.03	0.23	0.86	0.28	0.75	2.27	0.72	0.14	8.25
CA926	4000	0.1	28.40011	84.2473	54.18	14.84	6.39	0.04	2.56	0.67	1.33	2.45	0.95	0.50	15.82
CA926	4000	0.5	28.40011	84.2473	62.43	13.77	6.72	0.05	2.33	0.80	1.52	2.36	0.78	0.30	8.28
CA927	4000	0.05	28.40011	84.2473	62.60	12.99	4.12	0.03	1.43	0.67	1.19	2.05	0.70	0.24	13.05
CA927	4000	0.55	28.40011	84.2473	61.03	13.81	7.46	0.04	1.86	0.61	1.16	2.23	0.83	0.21	10.72
CA928	4085	0.25	28.40161	84.25102	62.23	14.24	6.50	0.05	2.38	0.67	1.23	2.36	0.71	0.21	9.75
CA929	3930	0.05	28.40371	84.25682	64.87	9.60	2.65	0.02	0.75	0.57	1.58	1.31	0.72	0.15	18.42
CA929	3930	0.15	28.40371	84.25682	67.08	11.25	5.97	0.03	2.46	0.36	1.53	0.90	0.64	0.11	9.10
CA929	3930	0.65	28.40371	84.25682	70.56	12.38	5.03	0.05	3.31	0.47	1.48	1.92	0.66	0.07	4.07
CA930	3930	0	28.40371	84.25682	54.87	9.24	4.49	0.03	1.50	0.52	1.19	1.15	0.59	0.24	25.97
CA931	3665	0.05	28.38847	84.26222	56.34	12.08	5.87	0.03	1.23	0.80	1.23	1.80	0.73	0.25	18.55
CA931	3665	0.25	28.38847	84.26222	58.90	14.46	7.20	0.04	1.74	0.59	1.07	2.04	0.80	0.16	11.87
CA931	3665	0.55	28.38847	84.26222	56.76	15.56	7.49	0.05	2.01	0.37	0.72	2.40	0.84	0.19	12.83
CA931	3665	0.85	28.38847	84.26222	63.90	15.46	5.84	0.08	3.53	0.68	1.71	1.09	0.61	0.16	6.85
CA931	3665	0.95	28.38847	84.26222	69.76	13.32	4.46	0.04	3.27	1.08	3.65	0.83	0.50	0.11	2.79
CA932	3635	0.05	28.39916	84.2607	47.07	11.69	4.60	0.04	1.11	0.40	0.56	1.95	0.60	0.35	31.07
CA932	3635	0.3	28.39916	84.2607	60.83	16.19	6.84	0.13	1.15	0.28	0.58	2.61	0.80	0.21	9.66
CA958	2945	0.95	28.36344	84.27742	60.83	16.19	6.84	0.13	1.15	0.28	0.58	2.61	0.80	0.21	9.66
CA10105A	2691	4.45	28.36259	84.29028	66.27	12.49	5.24	0.03	2.35	0.55	1.62	1.13	0.68	0.13	8.90
CA10105C	2691	2.15	28.36259	84.29028	62.80	15.22	6.50	0.12	3.80	2.87	1.55	2.66	0.74	0.14	4.48
CA10105D	2691	1.45	28.36259	84.29028	63.72	14.47	6.25	0.10	2.95	1.95	1.43	2.21	0.74	0.14	6.41
CA10105E	2691	1.15	28.36259	84.29028	58.60	16.00	6.53	0.08	2.77	0.98	0.64	2.14	0.74	0.13	12.29
CA10105F	2691	0.55	28.36259	84.29028	55.25	15.34	6.15	0.05	2.46	0.92	0.74	2.08	0.70	0.15	16.71
CA10105G	2691	0.3	28.36259	84.29028	59.58	14.42	5.56	0.06	2.06	0.95	1.02	2.14	0.59	0.12	14.00
CA10105H	2691	0.2	28.36259	84.29028	56.80	14.01	5.65	0.04	1.95	1.03	1.15	2.16	0.64	0.16	16.97
CA11108A	0	0.3	28.361767	84.3095	58.02	14.75	7.44	0.09	1.63	0.48	0.71	2.22	0.91	0.26	12.85
CA11108B	0	0.5	28.361767	84.3095	60.52	14.13	7.46	0.08	1.75	0.49	0.73	2.10	0.87	0.22	11.19
CA11108C	0	1	28.361767	84.3095	61.88	15.43	6.74	0.07	3.78	0.61	1.10	1.88	0.79	0.13	7.30
CA11108D	0	1.5	28.361767	84.3095	62.99	15.67	6.38	0.03	4.20	0.56	1.53	1.04	0.80	0.16	5.95
CA11109	0	0.3	28.354717	84.318233	64.49	13.53	6.36	0.07	4.02	0.89	1.72	2.66	0.81	0.15	4.06

TABLE 4.3 – Geochemical compositions of soils profiles of the Khudi basin.

Ech.#	Total	Fe/Al mol:mol	Na/Al	K/Al	Ca/Al	Mg/Al	Al/Si	Si/Al	TOC [%]	δ13Corg [‰]	H2O+ [%]	δD [‰]	H2O+/Al mol:mol
LH soils													
CA904	99.42	0.2870	0.0322	0.1905	0.0512	0.5086	0.2319	4.3126					
CA904	99.67	0.3024	0.0212	0.1794	0.0412	0.5161	0.2428	4.1187					
CA904	100.27	0.2941	0.0171	0.1739	0.0344	0.5041	0.2507	3.9893					
CA905	99.18	0.2184	0.0351	0.2194	0.0290	0.2500	0.3157	3.1677					
CA905	100.95	0.1957	0.0308	0.2136	0.0496	0.2276	0.3830	2.6110					
CA906	99.98	0.2482	0.0150	0.1378	0.0202	0.1924	0.4196	2.3834					
CA907	99.61	0.1941	0.0103	0.2181	0.0054	0.2734	0.3059	3.2689	1.40	-22.8			
CA907	100.32	0.2008	0.0177	0.1544	0.0154	0.1930	0.3759	2.6600	1.19	-21.9	5.71	-93.7	0.8577
CA907	100.00	0.2154	0.0079	0.0918	0.0216	0.2239	0.5434	1.8402	0.45	-22.2	7.74	-84.3	0.9555
CA907	100.97	0.2164	0.0281	0.1566	0.0434	0.2533	0.3541	2.8243	0.34	-23.8			
CA908	100.00	0.2737	0.0114	0.3614	NA	0.1993	0.3211	3.1141	0.84	-25.8	3.50	-92.0	0.5840
CA908	99.60	0.3266	0.0104	0.3619	NA	0.2440	0.2649	3.7756	0.70	-25.7	3.12	-92.3	0.6518
CA909	99.94	0.2377	0.0178	0.4551	0.0019	0.1918	0.4165	2.4011	0.99	-25.8	3.34	-95.3	0.3882
CA910	100.26	0.2653	0.1198	0.3465	0.0089	0.2470	0.2291	4.3648					
CA912	100.21	0.2667	0.0804	0.2664	0.0107	0.2218	0.3107	3.2186	3.47	-23.3	3.84	-88.4	0.5452
CA912	100.48	0.2699	0.2163	0.2940	0.0073	0.1897	0.3123	3.2018	0.75	-25.1	2.82	-92.9	0.4714
CA912	100.48	0.2626	0.2530	0.3266	0.0176	0.2276	0.3392	2.9479					
CA913	100.20	0.2786	0.0358	0.1812	0.0107	0.1712	0.3293	3.0367	3.67	-26.1			
CA913	100.69	0.2892	0.0249	0.1655	0.0089	0.1746	0.3571	2.8000	1.28	-25.6			
CA913	99.29	0.3061	0.0531	0.2823	0.0042	0.1955	0.3534	2.8294	0.46	-29.5			
CA913	100.65	0.2811	0.0523	0.3651	0.0026	0.1365	0.3507	2.8516	0.19	-3.2			
CA913	99.26	0.2002	0.1036	0.3690	0.0046	0.1799	0.3389	2.9506	0.11	-31.5			
CA972	99.61	0.1929	0.1077	0.2336	0.0719	0.2421	0.3123	3.2020					
HHC soils													
CA914	99.91	0.3143	0.0556	0.1180	0.0257	0.1264	0.3081	3.2454	2.27	-25.5			
CA914	98.96	0.2761	0.0324	0.1472	0.0143	0.1632	0.3837	2.6061	1.25	-24.7			
CA914	98.94	0.2837	0.1041	0.1436	0.0241	0.1771	0.3773	2.6506	0.18	-24.4			
CA914	100.52	0.3099	0.1506	0.1413	0.0234	0.2218	0.2078	4.8112	0.62	-24.3			
CA915	99.56	0.3337	0.0490	0.1190	0.0165	0.1143	0.3317	3.0149	3.89	-25.6			
CA915	99.43	0.2778	0.0324	0.1374	0.0149	0.1580	0.3760	2.6593	1.75	-26.1			
CA915	100.34	0.2628	0.1344	0.1059	0.0278	0.1891	0.2462	4.0612	0.27	-29.4			
CA916	100.93	0.3212	0.1132	0.1261	0.0477	0.1477	0.1979	5.0541	5.40	-26.6			
CA916	100.50	0.3202	0.0732	0.1173	0.0272	0.1123	0.2752	3.6339	8.12	-26.4	3.44	-88.6	0.7729
CA916	100.00	0.3005	0.0401	0.1380	0.0233	0.1720	0.3473	2.8795	0.77	-24.5			
CA916	100.64	0.2673	0.1090	0.0815	0.0661	0.2067	0.1883	5.3099	0.84	-25.2			
CA916	100.61	0.2569	0.1299	0.1789	0.0952	0.2445	0.1761	5.6801	0.33	-27.0			
CA917	99.82	0.2393	0.1307	0.1698	0.0531	0.3403	0.2147	4.6577					
CA918	100.23	0.2886	0.2262	0.0984	0.0409	0.2134	0.2172	4.6036					
CA918	100.18	0.2774	0.2483	0.1165	0.0379	0.2055	0.1988	5.0310	1.44	-25.9	1.92	-88.6	0.4592
CA918	100.63	0.2792	0.2292	0.1131	0.0355	0.2032	0.2067	4.8381	1.33	-26.0	1.98	-94.8	0.4563
CA918	100.00	0.3097	0.2374	0.1114	0.0330	0.1995	0.2041	4.8993					
CA922	100.06	0.2963	0.1822	0.1074	0.0448	0.1784	0.2357	4.2419	3.58	-26.5	2.52	-92.8	0.5555
CA924	100.15	0.2970	0.0972	0.2013	0.0336	0.0988	0.2298	4.3512					
CA924	99.63	0.2873	0.0676	0.1712	0.0212	0.1550	0.3358	2.9781					
CA924	99.78	0.2052	0.0658	0.1307	0.0137	0.0582	0.3598	2.7790					
CA926	99.75	0.2747	0.1477	0.1788	0.0413	0.2185	0.3228	3.0977	6.23	-25.4	3.62	-93.4	0.6915
CA926	99.33	0.3116	0.1812	0.1853	0.0527	0.2137	0.2599	3.8471	1.29	-28.2	2.22	-14.5	0.4558
CA927	99.06	0.2024	0.1502	0.1711	0.0465	0.1390	0.2446	4.0886					
CA927	99.96	0.3447	0.1384	0.1745	0.0402	0.1707	0.2666	3.7508					
CA928	100.34	0.2915	0.1419	0.1797	0.0426	0.2118	0.2697	3.7084					
CA929	100.63	0.1761	0.2705	0.1476	0.0535	0.0992	0.1743	5.7369	9.25	-24.8	2.67	-97.6	0.6142
CA929	99.42	0.3387	0.2237	0.0864	0.0288	0.2772	0.1976	5.0598	1.21	-25.5	2.68	-116.2	0.6762
CA929	100.00	0.2592	0.1966	0.1681	0.0347	0.3380	0.2068	4.8353	0.32	-27.6			
CA930	99.79	0.3106	0.2120	0.1352	0.0516	0.2053	0.1983	5.0419					
CA931	98.91	0.3101	0.1675	0.1610	0.0600	0.1283	0.2527	3.9569	4.88	-26.6			
CA931	98.84	0.3176	0.1213	0.1525	0.0368	0.1519	0.2893	3.4565	3.13	-26.0	3.53	-96.6	0.6914
CA931	99.21	0.3071	0.0762	0.1667	0.0217	0.1637	0.3230	3.0959	3.96	-26.4	4.59	-98.3	0.7392
CA931	99.91	0.2411	0.1823	0.0765	0.0399	0.2887	0.2852	3.5067	0.30	-26.6			
CA931	99.80	0.2139	0.4511	0.0675	0.0739	0.3103	0.2250	4.4443	0.62	-26.8			
CA932	99.43	0.2512	0.0786	0.1807	0.0310	0.1206	0.2925	3.4182					
CA932	99.26	0.2695	0.0587	0.1745	0.0154	0.0898	0.3137	3.1877					
CA958	99.26	0.2695	0.0587	0.1745	0.0154	0.0898	0.3137	3.1877	1.24	-26.5			
CA10105A	99.37	0.2676	0.2127	0.0981	0.0397	0.2376	0.2221	4.5025			2.45	-92.5	0.5457
CA10105C	100.86	0.2726	0.1672	0.1890	0.1716	0.3158	0.2855	3.5025	0.77	-26.6			
CA10105D	100.36	0.2756	0.1629	0.1654	0.1224	0.2581	0.2675	3.7381	0.29	-25.8			
CA10105E	100.89	0.2607	0.0660	0.1451	0.0556	0.2191	0.3217	3.1089	1.86	-25.2	2.45	-92.5	0.4269
CA10105F	100.55	0.2559	0.0796	0.1471	0.0543	0.2026	0.3272	3.0563	3.28	-25.9			
CA10105G	100.49	0.2463	0.1159	0.1610	0.0598	0.1807	0.2852	3.5066	2.38	-26.2			
CA10105H	100.55	0.2573	0.1349	0.1672	0.0670	0.1760	0.2906	3.4416	4.22	-26.5			
CA11108A	99.37	0.3220	0.0790	0.1631	0.0298	0.1401	0.2995	3.3391			3.98	-83.5	0.7640
CA11108B	99.55	0.3369	0.0851	0.1610	0.0317	0.1569	0.2750	3.6359					
CA11108C	99.69	0.2790	0.1169	0.1317	0.0360	0.3103	0.2938	3.4042	0.85	-19.8			
CA11108D	99.29	0.2600	0.1603	0.0716	0.0323	0.3395	0.2931	3.4116					
CA11109	98.74	0.3000	0.2092	0.2125	0.0598	0.3763	0.2472	4.0453	0.30	-26.1	2.39	-87.6	0.2749

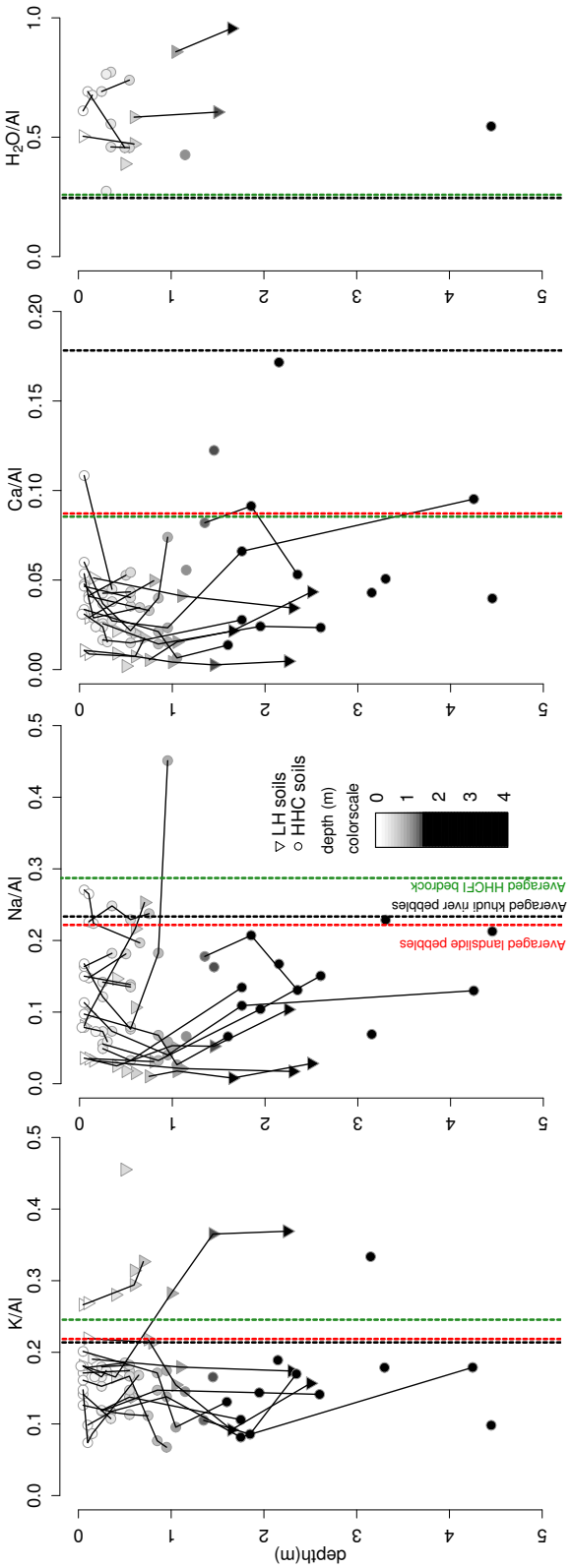

FIGURE 4.2.5 – Mobile elements and hydroxyles content of soils along deep profiles. As pristine rocks references, Khudi khola pebbles (dashed black line), landslides pebbles (dashed red line) and HHC bedrock (dashed green line) compositions also represented.

Most soils profiles do not correspond to well organized weathering pattern in soils. K/Al, Na/Al and Ca/Al ratios do not show progressive depletion trend along soils horizons (c.f. figure 4.2.5). Still, merely all soil compositions are depleted in mobile cations K, Na, Ca compared to the bedrock references (HHCFI bedrock, Khudi river pebbles and landslide pebbles) (figures 4.2.4 & 4.2.5). The loss of mobile cations is also corroborated by mineral hydration content [H_2O+] that are noticably higher than those of bedrock references. This tracer, more than majors elements seem very sensitive to weathering as expressed by the very high soils hydration values that reach 2 to 3 fold the intial water content in the bedrock.

Several factors may be at the origin of the scattering of soils profiles : 1- the initial heterogeneity of bedrock composition may overprint the losses of cations induced by weathering, 2- colluvial and soil creeping may generate perturbed soil profile and in some case saprolite fragment were observed at higher levels of the profiles ; finally, the weathering front appears in most case to be very deep so that we never sampled real protolith. Soils profiles CA 918 and 931 show Na/Al ratios higher than river sediments or other soils. These are likely developed on more sodic protolith. This variability can be explained by migmatitic zones in gneisses, that could express locally Na-rich leucosome [Barbey 96].

Classically, soil organic carbon (TOC) is abundant in the upper horizon (2 to 5 wt% above 60 cm) and decrease bellow 1% in deeper levels. $\delta^{13}C$ of TOC are low between -24 and -28‰ with an average of -25.5‰ in HHC soils. Such values are consistant with the C3 nature of the flora.

4.2.5.4 Landslides sediments compositions

The Saituti landslide is developed on HHC gneisses on the western flank of Khudi basin. Sands from the stream draining the landslide was collected in the inner part of the landslide and at the outlet ∼5m upstream of the confluence with the Khudi. Their compositions overlap with those of the Khudi SL (table 4.2 and figure 4.2.4). Nevertheless some scatter in K, Ca and Mg is likely due the poor mixing capacity of the stream draining the landslide. The average composition of ∼100 pebbles randomly collected at the outlet of the landslide is also very similar to the Khudi SL except for Na which appears slightly enriched. Because the Saituti landslide deeply samples the hill slope where it is developed,

compositions derived from the landslide sand and moreover of the pebbles represent the best estimate of the HHC Khudi crust. Their water concentration closely match those of the HHCF1 gneisses which confirm that their alteration is very low. Hence, we think that Khudi HHC crust is poorer in Na and richer in Ca than HHCFI rocks dataset would let suppose.

4.2.5.5 Physical and chemical erosion fluxes in Khudi basin

Physical erosion

For the year 2010, we estimated the physical erosion flux from the integration of surface SL concentrations and daily discharges and includes extrapolate values for the dry season. The discharge is derived from water level gaging at the Intake station and was calculated to be 397 $\times$ 10^6 m^3 for 2010 . This rough estimate gives a flux of 1.5 Mt/yr equivalent to 4.1 mm/yr. During the monsoon 2012 we performed a more complete survey of the river including permanent turbidity measurements and daily sampling of depth and surface SL [Gallo 14b]. This approach allowed a more realistic estimate because (1) it takes into account the gradient of SL concentration with depth which are two to four time higher than in the surface, and (2) the turbidity record better capture the daily increase of discharge and SL concentration that generally occur overnight. The calculated sediment flux for 2012 is 1.7 Mt/yr equivalent to 4.7 mm/yr. In 2012 the annual discharge was lower at 335 $\times$ 10^6 m^3. Extrapolating this calibration to the 2010 hydrogram gives a sediment flux of 2.25 Mt/yr equivalent to 9.5 mm/yr.

These figures are substantially higher than estimates of 2.0±0.6 mm/yr from [Gabet 08]) based on a 2000-04 survey but based only on surface SL concentrations. TCN analysis gave variable erosion rates : 2.7 mm/y (1.0 Mt/y) [Godard 12, Godard 14], 3.5 mm/yr (1.3 Mt/y) with estimated proportion of landslide derived sediment of 96% (3.35 mm/yr and 1.2 Mt/y) [Niemi 05], while TCN analysis on grain-size fractions gave erosion rates from 0.8 to 4.4 mm/y (0.3 to 1.6 Mt/yr) [Puchol 14]. Thermochronologic data give a range between 1.8 to 3.7 mm/y (0.7 to 1.3 Mt/y) [Whipp 07, Blythe 07].

Chemical erosion

Dissolved cations and anions concentrations of the Khudi river at intake station are presented in table 4.2.7 and figure 4.2.6 and 4.2.8.

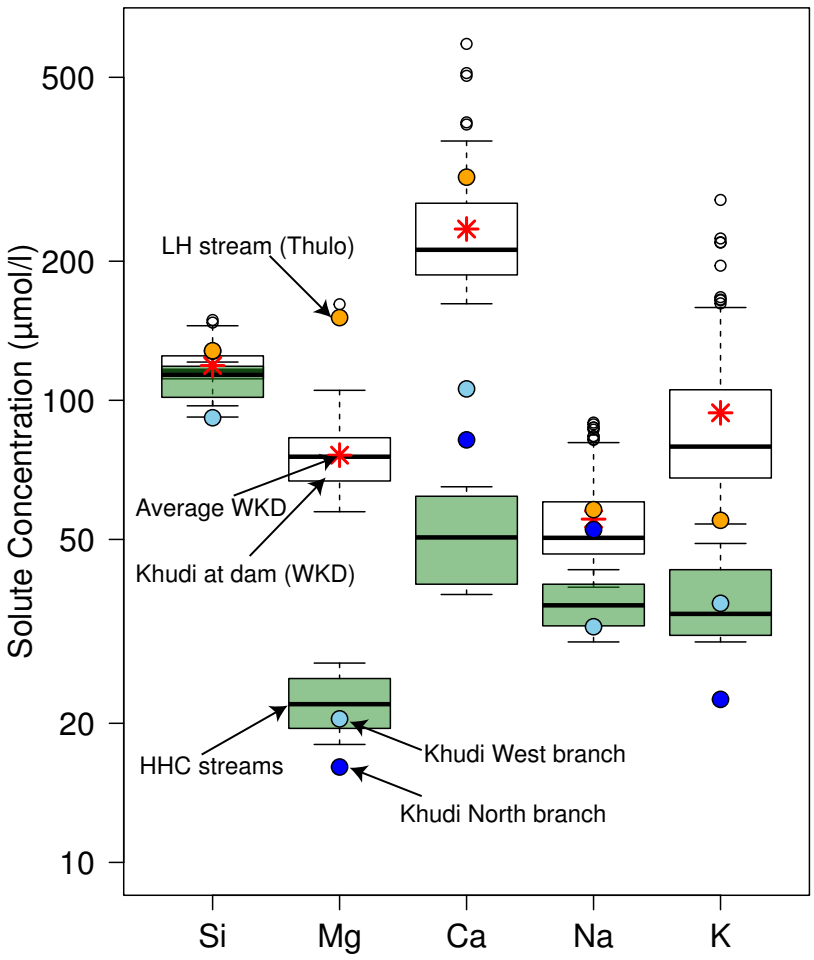

FIGURE 4.2.6 – Khudi river, HHC and LH tributaries, upper Northern and Western branchs cations compositions

Ech.	North	East	SL conc. [g/L]	Julian day	Date	Sum Cat. [mg/L]	Sum Cat. µM	Si µM	Mg	Ca	Na	K	Ba	Sr	Mg/K mole:mole	Mg/Na	Ca/Na	Ca/Sr
Khudi at Dam intake																		
CA12W20	28.3056	84.3301		124	03/05/12	18.7	563.7	131.4	64.6	239.7	75.3	52.7	0.08		1.23	0.86	3.18	
WKD1	28.3056	84.3301	3.38	161	11/06/10	22.3	670.3	143.4	83.2	281.4	86.4	75.8	0.08	0.25	1.10	0.96	3.26	1119
WKD2	28.3056	84.3301	0.75	162	12/06/10	22.5	676.7	145.0	83.9	284.4	88.7	74.7	0.10	0.25	1.12	0.94	3.21	1125
WKD3	28.3056	84.3301	7.23	163	13/06/10	22.3	670.6	144.4	80.6	279.9	87.3	78.3	0.11	0.25	1.03	0.92	3.21	1140
WKD4	28.3056	84.3301	0.08	164	14/06/10	22.0	665.1	147.3	81.0	279.4	89.5	67.9	0.10	0.24	1.19	0.91	3.12	1152
WKD5	28.3056	84.3301	0.22	165	15/06/10	21.0	634.0	141.2	77.2	267.7	83.6	64.2	0.10	0.23	1.20	0.92	3.20	1145
WKD6	28.3056	84.3301	0.84	166	16/06/10	21.5	649.0	142.5	78.1	272.7	87.3	68.4	0.11	0.24	1.14	0.90	3.13	1144
WKD7	28.3056	84.3301	0.94	167	17/06/10	21.4	646.6	144.8	79.5	266.7	83.6	71.9	0.10	0.23	1.11	0.95	3.19	1153
WKD8	28.3056	84.3301	0.26	168	18/06/10	20.5	618.9	139.5	75.5	257.2	82.4	64.2	0.09	0.23	1.17	0.92	3.12	1137
WKD9	28.3056	84.3301	0.63	169	19/06/10	21.0	635.5	138.1	84.0	267.0	80.6	65.8	0.10	0.22	1.28	1.04	3.31	1221
WKD10	28.3056	84.3301	9.75	170	20/06/10	20.2	600.1	127.2	69.2	224.7	64.3	114.5	0.10	0.25	0.60	1.08	3.49	909
WKD11	28.3056	84.3301	1.58	171	21/06/10	20.8	622.8	128.0	83.6	261.7	72.3	77.3	0.10	0.22	1.08	1.16	3.62	1213
WKD12	28.3056	84.3301	0.90	172	22/06/10	20.2	609.8	135.2	72.4	251.7	81.0	69.4	0.09	0.23	1.04	0.89	3.11	1086
WKD13	28.3056	84.3301	2.37	173	23/06/10	21.6	646.5	135.2	80.9	270.7	78.8	80.8	0.09	0.23	1.00	1.03	3.43	1187
WKD14	28.3056	84.3301	2.00	174	24/06/10	20.4	610.7	124.8	83.0	250.2	68.7	84.0	0.09	0.21	0.99	1.21	3.64	1220
WKD15	28.3056	84.3301	3.64	175	25/06/10	19.8	593.5	118.4	90.2	248.6	61.5	74.9	0.09	0.19	1.20	1.47	4.04	1313
WKD16	28.3056	84.3301	0.85	176	26/06/10	22.6	678.4	132.1	105.1	292.9	72.5	75.8	0.10	0.22	1.39	1.45	4.04	1343
WKD17	28.3056	84.3301	3.88	177	27/06/10	22.4	669.0	136.9	89.3	281.2	73.5	88.1	0.09	0.23	1.01	1.22	3.83	1246
WKD18	28.3056	84.3301	16.64	178	28/06/10	22.0	645.7	130.3	71.4	251.7	65.2	127.0	0.08	0.27	0.56	1.09	3.86	931
WKD19	28.3056	84.3301	3.72	179	29/06/10	20.8	621.6	126.8	85.6	269.0	67.3	73.0	0.09	0.22	1.17	1.27	4.00	1242
WKD20	28.3056	84.3301	4.32	180	30/06/10	20.6	615.5	130.9	84.9	263.5	65.8	70.5	0.08	0.21	1.20	1.29	4.01	1262
WKD21	28.3056	84.3301	8.53	181	01/07/10	19.3	576.5	122.4	73.7	232.3	62.1	86.1	0.07	0.22	0.86	1.19	3.74	1058
WKD22	28.3056	84.3301	7.55	182	02/07/10	19.6	579.1	113.8	77.8	234.6	55.9	97.1	0.09	0.21	0.80	1.39	4.20	1121
WKD23	28.3056	84.3301	64.84	183	03/07/10	36.4	1015.0	131.7	88.3	510.7	64.8	219.4	0.15	0.35	0.40	1.36	7.89	1475
WKD24	28.3056	84.3301	32.45	184	04/07/10	30.5	860.6	128.5	82.0	395.2	59.2	195.6	0.13	0.29	0.42	1.39	6.68	1346
WKD25	28.3056	84.3301	18.47	185	05/07/10	26.8	769.9	121.5	92.1	339.8	57.7	158.8	0.13	0.26	0.58	1.60	5.89	1317
WKD26	28.3056	84.3301	25.15	186	06/07/10	27.8	794.0	122.8	89.0	364.0	56.2	162.1	0.12	0.27	0.55	1.58	6.48	1339
WKD27	28.3056	84.3301	7.62	187	07/07/10	21.9	637.4	115.3	83.9	267.2	49.3	121.8	0.10	0.21	0.69	1.70	5.42	1251
WKD28	28.3056	84.3301	2.82	188	08/07/10	18.4	546.9	115.9	78.2	223.4	48.2	81.3	0.08	0.17	0.96	1.62	4.64	1352
WKD29	28.3056	84.3301	1.67	189	09/07/10	18.0	539.2	120.1	78.7	219.1	51.1	70.3	0.08	0.17	1.12	1.54	4.29	1301
WKD30	28.3056	84.3301	5.79	190	10/07/10	18.4	545.6	113.6	77.8	228.1	49.2	76.9	0.08	0.17	1.01	1.58	4.64	1348
WKD30F	28.3056	84.3301	71.62	190	10/07/10	37.0	1046.7	136.4	104.7	503.7	82.1	219.8	0.09	0.55	0.48	1.28	6.14	913
WKD31	28.3056	84.3301	42.10	191	11/07/10	28.9	812.8	114.6	83.9	399.5	47.6	167.2	0.11	0.23	0.50	1.76	8.39	1717
WKD32	28.3056	84.3301	7.35	192	12/07/10	19.8	576.8	110.7	74.2	247.6	43.7	100.5	0.08	0.16	0.74	1.70	5.66	1533
WKD33	28.3056	84.3301	3.11	193	13/07/10	16.9	504.2	114.2	69.4	206.4	43.3	70.8	0.08	0.14	0.98	1.60	4.76	1445
WKD34	28.3056	84.3301	1.27	194	14/07/10	16.8	502.7	115.8	71.0	204.4	46.1	65.4	0.07	0.15	1.09	1.54	4.43	1371
WKD35	28.3056	84.3301	5.52	195	15/07/10	17.2	509.9	113.2	65.5	205.2	45.3	80.7	0.08	0.15	0.81	1.44	4.53	1335
WKD36	28.3056	84.3301	2.87	196	16/07/10	18.0	538.8	122.9	71.1	215.3	51.8	77.6	0.09	0.16	0.92	1.37	4.15	1330

FIGURE 4.2.7 – Dissolved cations and anions concentrations of the Khudi river at intake station.

Ech.	North	East	SL conc. [g/L]	Julian day	Date	Sum Cat. [mg/L]	Sum Cat. µM	Si µM	Mg	Ca	Na	K	Ba	Sr	Mg/K mole:mole	Mg/Na	Ca/Na	Ca/Sr
WKD37	28.3056	84.3301	3.26	197	17/07/10	15.8	474.5	114.6	62.0	188.1	45.4	64.4	0.07	0.14	0.96	1.37	4.15	1328
WKD38	28.3056	84.3301	1.66	198	18/07/10	16.9	508.6	125.1	66.9	199.4	53.1	64.1	0.07	0.16	1.04	1.26	3.75	1285
WKD39	28.3056	84.3301	1.67	199	19/07/10	16.0	482.5	115.9	67.0	188.8	49.9	60.8	0.07	0.14	1.10	1.34	3.78	1339
WKD40	28.3056	84.3301	6.52	200	20/07/10	16.9	496.0	102.4	57.4	195.5	41.5	99.1	0.09	0.16	0.58	1.38	4.71	1195
WKD41	28.3056	84.3301	1.73	201	21/07/10	15.7	470.8	112.9	64.5	186.7	45.5	61.2	0.08	0.14	1.05	1.42	4.10	1329
WKD42	28.3056	84.3301	8.33	202	22/07/10	18.0	523.6	100.9	64.4	217.8	39.4	101.1	0.09	0.15	0.64	1.64	5.53	1424
WKD43	28.3056	84.3301	2.15	203	23/07/10	14.9	444.8	105.0	58.8	172.3	40.7	68.0	0.07	0.13	0.86	1.44	4.23	1341
WKD44	28.3056	84.3301	5.11	204	24/07/10	15.6	465.4	107.0	58.9	176.6	46.8	76.1	0.07	0.14	0.77	1.26	3.77	1285
WKD45	28.3056	84.3301	2.84	205	25/07/10	14.5	437.5	107.0	60.0	167.6	41.8	61.2	0.07	0.13	0.98	1.44	4.01	1296
WKD46	28.3056	84.3301	2.30	206	26/07/10	15.7	471.2	110.0	65.8	178.3	44.2	72.8	0.07	0.14	0.90	1.49	4.03	1305
WKD47	28.3056	84.3301	30.61	207	27/07/10	23.2	659.2	103.8	65.6	299.9	46.8	143.1	0.13	0.23	0.46	1.40	6.41	1307
WKD48	28.3056	84.3301	0.97	209	29/07/10	15.3	462.2	116.2	65.0	174.1	46.5	59.3	0.08	0.13	1.10	1.40	3.75	1337
WKD49	28.3056	84.3301	11.28	210	30/07/10	16.3	477.4	97.3	57.5	190.1	40.4	92.0	0.08	0.16	0.62	1.42	4.71	1208
WKD50	28.3056	84.3301	5.80	211	31/07/10	15.3	455.8	97.7	58.5	173.9	44.4	81.3	0.09	0.14	0.72	1.32	3.92	1249
WKD51	28.3056	84.3301	1.31	212	01/08/10	14.7	447.4	114.0	65.3	170.6	43.1	54.3	0.06	0.12	1.20	1.51	3.95	1388
WKD52	28.3056	84.3301	1.62	213	02/08/10	15.0	456.0	117.0	65.4	167.5	46.9	59.1	0.07	0.15	1.11	1.40	3.57	1137
WKD53	28.3056	84.3301	11.40	214	03/08/10	16.5	492.3	113.7	62.5	189.8	45.8	80.6	0.08	0.16	0.78	1.36	4.14	1180
WKD54	28.3056	84.3301	3.15	215	04/08/10	15.1	456.6	113.1	60.0	169.8	48.5	65.1	0.06	0.14	0.92	1.24	3.50	1237
WKD55	28.3056	84.3301	11.10	216	05/08/10	16.2	482.0	110.5	58.0	186.8	44.3	82.4	0.08	0.16	0.70	1.31	4.22	1191
WKD56	28.3056	84.3301	1.61	217	06/08/10	14.4	439.1	116.0	59.2	161.8	45.5	56.6	0.07	0.13	1.05	1.30	3.55	1277
WKD57	28.3056	84.3301	0.48	218	07/08/10	15.4	469.8	120.2	67.0	174.5	53.6	54.4	0.07	0.13	1.23	1.25	3.25	1326
WKD58	28.3056	84.3301	0.39	219	08/08/10	15.3	466.8	119.4	65.2	177.4	50.9	54.0	0.07	0.14	1.21	1.28	3.49	1300
WKD59	28.3056	84.3301	0.38	220	09/08/10	15.2	464.2	119.6	65.2	174.7	49.4	55.4	0.07	0.14	1.18	1.32	3.54	1289
WKD60	28.3056	84.3301	0.43	221	10/08/10	16.4	497.9	122.2	69.5	190.0	52.7	63.5	0.09	0.15	1.10	1.32	3.60	1256
WKD61	28.3056	84.3301	15.51	223	12/08/10	23.0	664.1	105.6	85.2	267.5	49.1	156.8	0.18	0.24	0.54	1.73	5.45	1119
WKD62	28.3056	84.3301	0.15	224	13/08/10	15.8	479.9	122.9	66.1	182.4	52.6	55.9	0.08	0.15	1.18	1.26	3.47	1239
WKD63	28.3056	84.3301	1.20	226	15/08/10	15.9	479.6	113.3	62.0	174.6	53.2	76.4	0.08	0.15	0.81	1.17	3.28	1199
WKD64	28.3056	84.3301	10.75	227	16/08/10	20.5	602.5	120.5	74.1	233.3	53.4	121.2	0.14	0.19	0.61	1.39	4.37	1230
WKD65	28.3056	84.3301	3.19	228	17/08/10	18.7	555.0	112.3	76.1	211.7	49.4	105.5	0.12	0.16	0.72	1.54	4.29	1310
WKD66	28.3056	84.3301	2.93	229	18/08/10	19.5	577.2	111.8	84.3	225.2	51.5	104.3	0.12	0.16	0.81	1.63	4.37	1369
WKD67	28.3056	84.3301	16.00	230	19/08/10	24.2	696.3	111.2	87.2	282.4	50.9	164.6	0.21	0.24	0.53	1.71	5.55	1157
WKD68	28.3056	84.3301	3.55	231	20/08/10	17.2	512.1	109.2	71.0	183.7	48.0	100.3	0.10	0.17	0.71	1.48	3.82	1085
WKD69	28.3056	84.3301	2.13	232	21/08/10	15.8	477.6	111.9	66.1	171.6	49.3	78.6	0.08	0.15	0.84	1.34	3.48	1157
WKD70	28.3056	84.3301	0.89	233	22/08/10	16.6	500.5	111.3	73.4	187.0	49.5	79.4	0.11	0.14	0.92	1.48	3.78	1304
WKD71	28.3056	84.3301	50.18	234	23/08/10	42.5	1186.7	104.0	161.4	590.6	59.4	271.4	0.28	0.42	0.59	2.72	9.95	1394
WKD72	28.3056	84.3301	7.23	235	24/08/10	21.3	629.0	121.8	93.1	250.5	53.2	110.4	0.13	0.16	0.84	1.75	4.71	1525
WKD73	28.3056	84.3301	0.77	236	25/08/10	15.8	479.8	116.8	68.2	178.5	49.7	66.6	0.10	0.13	1.02	1.37	3.59	1325
WKD74	28.3056	84.3301	0.33	237	26/08/10	15.8	481.5	120.9	68.7	177.7	52.5	61.8	0.08	0.14	1.11	1.31	3.39	1283
WKD75	28.3056	84.3301	22.67	239	28/08/10	29.5	852.0	149.2	95.2	317.4	66.2	224.0	0.24	0.43	0.42	1.44	4.80	734

Ech.	North	East	SL conc. [g/L]	Julian day	Date	Sum Cat. [mg/L]	Sum Cat. µM	Si µM	Mg	Ca	Na	K	Ba	Sr	Mg/K mole:mole	Mg/Na	Ca/Na	Ca/Sr
WKD76	28.3056	84.3301	1.77	240	29/08/10	17.1	511.7	111.5	73.5	195.3	48.0	83.4	0.11	0.14	0.88	1.53	4.07	1364
WKD77	28.3056	84.3301	3.16	241	30/08/10	18.1	537.7	110.2	75.6	194.2	51.3	106.4	0.10	0.18	0.71	1.47	3.78	1080
WKD78	28.3056	84.3301	7.25	242	31/08/10	18.7	551.6	104.8	81.6	207.7	45.1	111.7	0.11	0.17	0.73	1.81	4.61	1231
WKD79	28.3056	84.3301	0.91	244	02/09/10	17.3	522.3	115.1	84.9	200.9	49.3	72.1	0.10	0.14	1.18	1.72	4.07	1473
WKD80	28.3056	84.3301	0.75	245	03/09/10	17.0	516.0	121.2	82.0	197.8	51.1	63.8	0.09	0.14	1.28	1.60	3.87	1441
WKD81	28.3056	84.3301	6.17	246	04/09/10	18.3	539.5	101.9	77.4	210.8	44.1	105.4	0.12	0.16	0.73	1.76	4.78	1356
WKD82	28.3056	84.3301	4.27	249	07/09/10	16.5	492.6	107.7	67.1	178.4	46.0	93.4	0.10	0.16	0.72	1.46	3.88	1139
WKD83	28.3056	84.3301	15.75	250	08/09/10	24.6	707.7	107.1	92.0	294.9	48.5	165.2	0.18	0.26	0.56	1.90	6.08	1146
WKD84	28.3056	84.3301	0.94	251	09/09/10	17.0	515.3	126.0	75.1	195.4	51.0	67.8	0.08	0.17	1.11	1.47	3.83	1164
WKD85	28.3056	84.3301		252	10/09/10	18.1	542.5	123.6	75.5	201.8	51.3	90.2	0.11	0.17	0.84	1.47	3.93	1208
WKD86	28.3056	84.3301		253	11/09/10	19.8	583.9	111.7	79.7	218.0	50.4	124.0	0.10	0.22	0.64	1.58	4.33	996
WKD87	28.3056	84.3301		255	13/09/10	18.5	552.2	113.9	82.5	215.7	49.3	90.8	0.12	0.17	0.91	1.67	4.38	1264
WKD88	28.3056	84.3301		257	15/09/10	22.5	653.9	106.5	99.1	273.7	46.2	128.4	0.17	0.20	0.77	2.14	5.92	1387
WKD89	28.3056	84.3301		258	16/09/10	16.7	501.8	115.4	71.2	186.0	48.2	81.0	0.10	0.14	0.88	1.48	3.86	1327
WKD90	28.3056	84.3301		259	17/09/10	17.6	521.9	102.5	80.9	203.2	45.2	90.2	0.13	0.15	0.90	1.79	4.50	1386
WKD91	28.3056	84.3301		260	18/09/10	20.2	594.1	113.2	80.9	227.9	49.5	122.6	0.14	0.17	0.66	1.63	4.60	1375
WKD92	28.3056	84.3301		261	19/09/10	17.6	531.5	116.5	75.7	196.6	60.3	82.4	0.10	0.16	0.92	1.26	3.26	1254
WKD93	28.3056	84.3301		262	20/09/10	17.2	519.5	123.7	76.3	196.0	50.9	72.6	0.11	0.15	1.05	1.50	3.85	1315
WKD94	28.3056	84.3301		263	21/09/10	15.8	480.7	122.5	68.8	182.0	47.4	60.1	0.10	0.14	1.14	1.45	3.84	1261
WKD95	28.3056	84.3301		264	22/09/10	17.4	511.6	100.3	69.7	194.3	41.8	105.4	0.10	0.16	0.66	1.67	4.64	1230
WKD96	28.3056	84.3301		265	23/09/10	15.8	474.4	110.4	69.0	180.2	42.5	72.2	0.10	0.13	0.96	1.62	4.24	1364
CA975	28.3056	84.3301		317	13/11/09	17.3	530.4		102.0	241.4	135.6	51.4			1.98	0.75	1.78	
ANNUAL DISCHARGE-WEIGHTED STREAM CHEMISTRY								118.5	74.2	218.8	60.0	82.7			0.90	1.24	3.65	
Upper Northern Khudi branch																		
CA11215B	28.3175	84.3564		317	14/11/11			127.8	16.1	82.1	52.5	22.5	0.02	0.13	0.71	0.31	1.56	649
Upper Western Khudi branch																		
CA11103	28.3652	84.3052		211	31/07/11			91.7	20.4	105.9	32.4	36.4	0.03	0.11	0.56	0.63	3.27	988
LH tributary (Thola Khola)																		
CA12w19	84.3322	28.325		124	03/05/12			128.0	151.0	304.0	58.0	55.0	0.10	0.15	2.75	2.60	5.24	2027
HHC tributaries																		
CA 11104	84.3052	28.3652		212	31/07/11			91.5	18.0	42.3	29.7	29.6	0.06	0.04	0.61	0.61	1.42	963
CA 11106	84.3076	28.3622		212	31/07/11			110.9	20.9	58.7	36.8	36.5	0.09	0.04	0.57	0.57	1.59	1492
CA 11107	84.3092	28.3616		212	31/07/11			120.8	26.9	38.3	43.1	49.1	0.07	0.04	0.55	0.62	0.89	960
CA 11110	84.3184	28.3546		212	31/07/11			116.4	23.1	64.5	34.9	31.6	0.06	0.03	0.73	0.66	1.85	1978
Average HHC streams								*109.9*	*22.2*	*50.9*	*36.1*	*36.7*	*0.07*	*0.04*	*0.62*	*0.61*	*1.44*	*1308*
Rain water (Wolff-Boesnish et al., 2009)										1.0	8.0	10.0	5.0					

Placed in ternary diagrams (c.f. figure 4.2.8), the Khudi waters compare well with gneiss derived rivers as reported by [Galy 99b] and to the Sun Kosi waters but are not in the range of silicate springs reported by [Quade 03] because their [Ca] and [Mg] are too high.

Few analyses of anions on 2013 monsoon sample show that X_{SO4}= [SO4]/([SO4]+[HCO3]) is around 0.2. $\delta^{13}C$ of total inorganic carbon is around -11‰, indicative of a mixed source between soil derived alkalinity and carbonate dissolution [Galy 99b]. [Cl] are remarkably low between 3 and 7 µmol/l, which is below the reported value for local rain water by [Galy 99b, Wolff-Boenisch 09]. The main identified source of chlorine is a hydrothermal spring (ratopani) on the Khudi bank near the village of Probi whose [Cl] is around 4000 µmol/l (unpublished). Therefore such spring plays a minor role on the chemical load of the river. In detail, about 13 samples out of hundred are associated to very high SL load and peak discharges and show high [K] and [Ca] that are unusual compared to known Himalayan rivers (c.f. figure A2 fig. 4.3.4) [Morin 14]. Hourly sampling of the Khudi in July 2013 revealed that episode of high discharge are characterized by a rise in K, Ca, HCO^{3-} and SO_4^{2-} whereas other elements are stable or diluted as [Si]. The process that releases these elements is unclear although it is associated to increased direct runoff peak subsequent to heavy precipitation, and higher suspended particle transport [Morin 14]. It could therefore be linked to the leaching of freshly fragmented rocks from the landslide. Alternatively, it could be supplied by soil litter leaching.

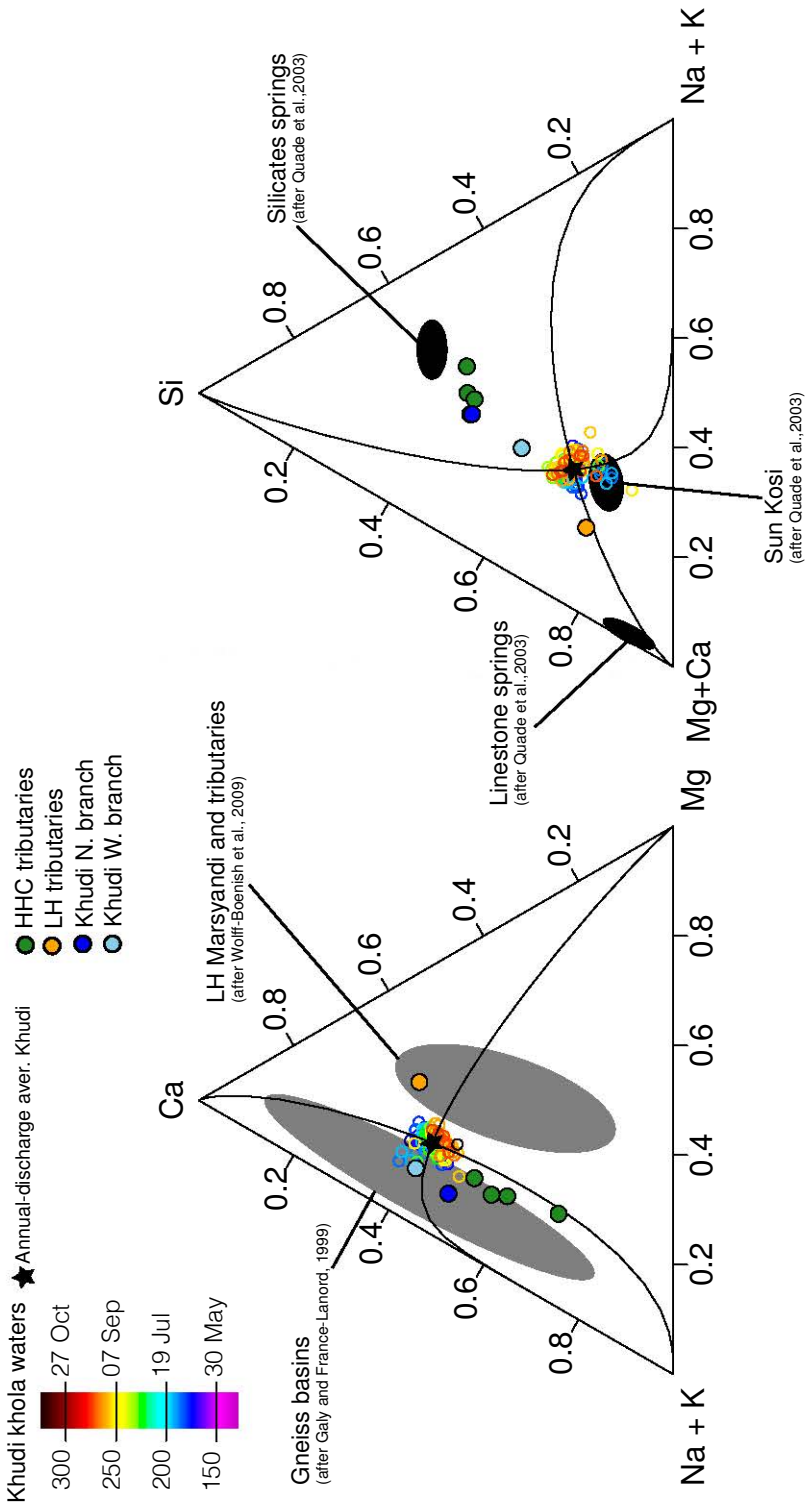

FIGURE 4.2.8 – Khudi river cations compositions are very similar to other Nepalese rivers draining gneisses and silicates.
Seti composition are from [Quade 03], Marsyandi water compositions from [Wolff-Boenisch 09]

On the basis of the 2010 set of monsoon daily SKD water samples, two pre-and post-monsoon samples, and combining with river discharge estimated from water level gaging, we calculated chemical erosion fluxes for the Khudi (Table 4.4).

CALCULATED FLUXES	Si	Mg	Ca	Na	K
t/y	1403	761	3696	581	1363
t/km2/y	11.8	6.4	31.1	4.9	11.4
t/ha/a	0.12	0.06	0.31	0.05	0.11
kmol/y	49955	31291	92221	25276	34847
kmol/km2/a	420	263	775	212	293
mol/ha/a	4198	2630	7750	2124	2928
ANNUAL DISCHARGE-WEIGHTED STREAM CHEMISTRY					
mg/L	3.33	1.80	8.77	1.38	3.23

TABLE 4.4 – Chemical erosion fluxes of the Khudi basin.

As mentioned by [Wolff-Boenisch 09], the diversity of calculation for this parameter makes comparison between studies awkward ; therefore we expressed our estimates with the different approaches. The calculation based on oxide weight [France-Lanord 03] makes the comparison of chemical and physical erosion possible whereas ionic fluxes are more relevant for CO_2 consumption estimates. Calculated erosion fluxes for 2010 compare relatively well with those estimated for the Khudi for 2001-02 [Wolff-Boenisch 09] of the Chepe khola [France-Lanord 03]. However the flux of K is significantly higher than that of Na which was not observed in earlier studies. This results from the link between discharge and highest [K]. Those peak discharge taking place most frequently overnight, they were probably not well sampled.

Carbonate and silicate weathering are estimated on the basis of [Galy 99b] (Table 4.5).

	fNa**	fK*	fMg*	fMg*sil x10^7 mol/yr	fCa*	fCa*sil	fSi*	Eros Carb t/yr	Eros Sil t/yr	SilWR t/yr	SilWR t/km^2/yr
Dissolved fluxes	1.49	2.58	2.47	1.29	7.13	0.60	3.94	7292	4902	4273.06	36.21239
Solid fluxes	108.87	150.00	153.54	58.56	58.56	58.56	2564.10		1.74 x10^6		
Dissolved as %Solids	1.35	1.69	1.58	2.16	10.86	1.01	0.15		0.28		

TABLE 4.5 – Dissolved and solid fluxes, carbonate and silicate weathering in the Khudi basin.

However we changed the Ca/Na_{sil} according to our estimate in the source rock of the HHC (0.39). Therefore the Ca silicate and carbonate proportions is calculated following :

$$[Ca]_{total} = [Ca]_{carbonate} + [Na] * \times 0.4$$

To assess runoff components on HHC and LH series, we also present cations concentrations of HHC tributaries, Khudi Western and Northern branch that drain HHCFI and LH tributrary. While silica $Si(OH)_4$ concentrations of waters collected in every part of the basin compare very well to Khudi Khola river concentrations Si ~100-120 µM, it is far to be the case with other elements. HHC tributaries have lower concentrations in all elements, [Ca]~50 µM, [Mg]~22 µM, [Na]~36 µM and [K]~37 µM, which represent respectively 67%, 10%, 60% and 45% of the Khudi river concentrations at Intake station. It is in agreement with waters from basin draining gneisses and silicates (figure 4.2.8).

Likewise, Khudi khola Northern branch and Western branch show comparable concentrations except in Ca for which they are 1.5 to 2 fold those of the HHC concentrations. On the contrary, LH tributary Thulo Khola (CA12w9) shows similar concentrations in [Na] = 58 µM, lower in [K] = 55 µM, but higher in [Ca] = 304 µM and [Mg] = 151 µM than the Khudi Khola. It is only a single sample but show the same concentrations as reported for LH series basins reported by [Wolff-Boenisch 09] and likely contain marbles. A simple composite mixing of HHC and LH tributaries compositions relative to their drainage area (86.6% HHC and 13.4% LH) results in explaining 95 % of Si and 86% of Mg concentrations in the Khudi khola water but only 27% Ca, 65% Na and 48% K, quite uncompatible with Khudi compositions. These discrepancies may first relate to the fact that tributary samples are mostly runoff waters and do not collect groundwaters compositions compared to the main river. Indeed Western and Northern branch also collect groundwaters and show sightly higher Ca concentrations. To some extent, we calculated Ca and Mg deriving from silicates weathering.

Silicate Ca and Mg are calculated using the Ca/Na and Mg/Na ratio of silicate rocks where Ca_{sil} is calculated as

$$Ca_{sil} = Na * \times \left(\frac{Ca}{Na}\right)_{silicate\,rock}$$

and Mg_{sil} is calculated as

$$Mg_{sil} = Na * \times \left(\frac{Mg}{Na}\right)_{silicate\,rock} \text{ or } Mg_{sil} = Na * \times \left(\frac{Mg}{Na}\right)_{silicate\,rock}$$

Na* is Na corrected for cyclic and hot spring inputs proposed and following X/Cl ratios of 0.16, 0.03, 0.10, 0.41, and 0.01 for the elements Ca, Mg, K, Na, and Si, respectively [Tipper 06c]. Rainwater input and [Cl^-] concentrations used are from [Wolff-Boenisch 09].

X_{sil}, the fraction of silicate cations to total cations is calculated on an equivalent basis as :

$$X_{sil} = \left(\frac{2\times Ca_{sil}+2\times Mg_{sil}+K+Na}{2\times Ca+2\times Mg+K+Na}\right)$$

The effect on Xsil of using different rock ratios has been assessed by using mutliple Ca/Na_{sil}, Mg/Na_{sil} and Mg/K_{sil} by [Pecher 78, Brouand 89, France-Lanord 97, Galy 99b, Quade 03, Wolff-Boenisch 09] and our estimation of Khudi basin HHC crust by landslide pebbles, which gives Ca/Na = 0.39, Mg/Na = 0.81 and Mg/K = 0.82.

Our calculations give for silicates cations fractions Xsil = 0.32±0.06, Silicate Weathering rate (Silicate cations including silica) SiWR=1027±62 mol/ha/y and Cations Weathering Rate (Silicate cations excluding silica) CatWR 611±67 mol/ha/a in agreement with [Wolff-Boenisch 09] . As already observed by these authors, it places the Khudi basin in high weathering basins. Indeed, when compared to other budgets established in High Himalayan basins of the Trisuli and Ganga basin by West et al. 2002, cations from silicate weathering in Khudi represent 1.9 kmol/ha/yr that is higher than Lirung basin (Trisuli basin) 1 kmol/ha/yr and of the order of Dokriani basin (head of Ganga basin) 2.5 kmol/ha/yr, while cations fluxes from carbonate weathering totalise 8.1 kmol/ha/yr which is high above 2.5 kmol/ha/yr and 5 kmol/ha/yr observed in Lirung and Dokriani basins. Carbonates weathering to silicates weathering ratio is hence of 4.3 in Khudi basin when it is 2.5 and 2 in Lirung and Dokriani respectively.

Such high carbonate weathering in the Khudi basin upstream our sampling station is quite astonishing given the fact that it is mainly draining (85%) the HHC, considered to countain low amounts of carbonates. However, considering the solid fluxes of 1.7 Mt/y and the carbonate content of 0.07% we measured in SL, it represents detrital carbonates fluxes of 119000 t/y that compared to 3700 t/y of dissolved Ca in the river. Hence, dissolving only 3% of the detrital carbonates exported by the river would be sufficient to explain the totality of Ca concentration of the Khudi. It may explain why the carbonate weathering seems not to make sense at first sight. Moreover, we observed quite astonishing correlation beween peak concentrations of dissolve K and Ca related to peak of water discharge, peak of solid concentrations resulting of intense rainfall events in 2010 (c.f. A2 figure 4.3.4) and

2013 [Morin 14]. We interpret this effect as resulting aither from the desorption of Ca and K adsorbed by organic matter or from flash dissolution of supergen sulfates. However, if the process involved is still unclear, such observation particularly enlights the impact of physical erosion on chemical erosion. In the Khudi basin where the physical erosion is completely dominant, chemical erosion likely occurs on slopes, in the groundwater tables, but also in the river drainage itself due to the high solid fluxes exported.

4.2.6 Discussion

4.2.6.1 Processes of physical erosion

Khudi khola

Sr-Nd isotopic compositions of Khudi khola sediment showed that 95 to 100% of the physical erosion occurs above the MCT in the HHC. While the Khudi is certainly a river where the proportion of sediments derived from landslide area is high [Niemi 05, Gabet 08, Puchol 13, Gallo 14a], the area covered by landslide in this basin is minor around 0.45% and the remaining 99.5% are very steep slopes exposed to to about 3m of rainfall annually, and hence represent potential sources of sediments. This includes forested area bellow 3500 m and the upper basin that is mostly barren and also undergoing high rainfall. In situ cosmogenic ^{10}Be measured on 10 bank samples of the river between 1997 and 2013 result in quite variable erosion rate between 0.7 and 2.5 mm/yr ([Gallo 14b] and refs. in). This suggests that there is an heterogeneity in the origin of the sediments. In addition the geochemical characteristics of the Khudi river sediment appears very similar to that of comparable rivers such as the Chepe and Dordi kholas but with no active landslides in their catchment. Therefore one of our objectives is to assess the proportion of erosion from the different components we measured i.e. landslide, soil and tributaries. Top soil and tributaries, both document the background slope erosion independent of active landslide and comprise material derived from soil washout and minor landslide. Soil erosion is estimated based on average composition of topsoil and is estimated from the composition of the upper 60 cm of soil samples. Tributary is based on average composition of 7 samples and Landslide is on average composition of 12 samples Table 4.2.

SL composition is the annual-discharge weighted SL composition calculated by integra-

ting over the monsoon season each SL sample composition multiplied by its concentration and river discharge at time of sampling. We finally calculated average geochemical composition of Khudi khola sediment by mixing average compositions of pebbles, banks and annual-discharge weighted SL in proportions of 10%, 25% and 65% respectively.

To propagate uncertainty in major elements compositions of each component : tributary, top soil and landslide, we randomly generated 10000 compositions based on covariance matrix of each dataset (c.f. A3 fig. 4.3.5). We verified their coherence with the sample compositions. Using major elements compositions of each component, we realized 2 sets of Monte Carlo mixing inversions (10000 iterations) to match the composition of Khudi khola sediments (c.f. figure 4.2.9) : one comprising : topsoils, tributaries and landslide, the second with only landslide including 5% of topsoils as calculated by carbon content and isotopic composition and topsoils.

The inversions realized with all components show that the landslide provides ~ 75-80 % of the river sediment while soils erosion is only 4.5-12.5 % as well as upper basin 5-12.5 %. The second inversions is for a mixing of landslide and topsoils with the composition of the landslide including 5% of HHC top soils as deduced from organic carbon data. The results of this inversion give a balance of 0-10% for top soils and 90-100% for landslide. It confirms that soils erosion represents a minor source of sediment compared to landslide derived sediment.

This corroborates with the 96% landslide proportion derived from TCN by [Niemi 05] in the Khudi basin. Because the Saituti landslide area is ∼0.5 km^2, calculated fluxes ∼75-90% of Khudi sediment fluxes coming from the landslide results in local erosion rates of ~1900-2300 mm/y, which is ∼400 times the mean erosion in the basin. Conversely, calculated topsoil erosion is 0.2 – 0.8 mm/yr reported to the total basin area. Erosion from upper basin tributary give the same order likely 0.2 mm/yr, which is in agreement with erosion rates of ∼0.14 mmm/yr measured by TCN [Niemi 05]. Surficial erosion in the Khudi basin is therefore estimated around 0.4 – 1.6 mm/yr. It is in agreement with erosion rates derived from sediment gauging ~0.15 – 2.12 mm/yr [Gabet 08] or TCN ~ 0.1 to 1.1 mm/yr [Godard 12, Godard 14] in the region of the Marsyandi basin.

This approach shows that the surficial erosion of soil is in the order of a mm/yr whereas landslide in the Khudi reach ~1900-2300 mm/yr, up to ~400 times the average erosion

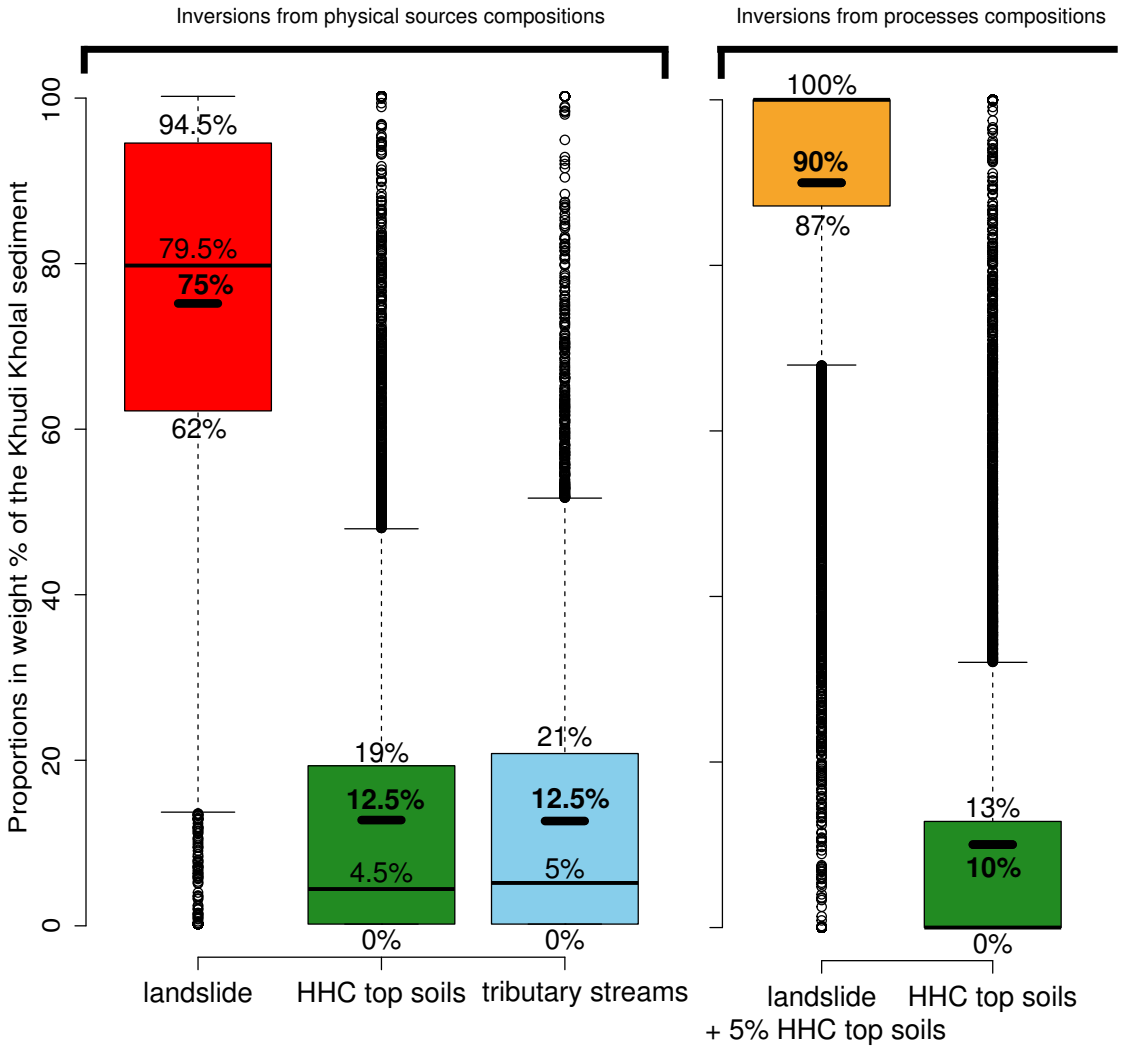

FIGURE 4.2.9 – Inverted proportions of erosion sources in the Khudi river sediment realised with major elements geochemical compositions.
Boxes represent modes of inversion ±50 quantiles while black bars represent the average of inversions. 1 – Inversions realised with averaged compositions of landslide sediments, top 60 cm of HHC soils, and sub-order tributaries banks. 2 – Inversions opposing landslide and top 60 cm of HHC soils result in 90% landslide against 10% of soils. Composition of the landslide includes 5% of HHC top soils as deduced from carbon content.

rates integrated over the whole basin ~3.5-5 mm/y. Such intense erosion is spatially limited to a very small area of the basin 0.45%, which highlights the huge spatial heterogeneity of physical erosion in such basin. As a consequence, hillslopes remain more or less quiescent in 99.5 % of the basin. The background erosion occurring on slopes is limited and partially explains why [Niemi 05] measured very low erosion rates on bedrock. It also implies that slopes remain exposed to weathering for long time. Based on this approach, surficial erosion rate calculated are between 0.1 – 0.4 mm/yr.

Comparison with Chepe and Dordi rivers

Chepe and Dordi river sediments have very similar geochemical signatures than those of the Khudi (Fig 4.2.2) suggesting that surficial soil erosion is also very low in these basins. On the other hand, they do not include large active landslide that could be identified using satellite imagery [Gallo 14a] , and available data on sediment transport by these rivers indicate low fluxes of sediments. Although there is no continuous record of SL on these rivers, hourly sampling over one day for the Dordi and two days for the Chepe during the monsoon 2013 showed that for both river surface SL concentrations varied between 0.05 g/l at low level and 0.30 g/l during overnight flood. This is much lower that the mean and median surface SL concentrations measured in the Khudi in 2010 : 8.5 and 3.1 g/l respectively. In addition repeated observations of these rivers show a clear visual contrast on SL concentrations (cf. A4). TCN on these rivers also show significantly higher [^{10}Be] than for the Khudi that is coherent with lower rate of erosion in the Dordi and Chepe relative to the Khudi (Godard et al. 2012, 2014).

In the absence of dilution by landslide derived sediments, the SL of these rivers should therefore show higher proportions of soil derived material corresponding to higher proportion of superficial erosion. The relatively "pristine" geochemical signatures of the Khudi and Chepe sediments imply therefore that sediment supply in these basin is mainly linked to erosion which can deliver sediments with low degree of weathering : (1) runoff of the high elevation part of the basin (>4000 m) where weathering is limited due to low temperature and lack of vegetation and where morainic material is available, (2) small landslides that are not easily observed with satellite imagery, and (3) physical processes such as pebble abrasion in the river bed and bedrock incision (Attal and Lavi, 2006).

Deciphering these processes goes beyond the scope of this study and would require additional observations on this type of basin. Because such processes must be dominant above soil erosion, the sediment geochemical signatures of river sediment do not show significant differences with the presence or not of an active landslide in the watershed.

4.2.6.2 Chemical erosion, soil production and weathering processes.

Basin scale chemical and physical erosion

The Khudi khola being one example of Himalayan basin undergoing extreme physical erosion, it is interesting to analyze whether this high physical erosion promotes chemical erosion or not. Comparing chemical and physical erosion relies mainly on the quality of discharge (Q) estimates but this term is present in both physical and chemical erosion rate which moderates the effect on Q uncertainty. Calculated fluxes presented in table 4.5 show that chemical erosion is about 0.8% that of total erosion (based on oxide fluxes of chemical erosion). Such proportion is quite extreme compared to other comparable basin, which are more frequently between 0.5 to 2% (e.g. [Galy 99b]). The proportion is highly dependent on the lithology as it is 0.2% and 82% for silicate and carbonate respectively. The very high proportion for carbonate is linked to the fact that there are only ≈5% of carbonate in the basin. Therefore such river belongs to the undersaturated rivers. On the opposite, silicate weathering appears very minor. Cation specific proportions of chemical erosion are between 0.15% for Si and 2.2 % for Mg (Table 4.5).

Weathering fluxes and rates calculated for the Khudi for 2010 appear notably higher than those calculated by [Wolff-Boenisch 09]. This is primarily due to the difference in runoff between the two studies. We argue that such high runoff is overestimated. [Putkonen 04] reported annual rainfall on five stations between 2000 and 4200m on the Khudi basin over the same working period. Only the two highest stations have precipitation above 3.2m/yr. The river runoff integrating additional evapotranspiration in the order of 1 m/yr in such area [Lambert 89], the river runoff should realistically be lower than 3 m/yr.

In order to compare different Himalayan basins, we plotted SilWR vs. Runoff for the Khudi from this study, Marsyandi tributaries of [Wolff-Boenisch 09], and Narayani tributaries of [France-Lanord 03]. Although datasets are not fully comparable, each of these

data results from an effort to establish annual discharge weighted concentrations and is based on sample sets that include monsoon sampling. This shows that there is a clear relationship between runoff and SilWR, suggesting a primary control by rainfall on silicate weathering rate (fig. 4.2.10).

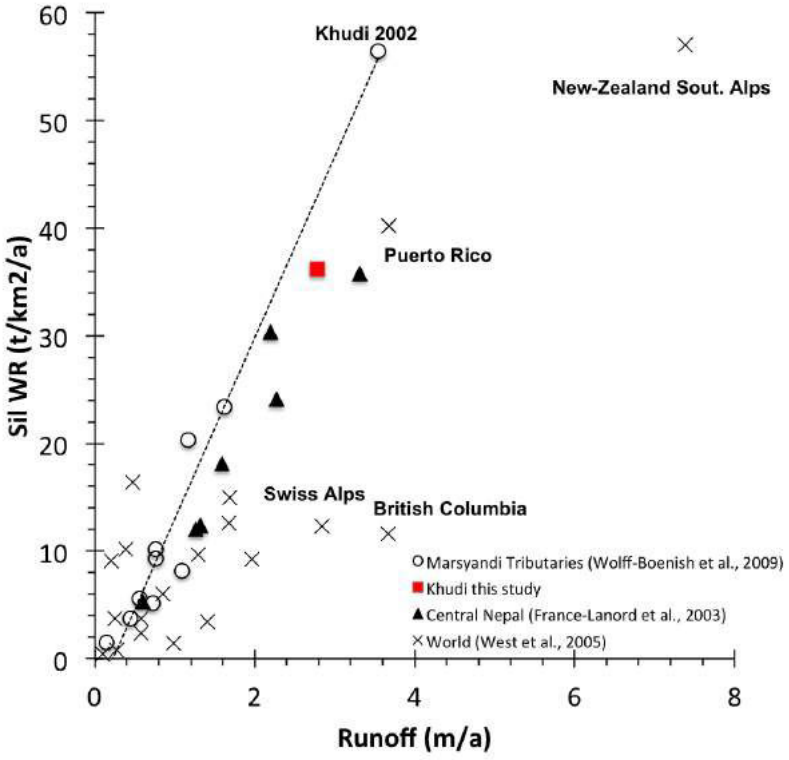

FIGURE 4.2.10 – SilWR vs. Runoff in Khudi basin compared to rivers in Nepal and world. SilWR vs. Runoff for the Khudi from this study, Marsyandi tributaries of [Wolff-Boenisch 09], Narayani tributaries of [France-Lanord 03, Wolff-Boenisch 09], World rivers of [West 05].

This is in spite of the variable proportion of carbonates in their watershed ; but the relationship between SilWR and Runoff normalized to silicate area remains well correlated Fig 4.2.11).

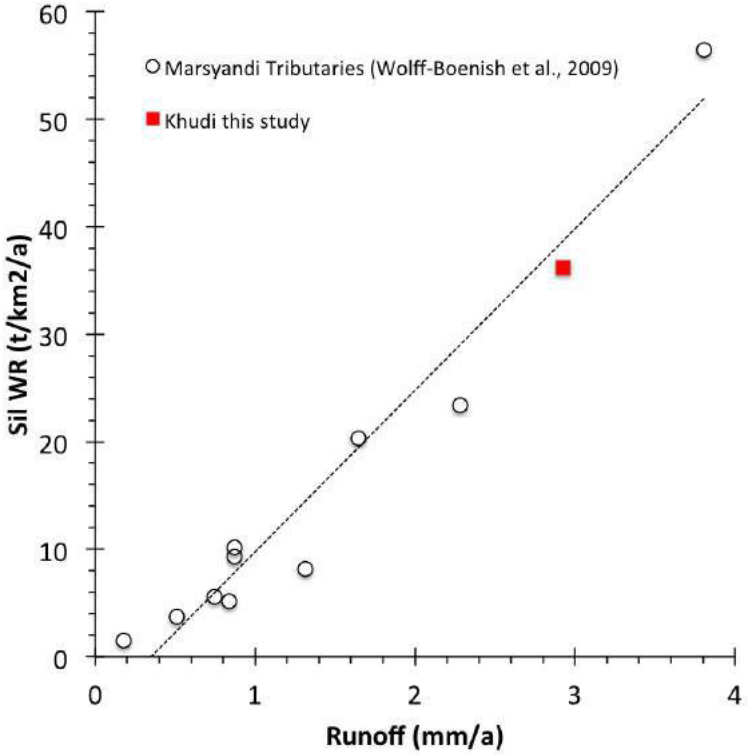

FIGURE 4.2.11 – SilWR vs. Runoff in Khudi basin compared to rivers in Nepal Khudi from this study, Marsyandi tributaries of Wolff-Boenish et al. (2009).

When compared to other data set based on worldwide watershed where silicate erosion is well documented ([Millot 02, West 05] and references in), SilWR of the Khudi appears in the general trend. High runoff basins of Puerto Rico are very close, but British Columbia and Swiss Alps are below the main tendency. This may point to a possible effect of temperature and vegetation. The comparison of SilWR with Physical denudation rate (fig 4.2.12) shows that there is no clear relationship, and that the Khudi, with the highest physical erosion, does not show exceptional SilWR.

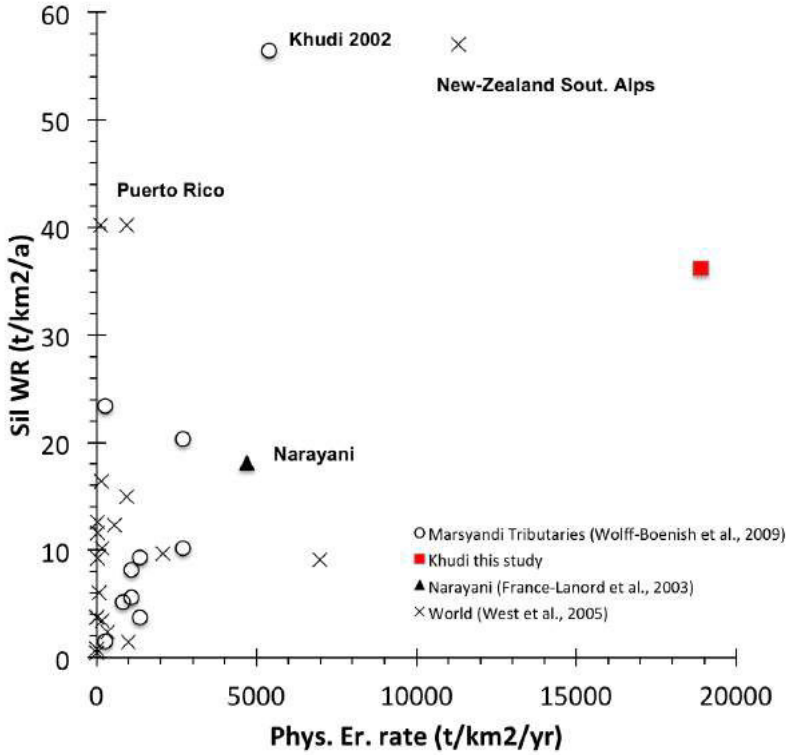

FIGURE 4.2.12 – SilWR vs. Physical denudation rate in Khudi basin compared to rivers in Nepal and world.

Rather there is likely a kinetic limitation to weathering in the Khudi. [West 05] proposed that climatic factors could limit weathering. In the case of the Khudi, the limiting factor could be the geomorphologic conditions, which trigger the landslide activity during a specific period.

Chemical erosion fluxes compared to inferred soil signature

Measured fluxes of dissolved elements lead to a chemical erosion that is in the order of 0.015 and 0.02 mm/yr for silicate and carbonate respectively. While there is significant uncertainty on such figures, the main source of uncertainty is the discharge estimate and an extreme upper boundary could be to increase the discharge by 50% leading to erosion rates of 0.02 and 0.03 mm/yr. The carbonate erosion rate likely largely relates to the marbles of the LH that cover a minor area of the watershed. If carbonate cover ≈5% of the basin area this would lead to a chemical erosion rate of 0.4 mm/yr for the carbonates,

which seems plausible in this context. On the silicate side, the estimated chemical erosion flux of 0.015 mm is in the range of 3 to 13% of the physical erosion of soil based on our estimate of 0.1 to 0.4 mm/yr. The crude comparison of these figures is difficult especially in the context of the Khudi river where landslide strongly hampers accurate estimate of soil erosion. Nevertheless, comparing average topsoil to landslide pebbles considered as an average pristine rock, we calculate that the loss of SiO_2, MgO, K_2O, Na_2O and CaO represents a chemical erosion of about 15% of the bedrock assuming constant Fe. Physical erosion of soil therefore appears roughly in the range of the chemical erosion.

The comparison of dissolved element fluxes to the soil depletion reveals more contrasted differences. Figure 4.2.13 shows the differences between landslide pebbles and soils relative to Al.

This shows that there is little losses of Mg and about equivalent losses of Na, K, and Ca. The Mg difference can be linked (1) to the fact we calculate Mg_{sil} from dissolved K concentration [Galy 99b] which is likely inadequate for Mg as it appears independent of K in the Khudi [Morin 14], and (2) to the high dispersion of $Mg/Al_{topsoil}$ which may lead to overestimation of this ratio (figure 4.2.13). The significantly higher flux of dissolved K relative to Na may be due to the difficulty to estimate initial bedrock composition, however, the differences between soil population and potential source rocks seem relatively robust. Rather we argue that top soils do not reflect the full weathering environment in the Khudi basin. Deeper levels in soil do not seem to show higher depletion in K than in Na. High K appears only to be correlated with peak discharge during the monsoon, which also preludes ground water influx which are more diluted during such event. The process that release K is therefore not identified yet. As mentioned earlier it may relate to rapid desorption from the suspended load during flood episodes or to leaching of the organic litter.

Soils erosion rates calculated are ~0.1 – 0.4 mm/y, and weathering on slopes does not seem to be hampered by physical erosion. Our observations tend to show that slopes are mantled by developed soils and that regolith thickness is important. Even down to 5 m depth, soils signatures do not present pristine bedrock signature corresponding more to sap-rock. The Khudi khola relatively high weathering characteristics were already explained by Wolff-Boesnish et al., 2009 through chemical kinetics modeling. They proposed that the climatic setting of Khudi basin with high temperatures ~20°C and precipitations

$\sim$3 m/yr induces rapid mineral weathering. On slopes, the regolith thickness is important and we suppose that it might results from deep fracturation resulting from hillslope destabilization.. Nevertheless, if evaluating deep-weathering is hard to tackle given that access accessing to groundwaters is quite impossible in such valley configuration, comparing compositions of runoff waters with soils compositions can give an idea on what happens in the regolith.

To do so, we modeled what happens to solid compositions if runoff HHC would result from the weathering of HHC Khudi bedrock (Landslide pebbles) (c.f. figure 4.2.13).

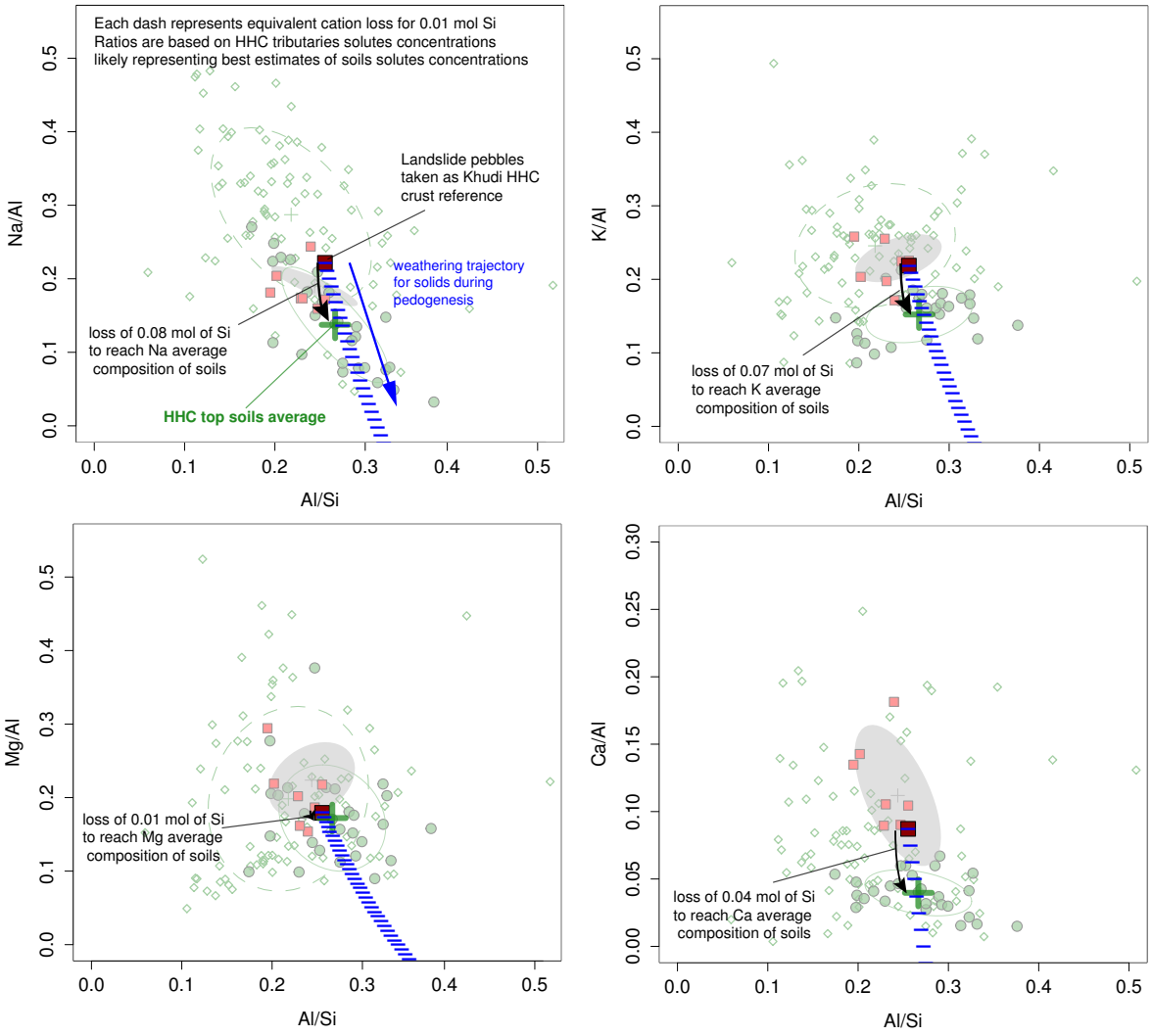

FIGURE 4.2.13 – Hillslopes solids weathering trajectory using waters composition estimated for soils waters : runoff waters of HHC tributaries.
Landslide pebbles are taken as reference for pristine bedrock of Khudi basin HHC crust. Each step corresponds to a loss of 0.01 mol Si and the cation equivalent loss calculated on the basis of HHC tributaries compositions.

Considering that HHC is mainly composed of silicates, we based other cations losses on their relative ratios to silica as expressed in HHC tributaries waters compositions. Multiple iterations corresponding to a loss of 0.01 mol of Si give the weathering trajectory of solids. Numbers of steps to reach soils compositions traduces the relative intensity of weathering

needed to explain soils compositions.

First, curves starting from landslide pebbles reach perfectly the average top soils compositions. It demonstrates 1-that landslide pebbles taken as bedrock reference seems to be the best estimate of Khudi HHC bedrock, and 2 – that compositions of runoff waters from HHC tributaries might well reflect soils waters compositions and illustrate the superficial weathering that occurs in soils. Now, on the numbers of relative mol of silica needed to reach top soils compositions, interpretation is more elusive. First, the same number of silica loss 0.07 and 0.08 mol of Si permits to reach Na and K soils compositions. It agrees relatively well with large scale interpretation that Himalayan weathering liberate Na and K in same quantity [Galy 99b]. Composition of soils is only reached for an equivalent silica loss of 0.04 mol. Hence, weathering of Ca-bearing minerals must be relatively rapid. Our interpretation is that such rapid weahtering maybe due to the fact that carbonates in traces are weathered quite instantly in soils. It would also provoke too high Ca concentrations of runoff waters compared to silicate waters if they were derived from carbonate free environnements, even if the latter remain minor in bulk solid. Still, the rapid weathering in Ca might occur very deep and quickly and certainly explains why Khudi has high dissolved Ca and low relatively low X_{sil}. Groundwater collecting deep weathering are likely more concentrated in Ca because of rapid carbonates traces weathering. Finally, Mg soils average composition is only reached for an equivalent 0.01 mol Si loss. If landslide pebbles compositions must not be put in cause as display compositions equivalent to HHC bedrock, it is possible that our estimates of soils composition in Mg is false given the high scattering observed in compositions for this element. But we think more likely that Mg is retained in soils by secondary minerals formation as clays and especially smectite that incorporates high amount of Mg. This observation corroborates with interpretation of Mg isotopic fractionations in the Marsyandi basin by Tipper et al. 2006a. Indeed, these auhtors propose that soils retain Mg by incorporation in secondary smectites and fractionating Mg isotopes. To summarize, Na and K released during superficial weathering of regolith may likely derive from simple processes and attain rivers without any disturbance as expected excepted potential K uptake by vegetation, whereas Ca must derive from much deeper weathering of hillslopes, and Mg may be retained by secondary phases crystallization as well as vegetation uptake.

4.2.7 Conclusion

The detailed analysis of the Khudi khola basin documents the variability and the characteristics of sediments exported in an Himalayan watershed exposed to intense physical erosion. These sediments analyzed over a full monsoon season define a relatively homogeneous range of composition that closely matches that of eroded material from the landslide. This is coherent with the earlier proposition that the landslide supplies most of the sediments to the river [Gallo 14a, Puchol 14].

Compared to source rocks, the Khudi river sediments have Sr-Nd compositions that clearly indicate their HHC origin. They have major element characteristics close to those of the HHC geological sample for Fe, K, Mg and H_2O+, and appear low in Na and high in Ca. These differences are not linked to chemical weathering, nor to the presence of trace carbonate. Rather they reflect bedrock characteristics different of previously documented gneisses of the HHC. This underlines the difficulty to identify representative source rocks and hampers attempt to quantify weathering in such context. The similarity of the Khudi sediments with those of the neighbor basins of the Chepe and Dordi suggests that this difference applies to a relatively large part of the basin.

Khudi sediment reflect no, or negligible signature of weathering as hydration is not detectable compared to source rocks and as the other cations seem very close to the signature of pebble average. This is quite consistent with the fact that sediments are derived mostly from a landslide, which is dominated by physical processes of sediment delivery. Nevertheless bedrocks in the landslide appear far from fresh, and show visible oxidation traces and extensive rock disaggregation. These appear however insufficient processes to alter markedly the sediment signature. Conversely, soils sampled in various positions in the basin show very clear signs of weathering with 40 to 60% depletions in K, Na, and Ca, and 100 to 200% hydration. This clear contrast allows estimating the soil contribution to the eroded sediment of the Khudi between 0 and 10%. Once again a very low contribution of surficial erosion to the Khudi sediments is not surprising given the predominance of landslide erosion. More significant is the observation that this contribution is equally low in the Chepe and Dordi khola which have no active landslide and are undergoing much lower erosion. This underlines that other process of erosion such as runoff of the upper part of the basin where chemical erosion is limited, and riverine

abrasion do supply sediments to the river with low alteration signature.

Chemical erosion estimated from dissolved element fluxes is high, around 100 t/km^2/yr, which is consistent with a subtropical basin exposed to very high runoff and covered with luxuriant vegetation. It shows however a strong decoupling with physical erosion. 60% in mass of the chemical erosion is linked to carbonate weathering that is concentrated in the Lesser Himalayan part of the basin and is a minor lithology. Silicate erosion represents 0.3% of the physical erosion. For major cations, the chemical erosion is in the order of 1 to 2% of that of the physical erosion. The present daily survey is the first of it's kind on an Himalayan watershed and shows that the chemical characteristics of the dissolved load respond strongly to the hydrological regime. Flood episode that occur mostly overnight and generate high runoff are not characterized by a classical dilution of the dissolved load. Rather, while discharge increases by a factor of two to four, the dissolved load stays essentially stable and shows a clear relative increase of K^+ and Ca^{2+}. This process is also parallel with much higher sediment load. This lead to fluxes of dissolved K^+ significantly higher than previously published and underline the need of high-resolution sampling to estimate reliably erosion fluxes. The processes that release K^+ and Ca^{2+} remain to be elucidated.

Overall, this study on the Khudi shows that, although weathering in the Himalaya is important and generate clearly depleted soils, it's translation in the sediments remain discrete. This is linked in part on the importance of transient processes such as landslide, but also to the overall low ratio of chemical to physical erosion. Deciphering weathering from bulk sediment compositions may therefore reveal to be very difficult on such system. Available data on the Narayani river indicate that signatures are quite comparable (see Chapter 5), although the mixing of source rocks is there much more complex. Because the actual weathering regime is probably close to the maximum, we expect that it will be even more difficult to trace weathering during period like the last glacial maximum when weathering intensity was likely reduced. This is indeed dependent on the chemical to physical erosion ratio but we do not expect a parallel drastic reduction of the physical erosion. This may be a limiting factor for interpreting sediments of the paleo-Gandak in term of weathering (see chapter 6). It will therefore be necessary to focus on the finest fractions of the sediment that are the most sensitive to weathering.

4.3 Appendices

A1

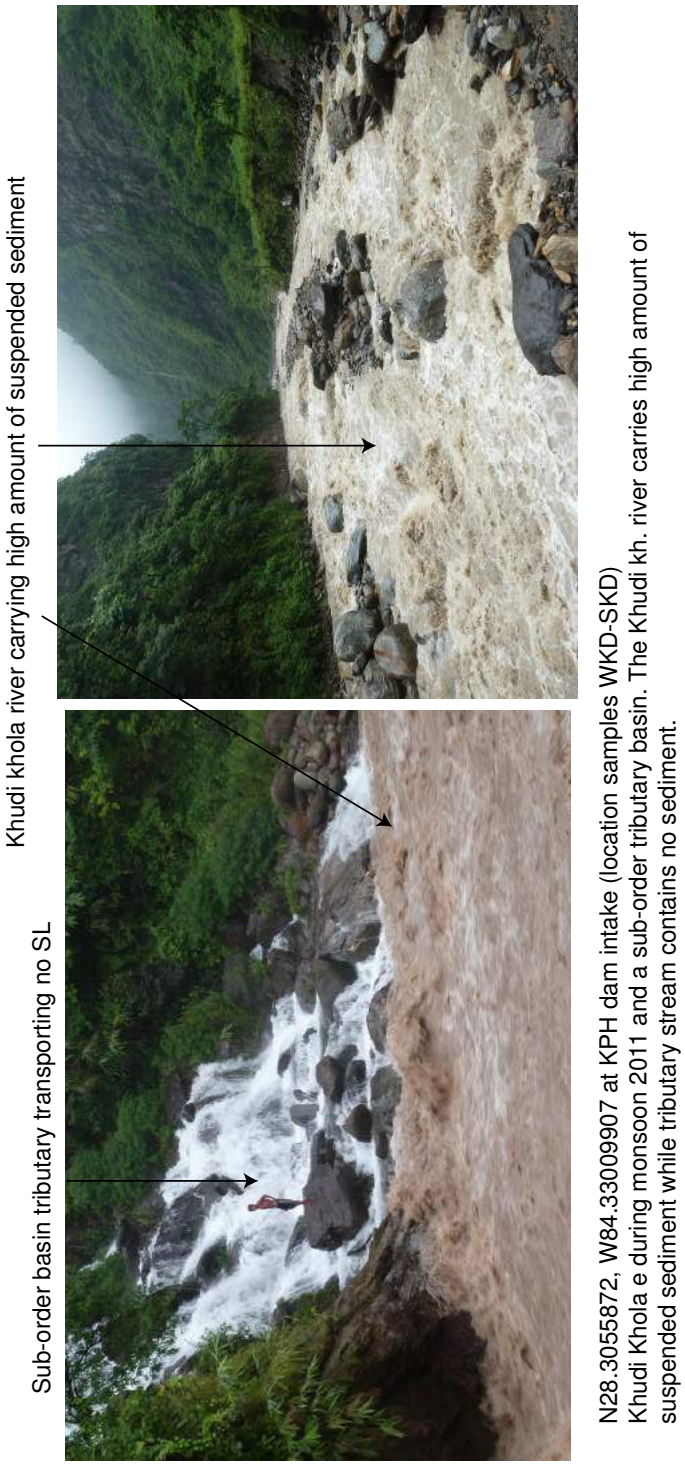

FIGURE 4.3.1 – Suspended sediment load in Khudi Khola river and tributaries during monsoon.

N28.37559,W84.28865 Sampling location CA950,CA12005,CA10112A,CA10112B,CA10112C.
Khudi western branch upstream landslides carries no suspended load.
Only minor proportions of sand and gravels.

FIGURE 4.3.2 – Suspended sediment load in Khudi Khola river in upper western branch.

N28.3174547 W84.3564019 Khudi Khola Northern branch (location samples WKD-SKD)
The Northern branch transport weak proportions of SL.
Hardly containing banks, the riverbed is composed of pebbles to boulders.

FIGURE 4.3.3 – Suspended sediment load in Khudi Khola river in upper western branch.

A2

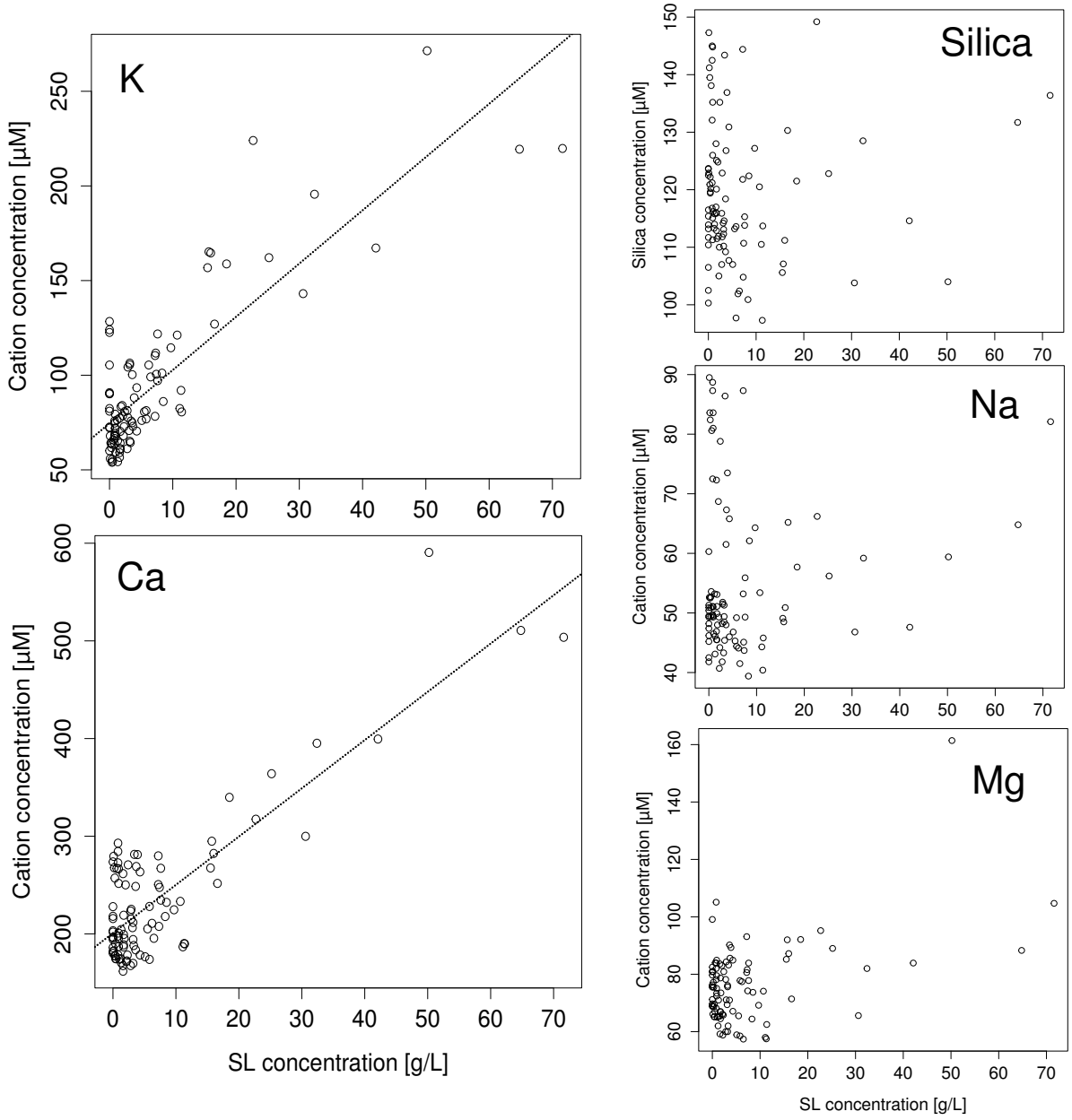

FIGURE 4.3.4 – K and Na dissolved loads correlation to suspended sediment load.

A3

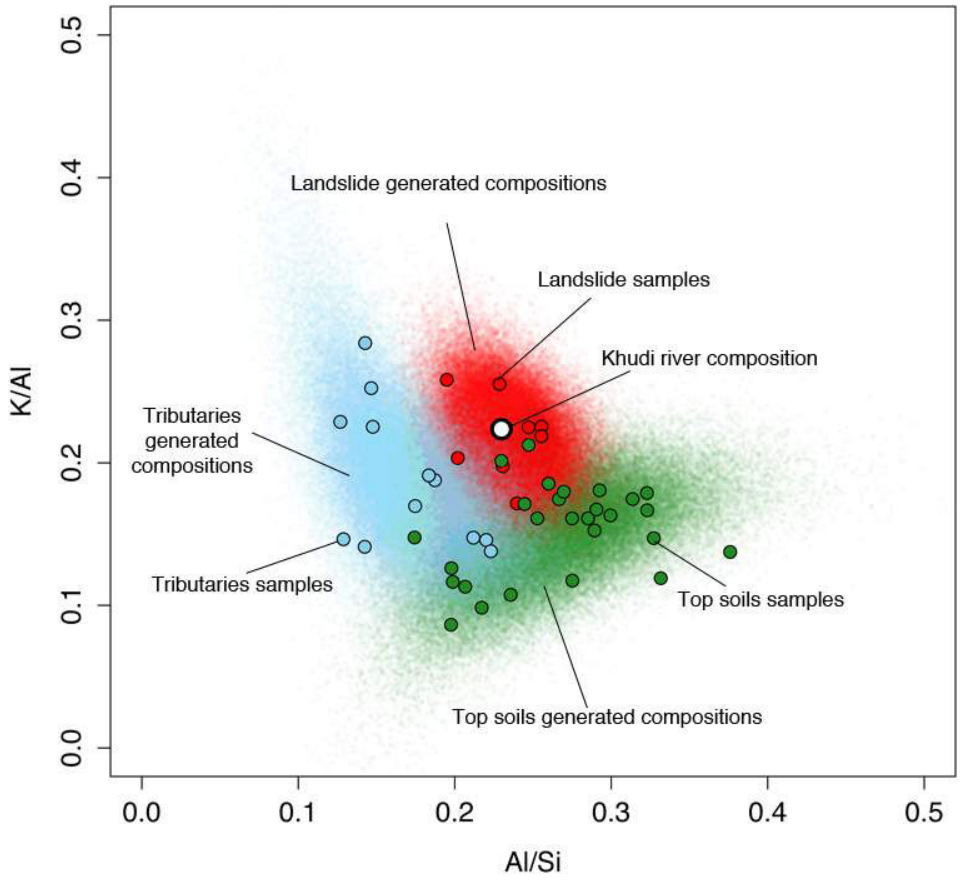

FIGURE 4.3.5 – Agreement between modeled compositions of tributaries, HHC topsoils and landslides sediments with mesured compositions.
Modeled compositions include 10000 randomly generated majors elements compositions based on covariance matrix of mesured data.

FIGURE 4.3.6 – Dordi and Khudi river during mosonn display visible suspended load concentrations contrast.

A4

4.4 Supplementary tables

S1 Central Nepal HHC FI rock compositions

Ech.#	SiO2	Al2O3	Fe2O3	MnO	MgO	CaO	Na2O	K2O	TiO2	P2O5	Pf	Total	Fe/Al	Na/Al	K/Al	Mg/Al	Ca/Al	Al/Si	H2O+	δD	H2O/Al
HHC FI	weight %												mol:mol						[%]	[‰]	mol:mol
715	74.1	12.6	4.63	0.07	0.98	0.64	0.94	3.59	0.65		1.53	99.73	0.23455	0.12273	0.38513	0.98428	0.46176	0.23814			
AP271	69.92	15.29	4.86	0.17	1.05	0.39	1.75	3.54	0.59		1.48	99.4	0.22886	0.18830	0.25695	0.86954	0.23189	0.25770			
AP278	84.46	8.25	1.61	0.06	0.59	0.65	1.88	1.15	0.39		1.24	1.28	0.12456	0.37490	0.15936	0.95345	0.71625	0.11518			
AP489	76.7	11.46	3.29	0.07	0.97	0.28	1.11	2.87	0.28		1.78	98.81	0.18325	0.15935	0.27117	0.17115	0.22212	0.17673			
AP683	70.99	14.72	5.3	0.08	1.4	0.48	1.74	3.53	0.76		0.81	99.81	0.22982	0.19447	0.25967	0.12369	0.29644	0.24435			
AP819	61.15	17.61	7.13	0.02	2.88	0.14	0.78	6.02	0.74		2.38	98.85	0.25844	0.72869	0.37157	0.26966	0.72273	0.33937			
BE106	68.49	12.95	6.32	0.07	3.72	1.51	2.4	3.13	0.9		0.96	1.45	0.31160	0.34895	0.26171	0.36353	0.16216	0.22282			
BE114	71.08	12	5.59	0.08	3.2	0.98	2.61	1.59	0.8		0.55	98.48	0.29734	0.35782	0.14347	0.33747	0.74242	0.19895			
BE300	70.67	12.83	4.8	0.08	1.78	1.6	2.57	3.88	0.78		0.75	99.74	0.23883	0.32955	0.32746	0.17557	0.11338	0.21394	0.90	-13.7	0.19791
BE307	70.51	12.87	4.77	0.06	1.7	1.43	3.04	3.1	0.72		0.84	99.4	0.23657	0.38866	0.26815	0.16716	0.11111	0.21596	0.96	-12.3	0.21128
BE310	67.9	14.25	5.67	0.08	2.27	2.39	2.73	2.86	0.93		1.7	1.15	0.25398	0.31518	0.21732	0.21593	0.15247	0.24731	1.19	-99.8	0.23735
E166	74.26	10.86	4.94	0.07	2.37	1.33	1.71	2.3	0.77		1.25	99.86	0.29349	0.25945	0.22932	0.27617	0.11133	0.17234			
E204	72.59	12.33	5.13	0.07	3.45	0	2.13	2.06	0.77		1.37	99.9	0.26557	0.28426	0.18962	0.35496		0.21661			
L01	71.21	13.09	3.59	0.06	1.17	0.67	2.69	4.71	0.4		1.64	99.23	0.17556	0.33881	0.38961	0.11311	0.46532	0.21662			
L12	83.38	7.48	1.53	0.02	0.29	0.03	0.8	3.41	0.23		1.34	98.51	0.13569	0.17595	0.49364	0.49638	0.36469	0.15717			
L36	67.41	14.67	5.36	0.09	1.37	1.05	2.16	3.28	0.71		2.3	98.4	0.23322	0.24223	0.24299	0.11818	0.65679	0.25645			
L44	74.59	10.94	4.11	0.05	2.08	0.94	2.26	2.35	0.68		1.59	99.59	0.23980	0.33986	0.23259	0.24686	0.78112	0.17284			
L46	79.16	9.95	2.68	0.04	0.7	0.64	2.38	2.7	0.37		1.66	1.28	0.17192	0.39352	0.29383	0.89376	0.58474	0.14812			
L54	63.97	16.77	5.46	0.07	1.56	0.62	1.96	4.71	0.93		2.63	98.68	0.27818	0.19228	0.34114	0.11772	0.33698	0.38937			
M102	68	12.8	5.82	0.07	4.54	0.69	1.52	3.21	0.9		1.37	98.92	0.29227	0.19536	0.27155	0.44886	0.49568	0.22182	1.79	-82.4	0.39654
M107	84.6	8.15	1.89	0.05	0.5	1.25	2.37	1.15	0.44		0.39	1.79	0.14822	0.47849	0.15279	0.77639	0.13943	0.11353			
M108	64.5	17.95	5.68	0.1	1.34	0.98	2.42	3.33	0.66		2.1	99.6	0.21979	0.22180	0.28765	0.94473	0.49633	0.32795			
M114	63.3	16.55	6.9	0.12	3.85	0.74	1.64	3.3	0.79		1.39	98.58	0.26612	0.16325	0.21596	0.29439	0.46482	0.38149	1.67	-94.7	0.28430
M200	78.2	9.15	4.37	0.03	1.98	1.98	1.81	1.84	0.69		0.76	1.81	0.34848	0.32544	0.21774	0.27385	0.19672	0.13789	0.97	-95.3	0.35748
M201	75	11.65	4.68	0.08	1	1.1	2.85	2.79	0.7		0.43	1.28	0.25641	0.42464	0.25931	0.18627	0.85837	0.18350			
MB301M	70.7	12.67	5.16	0.06	1.9	1.24	2.79	3.06	0.65	0.19	0.86		0.25995	0.36227	0.26151	0.18978	0.88972	0.21118			
MB363M	72.02	13.33	4.24	0.07	1.41	1.26	3.52	3.15	0.58	0.17	0.64		0.23295	0.43443	0.25588	0.13386	0.85936	0.21811			
MB364M	70.42	13.42	5.77	0.06	1.43	1.3	3.15	3.48	0.65	0.18	0.78		0.27444	0.38616	0.28786	0.13485	0.88639	0.22457			
MB368M	65.84	13.14	7.22	0.28	2.57	2.46	2.7	3.33	1.08	0.36	0.7		0.35724	0.33847	0.27449	0.24752	0.17195	0.23519			
MB369M1	72.67	12.65	4	0.09	1.46	3.46	2.93	1.67	0.76	0.18	0.18		0.21833	0.38153	0.14295	0.14659	0.24865	0.25135			
MB369M2	73.42	11.84	3.6	0.11	1.03	4.51	2.8	0.94	0.68	0.16	0.58		0.19478	0.38958	0.85966	0.11975	0.34628	0.19385			
MB369M3	61.18	16.86	6.26	0.12	2.51	2.55	2.65	6.09	1.01	0.2	0.68		0.23700	0.25858	0.39112	0.18842	0.13750	0.32475			
MB370M	64.4	15.11	6.06	0.11	2.69	3.22	3	3.38	1.02	0.19	0.65		0.25600	0.32664	0.24222	0.22530	0.19374	0.27649			
MB373M	62.47	16.68	6.1	0.07	2.3	1.23	2.96	5.72	0.91	0.8	1.74		0.23343	0.29195	0.37133	0.17456	0.67373	0.31466			
MB374M	69.48	13.75	5.21	0.07	1.85	1.41	2.64	3.48	0.89	0.22	1.14		0.24186	0.31588	0.27447	0.17268	0.93223	0.23322			
MB426M	77.14	8.06	5.21	0.04	3.34	0.95	1.12	2.65	0.76	0.3	0.81		0.41260	0.22868	0.35683	0.52442	0.17159	0.12313			
MB427M	82.68	8.47	2.1	0.02	1.6	0.51	2.33	1.34	0.48	0.11	0.56		0.15826	0.45257	0.17135	0.23957	0.54739	0.12722			
MK010	90.67	4.57	1.99	0.05	0.55	0.1	0.58	0.94	0.24		0.58	1.27	0.27795	0.28796	0.22273	0.15234	0.19893	0.59396			
MK013	65.82	16.09	6.34	0.08	1.71	0.29	0.46	4.35	0.84		2.49	98.47	0.25152	0.47338	0.29274	0.13449	0.16385	0.28873			
MK014	77.5	8.8	3.36	0.05	2.08	1.98	1.2	1.69	0.4		1.15	98.21	0.24371	0.22434	0.27947	0.29912	0.24545	0.13389			
MK015	49.75	17.54	8.77	0.11	6.2	2.67	1.7	5.63	0.97		4.69	98.3	0.31915	0.15945	0.34756	0.44733	0.13838	0.41547			
MK143	61.58	16.38	5.88	0.11	3.43	1.57	2.15	4.87	0.76		1.69	98.42	0.22913	0.21594	0.32193	0.26500	0.87136	0.31346			
MK302	72.83	11.66	4.94	0.05	4.25	0.2	2.09	1.82	0.73		1.18	99.75	0.27429	0.29489	0.16914	0.46127	0.15593	0.18867			
MK316	71.05	11.84	4.93	0.04	3.95	0.79	2.39	1.73	0.69		1.32	98.73	0.26578	0.33289	0.15821	0.42219	0.66572	0.19638			
MK324	66.86	14.29	5.38	0.15	2.3	1.96	3.29	2.36	0.55		2.11	99.25	0.24319	0.37877	0.17883	0.23686	0.12469	0.25187			
MK340	71.13	12.14	4.93	0.04	3.45	0.39	3.44	1.59	0.69		1.34	99.14	0.25930	0.46617	0.14182	0.35964	0.29247	0.21127			
NA023	65.45	15.81	6.38	0.09	2.84	0.59	2.82	3.02	0.81	0.8	1.24	99.13	0.25758	0.29344	0.26835	0.22733	0.33926	0.28466			
NA028	65.42	18.58	5.96	0.06	1.41	0.5	2.01	3.65	0.65		2.5	1.29	0.24752	0.17797	0.21271	0.96370	0.24464	0.33469			
NA041	67.64	14.83	7.62	0.06	2.96	0	0.87	3.52	0.88		0.76	99.14	0.32797	0.96513	0.25714	0.25259		0.25837			
NA058	65.19	15.57	5.58	0.1	2.33	3.25	3.3	2.59	0.85	0.12	0.73	99.61	0.22875	0.34869	0.18119	0.18938	0.18976	0.28146			
NA363	51.93	22.38	9.36	0.12	3.92	3.22	2.6	4.08	1.08	0.6	1.5	1.25	0.26696	0.19113	0.19742	0.22166	0.13799	0.57862			
NA366	58.93	17.72	7.53	0.1	3.31	3.75	2.86	3.11	0.78	0.7	0.87	99.3	0.27125	0.26553	0.19443	0.23639	0.19239	0.35435			
NA410	82.35	7.8	2.93	0.04	1.19	0.68	2.25	1.22	0.49	0.1	0.38	99.34	0.23978	0.47457	0.16936	0.19371	0.79255	0.11162			
NA411	63.75	15.34	7.64	0.1	3.87	0.5	1.76	4.05	0.87	0.12	1.33	99.33	0.31796	0.18875	0.28588	0.31926	0.29631	0.28356			
NL059	73.94	10.53	5.43	0.08	2.59	0.48	1.66	2.82	0.97	0.18	0.94	99.62	0.32916	0.25935	0.28998	0.31127	0.41444	0.16782	1.15	-80.6	0.39765
NL074	72.4	12.73	3.89	0.06	1.17	0.92	1.97	4.1	0.73		0.96	98.93	0.19549	0.25459	0.34874	0.11631	0.65728	0.27230	0.98	-76.1	0.21791
NL075	79.74	9.65	2.69	0.05	0.65	1.16	2.37	1.62	0.44		0.69	99.6	0.17793	0.44448	0.18178	0.85242	0.19279	0.14261	0.68	-79.5	0.19886
NL076	74	12.3	4.17	0.08	1.18	1.56	2.66	2.6	0.62		0.68	99.85	0.21640	0.35578	0.22889	0.12147	0.11530	0.19587			
NL081	65.06	17.6	6.21	0.1	1.67	1	2.66	3.88	1.16	0.23	0.9	1.47	0.22522	0.24864	0.23879	0.12795	0.51653	0.31879			
NL085	81.41	9.49	2.66	0	0.5	0.65	2.04	3.17	0		0.53	1.45	0.17891	0.35365	0.36169	0.66676	0.62267	0.13737			
NL086	73.99	11.91	4.36	0.09	1.08	0.99	2.09	2.73	0.73		0.87	98.84	0.23367	0.28870	0.24820	0.11476	0.75567	0.18969	0.94	-112.6	0.22248
NL093	82.6	8.19	1.85	0.07	0.58	1.76	2.01	0.66	0.33		0.52	98.57	0.14418	0.43758	0.87259	0.89629	0.19536	0.11684	0.46	-73.0	0.15824
NL100	81.53	8.86	1.95	0.04	0.51	1.31	2.6	1.01	0.32		0.57	98.7	0.14483	0.48278	0.12343	0.72845	0.13441	0.12863			
NL124	73.48	12.49	4.86	0.09	1.2	0.48	1.95	3.42	0.7	0.19	1.15	1.1	0.24837	0.25686	0.29649	0.12159	0.34937	0.23767			
NL133	74.56	11.9	4.03	0.06	1.14	0.8	2.11	2.8	0.61		0.57	98.58	0.21616	0.29176	0.25478	0.12123	0.61115	0.18881			
NL136	69.44	14.07	6.07	0.1	1.78	1.16	2.25	2.92	0.98	0.23	0.92	99.92	0.27538	0.26385	0.22472	0.16999	0.74950	0.23877	1.00	-82.4	0.27346
NL143	77.59	10.27	3.3	0.06	0.61	1.39	2.88	1.36	0.77	0.26	0.56	99.5	0.25158	0.46135	0.14339	0.75167	0.12342	0.15598			
NL146	74.46	12.06	4.44	0.08	1.08	0.66	2.1	3.76	0.63	0.1	0.68	1.5	0.23500	0.28648	0.33759	0.11333	0.49751	0.19866	0.84	-90.2	0.19659
NL150	76.3	11.37	4.31	0.08	1.2	1.03	1.92	2.76	0.7	0.12	0.65	1.44	0.24196	0.27782	0.26284	0.13356	0.82354	0.17566			
NL158	67.61	16.22	5.72	0.04	1.88	0.18	1.15	3.89	1.09	0.8	1.86	99.72	0.22596	0.11664	0.25969	0.14668	0.18856	0.28271	2.73	-17.5	0.47217
NL172	78.65	10.14	3.07	0.07	0.65	0.94	2.46	2.16	0.34	0.1	0.62	99.2	0.19325	0.39912	0.23656	0.81122	0.84275	0.15193	0.66	-78.8	0.16922
NL301	66.71	14.91	7.23	0.15	1.82	1.15	2.31	3.58	0.8	0.4	0.84	99.54	0.39517	0.25488	0.25999	0.15448	0.71177	0.26338	1.13	-83.9	0.21393
NL302	79.53	9.57	3.33	0.07	0.81	0.7	1.92	2.61	0.55		0.48	99.57	0.22214	0.33638	0.29540	0.17112	0.66496	0.14183			
NL413	75.27	11.59	4.52	0.07	1.94	0.96	2.25	2.09	0.84		0.9	1.43	0.24894	0.31938	0.19526	0.21183	0.75324	0.18145	0.88	-85.0	0.21472
NL414	74.99	10.59	4.47	0.05	3.27	0.11	2.13	2.12	0.65	0.1	0.99	99.38	0.26942	0.33896	0.21677	0.39766	0.94429	0.16642	1.37	-8.3	0.27751
NL418	70.58	12.71	5.34	0.05	3.78	0.64	1.73	2.48	0.74	0.1	0.93	99.8	0.26818	0.22393	0.21128	0.37637	0.45776	0.21221	1.29	-86.1	0.28827
NL420	71.42	13.49	4.82	0.03	2.3	0	1.87	2.88	0.75	0.2	1.41	99.17	0.22865	0.22854	0.23117	0.21577		0.22259			
NL499	74.83	10.28	4.42	0.07	2.25	1.67	2.06	2.03	0.79		0.84	99.24	0.27444	0.32967	0.21382	0.27698	0.14768	0.16190			
NL512	71.34	11.34	6.23	0.1	2.15	1.07	2.18	2.68	1.25	0.28	0.83	99.45	0.35670	0.31627	0.25594	0.23993	0.85778	0.18732	1.16	-79.8	0.28956
NL515	68.52	14.19	6.2	0.11	2.56	0.67	1.48	3.08	0.76	0.29	0.83	98.69	0.27889	0.17159	0.23527	0.22839	0.42924	0.24445			
NL517	65.58	14.13	3.17	0.09	2.49	2.47	2.28	3.37	0.71	0.23	4.93	99.45	0.14320	0.26546	0.25825	0.22390	0.15891	0.25397	1.35	-94.3	0.27248
NL519	77.14	9.67	3.95	0.08	1.61	0.73	1.5	2.38	0.75	0.16	1.9	99.6	0.26732	0.25520	0.26652	0.21700	0.68628	0.14772			
NL520	67.4	15.72	5.55	0.1	2.46	0.26	0.54	3.9	0.82	0.15	1.86	98.76	0.22535	0.56513	0.26863	0.19838	0.15359	0.27486	1.97	-78.3	0.35566
BE302	71.52	16.45	1.03	0.01	0.38	1.36	3.84	4.41	0.13		1.15	1.28	0.39966	0.38438	0.29283	0.29234	0.75159	0.27146	0.79	-88.5	0.13655
BE317	75.76	14.34	0.54	0.01	0.37	0.8	4.87	3.03	0.08		0.68	1.48	0.24363	0.55871	0.22879	0.32653	0.57164	0.22356			
DK402	72.62	15.37	1.75	0.05	0.33	1.69	4.4	2.96	0.28	0.11	0.81	1.37	0.72675	0.47964	0.28529	0.27180	0.99959	0.24941			
L34	73.55	14.83	0.99	0.03	0.29	1.33	3.88	3.29	0.01		1.66	99.86	0.42616	0.43427	0.24217	0.24747	0.81537	0.23769			
MANA	73.94	14.76	0.81	0.02	0.13	0.46	4.14	4.48	0.07	0.13	0.72		0.35285	0.46145	0.32866	0.11147	0.28332	0.23524			
MANC	74.04	14.67	0.84	0.02	0.18	0.5	4.06	4.5	0.07	0.14	0.79		0.36549	0.45538	0.33215	0.15528	0.39847	0.23349			
MB309M	75.43	13.03	1.31	0.03	0.3	0.63	3.71	4.42	0.26	0.15	0.44		0.64173	0.46842	0.36735	0.29137	0.43955	0.23566			
MB366M1	75.76	13.63	1.09	0.02	0.15	0.4	3.75	4.24	0.14	0.11	0.64		0.51460	0.45264	0.33684	0.13928	0.26679	0.21212			
MB366M2	76.86	13.87	0.94	0.03	0.13	0.31	3.15	3.19	0.14	0.14	1.5		0.43259	0.37364	0.24937	0.11861	0.23185	0.21266			
MB380M	73.67	14.92	1.99	0.04	0.3	1.63	3.76	3.23	0.11		0.49		0.85135	0.41460	0.23441	0.25446	0.99318	0.23866			
MB429M	71.3	12.9	0.8	0.1	2.58	0.88	2.33	2.79	0.71	0.1	1.56		0.39584	0.29715	0.23419	0.25312	0.62155	0.21328			
NA469	74.44	13.74	1.22	0.06	0.09	0.31	3.27	4.66	0.1	0.2	0.77	98.86	0.56676	0.39153	0.36724	0.82894	0.25178	0.21751			
NL288	70.39	15.27	2.66	0.01	2.06	0	0.34	4.99	0.73	0.2	2.31	98.78	0.11120	0.36640	0.35384	0.17724		0.25564			
NL518	69.44	12.78	1.74	0.02	1.28	0	0.21	4.35	0.82	0.8	7.92	98.64	0.86945	0.27332	0.36856	0.12675		0.21688			
MB421F	75.07	11.59	3.72	0.05	1.46	1.46	2.95	2.31	0.74	0.11	0.64		0.24872	0.41874	0.21581	0.15942	0.11452	0.18194			
MB421G	59.47	17.7	6.83	0.1	2.73	1.14	2.61	5.59	1.05	0.12	1.44		0.24634	0.24259	0.34197	0.19519	0.58552	0.35735			
MB301LK	71.73	15.12	0.48	<0.01	0.3	1.02	2.83	6.74	0.08	0.26	0.71		0.22634	0.37924	0.48268	0.25193	0.61328	0.24843			
MB301L	74.25	14.62	0.47	0.01	0.08	1.11	3.37	5.52	0.04	0.16	0.47		0.25198	0.37922	0.48828	0.69249	0.69213	0.23236			

Ech.#	SiO2	Al2O3	Fe2O3	MnO	MgO	CaO	Na2O	K2O	TiO2	P2O5	Pf	Total	Fe/Al	Na/Al	K/Al	Mg/Al	Ca/Al	Al/Si	H2O+	δD	H2O/Al
HHC FI	weight %												mol:mol						[%]	[‰]	mol:mol
MB309L	73.98	14.13	1.82	0.1	0.03	0.5	3.1	5.65	0.22	0.15	0.54		0.82215	0.36934	0.43297	0.26869	0.32169	0.22578			
MB364L	72.9	15.21	0.4	0.02	0	1	3.36	6.92	0.03	0.16	0.34		0.16786	0.36343	0.49264		0.59769	0.24587			
MB366L	73.44	14.68	0.65	0.02	0.12	0.09	2.76	6.34	0.05	0.23	0.59		0.28263	0.39383	0.46765	0.13448	0.55734	0.23556			
MB370L	69.63	14.58	3.25	0.06	1.43	3.08	3.2	3.13	0.52	0.12	0.66		0.14228	0.36178	0.23245	0.12413	0.19244	0.24675			
MB373L	71.36	15.25	1.41	0.03	0.6	1.76	4.14	4.13	0.17	0.15	0.8		0.59164	0.44663	0.29324	0.49796	0.14918	0.25184			
MB374L	74.84	13.71	1.2	0.03	0.32	2.53	4.13	1.63	0.23	0.53	1.12		0.55869	0.49559	0.12874	0.29538	0.16777	0.21588			
MB380L1	73.41	15.13	0.51	0.02	0	0.97	3.22	5.77	0		0.28		0.21516	0.35127	0.41294		0.58283	0.24288			
MB380L2	73.3	14.89	1.72	0.03	0.19	1.53	3.75	3.6	0.08		0.46		0.73732	0.41433	0.26179	0.16148	0.93412	0.23938			
MB426L	72.27	15.6	1.19	0.03	0.88	3.85	4.77	0.48	0.15	0.2	0.37		0.48697	0.53397	0.33317	0.71388	0.22436	0.25437			
MB427L	76.94	14.53	0.56	0.01	0.41	1.3	5.1	0.34	0.14	0.1	0.36		0.24666	0.57745	0.25337	0.35795	0.81336	0.22254			
MB429L	78.04	12.75	1.47	0.03	0.77	1.49	4.23	0.84	0.25		0.47		0.73592	0.54586	0.71338	0.76427	0.16239	0.19253			
MB301LP	74.88	13.89	0.43	<0.01	0.36	1.86	4.36	2.34	0.15	0.24	0.76		0.19761	0.51648	0.18242	0.32799	0.12174	0.21860			
MB309P	73.73	13.98	1.76	0.15	0.13	0.4	2.84	6.44	0.16	0.19	0.31		0.83580	0.33421	0.49882	0.11768	0.26112	0.22344			
MB363P	75.62	13.17	0.68	0.02	0	0.47	2.4	6.64	0.03	0.23	0.39		0.32957	0.29982	0.54592		0.32443	0.25236			
MB366P	74.81	14.57	0.73	0.02	0.12	0.35	3.79	3.97	0.09	0.25	0.61		0.31987	0.42795	0.29540	0.14229	0.21838	0.22951			
MB368P	71.41	14.93	0.47	0.13	0.17	1.66	2.65	7.03	0	0.3	0.36		0.29378	0.29279	0.59853	0.14497	0.11778	0.24638			
MB369P	75.57	12.78	0.47	0.06	0.18	2.17	2.51	4.62	0.07	0.23	0.48		0.23474	0.32312	0.39144	0.17825	0.15437	0.19929			
MB301R	67.84	11.67	7.61	0.09	2.97	0.82	1.47	4.1	1.26	0.29	1.4		0.41623	0.27231	0.38420	0.32273	0.63878	0.22717			
MB373R	52.1	19.69	10.45	0.12	4.52	0.93	2.12	6.75	1.69	0.15	1.74		0.33876	0.17713	0.37120	0.29578	0.42938	0.44536			
MB374R	66.63	14.67	6.3	0.07	2.33	1.08	1.57	4.78	1.15	0.38	1.48		0.27412	0.17667	0.35282	0.29976	0.66927	0.25946			
MB426R	59.85	14.78	11.54	0.15	5.95	0.84	0.98	4.08	1.19	0.19	1.28		0.49837	0.19838	0.29896	0.59457	0.51667	0.29114			
MB427R	71.85	11.46	5.75	0.05	4.41	0.12	0.76	3.23	0.89	0.12	1.5		0.32263	0.19132	0.35188	0.48699	0.95193	0.18796			
MB429R	56.35	19.97	8.99	0.14	5.85	0.37	0.93	4.37	1.04	0.26	1.18		0.28735	0.76615	0.23695	0.37717	0.16843	0.41763			
MB429gw	79.94	9.89	4.16	0.08	1.98	0.59	1.98	2.26	0.76	0.7	0.75		0.26849	0.32936	0.24744	0.25336	0.54233	0.14579			

S2 Central Nepal LH rock compositions

Ech.#	SiO2	Al2O3	Fe2O3	MnO	MgO	CaO	Na2O	K2O	TiO2	P2O5	Pf	Total	Fe/Al	Na/Al	K/Al	Mg/Al	Ca/Al	Al/Si	H2O+	δD	H2O/Al
HHC FI	weight %												mol:mol						[%]	[‰]	mol:mol
A78	51.92	8.78	3.46	0.2	7.73	1.21	0.68	1.97	0.38	0.7	15.2		0.25154	0.12742	0.24295	1.11417	1.57155	0.19928			
AL49	8.69	9.5	2.64	0.4	1.14	0.8	1.52	2.6	0.45		1.61	99.28	0.18620	0.27631	0.24647	0.15941	0.83616	0.13218	1.15	-78.0	0.36368
AL71	86.8	5.76	1.83	0.6	0.31	0.7	0.61	1.94	0.31		1.6	98.75	0.22793	0.17423	0.36469	0.68190	0.11480	0.78254	0.91	-84.0	0.44763
AL147	7.9	14.26	1.97	0.1	1.84	0.22	0.52	4.75	0.66		4.6	99.73	0.88186	0.59992	0.36682	0.16329	0.14252	0.23716	2.40	-64.5	0.47686
AL174	62.45	19.76	5.57	0.3	2.1		0.33	5.42	0.61		3.77	1.4	0.17993	0.27475	0.29735	0.13449		0.37287	4.87	-66.0	0.69830
AL185	84.58	7.64	1.89	0.4	0.45	0.15	1.12	2.43	0.42		1.4		0.15794	0.24118	0.34440	0.74539	0.17849	0.16446			
AL212	75.5	11.46	4.26	0.2	1.54		0.2	3.21	0.48		3.6	99.55	0.23727	0.28711	0.33299	0.17596		0.17887	2.80	-79.0	0.69226
AL214	65.89	16.23	4.8	0.2	1.99		0.6	4.98	0.72		3.89	98.58	0.18878	0.68193	0.33225	0.15517		0.29278	3.47	-81.4	0.65771
AL31	73.42	11	3.2	0.2	2.84	0.1	0.27	3.31	0.53		4.64		0.17524	0.43812	0.32583	0.32673	0.82645	0.17656			
AL54	47.7	14.48	12.8	0.13	13.26	0.23	0.2	0.52	2.57		8.3		0.56424	0.22723	0.38885	1.15888	0.14440	0.35773			
AP9	81.13	8.52	3.11	0.2	1.58		0.5	2.32	0.21		2.14	99.8	0.23299	0.96547	0.29485	0.23468		0.12375	2.15	-66.0	0.71498
AP13	81.3	9.69	2.53	0.3	1.4		0.14	3.3	0.37		1.97		0.16666	0.23769	0.33859	0.18284		0.14923			
AP136	82.88	7.78	2.31	0.2	0.75		0.26	3	0.35		1.33		0.18952	0.54980	0.41753	0.12200		0.11621			
AP167	77.16	1.69	3.4	0.3	1.34	0.15	1.62	1.91	0.63		2.7	99.27	0.18152	0.24931	0.19347	0.15863	0.12756	0.16326	1.79	-73.7	0.47444
AP197	93.9	3.49	0.84	0.3	0.39		0.39	0.76	0.17		0.6	99.76	0.15363	0.18384	0.23580	0.14142		0.44190	0.60	-62.3	0.48716
AP198	85.35	7.72	1.67	0.7	0.91	0.21	1.11	1.84	0.48		1.11		0.13877	0.23655	0.25877	0.14917	0.24729	0.16594			
AP199	53.81	23.32	9.86	0.15	2.23	1.4	0.98	4.75	1.14		2.96	1.24	0.26989	0.69136	0.22554	0.12116	0.45426	0.51747	3.47	-63.3	0.42198
AP23	95.47	0.93	1.75	0.3	0.41			0.4			0.94		1.21981		0.46572	0.55791		0.11479			
AP242	63.38	17.59	8.27	0.5	2.99	0.15	0.48	3.89	0.99		2.44		0.39798	0.44894	0.23946	0.21511	0.77523	0.32753	2.26	-81.1	0.36463
AP25	44.69	14.94	13.73	0.6	14.81		0.1	0.44	1.94		7.97		0.58662	0.11118	0.31890	1.25450		0.39395			
AP253	68.52	14.24	5.15	0.13	1.97	1.4	2.5	3.5	0.63		1.95		0.23846	0.23684	0.23192	0.17574	0.89377	0.24495			
AP298	66.37	17.39	6.18		1.63		0.24	4.9	0.43		2.15		0.22684	0.22749	0.35126	0.11862		0.38768	2.44	-81.2	0.39699
AP33	65.7	15.86	4.31	0.1	3.11	0.83	0.35	5.1	0.5		3.9		0.17346	0.36356	0.34819	0.24815	0.47575	0.28447			
AP334	56.99	22.56	7.72	0.11	2.45	0.8	0.97	4.79	0.66		3.84	1.17	0.21842	0.77361	0.22994	0.13743	0.32237	0.46649	4.28	-6.3	0.53739
AP343	56.39	15.1	7.74	0.3	5.24	7.7	0.48	2.18	0.3		4.14		0.32718	0.52297	0.15633	0.43916	0.46358	0.31556			
AP346	6.38	2.63	6.66	0.5	2.43	0.4	0.48	5.28	0.56		3.25	1.12	0.26622	0.38278	0.27713	0.14964	0.17627	0.42634	2.98	-57.0	0.49275
AP359	73.68	13.24	2.46	0.9	0.83	0.5	0.5	7.6	0.58		1.7	99.56	0.11860	0.62128	0.57739	0.79333	0.34331	0.21176	0.94	-74.0	0.21158
AP375	73.56	13.55	4.25	0.2	1.32	0.48	0.92	3.39	0.13		2.15	99.77	0.22413	0.11180	0.27942	0.12328	0.32240	0.21771	2.24	-85.2	0.46890
AP385	62.47	19.35	6.94	0.2	1.89		0.52	5.19	0.46		3.26	1.1	0.22893	0.44212	0.29426	0.12368		0.36518	3.39	-82.0	0.49638
AP39	64.69	18.9	5.44	0.2	1.51		0.18	4.88	0.56		4.72	1.9	0.19195	0.16370	0.29299	0.15634		0.32954	4.60	-76.5	0.63589
AP47	62.67	18.22	6.39	0.8	2.38	0.7	0.36	5.89	0.85		3.36	1.27	0.22386	0.32559	0.35388	0.16538	0.34927	0.34264	3.60	-88.3	0.55912
AP417	54.42	23.47	6.34	0.7	0.95		0.33	6.99	0.37		5.48	98.42	0.17242	0.23132	0.32249	0.51224		0.58228	4.69	-66.4	0.56676
AP44	84.78	6.89	1.88	0.5	0.44	0.39	1.16	1.92	0.36		0.92	98.79	0.17417	0.27698	0.31739	0.88162	0.51458	0.95771	0.77	-7.0	0.31664
AP447	54.48	22.63	6.71	0.5	3.62	0.25	1.6	4.99	0.52		5.4		0.18926	0.77614	0.23876	0.22437	0.14298	0.48950			
AP454	81.28	9.55	2.45	0.8	1.15	0.35	1.25	2.12	0.4		1.52		0.16375	0.21534	0.24378	0.15239	0.33317	0.13846			
AP473	67.29	15.13	5.77	0.1	1.98	1.44	1.29	4.74	0.59		2.2	1.35	0.24342	0.14268	0.33923	0.16561	0.86523	0.26497	1.87	-74.0	0.35187
AP524	56.22	22.18	8.56	0.11	2.65		0.7	5.44	0.7		3.78	1.34	0.24634	0.51921	0.26557	0.15120		0.46492	4.30	-45.0	0.51483
AP537	77.6	1.29	4.84	0.7	0.97		0.35	3.8	0.42		2.15	99.23	0.32295	0.55958	0.32414	0.11929		0.15736	1.83	-9.0	0.53887
AP545	78.33	9.75	4.2	0.6	1.34		0.14	2.38	0.43		2.14	98.77	0.27496	0.23623	0.26431	0.17393		0.14668	2.30	-81.4	0.66838
AP546	62.4	19.34	5.84	0.6	1.81		0.16	5.48	0.52		3.88	99.49	0.19274	0.13614	0.36813	0.11844		0.36524	3.79	-81.3	0.55524
AP559	58.42	19.26	1.8	0.13	1.93		0.36	3.97	1.12		4.58		0.33462	0.37568	0.22319	0.12681		0.38857	4.69	-68.3	0.68972
AP572	44.22	14.54	8.64	0.11	1.73	0.63	0.94	1.59	0.93		25.49		0.37929	0.16358	0.11848	0.15573	0.39390	0.38749			
AP589	63.49	14.59	9.73	0.4	2.71	0.2	0.16	4.6	1.9		3.5		0.42568	0.18415	0.34140	0.23562	0.12462	0.27835			
AP59	61.84	16.63	3.95	0.5	7.16	0.4	0.15	4.5	1.18		4.82		0.15161	0.14840	0.26371	0.54486	0.21866	0.31694			
AP592	95.41	1.53	0.58	0.2	0.43		0.4	0.37	0.1		0.47		0.24197	0.43175	0.26185	0.35567		0.18897			
AP61	96.86	1.38	0.46		0.26		0.5	0.3	0.1		0.68		0.21277	0.59673	0.23539	0.23843		0.16790			
AP63	57.35	17.41	11.29	0.4	3.22	0.1	0.18	5.14	1.26		3.58		0.41392	0.17913	0.31968	0.23457	0.52217	0.35774			
AP645	63.9	16.55	5.83	0.5	3.9	0.21	0.4	5.12	0.71		4.56		0.22486	0.39762	0.33498	0.23628	0.11535	0.39134			
AP657	57.77	21.98	7.76	0.9	2.8	0.23	0.64	4.98	0.7		2.67	99.62	0.22535	0.47928	0.24533	0.16121	0.95128	0.44836	3.17	-75.3	0.48630
AP693	67.9	15.43	5.4	0.4	2.34	0.6	0.84	3.3	0.71		3.88		0.22338	0.89562	0.23158	0.19192	0.35353	0.26779			
AP7	74.77	11.53	4.37	0.5	1.83		0.64	2.43	0.41		2.71		0.24192	0.91319	0.22826	0.28570		0.18172			
AP728	59.1	12.53	1.55	0.9	6.69	4.2	1.92	2.21	1.36		1.28		0.53743	0.25292	0.19981	0.67568	0.29166	0.25224			
AP746	55.31	26.1	9.71	0.7	1.63		0.36	4.74	0.59		2.2	1.35	0.23747	0.22692	0.19665	0.79337		0.55685	2.57	-96.4	0.27899
AP768	74.2	12.49	2.97	0.1	2.74	0.18	3.16	2.6	0.3		1.6		0.15179	0.41623	0.17859	0.27762	0.13114	0.19885			
AP781	67.1	12.26	3.91	0.7	2.67	9.57	1.7	0.17	0.46		1.63	99.45	0.23569	0.22812	0.15144	0.27564	0.79625	0.21563			
AP81	6.62	17.37	8.51	0.8	3.85	1.63	0.3	4.11	1.6		2.88		0.31272	0.28414	0.25627	0.28496	0.85395	0.33767			
AP87	65.59	9.94	4.64	0.6	3.8	1.88	0.77	1.46	0.4		1.95		0.29796	0.12744	0.15943	0.48380	0.17195	0.17859			
AP88	61.79	17.99	6.3	0.1	3.65	1.99	1.31	3.71	0.6		2.8		0.22353	0.11980	0.22332	0.25676	0.15692	0.34397			
AP813	62.47	16.73	7.69	0.4	3.89	0.16	0.33	4.74	0.9		2.57		0.29340	0.32459	0.36783	0.29425	0.86942	0.31559			
AP815	95.8	2.26	0.38	0.3	0.15	0.15	0.36	3.73	1.2		2.37	1.48	0.17324	0.26262	1.78713	0.83994	0.63379	0.28167	0.30	-87.5	0.37616
AP816	39.38	8.87	3	0.8	11.51	14.23	0.9	3.87	0.49		18.8		0.21588	0.16693	0.47243	1.64217	1.45845	0.26543			
AP822	49.8	16.55	1.92	0.55	5.75	7.2	0.24	3.56	1.3		3.68		0.42117	0.23857	0.23292	0.43968	0.38568	0.39163	2.81	-92.3	0.48169
AP823	46.89	28.77	5.31	0.4	2.4	0.75	1.74	8.4	1.2		3.86	99	0.11789	0.99499	0.31615	0.89734	0.23699	0.72343	3.75	-67.5	0.36938
AP825	68.21	12.41	2.46	0.3	2.12	0.56	0.78	2.62	0.57		1.59	1.35	0.12653	0.13426	0.22861	0.21619	0.41226	0.21442	2.61	-57.0	0.59589
AP826	97.85	1.4	0.49		0.11			0.3	0.16		0.28	1.23	0.37365		0.31235	0.13385		0.12525	0.33	-76.9	0.89938
AP828	9.14	4.46	2.32	0.2	0.82			1.4	0.27		0.83		0.33229		0.25249	0.23267		0.58371			
AP83	64.69	17.9	6.34	0.4	1.93	0.55	0.66	4.76	0.76		3.52	1.34	0.23679	0.63535	0.31589	0.14292	0.29257	0.31132	2.71	-69.8	0.44997
AP834	8.1	9.76	3.2	0.2	0.8		1.46	2.55	0.5		1.1		0.29278	0.24700	0.28294	0.13732		0.14359			
AP857	82.78	8.84	2.45	0.3	0.87		0.48	2.6	0.38		1.27		0.17694	0.89332	0.31847	0.12455		0.12584			
AP862	93.85	3.17	1.6	0.3	0.46		0.16	1.16	0.2		0.21		0.21344	0.83365	0.39624	0.18364		0.39842			
AP874	55.39	24.47	5.77	0.6	1.55		0.49	6.96	0.5		4.81	1	0.15600	0.32944	0.37981	0.81696		0.52633	4.70	-69.0	0.47126
AP888	72.2	14.44	4.32	0.3	1.79	0.1	1.2	3.36	0.5		2.71	1.47	0.19959	0.11629	0.25195	0.15687	0.62956	0.23569	2.71	-59.0	0.53175
AP9	81.13	8.52	3.11	0.2	1.58		0.5	2.32	0.21		2.14		0.23299	0.96547	0.29485	0.23468		0.12375			
AP955	83.53	8.3	1.63	0.2	1.25		0.83	1.36	0.42		2		0.12957	0.17478	0.18339	0.19700		0.11329			
AP969	64.35	17.8	6.12	0.4	1.61		0.9	4.55	0.63		4.6	99.25	0.21946	0.83182	0.27678	0.11446		0.32597	3.88	-78.7	0.61833
AP972	64.9	16.91	8.29	0.3	1.61		0.4	4.21	0.89		4.42	1.49	0.31293	0.38916	0.26959	0.12489		0.31926	3.95	-81.0	0.66184
AP99	56.35	22.11	7.59	0.5	2.81		0.33	5.96	0.57		4.26	1.3	0.21912	0.24555	0.29188	0.16836		0.46239	4.51	-77.9	0.57794
AP991	74.15	11.61	5.98	0.6	2.32		0.94	2.37	0.35		2.55	1.33	0.32877	0.13320	0.22137	0.25288		0.18451	2.84	-75.0	0.69387
AP994	46.5	14.1	14.43	0.19	6.78	2.3	2.43	2.36	1.13		9.93		0.65743	0.28535	0.18240	0.61243	0.14924	0.35852			
BE127	85.73	7.55	1.75	0.2	0.52	0.7	1.78	1.84	0.22		0.86		0.14795	0.38787	0.26389	0.87169	0.84287	0.13781			
BE13	69.4	12.94	5.65	0.9	2.71	0.63	1.91	2.76	0.8		2.9		0.27874	0.24283	0.23953	0.26533	0.44262	0.22875	2.88	-87.0	0.45712
BE135	58.3	19.2	7.61	0.2	2.97	0.9	1.18	6.51	0.83		3.32		0.25539	0.12657	0.37612	0.19762	0.43169	0.38624	2.96	-91.8	0.44156
BE165	7.98	12.95	1.25	0.2	1.14		0.4	4.27	0.7		8.68		0.61612	0.58158	0.35732	0.11144		0.21500			
BE241	65.58	16.58	5.11	0.3	2.6	0.16	1.58	3.78	0.63		3.8		0.19673	0.15678	0.24686	0.15723	0.87729	0.29793			
BE246	65.42	16.64	7.24	0.3	2.18	0.29	0.89	3.62	0.62		3.13		0.27773	0.87992	0.23556	0.16579	0.15844	0.29974	3.46	-72.1	0.58919
BE3	59.58	2.65	5.77	0.3	2.86		0.19	5.95	0.91		4.33		0.17835	0.15138	0.31199	0.17527		0.48436	4.48	-69.3	0.55546
BE41	48.14	16.2	9.11	0.9	15.29		0.54	1.4	2.26		7.66		0.36298	0.55455	0.72943	1.27842		0.39216	8.68	-8.2	1.42692
E112	41.84	14.78	17.64	0.6	13.58	0.9	0.8		3.5		7.64		0.76181	0.89480		1.16276	0.55357	0.41628			
E196	74.45	14.6	1.9	0.3	0.4	0.2	6.62	0.92	0.5		1		0.49484	0.77467	0.78519	0.36392	0.12932	0.22255			
E199	58.83	19.52	7.62	0.6	2.62		0.51	4.7	0.67		4.8		0.24917	0.42983	0.22577	0.16986		0.39177			
E26	66.49	16.26	5.71	0.3	1.94	0.19	0.74	3.35	0.56		3.22		0.22415	0.74872	0.22387	0.15989	0.16228	0.28818			
E211	65.53	18	4.33	0.3	2.6		0.44	4.8	0.58		3.77		0.15355	0.42155	0.28875	0.18280		0.32370			
E33	73.35	1.73	0.92	0.1	0.96	0.1	0.68	3.15	0.5		8.31		0.54728	0.14260	0.31788	0.11322	0.84724	0.17239			
E41	19.36	2.52	2.6	0.6	14.22	25.17	0.5	0.61	0.8		35.47		0.52178	0.32643	0.26217	7.14185	9.88659	0.15340			
E68	85.29	7.64	1.69	0.3	0.25	0.25	1.23	2.62	0.28		0.83		0.14119	0.26486	0.37133	0.41416	0.29748	0.15564			
E97	61.91	13.75	6.16	0.2	5.21	1.85	0.31	5.5	0.64		5.19		0.28596	0.38000	0.39768	0.47951	0.12231	0.26173			
L81	76.5	11.43	3.4	0.4	0.99	0.42	1.49	2.74	0.31		1.94		0.16977	0.21446	0.25957	0.19620	0.33449	0.17672			
L82	53.18	23.87	5.81	0.6	2.29	0.1	0.68	7.8	0.5		4.5		0.15536	0.46867	0.32117	0.12148	0.38858	0.52894			
LS18	56.22	22.25	7.72	0.15	2.71	1.43	1.37	3.72	0.75		3.85		0.22147	0.11298	0.18135	0.15414	0.58427	0.46638			
LS11	57.42	15.63	13.46	0.1	2.32	2.15	2.38	3.3	1.27		1.2		0.54968	0.25518	0.29999	0.18784	0.12559	0.32775			
LS112	57.92	15.3	13.19	0.28	3.2	3.81	0.78	1.83	1		2.29		0.55271	0.83880	0.12951	0.26468	0.22638	0.31129			

V

Chapitre 5

Dynamiques des transports sédimentaires et bilan des processus d'érosion au Népal central

Annual sediment transport dynamics in the Narayani basins Central Nepal, assessing erosion processes impact in the annual sediments budget

Annual sediment transport dynamics in the Narayani basins Central Nepal, assessing erosion processes impact in the annual sediments budget

(In preparation)

Guillaume P. Morin[1*], Jérôme Lavé[1], Christian France-Lanord[1], Ananta Prassad Gajurel[2], Rajiv Sinha[3], Gaurav Kumar[4].

1- Centre de Recherche Pétrographique et Géochimique (CRPG) CNRS UMR 7358, Université de Lorraine, 15 rue Notre Dame des Pauvres, F-54500 Vandoeuvre-lès-Nancy, France ; 2- Department of Geology, Tribhuvan University, Ghantaghar, Kathmandu, Nepal ; 3- Department of Earth Sciences, Indian Institute of Technology, Kanpur 208 016, India ; 4- Institut de Physique du Globe de Paris, 1 Rue Jussieu, 75005 Paris CEDEX 05, France

5.1 Introduction

Understanding how climate changes affect the earth surface is one of the most challenging issues in earth sciences. It has implications at all time scales, and more particularly on the long-standing debate related to the retroactions between tectonic, climate and erosion during topographic construction of orogens. Through mostly variations in precipitation and temperature, the climate directly controls the vegetation cover, the weathering processes and soil production, but also the snow cover, the hydrology and all the chain of sediment transport from topographic highs down to foreland basins or the oceans.

The influence of climate on erosion has been largely disputed over the last decades, and contrasted conclusions have arisen. Despite most erosional processes are dependent on water flux or water ground/soils saturation, several studies have failed to find a correlation between erosion intensity and annual or seasonal precipitations. [Riebe 01]'s study tend to indicate that the erosion rates as measured from ^{10}Be cosmogenic nuclides in small catchments of the Sierra Nevada do not depend on temperature or precipitation. At larger scale, and using low temperature thermochronologic methods,[Burbank 03] also concluded that long term denudation rate is independent from average rainfall amount in central Nepal, despite the study was spanning a region with a tenfold variation in rainfall amount.

However, other studies reached opposite conclusion, i.e. that average precipitation have a primarily control on long term denudation rates [Reiners 03]. Part of the problem is coming from the diversity of processes (hillslope, fluvial, glacial) that do not act in the same place in the landscape and are sensitive in a different way to climatic variables. So far, it is also not clear how, for example, higher precipitation influence soil erosion, since their make easier the loose sediment transport in channelized flows but also favour vegetation development, which in turn limit the soil erosion by root anchoring of the soil and reducing runoff. Along that line, it has been proposed that intermittency of wet and dry climates could have larger influence on the hillslope erosion average rates than average rainfall values, by continuously pushing the system out of equilibrium [Molnar 04], with alternating periods of soil production during wet phases and of soil striping off at the onset of drier and vegetation-cover-depleted phases. It is also not clear how weathering is coupled to physical erosion and if enhanced physical erosion of mountain ranges, as suspected during the last 2-4 Myr (e.g. [Peizhen 01]), leads to enhanced chemical weathering or not [Willenbring 10].

Among regions of the world where active tectonics and climate interact, giving rise to massive erosion of mountainous landscapes, the Himalayas appear as a remarkable laboratory to test and understand the role of climate on denudation, and to address above questions. The rapid rise from the lowlands of northern India up to the high elevation of the Himalaya peaks and the Tibetan Plateau profoundly affect both the average temperature structure of the atmosphere responsible for the seasonal winds and the localization of heavy precipitation that characterize the Asian monsoon [Molnar 10, Boos 10]. Monsoonal precipitations along the Himalaya generate one of most important erosional flux of the planet.

This surface mass transfer is presumed to have acted on the thermal structure and the stress field of the range, and partly determined its morphology (e.g. [Beaumont 01]), whereas, at larger scale, the Himalayan erosion is suspected to have actively participated in the global drawdown of atmospheric CO_2 responsible for the Cenozoic global cooling through organic carbon burial and silicate weathering [Raymo 92, France-Lanord 97].

Presently, the Ganga-Brahmaputra system delivers $\sim$1 Gt/a of sediments toward the ocean, which corresponds to $\sim$10% total worldwide sediments fluxes and ranks first amongst all contributing fluvial systems. Whereas coarsest Himalayan sediments are trapped into

the Indo-Gangetic foreland basin, a vast majority of this flux goes to the ocean and contributes to building the Bengal fan [Métivier 99b, Clift 06]. Both sedimentary deposition areas represent important archives that direct record past erosion history of the south Tibet-Himalayan, that could help untangling the issue of the climatic control on erosion . However, reading and interpreting these archives (e.g. [Goodbred 00, Goodbred 03, Clift 08]) in terms of erosion intensity, localisation and climatic or tectonic controls, require a prior detailed understanding of the present erosional system in Himalaya in order to document the dominant erosional processes, their response to climatic variables and the associated fluxes. Former studies led within the Himalayan range have drawn contrasted conclusions. More than others processes, landslides are considered as majors agents in mountain ranges erosion and landscape evolution [Hovius 97, Korup 10]. In the Himalayan range, slopes failures and landslides are very common, and display high diversity and variability [Shroder 98b, Shroder 98a, Weidinger 06, Fort 09, Gallo 14a]. As in other mountain settings, the factors that control their distribution, evolution and behaviour, may be as diverse as earthquakes (e.g. [Meunier 08]), rainstorms [Iverson 00], or cumulated seasonal rainfall through ground water saturation [Gabet 04a, Dahal 08]. Coincident scaling between topography and precipitation was observed in steep relief of Greater Himalaya suggesting a direct impact and imprint of rainfall amount on bedrock strength and hillslope angle of repose [Gabet 04b]. On the other hand, glacial erosion is considered in mountain areas to be more efficient than landslide erosion when driven by fluvial incision (e.g. [Hallet 96]), even if such inference was recently questioned [Thomson 10]. The high Himalayas is covered by numerous glacier and large U-shaped valleys down to 3000m attest of past glacier erosion. [Gabet 08] documented in that sense dominant control of glacier erosion in sediment export in the rivers draining the northern sides of the high summits of central Nepal. [Godard 12] concluded also in the same area that present glacier erosion can exceed by two to three folds the long term erosion, and leaves an imprint in the river sediments further downstream. Finally, in the Northern-Western part of the range, intermediate control was found with massive erosion events coincident with both extreme rainfalls and glacial outburst [Wulf 10, Wulf 12]. At the scale of the range, to untangle the role of climate in Himalayan denudation, longer term approaches have been conducted, but again led to contrasted inferences. Some concludes that present-day rainfall spatial distribution [Bookhagen 06, Bookhagen 10] would scale with long-term exhumation rates [Thiede 04, Deeken 11], whereas other studies highlight a lack of correlation between cli-

matic settings and erosion, and rather propose a dominant long-term control of tectonics on erosion .

In a climatic setting with well defined rainfall seasonality like in the Himalayas, studying during a whole climatic cycle the flux and characteristics of the sediment transported by major rivers offers the alternative possibility to assess the relations between erosion processes or intensity and rainfall chronicles.

In that perspective, and although large rivers might dampen or delay the original signals associated to the sources of the eroded material from hillslopes or glaciers, documenting the sediments of a large river system at its outlet from the mountain range offers several advantages : 1- smoothing the stochastic effects of landslide mass-wasting ; 2- providing an overall view on the erosion of a whole Himalayan section, including glaciated high peaks ; 3- and perhaps more importantly, yielding a direct understanding of the sedimentologic and geochemical message that can have be left in the sedimentary archives of the Indo-Gangetic foreland basin.

In the present study, in order to tackle such issues, we combined hydrologic and meteorological datasets with new measurements on sediment concentrations and geochemical characteristics from suspended load of the Narayani river, one of the major rivers draining and eroding central Himalaya. Specific focus is given to the period of monsoon, when most of rainfall (~80%) occur [Andermann 11], but also to pre- and post- monsoon periods. Our results combines two types of datasets : 1 : a daily sampling during 2010 monsoon that complements suspended load concentrations chronicles recorded by the Department of Hydrology and Meteorology of Nepal (DHM), and brings information on the evolution of grain-size, and geochemical characteristics (Major elements, carbonates content, δD in hydrated silicates phases, and total organic carbon) of these sediments ; 2 : suspended sediment depth-sampling associated with ADCP current measurement during monsoon 2011, in order to document spatial variability of sediment concentration and characteristics through a river cross section, and to improve both our analysis and the total sediment fluxes calculations.

After a general presentation of the different datasets and daily records, we propose an analysis of their fluctuations in the light of the climatic and hydrologic chronicles, and try unravelling in the Narayani basin the relative timing and contributions of the erosion processes that are glacier erosion, soils erosion and mass-wasting by landslides.

5.2 Geologic, climatic and geomorphologic settings

The Narayani river drains the Central Nepal Himalaya range, and represents the most important tributary of the Ganga in term of discharge and sediment flux (e.g. [Singh 08a, Lupker 12a, Andermann 12b]).

The Narayani drains a 32000 km^2 mountain catchment whose elevation varies from 8147 m down to 180 m. The drainage system is divided in five major Himalayan tributaries that are, from West to East : Kali Gandaki, Seti, Marsyandi, Bhuri and Trisuli. The Kali and Trisuli are transhimalayan rivers which drain a part of the Tibetan plateau corresponding to respectively 39 % and 40 % of their basins areas. The Narayani basin drains 5 main Himalayan geological units that are from North to South : 1- the Tethyan Sedimentary Series (TSS), low-grade Palaeozoic–Eocene sedimentary series of the passive northen Indian margin, which include a large proportion of limestone and carbonates, 2- the High Himalayan Crystalline (HHC) formations, high-grade metamorphic gneisses and migmatites, 3 – the High Himalayan Leucogranite (HHL), Miocene leucogranite massives intrusive in HHC and TSS, 4- the Lesser Himalaya (LH) formations, variably metamorphosed Indian crust material of Precambrian to Palaeozoic age, and 5- the Mio-Pliocene Siwaliks, sediments of the foreland basin exhumed by the most recent frontal thrusts [Colchen 86]. According to geologic map (Department of Mines and Geology of Nepal), the respective surface proportions of outcropping lithologies drained by the Narayani basin are ~30% of TSS, ~24% of High Himalayan gneisses and leucogranites (HHC+HHL) and ~46% of LH units, whereas the drained surface of Siwaliks units by the Narayani basin upstream of Narayanghad is negligible.

The Narayani basin is highly exposed to Indian Summer Monsoon (ISM), which generates flooding season that concentrates most of the annual discharge. It starts in mid June and last until mid to late September, and represents around 80% of the 1400 mm/yr to 1900 mm/yr annual rainfalls [Shrestha 00, Bookhagen 10, Andermann 12b, Andermann 12c] . Winds bring north-westward the moisture generated at the surface of the Bay of Bengal to the mountain range, where it generates intense precipitations by hitting the topography [Anderson 06]. The variability of rainfall along the Narayani basin is extreme with annual amounts ranging from 50mm in Mustang area (most NW part of the watershed) up to 5000mm at the Annapurnas foothills. This variability primarily reflects

the interplay of moisture supply and topography. The morphologic transition from the Lesser Himalaya lowlands and middle hills to the High Himalaya is indeed characterized in central Nepal by a sharp break in slope in the topography, that forms the principal orographic barrier that stops monsoon clouds at an elevation ~4000 m.

Consequently the High Himalayan foothill region undergoes the maximum of precipitations in Nepal (e.g. [Burbank 03]). In the Narayani basin such effect is enhanced by the relatively lower elevation of the frontal Mahabharata range SW of Kathmandu, which favours cloud penetration into the interior of the range, and probably explains that the precipitation are more intense in front of the Annapurna massive than anywhere else in Nepal. Because of the orographic effect, the Northern part of the watershed is much more arid. There, rainfall amounts are close to the arid southern Tibetan plateau values and can locally drop below 0.2 m/a. In between, the High Himalaya, that includes several of the highest summits in Nepal, received abundant snowfall, up to 1 m of equivalent water, mostly during winter season [Burbank 03, Putkonen 04]. As a consequence, glaciers cover most of the principal massive and represents ~9% of the Narayani watershed area (Glims database). Because of the limited glacier cover extent and because of the abundant liquid precipitation during ISM up to 5500 to 6000m, the contribution of snow and glaciers melt to the hydrological cycle remains minor, around 10% of the annual Narayani discharge, [Bookhagen 10, Andermann 12c](Bookhagen and Burbank 2010 ; Andermann et al. 2012c). And despite it peaks in early July, its influence is mostly noticeable in river discharge during the pre-ISM season [Immerzeel 10, Bookhagen 10].

Combined to contrasted tectonic activity along a NS transect [Lavé 01], the pattern of precipitation and climate directly influences erosion intensity and relief shaping in the central Himalayan landscapes. Whereas the Lesser Himalaya is characterized by subdued erosion rates, between 0.1 and 0.5 mm/yr [Godard 12], the 2 to 4 m of precipitation falling on the steep south Himalayan flank over the monsoon season generate massive erosion associated to landslide, runoff, glaciers and river incision, which roughly permit equilibration of denudation rates (up to 3-5 mm/yr) with high uplift rates above a mid-crustal ramp [Lavé 01, Burbank 03, Godard 06] . In the High Himalaya, present snowline is located above 5000 m, which limits the extent of active glacier and peri-glacial perosion, but large open U–shape valleys down to 3000 m attest for efficient glacier erosion during glacial stages. In the most northern part of the Narayani watershed, relief is lower than in the HH, and, due also to the arid conditions, the present erosion rates (~0.1 mm/yr)

appear much reduced [Gabet 08].

The sediments produced by the Himalayan erosion are, today, actively and efficiently transported by the main tributaries of the Narayani river, as suggested by numerous bedrock-floored channel segments across the High Himalaya, and across the Mahabharata hills upstream of the MBT. Nevertheless, the presence of large and thick fluvial or debris-flow terraces in the Lesser Himalaya [Fort 87a, Lavé 01] attest for periods of episodic and extensive alluviation of the lower valleys of the Narayani basin. The presence of these sediments reservoirs or storage volumes have been thus suspected to introduce a potential lag time in the Himalayan sediment routing system and to delay the erosion signal [Blöthe 13]. At the scale of the Marsyandi river, because of their relatively old age of formation, the contribution of the LH terraces to present sediment budget are, however, considered as negligible [Attal 06]. We thus consider in the following that a specific geochemical signature in Narayani sediments can be directly attributed to the corresponding pristine outcropping unit in Narayani catchment.

Finally, recent studies have proposed a range of estimates for the annual suspended load flux carried by the Narayani river, with values of 100±50 Mt/a [Andermann 12b, Sinha 94], whereas ^{10}Be cosmogenic nuclides on river sand collected over different years [Lupker 12a] estimated longer term sediment fluxes between 110 and 184 Mt/a, i.e. an equivalent mean erosion rates of ~1.7 mm/a. With both methods, it was in addition demonstrated that the Narayani basin presents the highest erosive activity in central Himalaya, which makes this system of particular interest.

5.3 Sampling and methods

5.3.1 Sampling location

In this study, we realized suspended sediment sampling during 2010 monsoon to complement available DHM dataset, and we also performed ADCP velocity current measurements associated to depth sampling at the basin outlet at Narayanghat – Bhâratpur (N27,700 ; E84,421), located in the Nepalese district of Chitwan. The DHM gauging station (Fig 5.3.1 and appendix A1) is located ≈3 km upstream of Narayanghat. This station has been reporting water level data for Narayani river since 1963 (DHM/FFS 2004). The

hourly water level for 2010 and 2011 were retrieved from telemetric online dataset from DHM website, which is dedicated to monitor instant river stages and alert population for floods hazards.

In the study area, the Narayani channel is relatively deep and narrow : it reaches between 15 to 20 m depth for a width of 170 – 190 m. Riverside-slopes are steep with rocky rivershores at the DHM gauging station, and partly sandy to partly constrained by concrete structures at the ADCP main site. Downstream Narayanghat, the Narayani enters into Chitwan Dun where the river channel widens (from 230 to 330 m), becomes shallower (10 to 15 m depth), and present large sandy or pebbly alluvial bars whereas riverside slopes are smoother. Bedload material of Narayani river in the studied area is only exposed along these alluvial bars, and is composed of coarse pebbles [Mezaki 84, Attal 06, Dingle 12] (see Appendix A4).

5.3.2 Narayani velocity distribution and discharges measurement by ADCP

ADCP measurements were conducted in two zones : 1- near to the DHM station dedicated to water level survey, and 2 : just upstream Narayanghat bridge where the suspended load were sampled (cf. figure 5.3.1).The velocity distribution in the water column was recorded using Acoustic Doppler Current Profiling (ADCP : Rio Grande, RD Instruments, 1200 kHz) mounted to the side of the boat, in order to measure instant water discharge and distribution through the channel (e.g. [Filizola 04, Muste 04]). We realized ADCP velocity current measurements (cross-sections or transects hereafter) across the river to compute river discharge. We also continuously recorded ADCP depth velocity during depth sampling (3.2) for suspended load to infer hydrodynamics conditions during sampling.

Velocity current measurements were acquired every 420 ms to 675 ms with a vertical resolution (or bin size) ranging from 43 cm to 67 cm depending on the instrument's configuration. Additionally, we used a GPS (Garmin etrex h) in combination with the ADCP to avoid possible moving bed bias [Lupker 11a] and provide a stable reference in order to derive absolute water velocity. We also associated an echosounder (Tritech PA200) to accurately detect the river bottom.

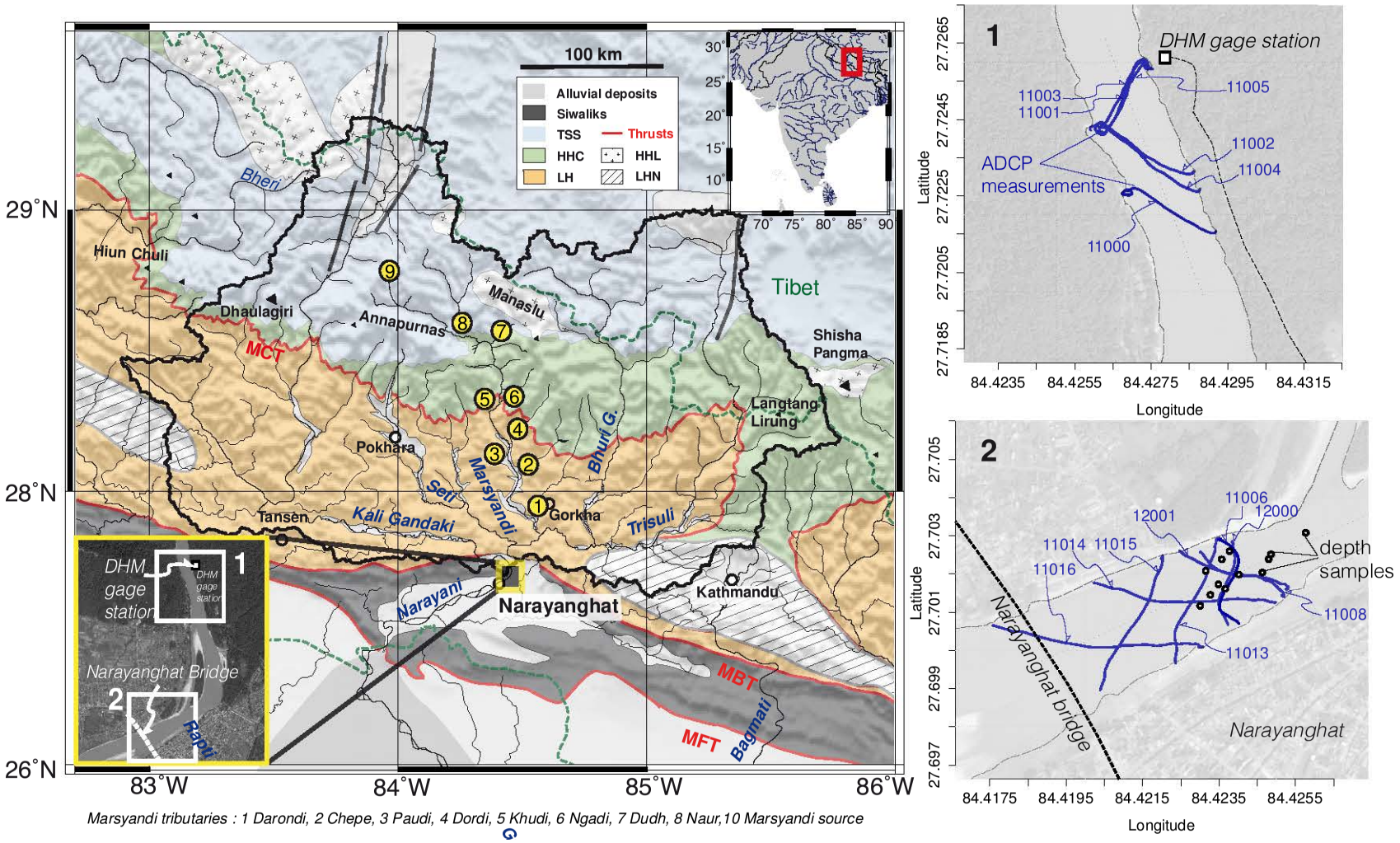

FIGURE 5.3.1 – Geographical settings of ADCP measurements and depth-sampling on the Narayani river at Narayanghat – Bhâratpur, Nepal.

Narayani basin drains 32000 km^2 of the central Nepal Himalayan range. Daily 2010 surface suspended sediment samples were recovered from the middle of Narayanghat bridge. To be representative, ADCP discharge measurements (blue lines) and depth-sampling (grey dots) were performed in an immediate area upstream the bridge, where hydrodynamic conditions might be considered analogue to daily samplings. In yellow dots),Marsyandi tributaries sampled for tracing glacial erosion in the basin (names are listed in the figure).

5.3.3 Sediment sampling

Narayani sampling includes (1) depth sampling to constrain sediment concentration with depth, and (2) daily sampling of surface water during the monsoon season 2010.

Distribution of the suspended load concentration *Cs(z)* in the water column is generally non uniform and depends on sediment concentration at the bottom, water depth, hydrodynamic conditions and sediment characteristics that are essentially grain-size and minerals properties (i.e. density and shape factor) [Garcia 08] . Depth sampling profiles were therefore carried out in order to constrain sediment fluxes across a whole river section and to evaluate the bias when considering only a homogeneous *Cs*, based only on surface samples. Six profiles were realized during 2005, 2007 and 2011 monsoons. Depth profiles sampled in 2005 and 2007 are composed of seven samples each, and an additional triple-sampling close to the river bed that documents boundary layer between bedload and suspended load. We used sediment depth sampling method as described in [Galy 08, Lupker 11b].

Sediment depth sampler consists in a 5L tube open at both ends and a closure system actuated by compressed air system and monitored from the boat. The boat was left drifting in full current on the axis of the river until the boat reached the desired locations of sampling. At the beginning of drifting, the sampling bottle ballasted by a 20 kg weight was immerged down to the desired depth and kept stabilized. Exact depth was obtained using a pressure gauge fixed on the sampler. Bottle closure was instantly triggered from the boat by compressed air system while the exact GPS position and depth was noted down. The triple-sampler was used in 2007. It consists in 3 x 1L horizontal Niskin bottles spaced by 50 cm mounted on a ballasted rigid frame that are pneumatically closed together when the sampler touches the bottom.

Synchronously to ADCP water velocities acquisitions in 2011, water and sediments were sampled along depth profiles including four samples each, systematically taken at regular depth-intervals from the surface down to the bottom along the channel middle axis, in order to account for vertical variability of the suspended load concentration in the river section. To assess lateral variability of sediment load along transversal river section at high stage, one depth sampling profile was done off-axis on the 06/08/2011.

Once brought on board, the sampler was kept sealed until the boat reached the riverbank, and then the sample was transferred into opaque plastic bags with special care to

avoid any loss of materials. Samples were stored in bags until filtration. The water and sediment samples were weighted and then filtered through 0.22 µm, 90 mm diameter, Poly Ether Sulfone (PES) filters in pressurised Teflon coated filtration unit, within the 6 to 48 h after collection. The sediment concentration is calculated by dividing the dried sediment weight by the weight of water.

In parallel, in order to document the daily variability of the suspended sediment flux in 2010, daily sampling was performed on the Narayani river. Two one-litre samples of surface water were taken daily at 8 am from the central part of the Narayanghat bridge (27.699963°N, 84.418537°E) where river flow is maximum (Fig 5.3.1 and Appendix A1). The samples were taken using an open bottle ballasted with a 10 kg load. In order to avoid over concentration of sediment in the bottle, the opening was protected from direct current by a deflector. Sampling was performed every four days from May 19th 2010 to June 16th 2010, then daily until October 10th 2010. This fully covers the monsoon season and allows to capture about 80% of the sediment discharge. Samples were weighted and filtered following the method described above.

Finally, suspended load samples are independently taken at the DHM station, also on a daily basis during monsoon, and once a week over the rest of the year. This dataset, made available by the Nepalese Department of Hydrology and Meteorology for 14 years (1976, 1977, 1979, 1985, 1986, 1993, 2001 to 2005 and 2010 to 2012) enabled us to eventually complement our own data during winter time, and to calculate average sediment flux over decades. Exact sampling protocol remains however unknown except that initial sampling were performed with a depth-integrative USGS bottle, whereas samples of the last decade have been taken at the surface from a small overhanging cliff on the left river bank.

5.3.4 Grain-size, major, trace elements and carbonates analysis

Sediments and filters were freeze-dryed and the filters were removed, then the samples were manually quartered with a sample splitter to obtain representative subfractions for further grain-size and chemical analysis. Special care was taken to recover any particles during all these steps. Samples subfractions dedicated to chemical analysis were powdered in agate mortar using a Retsch® grinder.

Particle-size measurements were performed using a Laser-Granulometer (Symantec's

HELOS/BF with a classic wet disperser SUCELL at LIEC, Nancy, France). Detailed grain-size distribution spectra were obtained after ultrasonic treatment of 30 s to break-up mineral clusters ; grain-size results are given in a range from 4.5 µm to 875 µm.

Major and trace elements were measured by ICP-AES and ICP-MS at Service d'Analyse des Roches et des Minéraux (SARM – CRPG, Nancy, France) on bulk aliquots of > 100 mg after metaborate lithium fusion [Govindaraju 87] . The uncertainties on major elements concentrations are less than 2%.

Carbonate content, carbon and oxygen isotopes were measured by phosphoric acid dissolution at 70°C on a gas-bench coupled to a MAT253 spectrometer and corrected for analytical fractionation, overall uncertainty is ± 0.9% for carbonate content, and is under ± 0.2 ‰ for δ^{13}C carbon isotopic compositions. Carbonate content, carbon and oxygen isotopes in the 2010 surface suspended load were also measured on 30–50 mg sample aliquots by classical phosphoric acid dissolution method on a manual vacuum extraction line [Sheppard 70, Galy 99b] . Calcite content was determined after 3 h at 25°C, and dolomite content was determined after additional 7 days reaction at 50 °C. The isotopic compositions of calcite and dolomite where measured on the released CO_2 by a modified VG-602 mass spectrometer and are reported using δ^{18}O (vSMOW) and δ^{13}C (vPDB) notations. The reported reproducibility is ±0.1‰.

Bulk organic mattter content, Corg is expressed as Total organic carbon concentration (TOC). TOC and carbon isotopic compositions were measured using an Elemental Analyser coupled to an Isoprime IRMS after removal of carbonates by diluted hydrochloric acid digestion following [Galy 07b]. TOC are reported in weight % of the decarbonated sediment and carbon isotopic composition are reported δ^{13}C using the delta-(δ) notation. Overall reproducibilities for TOC and δ^{13}C measurements are 0.02 % and 0.25 ‰ respectively.

Hydroxyl content [H_2O+] and D/H isotopic compositions measured in our samples corresponds to the amount of hydroxyl linked to mineral particles i.e. dominantly mica and clay phylosilicates and also minor amount of hydroxydes and other hydrated minerals. Total hydroxyls includes primary water inherited from metamorphic source rock, secon-

dary water due to hydration during weathering reactions and minor amount of hydrogen associated to organic matter. The analytical procedure [Lupker 12b] includes a first step of heating to remove adsorbed and interlayer water. Samples were heated at 120°C under vaccum for 48h and preserved from air moisture until analysis by EA [Sharp 01] . D/H is reported as δD and is normalized against SMOW. The overall reproducibility on sediments and rocks is 2‰ for δD and 0.1% for [H_2O+] [Lupker 12b].

For a question of time and cost, grain size, carbonate content and TOC were measured for each sample, whereas hydroxyl content and major elements were analyzed only for one sample over three.

5.4 Results

5.4.1 Water discharge and hydroclimatic record

5.4.1.1 Narayani river discharge calculation from ADCP measurements and comparison to DHM record

While ADCP measurement is a relatively standard technique, operating on the Narayani revealed to be challenging for several reasons. First, velocity as high as 6 m/s made it difficult to maintain simple transect trajectory. Second, in spite of the fact we detected bottom using an echo-sounder with a narrow solid-angle (12° conical) and a greater vertical resolution (1mm) we recorded important inconsistencies in the channel bottom marked by spikes in its topographic profile.

We suspect high turbulences including vertical eddies, possible highly concentrated sediment plumes near to the river bottom, and/or waves at the surface associated to high boat rolling, to have induced these bottom-detection errors. These abnormal spikes in the bottom profile had to be corrected to accurately compute water discharges (Figure 5.4.1 top).

Note that in absence of any corrections, water discharges computed by ADCP (QADCP) underestimate by more than 25% the DHM discharges (QDHM) independently recorded during our survey duration.

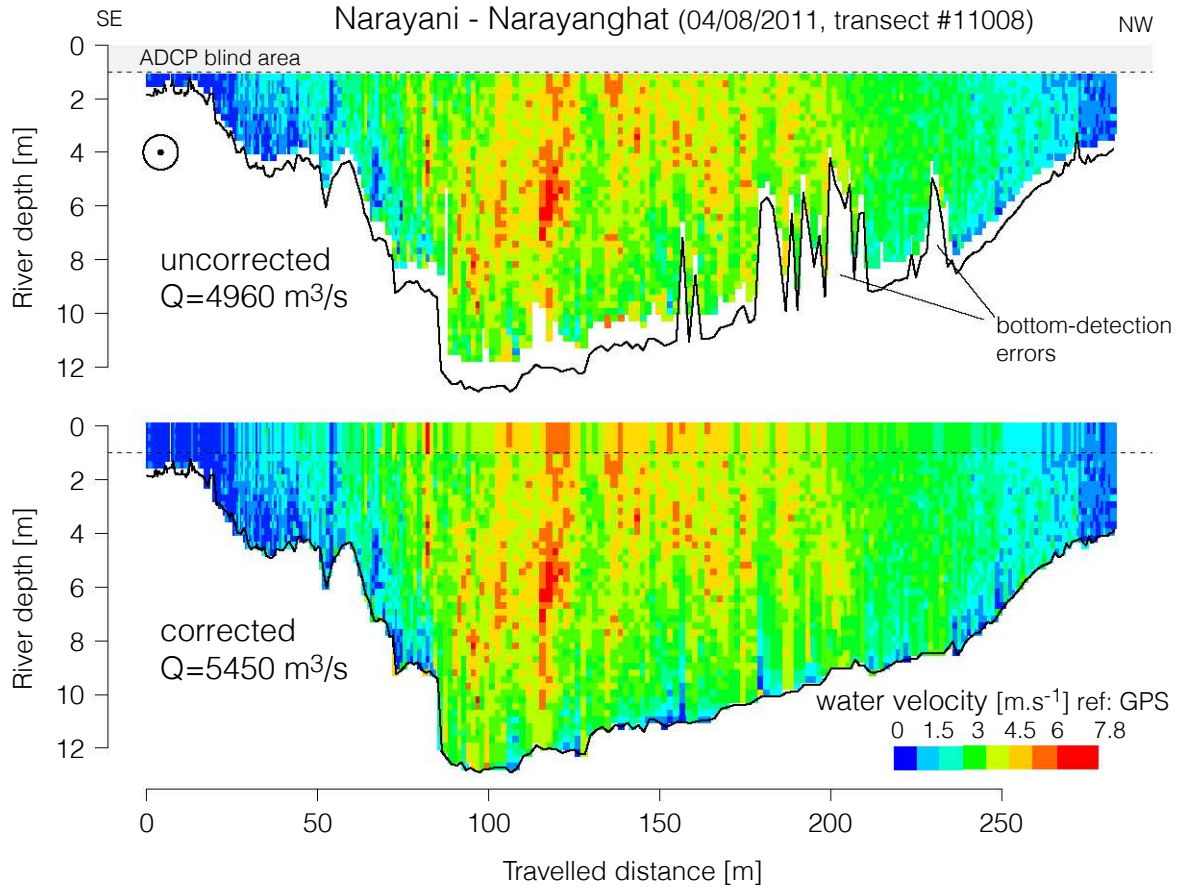

FIGURE 5.4.1 – Comparison between corrected (top) and uncorrected (bottom) ADCP measurement (transect # 11008).
Y axe represents the distance travelled by the boat. River bottom topography (blanks in upper section) were corrected and water velocities at top (above dashed line) and at the bottom were extrapolated by fitting existant velocity data. Water velocity can reach ~ 7.8 m/s in the central part of the channel which partially explains why technical limits were attained.

In order to assess the real topography, we plotted all transects in a geolocalised 3D representation. After corrections of bottom topography, pixels with missing velocity data were linearly interpolated from surrounding measurement. Moreover, the ADCP transducer measures water velocity within a zone going from a depth of ∼1.2 m at the top (the immerged ADCP bottom lies 0.7 m below the surface, and the first and shallowest recorded echo is ∼0.5 cm equivalent to two cells height) and down to roughly 0.5m above

channel bed at the bottom of the channel. Computing water discharge over the whole section therefore requires completing top and bottom velocity profiles. We fitted raw velocity profiles by a power-law for each ensemble (single ADCP sounding) and extrapolated missing velocity values in error-depth areas, as well as at the bottom and at the surface of the sections, i.e. we completed velocity profiles *u(z)* over the whole water column (see figure 5.4.1 bottom).

To compute ADCP water discharge after correction of missing velocity data, we first orthogonally projected absolute water velocity vector onto the normal to the local boat and then doubly integrated the values of the projected velocity component over the local water depth and across the whole section.

The so-obtained ADCP-derived discharge values are in good agreement with discharges calculated independently from the contemporaneous water level measured (hourly data) at the DHM station located 3 km upstream, and converted into discharge using DHM rating curve (figure 5.4.2). Despite large variations of water level during our 4-days campaign, the 12 ADCP discharge values only differ from DHM values by ± 5% or less, bringing confidence in the accuracy and reliability of both dataset, in particular in the ADCP water velocity measurements and interpolations before its use for sediment flux integration.

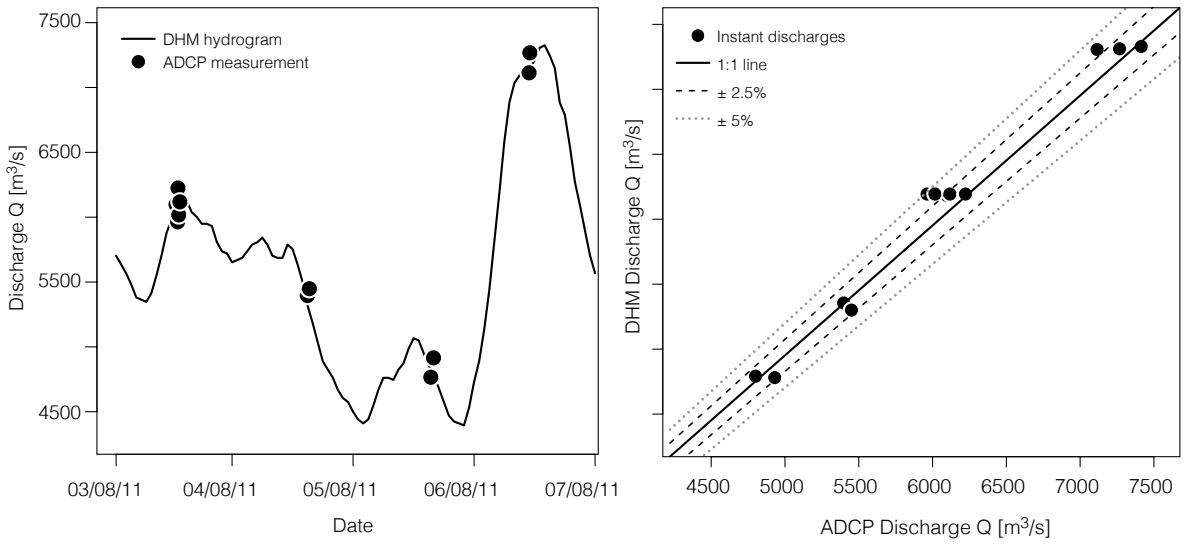

FIGURE 5.4.2 – Comparison between ADCP instant discharges measurements and DHM discharges from telemetric water level data.
Water discharges measured by ADCP compared to the hydrogram obtained from DHM water level between August the 4th and the 7th 2011 (on the left). Corrected ADCP discharges show good agreement with DHM estimations based water level extrapolated by rating curve, all errors are $<\pm 5\%$ and mostly $<\pm 2.5\%$ (linear model sets QDHM = 1.008·QADCP with $r^2 = 0.9996$) (on the right).

ADCP data associated with depth sampling were realised in the beginning of August 2011, when monsoon is well established and the river continuously at high stages. Compared to historical measurements (DHM daily record) that cover 50 years since 1962, this study documents the upper 25 % of Narayani river discharge (figure 5.4.3).

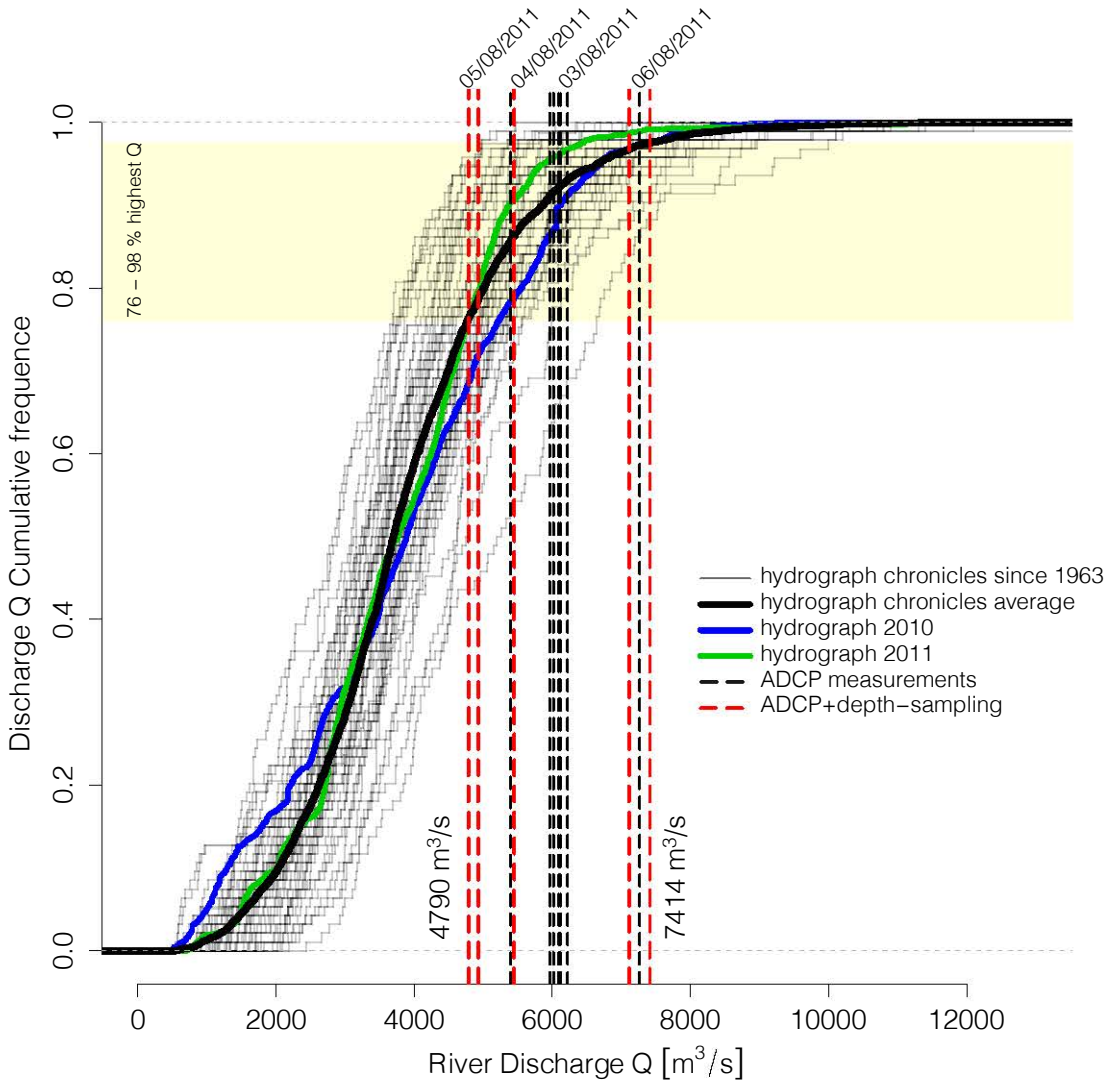

FIGURE 5.4.3 – Cumulative frequency of Narayani river discharges during monsoon (15-June to 15-September).
Monsoons 2010 (blue) and 2011 (green) river discharges are presented in comparison with 50 years discharges chronicles (light black) and their average (thick black). Discharges data are provided by DHM and span a period from 1963 to 2012 (C. Anderman, personnal communication). ADCP measurements alone (dashed black) and coupled to depth-sampling (dashed red) cover the ~30 % highest discharge-events reported ever, and hence documents major flow stages and erosion events of the river.

Though our direct observations missed most extreme floods (Q>10000 m^3/s), and ra-

ther caught moderate to high food events, we probably documented most representative flow conditions for bulk suspended load transportation [Wolman 60, Andermann 12b] .

5.4.1.2 Flow separation, snow/ice melt and hydroclimatic record

River hydrographs result from the contribution of various hydrologic components originating from different compartments of the watershed hydrologic system. The hydrologic components respond to rainfall events with distinct delays and smoothing, and therefore can be isolated from each others, providing a potential link between surface hydrology and erosion locus or process [Andermann 12b]. In most flow separation models, discharge is separated in two main components : the baseflow component, Qb, that represents the contribution from groundwater reservoir which slowly respond to rainfall events ; and the direct runoff or storm runoff component, Qd, which might represent the sum of infiltration and saturation excess overland flow, and is characterized by short response and transfer times after a rainfall events.

Many digital filters have been proposed to separate the two components (e.g. [Eckhardt 05, Furey 01]) and were efficiently applied on natural basins (e.g. [Tolorza 14, Struck 15]). More specifically in Nepal, [Andermann 12c] used a generic digital filters based on daily discharges adapted from[Eckhardt 05], setting for all the studied rivers the parameter a (the recession constant) at 0.98 and $BFImax$ (the ratio of annual baseflow to annual streamflow) at 0.8. Here, in order to separate the 2010 Narayani hydrograph, we use the same digital filter (Figure 5.4.4), but $BFImax$ value was set at 0.75 rather than 0.8 to improve hydrograph fitting. We also adapted the filter to hourly discharge dataset following [Eckhardt 08] by adapting a parameter to a hourly discharge varying by a non-linear relationship 0.987, at low flow, and 0.9, at highest flow. Results closely models recession phase of the hydrograph during the post-monsoon season (beginning in 2010 on julian day 266), that slightly departs from an exponential curve. Based on daily integration of Q dataset for the year 2010, annual Narayani discharge Q_{total} reaches 48.1 km^3/yr while annual direct runoff Qd_{total} =11.5 km^3/yr ($\sim$ 24% of Q_{total}) and total groundwater Qb_{total} represents 76% (coherent with $BFImax$ set at 0.75), in close agreement with previously reported values [Andermann 12b, Andermann 12c].

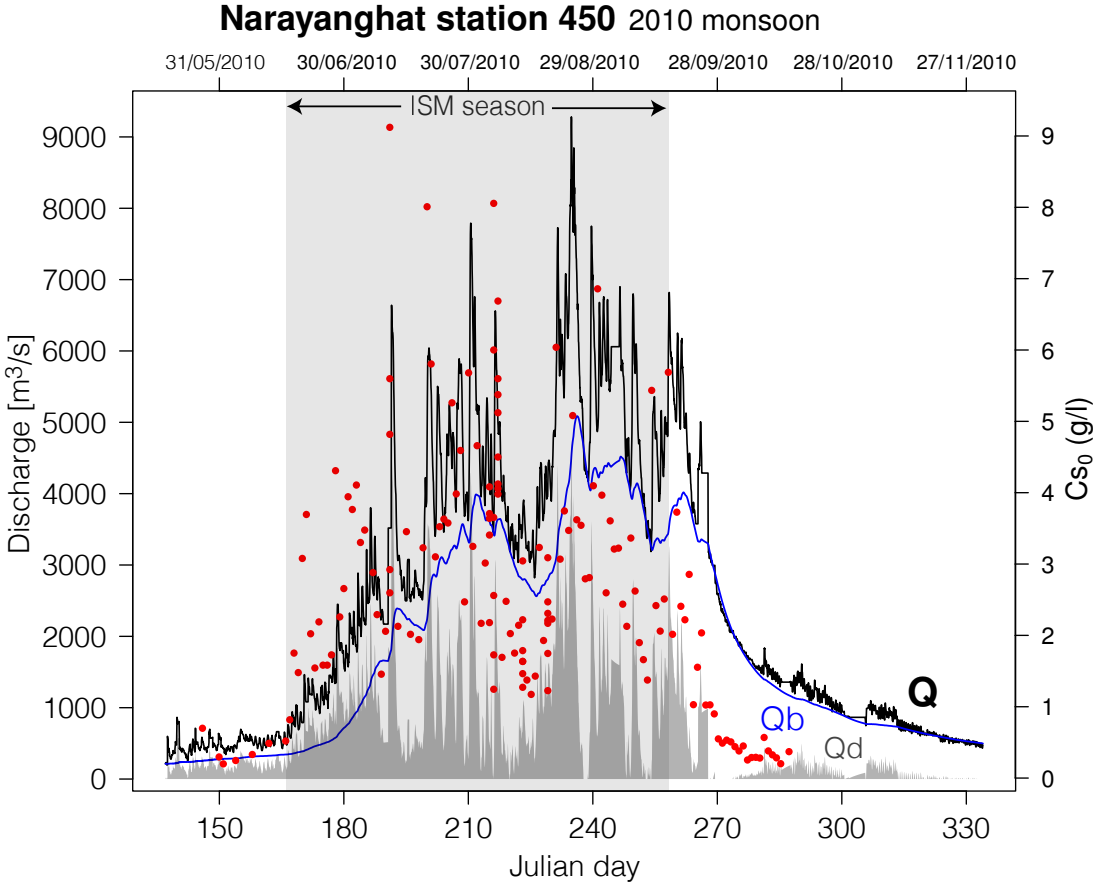

FIGURE 5.4.4 – Hourly Narayani river discharge hydrograph during 2010 monsoon and surface sediment sediment Cs_0.
Increased discharges (> 1000 m3/s) and increased sediment concentrations (> 1g/l) starts at the beginning of the monsoon in mid-June (~ 166th Julian day) and ends mid-September (~259th Julian day). The coeval pattern demonstrates the first order climatic control of monsoon over erosion i.e. sediment production/transport. General coherence between *Cs0* and discharges peaks indicates the probable effects of rainstorms on sediment delivery to the river drainage. Also presented, Narayani discharge Q, groundwater component Qb anf direct runoff component Qd as calculated by modified filter after [Eckhardt 05, Eckhardt 08, Andermann 12b, Andermann 12c].

The daily precipitations that fall on Narayani basin, as recorded by 80 DHM weather stations, display a remarkable agreement with the direct runoff component from early July until the monsoon end (fig. 5.4.4.b). They also clearly indicate that significant runoff

by overland flow can not take place as long as the soil has not been saturated by pre-monsoon rainfall on May and early June. During that period (Julian days 100 to 165), moderate daily rainfall and intense evapotranspiration delay soil infiltration and soil saturation [Bookhagen 10, Andermann 12c], groundwater recharge and therefore significant increase in Narayani discharge or direct runoff.

Finally, it has to be noted that above calculations to separate flow components can not account for ice and snow melting respective contributions. However, if we assume that a major fraction of glacier melt is efficiently channelized and rapidly join the river network, ice melt will mostly contribute to direct runoff. Conversely, melting of the snow pack, mostly during spring time, will rather go into infiltration and join the groundwater component. Based on estimate from hydrological model [Nepal 14] applied to the Dudh Kosi basin (Eastern Nepal), that indicates roughly equal partition between snow and ice melting in the hydrologic budget of this basin, we suspect that including melting will modify flow separation during the pre-ISM period, but that the relative annual proportion of the two components will remain unchanged.

5.4.2 Suspended load and sediment fluxes

5.4.2.1 Daily record of the surface concentrations

Temporal variations of surface suspended sediment Cs_0 (table 5.1 and figure 5.4.4) during 2010 monsoon roughly mimic the river hydrograph.

Ech.#	Type	Charge [g/l]	Julian day	Date	Al/Si [mol:mol]	TOC [%]	δ13Corg [‰]	H2O+ [%]	δD [‰]	Carb.Cont. [%]	δ13C.Carb [vPDB]	δ18O.Carb [vSMOW]	Calc.Cont. [%]	Dol.Cont. [%]	δ13C.Calc [vPDB]	δ13C.Dol [vPDB]	δ18O.Calc [vSMOW]	δ18O.Dol [vSMOW]	<4.5µm [%]	D10 (µm)	D16 (µm)	D50 (µm)	D84 (µm)	D90 (µm)	D99 (µm)
2010 monsoon daily surface suspended load																									
SNG1	SL	0.68	138	18/05/06		1.27	-25.7			8.03	-0.39	17.38	6.72	1.31	-1.41	-2.13	17.79	16.99	11	4	6	21	58	75	174
SNG2	SL	0.12	142	22/05/06																					
SNG3	SL	0.7	146	26/05/06		1.33	-26.4			3.81	-1.51	17.68	2.79	1.02	-1.13	-2.56	17.85	17.22	12	4	6	21	58	76	171
SNG4	SL	0.3	150	30/05/06	0.325711	0.90	-24.9												16	3	4	19	100	147	401
SNG5	SL	0.2	151	31/05/06		0.82	-24.9												16	3	4	20	111	152	298
SNG6	SL	0.25	154	03/06/06						16.29	-7.88		13.51	2.78	-0.99	-1.28	16.98	17.70	15	3	5	22	124	176	393
SNG7	SL	0.34	158	07/06/06						19.85	-0.70	17.02	17.47	2.38	-0.66	-0.95	16.92	17.74	20	3	4	14	86	137	334
SNG8	SL	0.49	162	11/06/06	0.332883	0.82	-24.4	3.03	-116.9	22.09	-0.40	16.26	19.85	2.24	-0.36	-0.77	16.18	16.95	21	2	4	14	81	132	350
SNG9	SL	0.52	166	15/06/06		0.53	-24.6			16.05			13.67	2.38		-1.04		16.94	16	3	4	26	253	336	494
SNG10	SL	0.82	167	16/06/06		0.82	-24.6			16.03	-0.17	16.53	12.87	3.16	-0.13	-0.30	16.22	17.77	22	2	3	13	75	113	310
SNG11	SL	1.75	168	17/06/06		0.78	-26.5			7.51	-1.51	17.28	4.99	2.52	-1.23	-2.05	17.32	17.19	14	3	5	22	101	142	311
SNG12	SL	1.48	169	18/06/06		0.76	-25.4			10.09	-0.78	16.26	7.48	2.61	-0.69	-1.05	15.82	17.51	14	3	5	23	139	210	453
SNG13	SL	3.08	170	19/06/06	0.330866	1.01	-26.6			7.82	-0.39	17.38	5.04	2.78	-1.20	-1.66	20.33	18.34	21	2	4	13	66	129	364
SNG14	SL	3.69	171	20/06/06		0.68	-25.3			18.79	-0.64	16.03	14.65	4.14	-0.58	-0.87	15.47	18.03	13	4	6	25	142	220	527
SNG15	SL	2.02	172	21/06/06		0.49	-25.0												11	4	7	31	146	210	473
SNG16	SL	1.55	173	22/06/06		0.48	-25.1			15.78	-0.54	17.26	12.99	2.79	-0.43	-1.06	17.21	17.50	14	3	5	25	135	191	364
SNG17	SL	2.19	174	23/06/06	0.254416	0.40	-25.1	2.04	-95.3	14.24	-0.44	17.35	11.85	2.39	-0.36	-0.85	17.25	17.81	9	5	9	73	271	304	412
SNG18	SL	1.58	175	24/06/06		0.59	-24.8			15.25	-0.55	17.09	12.42	2.83	-0.46	-0.93	16.97	17.58	10	4	7	45	261	320	510
SNG19	SL	1.58	176	25/06/06															14	3	5	27	151	210	394
SNG20	SL	1.73	177	26/06/06	0.28527	0.54	-25.0	2.46	-99.7	15.97	-0.43	16.95	12.99	2.98	-0.33	-0.87	16.93	17.06	16	3	5	19	77	108	257
SNG21	SL	4.3	178	27/06/06		0.49	-25.4				-0.93	19.43	9.89		-0.93		19.43		11	4	7	35	142	182	303
SNG22	SL	2.26	179	28/06/06		0.44	-24.6												12	4	6	25	98	143	293
SNG23	SL	2.65	180	29/06/06		0.44	-24.7												15	3	5	24	123	167	310
SNG24	SL	3.94	181	30/06/06		0.41	-25.2												10	5	7	47	184	227	358
SNG25	SL	3.76	182	01/07/06	0.244607	0.49	-25.4	2.32	-95.0	14.29	-0.80	18.25	10.69	3.6	-0.76	-0.91	18.15	18.57	5	9	16	71	164	196	314
SNG26	SL	4.1	183	02/07/06	0.227329			1.92	-95.1	10.03	-0.85	17.00	7.64	2.39	-0.82	-0.94	16.99	17.04	7	6	10	51	145	180	330
SNG27	SL	3.3	184	03/07/06		0.40	-25.4			11.33	-0.87	16.82	8.62	2.71	-0.88	-0.86	17.02	16.20	7	6	10	51	145	180	330
SNG28	SL	3.47	185	04/07/06		0.44	-25.7			10.65	-0.92	16.48	7.9	2.75	-0.88	-1.06	16.31	16.97	7	7	11	66	236	287	449
SNG29	SL	2.88	187	06/07/06		0.41	-25.4			10.27	-0.81	16.85	7.55	2.72	-0.74	-1.00	16.73	17.19	10	5	8	40	125	158	277
SNG30	SL	2.29	188	07/07/06		0.34	-25.2			8.36	-0.72	16.87	5.72	2.64	-0.61	-0.94	16.73	17.16	9	5	8	41	129	164	279
SNG31	SL	1.46	189	08/07/06	0.249345	0.36	-24.8	1.87	-96.6	20.4	-0.60	17.80	17.14	3.26	-0.50	-1.10	17.76	18.04	12	4	6	37	138	182	357
SNG32	SL	2.06	190	09/07/06		0.32	-24.9			19.14	-0.44	17.28	15.9	3.24	-0.37	-0.79	17.15	17.96	10	4	7	47	168	211	376
SNG33	SL	2.13	193	12/07/06		0.41	-25.1			18.31	-0.76	17.48	14.65	3.66	-0.70	-1.04	17.37	17.93	12	4	6	40	156	199	329
SNG34	SL	3.45	195	14/07/06		0.69	-25.9				-0.52		5.38		-0.52		14.38		9	5	7	27	76	100	220
SNG35	SL	2.01	196	15/07/06		0.42	-25.9			20.7	-0.57	17.30	17.02	3.68	-0.49	-0.92	17.29	17.35	11	4	7	35	130	172	387
SNG36	SL	1.94	198	17/07/06	0.289116	0.45	-24.0	2.03	-110.7	24.85	0.02	16.80	21.89	2.96	0.09	-0.56	16.62	18.11	16	3	4	21	86	116	238
SNG37	SL	3.23	199	18/07/06		0.26	-24.1												11	4	7	44	155	196	342
SNG38	SL	7.99	200	19/07/06	0.307437	0.51	-24.6	2.51	-107.5	20.14	-0.44	16.70	17.39	2.75	-0.38	-0.83	16.48	18.07	14	3	5	24	87	115	237
SNG39	SL	5.79	201	20/07/06		0.38	-24.1												12	4	6	32	118	157	321
SNG40	SL	3.1	202	21/07/06		0.45	-24.1				-0.54	17.10	15.9		-0.54	-0.87	17.10	17.71	13	4	6	29	96	121	216
SNG41	SL	3.52	203	22/07/06	0.233816	0.38	-25.5	1.79	-95.9	18.83	-0.62	17.26	14.61	4.22	-0.54	-0.89	17.04	18.01	10	5	8	52	190	244	483
SNG42	SL	3.62	204	23/07/06		0.30	-24.9												11	4	7	39	130	165	294
SNG43	SL	3.57	205	24/07/06		0.26	-24.2			18.4	-0.54	17.25	13.93	4.47	-0.43	-0.86	16.99	18.07	12	4	6	36	148	191	335
SNG44	SL	5.25	206	25/07/06		0.31	-24.7				-0.72	16.82	10.65		-0.72	-1.07	16.82	17.54	10	5	7	31	105	147	300
SNG45	SL	3.98	207	26/07/06	0.261975	0.49	-25.2	2.22	-98.3	23.24	-0.72	18.11	19.79	3.45	-0.67	-1.01	18.12	18.03	15	3	5	22	85	113	233
SNG46	SL	4.58	208	27/07/06		0.26	-24.9												10	5	7	50	203	254	431
SNG47	SL	2.47	209	28/07/06		0.28	-24.7												10	4	7	50	203	260	472
SNG48	SL	5.67	210	29/07/06	0.238619	0.31	-25.0				-0.67	17.29	11.99		-0.67	-0.99	17.29	17.68	7	6	11	55	175	220	353
SNG49	SL	3.24	211	30/07/06		0.37	-24.9			17.49	-0.74	16.99	12.44	5.05	-0.69	-0.88	16.80	17.46	9	5	8	44	159	206	377
SNG50	SL	4.65	212	31/07/06		0.25	-24.4				-0.24	16.73	11.96		-0.24	-0.83	16.73	17.53	8	5	9	62	180	218	352
SNG51	SL	2.17	213	01/08/06	0.217747	0.29	-24.2	1.71	-104.6	17.91	-0.31	17.21	14.15	3.76	-0.16	-0.87	16.98	18.09	11	4	7	47	161	199	321
SNG52	SL	3.01	214	02/08/06		0.51	-25.7												10	5	8	39	136	173	295
SNG53	SL	4.08	215	03/08/06		0.21	-24.3			14.09	-0.54	16.71	10.68	3.41	-0.40	-0.98	16.55	17.22	6	8	15	98	242	285	434
SNG54	SL	8.04	216	04/08/06	0.23338	0.24	-24.6	2.10	-90.3	8.5	-0.87	18.14	6.42	2.08	-0.80	-1.11	18.27	17.73	6	7	12	59	177	223	403

TABLE 5.1 – Geochemical compositions and grain-size of Narayani suspended load sediments sampled at the basin outlet, Narayanghat (N27,700 ; E84,421).

Ech.#	Type	Charge [g/l]	Julian day	Date	Al/Si [mol:mol]	TOC [%]	δ13Corg [‰]	H2O+ [%]	δD [‰]	Carb.Cont. [%]	δ13C.Carb [vPDB]	δ18O.Carb [vSMOW]	Calc.Cont. [%]	Dol.Cont. [%]	δ13C.Calc	δ13C.Dol	δ18O.Calc [vSMOW]	δ18O.Dol [vSMOW]	<4.5µm [%]	D10 (µm)	D16 (µm)	D50 (µm)	D84 (µm)	D90 (µm)	D99 (µm)
2010 monsoon daily surface suspended load (cont.)																									
SNG55	SL	4.12	217	05/08/06		0.23	-24.1			14.41	-0.71	17.47	10.56	3.85	-0.39	-1.61	17.24	18.09	7	6	11	74	212	253	410
SNG56	SL	1.69	218	06/08/06		0.31	-24.3			18	-0.17	16.62	14.55	3.45	-0.05	-0.67	16.28	18.06	13	4	6	37	141	181	322
SNG57	SL	2.48	219	07/08/06	0.259681	0.39	-24.8			16.67	0.03	16.59	13.7	2.97	0.20	-0.79	16.36	17.66	13	4	6	26	90	114	193
SNG58	SL	2.03	220	08/08/06		0.24	-24.7												10	4	7	37	129	166	295
SNG59	SL	1.75	221	09/08/06		0.52	-25.7			17.87	-0.16	16.86	14.37	3.5	-0.04	-0.63	16.52	18.27	11	4	7	34	109	140	251
SNG60	SL	2.14	222	10/08/06	0.28111	0.42	-24.8			16.1	-0.03	17.47	12.88	3.22	0.28	-1.26	17.34	17.98	12	4	6	31	127	170	314
SNG61	SL	3.04	223	11/08/06		0.31	-24.3			18.7	-1.02		14.63	4.07	-1.31		18.11		8	5	9	53	162	197	294
SNG62	SL	1.38	224	12/08/06		0.33	-24.6				-0.53	16.02	19.85		-0.53		16.02		12	4	6	36	136	173	293
SNG63	SL	1.18	225	13/08/06	0.264851	0.41	-25.0	2.14	-97.8	21.62	-0.41	17.73	18.19	3.43	-0.32	-0.90	17.68	18.02	12	4	6	30	117	154	298
SNG64	SL	1.43	226	14/08/06		0.25	-24.5												11	4	7	49	165	205	345
SNG65	SL	3.23	227	15/08/06		0.29	-25.0			10.15	-0.70	17.59	8.03	2.12	-0.19	-2.63	17.48	18.00	10	5	7	32	95	123	265
SNG66	SL	1.93	228	16/08/06		0.30	-23.9			19.88	-0.86	17.58	16.94	2.94	-0.71	-1.74	17.52	17.92	11	4	7	38	119	150	279
SNG67	SL	2.17	229	17/08/06		0.38	-25.4			17.49	-0.55	16.99	14.54	2.95	-0.50	-0.76	16.79	17.95	11	4	7	37	144	186	301
SNG68	SL	2.23	230	18/08/06	0.255687	0.40	-24.8	1.99	-109.3	20.3	-0.18	16.93	17.02	3.28	-0.08	-0.67	16.73	17.96	13	4	6	32	124	164	324
SNG69	SL	6.03	231	19/08/06		0.35	-24.9												15	3	5	25	131	193	393
SNG70	SL	3.07	232	20/08/06		0.34	-24.6			18.82	-0.01	17.17	14.76	4.06	0.21	-0.81	16.85	18.32	14	3	5	28	141	194	403
SNG71	SL	3.74	233	21/08/06		0.25	-24.4			16.72	-0.12	17.35	13.69	3.03	0.01	-0.72	17.17	18.19	9	5	8	62	217	272	462
SNG72	SL	3.47	234	22/08/06		0.23	-24.9												7	6	11	78	212	253	425
SNG73	SL	5.07	235	23/08/06	0.249316	0.46	-25.8	2.02	-96.1	17.45	-0.61	17.66	14	3.45	-0.49	-1.13	17.64	17.73	10	4	7	47	171	216	365
SNG74	SL	3.62	236	24/08/06		0.25	-24.9			18.71	-0.28	17.32	14.86	3.85	-0.14	-0.85	17.19	17.82	9	5	9	66	202	244	385
SNG75	SL	3.54	237	25/08/06		0.31	-24.5												14	3	5	40	268	323	418
SNG76	SL	2.79	238	26/08/06	0.20214	0.34	-25.2			18.15	-0.37	17.16	14.26	3.89	-0.22	-0.92	16.83	18.38	7	6	12	95	247	294	443
SNG77	SL	2.81	239	27/08/06	0.225504	0.40	-25.6	1.76	-98.1	16.72	-0.45	16.88	12.95	3.77	-0.30	-0.94	16.54	18.03	9	5	9	58	214	273	462
SNG78	SL	4.09	240	28/08/06		0.19	-24.6												7	6	11	98	274	322	473
SNG79	SL	6.84	241	29/08/06	0.214117	0.24	-24.9	1.60	-100.5	16.8	-0.76	17.76	13.31	3.49	-0.51	-1.72	17.76	17.74	7	6	11	100	240	277	420
SNG80	SL	3.96	242	30/08/06		0.33	-25.3			14.09	-0.61	16.99	10.91	3.18	-0.53	-0.85	16.65	18.15	6	9	17	118	257	292	406
SNG81	SL	2.59	243	31/08/06		0.24	-24.1												8	6	10	95	252	291	429
SNG82	SL	3.6	244	01/09/06	0.256601	0.42	-25.1	2.27	-97.5	13.38	-0.20	16.66	11.52	1.86	-0.11	-0.81	16.51	17.55	9	5	8	56	187	227	339
SNG83	SL	3.21	245	02/09/06		0.27	-24.6												8	5	9	75	233	281	432
SNG84	SL	3.22	246	03/09/06		0.38	-25.8												10	4	7	48	192	238	385
SNG85	SL	2.44	247	04/09/06		0.66	-25.5			23.17	-0.18	17.67	19	4.17	0.14	-1.66	17.51	18.39	12	4	6	41	170	212	355
SNG86	SL	2.13	248	05/09/06	0.237737					19.56	-0.06	17.20	15.53	4.03	0.13	-0.78	17.03	17.83	12	4	6	37	168	208	341
SNG87	SL	3.36	249	06/09/06															9	5	8	46	150	189	333
SNG88	SL	2.62	250	07/09/06		0.36	-25.2												10	4	7	36	136	181	388
SNG89	SL	1.9	251	08/09/06		0.31	-25.5			15.88	-0.37	17.37	12.23	3.65	-0.24	-0.79	17.12	18.20	9	5	9	53	176	223	411
SNG90	SL	1.66	252	09/09/06	0.237223	0.24	-25.1	1.87	-92.0	15.46	-0.33	17.12	11.54	3.92	-0.15	-0.85	16.94	17.64	9	5	9	52	157	195	314
SNG91	SL	1.38	253	10/09/06		0.30	-25.4												9	5	8	46	144	178	300
SNG92	SL	5.43	254	11/09/06		0.39	-26.1			14.14	-0.99	18.13	11.03	3.11	-0.96	-1.08	18.16	18.05	8	5	8	36	120	161	336
SNG93	SL	2.42	255	12/09/06	0.256644	0.31	-25.8	2.40	-87.6	12.83	-0.87	16.53	9.51	3.32	-0.86	-0.90	16.49	16.65	8	5	9	43	134	171	322
SNG94	SL	2.06	256	13/09/06						12.56	-0.89	17.37	9.73	2.83	-0.79	-1.21	17.36	17.43	7	7	11	65	197	245	404
SNG95	SL	2.51	257	14/09/06		0.45	-25.8			12.15	-0.83	16.30	9.13	3.02	-0.81	-0.91	15.99	17.22	8	6	9	44	135	170	294
SNG96	SL	5.68	258	15/09/06	0.288325	0.25	-25.5	2.53	-87.6	7.38	-1.42	18.34	5.49	1.89	-1.01	-2.62	18.42	18.12	7	7	11	50	157	205	411
SNG97	SL	2.01	259	16/09/06		0.31	-25.9												10	5	8	52	183	220	332
SNG98	SL	3.72	260	17/09/06		0.29	-25.8			7.93	-0.78	16.72	5.04	2.89	-0.70	-0.92	16.33	17.42	8	5	9	43	141	186	355
SNG99	SL	2.41	261	18/09/06		0.32	-24.9												13	4	6	24	84	116	295
SNG100	SL	2.22	262	19/09/06	0.255155	0.26	-24.7			13.11	-0.89	16.93	9.58	3.53	-0.79	-1.15	16.59	17.87	9	5	8	44	161	211	379
SNG101	SL	2.85	263	20/09/06		0.24	-24.7			9.96			6.84	3.12		-1.10		17.64	7	7	11	57	164	205	353
SNG102	SL	1.03	264	21/09/06		0.30	-25.1			14.26	-0.79	17.38	10.48	3.78	-0.71	-1.00	17.16	18.00	9	5	8	45	143	182	328
SNG103	SL	1.55	265	22/09/06		0.33	-26.0			13.98			12.18	1.8	-0.81		17.96		7	6	11	69	191	231	362
SNG104	SL	2.04	266	23/09/06	0.238198	0.27	-24.9	1.89	-92.5	15.37	-0.99	16.85	11.59	3.78	-0.98	-1.05	16.55	17.77	8	6	10	58	201	246	417
SNG105	SL	1.03	267	24/09/06		0.30	-25.4			16.9			12.23	4.67	-0.76		17.22		10	5	8	46	149	188	329
SNG106	SL	1.03	268	25/09/06		0.29	-25.5			15.18	-0.79	16.94	13.77	1.41	-0.77	-1.00	16.86	17.76	8	5	9	59	190	229	360
SNG107	SL	0.9	269	26/09/06	0.217685	0.32	-25.1			16.83	-0.85	17.65	15.48	1.35	-0.82	-1.20	17.58	18.40	8	5	9	62	178	214	354
SNG108	SL	0.55	270	27/09/06		0.44	-25.5			17.58	-1.06	16.96	15.96	1.62	-0.77	-3.90	16.75	19.06	11	4	7	35	112	145	266

Ech.#	Type	Charge [g/l]	Julian day	Date	Al/Si [mol:mol]	TOC [%]	δ13Corg [‰]	H2O+ [%]	δD [‰]	Carb.Cont. [%]	δ13C.Carb [vPDB]	δ18O.Carb [vSMOW]	Calc.Cont. [%]	Dol.Cont. [%]	δ13C.Calc	δ13C.Dol	δ18O.Calc [vSMOW]	δ18O.Dol [vSMOW]	<4.5µm [%]	D10 (µm)	D16 (µm)	D50 (µm)	D84 (µm)	D90 (µm)	D99 (µm)
2010 monsoon daily surface suspended load (cont.)																									
SNG109	SL	0.49	271	28/09/06		0.38	-25.5												11	4	7	40	135	170	287
SNG110	SL	0.54	272	29/09/06															9	5	9	63	185	226	377
SNG111	SL	0.51	273	30/09/06	0.21167	0.32	-25.2	1.86	-99.6	16.08	-0.85	16.62	12.39	3.69	-0.80	-1.03	16.13	18.26	8	5	9	71	220	271	451
SNG112	SL	0.45	274	01/10/06		0.37	-25.6			15.95	-1.16	17.71	11.98	3.97	-0.59	-2.87	17.52	18.29	7	6	11	83	219	272	446
SNG113	SL	0.38	275	02/10/06															8	5	9	62	209	267	487
SNG114	SL	0.45	276	03/10/06		0.29	-25.4			14.11	-1.26	17.79	10.5	3.61	-0.66	-3.01	17.57	18.41	7	7	12	101	276	318	459
SNG115	SL	0.26	277	04/10/06	0.246399														10	4	7	39	129	166	304
SNG116	SL	0.29	278	05/10/06		0.43	-26.0												7	6	11	76	202	242	393
SNG117	SL	0.3	279	06/10/06															7	7	12	85	224	265	421
SNG118	SL	0.28	280	07/10/06															7	7	12	77	211	256	399
SNG119	SL	0.57	281	08/10/2006	0.22021	0.55	-26.0	1.91	-100.6	12.89	-1.37	17.76	9.86	3.03	-0.92	-2.84	17.64	18.17	4	11	20	96	231	276	430
SNG120	SL	0.38	282	09/10/2006															5	10	18	110	270	318	477
SNG121	SL	0.33	283	10/10/2006		0.31	-25.4												4	13	25	137	295	342	513
SNG122	SL	0.29	284	11/10/2006		0.30	-25.7			14.4	-1.67	17.89	10.72	3.68	-0.78	-4.29	17.66	18.55	4	12	24	145	298	343	506
SNG123	SL	0.21	285	12/10/2006	0.20643														4	12	22	124	288	332	481
SNG124	SL	0.17	286	13/10/2006															6	8	14	82	214	259	422
SNG125	SL	0.37	287	14/10/2006		0.24	-25.5												2	25	49	183	324	361	489
2010 monsoon surface suspended load composite																									
SNG 9-34	. comp.	0	166-195	16/06-15/07/2010	0.26632																				
SNG 35-64	. comp.	0	195-226	16/07-15/08/2010	0.24823																				
SNG65-95	. comp.	0	227-257	16/08-15/09/2010	0.23371																				
SNG96-125	. comp.	0	258-287	16/09-15/09/2010	0.25927																				
2005 depth profiles																									
PB 60	SL 0	2.59	191	11/07/2005	0.27009	0.34	-24.5																		
PB 58	SL 0	2.92	191	11/07/2005	0.27058	0.33	-24.7	1.97	-96.0	21.75			16.15	5.6	-0.55		17.07	-13.42	13	4	5	22	74	97	207
PB 57	SL 2	4.81	191	11/07/2005	0.22999	0.24	-24.3	1.59	-95.1				14.73		-0.64		17.05	-13.45	9	5	8	44	123	150	303
PB 56	SL 4	5.59	191	11/07/2005	0.21507	0.21	-24.3	1.47	-96.2				13.87		-0.63		17.14	-13.35	4	9	14	77	171	210	425
PB 55	SL 6	9.10	191	11/07/2005	0.20543	0.20	-24.3	1.39	-97.2	17.22			12.57	4.65	-0.68	-0.89	17.15	-13.34	5	8	13	71	180	222	416
PB 54	SL 8	10.24	191	11/07/2005	0.19172	0.18	-24.2	1.26	-96.7	16.3			11.7	4.6	-0.71	-1.09	17.14	-13.36	3	11	20	102	235	281	452
2007 depth profiles																									
LO 757	SL 0	1.46	223	12/08/2007	0.24687	0.28	-24.4	1.68	-101.5	22.5	-0.33	17.38	18.33	4.17	-0.23	-0.78	17.33	17.62							
LO 756	SL 3.3	1.64	223	12/08/2007	0.23527	0.21	-24.0	1.61	-103.4	20.1	-0.33	17.38	16.32	3.78	-0.26	-0.62	17.29	17.77							
LO 754	SL 6	2.22	223	12/08/2007	0.21734	0.21	-23.9	1.46	-101.5	17.23	-0.39	17.38	13.68	3.55	-0.33	-0.64	17.26	17.86							
LO 755	SL 8	1.79	223	12/08/2007	0.22787	0.29	-24.0	1.61	-102.8	17.84	-0.39	17.37	14.31	3.53	-0.34	-0.61	17.30	17.67							
LO 758 A	SL 7.5	1.27	223	12/08/2007	0.24971	0.36	-24.4	1.84	-103.0																
LO 758 B	SL 8	1.64	223	12/08/2007	0.23173	0.30	-24.1	1.62	-102.1																
LO 758 C	SL 8.5	30.90	223	12/08/2007	0.14326	0.16	-25.3	0.98	-97.9																
2011 depth profiles																									
CA11117	SL 0	2.18	215	04/08/2011	0.29272	0.44	-25.3	2.57	-94.0										13	4	6	26	83	107	206
CA11118	SL 2.3	3.40	215	04/08/2011	0.24338	0.31	-25.0	1.99	-92.0										8	6	9	54	182	229	377
CA11116	SL 5.5	3.70	215	04/08/2011	0.24369	0.26	-25.0	2.01	-92.1										8	5	9	53	193	239	384
CA11119	SL 8.5	3.63	215	04/08/2011	0.23270	0.26	-25.5	1.89	-92.1										7	6	11	69	223	271	404
CA11123	SL 0	1.73	216	05/08/2011	0.26604	0.37	-25.0	2.25	-96.0										12	4	6	29	103	142	384
CA11124	SL 2	2.56	216	05/08/2011	0.22567	0.30	-25.5	1.86	-93.1										8	5	9	61	197	239	370
CA11122	SL 5.5	3.65	216	05/08/2011	0.20790	0.20	-25.2	1.66	-88.3										6	7	13	98	241	283	423
CA11121	SL 9.3	5.99	216	05/08/2011	0.19061	0.20	-25.4	1.45	-95.6										4	13	27	166	344	395	584
CA11127	SL 0	4.05	217	06/08/2011	0.26273	0.51	-25.4	2.30	-95.9										13	4	6	30	103	133	276
CA11126	SL 3	4.49	217	06/08/2011	0.24169	0.43	-25.3	2.00	-96.2										10	5	7	46	162	205	364
CA11125	SL 5	5.37	217	06/08/2011	0.22847	0.35	-24.9	1.89	-90.1										10	5	8	50	175	222	373
CA11128	SL 8	6.67	217	06/08/2011	0.21366	0.30	-25.1	1.67	-99.7										7	7	13	107	281	327	472
CA11130	SL 0	3.97	217	06/08/2011	0.25720	0.40	-24.6	2.15	-102.9										11	4	7	39	139	179	352
CA11131	SL 2	5.11	217	06/08/2011	0.23208	0.42	-25.8	2.00	-97.9										10	5	8	53	172	213	369
CA11129	SL 6.3	5.59	217	07/08/2011	0.22899	0.38	-25.3	1.95	-95.8										9	5	9	62	189	228	359

Cs_0 is quite low during the pre-monsoon period, and only starts exceeding 1 g/L when the monsoonal precipitations begin in mid-June (166th Julian day) and while Narayani discharges display values above 1000 m^3/s. Until the end of July (212th Julian day), flood peaks corresponding to intense direct runoff events engender quite immediate rise of Cs_0 above 4 g/l up to 8 g/l. From the end of July to mid-Sepetember (212th to 266 Julian day), Cs_0 variations still mimics peaks of discharge while Narayani displays higher discharges values. Cs_0 never exceed 7 g/l although comparably intense direct runoff events (storm rainfall) occur. Finally, when precipitation stop during the limb of monsoon from mid-September (260th Julian day), Cs_0 rapidly drops to values < 0.5 g/l, whereas direct runoff reaches nearly null values.

Over the year, suspended sediment Cs_0 compared to Narayani discharges display a clockwise hysteresis loop (figure 5.4.5). This pattern was already interpreted as the dilution effect by increased contribution of groundwaters seeping to the streamflow at the climax and at the end of the ISM (Andermann et al. 2012b). In 2010, it corresponds to a period going from the end of July to mid-September (210 – 260th Julian day) during which groundwater seeping Qb display values higher than 2500 m^3/s.

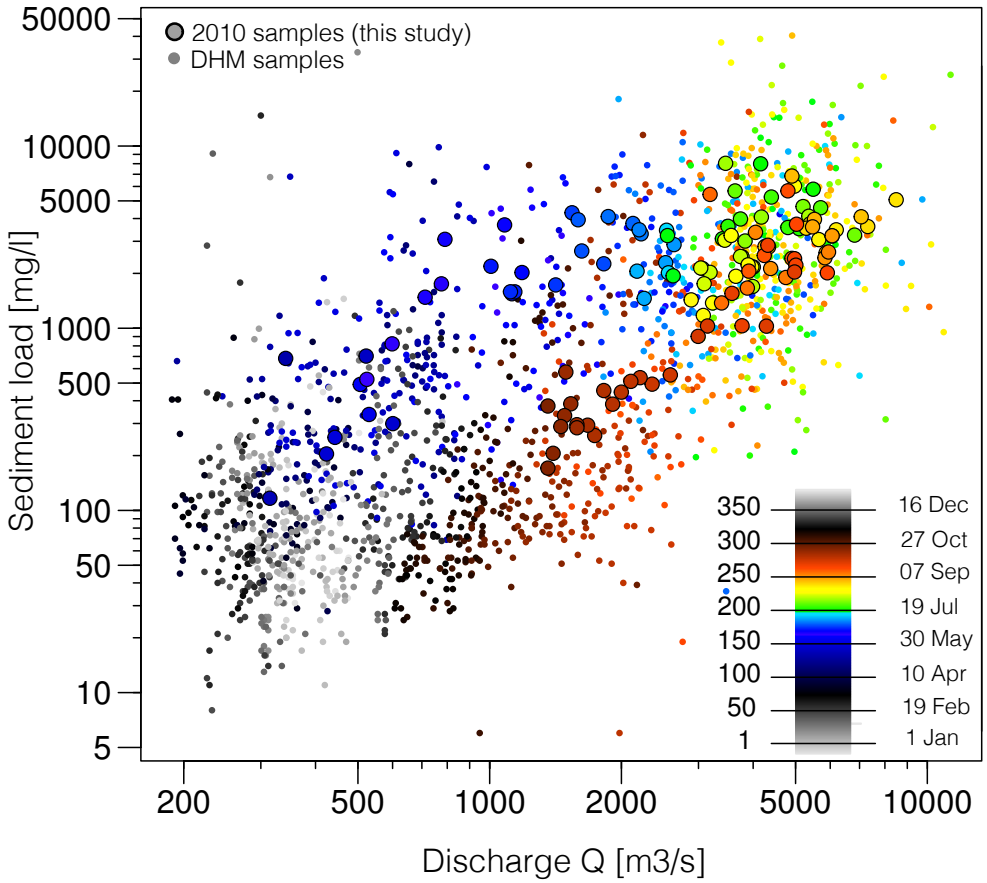

FIGURE 5.4.5 – Narayani surface suspended sediment concentrations relative to river discharge (log-log-scale).
DHM *Cs0* historical chronicles are represented by open symbols, this study 2010 surface suspended sediment concentrations are represented by filled symbols. 2010 samples span a period from May the 18th (138th julian) to October the 14th (287th julian) and ca the overall yearly clockwise hysteresis loop observed in DHM samples chronicle.

Reduction or annihilation of the hysteresis is observed when groundwater seepage component is removed from discharge, i.e. when Cs_0 is displayed versus the direct runoff component Qd (figure 5.4.6), as proposed by Andermann et al. (2012b). During the monsoon 2010, our data display in addition a linear relationship between Cs_0 and Qd (figure 5.4.6).

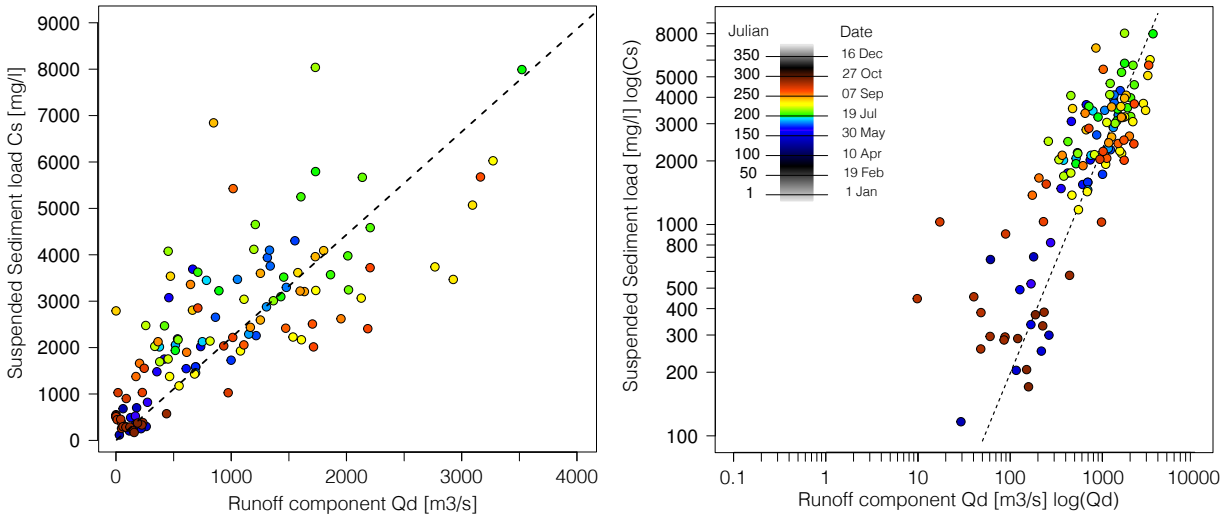

FIGURE 5.4.6 – Detailled monsoon 2010 surface suspended load *Cs0* compared to direct runoff *Qd* as calculated by modified filter after [Eckhardt 05, Eckhardt 08, Andermann 12b, Andermann 12c] represented in linear scale (left) and log-log scale (right).
Dashed line corresponds to the relation between *Cs* and *Qd*. 2010 *Cs0* comparison to *Qd* differenciates two populations : 1 – in violet and red, low sediment concentrations and direct runoff identical for pre-ISM (until mid-June) and post-ISM (after mid-September) seasons ; 2- in blue to orange, high sediment loads (above 1000 mg/L) and direct runoff (above 500 m^3/s) analog for all samples taken during months of ISM.

On the other hand, comparison of our Cs_0 data with DHM measurements indicates an overall good correspondence between both data sets (figure 5.7.2 Appendix A2). Except for the period of recession at the end of September during which our data are systematically higher than DHM's ones, more than two thirds of the data do differ by less than 50%. More importantly, the correlation slope between for the two data sets is very close to one (1.02 and 1.18 including or not the two main outliers). This suggests that lateral turbulent mixing of surface sediments between the central part of the channel and the river banks is relatively efficient, leading to roughly uniform suspended load concentration.

5.4.2.2 Suspended sediments segregation in the water column : concentration and grain size depth increase

The vertical sampling profiles, carried out in 2005, 2007, 2010 and 2011 display variable surface concentration values, Cs_0 , ranging from 1.4 to 4 g/l, with an average of 2.44 g/l (Table 5.1 and figure 5.4.7).

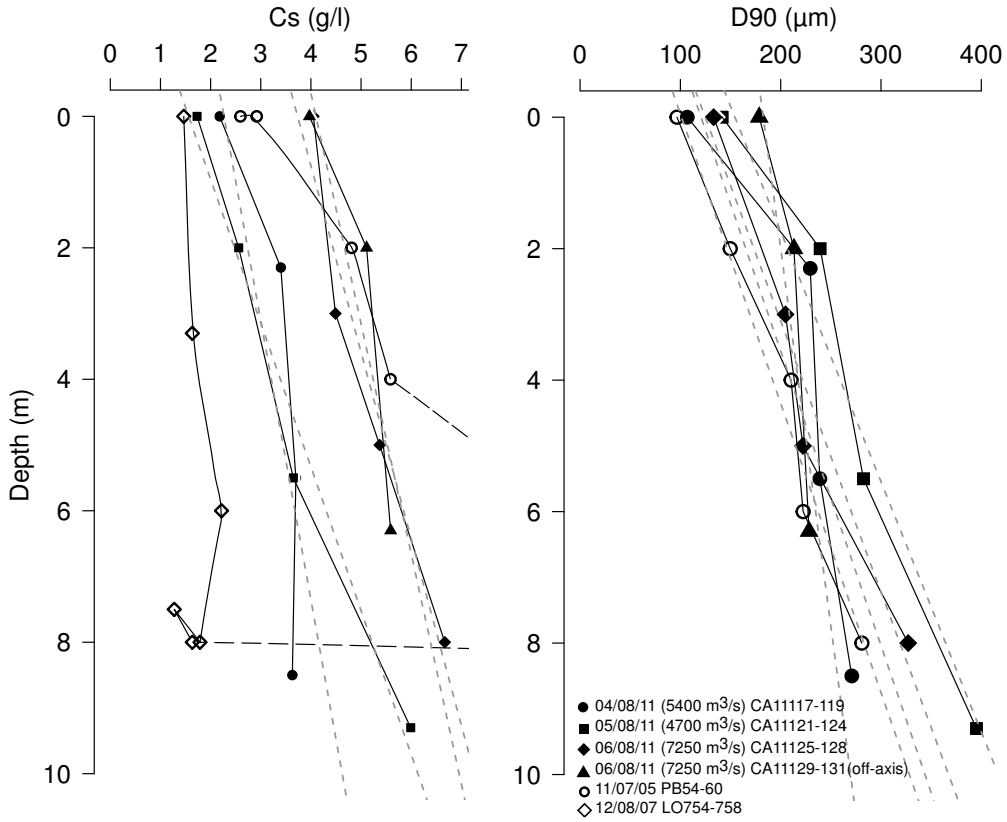

FIGURE 5.4.7 – Vertical profile of suspended sediments concentrations and grain-size measured by depth sampling along Narayani river water column in 2011, 2005 and 2007.
Both concentrations and grain-size D90 show linear increase with depth toward bottom.

Whatever this surface value, the profiles systematically show an increase with depth of the suspended load concentration with near bottom values reaching 1.8 to 10.2 g/l (at the bottom) i.e. 1.3 to 4 times the surface values (figure 5.4.7) depending on the depth-profile considered. At first order, the *Cs* increase with depth follows a nearly linear relationship

that can be expressed as :

$$C_s(z,t) = (1 + K_z) \cdot C_z(0,t) \quad (1)$$

where *Cs(z,t)* is the suspended load concentration at depth z and instant t, *Cs(0,t)* is the surface concentration, and K_z is the slope value of the linear increase of *Cs* with depth. Surprisingly, we observed low to no correlation between the concentration gradient K_z and the hydrodynamics conditions in particular for the vertical profiles sampled in 2011, despite river discharge varying from 4500 m^3/s up to 7000 m^3/s. The 2005 profile also indicate almost uniform gradient and vertical mixing although it was sampled under still lower discharge ($\sim$3000 m^3/s), that would in theory favour vertical segregation.

We assessed lateral variability of *Cs(z)* by realizing two depth profiles on the same day 07/08/11 between 10 :00 and 11 :30 AM, at the same hydrological stage. The first profile (samples # CA11125-CA11128) was realized on the axis of the river, whereas the profile "off-axis" (samples # CA11129-CA11131) was realized at a distance of $\frac{1}{4}$ the channel width from the right bank. Both "on-axis" and "off-axis" profiles display the same slope of *Cs(z)* with depth that supposes a relatively good lateral diffusion of turbulence over the whole river section. Such result is furthermore coherent with the observed similarity of the surface concentrations measured at the middle and along the bank of the river, at Narayangad bridge and DHM gauging station respectively (see previous section).

The concentrations measured near to the bottom in 2011 depth-sampling correspond to suspended sediments. Dredging sample bedload was not feasible in 2011 due to high flow conditions at that time. Nonetheless, former depth-profiles sampled in 2005 and 2007 (PB and LO) including tri-sampling, provide constraints on bottom suspended suspended and bedload concentrations. As expected, bottom samples PB 54 and LO 758C show very high concentrations : 10.24 g/l and 30.90 g/l respectively, illustrating sharp concentrations increase at the transition-layer between suspension and bedload transport. However, the available data are too limited to unravel the exact profile of this near-bottom *Cs(z)* increase, and to go much further than qualitative description.

Narayani river suspended sediments are principally composed of fine to medium sand (following Wenworth grain-size chart), and mainly display unimodal grain-size distribution. The 2011 samples depth-profiles display an overall downward coarsening. Whereas surface suspended sediments present median size, D50, and D90 (grain-size under which

50% and 90% of the sediment is distributed) of 44 and 199 µm respectively, it increases up to 295 - 395 µm at the bottom. Considering separated grain-size classes, clays fraction (<4.5µm) represents on average ~10% of the surface sediment, but only ~6% in the bottom samples ; silt fraction represents between 17 and 75% (on average 50%) of the surface sediments but only 22-41% at the bottom. Segregation of coarse particles in the water column is reverse, with sand fraction representing 14-80 % (on average 41%) of the suspended sediment at the surface, and rising up to 50-75% in the bottom sample. If grain size fraction is combined to suspended load concentration in order to assess absolute concentration in the different size fraction, it is shown that the sand fraction is the most affected by settling processes : sand fraction is more concentrated in the bottom sample whereas clay and silt are more uniformly distributed along the water column, as expected from Rouse or other suspension theories [Rouse 50].

Nevertheless, grain-size segregation in the Narayani River is rather limited if compared to the biggest rivers as Amazon, Ganga or Congo [Bouchez 11a, Bouchez 11b, Lupker 11b], where 2 to 7 fold increase of D90 are commonly observed between surface and bottom. In addition, and in contrast with what we would expect from Rouse theory [Garcia 08], we do not observe any variation of the gradient of the grain size when discharge varies, as also for concentration. Despite large discharge variations, between 3000 and 7000 m^3/s during 2007 and 2011 depth-samplings campaigns, grain-size (D90) display very similar and simple linear relationship with depth (figure 5.4.7).

The exact reasons for which concentration and grain size display a roughly uniform gradient with depth, and seem, more surprisingly, invariant whatever discharge amplitude is, remains beyond the scope of present study. In the following, we will just build on these linear relations that appear valid for discharge values between 3000 and 7000 m^3/s, i.e. 70% of the flood values during monsoon, to perform depth integration and simply derive sediment flux through the whole river section from surface suspended sediment concentration. To perform depth integration in sediment fluxes calculation and to assess related uncertainty, we thus consider a uniform vertical gradient of concentration $K_z = 0.36 \pm 0.09$ g/l/m, as deduced from the depth-sampling profiles.

5.4.2.3 Sediment flux calculation

In order to compute the total flux of suspended load transported by the Narayani river during the monsoon, we need to perform a triple integration over the water depth, over the width and over time. To proceed, we first modelled a synthetic topography of the river channel by considering the channel profiles sounded during ADCP cross-sections #11006, 11008, 12000, and 12001, and that encompass the zone where we realized sediments depth-samplings (figure 5.4.7).

Then, we orthogonally projected ADCP bottom channel topography with respect to the river axis, and averaged all transects into a Synthetic transversal River Section (SRS) (cf. figure 5.7.3 Appendix A3). We then derived a rating curve for this mean transversal section by computing water discharge, Q, through that section for any local water height, H, spanning from 0 to 14 m. To estimate the water velocity distribution in the section, we hypothesize that the law of the wall apply to the whole water column (details in Appendix A 4), so that :

$$Q(H) = \int_{X_{lb}(H)}^{X_{rb}(H)} \int_0^{z(x)} u_{(x,z,H)} dx dz \cong$$
$$\sqrt{g} \int_{X_{lb}(H)}^{X_{rb}(H)} \int_0^{z_B(x)} \frac{\sqrt{S_e(H)}\sqrt{z_B(x,H)}}{\kappa} \cdot ln\left(\frac{30(z_B(x,H)-z)}{k_s}\right) dx dz \quad (2)$$

where, *u(z,x)* is the water velocity at depth z and lateral position x, $[X_{\mathrm{lb}}, X_{rb}]$ represents the left and right bank abscissa, *Se(H)* the energy slope for a water elevation H, g the gravity constant,κ the Von Karman constant taken at 0.41, $z_{\mathrm{B}}(x)$ the local bottom depth counted from below the water surface, and *ks* the effective roughness height here defined by 3×D50 = 0.22 m from pebble median size as measured on local Narayani gravel bars [Mezaki 84, Attal 06, Dingle 12] (see Appendix A4). In above equation, the energy slope of the flow, *Se,* that depends on multiple factors at established regime (channel geometry and topography, discharge) is an unknown variable. Based on the results of ADCP section and integrations, that provide a direct relation between H and Q at the studied section, the energy slope was found almost constant, at ∼0.05%, and half of the mean channel gradient around Narayangad, i.e. 0.11 %. Such constant value was therefore used for any water height to compute water velocity and to derive a rating curve *H=f(Q)* at the SRS.

Then to compute the total flux of suspended load, we rely on the assumptions that the surface concentration presents, at a given time, a uniform value, and that depth profile in *Cs(z)* follows a linear trend of constant slope as described in the previous section. The

instantaneous sediment flux can thus be simplified, according to equations (1) and (2), into :

$$Q_s(t) = \int_{X_{lb}(t)}^{X_{rb}(t)} \int_0^{z(t,x)} C_s(z,t) \cdot u_{s(x,z,Q(t))} dxdz = C_{s0}(t) \left(Q(t) + K \int_{X_{lb}(t)}^{X_{rb}(t)} \int_0^{z_B(t,x)} z \cdot u_{s(x,z,Q(t))} \right) dxdz \quad (3)$$

Finally to realize time integration, we can follow distinct pathways. Discharge measurements from DHM provide hourly record, whereas suspended load sampling was performed on a daily basis. In order to compute sediment flux over monsoon or over the year, we can assume that hydrology of the Narayani river is slowly varying and that concentration measured each day at 8 AM is representative of the mean concentration during that day. In that first case (case DMC), we simply assess the mean daily discharge from the daily value measured at the DHM gauging station, derive the water height at the SRS from the synthetic rating curve, inject the measured surface concentration into equation (3), interpolate values between bi-weekly measurements out of the monsoon period and sum over the year the mean sediment daily fluxes.

In a second approach, we recognize that large daily variations observed in our *Cs(t)* data might be related to higher frequency variations during a day. In that case we need to define an empiric sediment rating curve. Classically, suspended load concentration is linked to water discharge through a power law. Such kind of relation makes sense when a river system is transport limited, i.e. when available sediment on channel bottom is unlimited and hydrodynamic conditions only determine the quantity of sediment that river can carry. However, as already argued by [Fuller 03] or [Andermann 12b], in active mountain range, rivers are mostly supply-limited, and a graph between discharge and concentration displays poor correlation or non-linear behaviour, including hysteresis (fig. 5.4.5).

In our case, we can rather take advantage of the linear relation between concentration and direct discharge (fig. 5.4.6), *Cs=f1(Qd)*, to define a less scattered sediment rating curve. Alternatively, [Andermann 12b] proposed to rather relate not the sediment concentration Cs, but the sediment flux Qs with the direct discharge, and to use a sediment rating curve *Qs=f2(Qd)*. Applied to our surface concentration data set, a graph of Qs vs Qd displays also a correlation between the two variables as good as the one between *Cs* and *Qd* for the samples taken during monsoon time (A5 fig. 5.7.5), that permits

to draw a linear sediment rating curve. However, a subtle counter-clockwise hysteresis is now emerging for pre- and post-monsoon samples, and indicates that a bijective relation is not fully adequate. Recognizing that the system is supply-limited, i.e. depending on sediment production on hillslope in particular due to landslides (see also discussion in 5.5.3), might appear as contradictory with the choice of a constant relation between *Qs* and *Qd*. The counter-clockwise hysteresis (Appendix A5 fig. 5.7.5) might illustrate a distinct sensitivity of the hillslope to erosion and sediment production during early and post- monsoon periods. To test such possibility, we have explored also a proportionality coefficient, *k(t)*, between *Qs* and *Qd*, that varies through time and which was calculated from surface sample concentration using a 9 days sliding window.

In order to document how sediment flux are sensitive to the different hypothesis, we provide in the following four calculation results (Table 5.2) : one summing daily values using measured concentration (case DMC), the three others by summing hourly values using concentrations estimated through rating curve *Cs=f1(Qd)* (case HCC), or rating curve *Qs=f2(Qd)* with constant (case HQCc) or variable proportionality coefficient (case HQCv). Note that the last approach can be viewed as a 9-days smoothed interpolation method.

Method	flux estimate	Hydrological timescale resolution	k coefficient	Qs Total sediment flux [Mt/a]	Equivalent erosion rate [mm/a] #
DMC0	measured Cs (no Cs depth gradient)	daily		108	1.28
DMC	measured Cs	daily		153 ± 15	1.80 ± 0.18
HCC	Cs = k1.Qd	hourly*	constant	152 ± 16	1.80 ± 0.19
HQCc	Qs = k2.Qd	hourly*	constant	158 ± 16	1.86 ± 0.2
HQCv	Qs = k2(t).Qd	hourly*	9 days sliding average	144 ± 15	1.70 ± 0.18

*daily data before May 17th and after Nov. 30th # using rock density of 2.65

TABLE 5.2 – Annual sediment flux estimate following the four different methods (see details on method in the text).

One of the aims of this study was first to improve former sediment flux estimates for the Narayani, in particular by integrating Cs along the water column based on depth-sampling measurements. Accounting for the concentration increase with depth, i.e. accounting for

the second integral member in eq. (3), lead to increase by ∼45% the sediment flux calculated without accounting for such depth variability (case DMC0 in Table 5.2). The time integration scheme has, in contrast, much less impact on the results : the four calculations using different time step integration or concentration estimate (cases DMC, HCC, HQCc, HQCv) lead to very similar estimates (Table 5.2), ranging between 144±14 and 156±15 Mt/an. The annual flux of suspended load in 2010 is thus estimated to be 150±20 Mt/a.

To document the timing of sediment delivery, cumulated fluxes were calculated along the year and are presented in figure 9 normalized to their respective total budgets and compared to the discharge and direct runoff Qd chronicles.

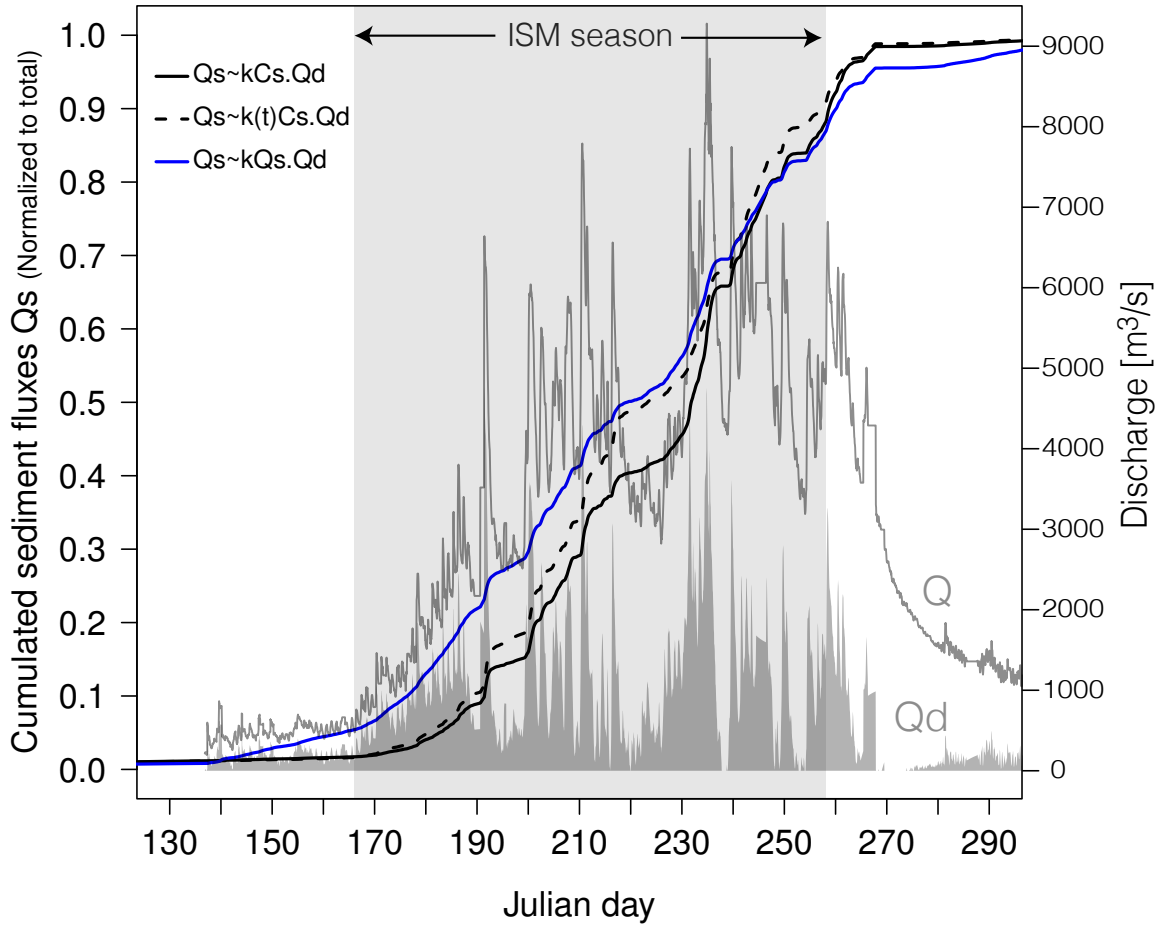

FIGURE 5.4.8 – Cumulated sediment fluxes obtained by different methods of integration (for total sediment budget report to table 5.2) along 2010 year.
In black lines, sediment fluxes obtained from calculation os sediment fluxes Qs with Cs regression to direct runoff Qd with a constant regression factor k (continuous line) and 9 days sliding average factor k(t) (dashed). In blue, fluxes obtained by Qs regression to Qd (continuous line constant value k, dashed 9 days averaged value k(t)). High slope of accumulation during runoff events demonstrate that sediment exports repond primarilly to direct runoff more than to total discharge.

A clear increase in sediment flux is evidenced during periods of sustained rainfall and intense runoff, whatever the mode of sediments fluxes calculation. More particularly, the

rainy period lasting around 1 week from julian day 230 to 238, yield 20 to 25% of the sediment yearly budget. However, much of the volume of suspended sediments exported by the Narayani river results from the cumulative effect of followed rainy days during the whole monsoon, rather from a few extreme events.

5.4.2.4 Average sediment flux over the last decades from DHM records

In active mountain ranges, landslides are usually considered as the major erosion process on hillslope, and therefore the major source of sediments provided to fluvial network. Because of the stochastic nature of landslide and the fact that erosional budget might be dominated by rare and very large landslides [Hovius 97], we suspect that sediment flux might be also stochastic by nature [Fuller 03], and vary from one year to another. Deriving a mean erosional flux for the Narayani basin requires therefore averaging sediment flux over several years or decades. Taking into consideration the concentration depth-increase using eq. (3), we therefore applied previous DMC approach to the 14 years of available DHM sediment record and corresponding daily discharge record, in order to derive sediment flux. We also used the HCC approach on a daily basis to derive direct runoff component, with the double objective to complement numerous gaps or missing data in the database, and to explore the temporal variation of the coefficient k1.

So-obtained results display basically two domains : before 2000, both the coefficient *k1* (Appendix A2 fig. 5.7.2) and the annual sediment flux (fig. 5.4.9) present large scattering with annual flux up to 150% higher than our reference year 2010, and large variations from one year to another.

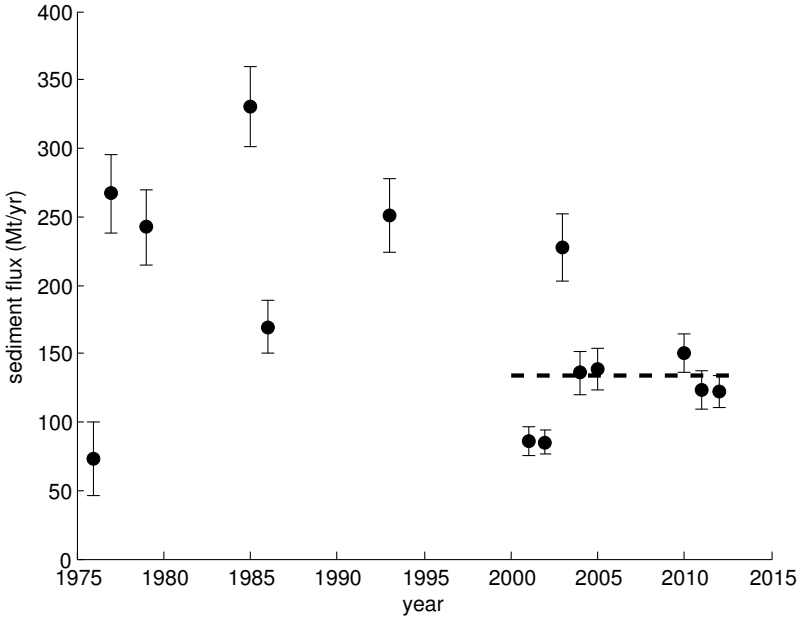

FIGURE 5.4.9 – Annual sediment flux derived from DHM daily suspended load data over 14 discontinuous years.
The average flux of 135 Mt/an (dashed line) was calculated only for records after the year 2000 (see text for justification).

In contrast, during the last decade, both k1 and the annual flux present less dispersed values. We partly ascribe the higher values before 2000 to the use of integrative USGS sampling bottles during the early recording years, which implies that concentration depth-increase is already accounted in the raw data. We donnot know, however, when the protocol shifted to surface sampling. In absence of further information, we limited our averaging period for mean flux calculation to the years posterior to 2000. Over the last decade, the average suspended load flux has been slightly lower than in 2010 and reach 135 ± 15 Mt/a.

5.4.3 Seasonal evolution of the suspended load characteristics

5.4.3.1 Evolution of the sediment granulometric distribution

Evolution of suspended sediment grain-size of during 2010 monsoon is presented in figure 5.4.10 (see also A6 fig. 5.7.6 for the whole cumulative distribution curves) and

compared to variations of Cs_0 and discharge. Despite large daily variations, there is a discrete grain-size rise through the 5 months investigated.

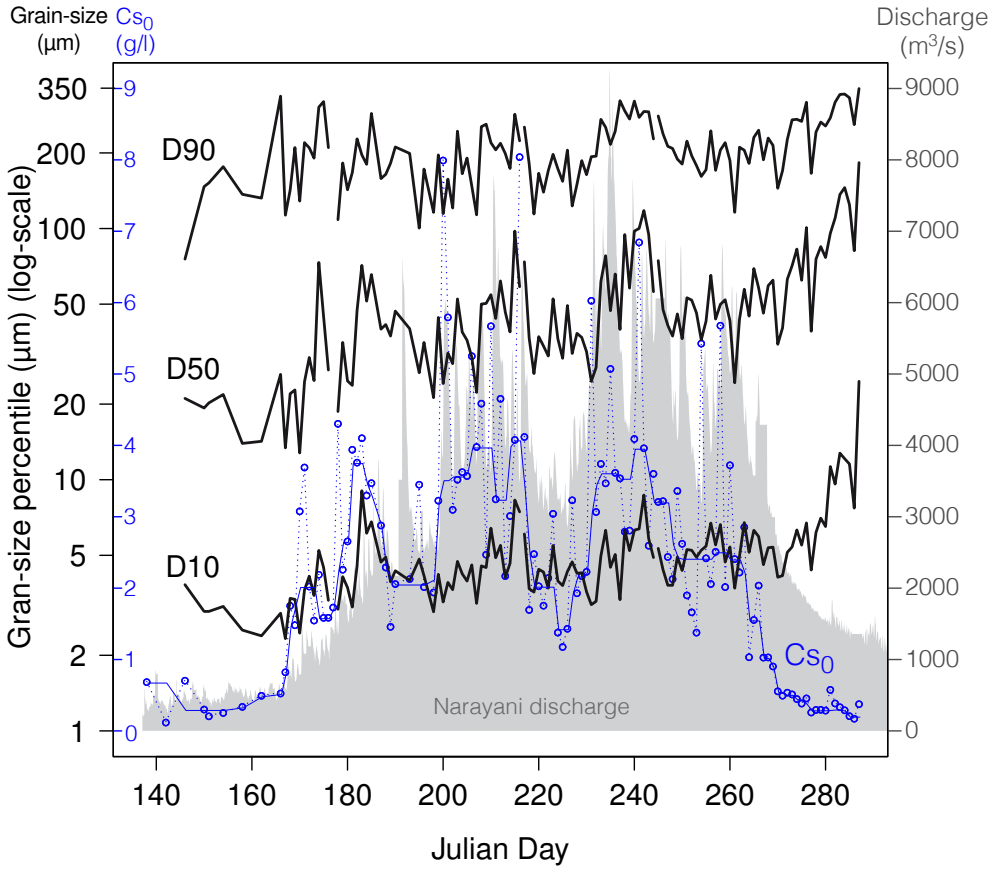

FIGURE 5.4.10 – Grain-size evolution of the 2010 surface suspended sediment (SNG) during monsoon.
D10, D50 and D90 correspond respectively to the 10th, 50th and 90th percentiles of bulk sediment. Surface sediment concentrations Cs0 are represented in blue dots and their smoothed evolution in blue line. Pulses of increasing grain-size seem to mimic pulses of sediment concentrations during monsoon as a response to sediment supply from hillslopes. Whereas, abrupt grain-size increase at the end of monsoon would indicate a progressive flush of the "washload" fraction and a transport relaxation f the system, seeing slow coarse particles arriving later at the outlet after sthe stop of supply by landslides (270th Julian day).

During the 3 months of monsoon, between mid-June (Julian day 166) and mid September (Julian day 258), D10, D50 and D90 start respectively around 3 µm, 20 µm, 100 µm

and rise up to finally values of 6 µm, 50 µm and 200 µm, respectively. After the monsoon, an abrupt increase in grain-size is observed : in about 3 weeks from end September to mid-October (Julian day 270 to 290), D10, D50 and D90 finally rise to 20 µm, 200 µm and 350 µm respectively.

Furthermore, superimposed on this seasonal grain size increase, higher frequency variations in grain-size display three rises reaching peak values on July the 1st, August the 3rd and August the 30th (Julian days 182, 215, 242) coincident with Cs_0 peaks at 4 g/l to 8 g/l, which strongly suggest that coarser sediments events are related to pulses of sediment supply. However, if high suspended load seem to be a necessary condition for observing grain size coarsening during monsoon period, the reverse is not true, in particular in June and July, since several peaks in sediment concentration are not associated to specific grain size coarsening.

5.4.3.2 Evolution of δD and carbonates content

In Narayani basin, carbonates are mostly derived from the Tethyan Sedimentary Serie (TSS) that form the High Himalayan range in the westerm part of the basin (Dhaulagiri and Annapurnas massives) [Galy 99b]. The small tributaries draining into the TSS display large disparities in carbonate content, with values reaching up to 65%, whereas the upper Marsyandi main tributaries, that average lithologies over large areas, present intermediate carbonate content of 25 to 30% (figure 5.4.11).

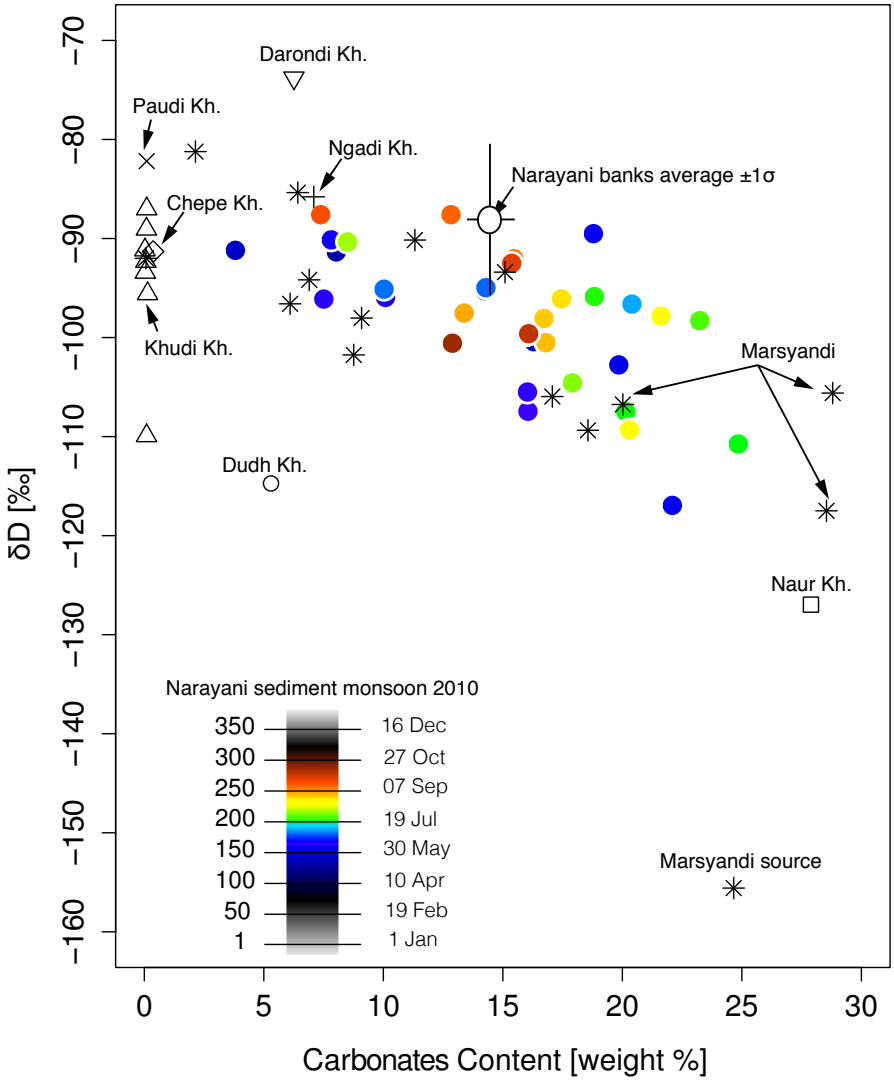

FIGURE 5.4.11 – Carbonates content versus δD values of 2010 Narayani SS (SNG), Marsyandi river and Marsyandi tributaries.

The anticorrelation of both tracers demsontrate that when sediment is derived from northern basin, high carbonates content and high proportion of TSS, hydration water is depleted in D showing more negative δD values relative to high altitude and glacial weathering environments. Small Marsyandi tributaries sediments compositions demonstrate the two poles : northern glacierized basins (Dudh kh., Naur Kh., Marsyandi source) with low δD values and/or high carbonates content, and southern not glacierized basins (Ngadi, Khudi, Chepe, Paudi, Darondi Kh.) showing les negative δD values and low carbonates content. Marsyandi and Narayani sediment sampled demonstrate this mixing. Monsoon Narayani sediments (SNG) does not display general evolution during monsoon. (same temporal color code as previous diagrams).

In contrast, rivers draining the south flank of the Himalaya carry much lower proportions of carbonate, between 0 and 10%, that mostly originate from the upper LH units [Colchen 86]. Narayani river sediments span a large variability in carbonates content from 5 to 25 % (fig. 5.4.12).

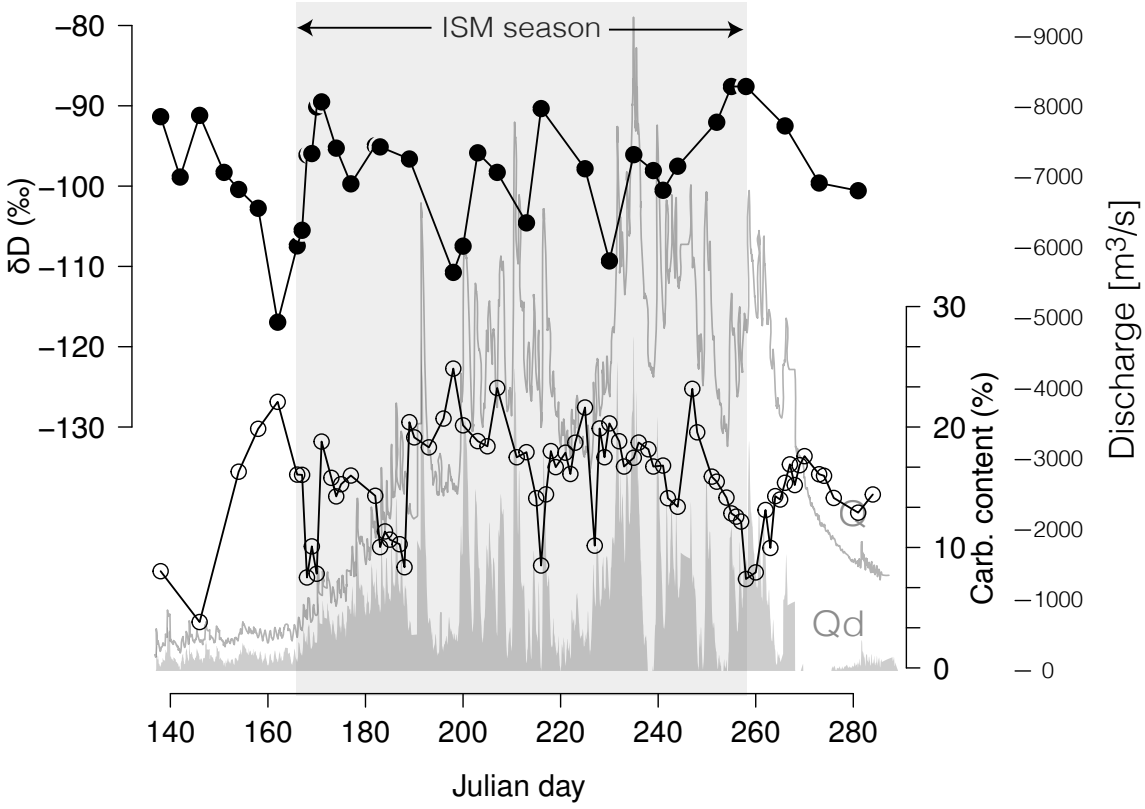

FIGURE 5.4.12 – Carbonates content and δD values evolution of 2010 Narayani SS (SNG).

Carbonates content is proposed as a tracer of TSS units, i.e. northern part of Narayani basin, while δD of hydration water as a tracer of elevation and glacial environments, corresponding to northern basin as well. And Both signals are anticorrelated, increase in δD values corresponding to decrease carbonates content. Evolution during monsoon, depsite high noise in the signal does not seem to show any trend with respect to time.

However, most values remain in the range 10-20% and the average content (sediment-flux weighted average) of the material delivered by the Narayani river from May or mid-October reach a value of 14.8%. Such value correspond to a large contribution of eroded

TSS material between 25 and 45%, roughly in proportion of TSS outcropping relative extension. (cf. table 5.3)

Ech.#	River	Elevation [m (a.s.l)]	North	East	H2O+ [%]	δD [‰]	Carb.Cont. [%]	δ13C.Carb [vPDB]	δ18O.Carb [vSMOW]	Calc.Cont. [%]	Dol.Cont. [%]	δ13C.Calc [vPDB]	δ13C.Dol [vPDB]	δ18O.Calc [vSMOW]	δ18O.Dol [vSMOW]
Marsyandi tributaries															
MAR-45.	Naur Khola	2639	28.561351	84.256863	1.57	-127.0	27.89	0.34	15.32	25.06	2.83	0.38	-0.05	15.09	17.43
MAR-52.	Dudh Khola	2092	28.534762	84.365727	0.45	-114.7	5.3	-2.14	15.38	4.6	0.7	-2.09	-2.43	15.51	14.54
SKD23	Khudi Khola	967	28.3055873	84.3300991	1.28	-92.3	0.07	-3.84	16.62						
SKD24	Khudi Khola	967	28.3055873	84.3300991	1.31	-91.2	0.03	-6.91	15.17						
SKD25	Khudi Khola	967	28.3055873	84.3300991	1.69	-89.1	0.09	-9.32	16.78						
SKD30	Khudi Khola	967	28.3055873	84.3300991	1.75	-109.9	0.09	-2.76	15.91						
SKD31	Khudi Khola	967	28.3055873	84.3300991	1.60	-87.0	0.10	-2.74	15.87						
SKD39F	Khudi Khola	967	28.3055873	84.3300991	1.40	-93.4	0.04	-8.76	17.13						
SKD79	Khudi Khola	967	28.3055873	84.3300991	1.79	-95.6	0.14	-3.22	16.32						
MAR-64.	Ngadi Khola	930	28.31541	84.40348	1.94	-85.8	7.09	-1.78	16.79	1.27	5.82	-4.69	-1.15	19.15	16.28
MAR-28.	Paudi Khola	524	28.11199	84.42655	1.61	-82.2	0.1			0.04	0.06				
MAR-26.	Chepe	453	28.05659	84.48038	0.90	-91.3	0.37			0.06	0.31		-1.77		16.07
MAR-10bis	Darondi	271	27.90773	84.54514	0.82	-73.8	6.26			1.73	4.53	-2.79	-1.01	16.43	15.83
MAR-40.	Sabche	3364	28.633765	84.106577	2.90	-90.2	11.32			9.58	1.74	-1.57	-2.77	17.77	17.19
Marsyandi river															
NAG 22	Marsyandi	4945	28.786227	83.963702	6.04	-155.6	24.66	0.69		20.05	4.60	0.87	-0.02	8.50	16.85
MAR-50.	Marsyandi	2250	28.530066	84.315895	0.90	-105.6	28.8			26.32	2.48	-0.44	-0.14	17.15	18.89
MAR-57.	Marsyandi	1665	28.465073	84.373153	1.07	-106.8	20.02			18.62	1.4	-0.25	-0.03	16.67	18.58
MAR-53.	Marsyandi	1685	28.482955	84.370631	0.91	-117.5	28.54			26.43	2.11	0.34	0.67	16.81	19.56
MAR-55.	Marsyandi	1665	28.465073	84.373153	0.70	-106.0	17.07			15.26	1.81	-0.59	-0.45	16.49	18.24
MAR-58.	Marsyandi	1378	28.440616	84.385446	0.55	-93.4	15.09			13.63	1.46	-0.87	0.01	16.36	18.28
MAR-61.	Marsyandi	1130	28.385815	84.403558	0.76	-109.4	18.56			16.26	2.3	-0.46	-0.18	17.01	17.90
MAR-29.	Marsyandi	570	28.130564	84.438402	0.84	-94.2	6.9			5.37	1.53	-1.06	-0.66	16.89	17.12
MAR-19.	Marsyandi	421	28.035269	84.463124	0.66	-96.6	6.1			4.25	1.85	-0.94	-0.63	16.51	16.98
MAR-68.	Marsyandi	867	28.277488	84.360624	0.91	-81.2	2.14			1.5	0.64	-0.96	-0.01	16.61	17.04
MAR-70.	Marsyandi	695	28.231132	84.383325	0.84	-85.4	6.42			4.93	1.49	-0.76	0.27	16.50	17.68
MAR-12.	Marsyandi	291	27.90803	84.539657	0.69	-101.8	8.76			6.96	1.8	-0.52	-0.50	16.11	18.78
MAR-12.	Marsyandi	291	27.90803	84.539657	0.72	-98.0	9.09			6.79	2.3	-0.61	-0.52	16.19	17.78

TABLE 5.3 – Carbonates content and δD values of Marsyandi river and its tributaries. Refer to figure 5.3.1 for tributary basins locations.

The values of δD in hydrated silicates reflect both the original bedrock composition (i.e. metamorphic water mostly contained in micas and chlorites and with an isotopic signature around -90‰, ; [France-Lanord 88]) and water adsorbed during weathering and secondary silicate minerals (mostly clay) formation [Savin 70]. The later depends on the isotopic composition of meteoric water, which in Himalaya is strongly dependant on elevation (e.g. [Gajurel 06, Garzione 08]). As a consequence, river sediments derived from high elevation and glaciated environments display low δD compositions, around -140 to -120 ‰, such as sediments of the northern Marsyandi, Naur and Dudh rivers, and more particularly such as the glacier flour sampled at the outlet of the pro-glacial tributaries in the Dudh watershed (figure 5.4.11). On the contrary, rivers from lower elevations and draining the south flank of the Himalaya have higher δD compositions between -95 and -85‰ (Khudi and Chepe khola on figure 5.4.11). A few samples of tributaries draining elevated TSS lithologies but along non-glaciated parts (Sabche or Bratang rivers in the upper Marsyandi) display also δD signature around -90 or above, i.e. close to pristine bedrock signature. This would suggest that negative δD more specifically sign sediments issued from glacier erosion and associated weathering.

As for carbonate content, the fraction of hydrated silicates in Narayani river sediments span a large variability in δD over the year, from -87 to-117‰ (fig. 5.4.12), with no obvious organisation but a high frequency content.

If most days present a δD higher than -100‰, consistent with dominant signature of unweathered bedrock or of weathered material issued from the southern Himalayan flank, a few ones display isotopic signature that requires a significant or even dominant contribution of sediment issued from the upper glacierized catchments. More specifically, the glacier sediment contribution can be evidenced during pre- and early monsoon periods, when it is compared to the contribution of ice melting to Narayani discharge (fig. 5.4.13).

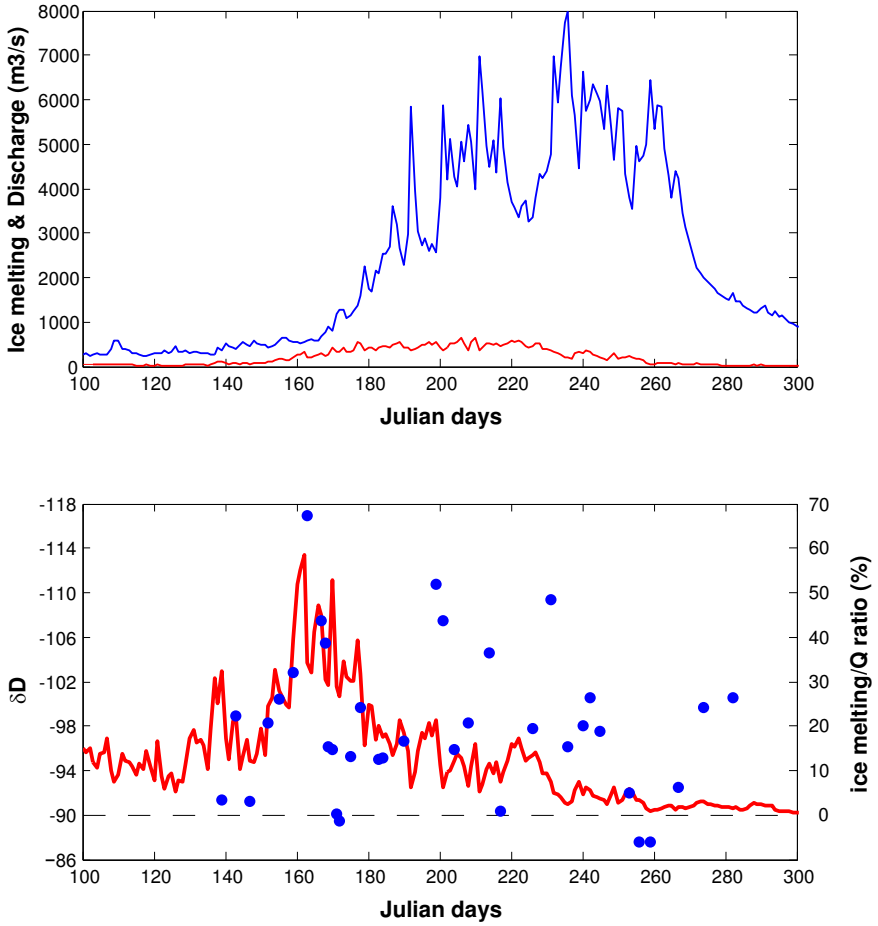

FIGURE 5.4.13 – (a) Summed ice melt flows in front of the glaciers of the Narayani basin, compared to the total discharge in Narayangad.
(b) δD signature of the hydrated silicate phase of Narayani suspended load superimposed on the curve of the relative contribution of ice melting to Narayani discharge sediments. Ice melting was computed from daily temperature recorded at 10 DHM weather stations located in the High Himalaya, from a Positive Degree Model (Rana et al., 1996)

During that period, the δD data appear to follow the curve of relative ice melting, with the most negative value recorded on mid June (Julian day 163), when ice melting has reached a maximum of $\sim$50% of relative contribution in Narayani discharge. This overall agreement during a month period is only interrupted by the first major monsoon rainfall event on Julian day 171 (fig. 5.4.4b), which gave rise to a 5-fold increase of suspended load concentration (fig. 5.4.4b) and which most probably diluted the glacier sediment

signal during a couple of days. In contrast, during monsoon, when relative contribution of ice-melting is lower than 10% no clear rational or correlation was found to explain variations in δD.

Daily samples of suspended sediments of the Narayani appear to cover almost the full spectrum of carbonate and δD compositions documented within the basin from north to south, and to show a rough anticorrelation (figure 5.4.11). Such anti-correlation is consistent with the fact that a large fraction of the Narayani glaciers, mostly in the western part of the basin, are presently eroding TSS carbonate-rich units. It is particularly obvious again during pre- and early monsoon periods, when the contribution of ice melting to Narayani discharge is maximal : it can be indeed observed similar rise and fall trend, similar maximum on Julian day 163, and low value excursion on Julian 171 after heavy monsoon rainfall event (fig. 5.4.12). Then during monsoon, the anti-correlation between the two variables becomes slightly messier (figure 5.4.12). We speculate that days of reverse correlation might correspond to increased glacier sediment input from granitic or gneissic glaciated massifs in the central and eastern part of the basin (example of day 231 for which δD is clearly more negative without any corresponding carbonate % increase), or days of increased TSS erosion by landslide or other hillslope erosion process (example of day 208 for which the carbonate content has clearly increased without any corresponding δD drop).

Nevertheless, probably the most important feature that the carbonate content and δD signals have in common is their high frequency content, i.e. values in both compositions that can vary abruptly from one day to another. Such feature indicates that the origin of sediments, whatever it is related to distinct geographic sources or an erosion process, may vary quite abruptly through the season, and rapidly respond to local events and meteorological conditions.

5.4.3.3 TOC Evolution

Total organic carbon concentrations (TOC) vary between 0.2 and 1.3 wt%. TOC are high around 1 wt% during the pre ISM period and drop to 0.2-0.5 % after the first heavy rainfall event and discharge take-off on Julian day 171, and until the post-monsoon season. Preferential association of organic carbon with fine grain particles has been described

previously in Himalayan sediments [Galy 08]. During the monsoon, TOC and grain size of Narayani suspended load seem to roughly follow this large Himalayana rivers grain-size control (Appendix A7 fig. 5.7.7), even if they display large scattering and lie mostly above this trend. In contrast, during the pre-monsoon period, the TOC values are well above Himalayan rivers average trend, and, despite being concomitant to an overall larger proportion of fine grain size in suspended load, cannot be explained only by grain size sorting in the water column when discharge and sediment suspension are low. We therefore suspect that high TOC during pre-ISM season in sediments carried by Narayani river might also reflect a source enriched in soil or litter, and that this component is absent or largely diluted once high sediment load associated to heavy rainfall and runoff events dominate the sediment budget during monsoon.

5.5 Discussion

5.5.1 Sediment flux calculation : depth sampling and general strategy

For Narayani river, previous estimates of suspended load flux reported values of $\sim$ 100 $\pm$ 50 Mt/a [Sinha 94, Andermann 12b]. Although falling within error bars of these previously values, our calculations for 2010 (150 $\pm$ 20 Mt/a) and for the last decade based on DHM data (135 $\pm$ 15 Mt/a) are significantly higher. This difference mostly arises from taking into account vertical increase of the concentration in water column, since we also obtain a flux around100 Mt/a, when this gradient is not included in calculation (case DMC0 in table 5.2). Even if the Narayani river is highly turbulent during monsoon floods, which favours vertical mixing, the vertical segregation remains of importance and must be integrated when calculating sediment flux, otherwise Narayani sediment flux can be underestimated by almost 50%. Our approach to integrate concentration over depth is simplified and based on measurements operated during only a few days. To perform depth integration on a more physical basis, a more elaborate study would be necessary in particular to document concentration gradient at low to intermediate flows (<3000 m^3/s) and very high flows (>7000 m^3/s). However, given the fact that the explored range of flow conditions during our sampling campaigns encompass >85% of the exported sediment flux (because of reduced load flux at low flow, and because of the too rare occurrence of the

highest flow conditions), we do not expect major bias in our calculation. Furthermore, the depth-integration term in eq. (3) is expressed only as a function of water discharge, Q, and can be applied to any future (or past) record of surface concentration in suspended load, without requirement of simultaneous depth sampling.

Relative to time integration of flux data, the different strategies we tested for the year 2010 indicate that the annual flux value is not very sensitive to these approaches (Table 5.2), regardless of considering hourly or daily integration, measured concentrations or interpolated ones based on a sediment rating curve. However, geomorphologic consideration, as well as highly variable rating curves obtained from DHM data between 1975 and 2012 (Appendix A8 fig. 5.7.8), suggest that in a supply limited system (see also discussion in section 5.5.4) deriving a unique and constant sediment rating curve is probably not relevant. Even if sediment production on hillslope seem roughly correlated to overland flow, as expressed by the relation between direct discharge and sediment flux (fig.5.7.5 Appendix A5), the stochastic nature of very large and contributive landslides or the influence of ground saturation in parallel to rainfall intensity in landslide triggering (Gabet et al., 2004 ; see also section 5.3), imply that above relation *Qs=f2(Qd)* can amply vary through time. The 14 yrs of DHM sediment chronicles suggest that variations have to be accounted at least on an annual basis. The small clockwise hysteresis observed in sediment flux in June 2010 (fig.5.7.5 Appendix A5) might suggest that variations would have to be considered even on a monthly to weekly basis.

In the case of a large watershed like the Narayani basin, in which discharge variations are gradual during the day, the best strategies for time-integration appear to be either a calculation on a daily basis using measured concentration (case DMC), or a hourly calculation interpolating concentration or flux from a variable sediment rating curve (*Cs=f1(t,Qd)* or *Qs=f2(t,Qd)* regressed from measured concentration with a sliding window (case HQCv). In both cases, it seems to us necessary to base calculation on continuous daily surface sediment sampling. Contrary to discharge rating curve *(Q=f(H))*, we doubt that sediment rating curve might be established and valid for long period of times.

5.5.2 Mean denudation rate

Deriving mean landscape denudation rate requires estimating bedload flux in addition to the suspended load flux. However, bedload fluxes were not investigated because of the technical difficulties for dredging bottom sediments during high floods. Bedload flux can only be inferred based on different approaches.

First by comparing to other worldwide rivers : if in upstream catchments, bedload has been suspected to represent up to 50 % a the total sediment load [Pratt-Sitaula 07], it would only represent a maximum of 10 % in rivers comparable in size (A > 30000 km2) to Narayani [Turowski 10].

Second, modeling of physical pebble abrasion, based on experimental data and the assumption of dominant landslide material, suggest that bedload fraction would represent a maximum of 12% at the Narayani outlet [Attal 06].

All together, above two arguments suggest that bedlod flux is lower than 13 Mt/an. And over the last decade, our best estimate for equivalent erosion rates in Narayani basin would be $1.6^{+0.3}_{-0.2}$ mm/a.

This rate is clearly higher than estimates obtained from suspended load in smaller subcatchments that drain either the active southern flank of the Himalayas of Nepal, with scattered values between 0.1 and 0.3 mm/yr and up to 2.8 mm/yr (Stations 0, 447 and 410 respectively, in [Andermann 12b]), or the upper and middle Marsyandi with erosion rates ranging between 0.1 and 0.7 mm/a except for a small subcatchment that reaches 1.3 mm/yr ([Gabet 08] _ note that for consistency reasons, we consider only suspended load).

If we consider, as discussed at length in section 5.4, that sediment transfer is quasi instantaneous at the scale of the monsoon season, and that no dilution or buffering effect of the sediment source signature is observed, it is not clear to us how we can reconcile above small rates with the one measured at the Narayani outlet, which might represent the sum of the sediment delivery from these subcatchments. Missing part might be coming from unsampled subcatchment (Buri and Seti rivers), higher bedload proportion in upstream areas, or, in the case of the Marsyandi river [Gabet 08], from the reduced recording duration (3 yrs) that could have missed characteristic years of heavy monsoon and higher hillslope erosion.

In contrast, the average erosion rate computed over the last decade appear in close agreement with the average denudation rate of 1.7 ± 0.2 mm/a calculated from ^{10}Be cosmogenic radio- nuclides (CRN) in Narayani river sand, which were sampled over several years at the same location [Lupker 12a]. In the specific case of the Narayani, CRN-derived values average erosion rates over a duration of ∼500 yrs, i.e. over one to two seismic cycles with estimated return period for large (Mw>=8) events every ∼200 yrs [Avouac 01].

Our result suggests therefore that erosion during the last decade has been representative of Late Holocene denudation, and that erosion by co-seismic landslides would not represent in Himalaya a significant contribution to long term landscape erosion in contrast with what observed along other Tibetan margin [Parker 11] . It is, however, expected that future studies on landscape and erosion responses, after last Mw=7.8 earthquake that hit central Nepal on April-25th 2015, will probably bring additional constrains on this issue.

5.5.3 The active erosion processes : climatic control and their respective contribution to Narayani sediment fluxes

River sediments transported by the Narayani are derived from three main processes : glacier erosion, shallow to deep seated landslides, and soil erosion. Deciphering how these processes contribute to the erosion flux is challenging but some constrain can be derived from the present set of data.

5.5.3.1 Erosion by landslides

In active mountain range, outside glaciated areas, the major erosion process involved in erosion is usually ascribed to landslides and more particularly deep-seated landslides. In Himalaya, landslides are frequent [Fort 87b, Shroder 98b, Shroder 98a], can mobilize volume of a few km^3 [Weidinger 06], and contribute to vast majority of the erosion budget [Gallo 14a]. Deep-seated landslides are mainly triggered by ISM precipitations [Iverson 00, Gabet 04a] that maintain high pore-water pressure in the subsurface and decrease slope stability . In central Nepal, [Gabet 04a] identified, besides the role of pore pressure and water table elevation, a second triggering factor for sediment production and supposedly for landslide activation : the daily rainfall intensity.

The correlation between *Cs* and the direct runoff, which is related to rainfall intensity (fig.5.4.4b) and to superficial runoff and water saturation in the soil and regolith, would support Gabet et al.'s view, that sediment production is proportionated to rainfall intensity. To explore this presumed double influence of ground water pore pressure and rainfall intensity, we redraw Gabet et al's graph (cumulated precipitation vs rainfall intensity) using instead the sediment flux amplitude as a function of groundbase flow and rainfall intensity (fig. 5.5.1).

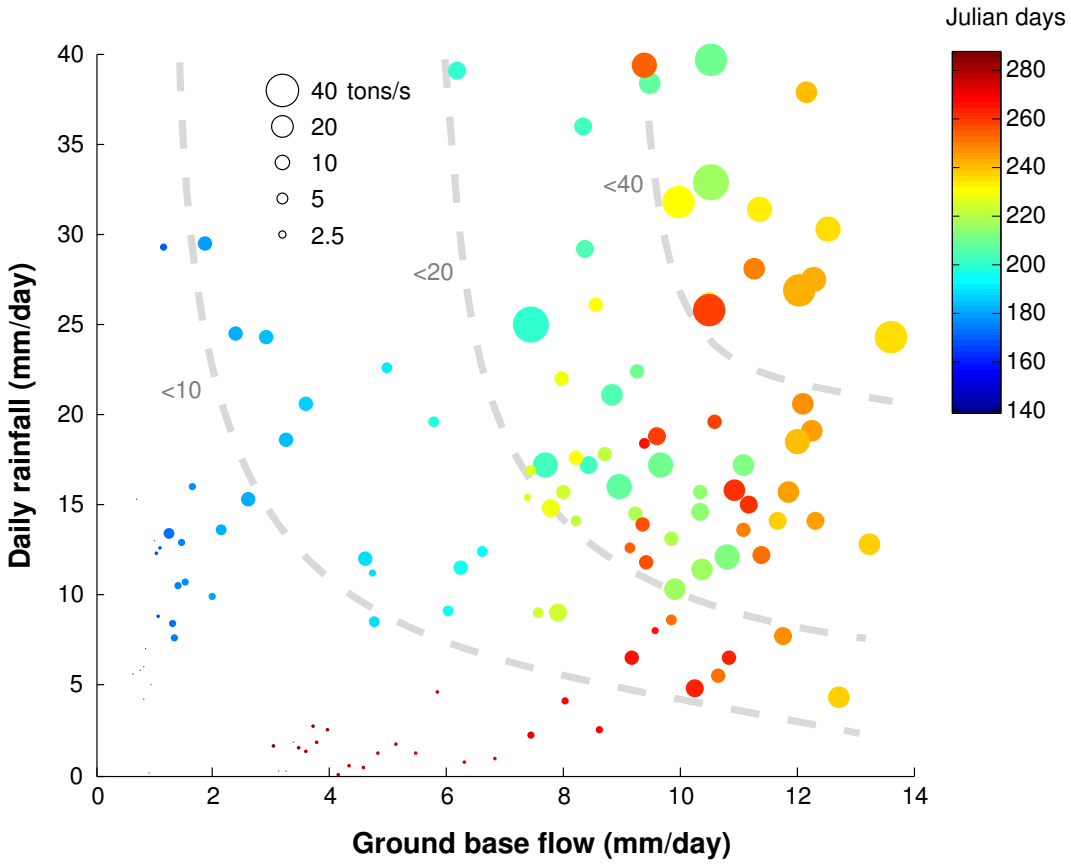

FIGURE 5.5.1 – Daily sediment flux as a function of ground base flow and daily rainfall amount.
Disk size is proportioned to flux amount, and colour code is related to the julian day.

In hydrologic model, as well as in the flow separation model used in this study (see also [Eckhardt 05]), the ground base flow is linearly related to the mean water table, so that in fig. 5.5.1 it can be considered as a reasonable proxy of pore pressure in the fractured rocky

substrate. This graph illustrates the double influence of rainfall intensity and water table depth on sediment delivery to the river network : intensity of erosional events increase both with water table height and rainfall intensity. The link between water table, pore pressure and landlide triggering factors suffers no physical ambiguity, so that we can clearly pinpoint the signature of landslides in erosion of the Narayani basin : a minimum groundbase flow of 2500 m^3/yr (∼6 mm/day of equivalent runoff on fig. 5.5.1, reached in 2010 after mid-July), seems required to trigger numerous or massive landslides and deliver sediment fluxes larger than 20 tons/s. The physical link between sediment flux and rainfall intensity is more equivocal. It could be related to erosion on hillslope : through a rapid increase of pore pressure either in high permeability fracture systems in the bedrock that would make easier deep seated landslides triggering, or in soil and regolith that would set off countless shallow landslides. It might be also related to sediment transport capacity in headwater and low-order channels : only high surface runoff events would be able to transport the sediment mobilized by landslides in upper and mid- valley slopes.

In both cases, hillslope erosion by landslides seem required either during the precipitation event, or in the days before in order to provide brecciated and finer material, unprotect by vegetation cover, avaible for transport by overland flows. Otherwise we would observe high sediment flux associated to heavy rainfall events during pre- and early monsoon, which is not the case.

The role of a minimum ground saturation on landslide triggering is also visible in fig. A5 between *Qs* and *Qd*, through the residual counter-clockwise hysteresis : *Qs* remains below the average trend during pre- and early monsoon as long as pore pressure in subsurface is still too low for landslide activation, and *Qs* is above the average trend on late September because high pore pressure compensates for mild rainfall intensity and permit significant erosion. Because the relation does not account for the role of water table in landslide triggering and sediment production, its therefore imposes for using it as a rating curve to vary the coefficient *k2* during monsoon.

If landslides overwhelmed any other signal after monsoon onset, tackling in our Narayani records sediment generation by erosion processes other than landslides require focusing on the pre- and early ISM season when landslides are not yet active. In the following we therefore try to identify glaciers and superficial soil erosion mostly during that period.

5.5.3.2 Glacier related sediments

Because glacier erosion is suspected to be locally of importance with rates outpacing the erosion rates in fluvial landscapes [Hallet 96] , we hypothetically suppose that glacier erosion might dominate sediment delivery or at least show up in load record during that pre-and early ISM season. According to melting models, based in particular on MODIS-data of temperature and snow cover, 10 to 12% of the annual water discharge is derived from ice and snowmelting [Bookhagen 10, Andermann 12a] in the Narayani watershed. Moreover, direct measurements at Himalayan glacier outlets [RANA 96, Shea 15]indicates that water discharge associated to melting, in particular ice-melting, begins rising on early June, peaks around mid- to end of July and has returned to 0 by the end of September.

For 2010, based on DHM daily temperature record and a positive degree day model (fig. 5.4.13), it was calculated for the Narayani a contribution to annual discharge of 7% of ice melting, peaking indeed on end-July. Contrary to ice melting studies, data on sediment fluxes produced by glaciers are relatively scarcer in Nepal. In Narayani watershed, sediment fluxes have been measured below glaciated areas in the Koto, Naur and Dudh khola catchments in the upper Marsyandi [Gabet 08] and in the upper Langtang located in the most eastern part of Narayani basin [Fukushima 87]. Equivalent erosion rates, derived from suspended load only, display important scattering, with values ranging between 0.07 (Naur) and 0.7 mmyr (Koto) for glaciated relative surfaces between 10 (Naur) and 38% (Langtang). If we assume that all the sediments are produced by glacier erosion, summing the sediment fluxes of the 4 watersheds and dividing by the sum of their glaciated surfaces provide an estimate of the maximum glacier-related erosion rate of $\sim$1.85 mm/yr. The Marsyandi and Langtang areas contain among the largest and probably fastest [Scherler 11] glaciers in the Narayani watershed. Whereas glaciers draining the wetter southern flank of the Himalayas are not included in above simplified analysis, we therefore suspect that above maximum glacier erosion rate is, to first order, representative of the erosion produced by Narayani glaciers on average : the maximum sediment flux derived from glacier erosion in Naryani watershed would be therefore $\sim$14 Mt/an. Glacier erosion is thus expected to represent less than 10% of the annual sediment flux.

In Himalayan glaciers, clockwise hysteresis in sediment load-discharge rating curve has

been described in the upper Marsyandi [Gabet 08] and further West in Garhwal Himalaya (India) [Gabet 08, Haritashya 10], and ascribed to the progressive depletion of the stock of glacier-derived sediment during the course of the melting season. Consequently, sediment flux as well as concentration in glacier sediments are generally peaking in July, whereas significant fluxes are also recorded in June [Fukushima 87, Hasnain 99, Gabet 08]. This clockwise hysteresis could be invoked to explain the hysteresis observed in Narayani suspended load record (fig. 5.4.5). However, it was shown that unglaciated catchments do present also a hysteresis similar to Narayani's one. Secondly, the "glacial sediments" hysteresis is shifted one month ahead the Narayani one : half of the sediments are delivered by mid-July in front of glaciated areas, whereas in Narayani sediment flux it occurred only by mid-August. Both arguments rule out a dominant role of the "glacial sediments" hysteresis further downstream, and confirm the role of dilution of landslide-derived sediment by groundbase flow in the origin the hysteresis observed in Narayani suspended load vs discharge.

At the Narayani outlet, glacier derived sediments are supposed to present a specific signature combining low δD composition, potentially high carbonate content and high proportion of low grain size associated to glacial flour production (median size of glacial flour ranges between ∼5 µm [Fairchild 99] and ∼30 µm [Thayyen 99, Haritashya 10]. During pre-monsoon times, a two weeks long period (Julian day 153 to 168) is characterized by relatively negative δD compositions which culminate on day 163 with δD dropping at -117 ‰. These samples correspond also to high proportion of fine grain sediment with 15 to 20% of <4.5 µm size fraction. These samples are also characterized by high carbonate proportions above 17 % that trace north range of the basin, where glaciated areas are more extensively developed. In addition, this period corresponds to the largest relative contribution (∼50%) of ice-melting to the Narayani discharge. After mid-June, despite ice-melting is still increasing until mid-July, the glacier-melt waters are diluted into increasing monsoon rainfall-derived water flux. After June 17th (Julian day 168), the δD return to more positive value, close to unweathered bedrock values (90 to 95‰), suggests that despite a probable correlative increase in glacier sediment flux until mid-July, this flux is largely hidden behind the massive supply of landslide material during the monsoon. However, a few excursions with low δD value (δD < -110 ‰) still occurred during the monsoon, such on Julian day 199. That day typically falls at the end of a one-week-long "drier" period characterized by lower precipitation, lower direct runoff and lower

concentration : during such a low monsoonal activity, isotopic imprint of glacier-derived sediments might therefore exceptionally show up in Narayani suspended load.

A basic mass balance, assuming two poles at -130 and -95 ‰ for the glacier and bedrock-derived sediment respectively, and assuming a similar degree of silicate hydration, indicates that glacial sediment may represent up to 70% (Julian day 163) of the Narayani sediments during the pre-monsoon period, and exceptionally ∼30% during low monsoon activity periods in July, like on day 199. However, during ISM, most δD values are typically between -100 and -90 ‰ values, more characteristic of south flank non glaciated areas. This rough geochemical approach, despite being limited by undersampling, confirms that the proportion of glacier-derived sediment is mostly visible during the pre monsoon period when landslide activity is weak, and accordingly that they are overwhelmed by landslide products during most of the ISM period.

5.5.3.3 Soils erosion

Soils erosion is usually expected providing fine sediments that are commonly rich in organic matter, in particular on the southern flanks of the Himalaya and further south, because of the well developed vegetation cover and associated thick soils. During the pre-ISM season, TOC values in Narayani sediments are high and sediments are fine, in clear contrast with the monsoon period, during which TOC values range around 0.2 and 0.4 % (figure 13) and sediment are coarser.

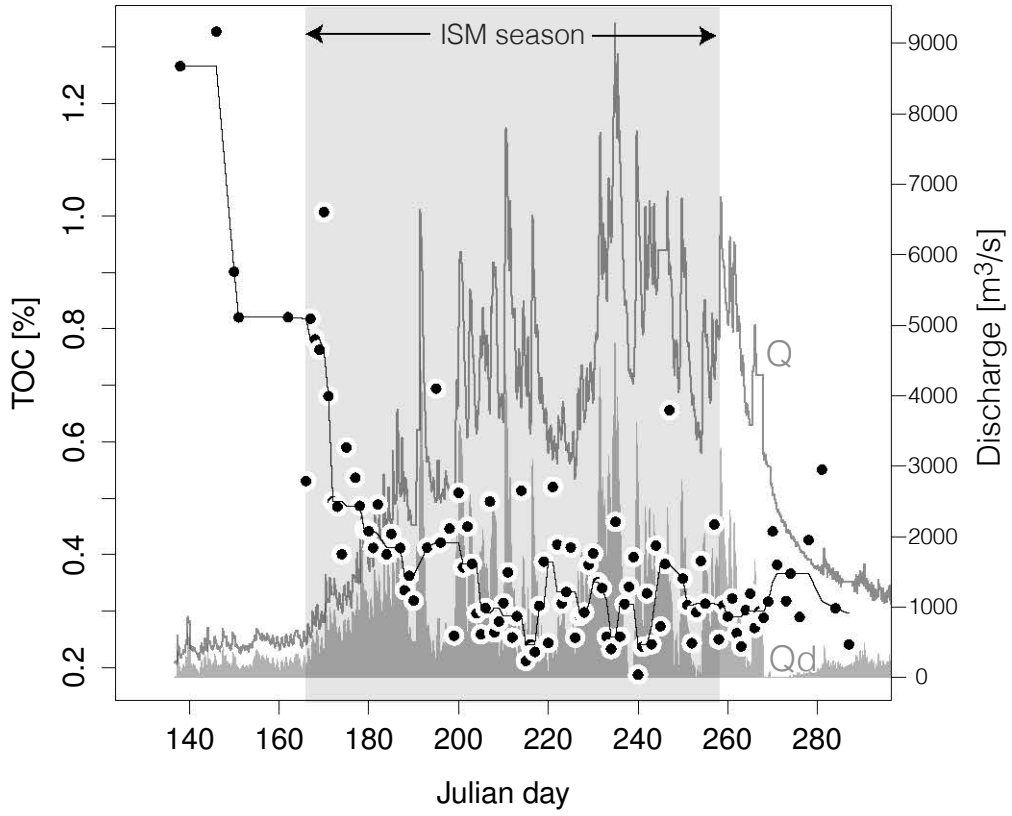

FIGURE 5.5.2 – Total Organic Carbon evolution of the 2010 monsoon Narayani suspended sediments (SNG).
Enriched in organic matter Corg in the pre-ISM-season, Narayani sediment composition reach values generally observed for bedrock during monsoon (Galy et al. 2008). This trend indicating that shallow soil erosion in pre-ISM season is dominated by landslides erosion during monsoon to become quite undetectable.

In detail, C_{org} exported with Narayani sediment describes two populations when compared to grain-size that depend on the period of sampling (A11 fig. 5.7.7). During monsoon, TOC values are comparable to Himalayan bedrock, C_{org}, and might partly correspond to graphitic carbon issued from metamorphic bedrock as described in Himalayan river sediments (Galy et al. 2007b). For this first population during monsoon, grain-size control on TOC is relatively weak, and it seems to follow the general trend identified in the major tributaries of the Ganga rivers (dashed line on fig. 5.7.7) [Galy 08]. In contrast, during the pre-ISM season, the TOC values are clearly higher than during the monsoon, and more

importantly two to three times higher than above mentioned grain-size control trend. This later observation confirm that these high TOC values are not an artefact controlled by grain size but do indicate significant addition of soil-derived material to Narayani load during pre-monsoon time. Concomitant smaller grain-size is also well compatible with a soil material signature, even if alternative explanations might be found, as low discharge and low turbulence limiting coarse grain suspension, or glaciers derived fine sediments [Thayyen 99].

In any case, combined C_{org} and small grain-size compared to average sediments let suppose that sediments derived from soils erosion occur during pre-ISM season in a sufficient proportion to be detected in the bulk sediment. To explain enrichment in soil-derived material during pre-ISM, we suppose that the first rainfall events trigger very shallow landslides, soil slides or export easily mobilized sediments produced by human activities such as agricultural practices, or might flush away dead vegetation (dead leaves) or litter that accumulated during the dry season within the low order channels and talwegs bottoms.

At the end of June (Julian day $\sim$180), Narayani sediment TOC reaches the bedrock value and then remains stable and low. For that period, we cannot, however, elucidate if easily mobilized Corg-rich material is depleted after having been flushed away during early monsoon, or if the soil-signature is simply overwhelmed by landslide-derived material.

Estimating an exact budget of soil-rich material in the Narayani sediment flux is out-of-reach from available data. However, considering that less than < 5 % of the annual sediment budget have transited in Narayani when soil erosion stops being detectable in the bulk sediment (i.e. around julian day 180), and considering that part of this flux is also related to glacier sediments, we suspect that soil erosion contributes only to a maximum of a few % to the Narayani erosional budget.

All above considerations, including sediment load response to rainfall and hydrology, cumulative curve of sediment flux (fig. 5.4.8) the relative stability during ISM of the geochemical signature in TOC and δD (except a few bursts of northern-derived sediments with δD excursions toward negative values) with values close to bedrock average signature, confirm that landsliding is the dominant erosion process in central Himalaya and that landslides-derived sediments overwhelm glacier and soil products from ISM onset.

5.5.4 Dynamics of the Himalayan supply-limited geomorphic system

Besides the geochemical signature or the load concentration that reflect specific provenance or a dominant erosion process, our data present a striking high frequency content whatever we consider concentration, TOC or carbonate content : compositions can vary abruptly from one day to another. Such feature indicates that the origin of sediments, whatever it is related to distinct geographic sources or erosional processes, may vary quite abruptly through the season. This suggests first that rapid changes essentially respond to local events and meteorological conditions, such as the intense rainfall event on day 171 which briefly interrupt the glacial sediment imprint, with a sudden rise in δD value and TOC, and a drop in carbonate, before a return to former tendency in only one or two days. It implies that residence or transfer time of suspended sediments in such wide Himalayan basin can be remarkably short.

Assuming average water velocities of 3 to 5 m/s in the Narayani river network during monsoon, the time transfer for water from headwater of major tributaries (over distance of 200 to 300km for Kali, Marsyandi, Trisuli) down to Narayangad range between 10 and 30 hours. The water transit time from the southern flank, which receives more precipitations, is around two times lower. This appears in good agreement with the absence of delay and remarkable time correspondence between daily rainfall and direct discharge.

High reactivity of the sediment export system suggests that suspended load travel almost as fast as water from the eroded hillslopes, and more importantly that there is no exchange or mixing with reworking of fine sediment storage along the river network channels. Field observations document several sand bars along the lower Trisuli for example. However, it seems that their volume or the dynamic of their re-erosion during flood is not sufficient to exchange in large proportions with transported load and to dampen geochemical signatures. In other words, the Narayani fluvial network does not present any memory with regard to silt and fine sand load. This fully demonstrates that the Narayani geomorphic system is definitively not transport-limited but supply-limited, and that carried sediment load is primarily depending on sediment delivered by landslides on hillslope.

Complementing that scheme, post-monsoon period is illustrative of how the system respond to sediment shortage from hillslope. As soon as the heavy monsoonal rainfall

stops, the sediment concentrations drops below 0.5 g/l. Concomitantly, we observe a drastic grain-size increase that cannot be attributed to sources effect as hillslope have stopped delivering material to the river network. This clear grain-size rise at the limb of monsoon corresponds more likely to processes occurring in the river network itself. Indeed, river discharges and consequently transport capacity are still high enough to transport sediment and also probably to partially move bedload on channel bottom. At least three processes, which are not exclusive from each other, can be invoked to interpret grain-size trend. First, a difference of travelling velocity between fine sand, that transit mostly as wash load and suspension, and coarse sand, that transit in suspension and saltation. The coarser particles would therefore be delayed and would arrive several days after their finer counterpart. Second, the re-erosion of sediment storages, as sand bars, that will tend to be increasingly depleted in fine grains during that process. Third, the remobilisation during bedload transport of the interstitial sandy fraction, which is generally much coarser than average suspended load.

5.6 Conclusion

The acquisition and analysis of a new dataset on the suspended load concentration and geochemical characteristics at the mountain outlet of one of the largest Himalayan rivers bring several important results and new perspectives.

1. From a methodological point of view, our depth sampling shows that even in a turbulent system like the Naryani river a vertical gradient in concentration is still persistent, and our study emphasises on the necessity for accounting this effect in order to calculate the sediment fluxes. Based on discrete depth sampling and on daily surface sampling of suspended load associated to flow characterization through ADCP measurements, we were thus able to provide a new model to integrate sediment flux across a river cross-section and over time. Bringing additional constrains on bedload flux, which can hardly be measured in such large and powerful river, we provide an estimate for 2010 year equivalent erosion rate of $1.8^{+0.35}_{-0.2}$ mm/a. Finally, by integrating over the last 15 years the past sediment load records from the Department of Hydrology and Meteorology of Nepal, we revised the previously proposed average erosion rates for Central Nepal erosion rate with a tighter estimate of $1.6^{+0.3}_{-0.2}$

mm/a. This rate is in close agreement with the longer term (∼500 yrs) denudation rates of 1.7 mm/a obtained from cosmonuclides in Narayani river sands (Lupker et al. 2012a), which suggests that long term Himalayan erosion budget is mostly driven by yearly monsoon impact. And even if variability in monsoon strength or mass-wasting on hillslope from one year to another seems to induce significant inter-annual variability in the sediment fluxes, the sporadic and extreme mass-wasting events, like the ones associated to co-seismic landslides, appear to have therefore little direct impact on the long term Himalayan erosion budget.

2. By analysing sediments fluxes and using geochemical compositions in δD, carbonates content and TOC, which we propose as possible tracers for glacier- and soil-derived material, we show that glacier and soil erosion contribute to annual erosion budget to less than 10% and a few % respectively. Their imprints in Narayani sediment is only visible during the pre- and early monsoon before being overwhelmed by landslide-derived material during the monsoon.

3. Our data confirm [Gabet 04a] inference that sediment export and possibly landslide triggering on Himalayan hillslopes are controlled both by pore pressure and daily rainfall intensity. The control by pore pressure, which is related to cumulated precipitation during monsoon, partly explains why the total sediment budget progressively builds up during two and half months rather than results from a few extreme events of heavy rainfalls. In any case, we confirm the previously proposed interpretation of a major control of ISM rainfalls on sediment mobilization through the triggering of bedrocks landslides [Andermann 12b].

4. The high variability of the daily geochemical signature in suspended load and the absence of delay between high rainfall episodes and sediment export despite distance of hundreds of kilometres between the sediment sources and the mountain outlet in Narayani basin suggest very short transfer time for silt and medium sand load. This implies a very reactive geomorphic system, which is strongly supply limited relative to the fine sediment fraction.

5. The fact that the total sediment flux is dominated by the signature from landslide-derived material, and that glacier- or soil-derived signatures would represent less than 10% each implies that in central Himalayas even a doubling of soil or glacier contribution to sediment budget might difficult to identify in sedimentary ar-

chives. This might explain why studies on sediment cores spanning the last glacial-interglacial transition, in the Ganga plain (Morin et al., in prep.) or in the Bengal fan [Lupker 13], show relatively unchanged provenances and were not able to evidence any past increase in glacial erosion during the LGM, or in soil stripping following a more arid climatic period.

5.7 Appendices

A1

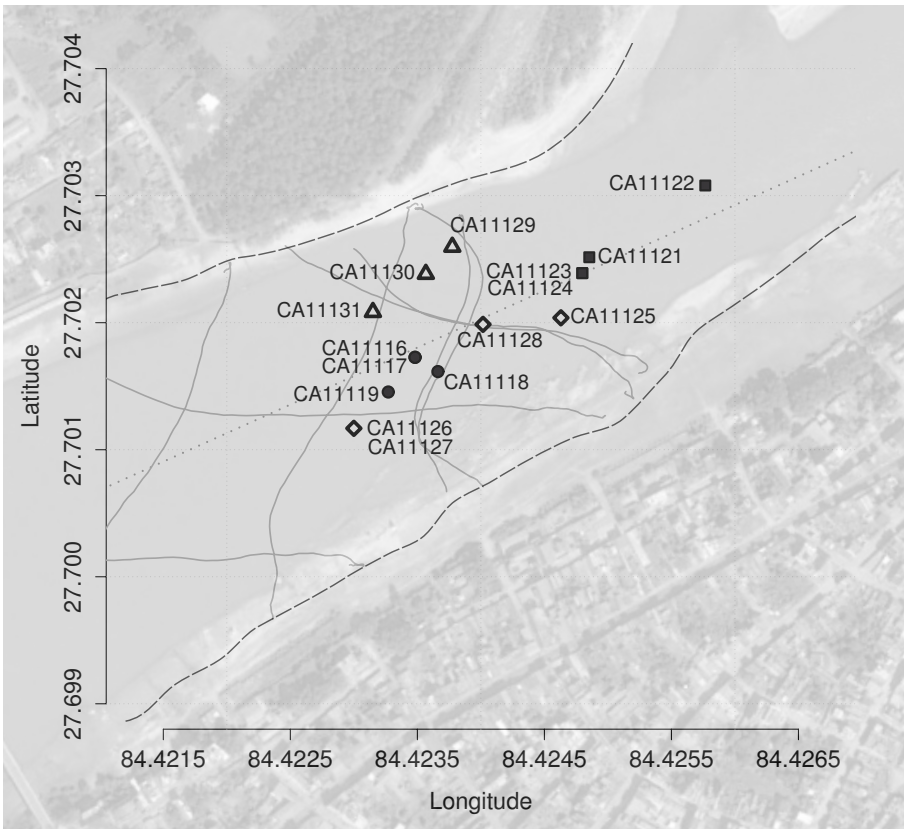

FIGURE 5.7.1 – Detailed locations of 2011 sediment depth-samples upstream Narayanghat bridge area.

A2

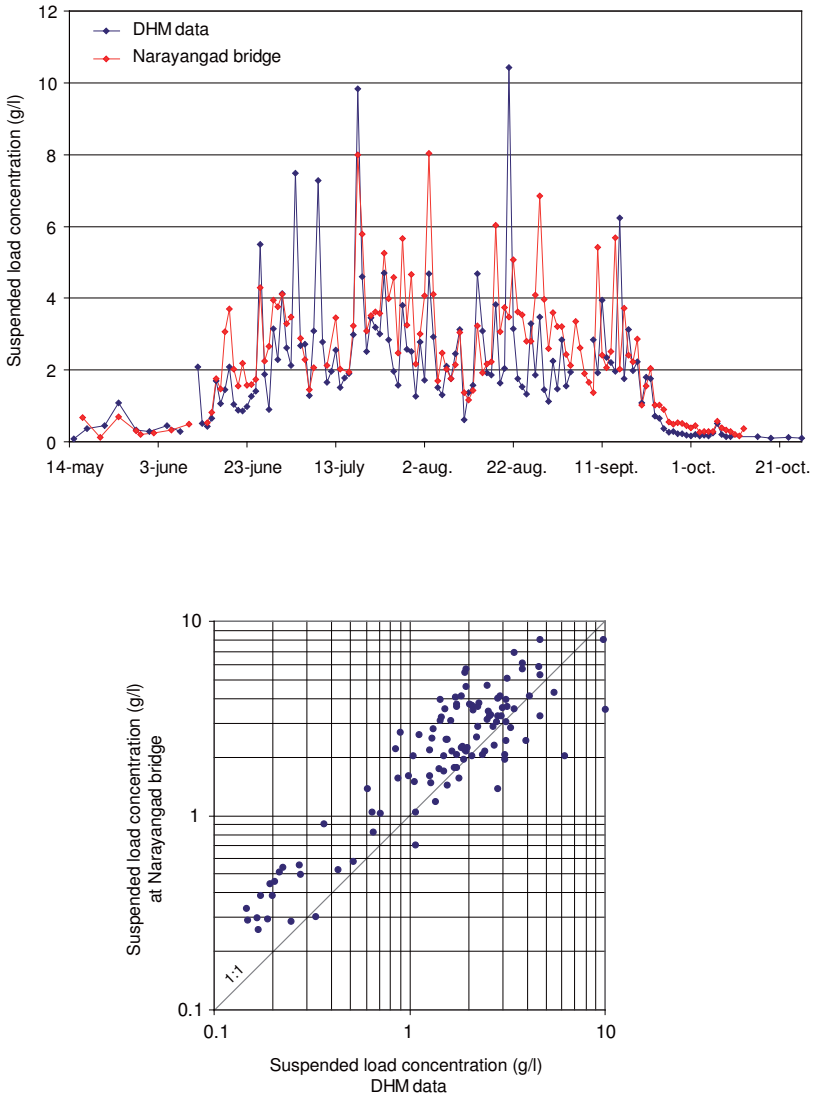

FIGURE 5.7.2 – Comparison between our daily measurements of suspended load made at the middle of Narayangad bridge
with DHM sampling on left bank of Narayani, 3km upstream at the DHM gauging station. (a) Daily comparison ; (b) XY graph comparison highlighting a 1 :1 slope between both datasets, but with a 1.18 factor difference.

A3

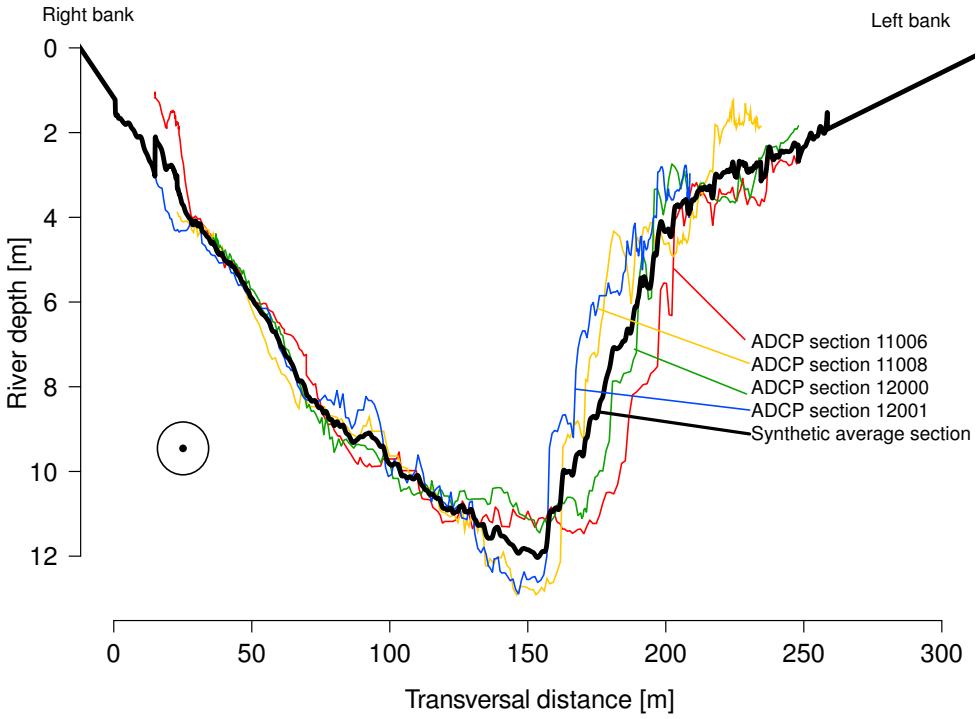

FIGURE 5.7.3 – Synthetic river channel topography in the zone of sampling defined by combining ADCP profiles # 11006, 11008, 12000, 12001.

A4

Water velocity depth-profile

Water velocity depth-profile Integration of the suspended sediment flux through a whole river wetted section requires the description of the water velocity over that section, assuming that suspended load is moving jointly with water, i.e. with similar horizontal velocity. The water velocity depth-profile is controlled by the bottom roughness z0 and the velocity u(z) at an elevation z above the local channel bottom and can be expressed using is the widely used law of the wall (Eq. 1) :

$\frac{u(z)}{u*} = \frac{1}{\kappa} ln\left(\frac{z}{z_0}\right)$ (Eq. 1)

where, u* is the shear velocity, related to the average boundary shear stress τb such that $u^* = (\tau b/\rho)^{1/2}$ (2)

κ the von Karman constant, z the depth, z0 the bottom grain-scale roughness. In theory such equation is considered as valid only for the lowest part ($\sim$1/3) of the water column, but following [Sime 07] we apply it to the whole water column.

Energy slope

In above equation, deriving the vertical velocity profile requires to first compute u* and therefore $\tau b = \rho \cdot g \cdot H \cdot Se$ by relationship to because (where ρ is the fluid density and g the gravity constant taken at 9.807 m.s^{-2}), which gives the expression of $u^* = (g \cdot H \cdot S)^{1/2}$. Empirical relationship between discharge Q and surface slope $Se = u^{*2}/g \cdot H$ was established based on the results of ADCP integrations and the rating cuve Q=f(H).

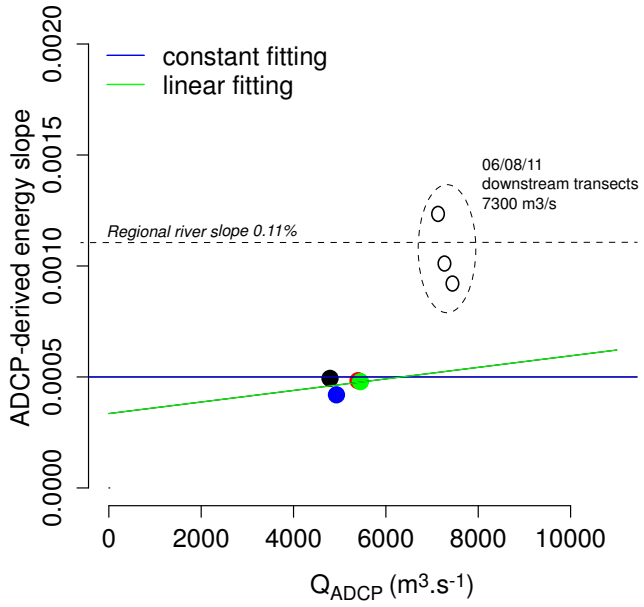

FIGURE 5.7.4 – River water surface slope relationship to discharge Q derived from u* computation measured by ADCP.

The linear relationship considered (see figure 5.4.1) was used to compute depth sediment fluxes qz detailled in results section 4.4. using the equation of the law of the wall integrated

along the water column in uniform regimes [Wilcock 96] (c.f. Eq. 2).

$u^* =< U > \cdot \kappa \cdot ln \cdot \left(\frac{e}{e \cdot z_0}\right)$ (Eq. 2)

where <U> is the velocity average, h the water depth (m), e the base of natural logarithms. We used Eq. 2 to compute shear velocity u* from velocity profiles measured by ADCP for all transects, a method that proved to provide a better estimate of u* from ADCP data than direct fitting of the law of the wall [Sime 07, Lupker 11a] .

Bedload roughness ks were deduced from gravel bars grain-size analysis.

Data are from literature and reported in the following table.

Gravel bar layer investigated	Average D50 (mm)	ks ~ 3*D50 (mm)	z0=ks/30 (10^{-3}m)	Sources
surface	100	150	5	[Mezaki 84]
surface	100	300	10	[Attal 06]
subsurface	70	210	7	[Attal 06]
surface	67	201	6.7	[Dingle 12]
average	*72*	*215*	*7.2*	

A5

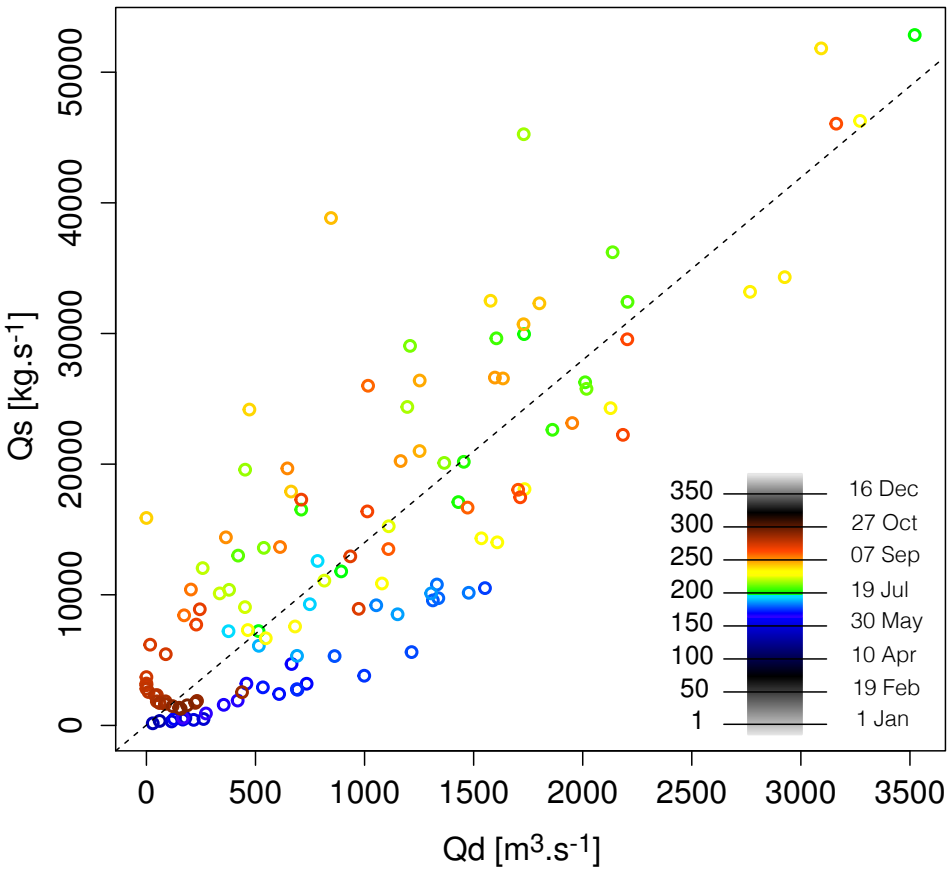

FIGURE 5.7.5 – Sediment discharge Qs as a function of direct runoff discharge Qd for the 2010 monsoon.

A6

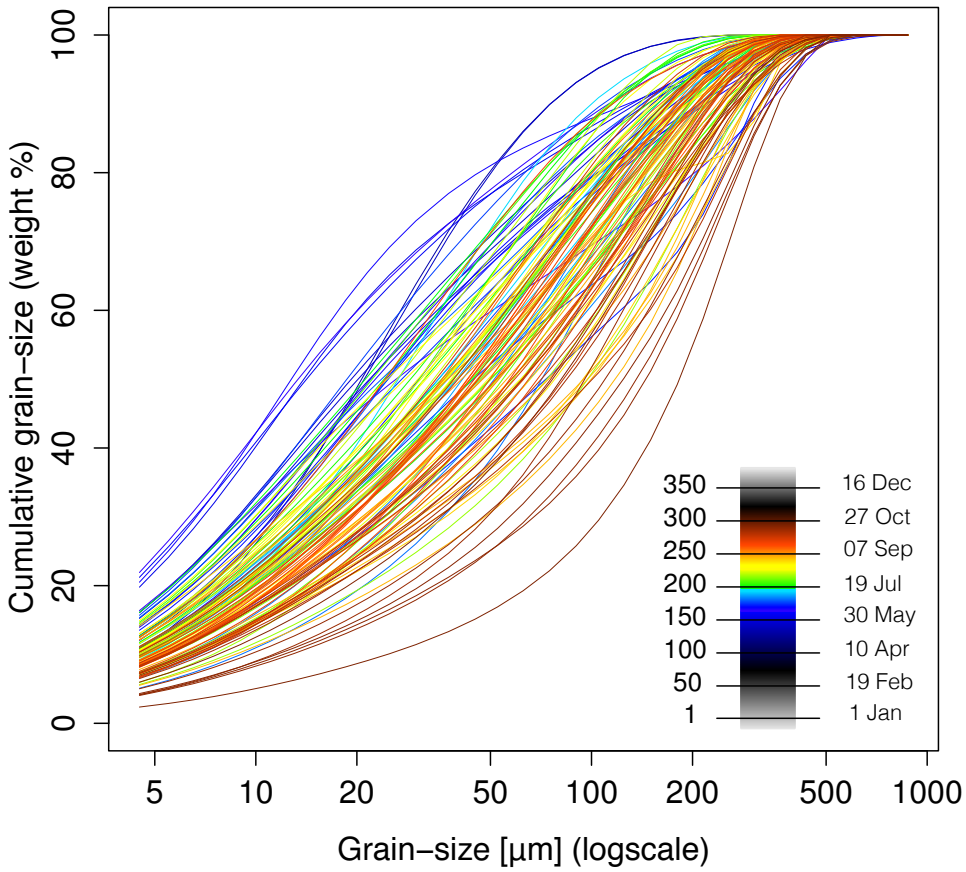

FIGURE 5.7.6 – Cumulative 2010 monsoon Narayani suspended sediment grain-size spectrum

showing clearly the progressive coarsening of grain-size from the pre-ISM season (blue lines) to the ISM season (green-yellow lines) corresponding to a change of supply from hillslope, and the washing relaxation of the river drainage corresponding to transport effect (dark red lines).

A7

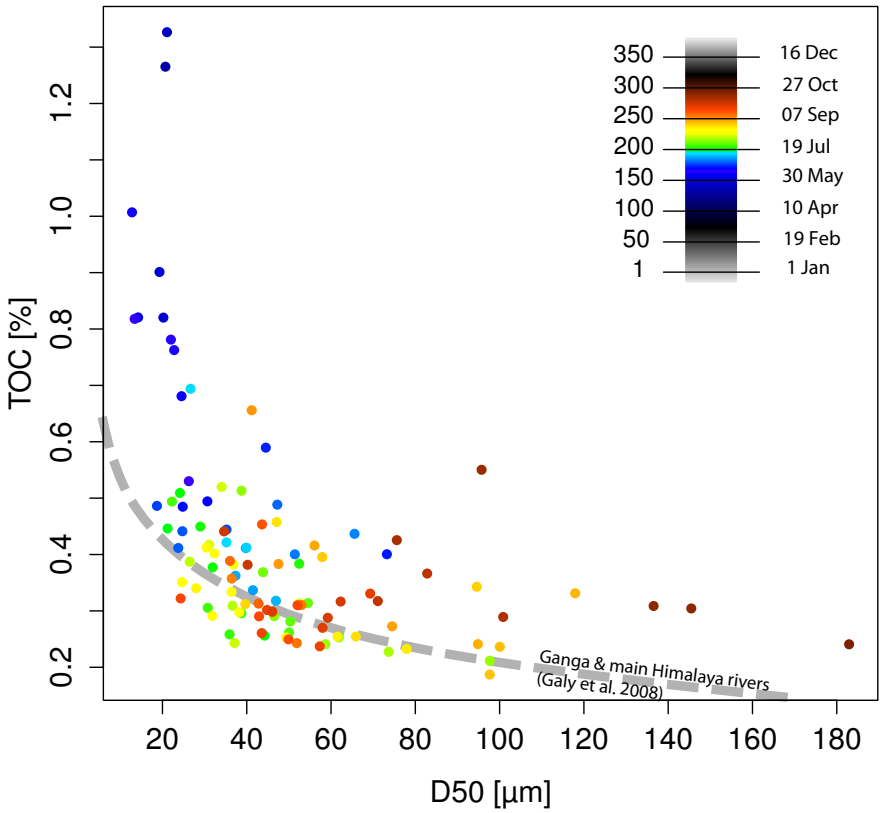

FIGURE 5.7.7 – Grain-size control on TOC in the monsoon Narayani suspended sediment (SNG).

Fine and Corg rich sediment during pre-ISM constitute an out-member population from the general monsoon Narayani sediment displaying coarse calibers and TOC comparable to bedrock. This could be explaind by two different hillslopes supplies, the pre-ISM sediment likely deriving from soil erosion while the monsoon rom landslides.

A8

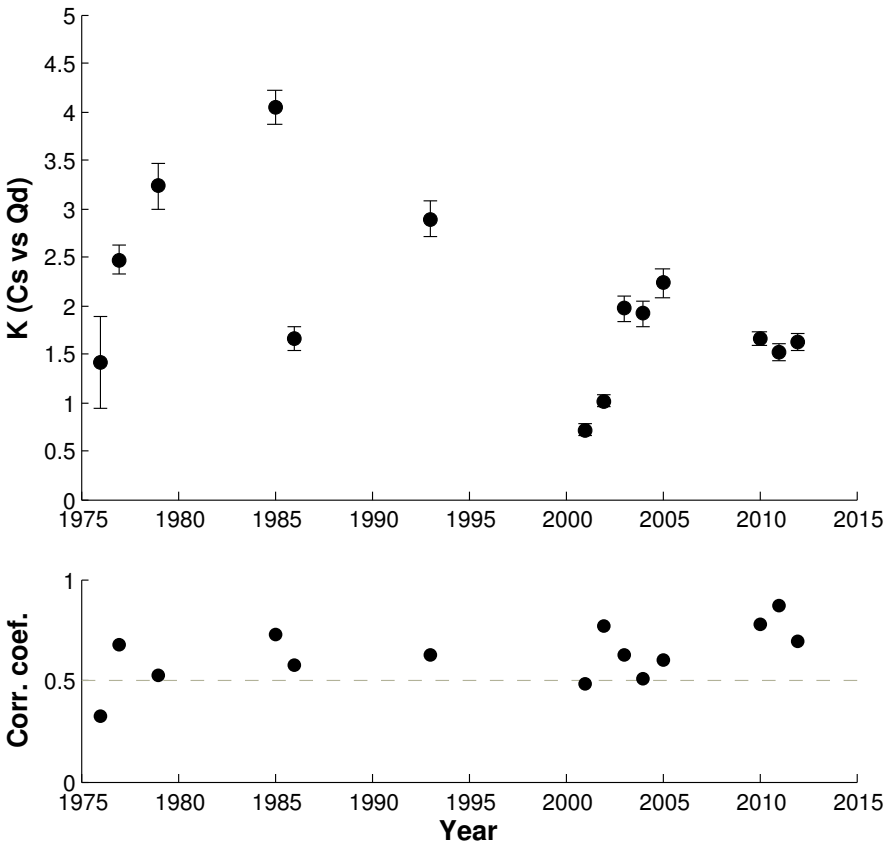

FIGURE 5.7.8 – (a) Annual variations of the slope coefficient k1 in the regressed rating curve between direct discharge and suspended load record of the DHM data set
(daily measurements over 14 discontinuous years). (2) Corresponding coefficient of correlation r^2.

VI

Chapitre 6

Évolution récente de l'érosion et de l'altération au Népal central par analyses des molasses de la plaine de la Gandak.

Nous avons réalisés trois forages dans la plaine de la Gandak pour regarder comment l'érosion de la chaîne du Népal central a répondu aux changements climatiques du Dernier Maximum Glaciaire et au cours de l'Holocène. L'investigation des provenances géologiques des sédiments ont été réalisés par l'analyse de leurs compositions isotopiques en Sr et Nd et par la détermination des proportions de carbonates. L'évaluation des proportions de sédiment provenant de chacun des agents érosifs (glissements de terrain, sols, glaciers) a été abordée avec les même traceurs qu'utilisés dans les sédiments de rivières actuelles : compositions en éléments majeurs, contenu en matière organique et hydratation pour le traçage des sols, proportions de carbonates et compositions isotopiques δD des hydroxiles d'hydratation pour le traçage des glaciers.

6.1 La plaine de la Gandak et le mégafan

La plaine du Gange est le bassin sédimentaire continental qui borde le sud de la chaîne himalayenne ; il est alimenté par les sédiments provenant des principales rivières Hi-

malayennes. La Narayani qui draîne le Népal central se prolonge dans la plaine Indo-Gangétique en prenant le nom de Gandak. La plaine d'inondation de la Gandak ainsi que le cône alluvial que la rivière représentent les structures sédimentaires principales du piémont du Népal central. Ces objets sont constitués des molasses Himalayennes et ont encore été assez peu étudiés jusqu'à présent.

Comme précédemment évoqués dans le Chapitre 2, les grands cônes alluviaux ou « mégafans » observés à l'embouchures des bassins himalayens dans la plaine du Gange, résultent probablement de la déviation des rivières himalayennes par la formation des reliefs Siwaliks. Ces dernières auraient été déviées par la formation des reliefs Siwaliks au front et capturées par les 4 rivières principales du Népal [Gupta 97]. Le mégafan de Narayani-Gandak a fait l'objet de peu d'études, et on ne reporte que deux études qui ont réellement caractérisé le mégafan, l'une portant sur la géomorphologie de la plaine de la Gandak [Mohindra 92], l'autre sur la stratigraphie en sub-surface [Sinha 14].

Localisations des forages

Les trois forages GR1, GR2 et GR3 atteignent 50 m (GR1 et GR3) et 55 m (GR2) de profondeur. Ils ont été forés en Inde près de la ville de Bettiah (GR1 : N26.9084 E84.2938 à Dhudhiwan Dharwan, GR2 : N26.8161 E84.1458 à Bhodhrahra Buzunge, GR3 : N26.7591 E83.9003 à Shapar Kaisa) cf. figure 6.1.1.

Le choix de la localisation des forages devaient répondre à trois critères :

1. Forer le fan de la Narayani-Gandak pour échantillonner les sédiments issus de l'érosion du bassin Himalayen de la Narayani.
2. Rester suffisamment loin du front de galets qui aurait stoppé la progression des forages (cas observé sur le mégafan de la Kosi, se reporter à l'article [Sinha 14]). La progression du font de galets, qui répond aux processus d'érosion et aux régimes hydrologiques, a été estimée à environ 15 à 20 km en aval du MFT [Dubille 15].
3. Être réalisés à la même distance de l'apex du fan pour prévenir les hiatus stratigraphiques potentiels dus aux avulsions fréquentes de la rivière.

Les forages ont été placés au pied de la structure de cône alluvial de la partie nord du mégafan que l'on nomme apex (cf. figure 6.1.1). Le mégafan de la Gandak ne présente que de faibles pentes en moyenne 0.02% (cf. figure 6.1.2) et se distingue moins dans la topographie que ses homologues de la Kosi ou la Tista dont les pentes moyennes sont de

0.03% et 0.05% respectivement [Chakraborty 10a, Chakraborty 10b]. Environ 70 km en aval de l'entrée de la Narayani dans la plaine, le choix des sites de forages permettait donc une bonne progression des carottages ainsi qu'un impact mineur des effets du transport dans la plaine sur la nature des sédiments. Un temps de séjour long dans la plaine est susceptible d'effacer le signal passé : mélange et remaniement du signal, altération des sédiments [Lupker 12b, Bouchez 12, Lupker 12a].

D'après les forages réalisés dans la plaine du Gange à l'IIT Kanpur, une profondeur de 50 m devait permettre d'atteindre des âges de 50 ka [Rahaman 09] et donc le dernier maximum glaciaire (DMG ou LGM) situé autour de 20-18 ka BP.

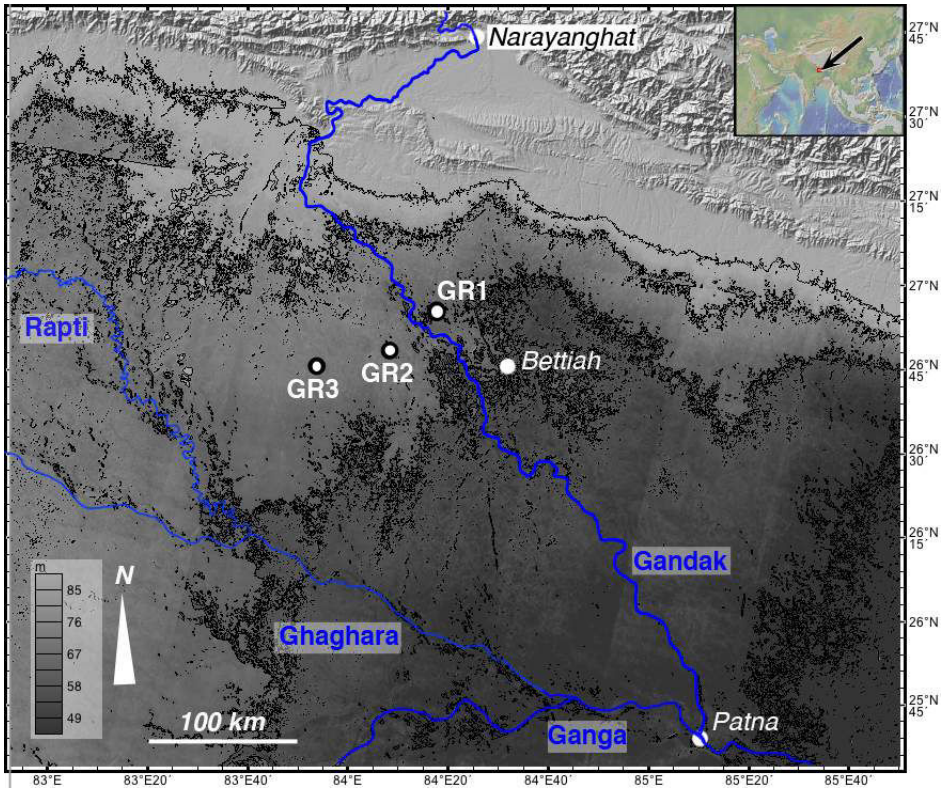

FIGURE 6.1.1 – Topographie et localisation des forages dans la plaine de la Gandak. (Données SRTM)
Les lignes de niveau sont espacées de 20 m en altitude. Cette résolution permet de visualiser la structure proximal du cône alluvial de l'apex du mégafan de la Gandak.

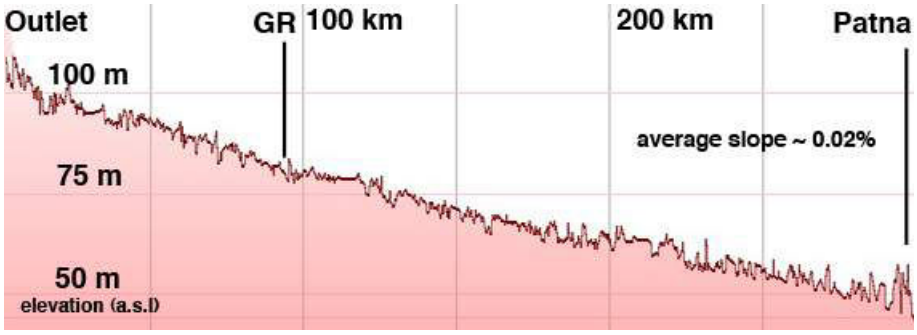

FIGURE 6.1.2 – Profil longitudinal du mégafan de la Gandak.
Le megafan présente de faibles pentes 0.02%, moins marquées que les mégafans de la Kosi et de la Tista.

Méthode de forage

Le diamètre de forage est de 5 cm (2 pouces) et les tubes de carottages sont en PVC. La progression du carottage se fait par étape de 2 m. À chaque progression de 2 m, le train de tige contenant le tube et la carotte sont remontés, le tube contenant la carotte est retiré et scellé, et est remplacé dans le train de tige par un tube neuf. Le train de tige est ensuite replacé à la profondeur précédente, la profondeur est contrôlée par la longueur du train de tige. Pour forer 50 m le procédé peut prendre plusieurs jours.

6.2 Stratigraphie des forages.

6.2.1 Article : « Shallow subsurface stratigraphy and alluvial architecture of the Kosi and Gandak megafans in the Himalayan foreland basin, India »

Cette étude est issue du travail d'exploitation des données acquises par sondage électrique vertical et des logs stratigraphiques des forages hydrologiques ou « puits » dont l'équipe disposait. Par comparaison empirique des résistivités avec les observations lithostratigraphiques réelles des puits, une architecture des dépôts alluvionnaires de subsurface a été proposée. Cette étude devait nous servir de diagnostique pour déterminer la présence en profondeur de paléo-chenaux enfouis, et déterminer la position des forages dans la plaine. Or, compte-tenu de la faible résolution spatiale de la méthode, et de l'absence de

diagnostic clair sur la présence de galets, nous avons préféré nous baser sur la topographie.

Je vous invite à vous reporter à l'annexe 1 pour de plus amples détails sur l'interprétation de l'architecture sédimentaire de subsurface de la plaine de la Gandak.

6.2.2 Lithostratigraphie des forages

Le *logging* lithostratigraphique des carottes de forages a été effectué à l'IIT Kanpur, dans les locaux du Core Archive and Analysis Facility au département de « Civil Engineering ».

Les forages de la plaine de la Gandak semblent analogues aux sables de rivière actuels en terme de granulométrie, nature et chimie, et présentent toutes les caractéristiques de paléo-chenaux enfouis. La variabilité des lithofaciès (cf. figure 6.2.1) balaie un spectre large en terme d'énergie de dépôts en variant de faciès sableux de haute-énergie correspondant à des paléo-chenaux, aux dépôts de faibles énergies dominés par les faciès silto-argileux de plaines d'inondation, parfois lacustres tels que des « oxbows-lakes »[Jain 03], une variabilité qui est décrite dans les sédiments du Gange [Singh 91].

Nous n'avons pas observé de structure érosive basale évidente pouvant témoigner d'une séquence stratigraphique fluviatile classique. Cependant, l'alternance de passées sableuses entrecoupées d'horizons argilo-silteux témoigne du caractère avulsif de la rivière. Le caractère résolument sableux de GR1 et GR2 et la présence de galets dans GR1 démontrent des niveaux d'énergie relativement importants.

Ils correspondent en tous points aux dépôts proximaux observés au niveau du mégafan de la Tista [Chakraborty 10a] et de la Kosi [Chakraborty 10b]. Au niveau de GR3, on distingue clairement deux « blocs » de paléo-chenaux entre 44 et 22 m puis entre 15 et 3 m espacés d'un épisode de plaine d'inondation de 22 à 15 m. Ces épisodes franchement argileux correspondent probablement à une période de quiescence lors de laquelle le site était éloigné de l'influence de la rivière et où les dépôts ont été alimentés par des rivières de plaines comme observé dans les parties distales du mégafan de la Tista [Chakraborty 10a].

Tout indique que les passées sableuses correspondent à des paléo-chenaux de la Narayani-Gandak et qu'il s'agit donc de sédiments issus de la chaîne du Népal central. C'est aussi l'interprétation qui en a été faite lors de la campagne géophysique de détermination de la stratigraphie sub-surface par sondages électriques [Sinha 14].

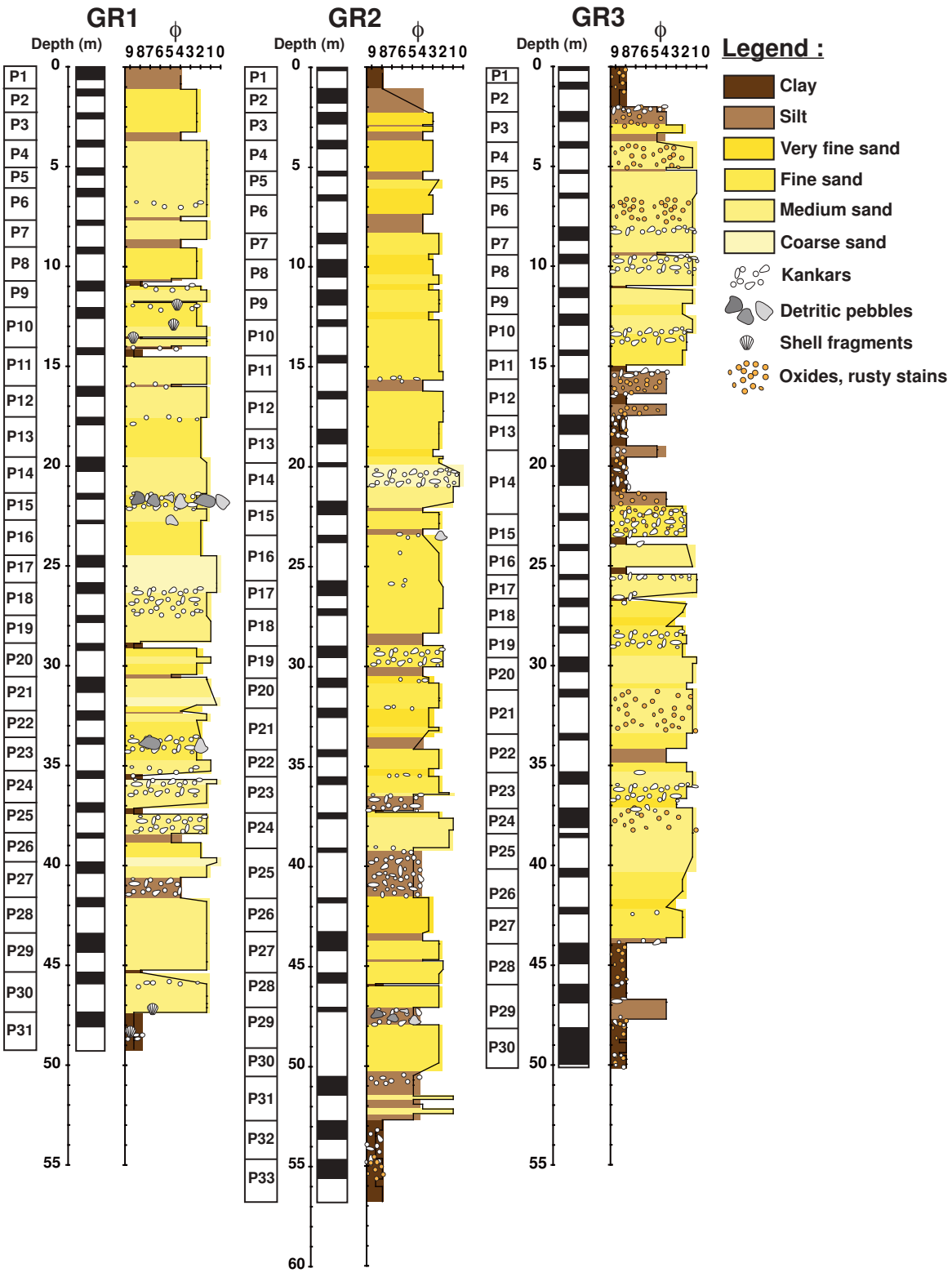

FIGURE 6.2.1 – Logs stratigraphiques des forages GR.
En ordonnées, la profondeur en (m), en abscisses le ϕ moyen des grains par observation à la loupe binoculaire, les taux de récupérations sont figurés en noir.
Les forages sont essentiellement constitués de sables de rivière fins à grossiers correspondant à des chenaux enfouis, et de passées argileuses correspondant à des dépôts de plaine d'inondation.

Le sable des carottes n'était pas induré (cf. figure 6.2.2 A) ce qui a compliqué la récupération lors du forage, la récupération moyenne se situe autour de 30% dans les parties des forages correspondant aux paléo-chenaux (cf. figure 6.2.1). À l'inverse, les faciès fins silto-argileux plus compétents (cf. figure 6.2.2 B) correspondant à des dépôts de plaine d'inondation ont permis de meilleurs taux de récupération de 75-90% (cf. figure 6.2.1). La lithologie des manques dans les séquences de forages ont été estimées par dilatation des lithologies observées dans les carottes. Ce procédé peut induire un biais mais nous a semblé raisonnable au vu de la faible variabilité des lithologies au sein des carottes, et entre deux carottes adjacentes.

FIGURE 6.2.2 – Exemples de carottes de forage.
En A, exemple typique d'une carotte de forage. Le facies dominant est constitué de sable grossier à moyen de type « *salt and pepper* » non induré. Ce type de facies correspond à un paléo-chenal enfoui (ici GR2P8). En B, exemple d'une carotte de forage dominée par des facies silto-argileux et contenant des carbonates pédogéniques « kankars ». Ce type de facies correspond à des dépôts de plaine d'inondation (ici GR3P28).

6.3 Datations des forages.

Dans ce contexte sédimentologique, les techniques de datations absolues se sont limitées aux matériaux dont nous disposions à savoir : les quelques charbons et résidus végétaux retrouvés et datés par ^{14}C, les sables contenant quartz et feldspaths ont été datés par OSL-IRSL en single-aliquot et single grain, et enfin la matière organique bulk des sables a été datée par ^{14}C après extraction séquentielle par pallier de température au « dirt-burner ».

Dans le premier forage noté GR1, nous avons trouvé des échantillons de résidus végétaux dont les datations se sont révélées cohérentes. Nous n'avons cependant pas eu cette chance dans GR2 et GR3. De tels échantillons de débris végétaux sont rarement rencontrés dans

ces types de dépôts principalement constitués de sables d'origine fluviatile. Face au faible nombre de charbons ayant permis une datation classique, et afin d'affiner les âges modèles de GR1 et d'obtenir des contraintes temporelles sur les enregistrements GR2 et GR3, nous avons opté pour des méthodes de datation par OSL et post-IR-IRSL.

Ces méthodes sont largement utilisées en archéologie pour dater des dépôts quaternaires, mais souffrent de contraintes techniques fortes : capacités du réseau cristallin des quartz à emmagasiner les électrons excités, terme de fuite ou « shading » désexcitation spontanée des feldspaths, dans le cas d'analyse en single-aliquot, les populations de grains peuvent aussi donner des âges très dispersés car ils n'ont séjourné qu'insuffisamment à la lumière du soleil (et partiellement « remis à zéro ») lors du transport fluviatile et avant leur enfouissement. Face aux difficultés de datations par méthode single-aliquot OSL - IRSL, nous avons commencé des datations par OSL-IRSL sur single grain. Cette piste semble prometteuse.

Nous avons aussi choisi d'explorer une piste de datation au ^{14}C par extractions séquentielles de la matière organique bulk des sédiments. Cette méthode qui demande d'analyser à l'AMS toutes les fractions extraites d'un seul échantillon s'est révélée onéreuse et les résultats « étonnants » sont sujet à discussion.

6.3.1 Datations ^{14}C des charbons par AMS

Les charbons ont été prélevés lors des deux missions de *logging* et d'échantillonnages des forages en février 2012 et mai 2013.

Description

Les résidus végétaux et composés organiques sont rarement rencontrés dans les forages de la plain du Gange. En effet, l'hydrogéologie y est gouvernée par le phénomène de mousson, et provoque une forte saisonnalité hydrique induisant alternativement un fort rabattement de nappe pendant la période sèche, et un ennoiement en surface lors d'inondations pendant la mousson. L'amplitude des variations de hauteur de la zone vadose est donc importante entre saison sèche et humide. Les sédiments déposés sont donc exposés à des épisodes oxiques chaque année. Ainsi, les résidus de matières organiques subissent certainement plusieurs cycles d'exposition à l'environnement vadose oxydant avant d'être suffisamment enfouis et de passer sous la limite de nappe à l'étiage, envi-

ronnement plus réducteur où ils sont plus susceptibles d'être conservés. Généralement inclus dans des dépôts très fins et argileux, les fragments végétaux retrouvés sont probablement issus de l'enfouissement de débris lors de phases d'inondation de la plaine et/ou de l'enfouissement de sédiments lacustres, comme en témoignent les coquilles de bivalves et gastéropodes retrouvés dans les facies fins. C'est probablement parce qu'ils étaient hermétiquement protégés dans leur gangues argileuses que les fragments végétaux ont été conservés. Les charbons prélevés sont constitués de petits morceaux de bois putréfié ou carbonisés d'échelle sub-centimétrique (cf. figure 6.3.1). Les conditions oxydantes, la dégradation par les micro-organismes présents dans les sols et les aquifères, et le remaniement des dépôts par migration de la rivière ne permettent de préserver ce types de débris végétaux que très rarement.

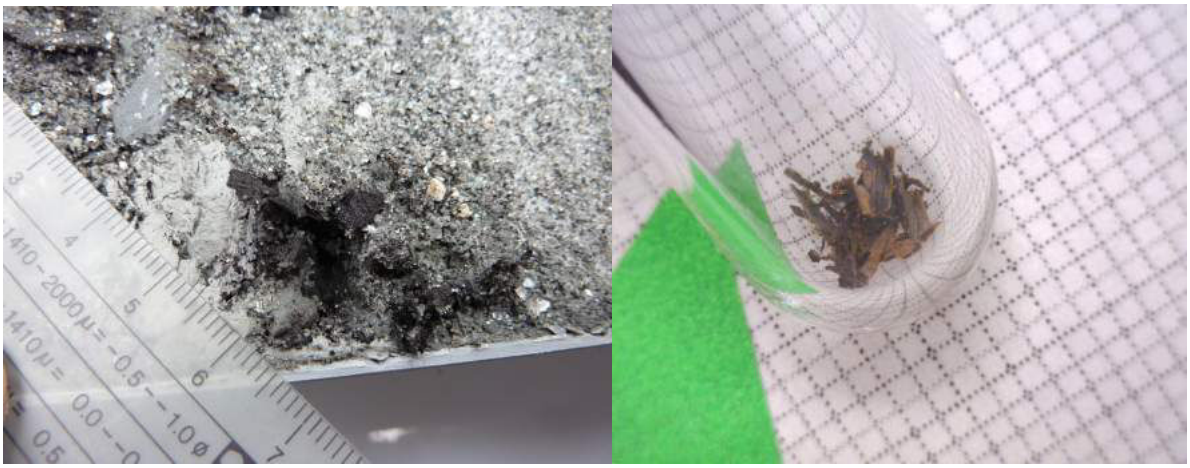

FIGURE 6.3.1 – Exemples de charbons et débris de bois putréfiés prélevés dans le forage GR1.
Les débris végétaux préservés d'échelle sub-centimétrique ont été trouvés inclus dans des facies argileux qui semblent les avoir protégés de la dégradation.

Analyses et résultats

Ces datations ont été réalisés par l'entreprise BETA-Analytics. Les échantillons ont été pré-traités par une méthode classique d'attaques séquentielles Acide - Base - Acide. Cela permet de supprimer toute trace de carbonates encore présents dans les échantillons. Les résidus subissent une combustion et le CO_2 produit est ensuite graphitisé avant passage à l'AMS.

Les résultats de datations des charbons du forage GR1 sont présentés si dessous (cf. tableau 6.1). Les âges obtenus à 13 et 14 m semblent jeunes mais restent probables si l'on considère que les chenaux en tresses de la Gandak sont susceptibles de déposer rapidement 5 à 10 m de sédiments, au cours de l'inactivation d'un bras ou de l'avulsion de la rivière. L'âge de ~32 ka obtenu à 36 m de profondeur laisse supposer que le fond des forages doit correspondre à des dépôts de 45 à 50 ka.

sample #	depth (m)	meas. radiocarb. age	conv. radiocarb. age	age 2s.d. calib. IntCal 13	Acc. rates (mm/a)
GR1P10 D	13	1760 +/- 30 BP	1740 +/- 30 BP	Cal BP 1714 to 1564	7.6 to 8.3
GR1P10 B	14	2370 +/- 30 BP	2370 +/- 30 BP	Cal BP 2490 to 2338	5.6 to 6
GR1P24 B	36	28080 +/- 130 BP	28260 +/- 130 BP	Cal BP 32661 to 31600	1.1 to 1.1

TABLE 6.1 – Datations au ^{14}C par AMS des charbons prélevés dans GR1. Les âges radiocarbone conventionnels ont été convertis en âges calendaires par la calibration IntCal13 [Reimer 13].

6.3.2 Autres méthodes de datation

Optically Stimulated Luminescence « OSL » et post - InfraRed - InfraRed Stimulated Luminescence « post-IR-IRSL »

Les datations OSL, post-IR - IRSL reposent sur un principe le piégeage d'électrons excités par le rayonnement naturel γ dans les irrégularités du réseau minéral.

Au cours du temps, les électrons sont accumulés dans ces pièges, lançant ainsi un chronomètre. Le seuls moyens de les libérer est de les exposer à la lumière du jour, à cet instant les électrons retournent à leur place en émettant de la lumière (phosphorescence). Ce phénomène s'appelle le « *bleaching* » et permet à tous les électrons piégés dans le minéral de se réorganiser, et ainsi remet le chronomètre à zéro. C'est ce qui arrive naturellement lors du transport des grains à la surface. Lors de leur dépôts, les grains enfouis et à l'abri de la lumière vont alors enregistrer le moment du dépôt.

Théoriquement, cette technique repose sur la mesure de la quantité d'électrons set e fait par mesure du rayonnement émis par l'échantillon lors de son excitation provoquée. L'intensité et le temps de l'émission permettent de remonter au temps d'accumulation, et donc à l'âge. Une mesure du taux de rayonnement γ de l'échantillon est nécessaire ainsi que la mesure du « nombre » de pièges disponibles dans le réseau pour recalculer cet âge (pour de plus amples informations, consulter [Rhodes 11].

Ces méthodes de datation utilisée en archéologie fonctionnent très bien lorsque les dépôts sont éoliens : dunes, loess [Prescott 97, Thiel 12]. Lors du transport fluviatile, le *bleaching* peut-être incomplet et la population de grains seulement partiellement remise à zéro, donnant lieu à des mesures d'âges beaucoup trop importants [Wallinga 02]. Enfin, tous les cristaux ne sont pas susceptibles d'emmagasiner des électrons, seuls 2 à 5% le sont [Botter-Jensen 10].

Plusieurs méthodes existent actuellement : la mesure peut être effectuée sur quartz (OSL) ou sur feldspaths (IRSL ou post-IR-IRSL). La mesure peut se faire sur échantillon entier dite « *single-aliquot* » ou grain par grain dite « *single-grain* ».

Nous avons débuté par la datation par méthode *single-aliquot* dans le laboratoire de géologie de Budapest. Cette méthode s'était révélée fructueuse auparavant pour les carottes de forages effectuées sur le Gange [Rahaman 09]. Pour nos échantillons, les résultats étaient inexploitables, les quartz étaient *dull* donc les mesures OSL impossibles. Les âges calculés sur les échantillons de surface par IRSL et post-IR-IRSL sur feldspaths étaient improbables. Par exemple, l'âge mesuré de 30 ky à 5 m de profondeur dans GR1, qui est le forage le plus proche de la rivière où les dépôts sont possiblement les plus récents, est en désaccord avec l'âge de charbons ~2 ka à 12 m de profondeur. Les sables ont visiblement mal subit le *bleaching* nécessaire à leur remise à zéro pendant le transport fluviatile. Les résultats de ces datations ne sont pas présentés ici et ne sont reportés qu'à titre indicatif dans la figure 6.3.3 récapitulative.

Nous avons engagé une collaboration avec Pierre Valla et Frederick Herman de l'Université de Lausanne pour effectuer des mesures par méthode *single-grain*. Cette méthode s'est montrée bien plus précise et plus efficace pour la datation de sédiments que la méthode *single-aliquot* [Duller 08]. Les quartz des échantillons himalayens se sont révélés *dull* et ont confirmé l'impossibilité de faire des mesures par OSL sur les quartz. Les résultats obtenus par IRSL sur feldspaths sont encore en cours d'étude mais semblent plus prometteurs. Ils ont aussi confirmé la dispersion des âges des grains, révélant un *bleaching* partiel, et expliquent les résultats incohérents des analyses single-aliquot. Les résultats sont présentés dans le tableau 6.2.

La technique a cependant permis de proposer des âges pour les échantillons analysés. Cette voie demande des analyses complémentaires afin de préciser avec plus de résolution

Sample #	Depth (m)	Age model cal.*	IR50°C age (ka)	postIR225°C age (ka)	Acc. rates (mm/a)
GR1P6 25-38	7	MAM	1.4 ± 0.9	1.9 ± 0.6	5.1 - 3.6
GR1P11 15-25	16	MAM	<2 ± /	1.9 ± 0.4	8 - 8.2
GR1P14 30-60	21	MAM	<2 ± /	1.6 ± 0.5	10.5 - 13.2
GR1P24 10-35	36	MAM	5.7 ± 0.8	12.8 ± 0.2	6.4 - 2.8
GR2P7 5-30	9	MAM	1.9 ± 0.5	5.6 ± 1.4	4.8 - 1.6
GR2P17 20-50	26	CAM	28.7 ± 7	39.7 ± 9.6	0.9 - 0.7
GR2P23 25-35	36	CAM	26.7 ± 7.6	35 ± 8.5	1.3 - 1
GR3P3 20-32	3	MAM	1.6 ± 0.4	1.5 ± 0.4	1.9 - 2

TABLE 6.2 – Résultats de datation OSL des forages par IR50°C et postIR225°C effectués à l'Université de Lausanne.
* Les âges modèles peuvent être déterminés en reportant soit le *Minimal-Age-Model* (MAM) qui rend compte que de l'âge de la population de grains les plus jeunes, soit le *Central-Age-Model* (CAM) qui rend compte de l'âge de la population de grains d'âges moyens. Les erreurs reportées sur les âges correspondent à 1σ de la population des âges de grains considérée.

les âges des échantillons et donc l'histoire des forages.

Datations ^{14}C des extractions séquentielles au « Dirt-burner »

Les extractions de carbone organique ainsi que les analyses ^{14}C des fractions extraites ont été réalisées en collaboration avec Valier Galy, au NOSAMS du WHOI (Woods Hole) aux États-Unis.

Cette méthode repose sur l'extraction séquentielle par pyrolyse de la matière organique bulk C_{org}suivant une rampe de températures. La matière organique des rivières est composée de deux *pools* : la fraction réfractaire pétrogénique « éteinte » composée de graphite, et la fraction biosphérique récente notamment composée d'acides gras à longues chaînes et de composés plus réfractaires [Galy 11a]. Si les acides gras peuvent être extraits par chromatographie, la séparation des fractions réfractaires est rendue difficile par la complexité des composés dont elle est constituée. Cependant, la technique d'extraction au dirt-burner permet de fractionner ces composés en collectant successivement les gaz produits pendant la montée en rampe de température [Rosenheim 12] (cf. figure 6.3.2).

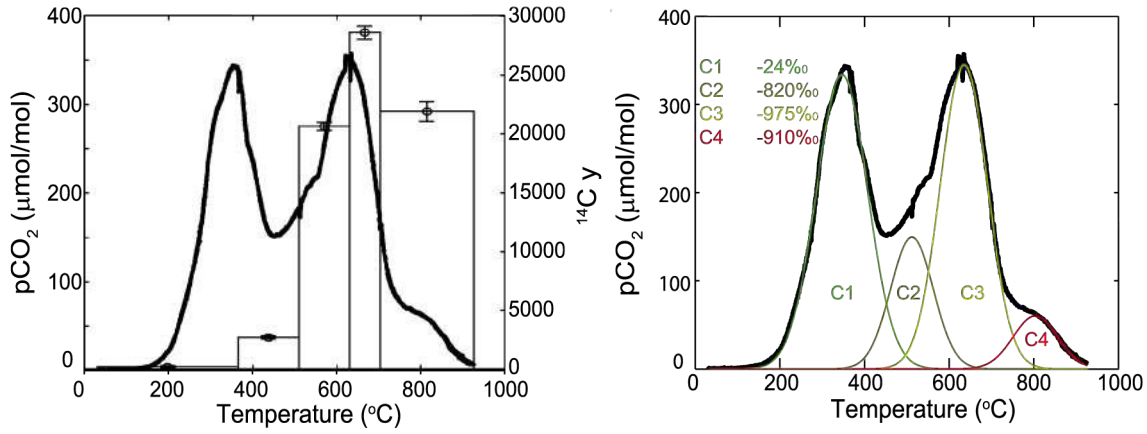

FIGURE 6.3.2 – Résultats d'extractions au dirt-burner sur un échantillon de MES de la Narayani collecté lors de la mousson 2005. (D'après [Rosenheim 12])
Rampe de pyrolyse et âges mesurés des fractions (à gauche) ; Déconvolution en modèles gaussiens simples basée sur 4 constituants majeurs (à droite).

Les fractions collectées aux températures froides sont constituées de la fraction biosphérique récente, puis les fractions extraites à plus hautes températures correspondent aux phases réfractaires biosphériques et pétrogéniques. Les compositions ^{14}C de ces gaz sont ensuite analysées et un modèle d'inversion basé sur un mélange de distributions gaussiennes permet de calculer les proportions des familles de composés, et de calculer l'âge de chacune des familles de composés (cf. figure 6.3.2).

Pour l'instant, nous n'avons analysé que les fractions extraites de 4 échantillons issus de GR1 et GR2. Les résultats de datations des fractions sont reportés dans le tableau 6.3. On constate que les fractions froides (F1) sont les plus jeunes et que les fractions plus chaudes présentent des âges supérieurs. L'âge ici reporté de ces fractions froides est l'âge maximal des composés biosphériques récents car l'âge des fraction inclus une partie de composés plus réfractaires.

Le travail de déconvolution n'est pas présenté ici et les résultats sont sujets à discussion. En effet, les deux échantillons les plus profonds GR1P26 et GR2P19 situés à 39 m et 30 m de profondeur respectivement semble très jeunes par rapport à ce que l'on peut attendre. En effet, cela impliquerait une accumulation de 30 à 40 m de sédiments en quelques 7000-8000 ans, ce qui nous semble très élevé.

Sample #	Depth (m)	F Modern	Fm Err	δ^{13}C Corr	Age	Age Err	Acc. rates (mm/a)
GR1 P9 34-41 F1	11.8	0.8942	0.0039	*	**900**	35	13.1
GR1 P9 34-41 F2	-	0.8716	0.0029	*	1100	25	
GR1 P9 34-41 F3	-	0.8322	0.0029	*	1470	30	
GR1 P9 34-41 F4	-	0.6543	0.0026	*	3410	30	
GR1 P26 0-10 F1	38.7	0.4042	0.0031	*	**7280**	60	5.3
GR1 P26 0-10 F2	-	0.0961	0.0029	*	18800	240	
GR1 P26 0-10 F3	-	0.0254	0.0025	*	29500	780	
GR1 P26 0-10 F4	-	0.0121	0.0026	*	35500	1700	
GR1 P26 0-10 F5	-	0.0282	0.0026	*	28700	730	
GR2 P11 31-37 F1	16.0	0.7879	0.0041	*	**1910**	40	8.4
GR2 P11 31-37 F2	-	0.8112	0.0038	*	1680	35	
GR2 P11 31-37 F3	-	0.6148	0.0026	*	3910	35	
GR2 P11 31-37 F4	-	0.1549	0.0023	*	15000	120	
GR2 P19 49-56 F1	30.4	0.3587	0.0030	*	**8240**	65	3.7
GR2 P19 49-56 F2	-	0.0921	0.0026	*	19150	230	
GR2 P19 49-56 F3	-	0.0329	0.0022	*	27400	530	
GR2 P19 49-56 F4	-	0.0144	0.0026	*	34100	1500	
GR2 P19 49-56 F5	-	0.0368	0.0036	*	26500	780	

TABLE 6.3 – Résultats des datations obtenues sur les fractions extraites au dirt-burner. * Les astérisques indiquent que les résultats radiocarbon ont été corrigés du fractionnement isotopique en utilisant les valeurs de δ^{13}C (non reportées) mesurées à l'accélérateur. La Fraction Moderne reportée ne requiert pas d'autre correction de fractionnement.

6.3.3 Conclusion et perspectives

Nous avons choisi de calibrer les âges des forages par rapport aux datations sur les charbons. Pour le moment, les autres résultats semblent encore à discuter.

Néanmoins, nous pouvons discuter ces datations en comparant les taux d'accumulation calculés pour la Gandak avec les taux d'accumulation publiés dans la littérature. Pour le mégafan de la Kosi, [Chakraborty 10b] proposent des taux d'accumulation de ~2 mm/a.

Les taux d'accumulation reportés dans la plaine du Gange, où l'accumulation est bien plus faible, sont estimés entre 0.41 ± 0.03 mm/a et 1.2 ± 0.7 mm/a [Rahaman 09] et équivalent aux taux d'accumulation long-terme observés dans les séries Siwaliks ~0.4 mm/a [Burbank 96b, Najman 05]. Les taux d'accumulation du mégafan de la Gandak sont certainement compris entre 0.5 et 2 mm/a. Les âges du charbon GR1P24B (à 36 m) et les

âges obtenus par IRSL single-grains pour GR2 et GR3 semblent compatibles avec ces taux. Au vu des taux d'accumulation importants de la plupart des datations obtenues, il semble que les âges mesurés sous-estiment les âges réels.

La figure 6.3.3 récapitule les résultats obtenus par les différentes méthodes de datations et illustre le travail qu'il reste encore à faire afin de proposer des âges modèles cohérents pour tous les forages.

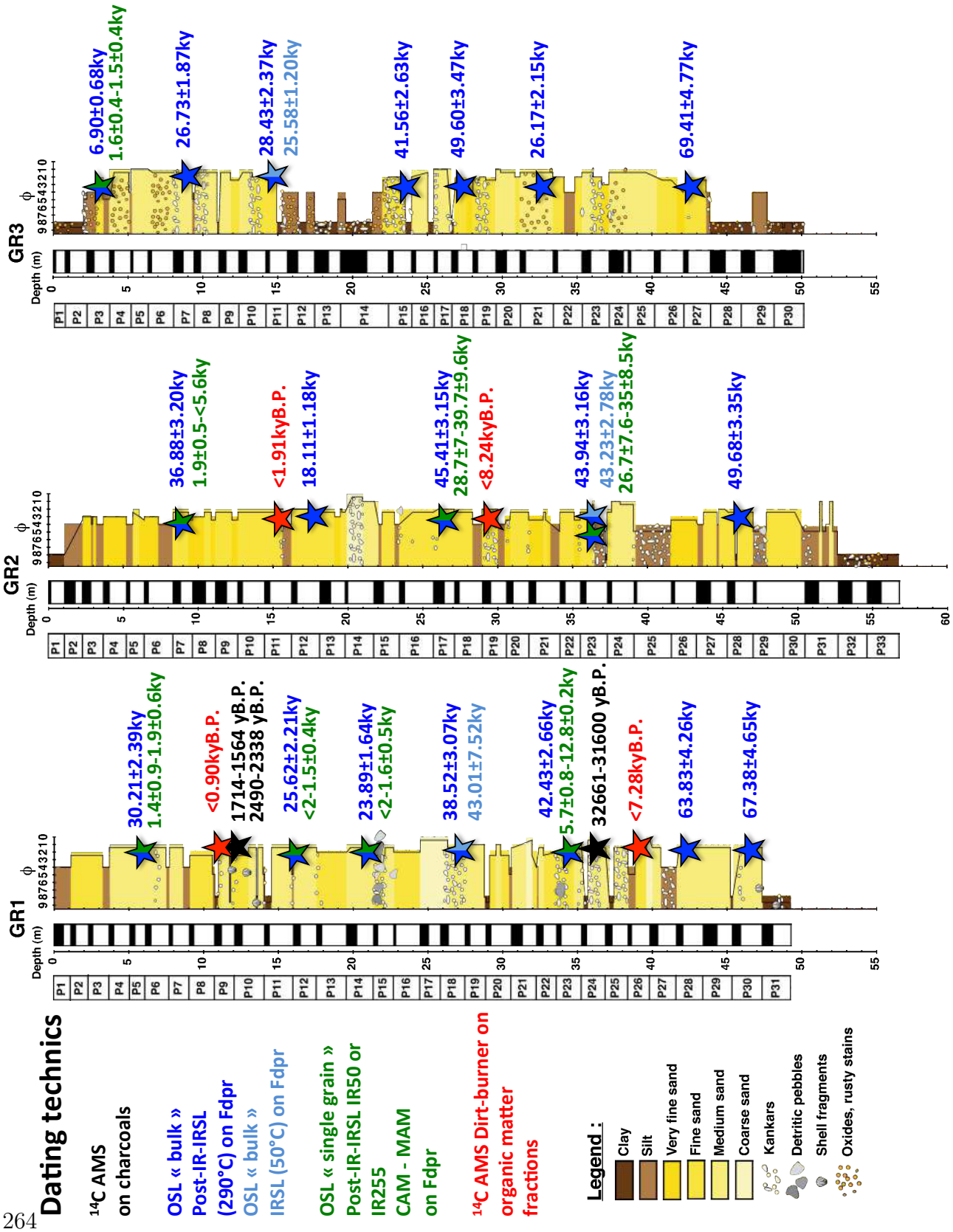

FIGURE 6.3.3 – Récapitulatif des datations des forages par les différentes techniques utilisées.

6.4 Variations de la géochimie des forages

Nous nous sommes attachés ici à présenter les compositions géochimiques des forages selon le même cadre de lecture qu'adopté dans les chapitres 4 et 5 afin de tracer les modifications des intensité d'altération et/ou les modifications des proportions des agents d'érosion.

Pour ce faire, nous présentons les résultats en éléments majeurs solubles, hydratation, les proportions de carbonates détritiques, et la concentration en matière organique. Les compositions chimiques des échantillons de forages sont reportés dans le tableau 6.4.

Sample #	Borehole	Depth [m]	SiO2	Al2O3	Fe2O3	MnO	MgO	CaO	Na2O	K2O	TiO2	P2O5	Pf	Total	Fe/Al	Na/Al	K/Al	Ca/Al	Mg/Al	Al/Si
GR1P1 24-31	GR1	0.5																		
GR1P1 60-67	GR1	1.1	57.05	12.78	4.636	0.0698	2.601	7.445	1.206	3.144	0.555	0.13	9.6	99.21	0.2315	0.1552	0.2664	0.5296	0.2576	0.2640
GR1P2 25-30	GR1	2.0																		
GR1P3 13-21	GR1	3.0																		
GR1P4 15-21	GR1	4.4																		
GR1P5 13-21	GR1	5.5	72.1	8.893	2.667	0.0528	1.545	5.072	1.452	2.115	0.33	0.09	4.71	99.03	0.1914	0.2686	0.2575	0.5185	0.2199	0.1454
GR1P5 32-37.5	GR1	6.0																		
GR1P8 13-21	GR1	9.9	67.89	8.374	2.718	0.0659	1.868	8.338	1.288	1.591	0.343	0.11	6.71	99.29	0.2072	0.2530	0.2057	0.9052	0.2823	0.1454
GR1P9 1-6	GR1	10.8	48.71	14.938	5.212	0.0778	3.081	9.507	0.9	3.917	0.609	0.12	12.43	99.5	0.2227	0.0991	0.2839	0.5786	0.2610	0.3614
GR1P9 34-41	GR1	11.8	54.86	10.333	3.897	0.0503	2.034	10.99	1.181	2.598	0.436	0.1	12.11	98.58	0.2407	0.1880	0.2722	0.9669	0.2491	0.2220
GR1P10 47-53	GR1	13.7	69.13	10.233	3.113	0.042	1.541	5.368	1.498	2.574	0.364	0.09	5.77	99.72	0.1942	0.2408	0.2724	0.4769	0.1906	0.1744
GR1P10 53-55	GR1	14.8	57.87	10.26	5.002	0.1247	1.799	7.718	1.234	2.525	0.414	0.13	11.62	98.69	0.3112	0.1979	0.2665	0.6839	0.2219	0.2089
GR1P11 20-32	GR1	15.5																		
GR1P12	GR1	16.8	59.98	14.41	7.068	0.0625	3.054	3.052	1.153	3.818	0.721	0.07	5.64	99.02	0.3131	0.1316	0.2869	0.1925	0.2682	0.2831
GR1P13 0-5.5	GR1	17.7	72.4	9.007	2.514	0.0695	1.192	5.411	1.465	1.84	0.283	0.08	4.62	98.88	0.1782	0.2676	0.2212	0.5461	0.1675	0.1466
GR1P13 17-27	GR1	18.6																		
GR1P15	GR1	21.6	73.57	9.648	2.245	0.0462	0.986	4.312	1.771	2.229	0.256	0.08	4.03	99.17	0.1485	0.3020	0.2502	0.4063	0.1293	0.1545
GR1P16 0-8	GR1	23.1																		
GR1P17 0-38	GR1	25.3	74.86	9.139	1.825	0.0388	0.879	3.975	1.821	2.178	0.23	0.07	3.66	98.67	0.1275	0.3278	0.2581	0.3954	0.1217	0.1439
GR1P20 6-9	GR1	29.2																		
GR1P20 16-20	GR1	29.7	69.17	10.698	2.804	0.0356	1.446	5.09	1.819	2.838	0.363	0.08	4.62	98.96	0.1673	0.2797	0.2872	0.4325	0.1711	0.1823
GR1P21 5-40	GR1	31.0	73.43	8.76	2.453	0.0682	1.248	5.204	1.47	1.862	0.266	0.08	4.25	99.08	0.1787	0.2761	0.2302	0.5401	0.1803	0.1406
GR1P22 5-15	GR1	32.5																		
GR1P23 25-33	GR1	35.0	74.72	9.091	2.464	0.0587	1.089	4.2	1.536	1.937	0.265	0.08	3.57	99.01	0.1730	0.2780	0.2307	0.4200	0.1516	0.1434
GR1P25 6-16	GR1	37.1																		
GR1P25 24-27	GR1	37.7																		
GR1P26 0-10	GR1	38.7	66.34	11.078	4.322	0.0683	2.194	5.323	1.495	2.759	0.522	0.09	5.91	100.09	0.2490	0.2220	0.2697	0.4368	0.2506	0.1968
GR1P26 21-23	GR1	39.7	69.55	9.526	3.685	0.0964	1.663	5.566	1.423	1.936	0.44	0.13	4.8	98.81	0.2469	0.2458	0.2201	0.5312	0.2209	0.1614
GR1P26 23-26	GR1	39.8	59.58	14.253	6.176	0.0545	3.34	3.915	1.224	3.929	0.747	0.07	5.56	98.85	0.2766	0.1413	0.2985	0.2497	0.2966	0.2819
GR1P29 24-40	GR1	44.0	68.74	9.835	2.94	0.0551	1.207	6.3	1.739	2.222	0.379	0.1	5.74	99.25	0.1908	0.2909	0.2446	0.5823	0.1553	0.1686
GR1P29 92.5-96	GR1	45.3																		
GR1P31 2-11	GR1	47.5	49.05	15.958	6.226	0.0773	2.582	8.131	0.679	3.482	0.661	0.11	12.52	99.48	0.2490	0.0700	0.2363	0.4632	0.2048	0.3834
GR1P31 24-32	GR1	48.0	50.17	16.408	6.144	0.0662	2.702	6.853	0.681	3.694	0.665	0.1	11.59	99.07	0.2390	0.0683	0.2438	0.3797	0.2084	0.3854
GR1P31 47-56	GR1	48.6																		
GR2P1 15-20	GR2	1.0																		
GR2P2 3-15	GR2	1.2	25.2	7.356	2.5	0.0384	2.132	31.91	0.737	2.082	0.391	0.06	27.81	100.21	0.2169	0.1648	0.3065	3.9436	0.3668	0.3440
GR2P2 59-69	GR2	2.1	48.3	6.18	2.295	0.0359	1.554	20.83	1.278	1.41	0.347	0.1	17.38	99.72	0.2370	0.3402	0.2470	3.0641	0.3182	0.1508
GR2P3 5-15	GR2	2.4																		
GR2P3 20-24	GR2	2.8																		
GR2P4 3-12	GR2	3.9	53.84	7.777	2.952	0.0417	2.033	16.203	1.306	2.022	0.367	0.08	13.59	100.21	0.2423	0.2763	0.2815	1.8940	0.3308	0.1702
GR2P5 20-24	GR2	6.2																		
GR2P6 7-15	GR2	7.1	54.2	7.278	3.271	0.0586	1.962	15.7	1.261	1.627	0.421	0.13	12.95	98.86	0.2869	0.2850	0.2421	1.9611	0.3412	0.1582
GR2P7 0-25	GR2	8.6																		
GR2P7 31-36	GR2	9.1	54.82	7.492	3.83	0.0622	1.978	15.343	1.206	1.764	0.486	0.13	12.11	99.21	0.3263	0.2648	0.2549	1.8617	0.3341	0.1611
GR2P8 43-63	GR2	10.5	63.52	8.714	2.925	0.0457	1.789	10.3	1.446	2.241	0.355	0.08	8.68	100.09	0.2143	0.2730	0.2785	1.0746	0.2598	0.1617
GR2P9 11-15	GR2	11.4																		
GR2P9 57-60	GR2	12.3																		
GR2P11 31-37	GR2	16.0	62.3	10.578	3.895	0.0719	1.853	8	1.27	2.431	0.477	0.12	8.38	99.37	0.2350	0.1975	0.2488	0.6875	0.2217	0.2001
GR2P13 10-36	GR2	18.7	73.05	9.236	2.756	0.0658	1.248	5.29	1.477	1.928	0.334	0.08	5.1	100.56	0.1905	0.2631	0.2260	0.5207	0.1710	0.1490
GR2P16 0-14A	GR2	23.8	33.94	6.933	2.993	0.1002	1.643	27.685	0.833	1.566	0.321	0.1	24.11	100.23	0.2756	0.1977	0.2446	3.6302	0.2999	0.2407
GR2P17 20-26	GR2	26.1	69.11	10.128	3.065	0.0523	1.337	5.979	1.69	2.337	0.428	0.13	5.71	99.96	0.1932	0.2745	0.2499	0.5367	0.1671	0.1727
GR2P17 57-63	GR2	26.8																		
GR2P18 26-30	GR2	28.7																		
GR2P19 6-30	GR2	29.4	74.13	8.984	2.076	0.0381	0.97	4.91	1.565	2.077	0.299	0.08	4.53	99.65	0.1475	0.2866	0.2503	0.4968	0.1366	0.1428
GR2P19 49-56	GR2	30.4	71.68	10.513	2.789	0.0348	1.46	4.3	1.686	2.537	0.357	0.07	4.39	99.82	0.1693	0.2638	0.2613	0.3718	0.1757	0.1728
GR2P20 30-35	GR2	31.6	72.45	9.534	2.555	0.0592	1.205	5.295	1.691	2.083	0.312	0.1	4.56	99.83	0.1711	0.2918	0.2366	0.5049	0.1599	0.1551
GR2P21 43-47	GR2	34.0	72.43	9.704	2.843	0.0645	1.202	4.624	1.618	2.183	0.316	0.09	4.61	99.67	0.1870	0.2743	0.2436	0.4332	0.1568	0.1579
GR2P23 37-40	GR2	37.2	41.92	10.463	11.32	0.4192	1.853	12.88	1	2.425	0.45	0.12	17.19	100.05	0.6906	0.1572	0.2510	1.1191	0.2241	0.2941
GR2P24	GR2	38.2	74.78	9.43	2.179	0.0329	1.048	4.244	1.568	2.161	0.288	0.07	4.15	99.94	0.1475	0.2736	0.2481	0.4091	0.1406	0.1486
GR2P27 70-96	GR2	45.0	72.19	9.142	2.739	0.0496	1.187	5.109	1.538	2.007	0.348	0.08	5.01	99.4	0.1912	0.2768	0.2377	0.5080	0.1643	0.1492
GR2P31 23-30	GR2	51.1	62.19	10.788	3.765	0.0407	1.78	7.773	1.23	2.817	0.516	0.13	9.28	100.31	0.2228	0.1876	0.2827	0.6550	0.2088	0.2044
GR2P31 49-54	GR2	51.7	59.2	10.083	3.091	0.0619	1.583	11.28	1.188	2.219	0.414	0.08	11.23	100.43	0.1957	0.1938	0.2383	1.0170	0.1987	0.2007
GR2P32 16-28	GR2	53.1	54.85	12.188	4.143	0.0379	1.808	9.307	1.365	3.026	0.534	0.14	13.78	101.17	0.2170	0.1843	0.2688	0.6942	0.1877	0.2619
GR2P32 63-69	GR2	54.0	37.41	13.746	5.655	0.0646	1.631	15.513	0.61	3.207	0.603	0.11	22.15	100.7	0.2626	0.0730	0.2526	1.0260	0.1502	0.4330
GR3P2 15-24	GR3	1.6	67.57	13.474	5.339	0.0641	1.075	1.395	0.738	2.674	0.664	0.12	5.93	99.04	0.2529	0.0901	0.2149	0.0941	0.1010	0.2350
GR3P3 24-33	GR3	3.1	74.04	11.243	3.832	0.0432	1.256	1.035	1.419	2.136	0.599	0.16	3.41	99.17	0.2176	0.2076	0.2057	0.0837	0.1414	0.1789
GR3P4 6-13	GR3	4.1	76.11	10.543	3.317	0.0761	0.921	1.269	1.675	1.936	0.376	0.12	2.19	98.54	0.2008	0.2614	0.1988	0.1094	0.1106	0.1632
GR3P5	GR3	5.7	78.19	10.315	3.007	0.0715	0.831	1.289	1.823	1.961	0.346	0.11	1.54	99.48	0.1861	0.2908	0.2059	0.1136	0.1020	0.1555
GR3P6 20-27	GR3	7.8	78.24	10.338	2.623	0.047	0.941	1.435	1.86	2.152	0.325	0.09	1.57	99.61	0.1620	0.2960	0.2254	0.1262	0.1152	0.1557
GR3P7 5-29	GR3	8.3	73.69	9.582	2.365	0.0337	0.921	4.288	1.705	1.941	0.294	0.08	3.98	98.87	0.1575	0.2927	0.2193	0.4068	0.1216	0.1532
GR3P9 35-40	GR3	12.0	72.31	9.966	2.718	0.0434	1.337	4.664	1.773	2.351	0.342	0.08	3.85	99.43	0.1741	0.2927	0.2554	0.4254	0.1698	0.1624
GR3P10 46-55	GR3	13.9	70.43	10.363	3.585	0.0983	1.404	4.945	1.623	2.184	0.366	0.09	3.7	98.79	0.2208	0.2577	0.2282	0.4338	0.1715	0.1734
GR3P12 13-26	GR3	16.1	65.88	14.818	5.288	0.0445	2.002	1.314	1.482	3.606	0.664	0.14	4.39	99.63	0.2278	0.1645	0.2635	0.0806	0.1710	0.2651
GR3P12 40-47	GR3	16.7	66.29	14.013	4.618	0.0362	1.694	2.11	1.315	3.333	0.602	0.11	5.14	99.26	0.2104	0.1544	0.2575	0.1369	0.1530	0.2491
GR3P13 51-62	GR3	18.4	67.28	13.342	4.954	0.0371	1.681	1.866	1.237	2.965	0.618	0.07	5.32	99.37	0.2370	0.1525	0.2406	0.1271	0.1594	0.2337
GR3P14 144-166	GR3	21.9	71.75	11.933	4.582	0.0585	1.219	1.099	1.341	2.381	0.58	0.11	3.73	98.79	0.2451	0.1849	0.2161	0.0837	0.1293	0.1960
GR3P15 0-20	GR3	22.8	75.64	10.443	3.078	0.0479	0.938	1.787	1.714	2.166	0.384	0.11	2.27	98.57	0.1881	0.2700	0.2246	0.1556	0.1137	0.1627
GR3P16 13-22	GR3	24.7	75.31	10.703	3.674	0.0951	0.942	1.919	1.746	2.058	0.378	0.13	1.87	98.82	0.2191	0.2684	0.2082	0.1630	0.1114	0.1675
GR3P18 10-40	GR3	27.4	73.01	9.362	2.399	0.0485	0.964	4.918	1.762	1.885	0.312	0.09	4.27	99.02	0.1636	0.3096	0.2180	0.4776	0.1303	0.1511
GR3P18 30-40	GR3	27.7	74.23	9.12	1.922	0.0331	0.861	4.538	1.827	1.926	0.263	0.09	3.87	98.67	0.1345	0.3296	0.2287	0.4524	0.1195	0.1448
GR3P20 38-43_6	GR3	30.4	72.51	9.919	3.187	0.0891	1.145	4.314	1.75	2.103	0.347	0.1	3.5	98.96	0.2051	0.2903	0.2296	0.3954	0.1461	0.1612
GR3P20 0-20_27	GR3	30.2	72.31	10.155	2.748	0.0536	1.172	4.055	1.775	2.284	0.343	0.09	3.69	98.67	0.1727	0.2876	0.2435	0.3630	0.1461	0.1655
GR3P21	GR3	32.3	79.03	8.963	2.038	0.053	0.611	2.608	1.609	1.829	0.246	0.08	2.23	99.29	0.1451	0.2953	0.2210	0.2645	0.0863	0.1336
GR3P22 27-34	GR3	35.1	73.97	9.61	2.939	0.0603	1.008	3.688	1.629	1.982	0.386	0.11	3.48	98.85	0.1952	0.2789	0.2233	0.3489	0.1327	0.1531
GR3P24 57-91	GR3	38.1	72.48	10.455	3.898	0.1283	1.062	4.023	1.466	1.793	0.441	0.13	3.71	99.59	0.2380	0.2307	0.1857	0.3498	0.1285	0.1700
GR3P26 8-15	GR3	40.7	70.5	10.067	2.624	0.0364	1.174	5.326	1.861	2.453	0.334	0.09	4.93	99.4	0.1664	0.3041	0.2638	0.4810	0.1476	0.1683
GR3P27 27-31	GR3	43.6	68.07	8.853	2.695	0.0413	1.513	7.08	1.457	2.064	0.409	0.12	6.93	99.23	0.1943	0.2708	0.2524	0.7270	0.2163	0.1533
GR3P27 31-33	GR3	43.7	64.29	12.146	5.141	0.0494	2.602	4.556	1.311	3.095	0.579	0.1	6.25	100.11	0.2702	0.1776	0.2759	0.3410	0.2711	0.2226
GR3P28 18-33	GR3	44.4	66.25	14.88	5.157	0.0238	1.272	1.255	0.734	2.959	0.749	0.05	6.77	100.1	0.2212	0.0812	0.2153	0.0767	0.1082	0.2647
GR3P29 25-31	GR3	46.6	62.58	15.535	6.281	0.0424	2.21	1.93	0.944	3.138	0.715	0.12	6.72	100.21	0.2581	0.1000	0.2187	0.1129	0.1800	0.2925
GR3P30 32-42	GR3	48.5	37	11.795	4.846	0.0832	1.638	20.603	0.593	2.825	0.52	0.1	20.22	100.22	0.2622	0.0827	0.2593	1.5880	0.1757	0.3757
GR3P30 89-101	GR3	49.1	59.42	12.832	4.846	0.045	1.892	7.182	1.394	3.041	0.627	0.16	8.47	99.9	0.2411	0.1787	0.2566	0.5088	0.1866	0.2545

TABLE 6.4 – Compositions géochimiques des échantillons de forages

Sample #	Borehole	Depth [m]	TOC [%]	δ13Corg [‰]	δD [‰]	H2O+/Al	δ13Ctot	δ18Ototpdb	δ18Ototsmow	%wt.Carb	Na/Al*	K/Al*	H2O/Al*
GR1P1 24-31	GR1	0.5					-1.2	-13.1	17.4	9.0			
GR1P1 60-67	GR1	1.1	0.41	-22.6	-92.2	0.5884	-1.5	-12.0	18.5	12.9	-0.0205	-0.0022	0.0945
GR1P2 25-30	GR1	2.0			-90.4		-1.1	-12.9	17.6	9.8			
GR1P3 13-21	GR1	3.0			-88.5		-0.9	-13.0	17.5	12.3			
GR1P4 15-21	GR1	4.4			-85.8		-0.9	-13.0	17.5	8.8			
GR1P5 13-21	GR1	5.5	0.11	-24.5	-95.9	0.2828	-0.9	-13.1	17.4	8.0	0.0084	-0.0078	-0.0460
GR1P5 32-37.5	GR1	6.0					-0.9	-12.8	17.7	7.1			
GR1P8 13-21	GR1	9.9	0.06	-24.2	-88.6	0.2411	-0.7	-13.0	17.5	13.0	-0.0072	-0.0596	-0.0876
GR1P9 1-6	GR1	10.8	0.77	-19.2	-92.3	0.5669	-0.8	-12.2	18.3	25.2	-0.0072	0.0127	-0.0624
GR1P9 34-41	GR1	11.8	0.97	-14.8	###	0.4387	-0.7	-11.9	18.6	19.7	-0.0176	0.0048	0.0034
GR1P10 47-53	GR1	13.7	0.39	-22.4	-99.0	0.4395	-1.1	-11.9	18.7	8.3	0.0014	0.0063	0.0703
GR1P10 53-55	GR1	14.8	1.61				-1.5	-10.2	20.4	13.1	-0.0171	-0.0006	
GR1P11 20-32	GR1	15.5					-0.9	-13.2	17.3	5.1			
GR1P12	GR1	16.8	0.14	-24.4	-93.7	0.5522	-1.1	-11.9	18.6	4.5	-0.0305	0.0178	0.0317
GR1P13 0-5.5	GR1	17.7	0.08	-23.2	-83.8	0.2492	-0.6	-11.6	18.9	7.7	0.0083	-0.0441	-0.0813
GR1P13 17-27	GR1	18.6					-0.4	-12.7	17.8	8.6			
GR1P15	GR1	21.6	0.09	-24.3	###	0.2715	-0.3	-10.9	19.7	6.6	0.0483	-0.0154	-0.0700
GR1P16 0-8	GR1	23.1					-0.8	-12.4	18.1	6.2			
GR1P17 0-38	GR1	25.3	0.08	-24.8	-94.1	0.2273	-0.5	-11.6	18.9	6.3	0.0666	-0.0072	-0.0994
GR1P20 6-9	GR1	29.2					0.4	-10.8	19.7	13.8			
GR1P20 16-20	GR1	29.7	0.10	-23.5	-94.9	0.2813	-0.3	-13.4	17.1	7.6	0.0458	0.0209	-0.0988
GR1P21 5-40	GR1	31.0	0.06	-25.8	-89.5	0.2145	-1.0	-12.3	18.2	7.9	0.0125	-0.0350	-0.1076
GR1P22 5-15	GR1	32.5					-0.7	-13.1	17.4	8.0			
GR1P23 25-33	GR1	35.0	0.08	-23.7	-96.7	0.2400	0.0	-12.8	17.7	6.0	0.0164	-0.0345	-0.0860
GR1P25 6-16	GR1	37.1					-0.7	-12.4	18.1	12.0			
GR1P25 24-27	GR1	37.7					-0.4	-12.8	17.7	8.8			
GR1P26 0-10	GR1	38.7	0.14	-23.8	-91.5	0.3983	-0.1	-12.8	17.7	6.0	-0.0016	0.0030	-0.0020
GR1P26 21-23	GR1	39.7	0.10	-18.5	-84.3	0.2632	-0.7	-12.4	18.1	9.3	-0.0030	-0.0457	-0.0879
GR1P26 23-26	GR1	39.8	0.18	-24.1	-86.4	0.4623	-0.5	-13.2	17.3	8.8	-0.0217	0.0294	-0.0565
GR1P29 24-40	GR1	44.0	0.09	-25.2	###	0.2854	-0.7	-12.6	17.9	7.8	0.0473	-0.0213	-0.0757
GR1P29 92.5-96	GR1	45.3					-0.8	-12.9	17.6	9.6			
GR1P31 2-11	GR1	47.5	0.31	-20.2	-97.0		0.5	-10.8	19.8	10.2	-0.0207	-0.0356	
GR1P31 24-32	GR1	48.0	0.30	-19.1	-93.3	0.6901	0.6	-10.7	19.9	12.1	-0.0210	-0.0281	0.0273
GR1P31 47-56	GR1	48.6					-1.0	-8.6	22.1	19.2			
GR2P1 15-20	GR2	1.0					-1.0	-12.0	18.5	40.4			
GR2P2 3-15	GR2	1.2	0.30	-18.5	-75.5	0.5266	-1.0	-11.6	19.0	56.6	0.0461	0.0357	-0.0785
GR2P2 59-69	GR2	2.1	0.52	-2.8	-78.5	0.3533	-0.7	-12.3	18.3	37.3	0.0839	-0.0184	0.0170
GR2P3 5-15	GR2	2.4					-1.0			15.1			
GR2P3 20-24	GR2	2.8					-0.9	-12.3	18.3	30.9			
GR2P4 3-12	GR2	3.9	0.11	-24.5	-75.8	0.3158	-0.8	-12.7	17.8	27.6	0.0338	0.0155	-0.0475
GR2P5 20-24	GR2	6.2					-0.9	-12.3	18.3	30.9			
GR2P6 7-15	GR2	7.1	0.08	-22.8	-71.7	0.2865	-0.8	-13.0	17.6	27.5	0.0340	-0.0236	-0.0602
GR2P7 0-25	GR2	8.6					-0.8	-12.6	17.9	27.0			
GR2P7 31-36	GR2	9.1	0.08	-25.1	-86.4	0.5134	-0.8	-12.9	17.6	18.2	0.0158	-0.0108	0.1628
GR2P8 43-63	GR2	10.5	0.12	-24.1	-98.1	0.2989	-0.8	-12.7	17.8	17.4	0.0244	0.0127	-0.0526
GR2P9 11-15	GR2	11.4					-0.8	-12.6	18.0	24.6			
GR2P9 57-60	GR2	12.3					-0.9	-13.3	17.2	15.5			
GR2P11 31-37	GR2	16.0	0.35	-17.8	-94.4	0.3849	-0.5	-12.1	18.5	13.3	-0.0237	-0.0180	-0.0200
GR2P13 10-36	GR2	18.7	0.10	-26.2	-97.9	0.2821	-0.9	-12.4	18.1	8.3	0.0055	-0.0394	-0.0517
GR2P16 0-14A	GR2	23.8	1.04	-1.0	-94.6	0.5431	2.2	-6.3	24.4	50.7	0.0054	-0.0233	0.0816
GR2P17 20-26	GR2	26.1	0.08	-23.0	###	0.2914	-0.5	-12.7	17.8	9.0	0.0338	-0.0162	-0.0754
GR2P17 57-63	GR2	26.8					-0.5	-11.9	18.6	9.1			
GR2P18 26-30	GR2	28.7					-0.4	-12.2	18.4	8.5			
GR2P19 6-30	GR2	29.4	0.08	-23.9	-99.0	0.2687	-0.5	-12.6	17.9	6.7	0.0246	-0.0149	-0.0566
GR2P19 49-56	GR2	30.4	0.11	-23.5	-99.0	0.2950	-0.4	-12.9	17.6	7.8	0.0232	-0.0048	-0.0720
GR2P20 30-35	GR2	31.6	0.08	-23.1	###	0.2206	-0.4	-13.1	17.4	7.3	0.0385	-0.0290	-0.1217
GR2P21 43-47	GR2	34.0	0.10	-22.9	-98.3	0.2575	-0.2	-12.2	18.3	31.9	0.0230	-0.0221	-0.0887
GR2P23 37-40	GR2	37.2	0.58	-18.7	###	0.5060	-0.4	-9.5	21.1	7.0	0.0030	-0.0184	-0.0298
GR2P24	GR2	38.2	0.08	-24.4	###	0.2689	0.0	-11.4	19.2	7.9	0.0157	-0.0172	-0.0643
GR2P27 70-96	GR2	45.0	0.07	-23.5	-99.5	0.2941	-0.6	-12.7	17.8	20.0	0.0193	-0.0277	-0.0400
GR2P31 23-30	GR2	51.1	0.15	-20.5	-93.7	0.4771	-0.3	-10.1	20.5	16.0	-0.0306	0.0158	0.0662
GR2P31 49-54	GR2	51.7	0.17	-19.3	-94.3	0.4434	0.7	-9.0	21.6	13.4	-0.0269	-0.0285	0.0377
GR2P32 16-28	GR2	53.1	0.24	-17.5	###	0.4851	-0.1	-12.9	17.6	28.9	0.0070	0.0003	-0.0057
GR2P32 63-69	GR2	54.0	0.49	-10.0	###	0.6803	1.1	-12.4	18.1	7.9	0.0176	-0.0206	-0.0487
GR3P2 15-24	GR3	1.6	0.21	-17.1	-88.3	0.6994	-1.0	-10.9	19.7	0.8	-0.1063	-0.0529	0.2459
GR3P3 24-33	GR3	3.1	0.08	-23.4	-91.5	0.5237	-9.2	-11.4	19.2	0.0	-0.0286	-0.0605	0.1482
GR3P4 6-13	GR3	4.1	0.07	-23.8	-95.1	0.3472	-8.2	-10.3	20.3	0.0	0.0139	-0.0670	-0.0064
GR3P5	GR3	5.7	0.05	-23.4	###	0.2655	-5.5	-11.7	18.9	0.0	0.0378	-0.0597	-0.0773
GR3P6 20-27	GR3	7.8	0.06	-23.2	###	0.2469	-6.3	-13.3	17.2	0.3	0.0432	-0.0402	-0.0963
GR3P7 5-29	GR3	8.3	0.07	-23.2	###	0.2753	-1.2	-12.7	17.8	5.4	0.0382	-0.0462	-0.0644
GR3P9 35-40	GR3	12.0	0.08	-23.5	-98.8	0.2548	-0.7	-13.5	17.0	6.3	0.0446	-0.0103	-0.0977
GR3P10 46-55	GR3	13.9	0.07	-23.0	-97.3	0.2169	-0.4	-12.7	17.9	6.3	0.0174	-0.0379	-0.1509
GR3P12 13-26	GR3	16.1	0.16	-19.9	-98.3	0.5048	-0.1	-9.6	21.0	0.6	-0.0104	-0.0051	0.0095
GR3P12 40-47	GR3	16.7	0.14	-19.1	-96.9	0.5273	1.2	-10.4	20.2	2.2	-0.0319	-0.0106	0.0542
GR3P13 51-62	GR3	18.4	0.08	-20.7	-96.2	0.5563	0.1	-7.5	23.2	1.9	-0.0448	-0.0271	0.1047
GR3P14 144-166	GR3	21.9	0.08	-22.3	-93.1	0.5280	-1.9	-8.5	22.2	0.2	-0.0393	-0.0506	0.1288
GR3P15 0-20	GR3	22.8	0.05	-23.4	###	0.3374	-0.7	-7.8	22.8	1.2	0.0222	-0.0412	-0.0155
GR3P16 13-22	GR3	24.7	0.05	-22.8	-99.1	0.2515	0.1	-7.0	23.7	1.1	0.0239	-0.0577	-0.1080
GR3P18 10-40	GR3	27.4	0.07	-22.3	-97.8	0.2293	-0.5	-13.4	17.1	6.7	0.0535	-0.0474	-0.1075
GR3P18 30-40	GR3	27.7	0.05	-23.3			-0.6	-13.1	17.4	6.3	0.0690	-0.0366	
GR3P20 38-43_6	GR3	30.4	0.06	-23.5	-93.5	0.2635	-0.6	-13.1	17.4	5.8	0.0413	-0.0362	-0.0873
GR3P20 0-20_27	GR3	30.2	0.08	-23.4	-96.1	0.2035	-0.5	-12.5	18.0	5.6	0.0417	-0.0223	-0.1533
GR3P21	GR3	32.3	0.04	-22.9			-0.4	-11.3	19.3	2.7	0.0268	-0.0440	
GR3P22 27-34	GR3	35.1	0.07	-23.2	-96.2	0.3019	-0.5	-12.4	18.1	4.7	0.0242	-0.0422	-0.0377
GR3P24 57-91	GR3	38.1	0.06	-22.8	-94.5	0.2442	-0.3	-12.6	17.9	4.9	-0.0120	-0.0803	-0.1189
GR3P26 8-15	GR3	40.7	0.06	-23.6	-97.7	0.2532	-0.8	-13.2	17.3	8.1	0.0603	-0.0021	-0.1074
GR3P27 27-31	GR3	43.6	0.11	-23.8	-68.2	0.3530	-0.3	-14.1	16.3	12.1	0.0162	-0.0131	0.0132
GR3P27 31-33	GR3	43.7	0.20	-24.6	-85.7	0.4842	-0.3	-13.8	16.7	7.4	-0.0276	0.0085	0.0479
GR3P28 18-33	GR3	44.4	0.10	-21.3	-89.8	0.6950	1.5	-7.7	23.0	1.3	-0.0941	-0.0533	0.2002
GR3P29 25-31	GR3	46.6	0.10	-21.3	-94.5	0.6950	0.8	-8.3	22.4	2.3	-0.0554	-0.0506	0.1614
GR3P30 32-42	GR3	48.5	0.15	-21.7			0.7	-9.4	21.2	37.2	-0.0135	-0.0123	
GR3P30 89-101	GR3	49.1	0.20	-24.2	-91.1	0.5111	-0.2	-13.0	17.5	11.7	-0.0038	-0.0117	0.0305

6.4.1 Géochimie des éléments majeurs et hydratation

Comme nous l'avons précédemment démontré dans les chapitre 4 et 5, les rapports Na/Al et K/Al permettent de distinguer les sols des roches sources non altérées. Dans le bassin de la Narayani, ces rapport sont aussi dépendant des proportions dérivées des HHC et du LH dans les sédiments. Nous démontrons (§6.5) que ces proportions sont stables dans les forages d'après les compositions isotopiques du Sr et du Nd.

Lors de l'altération, les rapports Na/Al et K/Al sont principalement diminués par l'hydrolyse de l'albite et la vermiculitisation des biotites. Dans les sols développés sur les gneiss du Haut-Himalaya, ces rapports peuvent être diminués de 0.05 à 0.1 (soit 30 à 50%) lors de la pédogénèse. Parallèlement, la concentration en H_2O+ augmente par hydratation et incorporation d'hydroxyles dans les vermiculites et les phases secondaires. Le rapport H_2O+/Al peut ainsi augmenter de 0.3 (soit x2).

Néanmoins, tous ces traceurs sont dépendants du tri minéralogique et granulométrique du sédiment effectué par la rivière. Ainsi, il convient de considérer ces rapports en fonction du rapport Al/Si qui est fortement corrélé à la granulométrie, comme le montrent les corrélations observées entre les rapports X/Al et Al /Si des matières en suspension de la Narayani moderne (cf. figure 6.4.1). Dans les sédiments grossiers et les *banks* (Al/Si<0.19), ces corrélations ne sont plus valables car les dépôts ont subi plusieurs épisodes de dépôt et de tri minéralogique. Nous attribuons la chute des rapports K/Al et H_2O+/Al au départ préférentiel des micas et des argiles. À l'inverse, leurs rapports Na/Al élevés peuvent s'expliquer par l'enrichissement en albites grossières et non-altérées relativement aux SL. Les échantillons de GR1 et GR2 sont très proches des sédiments modernes (cf. figure 6.4.1). Ainsi, le signal sédimentaire enregistré par ces forages et provenant de la chaîne ne semble indiquer aucune modification marquée des régimes d'altération. Les proportions de sols dans les sédiments de forages semblent être mineures, tout comme dans la Narayani actuelle. Par contraste, GR3 présente des échantillons clairement hors de ces corrélations.

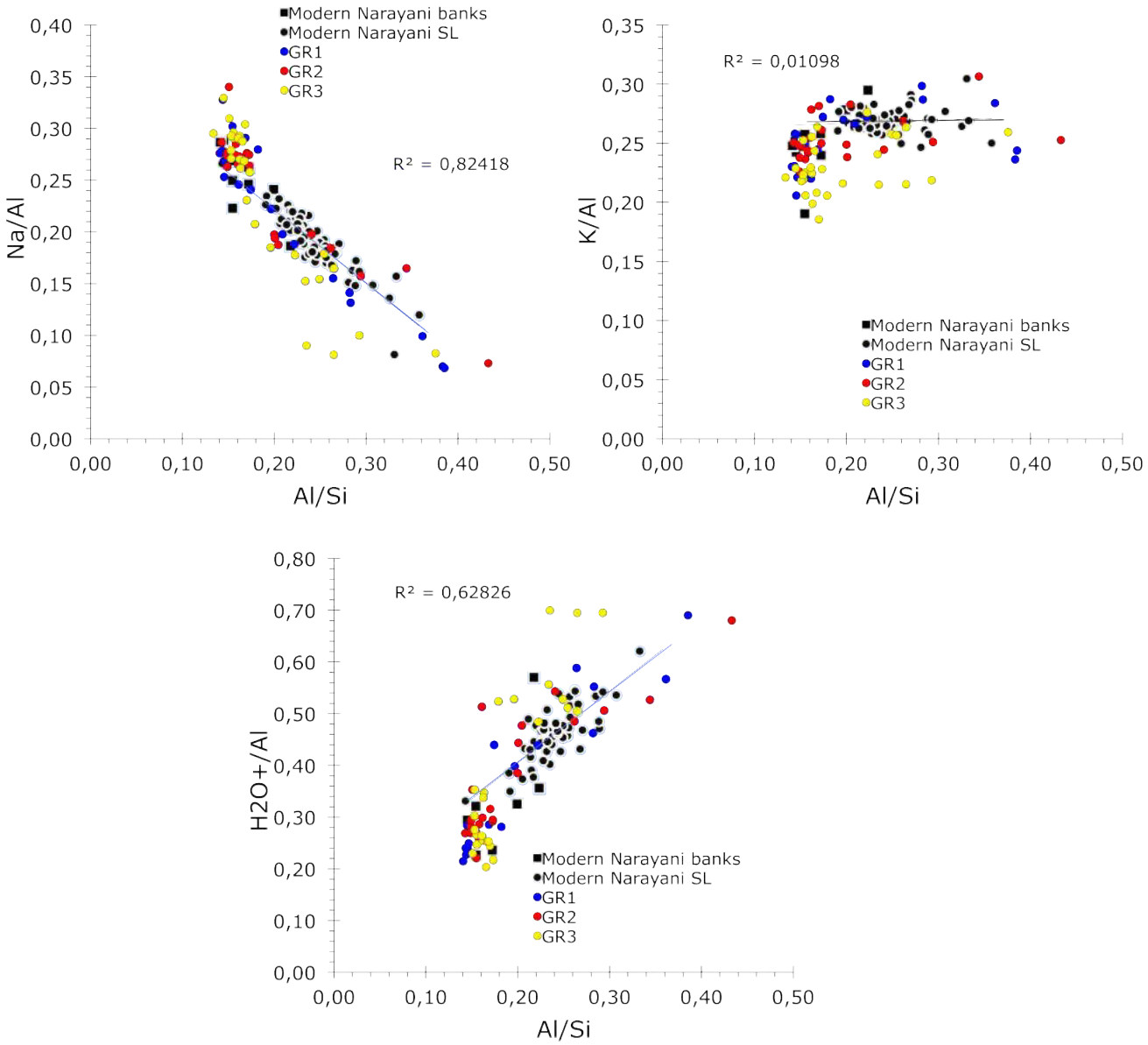

FIGURE 6.4.1 – Rapports Na/Al, K/Al et H_2O+ /Al en fonction de Al/Si des sédiments des forages comparés aux sédiments de la Narayani moderne.

L'écart des rapports X/Al des sédiments des forages par rapport aux corrélations dans les SL modernes sont notés X/Al* (avec X = Na, K ou H_2O+). Ils témoignent d'un changement de composition des sédiments par rapport au mélange canonique que la rivière

moderne produit. L'altération est associée à des pertes en Na, K et un gain en H_2O+ , i.e. Na/Al* et K/Al* diminuent et H_2O+ /Al* augmentent par rapport aux sédiment modernes.

Les rapports X/Al* (avec X = Na, K ou H_2O+) de GR3 ont été reportés en fonction de la profondeur et comparés aux logs stratigraphiques (cf. figure 6.4.2). Dans GR3, les horizons sableux montrent, comme dans les banks modernes, des rapports Na/Al* légèrement supérieurs, K/Al* et H_2O+/Al* légèrement inférieurs aux MES de la Narayani. Par contraste, les échantillons entre 50 et 44 m, 22 et 15 m, et entre 2 m et la surface, sortent fortement des corrélations et montrent des rapports Na/Al* très inférieurs et des rapports H_2O+/Al* très supérieurs aux SL modernes. Ils montrent donc des signatures d'altération prononcées.

Or, stratigraphiquement, ces échantillons sont liés aux dépôts silto-argileux qui ont été attribuées à des dépôts de plaine d'inondation. Ce dépôts fins montrent aussi des rapport K/Al* équivalents aux *banks* bien inférieurs aux SL modernes, ce qui témoigne d'une perte en K et renforce l'hypothèse de l'altération de ces sédiments. Il est probable que l'altération des sédiments ait eu lieu après leur dépôt par pédogénèse. Si, peu de traces de bioturbation ont été constatées, la présence de carbonates pédogéniques dans ces horizons apporte une preuve supplémentaire de la probable pédogénèse qui s'y est déroulée. Mis à part cette altération *in-situ*, GR3 est semblable aux autres forages et ne semble pas non plus avoir enregistré de variation d'altération des sédiments provenant de la chaîne lors des derniers 50 ka.

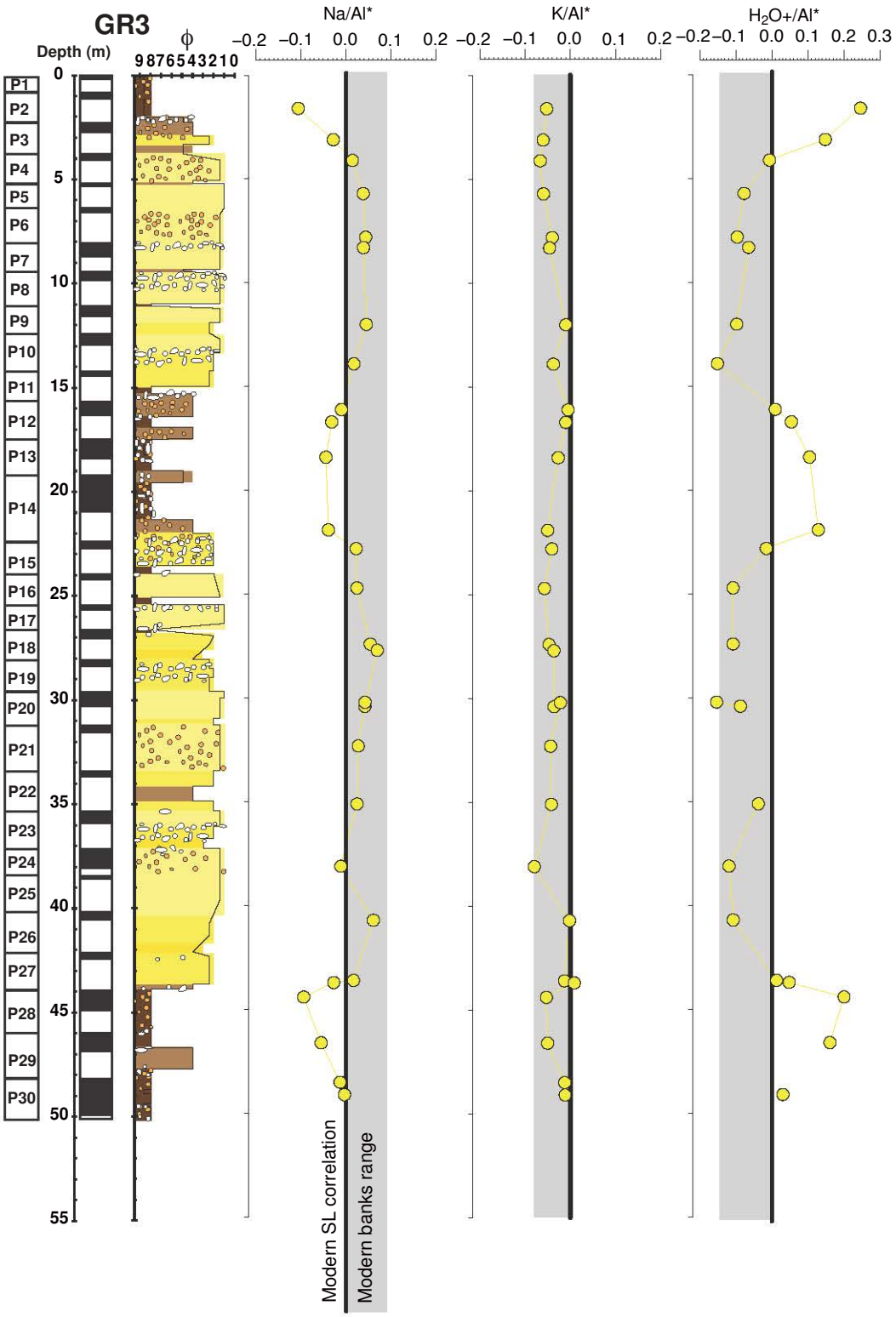

FIGURE 6.4.2 – Rapport X/Al* (avec X = Na, K ou H_2O+) des sédiments de GR3. 0 correspond à la corrélation des SL de la Narayani moderne.

6.4.2 Carbonates détritiques

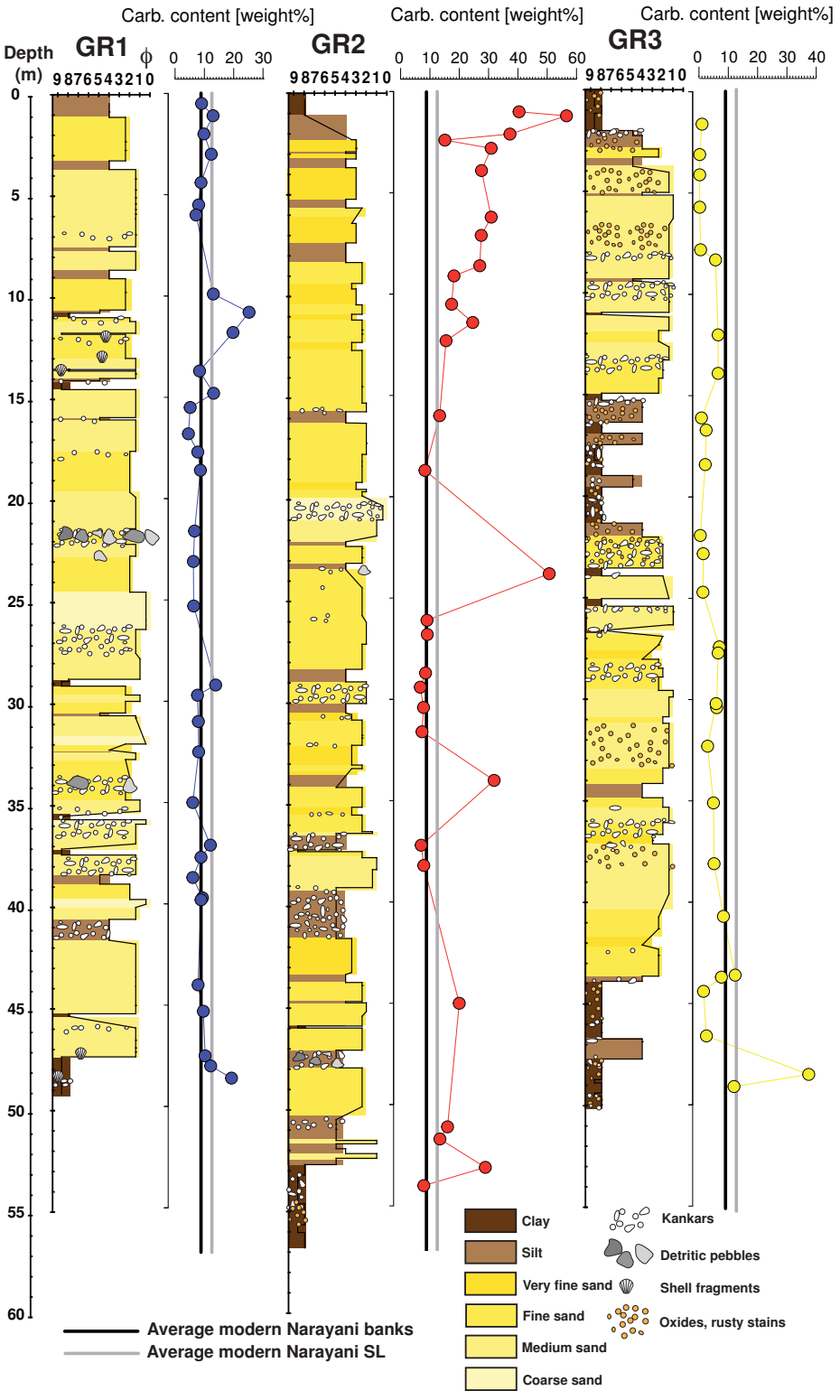

FIGURE 6.4.3 – Concentrations de carbonates dans les forages GR.

Les concentrations de carbonates dans les forages sont reportées dans le tableau 6.4, et présentées dans la figure 6.4.3.

Les concentrations moyennes des SL et banks de la Narayani moderne sont reportées à titre de comparaison. Les forages montrent des concentrations de carbonates différentes comparées aux sédiments modernes. La quasi totalité des sédiments de GR1 montrent des concentrations équivalentes à la rivière moderne excepté autour de 10 m de profondeur où les concentrations atteignent 20-25%. Si les concentrations de GR1 semblent identiques à celle de la rivière actuelle, les sédiments de GR2 montrent des épisodes de très fortes concentrations allant de 20 à 60%, alors que les concentrations observées dans GR3 sont très faibles et inférieures aux valeurs de la rivière actuelle.

La présence de carbonates pédogéniques ou kankars dans les forages soulève un doute sur une possible contamination des échantillons présentant des concentrations élevées, bien qu'un soin particulier ait été pris afin d'enlever les fragments de kankars rencontrés avant porphyrisation des sables.Les compositions isotopiques d'oxygène et de carbone des roches totales apparaissent clairement proches de celles des sédiments de la Narayani actuelles et des compositions connues pour les roches des TSS. En revanche les compositions des kankars sont clairement enrichies en ^{18}O (-5 à 2‰) et appauvries en ^{13}C (-10 à -4‰) [Quade 95] par rapport aux sédiments de rivières (autour de -18‰ et 0‰) (cf. 6.4.4). Ainsi, ces passées carbonatées semblent témoigner d'épisodes érosifs importants dans les bassins versants TSS. Dans GR3, les très faibles concentrations de carbonates pourraient être dues à la contamination de ce forage par des rivières drainant les Siwaliks mais les compositions isotopiques de C et d'O qui y sont observées sont incompatibles avec cette hypothèse [Lupker 12b]. Notre hypothèse, afin d'expliquer ces très faibles concentrations en carbonates, réside dans le fait que ce forage semble avoir subi une altération in-situ poussée comme nous l'avons observé avec les éléments majeurs (cf. section 6.4.1). Les carbonates, qui sont très sensibles à l'altération chimique, ont pu être dissous par lessivage parce que ce forage est possiblement plus ancien, et qu'il est désormais situé loin de l'influence de la nappe de la Narayani dont les eaux sont saturées vis à vis des carbonates.

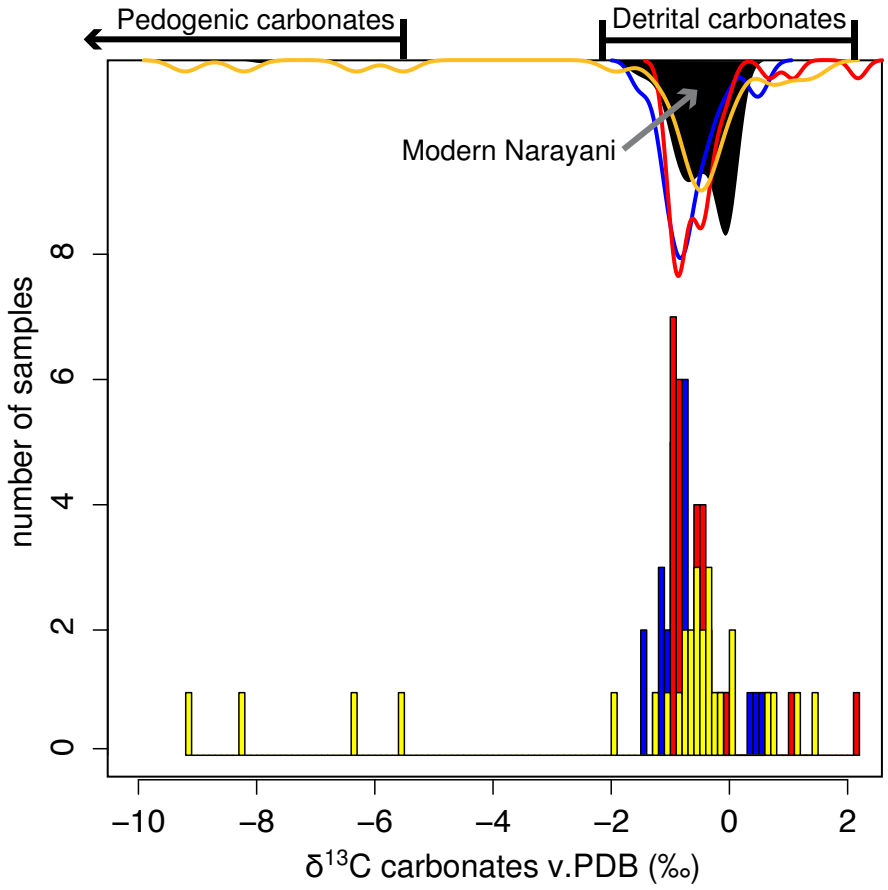

FIGURE 6.4.4 – Compositions isotopiques δ^{13}C (‰ v.PDB) des carbonates bulk des forages.
Les valeurs isotopiques δ^{13}C des sédiments de la Narayani moderne sont reportées à titre de comparaison. Les gammes des valeurs isotopiques δ^{13}C des carbonates détritiques et pédogéniques sont issues des valeurs de sédiments de rivières et de coquilles de gastéropodes des Siwaliks d'après [Lupker 12b, Gajurel 06]. Le code couleur est le même qu'utilisé précédemment, GR1 en bleu, GR2 en rouge, GR3 en jaune.

La variation des concentrations de carbonates couplées aux mesures de δD des hydroxyles des silicates s'est révélée être, dans les sables de la Narayani actuelle, un bon traceur des apports des bassins versants TSS et englacés du Nord Himalaya (cf. Chapitre 5). Une contribution plus importante de ces bassins provoquerait une augmentation des concentrations de carbonates et des δD plus négatifs. Or, cette corrélation n'est pas observée dans les sédiments de forages. Les épisodes de très fortes concentrations ob-

servés dans GR1 et GR2 ne sont pas accompagnés de valeurs plus négatives en δD des hydroxyles des silicates (cf. figure 6.4.5). Une interprétation directe correspondant à des apports détritiques accrus des bassins du Nord Himalaya au niveau de ces horizons est donc discutable.

Les compositions δD des forages sont en moyenne très comparables avec respectivement -94.0, -94.2, -94.7 ‰ pour GR1, GR2 et GR3. De plus, leur étonnante stabilité au cours du temps informe qu'aucune variation sensible des apports glaciaires n'est constatée, même dans le fond des forages probablement contemporains de la dernière phase glaciaire. Ce constat soulève la question de la conservation de l'information isotopique par les phases hydratées. Il est en effet possible que les hydroxyles contenus par les phases silicatées soient échangés avec l'eau environnementale dans des laps de temps correspondant à plusieurs milliers d'années. Les enregistrements sédimentaires se révèleraient alors peu informatifs. Cependant, cette hypothèse se révèle peu probable puisque les sédiments du cône du Bengale montrent une variation du signal alors qu'ils ont été stockés plusieurs milliers d'années dans l'eau de mer par définition à 0‰ δD.

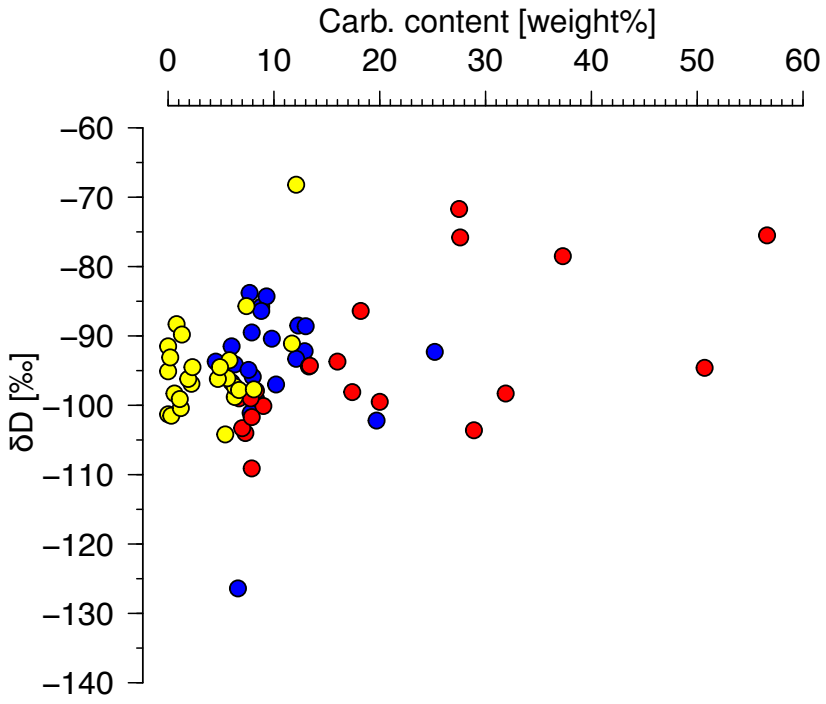

FIGURE 6.4.5 – Compositions isotopiques δD comparées aux concentrations de carbonates des forages.

6.4.3 Matière organique Corg

Les concentrations en matière organique C_{org}dans les forages sont reportées dans le tableau 6.4, et présentées dans la figure 6.4.6.

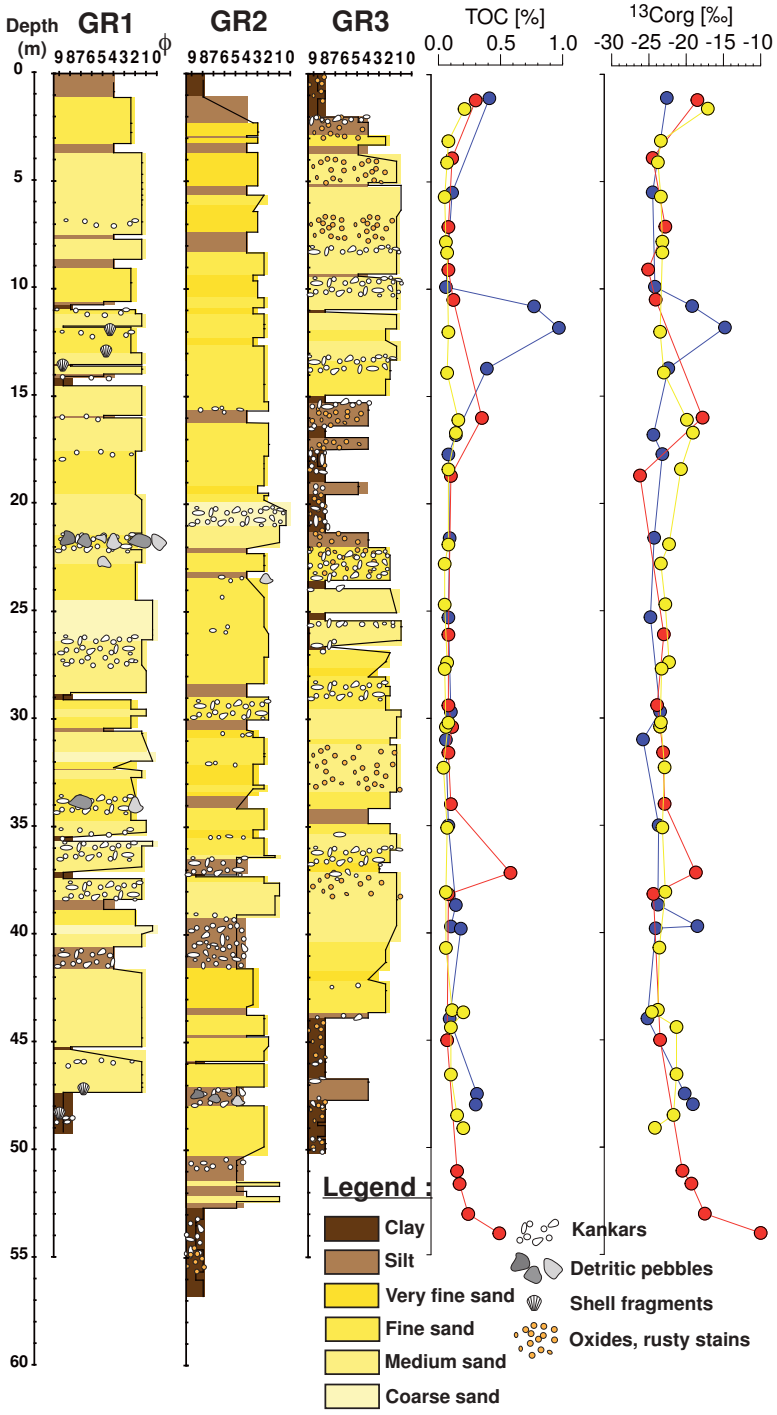

FIGURE 6.4.6 – Concentrations en matière organique C_{org} (TOC [%]) et compositions isotopiques $\delta^{13}C_{org}$des forages.

Les analyses du carbone organique ont été effectuées après avoir décarbonaté les échantillons avec de l'HCl (4% weight) à 80°C pendant 40 min selon [Galy 07b].

Les [C_{org}] et les compositions isotopiques sont particulièrement stables le long des trois forages mis à part deux échantillons dans GR1 à 12 - 13 m de profondeur, et trois dans GR2 à 16 m, 37 m et 54 m de profondeur. Les 4 échantillons anormaux exhibent des TOC plus élevés ~0.5 - 1% associés à des $\delta^{13}C_{org}$moins négatifs -15 à -10‰. Ces valeurs anormales ne sont pas observées dans les parties argileuses des forages qui ont la plus forte probabilité d'avoir subi la pédogénèse, mais elles sont issues des sables. Dans l'hypothèse où le carbone détritique est échangé avec du carbone de plaine, ce sont dans les dépôts de plaine d'inondation qu'un tel processus serait le plus efficace. Or dans les parties de plaines d'inondations de GR3 où les autres traceurs semblent indiquer que la pédogénèse a été importante, aucune variation significative des $\delta^{13}C_{org}$ n'est observée. Malgré la décarbonatation préalable, nous pensons que ces échantillons contenaient encore des traces de carbonates résistants à la dissolution (par exemple de sidérites) qui ont biaisé les valeurs isotopiques.

Si l'on exclut les valeurs anormales, les C_{org} des forages GR1, GR2 et GR3 montrent respectivement des TOC moyens de 0.15% 0.17%, 0.09% et des compositions isotopiques $\delta^{13}C_{org}$moyennes de -23.2 ‰, -22.2 ‰, -22.5 ‰. Les TOC faibles s'expliquent simplement par le fait que la matière organique détritique est contrôlé par la granulométrie moyenne du sédiment, sa surface spécifique et son taux de particules fines [Galy 08] et elle est faiblement associée aux sables grossiers. Les rapports Al/Si moyens des forages sont de 0.21% dans GR1, et 0.20% dans GR2 et GR3 ce qui se traduit par un TOC entre 0.17% - 0.20 % d'après les corrélations observées dans les rivières himalayennes issues de [Galy 08]. Ces valeurs sont comparables aux valeurs de GR1 et GR2, alors que GR3 semblent montrer des TOC faibles. Il est possible que la matière organique de GR3 ait été altérée et ait subi plus d'oxydation.

Les TOC ne semblent pas évoluer sensiblement au cours du temps, de même, aucune variation à long terme des compositions isotopiques n'est observée le long des forages. Les valeurs de $\delta^{13}C_{org}$ sont un peu élevées que celles de la Narayani actuelle qui est de -25.0‰ (valeur compatible avec les valeurs publiées pour les rivières Himalayenne de -24.8 ‰ [Galy 08]). Les compositions des forages sont plutôt comparables aux valeurs du Ganges

- Brahmapoutre autour de -22.4 à -20 ‰ [Galy 08]. Le carbone organique d'origine détritique provenant de l'Himalaya est majoritairement dérivé de plantes en C3 ($\delta^{13}C_{org}$ de -30 à -23‰) [Cerling 99]. Dans les forages, il a pu être partiellement échangé avec le carbone originaire de plantes C4 (-15 à - 10‰) issu de la plaine comme c'est le cas dans les sédiments du Gange [Galy 11b]. Cet échange ne peut cependant avoir dépassé 10 à 15 % du carbone total.

Les compositions [Corg] et $\delta^{13}C_{org}$ des forages ne semblent pas avoir évoluées au cours du temps. Ils restent compatibles avec les valeurs des sédiments actuels issus de la chaîne modulo un échange partiel avec la plaine. Les sédiments de GR3 semblent cependant avoir subi une altération accompagnée de la perte, probablement par oxydation, d'une partie de la matière organique initiale.

6.4.4 Conclusion

L'application des traceurs géochimiques diagnostiques de l'altération et/ou des provenances d'environnements glaciaires montrent une grande stabilité tout au long des forages si bien que le degré d'altération des sédiments au cours des derniers 50 ka ne semble pas avoir varié. Seul des épisodes très riches en carbonates dans GR1 et GR2 semblent témoigner d'épisodes érosifs brutaux et brusques qui ont eu lieu dans les parties drainant les TSS au Nord du bassin versant. GR3 semble avoir subit une altération post-dépositionnelle poussée qui a conduit à une lixiviation des carbonates, des pertes en Na, K ainsi qu'une partie de la matière organique, et un gain en hydratation. Les dépots de ce forage, loin de l'influence actuelle de la rivière sont certainement plus anciens.

6.5 *Unprecedented erosion increase in Central Nepal Himalaya aroused by recent anthropogenic activities*

Unprecedented erosion increase in Central Nepal Himalaya aroused by recent anthropogenic activities

(To be submitted)

Guillaume P. Morin[1*], Christian France-Lanord[1], Jérôme Lavé[1], Ananta Gajurel[2], Albert Galy[1], Clio Bosia[3], Rajiv Sinha[4].

1- Centre de Recherche Pétrographique et Géochimique (CRPG) CNRS UMR 7358, Université de Lorraine, 15 rue Notre Dame des Pauvres, F-54500 Vandoeuvre-lès-Nancy, France ; 2- Department of Geology, Tribhuvan University, Ghantaghar, Kathmandu, Nepal ; 3- Laboratoire d'Hydrologie et de Géochimie de Strasbourg (LHyGES), EOST, Université de Strasbourg and CNRS, 1 Rue Blessig, 67084 Strasbourg Cedex, France ; 4- Department of Earth Sciences, Indian Institute of Technology, Kanpur 208 016, India

Abstract

Evolution of the erosion of continental surfaces through geologic times provides key evidences to assess the interplay of controls exerted by tectonics, topography, climate, and lately, human activities. Mountains belts, and more than others Himalayan range, has the particularity to present very high tectonics activity, contrasted seasonnality marked by the monsoon, developped topography and recent socio-economic development, which makes it a model to assess main issues on these complexe interactions.

Taking advantage of the large Sr and Nd isotopic contrasts of the main geological and physiographic Himalayan units, this study explores the time variations of the spatial distribution of erosion in Central Himalayas. Compiling Sr and Nd isotopic compositions of rivers sediments from many tributaries within the Narayani basin in central Nepal, we first define the mean Sr and Nd isotopic compositions of the three main Himalayan geological units in this region. Then we present isotopic chronicles of river sediments sampled at the outlet of the Narayani basin during 16 years, and ~50-kyr-long sedimentary archives drilled in the foreland basin.

Using Sr and Nd isotopic compositions to trace relative geological provenances and contribution, we demonstrate that erosion in the Narayani basin has remained stable for ~50 kyr up to the end of the 20th century. During this period, sediment fluxes were primarily derived from the High Himalayan regions (~ 80 %), i.e. from the areas presenting high reliefs and steep slopes. Fluxes stability during the major Pleistocene-Holocene climatic transition provides new evidence for a primary control of erosion by tectonic forcing rather than climatic forcing in the Himalayas. Since 2000s, a clear shift of the sediment compositions reveals a major and progressive intensification of erosion in the Lesser Himalaya (from ~20 to ~45% of the sediment budget) despite unchanged tectonic or climatic settings.

We propose that this strong increase by 3 fold of erosion of the Lesser Himalayan region is a consequence of recent human activities, and most likely, roads constructions in the Middle Hills of Nepal, highlighting the crucial role of anthropic activities as major erosion agents on sensitive environments such as can be mountain ranges.

6.5.1 Introduction

The evolution and erosion of the continental landscapes are of particular importance in Earth sciences since they correspond to the interface between internal and external Earth's envelopes. The possibility of a major climate change over the next century makes also crucial the issue of the response of the continental surfaces, on which we live, to such climatic change. For both reasons, understanding the sensitivity of the landscape to climatic conditions is thus a major objective for the geomorphological community. Beyond the comprehension of the continental surfaces behaviour, the detection of possible changes of these surfaces and of its erosion over the next century also requires a detailed description of the current state of the system, including the identification of possible anthropogenic effects that would have already significantly altered the landscape. Recent evolution of worldwide riverine sediment delivery to the ocean indicates indeed that the Anthropocene is marked by the modification of both the production of terrestrial sediments and the transport through major rivers due to human transformation of the environment. During the 20th century, global sediment export has been enhanced by soil erosion due to land clearance and agricultural practices [Walling 06]. Major river sediment fluxes to the oceans have been, however, reduced since the 1960's by sequestration of sediment

by reservoirs behind dams [Syvitski 05, Walling 06, Syvitski 07]. The various factors that control the erosion and the evolution of the continental Earth's surface generally correspond to different time scales : tectonics modulations act over hundred thousands to millions of years, the climate changes evolves at millennial to hundred thousands years scale, whereas human impact can occur rapidly over a decade or a century. These timing differences might in theory permit to study separately the influence of each factor. At the scale of the Late Pleistocene or of the Holocene for example, the long wavelengths of the topography can be considered as almost fixed and any variation of erosion can, in most cases, be attributed to either climate or human activities.

Of all the landscapes, mountain landscapes are considered as highly vulnerable, especially because they can be strongly affected both by temperature variations and by a change in precipitation. Exposure of steep slopes to erosion or slope destabilization following a change in the vegetation cover [Lavé 04] partial melting of the permafrost at high elevation [Fischer 06], variable exposure to frost cracking [Delunel 10], or the fluctuations of glaciers extent, are all phenomena that contribute to sharply modulate the erosional activity along mountain slopes in phase with climate variations. Similarly, steep slopes make these setting quite vulnerable to human activities and deforestation.

Among all the mountain ranges on Earth, the Himalaya ranks first as source of sediments to the ocean [Milliman 83, Milliman 11] combining the ~600 and ~400 Mt/yr sediment mass flux exports of the Brahmaputra and Ganga respectively, [Lupker 11b], after a long transfer within the densely populated Ganga plain. Therefore, any change of erosion in the Himalayas makes it of particular significance even at global scale. The high sediment fluxes are direct consequences of the extreme Himalayan topographic slopes but also of intense monsoonal precipitations. During the Late Quaternary, the Himalayas have presumably faced large variations of precipitation in relation with varying intensity of the Indian summer monsoon (ISM) phenomenon (e.g. [Gu 93, Enzel 99, Cai 10]). They were also exposed to temperature changes with significant glaciers advance during glacial times. Nevertheless, the response of the Himalayan erosion to the Quaternary climatic variations has, so far, remained quite disputed. In the western Himalayas, sedimentary records from the Indus fan [Clift 08] indicate that during the early to mid-Holocene climatic optimum, the Lesser Himalaya (LH) was eroded faster than today relatively to the High Himalaya (HH) domain, in relation with an intensification of the precipitation on low elevation reliefs in front of the range. On the opposite, [Bookhagen 05b] observed highly

erosive events in the sediments of mountain lakes located in the High Himalayas of the Western Himalayas and Ganga headwater : according to this study, intensified monsoons during the mid-Holocene would have rather impacted the High Himalayas, triggering numerous landslides and increasing slopes erosion. Additional disagreement was found by [Rahaman 09] in the Ganga sediments originated from the central-west Himalayas, since higher proportion of sediment derived from the Lesser Himalaya was found during glacial periods, and hypothetically ascribed to limited erosion of the northern Himalayan as result of ice cap protection. In the central and Eastern Himalayas, the conclusions of various studies might also appear in partial contradiction : on one side [Lupker 13] did not observe any change of provenance between 21 ka and today, suggesting any modification of the erosion balance between the Ganga and Brahmaputra basins or the northern HH and southern LH ; on the other hand, [Goodbred 00], based on sediment volume reconstruction in Bangladesh, document a major increase in sedimentation during the early Holocene, even if it is difficult to ascribe it to erosion increase in the Himalayas or to a sedimentary response to the pre-Holocene sea level rise.

Contradictory results also characterize the impact of recent human activities on the erosion in the Himalayas. Deforestation, land use and agriculture were reported to promote the Himalayan environmental degradation [Ives 89] whereas investigations on soils erosion due to agricultural practices in the middle hills were concluding, on the contrary, that traditional terracing practices seem to prevent soil loss and hillslope erosion [Gardner 03, Smadja 92, Tiwari 09].

bove discrepancies between the variations of erosion and the climatic or anthropic forcing probably arise from various difficulties. On the short term, because of the stochastic nature of the hillslope erosion by landslides, the sediment load in rivers can vary significantly on an annual basis. In Nepal for example, the suspended load measurements over the last decades [Andermann 12b, Gabet 08] are found in general to poorly reflect, and mostly to largely underestimate along the southern flank of the HH, the millennial-scale erosion rates as provided by the ^{10}Be measured in the quartz fraction of the river sands [Godard 12, Puchol 14]. At longer time scale, estimating sediment flux requires to reconstruct in 3D the deposited volume of sediments. In the Himalayas, where 90% of the sediments are exported toward the ocean [Lupker 11b] and mixed with sediments of many rivers, such approach is therefore not possible. To overcome these difficulties, many studies rely not on absolute but rather on relative erosion rates based on the large geochemical

and isotopic spatial heterogeneities of the Himalayan geologic units, which are roughly correlated to the main physiographic units of the range. In case of contrasted erosive impact on the lower and higher Himalayas respectively, it is possible to track change through time of the sediment provenance and to identify climatic and anthropic changes. Following this general approach, in order to assess and interpret the evolution of the erosion signal in central Nepal, we document in the present study the provenance of the sediment deposited in the Narayani-Gandak floodplain over the last ~50 ka based on Sr-Nd isotopic tracing, and compare it to that of modern Narayani river sediments sampled over the last 16 years. This spatially integrative method has been first applied to isotopically trace the evolution of the Himalaya from the record of the Bengal fan [Bouquillon 90, France-Lanord 93], and later used in number of other provenance studies including paleo-erosion from Siwaliks sediments (e.g. [Huyghe 01, Najman 08, Robinson 01]). In the following, after a presentation of the isotopic measurements made on the main units outcropping in the Narayani watershed, on the Narayani-Gandak floodplain core sediments and on the modern sediment carried by the Narayani, we discuss how the relative proportions of sediments issued from the Lesser Himalaya and Higher Himalaya respectively have evolved through time, in particular during the last decade.

6.5.2 Setting

The Narayani watershed is one of the three major river networks draining the Nepal Himalaya. It covers a ~210 km E-W Himalayan segment of Nepal for an area of 32000 km^2. Four main transhimalayan rivers compose the basin, which are from West to East : Kali Gandaki, Marsyandi, Bhuri Gandaki and Trisuli. These main rivers drain across the main physiographic units from the South Tibet or Northern Himalaya, characterized by mountains at high elevation (>5000m) and arid climate ; the High Himalayan range that encompass in central Nepal numerous >7000m high summits and which is characterized by maximum relief ; the Middle Hills or Lesser Himalaya which contrasts in Central Nepal by low elevation mountains (<1500m) and more subdued relief. The Narayani river strictly speaking starts downstream of the confluence of Trisuli and the Kali Gandaki at Devghat and it cuts across the Siwaliks range, the most frontal Himalayan Hills including the piggy back basin of the Chitwan Dun. South of the front range, the Narayani takes the Gandak name and expands southeastward in the floodplain. The Gandak is a one-to-six-

km wide braided river that builds a smooth alluvial fan and converge with the Ganga after ~ 230 km. The Narayani is the most important Himalayan contributor to the Ganges in term of sediment flux (~ 100 Mt/yr ; [Andermann 12b]) and discharge (~ 50 km3/yr ; [DHM 03, DHM/FFS 04]).

The Narayani watershed undergoes very intense precipitation, ~1.3 m/yr, due to high monsoon rainfall especially in front of the Annapurna range [Putkonen 04, Bookhagen 10, Andermann 12b]. High precipitation combined with high relief and steep slopes in particular in the High Range lead to rapid erosion through glacier, river inscision, and landsliding [Gabet 04b, Gallo 14a]. Estimates of average erosion rates range from 0.8 to 2.7 mm/yr based on modern sediment flux (Andermann et al., 2012) and 1.7±0.4 mm/y based on concentrations of in situ 10Be in the quartz fraction of the Narayani sediments [Lupker 12a].

The Himalayan physiographic units partially overlap with the four main E–W trending geologic units of the range (e.g. [Le Fort 75, Colchen 86]), which are from North to South : 1- the Tethyan Sedimentary Series (TSS) composed of variably metamorphosed Palaeozoic–Eocene sedimentary series of the passive northern Indian plate margin ; 2- the High Himalayan Crystalline formations (HHC) composed of high-grade metamorphic gneisses and migmatites and locally marbles ; 3- the Lesser Himalayan formations (LH) that include variably metamorphosed Precambrian to Palaeozoic metasediments of the Indian craton ; 4- the Miocene to Pleistocene Siwaliks sediments that correspond to the foreland basin deposits exhumed by Late Cenozoic thin skin tectonics. Unlike most other Himalayan sections, the TSS units are largely exposed in the High Himalaya of Central Nepal, in particular along the Dhaulagiri and Annapurna massifs above 4000m. As a consequence, the Narayani sediments carry an unusually high proportion of carbonates between 5 and 20% ([Galy 99b, Lupker 12b] Table 6.7). Downstream the Siwalik front, the Gandak river drains into a wide floodplain that is a part of the low-gradient Himalayan foreland basin, building a megafan of alluvial deposits (Fig 6.5.1). The megafan is characterized by its subtle topographic fan shape and the presence of abandoned meanders and oxbow lakes [Mohindra 92, Sinha 05, Sinha 94].

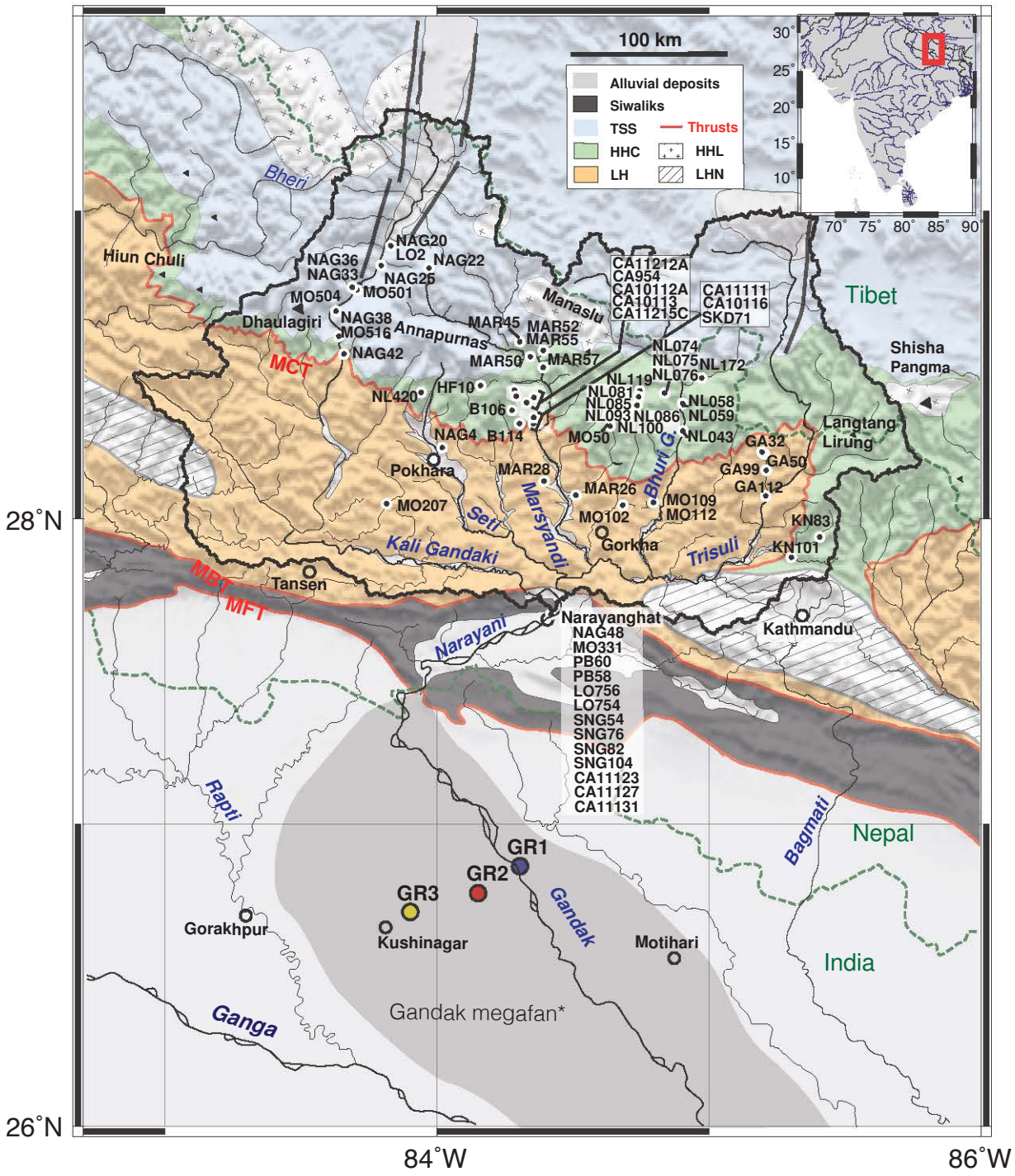

FIGURE 6.5.1 – Geographical setting of the Narayani-Gandak basin across the Central Himalayan mountain range and along the Northern Ganga plain.
Black dots with sample numbers correspond to small catchments draining the main lithologic units outcropping in the Himalayas and which sediments are used to document the Sr and Nd isotopic signature of these units (see Table 1). The sediment samples of the Narayani river were taken at Narayanghat from 1995 to 2011. The blue, red and yellow dots report the location of the 3 boreholes drilled into the upper part of the Gandak megafan (megafan limits as follows [Mohindra 92]).

In the Narayani catchment, topography, relief and climate have strongly conditioned the distribution of the population. If the total Narayani basin population reaches ~3.3 million inhabitants, with an average density of 122 per/km^2 (Nepalese population data survey), the repartition is very contrasted between the Lesser Himalayan districts where population density reaches 200-250 per/km^2, up to 320 per/km^2, and the drier and colder High Himalayan districts, where density is <50 per/km^2 and in some parts as low as 3.8 per/km^2. In the dry and elevated southern Tibetan part of the Narayani basin (15% of the whole catchment located north to the Nepal/China border), the population density is also very low and estimated to be <5 per/km^2 (the mean Tibet population density is 2.2 per/km^2). Therefore, human pressure on the environment varies in intensity between high mountainous catchments and the middle Hills, with an almost 100 times southward increase of population density.

6.5.3 Samples and methods

6.5.3.1 Sources signatures

In spite of number of isotopic studies on the various lithologies of the main Himalayan units, the isotopic characteristics of the Tethyan Sedimentary series, which is particularly well exposed in the northern part of the Narayani basin, is still poorly documented. Here, we therefore expand existing database and provide a general synthesis on the isotopic signature of the main Himalayan units in central Nepal putting a special emphasis on the Tethyan sediments. Because river sediments tend to integrate the isotopic signature of lithologies eroded in a catchment, we first expanded former ($^{87}Sr/^{86}Sr$, εNd) database based on bedrock samples, with measurements made on river sediments in order to document the average signature of the 3 main geological units (HHC, TSS and LH). This sampling includes both suspended and bank sediments sampled during monsoon and the dry season. We preferentially selected watersheds draining single geological unit in order to properly define their isotopic signature. The sampling also includes sediments from what we will call "dual basins" that drain dominantly (in terms of drainage area) through a given unit, but also encompass a minor area of a different unit.

6.5.3.2 Modern Narayani river

The sample set of the Narayani cover a 16 years range so that their isotopic compositions can be documented since 1995. Most samples have been taken at Narayanghat (Nepal, N 27.700, E 84.420) at the outlet of the Himalayan range. The overall data include bank sediment sampled on riversides at Narayanghat (1995), surface suspended loads sampled in the center of the river from Narayanghat Bridge (1998 to 2010) and suspended sediment depth profiles sampled in the center of the river at Narayanghat during monsoon 2005, 2007 [Galy 08], and 2011.

6.5.3.3 Gandak floodplain borehole samples

Three 50-m-long boreholes (Sites GR1, GR2, GR3) were drilled in Bihar (India) close to Bettiah (GR1 : N 26.9084 E 84.2938 at Dhudhiwan Dharwan, GR2 : N 26.8161 E 84.1458 at Bhodhrahra Buzunge, GR3 : N 26.7591 E 83.9003 at Shapar Kaisa). The locations of the boreholes were chosen based on electrical resistivity exploration of two transects [Sinha 14]in order to drill into the Narayani/Gandak fan, i.e. into sediments issued from the erosion of the Narayani Himalayan watershed, and to core far enough from the gravel front [Dubille 15] to prevent drilling into pebbly layers that would have hindered the drilling process. To outbalance potential hiatuses in the records due to the very avulsive nature of these rivers, three boreholes were made at a similar distance from the fan apex but at various lateral distances from present Gandak river. According to other boreholes dated in the Ganga floodplain by [Rahaman 09], these ~50-m-long stratigraphic sequences correspond to several tens of ka. The drilling was performed using bentonite as fluidizing agent.

The drilling progress were limited to two meters steps, and the string of rods containing the core liner were brought to surface each time. Recovery rarely exceeded 40% because of the loss of unconsolidated sand during coring. Nevertheless, the original sedimentary texture was sufficiently well preserved in the remaining core segments to permit characterization of facies and granulometry, and to sampling for geochemical analysis.

The drilled sediments appear very similar to modern river sand deposits in terms of grain-size, nature and chemistry, and present all characteristics of buried paleo-channels [Sinha 14]. Lithofacies variability span high-energy level deposits composed of sandy facies of burried multi-storeyed river channels, to mud-dominated overbanks and interfluve

deposits with a few oxbow lakes sediments layers [Jain 03]. This compares with variability described in current Ganga floodplain deposits [Singh 91].

In the 3 boreholes, sandy facies were preferentially sampled for Sr – Nd analysis in order to both minor mineralogical effect on $^{87}Sr/^{86}Sr$ (see section 5.1), and to study sediment a priori directly derived from the Himalayan range, and not potentially reworked from the fine interfluve deposits. Special care was also taken to sample the most well preserved zone in the center of the cores to avoid drilling disturbance and/or contamination at the periphery of the cores. According to above granulometric requisites, the samples were picked every 3 to 5 m along the three holes.

6.5.3.4 Sr-Nd analysis

Nd and Sr separation and analysis were performed at CRPG following an adapted procedure after [Pierson-Wickmann 01]. Because Narayani sediments contain 5 to 20% of calcite and dolomite characterised by low $^{87}Sr/^{86}Sr$ derived from their marine origin [Galy 99a], all samples were decarbonated prior analyses. Analyses therefore reflect the signature of the silicate fraction of these sediments. The pre-treatment consists in a decarbonation with low concentration 0.5 N HCl acid at 80°C for an hour with intermittent ultrasonic treatment and vortex agitation following [Galy 10, Singh 08b]. After centrifugation, the residue was washed with Milli-Q water and freeze-dried. The completeness of the decarbonation were then tested for carbonates concentration on a gaz-bench coupled to MAT253 by phosphoric acid at 70°C. Samples were then ashed at 600° C during 8h to oxidize organic matter. Aliquots of known weights ~100 mg sediments were transfered to Savillex vials and dissolved in HF-HNO_3 with a small amount of $HClO_4$. Sr and Nd were separated using Eichrom Sr-spec, TRU-spec and Ln-spec resins. Sr isotopic compositions were measured by TIMS using a Triton Plus operated in static mode.

The $^{87}Sr/^{86}Sr$ ratios for the standard NBS 987 was 0.710233 ± 0.00005 (2σ), and all ratios were corrected for mass fractionation $^{86}Sr/^{88}Sr = 0.1194$. Nd isotopes were measured on a Neptune Plus MC-ICP-MS and Nd isotopic ratios were normalized to $^{146}Nd/^{144}Nd$ =0.7390. Isotopic compositions are reported in εNd calculated using the CHUR value given by [Jacobsen 80]. Nd and Sr procedural blanks are taken into account in overall reproducibility for $^{87}Sr/^{86}Sr$ and εNd that are given at 2 $.10^{-5}$ for Sr and 0.5 ε unit for Nd.

6.5.3.5 Carbonates analysis

Because above isotopic measurements were conducted on the silicate fraction of the sediments, the relative budgets in HH, LH and TSS units, presented in the discussion section, have to be corrected for the carbonate content. For this reason we have also systematically measured the carbonate content, as well as the carbon isotopic signature, of the main units outcropping in Narayani catchment and of the sampled sediments by phosphoric acid dissolution at 70°C, and CO_2 analysis on a gas-bench coupled to a MAT253 spectrometer and corrected for analytical fractionation. The overall uncertainty is ± 1.5% for carbonate content, and is under ± 0.2 ‰ for δ13C carbon isotopic composition.

6.5.4 Results

6.5.4.1 Isotopic signatures and carbonate content of main geological units of Central Nepal

The average isotopic signature of the TSS is mostly documented by samples from the upper Kali Gandaki and upper Marsyandi rivers and few of their tributaries (Figure 6.5.2 and 6.5).

Sample #	River	Locality	Geological units	Type	North	East	Date	Rb Sil [ppm]	Sr Sil [ppm]	$^{87}Sr/^{86}Sr$	2 s.d.	Nd Sil [ppm]	Sm Sil [ppm]	$^{143}Nd/^{144}Nd$	2 s.d.	εNd_0
TSS																
NAG 22	Marsyandi	source	TSS	BL	28.7862	83.9637	28/11/95	218.0	93.6	0.721900	<1.5E-5	64.3	10.1	0.511790		-16.6
MAR-50	Marsyandi	Temang	TSS	BL	28.5301	84.3159				0.731500	<1.5E-5			0.511750		-17.3
MAR-45	Naar k.	RG	TSS	BL	28.5614	84.2569				0.722066	<1.5E-5			0.511807		-16.2
MO 501	Kali	Tukuche	TSS	SL	28.7034	83.6345	26/07/98	172.5	156.5	0.723111	<1.5E-5	30.3		0.511749		-17.2
NAG 33	Kali	Koketani	TSS	BL	28.6473	83.5942	02/12/95	136.7	95.8	0.729111	<1.5E-5	38.4	6.8	0.511758		-17.2
NAG 36	Kali	Kopchepani	TSS	BL	28.6473	83.5942	02/12/95	223.7	153.2	0.724852	<1.5E-5	38.5	6.7	0.511810		-16.2
TSS average			**TSS**					187.7	**124.8**	**0.725423**		**42.9**	7.9	**0.511777**		**-16.8**
LO2	Kali	Kagbeni	mixed TSS basin	BL	28.8407	83.7844	16/05/93	159.3	95.9	0.731960	<1.5E-5	30.0	5.3	0.511837		-15.6
NAG 20	Kali	Kagbeni	mixed TSS basin	BL	28.8407	83.7844	25/11/93	157.0	96.0	0.731627	<1.5E-5	19.3	3.6	0.511928		-13.8
NAG 25	Kali	Jomoson	mixed TSS basin	BL	28.7846	83.7344	01/12/95	248.0	162.4	0.722487	<1.5E-5	47.5	8.5	0.511898		-14.4
MO 504	Yamkim	outlet	TSS	SL	28.7112	83.6412	26/07/98		56.3	0.759400	<1.5E-5	29.5		0.511660		-18.9
MO 516	Kali		mixed TSS basin	SL	83.6358	28.5579	27/07/98		195.9	0.721980	<1.5E-5	34.9		0.511816		-15.9
NAG 38	Kali	Dana	mixed TSS basin	BL	28.5579	83.6358	03/12/95	157.0	135.0	0.730227	<1.5E-5	32.2	5.9	0.511823		-15.9
NAG 42	Kali	Tatopani	mixed TSS basin	BL	28.4962	83.6542	05/12/95	153.2	142.9	0.729763	<1.5E-5	28.9	5.2	0.511775		-16.8
MAR-52	Dudh k.	Darapani	mixed TSS basin	BL	28.5348	84.3657				0.731861	<1.5E-5			0.511712		-18.1
MAR-57	Marsyandi		mixed TSS basin	BL	28.4651	84.3732				0.729856	<1.5E-5			0.511782		-16.7
MAR-55	Marsyandi	Tal	mixed TSS basin	BL	28.4668	84.3728				0.731092	<1.5E-5			0.511726		-17.8
HF 10	Seti		mixed TSS basin	BL				128.6	47.3	0.737782	<1.5E-5	22.3	3.8	0.511748		-17.4
HHC																
MO 50	Chepe	Vallon	HHC	BL			06/05/97			0.753712	<1.5E-5			0.512002		-12.4
MAR-26	Chepe		HHC	BL	28.1120	84.4266				0.754397	<1.5E-5			0.511824		-15.9
KN 101	Likhu		HHC	BL	27.8912	85.2492		301.9	106.4	0.750994	<1.5E-5	31.7	6.1	0.511812		-16.1
KN 83	Tadi		HHC	BL	27.8912	85.2492	06/05/97	117.0	131.0	0.750860	<1.5E-5	29.5		0.511838		-15.6
CA11215C	*Khudi k. N*	*Branche Nord*	*HHC*	*Sand/Gravels*	*28.3175*	*84.3564*	*14/11/11*			*0.755024*	*1.E-05*			*0.511867*	*3.E-06*	*-15.0*
CA10112A	*Khudi k. W*	*Branch W*	*HHC*	*Bank*	*28.3652*	*84.3054*	*15/11/10*			*0.757583*	*8.E-06*			*0.511893*	*2.E-06*	*-14.5*
SKD71	*Khudi k.*	*Khudi*	*HHC*	*SL*	*28.3056*	*84.3301*	*23/08/10*			*0.762701*	*1.E-05*			*0.511894*	*3.E-06*	*-14.5*
CA11212A	*Khudi*	*Nord W basin*	*HHC*	*Sand/Gravels*	*28.4053*	*84.2629*	*10/11/11*			*0.748403*	*1.E-05*			*0.511835*	*3.E-06*	*-15.7*
CA10113	*Khudi basin*	*HHC Trib*	*HHC*	*Bank*	*28.3648*	*84.3047*	*15/11/10*			*0.756553*	*7.E-06*			*0.511862*	*4.E-06*	*-15.1*
CA954	*Khudi basin*	*Landslide*	*HHC*	*Bank*	*28.3718*	*84.2940*	*11/11/09*			*0.761857*	*7.E-06*			*0.511880*	*2.E-06*	*-14.8*
Khudi average	***Khudi basin***		***HHC***							***0.757020***				***0.511872***		***-14.9***
HHC average			**HHC**					209.5	**118.7**	**0.753397**		**30.6**	6.1	**0.511870**		**-15.0**
GA 32	Mailung	Paigutang	mixed HHC basin	Bank	28.2217	85.1875	06/10/99	127.4		0.754785	<1.5E-5			0.511686		-18.6
CA10116	Khudi k.	Khudi Power house	mixed HHC basin	Bank	28.2880	84.3451	16/11/10			0.761467	1.E-05			0.511871	3.E-06	-15.0
CA11111	Khudi k.	Khudi Power house	mixed HHC basin	SL	28.2885	84.3452	29/07/11			0.762997	2.E-05			0.511857	3.E-06	-15.2
B106	6.1	0.8	HHC bedrock							0.765060	<1.5E-5			0.511903		-14.3
B114	3.0	0.8	HHC bedrock							0.757940	<1.5E-5			0.511925		-13.9
NL43	3.9	0.7	HHC bedrock							0.747452	<1.5E-5			0.511810		-16.2
NL58	3.1	0.7	HHC bedrock							0.745126	<1.5E-5			0.511918		-14.0
NL59	1.1	0.7	HHC bedrock							0.733112	<1.5E-5			0.511866		-15.1
NL74	2.0	0.7	HHC bedrock							0.733546	<1.5E-5			0.511844		-15.5
NL75	5.5	0.8	HHC bedrock							0.754950	<1.5E-5			0.511777		-16.8
NL76	1.4	0.7	HHC bedrock							0.733218	<1.5E-5			0.511852		-15.3
NL85	2.0	0.7	HHC bedrock							0.745317	<1.5E-5			0.511706		-18.2
NL93	0.4	0.7	HHC bedrock							0.734352	<1.5E-5			0.511713		-18.0
NL420	19.2	0.8	HHC bedrock							0.806501	<1.5E-5			0.511841		-15.5
LH																
NAG 4	Bijaipur	Kundahar	LH	BL	28.2449	84.0003	11/11/95	106.8	44.8	0.879796	<1.5E-5	30.1	5.4	0.511349		-25.1
MO 112	Isul k.	Bhuri G.	LH	BL	28.0482	84.8084	12/05/97			0.874814	<1.5E-5			0.511324		-25.6
MO 102	Marsel k.	Darondi	LH	BL	28.0411	84.6694	11/05/97		48.9	0.840096	<1.5E-5			0.511418		-23.8
MO 109	Mati k.	Bhuri G.	LH	BL	28.0446	84.8061	12/05/97		50.2	0.853771	<1.5E-5			0.511577		-20.7
MO 207	Andi	Kali Gandaki	LH	BL	28.0429	83.7903	18/05/97			0.892148	<1.5E-5			0.511319		-25.7
GA 99	Mailung	landslide	LH	Bank	28.1478	85.1994	11/10/99		74.8	0.822903	<1.5E-5	31.6		0.511452		-23.0
GA 112	Mailung	Camp	LH	Bank	28.0817	85.2067	12/10/99		62.2	0.855181	<1.5E-5	30.1		0.511343		-25.1
MAR-28	Paudi k.	RG	LH	BL	28.1231	84.4083				0.824000	<1.5E-5			0.511392		-24.3
MAR-64	Ngadi Khola	RG	LH	BL	28.3098	84.4043				0.814000	<1.5E-5			0.511423		-23.7
LH average			**LH**					106.8	**56.2**	**0.850745**		**30.6**	5.4	**0.511400**		**-24.1**
GA 50	Mailung	Col	LH bedrock	Bank	28.2180	85.1813	08/10/99		19.8	0.885761	<1.5E-5	32.7		0.511587		-20.4

TABLE 6.5 – Sr and Nd silicates isotopes of lithology units in the chain of central Nepal Himalaya

To the exception of the Yamkim khola (MO 504), all compositions are grouped in a narrow range. Excluding this outlier of the most western and drier part of the Narayani catchment, the averaged isotopic compositions of the TSS based on mainstream rivers defines a pole with $^{87}Sr/^{86}Sr = 0.725 \pm 0.004$ (1σ) andεNd = -16.8 ± 0.5 (1σ). These values are further strengthened by Kali Gandaki, Marsyandi and Seti sediments sampled downstream of the TSS in the HHC domain but fed in a large majority by TSS erosion products (light blue circles in figure 6.5.2). These samples show indeed compositions identical to intermediate between TSS and HHC. On the other hand, the average concentrations of Sr and Nd in silicate fractions of the TSS rocks reach $[Sr]_{sil} \approx 125$ ppm and $[Nd]_{sil} \approx 43$ ppm. More than any other Himalayan formations, the TSS are very rich in carbonated rocks. This is dominantly calcite and the carbonate concentration of the Kali Gandaki and Marsyandi sediments in the TSS vary between 10 and 60%.

The HHC is documented by 10 samples of HHC tributaries of main rivers and by published bedrock data. The average compositions of HHC watersheds are $^{87}Sr/^{86}Sr = 0.756 \pm 0.005$ (1σ) and εNd = -15.0 ± 1 (1σ) (Fig 6.5.2). The bedrock data (listed in annexe A1) comprise 61 Sr data and 97 Nd data with limited combined Sr-Nd couples : their mean isotopic values, $^{87}Sr/^{86}Sr = 0.765$ (median = 0.752) and εNd = -15.6 (median = -15.5), are found in close agreement with HHC basins average. The Sr and Nd average concentrations in HHC silicate fractions are close to those of TSS with $[Sr]_{sil} \approx 119$ ppm and $[Nd]_{sil} \approx 31$ ppm. In spite being mostly silicated and gneissic, the HH units contain also a few calc-gneisses units, and on average its carbonate (mostly calcite) concentration reach 1%.

Finally, LH is characterized based on 8 river sediments from tributaries draining solely the LH. Isotopic data show higher dispersion than for HHC and TSS with εNd between -20.3 and -25.7 and $^{87}Sr/^{86}Sr$ between 0.823 and 0.892. This reflects the diversity of nature and age of the LH bedrocks. Nevertheless, LH river data confirm the strong isotopic contrast with HHC and TSS and return the following average compositions $^{87}Sr/^{86}Sr = 0.859 \pm 0.026$ (1σ) and εNd = -23.7 ± 2 (1σ), while $[Sr]_{sil} \approx 56$ ppm, $[Nd]_{sil} \approx 31$ ppm. The Nd isotopic composition is in good agreement with the bedrock mean value of -23.9 (median = -24.0 and n=45) (Appendix A2). On the contrary the $^{87}Sr/^{86}Sr$ of LH river sediments is less radiogenic than that of bedrock (mean=1.057) probably because the latter is only based on 10 samples. The presence of dolomitic units within the upper LH sequence [Pecher 78] is reflected in the sediments of rivers draining LH units by an average

content in carbonate of 1.1 %.

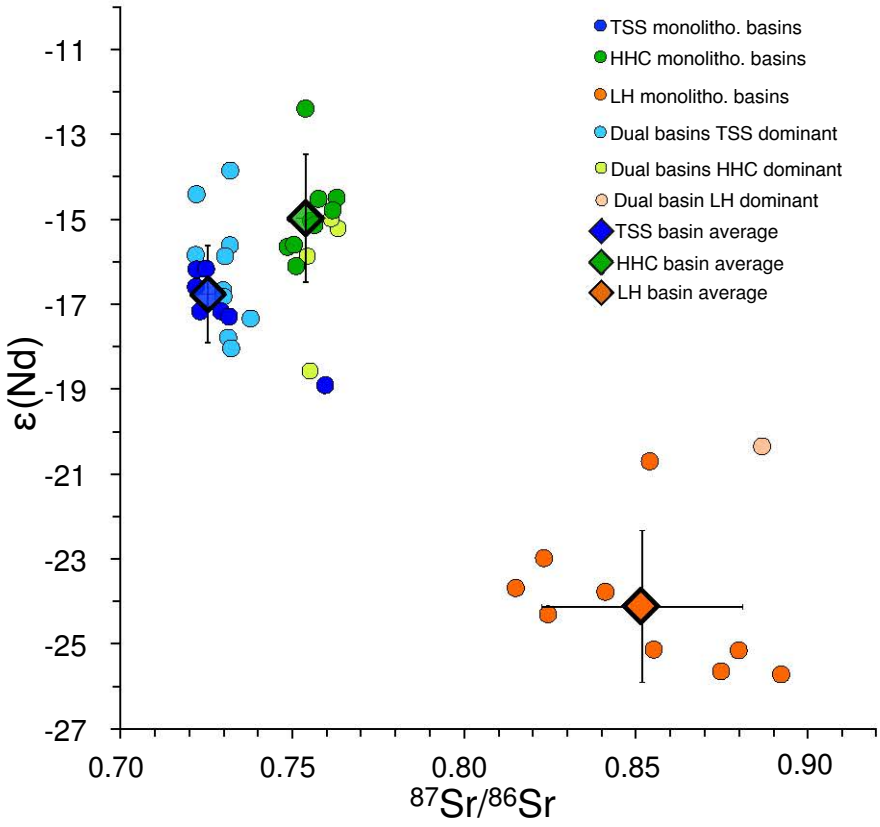

FIGURE 6.5.2 – εNd and $^{87}Sr/^{86}Sr$ compositions of monolithological or dual geological units Himalayan tributaries in Narayani river basin.
Pure TSS basins (blue dots) define a narrow compositional space around a mean value of $^{87}Sr/^{86}Sr$ = 0.72542±0.0400 and εNd = -16.8±0.5 (blue diamond) supported by TSS dominated mixed TSS-HHC basins light blue dots. Pure HHC basins (green dots) define compositional space around a mean value of $^{87}Sr/^{86}Sr$ = 0.75638±0.0502 and εNd = -15.0±1 (green diamond) also supported by mixed HHC dominant basins light green dots. Pure LH basins (orange color dots) compositions are more spread and occupy a larger space with an average $^{87}Sr/^{86}Sr$ = 0.85872± 0.2604 and εNd = -27.7±2 (orange color diamond). Error bars associated to the average poles correspond to 1σ-error.

6.5.4.2 Borehole sediments from the Gandak floodplain

Boreholes sediment dating

We have three ^{14}C ages obtained on wood debris recovered in muddy cores of GR1 ; carbon isotopic compositions were measured on AMS by BETA Analytics after classical acid/alkali/acid pre-treatment. These wood debris were embedded in anoxic environment that likely prevented their oxidation. The two shallowest samples, 13 and 14 m deep, give an age of 1714 to 1564 BP (GR1P10-D-20 _ conventional ^{14}C-age BP : 1740 ± 30) and 2490 to 2338 BP (GR1P10-B-46-47 _ conventional ^{14}C-age BP : 2370 ± 30) respectively. The deepest sample at 36 m depth gives an age of 32660 to 31600 BP (GR1P24-B-10 _ conventional ^{14}C-age BP : 28260 ± 130) (calibration were made using IntCal13 [Reimer 13] see appendix A2). These ages represent mean sedimentation rates of 7.9 mm/yr, 5.8 mm/yr and 1.1 mm/yr, respectively. The two shallowest wood-debris sampled in the same core segment GR1P10 gives very high sedimentation rates compared to the mean sedimentation rate of 0.9 to 1.2 mm/yr observed during the Holocene in a nearby site close to the Narayani MFT outlet but fed by small Siwaliks-draining rivers [Gurung 05]. The Gandak river channel presently displays active braided forms and its depth reaches ~8 m [Jain 03] : lateral channel migration following sudden avulsion can induce bank erosion or new channel formation and therefore locally produces rapid sedimentation of thick braided channel deposits, which might potentially explain the young sediment ages obtained at 12-13 m depth.

On the basis of the deepest and oldest wood sample, we extrapolate that the bottom sediment of the boreholes could be aged around 40 to 50 ka BP. We underline that the large variations of sedimentation rates observed in the upper part of the GR1 borehole might also be present in the lower portion of the holes and preclude providing more precise sediment age framework. However, the main purpose of this study is to document the very recent evolution of the isotopic signature of Gandak/Narayani sediments and to compare it to the Late Pleistocene and Holocene. For this purpose, an exact age control was not an essential requisite.

Isotopic results

The data of the three Gandak boreholes are listed in Table 6.6, and presented in Fig 6.5.3.

Sample #	Sample depth (m)	Grain-size	Al/Si	$^{87}Sr/^{86}Sr$	2 s.d.	$^{143}Nd/^{144}Nd$	2 s.d.	εNd_0	Carbonates cont. %wt.	$\delta^{13}C$ carb. vPDB	$\delta^{18}O$ carb. vSMOW
GR1P1 60-67	1.1	very fine sand to silt	0.264	0.776231	9.E-06	0.511640	5.E-06	-19.5	12.9	-1.54	18.51
GR1P5 13-21	5.5	medium sand	0.145	-	-	0.511709	1.E-05	-18.1	8.0	-0.90	17.45
GR1P8 13-21	9.9	fine sand	0.145	0.743296	5.E-06	-	-	-	13.0	-0.74	17.53
GR1P9 1-6	10.8	silt to clay	0.361	0.794973	7.E-06	0.511618	5.E-06	-19.9	25.2	-0.84	18.29
GR1P9 34-41	11.8	fine sand	0.222	0.752141	8.E-06	0.511715	5.E-05	-18.0	19.7	-0.71	18.60
GR1P10 47-53	13.7	medium sand	0.174	0.752929	2.E-05	-	-	-	8.3	-1.09	18.66
GR1P12	16.8	medium sand	0.283	0.757756	9.E-06	0.511704	4.E-05	-18.2	4.5	-1.10	18.62
GR1P13 0-5.5	17.7	medium to fine sand	0.147	0.747730	1.E-05	-	-	-	7.7	-0.64	18.92
GR1P20 16-20	29.7	medium to coarse sand	0.182	0.746503	2.E-05	-	-	-	7.6	-0.32	17.13
GR1P26 0-10	38.7	fine to medium sand	0.197	0.753032	2.E-05	0.511725	2.E-05	-17.8	6.0	-0.06	17.72
GR1P29 24-40	44.0	medium sand	0.169	0.744560	1.E-05	0.511670	2.E-05	-18.9	7.8	-0.66	17.92
GR1P31 24-32	48.0	clayey silt	0.385	0.767885	3.E-05	0.511695	2.E-05	-18.4	12.1	0.64	19.88
GR2P2 3-15	1.2	clayey silt	0.344	0.743181	6.E-06	-	-	-	56.6	-0.97	18.95
GR2P2 59-69	2.1	very fine sand	0.151	0.743681	5.E-06	0.511748	2.E-05	-17.4	37.3	-0.72	18.28
GR2P4 3-12	3.9	fine to very fine sand	0.170	0.741436	3.E-05	0.511709	6.E-06	-18.1	27.6	-0.80	17.83
GR2P6 7-15	7.1	fine to very fine sand	0.158	0.738372	8.E-06	0.511746	9.E-06	-17.4	27.5	-0.81	17.56
GR2P7 31-36	9.1	fine sand	0.161	0.801433	6.E-06	0.511780	6.E-06	-16.7	18.2	-0.81	17.56
GR2P13 10-36	18.7	fine sand	0.149	0.749735	1.E-05	0.511715	6.E-06	-18.0	8.3	-0.92	18.14
GR2P19 49-56	30.4	very fine sand to silt	0.173	0.748360	1.E-05	0.511716	8.E-06	-18.0	7.8	-0.39	17.61
GR2P23 37-40	37.2	silt	0.294	0.744328	2.E-05	0.511715	2.E-05	-18.0	7.0	-0.40	21.11
GR2P27 70-96	45.0	fine to medium sand	0.149	0.748416	6.E-06	0.511728	6.E-06	-17.7	20.0	-0.56	17.79
GR2P31 23-30	51.1	silt	0.204	0.741129	1.E-05	0.511728	5.E-06	-17.7	16.0	-0.33	20.46
GR2P32 16-28	53.1	silt to clay	0.262	0.738715	1.E-05	0.511747	4.E-06	-17.4	28.9	-0.13	17.63
GR3P4 6-13	4.1	medium sand	0.163	0.746701	9.E-06	0.511698	5.E-06	-18.3	0.0	-8.22	20.29
GR3P7 5-29	8.3	medium sand	0.153	0.746401	1.E-05	0.511725	9.E-06	-17.8	5.4	-1.15	17.82
GR3P9 35-40	12.0	fine sand	0.162	0.746129	5.E-06	-	-	-	6.3	-0.67	17.01
GR3P12 40-47	16.7	silt to clay	0.249	0.748300	9.E-06	0.511720	6.E-06	-17.9	2.2	1.25	20.18
GR3P16 13-22	24.7	fine to medium sand	0.167	0.747781	1.E-05	0.511752	1.E-05	-17.3	1.1	0.12	23.69
GR3P18 30-40	27.7	fine sand	0.145	0.746445	1.E-05	-	-	-	6.3	-0.59	17.40
GR3P21	32.3	medium sand	0.134	0.746774	2.E-05	0.511744	7.E-06	-17.4	2.7	-0.38	19.28
GR3P26 8-15	40.7	fine sand	0.168	0.744442	1.E-05	0.511743	6.E-06	-17.5	8.1	-0.75	17.28
GR3P27 27-31	43.6	fine sand	0.153	0.747174	8.E-06	0.511714	5.E-06	-18.0	12.1	-0.31	16.34
GR3P30 89-101	49.1	silt to clay	0.254	0.752346	9.E-06	0.511730	5.E-06	-17.7	11.7	-0.25	17.48

TABLE 6.6 – Sr, Nd silicates isotopes and carbonates contents and isotopes in boreholes samples of Gandak plain

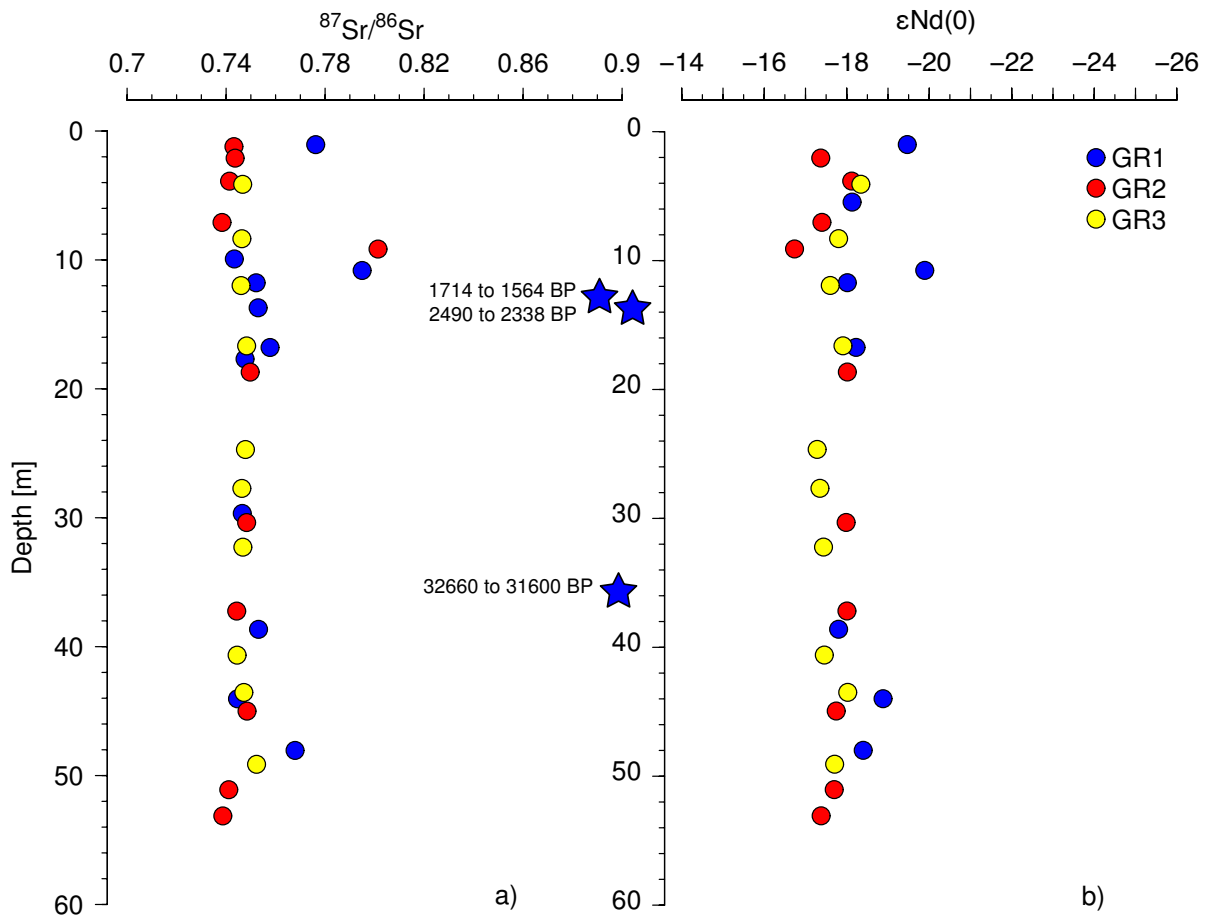

FIGURE 6.5.3 – εNd (a) and $^{87}Sr/^{86}Sr$ (b) composition of boreholes GR1 (blue dots), GR2 (red dots), GR3 (yellow dots) relative to depth.
Despite limited dating constrains, the three sites show essentially constant compositions for at least 32 kyr (oldest carbon dating 32 kyr BP at 36 m depth in GR1) that reveals stable mixing since at least last glacial and glacial-interglacial transition. Site GR1 shows two excursions away from the mean and constant trend at 1.1 and 10.6 m, which can be associated to events of higher LH erosion.

To the exception of four samples out of the ranges, both Sr and Nd isotopic data are remarkably homogeneous with average compositions of 0.747 ± 0.004 and -17.9 ± 0.4 for Sr and Nd respectively. The Nd standard deviation obtained along the boreholes is

very low close to the analytical uncertainty. Two samples from Site GR1 (P1 60-67, P9 34-41) have higher $^{87}Sr/^{86}Sr$ and lower εNd but remain compatible with the mixing space defined by the Narayani-Gandak sources (Fig 6.5.4).

One sample of GR2 (P7 31-36) shows distinctly higher $^{87}Sr/^{86}Sr$ (0.817) and the highest εNd (-16.7) of the borehole samples. This sample falls out of the mixing space defined by the Narayani-Gandak sources (Fig 6.5.4). Such extreme Sr composition could be linked to exceptional concentration in biotite although reported value for Ganga biotite is slightly less radiogenic (0.812 in [Garçon 14]) and there is no indication from major elements or direct observation of unusual mineralogical characteristics. Therefore we have no satisfying explanation for this sample and will further consider it as an outlier.

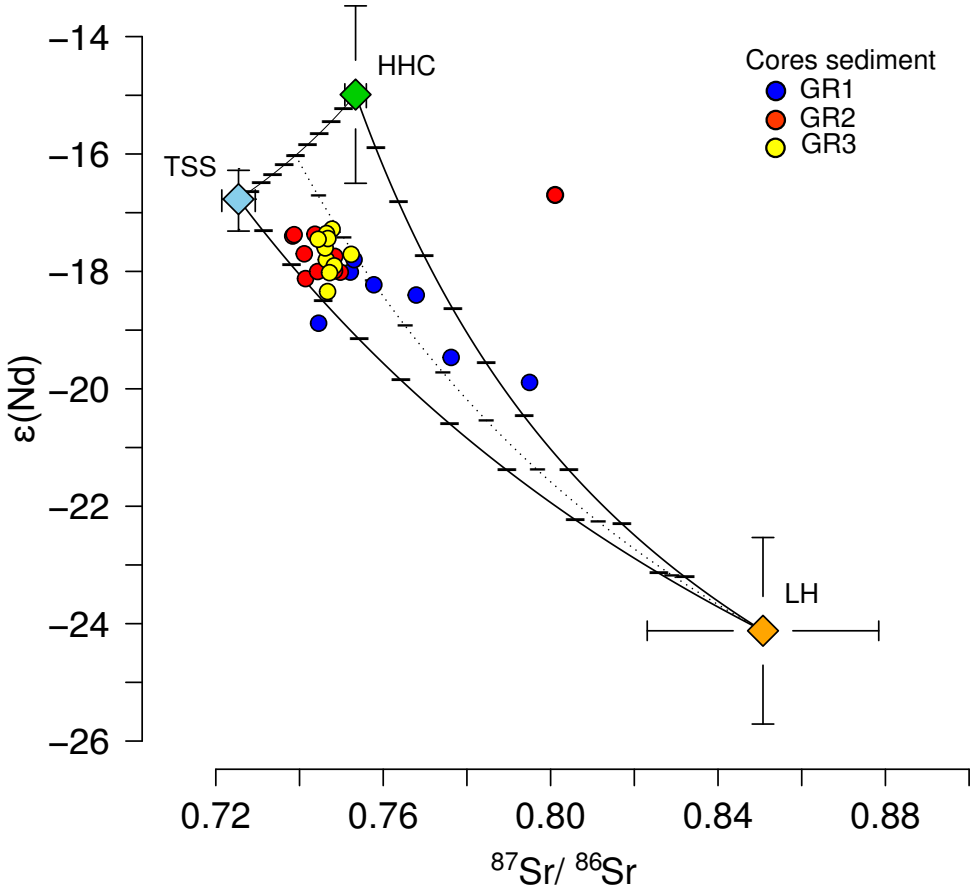

FIGURE 6.5.4 – εNd and $^{87}Sr/^{86}Sr$ compositions of boreholes (same color as in 6.5.2 and 6.5.3) compared to Himalayan lithology units averages (filled diamonds), the TSS units in blue, the HHC units in green and the LH units in orange color.

Graduated lines represent relative proportion of mixing between these 3 lithologic poles. Boreholes samples present very homogeneous compositions in agreement with a dominant proportion (~80 %) of Higher Himalayan units (TSS + HHC) over LH units. On this diagram, it is clear that the excursions away from the mean borehole compositions, already observed on εNd and $^{87}Sr/^{86}Sr$ GR1 profile of 6.5.3, are associated to pulses of increased sediment inputs from LH units.

6.5.4.3 Modern Narayani samples

Modern Sr-Nd compositions of Narayani sediments are reported in 6.7, 6.5.5 and 6.5.6.

Sample #	River	Location	Type Depth	Date	$^{87}Sr/^{86}Sr$	2 s.d.	$^{143}Nd/^{144}Nd$	2 s.d.	εNd_0	Carbonates cont.%wt.	$\delta^{13}C$ carb. vPDB	$\delta^{18}O$ carb. vSMOW
NAG 48	Narayani	Narayanghat	BL -	11/12/95	0.753632	<15.E-6	0.511672	-	-18.8	13.8	-0.8	17.7
MO 331	Narayani	Narayanghat	SL surf	10/07/98	0.751348	<15.E-6	0.511752	-	-17.3	-	-	-
BR 310	Gandak	Hajipur	Bank Int	07/05/04	0.747380	5.E-04	0.511684	-	-18.6	-	-	-
BR 335	Gandak	Barauli	Bank Cl	11/05/04	0.771122	5.E-04	0.511656	-	-19.2	-	-	-
PB 60	Narayani	Narayanghat	SL surf	11/07/05	0.758635	-	0.511647	-	-19.3	-	-	-
PB 58	Narayani	Narayanghat	SL surf	11/07/05	0.756602	-	0.511647	-	-19.3	21.8	-	
LO 754	Nayayani	Narayanghat	SL 6m	12/08/07	0.759287	-	0.511703	-	-18.2	17.2	-0.39	17.38
LO 756	Nayayani	Narayanghat	SL 3.3m	12/08/07	-	-	0.511680	-	-18.7	20.1	-0.33	17.38
SNG54	Narayani	Narayanghat	SL surf	05/08/10	0.790372	1.E-05	0.511613	4.E-05	-20.0	8.5	-0.87	18.14
SNG76	Narayani	Narayanghat	SL surf	27/08/10	0.750845	1.E-05	0.511631	3.E-05	-19.6	18.2	-0.37	17.16
SNG82	Narayani	Narayanghat	SL surf	02/09/10	0.773771	1.E-05	0.511650	2.E-05	-19.3	13.4	-0.20	16.66
SNG104	Narayani	Narayanghat	SL surf	24/09/10	0.769489	2.E-05	-	-	-	15.4	-0.99	16.85
SNG35-64	Narayani	Narayanghat	SL surf comp*	16/07-15/08/2010	-	-	0.511670	2.E-05	-18.9	-	-	-
SNG65-95	Narayani	Narayanghat	SL surf comp*	16/08-15/09/2010	-	-	0.511658	3.E-05	-19.1	-	-	-
SNG96-125	Narayani	Narayanghat	SL surf comp*	16/09-15/09/2010	-	-	0.511599	2.E-05	-20.3	-	-	-
CA11122	Narayani	Narayanghat	SL 5.5m	05/08/11	0.776275	2.E-05	-	-	-	-	-	-
CA11123	Narayani	Narayanghat	SL surf	05/08/11	0.768999	2.E-05	0.511623	1.E-05	-19.8	-	-	-
CA11127	Narayani	Narayanghat	SL surf	06/08/11	0.760857	1.E-05	0.511608	2.E-05	-20.1	-	-	-
CA11131	Narayani	Narayanghat	SL 2m	06/08/11	0.759556	1.E-05	0.511645	4.E-05	-19.4	-	-	-

SL surf comp* : composite sample created by weighted average daily discharge and concentration

TABLE 6.7 – Sr and Nd isotopes of recent Narayani river sediments sampled at Narayanghat from 1995 to 2011

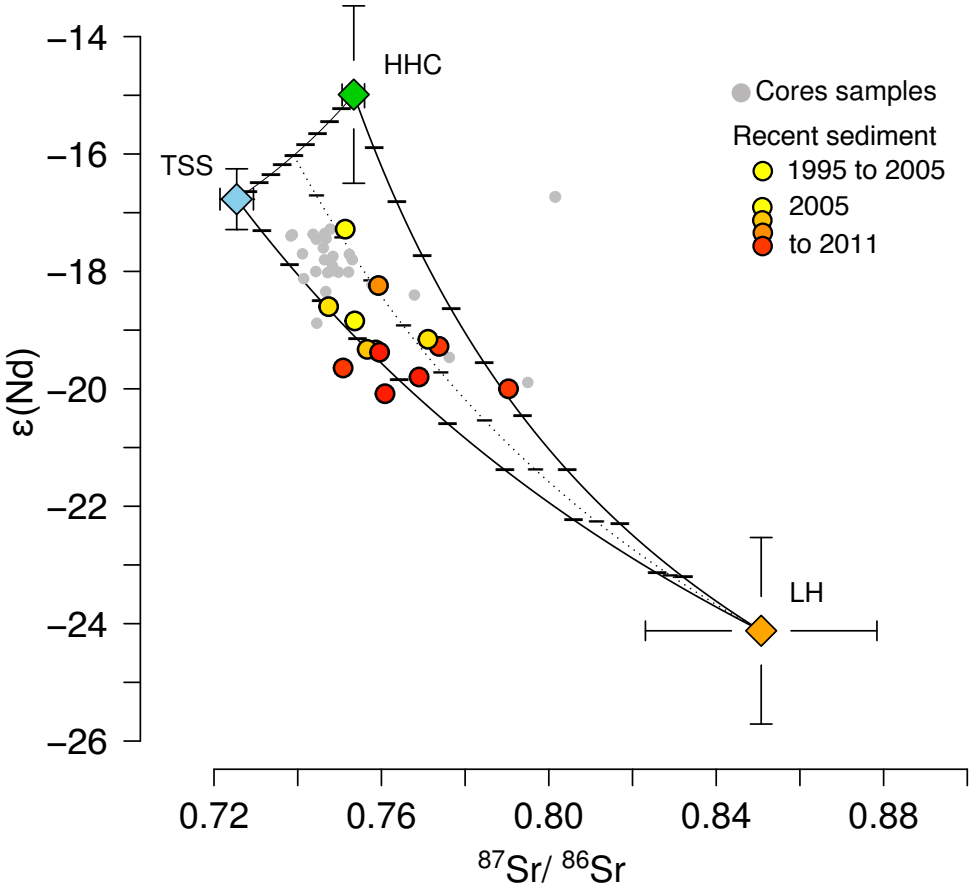

FIGURE 6.5.5 – εNd vs $^{87}Sr/^{86}Sr$ of the Narayani river sediment over the past 16 yrs in a mixing model with the 3 main Himalayan geological units.
The color scale from yellow (1995 – 2005) to red (2011) highlight a progressive shift in sediments compositions from ~80% of HHC+LH, close to the Late Pleistocene compositions as seen in the boreholes (gray dots), toward higher LH proportions of ca. 40-50% mostly since 2005. Spatial distribution of erosion is consequently interpreted as shifting from HH- to LH-dominated during the last 10 years.

The isotopic data are much more variable than for the Gandak borehole samples. The extrema are MO331 sampled in 1998 with $^{87}Sr/^{86}Sr$ = 0.75135 and εNd = -17, and

SNG54 sampled in 2010 with $^{87}Sr/^{86}Sr$ = 0.79037, εNd = -20.0. Overall there is a very limited overlap between modern Narayani samples and Gandak borehole samples. Closer examination of modern samples shows that there is a co-evolution of Sr and Nd isotopic compositions with time. Earlier data during the nineties show compositions close to those of the borehole samples whereas more recent samples suggest a gradual increase of the LH proportions in Narayani sediment (Fig 6.5.6).

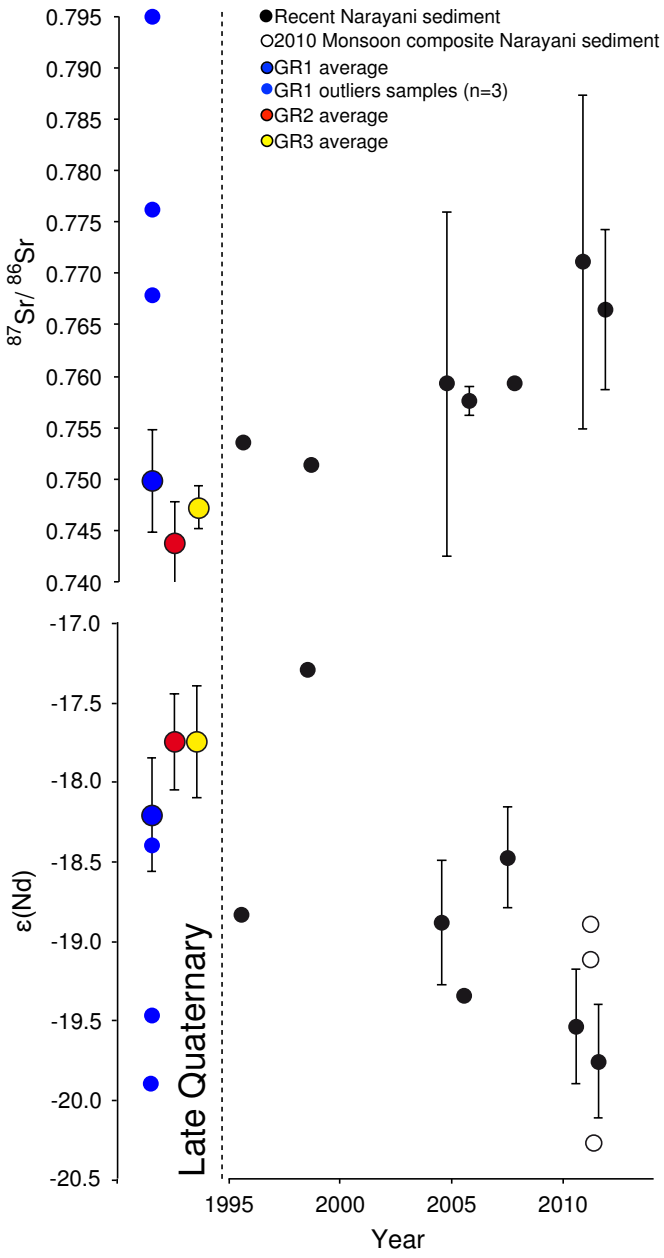

FIGURE 6.5.6 – Recent river sediment εNd and $^{87}Sr/^{86}Sr$ evolution through time compared to Late Quaternary boreholes samples sediments.
The black dots reports the yearly averaged values of Sr and Nd isotopes over the last 16 years (errors bars = 1σ). The blue, red and yellow dots report averaged GR1, GR2 and GR3 isotopes values (errors bars = 1σ). The co-evolving increase in $^{87}Sr/^{86}Sr$ values and decrease in εNd values traduces a general rise in Lesser Himalaya proportions in the Narayani sediment.

6.5.5 Discussion

6.5.5.1 Geological provenance inversion

In order to properly interpret the Sr and Nd isotopic data of Narayani-Gandak samples in terms of source mixing and subsequently in terms of variations of the relative erosion between the different physiographic units of the central Himalayas, we need to consider the sources of uncertainty associated to these tracers. This includes the mineralogical control on the isotopic signature of the sediment mixture, the uncertainty on the compositions of the geological units, and the analytical uncertainties.

The mineralogical control has been examined on Ganga sediment that are quite comparable to those of the Narayani [Garçon 14]. It is important for Sr for which the heterogeneity is high : muscovite, biotite and fine silt fraction are significantly more radiogenic (0.782 to 0.831) than other minerals (0.712 for epidote, 0.746 for clay, 0.757 for K feldspar). On the contrary, the mineralogical heterogeneity is minor for Nd isotopic compositions amongst the few minerals (monazite, clay, and biotite) that carry most of the Nd [Garçon 14]. Mineral sorting induced by hydrological processes are known to segregate particles in the river column : coarse, round, dense minerals being enriched in the bottom whereas fine, platty or light minerals being enriched towards the surface (e.g. [Galy 07a, Garzanti 10, Garzanti 11, Lupker 11b]). This generates a relative enrichment in quartz and dense minerals towards bottom and in clays and micas towards surface. This process can generate Sr isotopic heterogeneity whereas Nd isotopic compositions remain even. Despite the fact that $^{87}Sr/^{86}Sr$ variations as high as 0.04 were documented between bottom and surface sediments of the Ganga in Bangladesh [Lupker 13], the data from depth profile in the Narayani in 2011 show only limited variations (0.007 between surface and 5.5 m deep). This is mainly due to the high turbulence that limits mineral fractionation in the water column. However, even if limited in the Narayani sediments, the fact that we analysed for the last 15 years both suspended load and bank sediment might bring an additional noise on $^{87}Sr/^{86}Sr$ signatures. It is therefore important to consider the co-evolution of Sr and Nd isotopic compositions as a diagnostic evidence for source evolution.

The second source of uncertainty is inherent to the geological unit characteristics. The

typical isotopic signatures of the TSS and HHC units cover narrow ranges but have overlapping εNd ranges and relatively discrete differences in $^{87}Sr/^{86}Sr$. Thus, the evaluation of TSS to HHC relative contributions is poorly constrained given the analytical uncertainties. The LH isotopic scattering is large but the average values are very different from those of TSS and HHC. The Sr-Nd isotopic signatures of river sediments are therefore expected to express clearly changes in ratio of LH to High Himalayan domain (HHC+TSS).

Finally, the analytical uncertainties (0.0005) are negligible for $^{87}Sr/^{86}Sr$ measurements as it represents 0.03% of the variations observed in sediments of the Narayani (from 0.738 to 0.790). On the contrary, the εNd uncertainty reaches 0.5 ε units, which represents 18% of the variation observed in the sediments.

To summarize, the Sr isotopic data are precise but suffer some dispersion due to mineralogical sorting and variability of the LH end-member. Nd data are less accurate but define more precise end-members and are unbiased by mineralogical sorting. In order to resolve the inversion of the source mixing we used a Monte Carlo approach to take into account both the dispersions on the isotopic values of the three geological units, and the analytical uncertainty for each sediment sample (see appendix A3). Calculated proportions of each geological unit are reported in table 4. Because these calculations only apply to the silicate fraction of the sediments, a subsequent estimate must be added for the carbonate fraction. As described in section 4.1, only the rivers draining the TSS carry a significant fraction of carbonate, up to 30-40% of calcite, whereas HHC- and LH-draining rivers carry only 0 to 5% of carbonate. We therefore add a TSS carbonate proportion adjusted on the measured calcite concentration in the Narayani sediment samples, assuming a constant 3% calcite average contribution from the HHC and LH domains. Overall the calculated proportions for the Narayani sediments vary as follow : TSS (18-48%), HHC (12-43%), and LH (18-57%) (Fig 6.5.5). The Gandak boreholes data show significantly lower LH proportions (20%) except for the three samples of Site GR1 showing peaks in LH proportion from (35 to 52%). For reasons mentioned above, the relative proportions of TSS and HHC have high uncertainties ; therefore the clear evolution observed on these samples will be discussed between LH versus High Himalaya (mentioned as HH hereafter) as the sum of TSS and HHC (Fig 6.5.7)

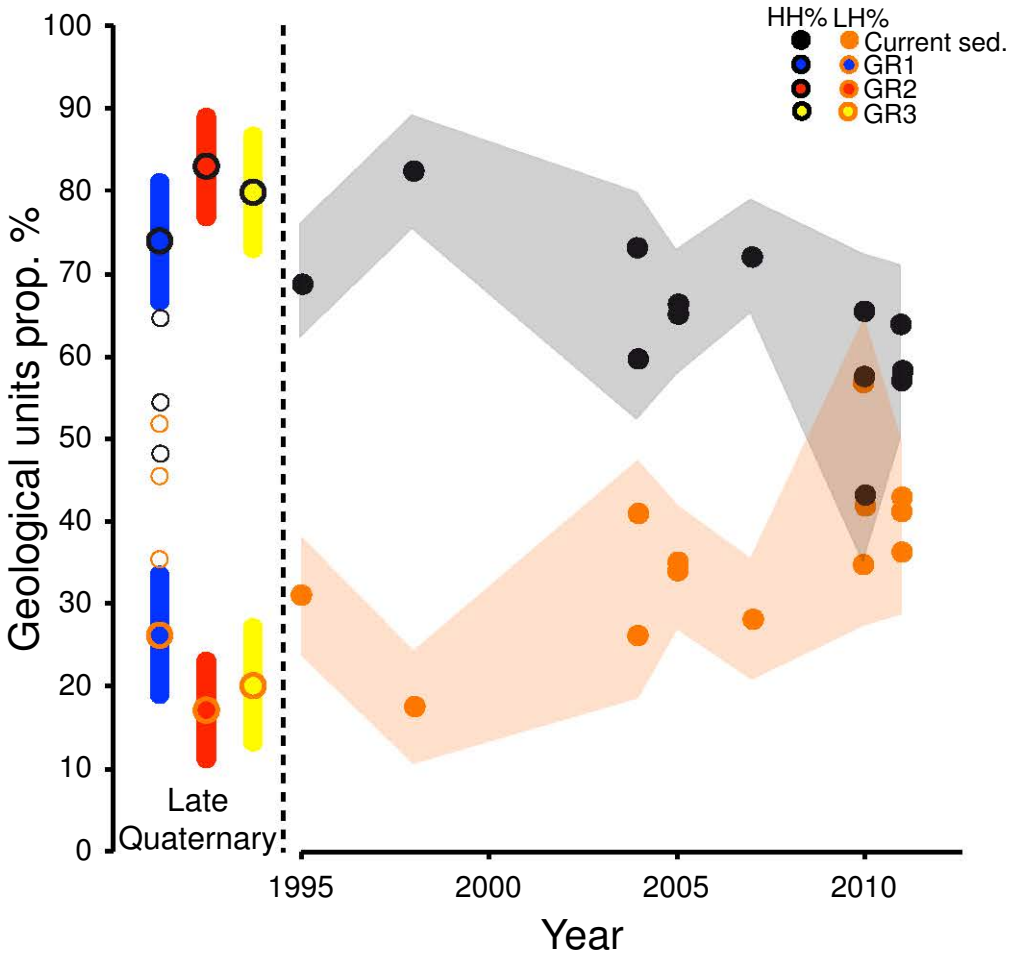

FIGURE 6.5.7 – Evolution since 1995 of LH and HH relative proportions in Narayani river sediment inverted from Sr and Nd isotopic compositions.

6.5.5.2 Late Quaternary erosion distribution stability in central Nepal

The Gandak borehole records are characterized by an overall remarkable stability of source mixing with few excursions toward higher proportion of LH in the upper part of Site GR1. This implies that erosion distribution in the Narayani basin has remained essentially stable over the last 40 ka in spite of the Late Quaternary climatic changes that have modified the glacier extent and the hydrological regime of rivers in Nepal (e.g. [Finkel 03, Gayer 06, Williams 06]. Our observation is at odd with previous evidence from Ganga flooplain boreholes near Kanpur [Agrawal 14, Rahaman 09] where a co-evolution of Sr and Nd isotopic compositions suggests that the ratio of LH/HHC erosion increased during the glacial episodes around 20 and 70 ka ago However, our results confirm former observations made at a broader scale in the Bengal Fan record over the last 20 ka that similarly show no evolution of erosion distribution [Pierson-Wickmann 01, Lupker 13], even if proximal floodplain deposition might not fully compare to the much more distal Bengal fan records. These later ones might indeed be affected by a buffer effect due to long time transfer and temporary sediments storage in the Ganga plain [Métivier 99a]. Similarly, the stability of the isotopic signal in the Gandak record could be potentially ascribed to such a buffer effect by the sediments stored in the northern floodplain and the Chitwan piggy back basin. However this effect has first been found minimal along the whole Ganga plain during the last millennia [Lupker 12a], and more importantly it should be more effective in the case of the Kanpur boreholes drilled into the Ganga floodplain, which are located in a more distal position in the floodplain.

On the other hand, in GR1, three samples show distinctly higher proportions of LH, up to 50-55% (Fig 6.5.7), whereas these episodes are not recorded in sites GR2 and GR3. They possibly reflect brief pulses of sediments with dominant supply from the LH following massive sediment supply by landslide or debris flows in LH parts of the Himalayan southern flanks. More importantly, the limited duration of these pulses suggest that the Narayani/Gandak rivers are able to convey rapidly large volumes of sediment with specific geochemical signature without signal dilution, i.e. without major buffering effect during sediment transfer down to the boreholes location.

Besides these three isolated pulses, we therefore interpret the general stability of the relative proportions of the main Himalayan geologic units found in the data of the Gandak boreholes as an evidence that the glacial to interglacial changes did not significantly

impact the overall erosion distribution in the Narayani basin.

From a quantitative point of view, the Gandak floodplain sediment record indicates that about 20 % of the sediment was derived from the LH and 80% from the High Himalaya including both HHC and TSS during pre-anthropic period. At the time scale of the Late Holocene period, an average erosion rate of 1.75±0.3 mm/yr for the whole Narayani watershed has been deduced from CRN in the quartz fraction of river sand [Lupker 12a]. Applying a simple budget calculation (Table 6.8), LH was therefore undergoing erosion rates of about 0.85±0.15 mm/yr and HH of about 2.4±0.4 mm/yr. These rates are quite consistent with the view that the HHC is eroded much faster than the LH whatever the considered time scale, according to thermochronology studies [Burbank 03, Herman 10], river profiles [Lavé 00, Lavé 01], CRN studies [Godard 14] or mineralogic mixing provenance using river sands from 2000 (i.e. before the most recent change discussed in next section) [Garzanti 07]. If such erosion pattern primarily results from much higher relief in the HHC, on the long term this might reflect higher uplift rates in the HHC as induced by the passive overthrusting of the Himalyan wedge over the ramp-flat geometry of the Main Himalayan Thrust [Lavé 01]. The general stability of the relative proportions of the main Himalayan geologic units found in the data of the Gandak boreholes might therefore reflect dominant tectonic forcing on spatial distribution of erosion.

6.5.5.3 Modern increase of the erosion of the Lesser Himalaya

When comparing Sr-Nd data in Gandak boreholes with those of recent sediments of the Narayani sediments, the proportion of LH appears clearly higher in the modern Narayani river sediments. The LH proportion is consistently between 15 and 30% in the Gandak boreholes whereas it is 30 to 55% in modern Narayani samples (Fig 6.5.7). This difference could be due to addition of different source of sediments between the Narayani sampling site and the Gandak borehole sites. As a matter of fact, Siwaliks tributaries are collected between Narayanghat and the coring sites. Such explanation is however unlikely for two reasons. First, the Siwaliks sandstones, as measured along the Tinau section located at 50km from Narayani outlet [Szulc 06], display isotopic compositions in Strontium and Neodymium very close to the Gandak boreholes values. Given that the Siwaliks drainage of the Gandak represents less than 10% of the total basin area, limited addition of Siwaliks

material appears insufficient to produce a significant shift of the most radiogenic Narayani samples. Secondly, the isotopic compositions of the carbonates in the Gandak boreholes are identical to those of the modern Narayani samples (see Table 6.7). Significant addition of Siwalik derived sediments would generate low $\delta^{13}C$ signatures characteristics of Siwaliks carbonates as observed in the Karnali river where Siwaliks contribution is high [Lupker 12b]. Therefore we consider that the present dataset represent robust evidence that there is a recent change in the erosion balance between the different Himalayan physiographic units within the Narayani watershed. Furthermore there is a tendency over the sixteen years of Narayani sampling for a progressive increase in LH supply in the Narayani.

Recent increase in LH proportion might reflect the signature or large mass wasting events, as hypothesized for the short excursions observed in Gandak Site GR1 and that we relate to massive landslide or debris flow imprints.. However, according to mapping on satellite images taken between 2002 and 2012, there is no evidence for enhanced activity of large natural landslides in the Lesser Himalaya [Gallo 14b] that could have fostered erosion of the LH. To the contrary, in the Marsyandi watershed for example, the major landslide recent activity has affected the HHC rather than LH [Gallo 14a].

On the other hand, no significant change in spatial pattern of the precipitation, like a relative rainfall increase over the Middle Hills, has been documented over the last 20 years to our knowledge. In absence of geomorphic or climatic reasons, we strongly suspect human activities are a plausible cause for evolution of the erosion spatial distribution. Among others, the building of new damming structures, change in land use activities or road constructions may have modified the relative contribution of LH and HH erosion fluxes.

First, retention of HH sediments behind dams must have enhanced relative proportion of the LH fluxes. However, no major dam was constructed so far in Central Nepal except the two medium size dams across the middle Marsyandi (commissioned in 2008) and across the middle Kali Gandaki (commissioned in 2002). These dams have, however, a limited retention capacity. With respective water storage volumes of 1.6×10^6 m^3 and 3.1×10^6 m^3, they would be able to intercept over a decade only ~1% of the Narayani modern sediment flux (48×10^6 m^3/yr _ [Andermann 12b]). In addition seasonal sediment flushing operations during monsoon time reduce the sediment storage upstream of the dams. Over a decade, it is estimated that ~8 Mt of sediments were deposited upstream of the Kali

Kandaki dam (Hydropower Plant Rehabilitation Project _ Nepal Electricity Authority, 2013). Retention of High Himalaya sediments by dam reservoirs seems therefore unable to explain the observed relative decrease of the HH units contribution.

An alternative is that erosion of the Lesser Himalaya has been enhanced by land use and/or infrastructures constructions. The strong growth of the Nepali population over the second half of the twentieth century was accompanied by massive deforestation because forest is a source of energy and exotic wood trading and also in order to increase cultivated lands. This was followed more recently by an extensive development of road construction (Fig 6.5.8).

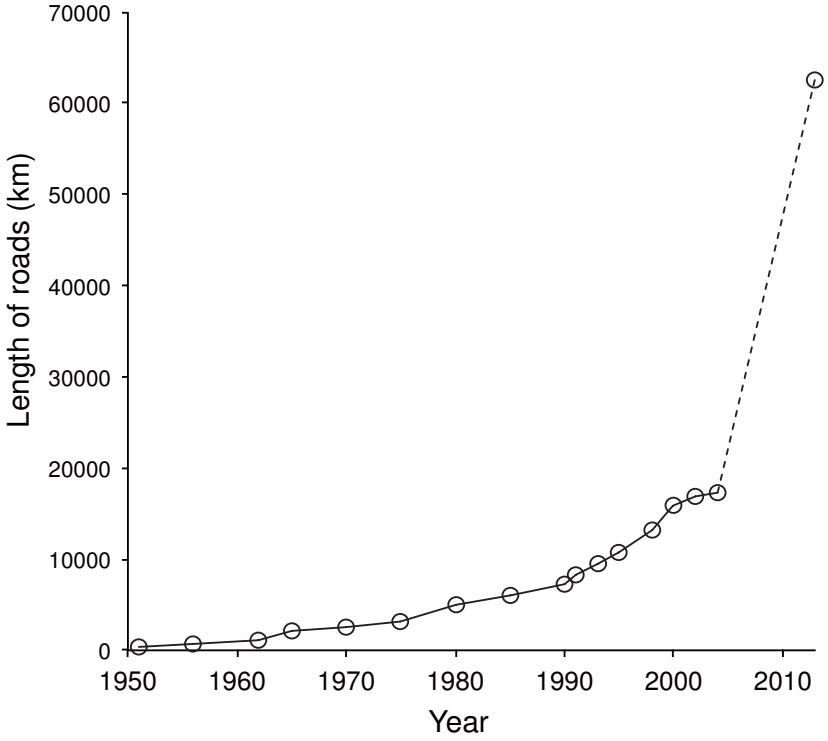

FIGURE 6.5.8 – Roads length evolution since 1950 showing the enormous increase in infrastructures development during the past 10 years.

The National road network in Nepal slowly developed between 1951, when the length of the network was only 376 km and 1985 with about 5925 km. It was followed by a very rapid increase up to 62579 km in 2013 with an annual increase rate around 10%

[Thapa 13]. The recent road increase that occurred after the civil war led to intense road construction in the Lesser Himalaya in order to connect the important villages on the ridges and valley slopes to roads usually present at the valley bottom. The vast majority of the mountain roads are unpaved and are far from being stabilized. They undergo frequent destruction during the monsoon, which has also been taken as responsible for increasing casualties since 1990 [Petley 07]. Although a large part of the population growth occurs in the Terai region (Himalaya front floodplain), Lesser Himalaya has been much more affected by deforestation and road construction than the High Himalaya where the population density is more than 5 times lower (<50 per/km^2 against 200-250 per/km^2) (cf. supplementary material S1 and S2). On the contrary, development of the High Himalayan villages declines and is hampered by rural out-migration [Banister 81].

A good example of erosion increased by roads expansion in the South part of the basin is the Mugling – Narayanghat road corridor, where numerous landslides have been induced by earth-works, excavations and embankments [Devkota 12, Regmi 13, Regmi 14]. Indeed, roads constructions are known to considerably impact mountainous regions, creating slopes destabilisations and inducing frequent landslides (e.g. [Larsen 97]). For example, in the High Himalayan part of the Kali Gandaki valley, 30 years of observation demonstrate the permanent sediment delivery to the river drainage by medium size landslides (10^5 to 10^6 m3) associated to roads [Fort 10]. Similar observations in South-East Asia puts badly planned road construction at first rank for enhancing slopes erosion in tropical mountains [Sidle 12].

Despite a precise quantification of the changes in erosion rates from the present Sr-Nd data set for the Narayani river is beyond the scope of this paper, we can roughly estimate (Table 6.8) the erosion increase in the Middle Hills due to road construction and other anthropic factors assuming that the erosion of the HH domain has remained constant and equal to its value over the last millennium as deduced from CRN [Lupker 12a]. Compared to the pre-anthropic period, a 45% contribution of the LH rocks over the last years correspond to an increase by a factor 3 of the erosion of the Middle Hills, from 0.85 mm/yr to 2.75 mm/yr (Table 6.8). The multiplication by 3 of LH middle hills erosion by recent human activities has therefore completely destabilised the natural control and highlight the sensitivity of mountainous environments to anthropic impact.

	LH	HHC	TSS	HH	Total
Area %*	41.55	24.97	30.83	55.8	97
Area km^2	13297	7991	9866	17857	32002
Modern er. %	45			55	
Modern er. 10^6 t/yr	43.74			53.46	97*
Modern sediment yield t/ km^2/yr	3290			2994	3037
Preanthropic er. %	20			80	
Preanthropic er. 10^6 t/yr	*13.37*			*53.46*	*67*
Preanthropic sediment yield t/km^2/yr	1005			2994	2088

* Hurtrez (PhD), ** Anderman et al. 2012

TABLE 6.8 – Comparison between preanthropic and modern erosion rates calculated from compositions of current Narayani sediments and drillings boreholes, assuming HH erosion has remained constant.

6.5.6 Conclusion

Our study reveals that the original pre-anthropic erosion balance calculated from Gandak floodplain sediment record implies that about 20 % of the sediment was derived from the LH and 80% from the High Himalaya including both HHC and TSS. These proportions are similar to previous landscape denudation rates calculated from fluvial incision and that naturally counter-balance the uplift at long-term scale. Over the past 30 ka these proportions were remarkably stable in spite of glacial extension and rainfall changes that appear to have altered the LH/HH ratios in other basins. It suggests that climatic changes during the Pleistocene - Holocene transition remain of a second order compared to the topographic and tectonic control on denudation [Burbank 03].

On the opposite, we observe that over the last 16 years, LH erosion has increased during nearly a decade to attain 3 times the initial long-term denudation rate in 2011. This shift in erosion distribution is attributed to a rapid population growth and infrastructure development in the LH mountains. Either deforestation and natural environment degradation due to human settlement or rapid roads development seem to be the major causes of this increasing sediment fluxes of about 70×10^6 t/yr, implying major issues in the downstream river management. The impact on river drainage and its ecology corresponds to direct

flushing of hundreds of small landslides [Fort 10].

The resulting increased sediment fluxes due to the enhanced middle hills erosion might represent a major concern in downstream water resources and civil engineering river management by : severely damaging hydropower infrastructures and reducing reservoir lifespan [Harden 93], increasing flooding hazards [Costa 75], and strengthening the risks of river avulsion over the embankments, a phenomenon which occurred on the Kosi river in 2008 [Sinha 09, Sinha 13a]. If not wisely planned, civil extension induced by economic development puts at risk an already fragile environnement, and exposes the population to higher risks.

Aknowledgments

This study was funded by ANR blanche "CALIMERO" including G. P. Morin PhD fellowship (co-funded by Région Lorraine). We thank Catherine Zimmerman, Christiane Parmentier and Laurie Reisberg for their help in the Sr-Nd analyse, and for helpful discussions on the data. We thank Henriette Lapierre who supervised the ^{87}Sr /^{86}Sr and εNd measurements of MAR-XX samples in Grenoble, ten years ago. Thomas Rigaudier is also thanked for his help during carbonates analysis. We also thank the SARM team at CRPG, Nancy for major elements analysis.

Appendices

Appendix A 1

Sample #	Geological unit	Formation	Source	Rb	Sr	87Rb/86Sr	87Sr/86Sr	Sm	Nd	147Sm/144Nd	143Nd/144Nd	$\varepsilon_{Nd}0$
HHC							*n=49*					*n=52*
ß 106	HHC	FI	Deniel et al., 1987					5	25.3	0.120	0.511903	-14.3
ß 114	HHC	FI	Deniel et al., 1987					4.5	25.5	0.107	0.511905	-14.3
ß 114	HHC	FI	Deniel et al., 1987	2.88	55.5	15.32	0.93943				0.511945	-13.5
NL 623	HHC	FII	Deniel et al., 1987	5	772.5	0.018	0.71411					
NL 428	HHC	FII	Deniel et al., 1987	190.5	231	2.39	0.73459					
U 48	HHC	FI	Deniel et al., 1987								0.511817	-16.0
NL43	HHC	FI	Deniel et al., 1987	211	157.5	3.89	0.74745	7.6	39.6	0.117	0.51181	-16.2
NL 58	HHC	FI	Deniel et al., 1987	142	132.5	3.10	0.74513	7.1	35.8	0.121	0.511918	-14.0
NL 59	HHC	FI	Deniel et al., 1987	105	267	1.14	0.73311	7.7	39.9	0.117	0.511866	-15.1
NL74	HHC	FI	Deniel et al., 1987	150	220	1.98	0.73355	8.1	37.7	0.130	0.511844	-15.5
NL 75	HHC	FI	Deniel et al., 1987	92	48.5	5.51	0.75495	4.7	22.9	0.124	0.511777	-16.8
NL 76	HHC	FI	Deniel et al., 1987	121.5	249.5	1.41	0.73322	6.2	30.2	0.126	0.511852	-15.3
NL81	HHC	FI	Deniel et al., 1987	227.5	156.5	4.22	0.74596	8.57	44.63	0.1161	0.511862	-14.9
NL85	HHC	FI	Deniel et al., 1987	111.5	163	1.99	0.74532	4.9	24.2	0.123	0.511706	-18.2
NL86	HHC	FI	Deniel et al., 1987	127.5	181.5	2.04	0.73799					
NL93	HHC	FI	Deniel et al., 1987	41.5	269.5	0.45	0.73435	4	20.1	0.121	0.511713	-18.0
NL 100	HHC	FI	Deniel et al., 1987	46	210.5	0.63	0.73113					
NL 119	HHC	FI	Deniel et al., 1987	312	171.5	5.27	0.73926					
NL 164	HHC	FI	Deniel et al., 1987	6	386.5	0.045	0.73047					
NL 172	HHC	FI	Deniel et al., 1987	76.5	225.5	0.98	0.72899					
NL 420	HHC	FI	Deniel et al., 1987	238	36	19.7	0.80650	6	32.1	0.115	0.511841	-15.5
NL 487	HHC	FI	Deniel, 1986	182.5	44	12	0.75190					
NL 493	HHC	FI	Deniel et al., 1987	332	59	16.34	0.77324					
NL499	HHC	FI	Deniel et al., 1987	102	104	2.84	0.74425					
NL 512	HHC	FI	Deniel et al., 1987	134	90.5	4.30	0.74872					
NL 506	HHC	FI	Deniel et al., 1987	82.5	30.5	7.95	0.78899					
L 102	HHC	FI	Deniel et al., 1987			5.37	0.77409					
M 102	HHC	FI	Deniel et al., 1987			13.93	0.78067	7.14	37.09	0.1165	0.551837	-15.4
M 107	HHC	FI	Deniel et al., 1987			0.77	0.73962					
M 108	HHC	FI	Deniel et al., 1987			3.38	0.76470	7.38	36.68	0.1216	0.512084	-10.6
M 114	HHC	FI	Deniel et al., 1987			7.54	0.76189	5.6	28.66	0.118	0.511901	-14.2
U757	HHC	FI	Vidal unpub.					10.09	55.38	0.1101	0.51165	-19.0
DK 400	HHC	FI	Deniel, 1986	102	199	1.49	0.75171					
DK 401	HHC	FI	Deniel, 1986	257	136	5.48	0.75578					
MB301L	HHC	FI	Brouand, 1989	138.1	85.8	4.692	0.78559					
MB301M	HHC	FI	Brouand, 1989	213.8	41.9	14.88	0.78743					
MB301R	HHC	FI	Brouand, 1989	308.7	21.3	42.28	0.79199					
MB373 L	HHC	FI	Brouand, 1989	122.6	256.8	1.386	0.74211					
MB373M	HHC	FI	Brouand, 1989	292.9	193	4.405	0.74169					

MB373R	HHC	FI	Brouand, 1989	438.2	116.4	10.93	0.74399					
M8374L	HHC	FI	Brouand, 1989	67.5	206.1	0.951	0.74248					
MB374 M	HHC	FI	Brouand, 1989	229.6	131.5	5.069	0.74192					
MB374R	HHC	FI	Brouand, 1989	312.9	76.8	11.83	0.74348					
M 8429L	HHC	FI	Brouand, 1989	32.1	78.6	1.191	0.79368					
M8429 ÇJW	HHC	FI	Brouand, 1989	88.4	32.3	7.986	0.79477					
MB429R	HHC	FI	Brouand, 1989	214	13	48.06	0.80012					
MB369M1	HHC	FI	Brouand, 1989	170	182	2.711	0.740314					
MB369M2	HHC	FI	Brouand, 1989	63	171	1.069	0.739658					
MB369 M3	HHC	FI	Brouand, 1989	389	255	4.428	0.739962					
MB369 P	HHC	FI	Brouand, 1989	164	250	1.904	0.742731					
HC46	HHC		Imayama et al., 2008						33.33	0.1256	0.511928	-13.9
HC47	HHC		Imayama et al., 2008						28.22	0.1324	0.511766	-17.0
502068	HHC	FI	Martin et al., 2005					6.96	35.38	0.1189	0.511877	-14.8
502069	HHC	FI	Martin et al., 2005					3.85	20.23	0.1150	0.511737	-17.6
502070	HHC	FI	Martin et al., 2005					6.39	33.01	0.1170	0.511843	-15.5
502071	HHC	FI	Martin et al., 2005					7.10	36.52	0.1176	0.511779	-16.8
502104	HHC	FI	Martin et al., 2005					5.94	29.63	0.1213	0.511935	-13.7
502105A	HHC	FI	Martin et al., 2005					6.79	34.09	0.1203	0.511897	-14.5
502105B	HHC	FI	Martin et al., 2005					7.30	37.89	0.1164	0.511783	-16.7
502106	HHC	FI	Martin et al., 2005					5.74	28.86	0.1203	0.511950	-13.4
502128	HHC	FI	Martin et al., 2005					7.93	41.30	0.1161	0.511804	-16.3
502129	HHC	FI	Martin et al., 2005					7.06	35.95	0.1188	0.511868	-15.0
502133	HHC	FI	Martin et al., 2005					5.99	29.84	0.1214	0.511933	-13.8
502132	HHC	FI	Martin et al., 2005					5.93	29.91	0.1199	0.511908	-14.2
502152	HHC	FI	Martin et al., 2005					5.73	28.85	0.1200	0.511903	-14.3
502149	HHC	FI	Martin et al., 2005					7.21	36.33	0.1200	0.511922	-14.0
502148	HHC	FI	Martin et al., 2005					8.40	43.60	0.1165	0.511818	-16.0
502147	HHC	FI	Martin et al., 2005					7.30	37.84	0.1166	0.511741	-17.5
402086	HHC	FI	Martin et al., 2005					6.04	30.81	0.1184	0.511928	-13.8
402088	HHC	FI	Martin et al., 2005					8.88	46.04	0.1166	0.511790	-16.5
402090	HHC	FI	Martin et al., 2005					5.22	28.01	0.1127	0.511671	-18.9
402092A	HHC	FI	Martin et al., 2005					1.59	8.50	0.1131	0.511691	-18.5
402092B	HHC	FI	Martin et al., 2005					5.08	26.20	0.1172	0.511753	-17.3
LT-33	HHC	FI	Parrish and Hodges, 1996						39.01	0.1177	0.511805	-16.2
LT-34	HHC	FI	Parrish and Hodges, 1996						11.87	0.1153	0.511741	-17.5
LT-21	HHC	FI	Parrish and Hodges, 1996						34.99	0.1169	0.511826	-15.8
LT-22	HHC	FI	Parrish and Hodges, 1996						45.54	0.119	0.511878	-14.8
LT-24	HHC	FI	Parrish and Hodges, 1996						43.54	0.1159	0.511816	-16.0
LT-29	HHC	FI	Parrish and Hodges, 1996						30.53	0.11	0.511691	-18.5
SLMI	HHC	FI	Inger and Harris, 1993	258.2	54-4	13.89	0.82545					
LM201	HHC	FI	Inger and Harris, 1993	109	31	10.25	0.78350					

SKM2	HHC	FI	Inger and Harris, 1993	99.3	34.9	8.31	0.80355					
SKM3	HHC	FI	Inger and Harris, 1993	153	35	12.78	0.81429					
LM207	HHC	FI	Inger and Harris, 1993	146	24	17.81	0.83052	5.65	28.8	0.119	0.51187	-15.0
LM209	HHC	FI	Inger and Harris, 1993	246	46	15.66	0.83156					
LM211	HHC	FI	Inger and Harris, 1993	299	45	19.54	0.87698					
SM201	HHC	FI	Inger and Harris, 1993	206	120	4.99	0.75768					
SM203	HHC	FI	Inger and Harris, 1993	307	180	4.96	0.75043					
SM202	HHC	FI	Inger and Harris, 1993	138	132	3.04	0.75294	6.38	29.29	0.132		
SM206	HHC	FI	Inger and Harris, 1993	112	91	3.58	0.75263			0.13	0.51192	-14.0
SSM6	HHC	FI	Inger and Harris, 1993	197	111.3	5.15	0.76231	7.81	38.07	0.124	0.51195	-13.4
RM201	HHC	FI	Inger and Harris, 1993	139	150	2.69	0.76075					
SNM2	HHC	FIII	Inger and Harris, 1993	234.7	131.4	5.2	0.76609					
NM203	HHC	FIII	Inger and Harris, 1993	239	79	8.81	0.77203					
9TBkal	HHC	FIII	Robinson et al., 2001						27.92	0.1533	0.512137	-9.8
12TBgh	HHC	FI	Robinson et al., 2001						37.85	0.1160	0.511814	-16.1
13TBru	HHC	FII	Robinson et al., 2001						41.77	0.1209	0.511946	-13.5
AG-105	HHC	FI	Robinson et al., 2001						8.85	0.1483	0.511836	-15.6
TSS							*n=0*					*n=9*
NA 178	TSS		Bouquillon et al., 1990					4	20.3	0.124	0.511795	-16.4
NA 181	TSS		Bouquillon et al., 1990					12.6	59	0.135	0.512405	-4.5
1TBkag	TSS	Chukh Fm	Robinson et al., 2001					16.50	84.95	0.1174	0.512322	-6.2
2TBpha	TSS	Dogger Fm	Robinson et al., 2001					4.75	33.22	0.0864	0.511805	-16.2
3TBjom	TSS	Jomson Fm	Robinson et al., 2001					9.05	53.17	0.1028	0.511673	-18.8
4TBSya	TSS	Tilicho Fm	Robinson et al., 2001					10.35	63.38	0.0987	0.511671	-18.9
5TBMar	TSS	Tilichio Fm	Robinson et al., 2001					11.80	64.50	0.1105	0.51175	-17.3
DD-31	TSS	Melmura Fm						5.84	29.59	0.1193	0.511734	-17.6
DD-33	TSS	Melmura Fm						6.71	35.99	0.1128	0.51161	-20.1
LH							*n=10*					*n=32*
NL 3	LH	Kunchha	Deniel et al., 1987	1	7.5	7.66	0.86772					
NL 4	LH	Kunchha	Deniel et al., 1987									
AP9	LH		France-Lanord & Le Fort 1988	143	11	40.08	1.50980					
AP 346	LH		France-Lanord & Le Fort 1988	252	21	38.07	1.68090	8.08	44		0.511397	-24.2
AP 385	LH		France-Lanord & Le Fort 1988	236	63	1348	1.03010	6.58	36.6		0.511331	-25.5
AP 440	LH		France-Lanord & Le Fort 1988	98	83	3.48	0.83318					
AP 524	LH		France-Lanord & Le Fort 1988	321	76	12&52	0.96411					
AP 825	LH		France-Lanord & Le	123	74	4.82	0.82573					

			Fort 1988										
AP 874	LH		France-Lanord & Le Fort 1988	366	56	19.58	1.01761						
AP 888	LH		France-Lanord & Le Fort 1988	126	44	8.48	0.89964						
NL 1	LH		France-Lanord & Le Fort 1988	114	19	17.79	0.93696						
MC49	MCTZ		Imayama et al., 2008					5.12	29.69	0.1042	0.511312	-25.9	
MC69	MCTZ		Imayama et al., 2008					1.94	9.06	0.1293	0.511420	-23.8	
MC74	MCTZ		Imayama et al., 2008					6.75	36.79	0.1110	0.511296	-26.2	
LC50	LLHS		Imayama et al., 2008					4.36	24.81	0.1062	0.511328	-25.6	
LC70	LLHS		Imayama et al., 2008					2.38	13.96	0.1030	0.511357	-25.0	
LC71	LLHS		Imayama et al., 2008					6.72	35.37	0.1149	0.511342	-25.3	
LC72	LLHS		Imayama et al., 2008					4.65	25.16	0.1118	0.511340	-25.3	
LC73	LLHS		Imayama et al., 2008					5.48	29.20	0.1135	0.511340	-25.3	
LC53	ULHS		Imayama et al., 2008					1.90	10.37	0.1108	0.511439	-23.4	
LC54	ULHS		Imayama et al., 2008					7.00	35.78	0.1182	0.511619	-19.9	
LC55	ULHS		Imayama et al., 2008					4.62	25.75	0.1084	0.511518	-21.9	
LC56	ULHS		Imayama et al., 2008					6.11	34.40	0.1074	0.511515	-21.9	
LC57	ULHS		Imayama et al., 2008					4.99	23.16	0.1303	0.511614	-20.0	
502075	LH	Kuncha	Martin et al., 2005					1.71	8.32	0.1244	0.511592	-20.4	
502108	LH	Kuncha	Martin et al., 2005					6.58	35.16	0.1131	0.511548	-21.3	
502097	LH	Kuncha	Martin et al., 2005					4.63	25.98	0.1077	0.511428	-23.6	
502130	LH	post-Kuncha Nawakot	Martin et al., 2005					5.45	29.00	0.1136	0.511616	-19.9	
502131	LH	post-Kuncha Nawakot	Martin et al., 2005					2.87	15.34	0.1130	0.511568	-20.9	
502136	LH	post-Kuncha Nawakot	Martin et al., 2005					3.80	21.94	0.1044	0.511477	-22.6	
502146	LH	Kuncha	Martin et al., 2005					5.74	32.08	0.1077	0.511440	-23.4	
602002	LH	Kuncha	Martin et al., 2005					7.53	40.92	0.1112	0.511462	-22.9	
402093	LH	Kuncha	Martin et al., 2005					4.94	28.95	0.1032	0.511449	-23.2	
402097	LH	Kuncha	Martin et al., 2005					6.61	37.52	0.1065	0.511384	-24.5	
LT-4	LH		Parrish and Hodges, 1996					4.83	26.36	0.1108	0.511356	-25.0	
LT-6	LH		Parrish and Hodges, 1996					5.79	31.96	0.1096	0.511348	-25.2	
LT-7	LH		Parrish and Hodges, 1996					10.08	54.75	0.1113	0.511429	-23.6	
LT-10	LH		Parrish and Hodges, 1996					7.01	38.68	0.1095	0.51133	-25.5	
LT-18	LH		Parrish and Hodges, 1996					8.14	43.34	0.1085	0.511296	-26.2	
LT-19	LH		Parrish and Hodges, 1996					6.75	38.13	0.107	0.511423	-23.7	
LT-20	LH		Parrish and Hodges, 1996					2.21	10.51	0.1273	0.511532	-21.6	

HHC stands for High Himalayan Cristalline, TSS for Tethyan Sedimentary Series, LH for Lesser Himalaya, LLHS for Lower LH, ULHS for Upper LH, MCTZ for Main Frontal Thrust Zone, After (Bouquillon et al., 1990; Brouand, 1989; Deniel, 1986; Deniel et al., 1987; France-Lanord and Le Fort, 1988; Imayama and Arita, 2008; Inger and Harris, 1993; Martin et al., 2005; Parrish and Hodges, 1996; Robinson et al., 2001)

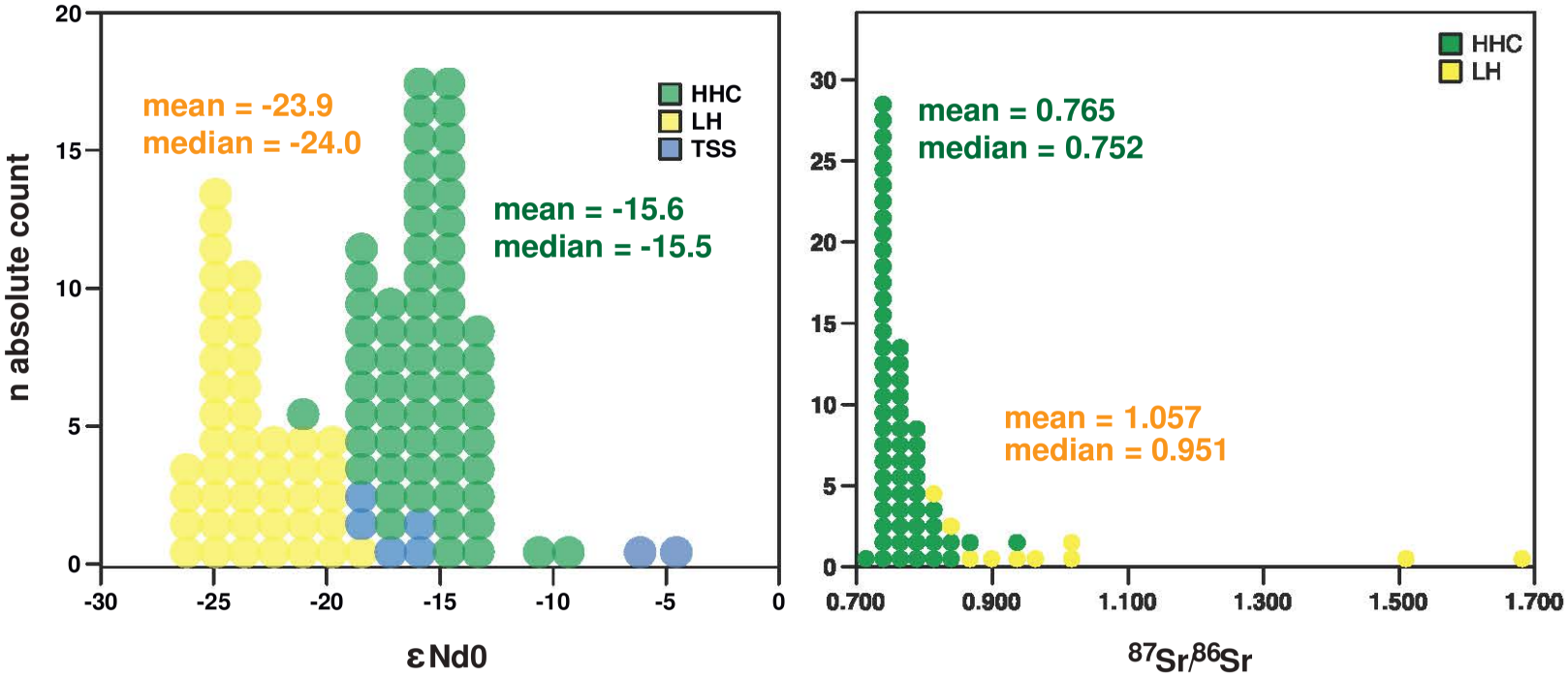

Appendix A 2

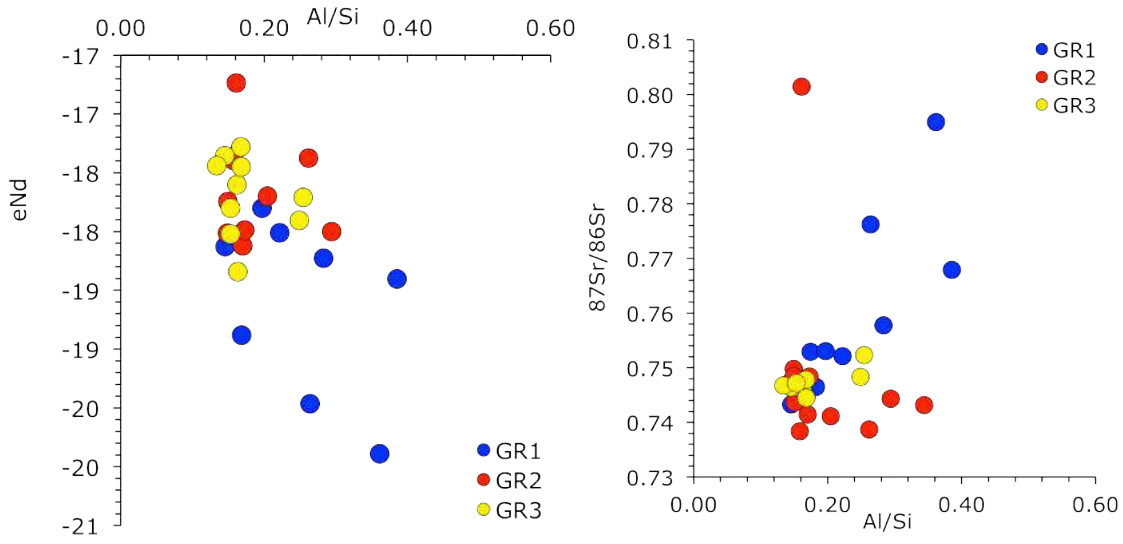

Appendix A 3

1. Geochemical ternary mixing

We describe here the formalisation of the ternary mixing equations established to solve lithological fractions in our samples.

Considering 1, 2 and 3 the different lithologies and f_i their respective fractions:

$$f + f_2 + f_3 = 1 \qquad \text{eq. 0}$$

For example with Sr isotopes we can write:

$$[^{87}Sr]_{mix} = f_1 \cdot [^{87}Sr]_1 + f_2 \cdot [^{87}Sr]_2 + f_3 \cdot [^{87}Sr]_3 \qquad \text{eq. 1}$$

$$[^{86}Sr]_{mix} = f_1 \cdot [^{86}Sr]_1 + f_2 \cdot [^{86}Sr]_2 + f_3 \cdot [^{86}Sr]_3 \qquad \text{eq. 2}$$

we divide eq.1 by eq. 2:

$$\frac{[^{87}Sr]_{mix}}{[^{86}Sr]_{mix}} = \frac{^{87}Sr}{^{86}Sr_{mix}} = \frac{f_1 \cdot [^{87}Sr]_1 + f_2 \cdot [^{87}Sr]_2 + f_3 \cdot [^{87}Sr]_3}{f_1 \cdot [^{86}Sr]_1 + f_2 \cdot [^{86}Sr]_2 + f_3 \cdot [^{86}Sr]_3} \qquad \text{eq. 3}$$

Since the range in isotopic compositions of Sr is usually small, ^{86}Sr is very nearly a constant fraction of total Sr, $[^{86}Sr]_i \approx k \cdot [Sr]_i$, so that $[^{87}Sr]_i = \frac{[^{87}Sr]_i}{[^{86}Sr]_i} \cdot [^{86}Sr]_i = \frac{^{87}Sr}{^{86}Sr_i} \cdot k \cdot [Sr]_i$

Replacing $[^{86}Sr]_i$ and $[^{87}Sr]_i$ in eq. 3:

$$\frac{^{87}Sr}{^{86}Sr_{mix}} = \frac{f_1 \cdot \frac{^{87}Sr}{^{86}Sr_1} \cdot k \cdot [Sr]_1 + f_2 \cdot \frac{^{87}Sr}{^{86}Sr_2} \cdot k \cdot [Sr]_2 + f_3 \cdot \frac{^{87}Sr}{^{86}Sr_3} \cdot k \cdot [Sr]_3}{f_1 \cdot k \cdot [Sr]_1 + f_2 \cdot k \cdot [Sr]_2 + f_3 \cdot k \cdot [Sr]_3}$$

$$\Leftrightarrow$$

$$\frac{^{87}Sr}{^{86}Sr_{mix}} = \frac{f_1 \cdot \frac{^{87}Sr}{^{86}Sr_1} \cdot [Sr]_1 + f_2 \cdot \frac{^{87}Sr}{^{86}Sr_2} \cdot [Sr]_2 + f_3 \cdot \frac{^{87}Sr}{^{86}Sr_3} \cdot [Sr]_3}{f_1 \cdot [Sr]_1 + f_2 \cdot [Sr]_2 + f_3 \cdot [Sr]_3} \qquad \text{eq. 4}$$

Which is equivalent to the classically proposed form:

$$\frac{^{87}Sr}{^{86}Sr_{mix}} = f_1 \cdot \frac{^{87}Sr}{^{86}Sr_1} \cdot \frac{[Sr]_1}{[Sr]_{mix}} + f_2 \cdot \frac{^{87}Sr}{^{86}Sr_2} \cdot \frac{[Sr]_2}{[Sr]_{mix}} + f_3 \cdot \frac{^{87}Sr}{^{86}Sr_3} \cdot \frac{[Sr]_3}{[Sr]_{mix}}$$

where $[Sr]_{mix} = f_1 \cdot [Sr]_1 + f_2 \cdot [Sr]_2 + f_3 \cdot [Sr]_3$

Now we can arrange eq. 4 to have linear relationship with respect to f_1, f_2, f_3:

$$\frac{^{87}Sr}{^{86}Sr_{mix}} \cdot \left(f_1 \cdot [Sr]_1 + f_2 \cdot [Sr]_2 + f_3 \cdot [Sr]_3\right) = f_1 \cdot \frac{^{87}Sr}{^{86}Sr_1} \cdot [Sr]_1 + f_2 \cdot \frac{^{87}Sr}{^{86}Sr_2} \cdot [Sr]_2 + f_3 \cdot \frac{^{87}Sr}{^{86}Sr_3} \cdot [Sr]_3$$

$$\Leftrightarrow$$

$$f_1 \cdot \left(\frac{^{87}Sr}{^{86}Sr_{mix}} \cdot [Sr]_1 - \frac{^{87}Sr}{^{86}Sr_1} \cdot [Sr]_1\right) + f_2 \cdot \left(\frac{^{87}Sr}{^{86}Sr_{mix}} \cdot [Sr]_2 - \frac{^{87}Sr}{^{86}Sr_2} \cdot [Sr]_2\right)$$

$$+ f_3 \cdot \left(\frac{^{87}Sr}{^{86}Sr_{mix}} \cdot [Sr]_3 - \frac{^{87}Sr}{^{86}Sr_3} \cdot [Sr]_3\right) = 0$$

$$\Leftrightarrow$$

$$f_1 \cdot [Sr]_1 \cdot \left(\frac{^{87}Sr}{^{86}Sr_{mix}} - \frac{^{87}Sr}{^{86}Sr_1}\right) + f_2 \cdot [Sr]_2 \cdot \left(\frac{^{87}Sr}{^{86}Sr_{mix}} - \frac{^{87}Sr}{^{86}Sr_2}\right) + f_3 \cdot [Sr]_3 \cdot \left(\frac{^{87}Sr}{^{86}Sr_{mix}} - \frac{^{87}Sr}{^{86}Sr_3}\right) = 0$$

eq.5

Similarly with Nd we classically have:

$$\frac{^{143}Nd}{^{144}Nd_{mix}} = f_1 \cdot \frac{^{143}Nd}{^{144}Nd_1} \cdot \frac{[Nd]_1}{[Nd]_{mix}} + f_2 \cdot \frac{^{143}Nd}{^{144}Nd_2} \cdot \frac{[Nd]_2}{[Nd]_{mix}} + f_3 \cdot \frac{^{143}Nd}{^{144}Nd_3} \cdot \frac{[Nd]_3}{[Nd]_{mix}}$$

or again, because $[Nd]_{mix} = f_1 \cdot [Nd]_1 + f_2 \cdot [Nd]_2 + f_3 \cdot [Nd]_3$, and as demonstrated above:

$$\frac{^{143}Nd}{^{144}Nd_{mix}} = \frac{f_1 \cdot \frac{^{143}Nd}{^{144}Nd_1} \cdot [Nd]_1 + f_2 \cdot \frac{^{143}Nd}{^{144}Nd_2} \cdot [Nd]_2 + f_3 \cdot \frac{^{143}Nd}{^{144}Nd_3} \cdot [Nd]_3}{f_1 \cdot [Nd]_1 + f_2 \cdot [Nd]_2 + f_3 \cdot [Nd]_3}$$

$$\Leftrightarrow$$

$$f_1 \cdot [Nd]_1 \cdot \left(\frac{^{143}Nd}{^{144}Nd_{mix}} - \frac{^{143}Nd}{^{144}Nd_1}\right) + f_2 \cdot [Nd]_2 \cdot \left(\frac{^{143}Nd}{^{144}Nd_{mix}} - \frac{^{143}Nd}{^{144}Nd_2}\right) + f_3 \cdot [Nd]_3 \cdot \left(\frac{^{143}Nd}{^{144}Nd_{mix}} - \frac{^{143}Nd}{^{144}Nd_3}\right) = 0$$

eq.6

We can adopt the ε_{Nd} notation: $\varepsilon\mathrm{Nd}_i = \left(\frac{\frac{^{143}Nd}{^{144}Nd_i} - \frac{^{143}Nd}{^{144}Nd_{std}}}{\frac{^{143}Nd}{^{144}Nd_{std}}} - 1 \right) \cdot 10000$

So $\frac{^{143}Nd}{^{144}Nd_i} = \frac{\varepsilon\mathrm{Nd_i}}{10000} - 1$ that we can replace in eq. 6:

$$f_1 \cdot [Nd]_1 \cdot \left(\frac{\varepsilon\mathrm{Nd_{mix}}}{10000} - 1 - \frac{\varepsilon\mathrm{Nd_1}}{10000} + 1 \right) + f_2 \cdot [Nd]_2 \cdot \left(\frac{\varepsilon\mathrm{Nd_{mix}}}{10000} - 1 - \frac{\varepsilon\mathrm{Nd_2}}{10000} + 1 \right) + f_3 \cdot [Nd]_3 \cdot \left(\frac{\varepsilon\mathrm{Nd_{mix}}}{10000} - 1 - \frac{\varepsilon\mathrm{Nd_3}}{10000} + 1 \right) = 0$$

$\Leftrightarrow$

$$f_1 \cdot [Nd]_1 \cdot \left(\varepsilon\mathrm{Nd_{mix}} - \varepsilon\mathrm{Nd_1} \right) + f_2 \cdot [Nd]_2 \cdot \left(\varepsilon\mathrm{Nd_{mix}} - \varepsilon\mathrm{Nd_2} \right) + f_3 \cdot [Nd]_3 \cdot \left(\varepsilon\mathrm{Nd_{mix}} - \varepsilon\mathrm{Nd_3} \right) = 0 \qquad \text{eq. 7}$$

Hence, combining equations Eq. 0, Eq. 6 and Eq. 7, the inverse problem consists in resolving the following system of linear equations with respect to f_1, f_2 and f_3:

$$\begin{cases} f + f_2 + f_3 = 1 \\ f_1 \cdot [Sr]_1 \cdot \left(\frac{^{87}Sr}{^{86}Sr_{mix}} - \frac{^{87}Sr}{^{86}Sr_1} \right) + f_2 \cdot [Sr]_2 \cdot \left(\frac{^{87}Sr}{^{86}Sr_{mix}} - \frac{^{87}Sr}{^{86}Sr_2} \right) + f_3 \cdot [Sr]_3 \cdot \left(\frac{^{87}Sr}{^{86}Sr_{mix}} - \frac{^{87}Sr}{^{86}Sr_3} \right) = 0 \\ f_1 \cdot [Nd]_1 \cdot \left(\varepsilon \mathrm{Nd}_{\mathrm{mix}} - \varepsilon \mathrm{Nd}_1 \right) + f_2 \cdot [Nd]_2 \cdot \left(\varepsilon \mathrm{Nd}_{\mathrm{mix}} - \varepsilon \mathrm{Nd}_2 \right) + f_3 \cdot [Nd]_3 \cdot \left(\varepsilon \mathrm{Nd}_{\mathrm{mix}} - \varepsilon \mathrm{Nd}_3 \right) = 0 \end{cases}$$

2. Numerical model for inversion

In our system, the terms indexed "mix" are the sample isotopic compositions and will now be indexed as "sample".
In a matricial form, the system to solve is written:

$$A \cdot x = b \qquad \text{eq. 8}$$

where:

$$A = \begin{pmatrix} 1 & 1 & 1 \\ [Sr]_1 \cdot \left(\frac{^{87}Sr}{^{86}Sr_{sample}} - \frac{^{87}Sr}{^{86}Sr_1} \right) & [Sr]_2 \cdot \left(\frac{^{87}Sr}{^{86}Sr_{sample}} - \frac{^{87}Sr}{^{86}Sr_2} \right) & [Sr]_3 \cdot \left(\frac{^{87}Sr}{^{86}Sr_{sample}} - \frac{^{87}Sr}{^{86}Sr_3} \right) \\ [Nd]_1 \cdot \left(\varepsilon \mathrm{Nd}_{sample} - \varepsilon \mathrm{Nd}_1 \right) & [Nd]_2 \cdot \left(\varepsilon \mathrm{Nd}_{sample} - \varepsilon \mathrm{Nd}_2 \right) & [Nd]_3 \cdot \left(\varepsilon \mathrm{Nd}_{sample} - \varepsilon \mathrm{Nd}_3 \right) \end{pmatrix}$$

$$x = \begin{pmatrix} f_1 \\ f_2 \\ f_3 \end{pmatrix} \text{ with } x \geq 0$$

and $b = \begin{pmatrix} 1 \\ 0 \\ 0 \end{pmatrix}$

The inverse problem is then a minimization problem:

$$\min\left(\left\| (A \cdot x - b) \right\|^2 \right) \text{, with } x \geq 0$$

which gives the best solution for $x = \begin{pmatrix} f_1 \\ f_2 \\ f_3 \end{pmatrix}$ with $x_i \supset [0,1]$.

We solve this problem by a constrained least square minimization routine on the open source software R. The routine used is called "nnls" and is available in the package "limSolve",

written by Karline Soetaert, Karel Van den Meersche, Dick van Oevelen and LAPACK authors (maintainer: Karline Soetaert karline.soetaert@nioz.nl).

3. Monte Carlo method for lithological fractions inversions

We used a Monte Carlo method to take into account both the dispersions on the Sr, Nd concentrations, and their isotopic values of the 3 geological units end-members, and the analytical reproductibility of each sample.

Our code randomly generates 10000 triplets of 3 pole values $[^{87}Sr/^{86}Sr, \varepsilon_{Nd}]_i$ (with i related to each of the 3 geologic unit end-members), such that they respect for each pole a normal distribution of average μ_i and standard deviation s_i, which correspond to the average and standard deviation as defined by monolithlogical basins, c.f. §4.1. For each random realization, a random triplet of $[[Sr], [Nd]]_i$ concentrations and a random value of the measured sample isotopic content $[^{87}Sr/^{86}Sr, \varepsilon_{Nd}]_{sample}$ are also generated, following again gaussian distribution.

And for each random realization we invert for x = (f1 f2 f3) according to eq. 8, so that at the end of the Monte Carlo process, we obtain a population of <10000 (remember that the reject the negative fi<0 and fi>1 solutions) for the geologic unit proportions. Final average proportions and associated standard deviations are directly computed from this population.
To asset the uncertainty of the sum of TSS+HHC propotions, we calculated the standard deviation of the algebric sum of two random variables as:

$$\sigma f_{HHC} \pm f_{TSS} = \sqrt{\sigma^2_{f_{HHC}} + \sigma^2_{f_{TSS}} \pm 2 \cdot \sigma_{f_{HHC}} \cdot \sigma_{f_{TSS}} \cdot \rho(f_{HHC}, f_{TSS})}$$, where $\rho(f_{HHC}, f_{TSS})$ is the correlation coefficient between the two random variables f_{HHC} and f_{TSS} (Saporta, 2006).

Supplementary

S1 Map of population density in the Narayani basin (outer red shape) and geological units area after Colchen, 1986

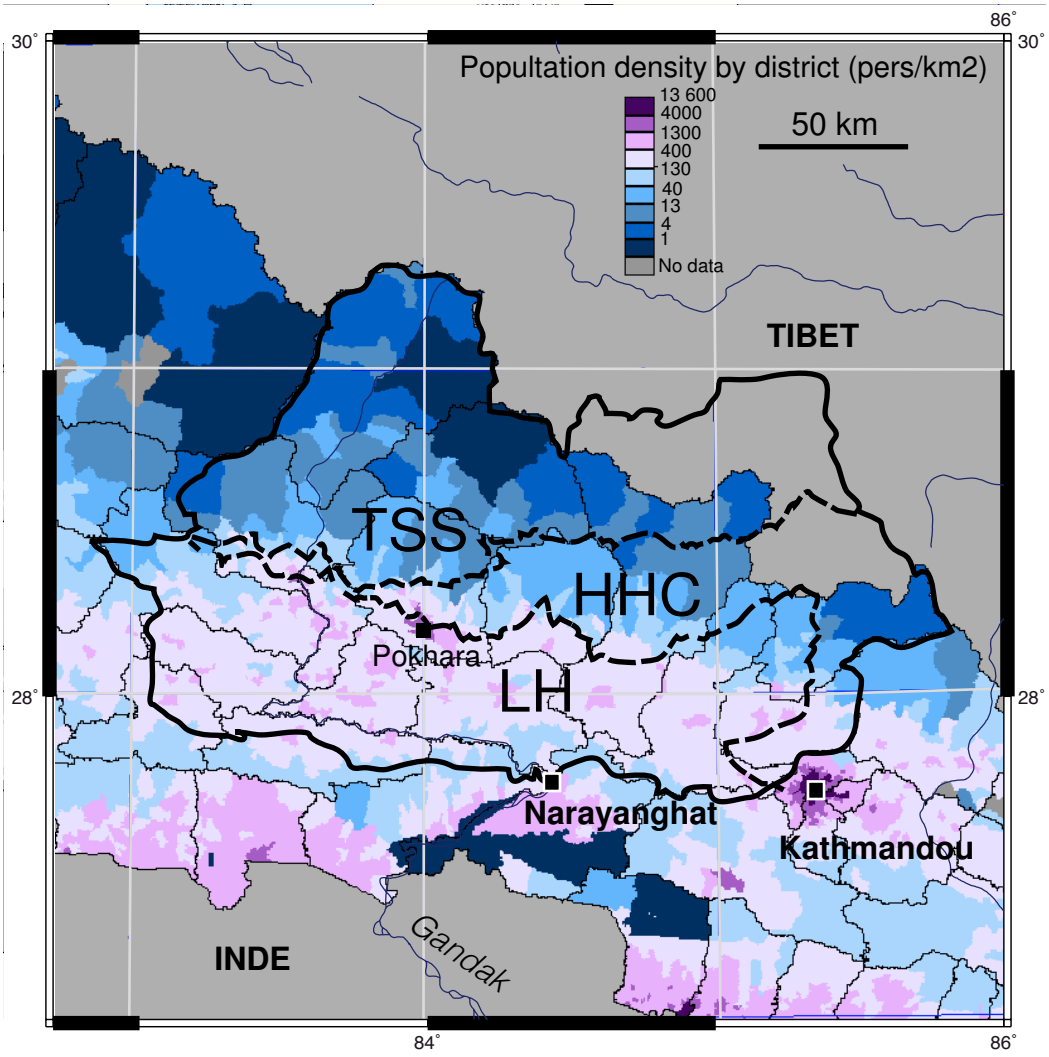

S2 S2 Map of roads length density in the Narayani basin and geological units area after Colchen, 1986

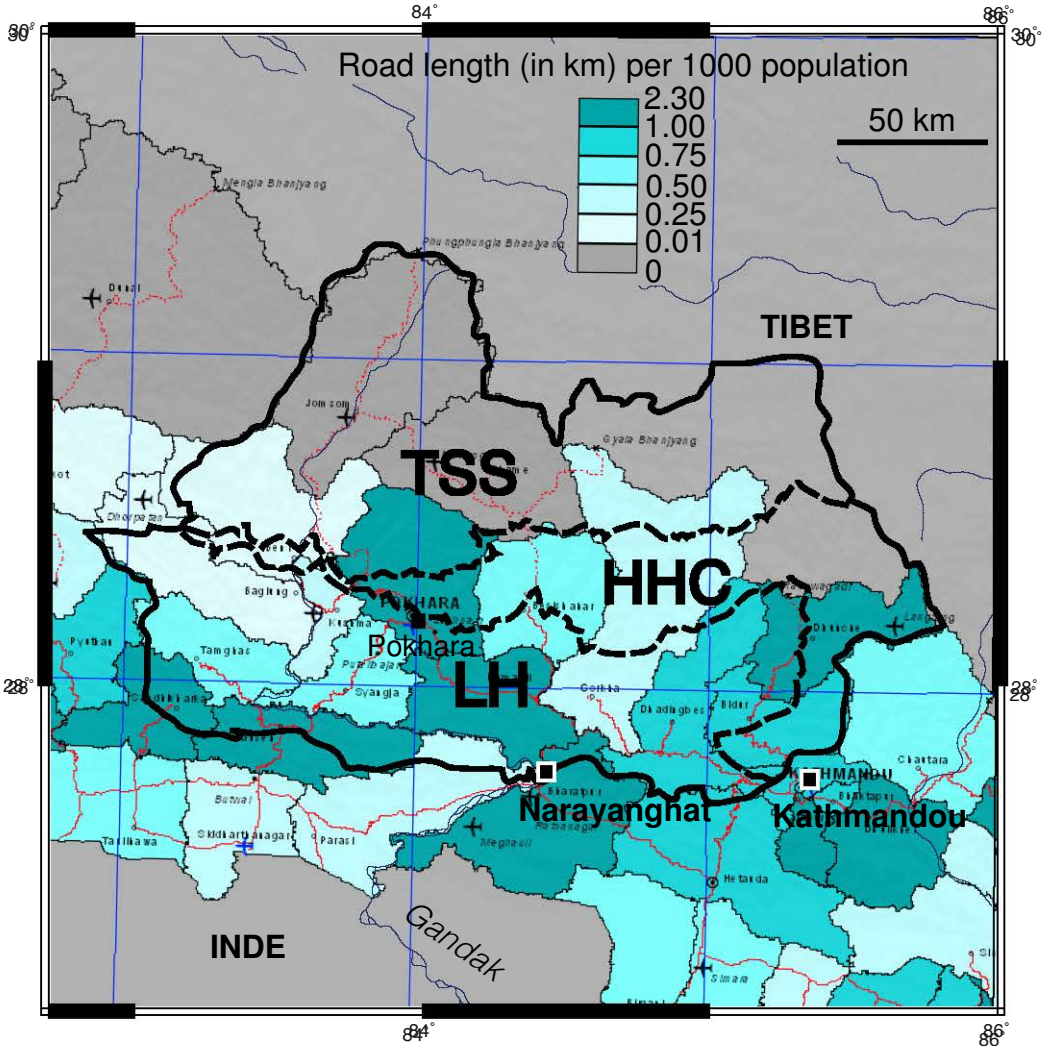

6.6 Paleo-taux d'érosion dans les forages par isotopes cosmogéniques ^{10}Be

6.6.1 Théorie générale

Le rayonnement cosmique qui frappe en permanence la Terre est constitué de particules de haute énergie : des protons (83%) et des particules-α (13%). Ces particules en rencontrant les molécules de l'atmosphère provoquent une cascade de réactions nucléaires libérant principalement des neutrons secondaires. Ces particules interagissent avec les atomes de la croûte terrestre par spallation, capture de neutrons thermiques ou de muons négatifs lents. Ces atomes produits dans les premiers mètres de la surface sont appelés d'isotopes dits cosmogéniques : ^{3}He, ^{10}Be, ^{14}C, ^{26}Al et ^{36}Cl, leur production est rapidement atténuée dans les premiers mètres.

Le flux de particules cosmiques provenant des étoiles est isotrope avant sa rencontre avec la magnétosphère (champ magnétique terrestre) mais va être dévié en fonction de la charge des particules et des caractéristiques du champ magnétique terrestres (intensité, orientation) : le flux de particules est donc plus important aux pôles qu'à l'équateur. Enfin, les variations du champ magnétique terrestre au cours du temps ont provoqué une modification des taux de production dont il convient de tenir compte lors de calculs des taux dans le passé.

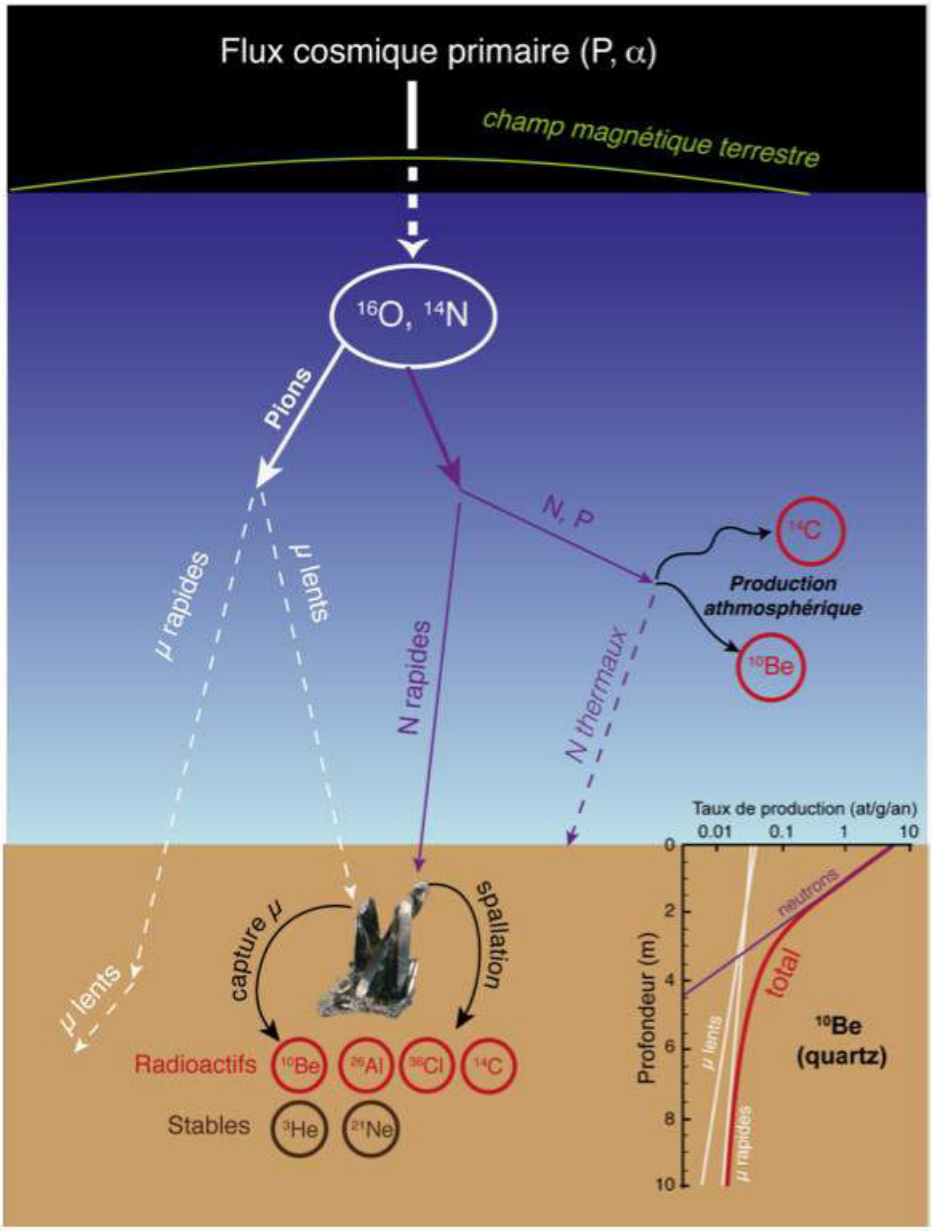

FIGURE 6.6.1 – Schéma de la cascade de réactions menant du flux cosmique primaire à la production d'isotopes cosmogéniques in-situ. (extrait de [Puchol 13])
Le flux de particules est atténué par sa rencontre avec les atomes de l'atmosphère et par le champ magnétique terrestre (fonction de la latitude). Un ensemble de particules secondaires (N : neutrons, P : protons, μ : muons) est créé dont une faible partie atteindra la surface de la Terre. Dans les premiers mètres, les taux de production cosmogénique décroissent exponentiellement avec des longueurs caractéristiques différentes selon les éléments.

La cascade réactionnelle qui a lieu dans l'atmosphère atténue l'intensité du flux, les taux de production sont ainsi dépendants de l'altitude (minimal au niveau de la mer), et les taux de production de référence sont donnés pour les hautes latitudes et au niveau de la mer (Sea Level High Latitude ou SLHL production rates). Enfin, une composante d'écrantage due à la topographie environnante du site d'échantillonnage est aussi à prendre en compte.
Le taux de production P (at/g/an) d'un isotope à une profondeur z s'exprime donc ainsi :

$$P(z) = \sum_i P_i(0) e^{-z\rho/\Lambda_i}$$

avec P_i les taux de production par spallation, capture neutronique et capture muonique, longueur d'atténuation Λ_i(g/cm) et ρ la masse volumique de la roche

6.6.2 Utilisation dans le calculs des taux de dénudation

La production des isotopes cosmogéniques a lieu à la surface et dans les premiers mètres du sol. Le minéral ainsi exposé accumule des isotopes cosmogéniques dans son réseau cristallin au cours du temps (exemple ^{10}Be dans le quartz). Si la surface est exposée pendant un temps suffisant avec un taux de dénudation constant, la concentration du grain atteint un état d'équilibre [Lal 91] qui s'exprime à une profondeur z par :

$$C(z) = \frac{P(z)}{\lambda + \rho\varepsilon/\Lambda}$$

avec λ la constante de désintégration de l'élément considéré.

Les effets conjoints de l'érosion, qui retire de la masse en surface et expose ainsi les minéraux, ainsi que de l'accumulation cosmogénique permettent de calculer un taux d'exhumation des minéraux. Un taux d'érosion élevé provoquant un déplacement rapide des minéraux vers la surface résultera d'un temps d'accumulation faible et donc de faibles concentrations en isotopes cosmogénique (et inversement).

[Granger 96] ont démontré qu'il était possible d'utiliser la concentration des sédiments de rivière pour calculer le taux d'érosion d'un bassin versant en calculant le taux moyen de production sur le bassin considéré. La concentration en un isotope cosmogénique d'un sable de rivière s'exprime alors en fonction des paramètres moyens sur l'ensemble du bassin amont :

$$\overline{C} = \sum_i \frac{\bar{P}_i}{\rho\bar{\varepsilon}/\Lambda_i}$$

avec P_i les taux de production moyen par spallation, capture neutronique et capture muonique et λ_i les longueurs d'atténuation respectives des trois processus.

Il faut cependant que le système réponde à certaines conditions

1. le taux de dénudation doit être constant pendant la période correspondant aux temps nécessaire pour éroder une épaisseur équivalente à la longueur d'atténuation, et ce temps être négligeable par rapport au temps de demi-vie de l'isotope radioactif (^{10}Be, ^{14}C, ^{26}Al et ^{36}Cl).
2. le minéral doit être présent de manière ubiquiste dans toutes les formations lithologiques (cas général du quartz).
3. la granulométrie du minéral cible doit être équivalente dans toutes les formations lithologiques du bassin versant.
4. l'altération chimique en profondeur doit être limitée.
5. le temps de transfert des sédiments dans le bassin doit être faible afin d'éviter une augmentation de la concentration par ré-exposition ou une diminution de la concentration par décroissance radioactive pendant le transport.

Dans le cas du bassin de la Narayani, nous avons choisi d'utiliser l'analyse du ^{10}Be dans le quartz, car ce minéral est ubiquiste et abondant dans les formations himalayennes. L'isotope cosmogénique ^{10}Be est produit par spallation neutronique et capture muonique sur les atomes d'oxygène avec un taux de production (SLHL) de 3.9 à 4.5 at/g/an [Nishiizumi 07, Balco 09].

Le but de cette étude est d'une part de comparer les données de taux de dénudation des forages avec les taux de dénudation dans les sables actuels de la Narayani reportés par [Lupker 12a], et d'autre part d'observer l'évolution temporelle du signal en ^{10}Be au cours de la transition glaciaire-interglaciaire du tardi-Pléistocène - Holocène, et au cours de l'Holocène.

6.6.3 Méthode

Afin de mesurer la variabilité du signal en ^{10}Be au cours du temps, de « gros » échantillons ont été prélevés régulièrement dans les carottes en respectant une résolution d'en-

viron 5 m de profondeur.

Le protocole suivant a été utilisé pour tous les échantillons analysés lors de cette thèse :

1. Une première étape de tamisage en voie sèche a été réalisée sur tous les échantillons sélectionnés et a permis d'isoler les fractions 0-50 µm / 50-125 µm / 125-250 µm / 250-400 µm / 400-800 µm / 800 µm et +. Compte tenu des masses initiales très limitées des échantillons prélevés dans les carottes, les fractions 125-250 µm / 250-400 µm ont été combinées pour obtenir des fractions 125-400 µm de masses plus importantes. Le choix de cette fraction a aussi été dirigé par le fait que les fractions granulométriques généralement analysées se situent autour de 125 µm, 250 µm et 500 µm. Les granulométries analysées dans les sables actuels de la Narayani [Lupker 12a] sont de 125-250 µm et 250-400 µm et ces auteurs n'ont pas observé de différences de concentrations entre les fractions, ce qui lève les effets possibles de la granulométrie sur les concentrations qui peuvent affecter l'analyse des isotopes cosmogéniques dans les petits bassins [Puchol 14].
2. Les sables ont ensuite été soumis à une étape de séparation magnétique permettant d'isoler les minéraux faiblement magnétiques : quartz, feldspaths, disthènes et muscovites.
3. Une pré-étape de dissolution des carbonates avec du HCl 1N a été effectuée avec les fractions non-magnétiques des échantillons car les sédiments des forages contiennent parfois jusqu'à 25% de carbonates.
4. Les grains de feldspaths et de muscovites ont été dissous séquentiellement dans une solution d'acide hexafluorosilicique H_2SiF_6 et d'acide chlorhydrique HCl (proportions 2 :1) pendant 5 à 15 jours.
5. (Facultatif) Les quelques échantillons qui présentaient encore des impuretés ont subi une solution diluée d'acides fluorhydrique et nitrique (HF 1%/HNO_3 1%) en cuve à ultrasons pendant 6h.
6. Passées ces étapes, les échantillons doivent être composés exclusivement de quartz. La composante atmosphérique ou météorique du ^{10}Be (dont la concentration peut-être 1000 fois plus importante que la composante cosmogénique in situ) est alors éliminée par 3 étapes de dissolution ménagée à l'HF qui permettent de dissoudre ~10% de la masse initiale des grains [Brown 91].

7. Les échantillons (quartz pur) subissent ensuite une dissolution complète avec de l'HF concentré après addition de 150 μL de solution d'entraîneur ^{9}Be. Malgrés toutes les précautions prises dans l'étape de dissolution séquentielle, quelques minéraux de disthène résiduels n'ont pas été dissous par l'HF. Ils ont été rincés, séchés et pesés très précisément afin de soustraire leur masse à la masse totale de quartz dissoute pour le calcul final des concentrations en ^{10}Be.
8. Le Be en solution est isolé par échanges ioniques sur colonnes. Le précipité final d'oxyde de Be est obtenu par un passage au four à 600°C pendant 2h.

Les mesures des rapports ^{10}Be /^{9}Be des échantillons ont été effectués par AMS (Accelerator Mass Spectrometer) par l'équipe ASTER (Accélérateur pour les Sciences de la Terre, Environnement, Risques) d'Aix-en-Provence. Grâce à ce rapport et à la masse d'entraîneur ajoutée, on calcule concentration en ^{10}Be (en at/g) de chaque échantillon par :

$$[^{10}Be] = \frac{\frac{^{10}Be}{^{9}Be}_{éch} - \frac{^{10}Be}{^{9}Be}_{blanc} N^{9}Be}{m_{quartz}}$$

avec $\frac{^{10}Be}{^{9}Be}_{éch}$ et $\frac{^{10}Be}{^{9}Be}_{blanc}$ les rapports isotopiques mesurés respectivement pour l'échantillon et le blanc, $N^{9}Be$ le nombre d'atomes de ^{9}Be et m_{quartz} la masse de quartz dissoute.

Les taux de production moyens sur chaque bassin et les facteurs de correction de la latitude et de l'altitude ont été calculés à partir d'un MNT SRTM de ~ 90 m de résolution [Stone 00]. Le taux de production SLHL du ^{10}Be retenu est de 3.9 ± 0.1 at/g/an [Balco 09], les longueurs d'atténuation « neutrons » , « μstop » et « μfast » respectivement de 160, 1500 et 4320 g/cm^2 [Braucher 01]. La densité du quartz retenue de 2.65 g/cm^3.

6.6.4 Résultats, discussion et perspectives

Les caractéristiques du bassin de la Narayani ainsi que les taux de production sont reportés dans le tableau 6.9 d'après [Lupker 12a].

Mean elev.	Glacier cov.	Basin area	P_n	P_{ms}	P_{mf}
(m)	(%)	(km^2)	(at/g/yr)	(at/g/yr)	(at/g/yr)
3030	9.2	31770	25.6	0.030	0.098

TABLE 6.9 – Résumé des caractéristiques du bassin de le Narayani. (D'après [Lupker 12a]) Rivière : Narayani, Localité : Narayanghat (°N27.703 °E84.427)

Nous utilisons les taux de production calculés à partir des caractéristiques actuelles du bassin. Si l'altitude, la superficie et le réseau de drainage ne doivent pas avoir été grandement modifiés au cours des derniers 45 ka, l'extension glaciaire et la couverture neigeuse a elle été réduite pendant la période interglaciaire, ayant un impact sur les taux de production moyens du bassin. Une analyse plus rigoureuse demandera d'évaluer l'impact de ce changement sur les taux de production afin d'affiner les résultats présentés ici. Les résultats des analyses et les taux de dénudation calculés dans les forages sont présentés dans le tableau 6.10 ainsi que dans les figures 6.6.2 et 6.6.3.

Les concentrations mesurées sur l'ensemble des forages semblent assez semblables aux concentrations mesurées dans les sables de la Narayani moderne et présentent une moyenne de 9.9×10^3at/g, et des concentrations comprises entre 6.3×10^3at/g et 13.5×10^3at/g ($\pm$ 2 σ). Les concentrations des forages GR1 et GR2 montrent une variabilité importante mais semblent compatibles jusqu'à 40 m de profondeur avec ces valeurs.

Par contraste, les échantillons de GR3 présentent des concentrations plus importantes avec 4 échantillons entre 15 et 18.5×10^3at/g ce qui témoigne d'une accumulation plus importante. L'échantillon GR2P10 avec une concentration de 29.6×10^3at/g semble constituer un *outlier* sans équivalent. Il est possible que cet échantillon ait été exposé pendant une période longue après son dépôt avant d'avoir été enfoui à l'occasion de l'avulsion de la rivière. Ce calcul peut être fait en considérant des taux de production Pn de 3.9 à 4.5 at/g/an à cette altitude, et en supposant que la concentration initial du sable à son dépôt ait été de 14×10^3at/g, soit une accumulation de 15×10^3at/g après dépôt, on déduit un âge d'exposition de 3800 à 3300 ans, ce qui semble important mais reste possible dans ce cadre d'environnement sédimentaire.

Drilling site	Sample core #	Depth (m)	^{10}Be (10^3at/g)	Denudation rate (mm/y)
GR1	GR1 P6	7	9.15 ± 2.36	1.88 ± 0.19
GR1	GR1 P12	17	13 ± 2.53	1.32 ± 0.12
GR1	GR1 P14	21	6.66 ± 1.75	2.58 ± 0.39
GR1	GR1 P17	25	8.65 ± 1.7	1.99 ± 0.26
GR1	GR1 P19	28	12.22 ± 2.19	1.41 ± 0.13
GR1	GR1 P21	31	9.57 ± 1.8	1.8 ± 0.17
GR1	GR1 P26	40	15.18 ± 2.42	1.13 ± 0.09
GR1	GR1 P29	44	18.86 ± 1.35	0.91 ± 0.07
GR1	GR1 P30	46	18.51 ± 3.38	0.93 ± 0.05
GR2	GR2 P7	9	12.57 ± 1.75	1.37 ± 0.19
GR2	GR2 P10	16	29.64 ± 1.26	0.58 ± 0.02
GR2	GR2 P13	19	13.41 ± 2.73	1.28 ± 0.09
GR2	GR2 P16	24	11.2 ± 0.92	1.54 ± 0.13
GR2	GR2 P19	29	15.29 ± 2.05	1.13 ± 0.08
GR2	GR2 P24	38	11.11 ± 0.56	1.55 ± 0.08
GR2	GR2 P27	45	12.46 ± 0.53	1.38 ± 0.06
GR2	GR2 P29	51	15.71 ± 3.37	1.09 ± 0.06
GR3	GR3 P7	8	9.62 ± 0.7	1.79 ± 0.13
GR3	GR3 P10	14	17.56 ± 4.16	0.98 ± 0.07
GR3	GR3 P15	23	15.9 ± 0.75	1.08 ± 0.05
GR3	GR3 P18	27	18.05 ± 0.98	0.95 ± 0.05
GR3	GR3 P21	32	12.09 ± 0.7	1.42 ± 0.08
GR3	GR3 P26	41	18.13 ± 4.42	0.95 ± 0.06

TABLE 6.10 – Résultats des mesures de ^{10}Be et taux de dénudation dans les forages. Les incertitudes sur les concentrations et les taux de dénudations correspondent à 1 σ

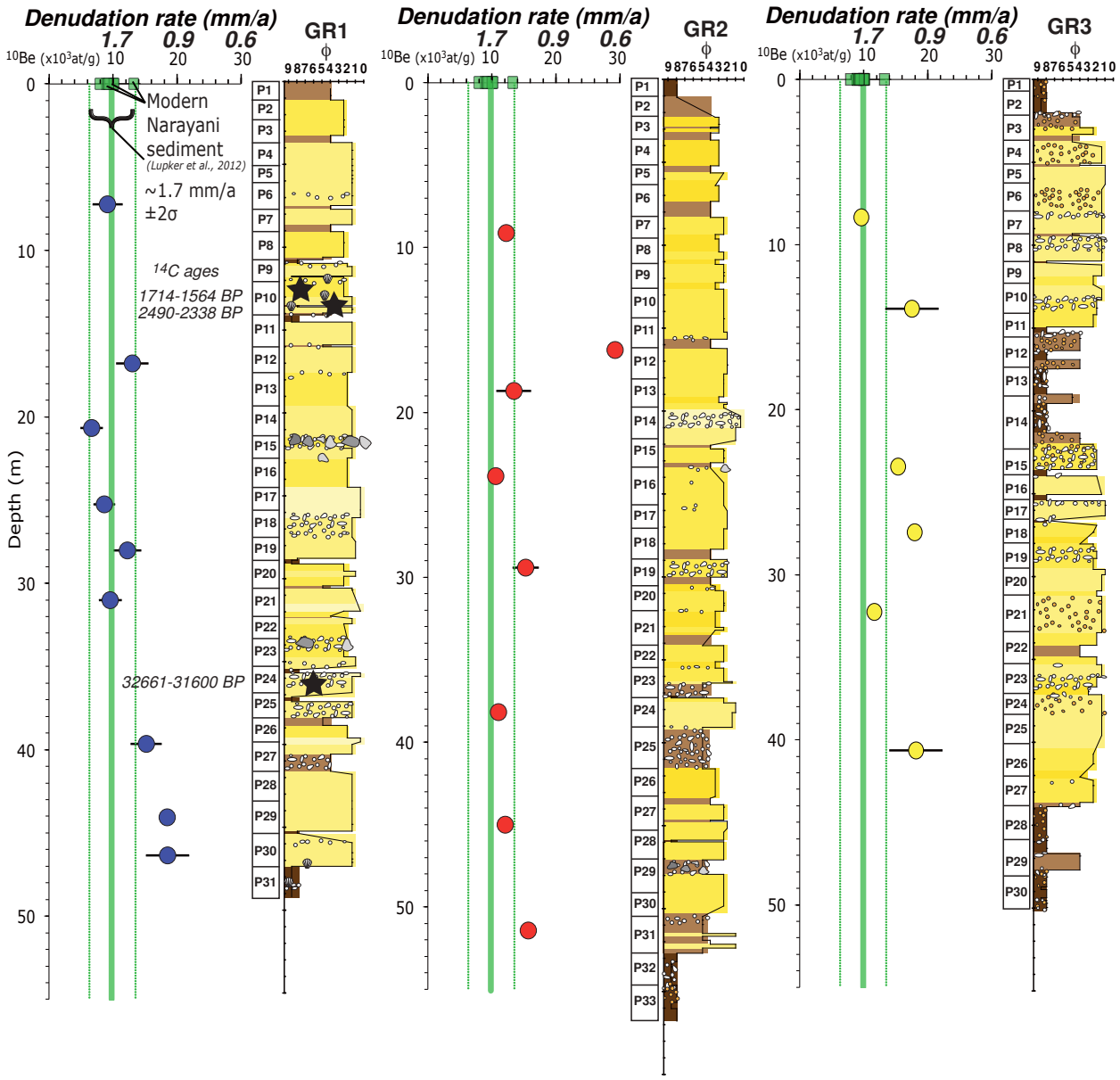

FIGURE 6.6.2 – Logs des concentrations en^{10}Be et taux de dénudation dans les forages. Les concentrations ^{10}Be en taux de dénudation des sédiments actuels de la Narayani sont issus de [Lupker 12a]. Les forages présentent des taux de dénudations comparables aux sédiments actuels ~1.7 mm/a ± 2σ exceptés le bas des forages GR1 et GR2, et 2/3 de GR3, qui montrent des taux de dénudation plus faibles de l'ordre de ~0.9-1.4 mm/a.

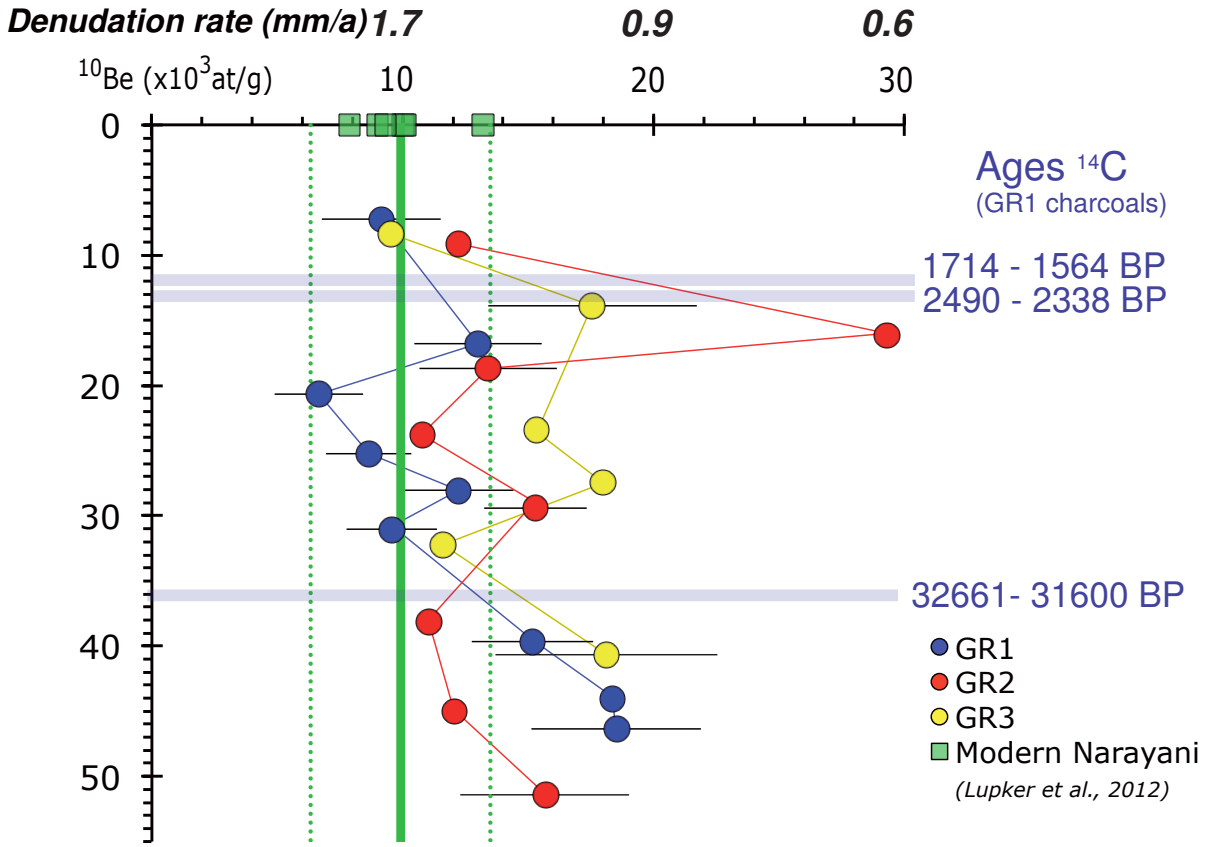

FIGURE 6.6.3 – Log compilé des concentrations en ^{10}Be et taux de dénudation des forages.

Si l'on considère les datations obtenues par charbons dans GR1 et que l'on estime ces âges comme représentatifs dans GR2 également, on en déduit que les taux de dénudation de GR1 et GR2 sont compatibles avec les taux actuels depuis au moins 32 ka.

Cela implique que la dernière transition n'a pas eu d'impact brutal sur les taux de dénudation mais que l'évolution s'est faite de manière continue (cf. figure 6.6.3). Les taux de dénudation de l'ordre de 0.9 à 1.1 mm/a observés dans le bas de GR1 et GR2 suggèrent que les régimes d'érosion étaient inférieurs d'un facteur de 30 à 50% lors de la glaciation du Pléistocène supérieur (Würm). L'interprétation des résultats obtenus dans GR3 reste encore difficile. Compte-tenu de son éloignement de la rivière actuelle, il est possible que ce forage n'ait pas été alimenté par la rivière à l'Holocène. Il présente des taux d'érosion faibles et inférieurs aux sédiments actuels avec des valeurs principalement comprises entre 0.9 et 1.4 mm/a. Sans contraintes chronologiques plus fortes sur ce forage, nos interpré-

tations restent spéculatives.

Néanmoins, nous pouvons exploiter les données à la lumière des datations obtenues par les charbons. Alors que la géochimie en éléments majeurs, l'hydratation, et les provenances des sédiments ne semblent pas présenter d'évolution sensible au cours des derniers ~45 ka, les taux de dénudation varient sensiblement. On observe une inflexion des concentrations vers des valeurs plus importantes que les sédiments modernes à 40 m et plus profond dans GR1 et GR2, et la quasi totalité de GR3. Cela semble indiquer que les taux de dénudations étaient plus faibles lors de la dernière glaciation.
Grâce aux compositions des isotopes du Sr-Nd dans les forages (cf. section 6.5), on ne note pas de variation de la distribution spatiale de l'érosion. En effet, le rapport des proportions de sédiments provenant du Haut-Himalaya (HH) et du Bas-Himalaya (LH) n'a que peu évolué pendant ces 45 ka avec un ratio constant de 80% HH contre 20% LH (cf. section 6.5).

Or on sait que les glaciers étaient très développés sur le Haut-Himalaya [Owen 02, Owen 09, Pratt-Sitaula 11, Owen 14]. La ELA était probablement 1000 m en dessous de la ELA moderne et donc le recouvrement glaciaire qui est actuellement de 10% devait plutôt avoisiner 20% de l'aire du bassin. On sait que les 2/3 de la surface des glaciers sont situés au dessus de la ELA, la semelle de cette partie est englacée et n'ablate pas la roche sous-jacente. Seul le tiers inférieur des glaciers situé sous la ELA est érosif via la fonte de la semelle, le glissement, et le développement du réseau de drainage sous-glaciaire.

Si l'on considère ces estimations, la superficie de l'érosion glaciaire actuelle doit correspondre à environ 3% de l'aire du bassin versant (1/3 de 10%) alors qu'elle devait être de 6 - 7% lors du LGM (1/3 de 20%). Au LGM, les flux sédimentaires glaciaires provenant du Haut-Himalaya étaient certainement supérieurs aux flux actuels d'un facteur $\times 2$, ce qui implique que la couverture glaciaire avait un rôle érosif et non protecteur comme proposé par [Rahaman 09]. De plus, les sédiments sous glaciaires, puisque protégés par la masse de glace sus-jacente, présentent des concentrations en ^{10}Be très faibles [Godard 12]. Une érosion glaciaire accrue au LGM aurait donc diminuée les concentrations en ^{10}Be. Ainsi, lors du LGM, une érosion glaciaire accrue voire dominante aurait provoqué des concentrations plus faibles en ^{10}Be, alors que nos résultats montrent des concentrations plus fortes.

Dans le bassin de la Narayani moderne, le flux de sédiments glaciaires semble mineur

comparé aux flux provenant d'autres agents d'érosion (cf. chapitre 5). Il est possible que l'érosion glaciaire accrue au LGM soit restée mineure par rapport à l'érosion provoquée par les autres agents d'érosion, et n'ait pu impacter sensiblement les concentrations en ^{10}Be des sédiments de la Narayani. De fait, la variation d'érosion glaciaire ne peut expliquer la modification des taux de dénudations lors de la glaciation.

En revanche, on sait que les régimes de mousson et les précipitations étaient moins intenses pendant l'ère glaciaire comme le montrent les enregistrements marins de la salinité dans la Baie du Bengale [Kudrass 01]. Ces régimes climatiques plus modérés ont certainement induit une réduction de l'intensité de l'érosion à l'ère glaciaire. [Clift 08] proposent que les moussons plus intenses de l'Holocène auraient déclenché des épisodes d'érosion intense dans le LH, donc à l'inverse une mousson réduite en période glaciaire doit avoir réduit les précipitations sur le LH et les flux sédimentaires associés.

Pour conserver un ratio stable entre HH et LH, les flux sédimentaires dérivés du HH doivent aussi avoir été réduits pendant le Pléistocène. Cette hypothèse impliquant une diminution des taux d'érosion sur l'ensemble de la chaîne lors de la période glaciaire du Pléistocène, semble être contradictoire avec l'extension des glaciers au LGM. Puisque les sédiments sont proches du pôle Haut-Himalaya, le système Sr-Nd n'est peut-être pas suffisamment sensible pour rendre compte de variations de l'ordre d'une dizaine de % dans le ratio HH -LH. Si l'érosion glaciaire devait être supérieure d'un facteur $\times 3$ et que les glissements de terrains et l'érosion des sols devaient être réduits par diminution des précipitations, le ratio HH-LH était probablement plus proche de 9 :1, ce qui semble difficile à détecter par les isotopes du Sr-Nd, mais qui semble cohérent avec la réduction des taux de dénudation.

La datation plus précise des forages et notamment de GR2 et GR3 permettront sans d'interpréter le signal avec une résolution temporelle supérieure, voire d'accéder à des enregistrements plus anciens que nous ne le supposons pour l'instant (probablement avec GR3).

6.7 Conclusion et perspectives

Pour le moment nous avons choisi de baser nos interprétations sur les âges^{14}C obtenus par datations des fragments végétaux dans GR1. L'âge d'environ 32 ka à 36 m laisse supposer que le fond des forages à 50 et 55 m doit correspondre à des dépôts de 45 à 50 ka, ce qui semblerait en accord avec les taux d'accumulation observés dans les autres mégafans de la plaine du Gange. Ces forages permettent ainsi de documenter les variations d'érosion et d'altération qui ont eu lieu dans le bassin de la Narayani et dans la chaîne du Népal central depuis la fin du Pléistocène, et incluent le LGM (Dernier Maximum Glaciaire) il y 18 - 20 ka ainsi que l'optimum climatique de l'Holocène il y a 6 -8 ka.

Étonnamment, la géochimie des forages semble indiquer que pendant ces derniers 50 ka, aucune variation du degré d'altération des sédiments n'a eu lieux. De même, l'analyse fine des provenances des sédiments semble indiquer que la distribution de l'érosion n'ait pas non plus été modifiée lors du passage de l'âge glaciaire à l'inter-glaciaire actuel. Les sédiments sont principalement produits dans le Haut-Himalaya à 80% contre seulement 20% dans le Bas Himalaya (LH), comme toutes les études précédentes tendent à le montrer (e.g. [Lavé 01, Galy 01, Singh 08b, Singh 02]).

Si la distribution de l'érosion au sein de la chaîne ne semble pas avoir varié aux cours des derniers 50 ka en conservant un ratio Haut-Himalaya - Bas-Himalaya de 9 :1 à 8 :2, les taux de dénudation semblent avoir augmenté à l'Holocène passant de 0.9 - 1 mm/a à l'ère glaciaire à 1.5 - 1.7 mm/a. L'intensification de la mousson observée à l'Holocène [Kudrass 01] a augmenté l'érosion de la chaîne sans en avoir changé sensiblement la distribution. L'impact anthropique récent a contribué à l'augmentation par $\times 3$ des taux d'érosion dans le Bas-Himalaya, ce qui n'avait pas été produit par la dernière transition climatique.

En apportant une meilleure résolution temporelle des enregistrements sédimentaires, l'obtention de datations plus nombreuses et cohérentes notamment par IRSL single-grain et ^{14}C des extractions séquentielles de Corg, devraient permettre de préciser l'évolution des taux de dénudation de la chaîne et résoudre les interprétations comparatives des forages, souvent hypothétiques pour le moment.

VII

Conclusion générale et perspectives

Relevant des interactions entre tectonique-climat-érosion, le fonctionnement et l'évolution des systèmes orogéniques actifs occupent une place importante dans les cycles physiques et chimiques du globe. Elles sont le lieu d'une activité géodynamique intense et du couplage de cette « Terre solide » aux cycles et fonctionnements des enveloppes externes de la surface de la Terre.

Nous avons choisi d'étudier ces liens érosion-climat par l'analyse fine des sédiments d'un système orogénique très actif : l'Himalaya. Les sédiments sont en effet les messagers des phénomènes et processus qui ont lieu dans la chaîne de montagnes et contiennent de grandes quantités d'informations concernant les processus et conditions par lesquels ils ont été produits, leur origine géographique, les agents qui les ont transportés etc. Lorsqu'il s'agit de remonter le temps, ils sont à même de délivrer leurs informations moyennant quelques précautions concernant les transformations qu'ils subissent après leur dépôt dans les bassins sédimentaires. Ce projet de thèse a consisté à tracer les sédiments depuis leurs zones de production dans la chaîne : au pied des glaciers, dans les sols développés sur les pentes des vallées, à la sortie des glissements de terrain ; jusqu'à leurs zones de dépôts dans le bassin d'avant-pays de la plaine de la Gandak. La majeure partie des analyses de ce travail a concerné les sédiments charriés par les rivières pour plusieurs raisons : elles sont le vecteur principal du transport des sédiments ; elles sont de bons intégrateurs des provenances et processus en amont et permettent d'établir des bilans quantitatifs à grande échelle ; ce faisant elles « échantillonnent » de grandes surfaces dont la caractérisation *in-situ* demanderait un temps et des moyens considérables ; l'analyse de la dynamique du transport sédimentaire fluviatile associée aux conditions hydro-climatologiques renseigne déjà sur certains aspects du couplage entre érosion et climat.

Les premières étapes de ce projet ont été d'étudier les caractéristiques granulométriques et chimiques des sédiments produits par chacun des agents érosifs : sols, glissements de terrains, glaciers afin d'en définir les traceurs diagnostiques dans les sédiments de rivières. Ensuite, il s'est agi d'évaluer la dynamique et les bilans de ces processus par la lecture du signal sédimentaire à l'échelle du Népal central. Enfin, il s'est agi d'appliquer la connaissance acquise sur le fonctionnement actuel du système afin d'interpréter les potentielles évolutions du fonctionnement de ces processus en réponse au changement climatique marqué de la dernière la dernière grande transition glaciaire-interglaciaire marquand la transitioni Pléistocène - Holocène.

Résultats et apports

Ce travail de thèse a donc tout d'abord débuté par tester si le traçage des processus érosifs était possible à partir de l'analyse des sédiments d'un petit bassin haut-himalayen typique du flanc sud : le bassin de la Khudi khola. Dans ce bassin, les conditions climatiques sont connues pour être intenses (précipitations >4 m/a), la lithologie et les conditions tectoniques y sont homogènes. Les taux d'érosion et de dénudation de ce bassin reportés dans ce bassin sont élevés entre 2.5 et 5 mm/a [Niemi 05, Whipp 07, Gabet 08, Blythe 07, Gallo 14b, Puchol 14]. Par sa taille modeste, le bassin de la Khudi constitue une « cellule » élémentaire et a servi de laboratoire d'étude pour réaliser un premier bilan érosif entre l'érosion des sols et des glissements de terrains. Les sols ont été échantillonnés sur les pentes et crêtes à plusieurs endroits du bassin versant. Les sédiments d'un glissement de terrain actif, le glissement de « Saituti », ont été échantillonnés sur plusieurs années ainsi que les sédiments transportés par les nombreux petits tributaires et dans le cours principal de Khudi.
Des compositions en éléments majeurs et des concentrations en hydroxiles d'hydratation des silicates H_2O+, nous sommes parvenus à la conclusion que : 1- les sols, par leurs compositions appauvries en éléments solubles comparés à la roche mère témoignent d'une altération chimique marquée sur les versants, 2- les sédiments des tributaires et de la rivière principale ainsi que ceux du glissement de terrain ne portent que peu de traces d'altération chimique. Une méthode de préparation préalable à la mesure de l'hydratation

dans les sols a été développée, et à notre connaissance, c'est la première fois que l'hydratation des silicates H_2O+ était appliquée à l'analyse des sols. La signature d'hydratation s'est révélée être très marquée dans les sols, ce qui fait d'H_2O+ un traceur diagnostique de la proportion de sol dans les sédiments de rivière.

Par inversion des compositions chimiques en éléments majeurs des sédiments des rivières et des sédiments des versants, nous avons calculé un bilan de l'érosion physique en terme de processus et concluons que 75 à 80 % des flux sédimentaires exportés du bassin par la rivière dérivent directement de la petite zone du glissement de terrain. L'érosion physique des sols ne correspond qu'à 5-10% de l'érosion totale ce qui, rapporté à l'aire du bassin, correspond à moins de 0.2 à 0.8 mm/a. L'érosion des sols et celle dérivée des petits tributaires constituent l'érosion superficielle « normale » des pentes dont le taux d'érosion est estimée entre 0.4 et 1.6 mm/a.

Dans ce bassin, le bilan marque la très grande focalisation de l'érosion physique circonscrite à une zone correspondant à 0.5% de l'aire totale du bassin versant, et en corollaire, illustre la relative quiescence de l'érosion physique superficielle sur les versants qui ne présentent pas de glissement. Ces derniers sont tout à fait comparables aux autres bassins versants voisins dans lesquels aucune zone de glissement n'a été détectée par photo satellite [Gallo, 2014]. Les signatures très peu altérées des sédiments de ces bassins semblent indiquer que l'érosion des sols y est aussi mineure. Les sédiments de rivières dériveraient plutôt de sédiments stockés sur les versants ou de l'attrition lors du transport fluviatile.

Les flux d'érosion chimique d'origine silicatée ont aussi été calculés dans la Khudi et sont faibles ~0.3% face aux flux physiques. Le « bruit » des compositions chimiques des sédiments et l'incertitude sur la composition de la croûte ne permettent pas de déterminer si ce bassin est à l'état d'équilibre ou non.

Néanmoins, les flux d'érosion chimique des silicates y sont intenses et semblent cohérents avec les corrélations observées entre érosion chimique des silicates et précipitation (ou écoulement spécifique) à d'autres endroits dans le monde. Cela ne distingue pas ce bassin des autres, bien qu'il montre un comportement pourtant exceptionnel en ce qui concerne l'érosion physique. Ce résultat conforte le modèle théorique de [West et al., 2005 ; Gabet et al., 2007, 2009] qui proposent que le contrôle de l'érosion chimique par l'érosion physique est beaucoup moins marquée dans les bassins dominés par les glissements.

Enfin, l'étude du fonctionnement du glissement de terrain réalisée en parallèle dans la thèse de F. Gallo [Gallo, 2014] démontre que le glissement est actif depuis plus de 40 ans

et que les taux d'érosion augmentent avec l'extension du glissement [Gallo et al., 2014]. De plus l'export par le réseau hydrographique des sédiments produits par les glissements est stochastique : les versants sont en régime *transport-limited* quand la rivière est en régime *supply-limited [Gabet 04b, Andermann 12b],* ce qui implique l'export sédimentaire dans ce bassin est contôlé par les précipitations.

Ce type de bassin alimente donc le réseau hydrographique régional par un flux important mais variable de sédiments alors que les bassins voisins semblent procéder d'une érosion moins intense. Ces bassins haut-himalayens typiques du flanc Sud exportent des sédiments dont les compositions chimiques sont très peu altérées, ou autrement dit « des sédiments frais ».

L'étude de la dynamique des flux sédimentaires a été réalisée à plus grande échelle à partir de l'analyse temporelle des signatures géochimiques et granulométriques des sédiments collectés à l'exutoire du bassin de la Narayani qui draine l'ensemble du Népal central. Cette étude précise les travaux de [Anderman et al., 2012] qui avait proposé un modèle de production et de transport des sédiments couplé au signal hydro-climatique sur plusieurs point :

1. La similitude des mesures de débit par ADCP avec celles des mesures de la hauteur d'eau à la station DHM montrent la cohérence des deux ensembles de données. L'utilisation couplée de mesures de courant par ADCP et d'échantillonnages en profondeur nous a permis de proposer un modèle de transport intégrant les flux de sédiments en profondeuret de calculer les taux d'érosion à partir de l'échantillonnage des MES de surface et des mesures des débits par la station DHM. Nous obtenons ainsi des taux d'érosion équivalents de 1.8+/-0.2 mm/a et de 1.6(+0.35/-0.2) mm/an pour respectivement l'année 2010 et le taux moyen au cours de la dernière décennie. Ces valeurs sont très proches des taux mesurés par isotopes cosmogéniques [Lupker et al., 2012] à plus long terme sur des temps d'intégration d'environ 500 ans.
2. La composante des débits directs (débits de ruissellement superficiel sur les pentes ou *runoff*) calculée à l'aide de filtres numériques à partir de l'hydrogramme annuel de la Narayani montre une bonne corrélation aux précipitations calculées à partir du réseau de stations DHM. Les débits sédimentaires de mousson ont montré une bonne corrélation aux débits directs ce qui conforte les conclusions de [Anderman et al.,

2012] qui proposent un contrôle des précipitations sur la production des sédiments au niveau des versants, qu'ils attribuent par hypothèse aux glissements de terrain.

3. Pour analyser l'érosion physique en terme de processus érosifs, nous avons affiné le calcul des flux sédimentaire en proposant un modèle de transport incluant les flux intégrés en profondeur, et nous avons comparé les flux sédimentaires aux signatures granulométriques et géochimiques des sédiments. Nous avons utilisé le taux de carbone organique Corg dans les sédiments comme traceur de l'érosion des sols. Afin de documenter l'érosion glaciaire provenant du nord du bassin où affleurent essentiellement les lithologies carbonatées des TSS, nous avons couplé les proportions de carbonates aux compositions isotopiques D/H (dépendantes de l'altitude et plus négatives dans les environnements glaciaires) dans les sédiments de rivière. L'anti-corrélation des deux traceurs dans les sédiments de la Narayani ainsi que dans ses tributaires (notamment la Marsyandi) permet, avec une bonne confiance, de tracer les contributions glaciaires à l'échelle du Népal central.
4. De l'analyse temporelle journalière des signatures géochimiques et granulométriques des sédiments, associée aux débits sédimentaires calculés par le modèle, nous concluons que les sols et glaciers contribuent de façon mineure aux bilans de l'érosion totale (<20%). L'érosion superficielle des sols est totalement « diluée » pendant la mousson par la production de sédiments par les glissements. Enfin, les contributions glaciaires semblent plus erratiques et ne semblent visibles qu'en période de pré-mousson ou durant des périodes moins arrosées de la mousson, périodes où le flux issus des glissements de terrain est fortement atténué et ne vient pas les masquer.

Nos observations de la dynamique de l'érosion physique à plus grande échelle confirment les observations faites au niveau du bassin de la Khudi : les régimes de la Narayani sont *supply-limited* et il est probable que les flux d'érosion soient principallement liés aux glissements de terrain, qui dominent ainsi complètement l'érosion de la chaîne du Népal central.

Actuellement, la majeure partie des sédiments est principalement exportée pendant la période de mousson. Ces sédiments ne sont que peu altérés car ils dérivent en majorité des glissements de terrain. Pendant l'interglaciaire actuel, l'Himalaya exporte des sédiments « frais » sensibles à l'altération chimique qui se déroule dans la plaine [Lupker et al., 2012 ; Bouchez et al., 2011].

L'analyse des séries détritiques correspondant aux dépôts des sédiments issus de la chaîne himalayenne du Népal central a été rendue possible par la réalisation de 3 forages dans la plaine de la Gandak, au niveau de la partie proximale (apex) du *megafan*. Les datations disponibles à ce jour démontrent que ces séries sédimentaires correspondent à un enregistrement d'environ 45 - 50 ka, documentant ainsi l'érosion et l'altération passées, et leur évolution au cours de la dernière transition climatique. Ces enregistrements incluent le LGM (~20 ka BP) et l'optimum climatique Holocène (~ 6 ka BP).

Les compositions géochimiques des sables et silts échantillonnés dans les forages indiquent que les degrés d'altération des sédiments sont restés stables depuis 50 ka. De même, le traçage des provenances des sédiments par les isotopes du Sr et du Nd montre que la distribution de l'érosion dans la chaîne n'a pas été modifiée lors de la déglaciation et au cours du réchauffement Holocène ; les flux dérivés du Haut-Himalaya comparés au Bas-Himalaya ont conservé un ratio d'environ 80% : 20%. Ces calculs de distribution de l'érosion au Népal central ont été réalisés grâce à l'utilisation du système isotopique du Sr et du Nd des fractions silicatées des sédiments. Utilisant les compositions publiées dans la littérature et en les complétant d'analyses nouvelles, nous proposons un calcul des proportions des unités géologiques dans les sédiments de rivières du Népal central basé sur une méthode de Monte Carlo avec inversions multiples des compositions isotopiques du Sr et du Nd.

Seules les proportions de carbonates détritiques montrent des « pulses » correspondant à de très forts épisodes d'érosion dans les bassins carbonatés TSS du Haut-Himalaya. Ces « pulses » de carbonates ne sont pas accompagnés de modification du signal D/H et ne semblent donc pas liés de manière simple à de l'érosion glaciaire. Nous proposons plutôt qu'ils témoignent d'épisode rares et probablement catastrophiques tels que celui de la Seti.

A contrario, les taux d'érosion calculés à partir des mesures des concentrations en [^{10}Be] cosmogénique dans les forages semblent progressivement augmenter depuis 50 ka depuis des valeurs ~0.9 mm/a pendant la dernière glaciation vers les valeurs actuelles ~1.7 mm/a. Ces résultats sont encore difficiles à interpréter finement par manque de contraintes chronostratigraphiques précises (notamment sur GR3) mais les tendances observées sur les trois forages documentent déjà à ce stade la réponse de l'orogène au réchauffement cli-

matique de l'Holocène. La dénudation s'est intensifiée d'un facteur $\times 1.5$ à $\times 2$ lors du réchauffement climatique, cette augmentation s'est accompagnée d'une probable diminution de l'érosion glaciaire d'un facteur $\div 2$, tandis que l'érosion des sols semble être restée mineure comme en témoigne les compositions en éléments majeurs, Corg et hydratation H_2O+ des sédiments des forages. Dès lors, nous supposons que l'érosion a été intensifiée par le déclenchement croissant de glissements de terrains en réponse à l'intensification de la mousson et des précipitations orographiques qui en ont été la conséquence [Kudrass et al., 2000]. Ces résultats apportent donc une réponse partielle à la réponse des orogènes actifs à un forçage climatique marqué :

1. l'érosion physique a été augmentée lors d'intensification des régimes de précipitations certainement par déclenchement progressif d'un nombre croissant de glissements de terrains,
2. la réponse de l'altération chimique semble plus difficile à interpréter ; la variation d'altération chimique et la production de sols qui ont certainement augmenté avec l'accroissement des températures n'est pas détectée dans les archives sédimentaires. Or, comme l'érosion des sols semble mineure par rapport à celle des glissements de terrain qui, elle, n'a cessé de s'intensifier à l'Holocène, il est probable que nous ne puissions pas détecter « sensiblement » la modification de l'altération par analyses des sédiments totaux.
3. le temps de réponse de l'érosion semble de l'ordre de celui imprimé par le changement climatique ; dès lors, dans un contexte global d'intensification de l'amplitude des phénomènes climatiques, il est à prévoir que les orogènes actifs et leurs environnements vont observer une augmentation de la fréquence et de l'amplitude des épisodes érosifs catastrophiques, notamment au travers du déclenchement d'un nombre croissant de grands glissements de terrains. Ces résultats illustrent ainsi la potentielle augmentation de l'aléa « glissement de terrain » et l'augmentation du risque encouru en aval par les infrastructures (barrages) et surtout les populations exposées.

Enfin, nous avons appliqué le modèle d'inversion des compositions isotopiques Sr-Nd des provenances géographiques à la comparaison des archives sédimentaires et à un ensemble d'échantillons de sédiments actuels de la Narayani qui couvre environ 16 ans depuis 1995 à aujourd'hui. Les ratios Haut-Himalaya : Bas-Himalaya (HH :BH) depuis le LGM et au

cours de l'Holocène, ainsi que des sédiments récents avant les années 2005 étaient tout à fait comparables et de l'ordre de 80 : 20%.

Depuis les années 2005, on observe une nette inflexion des proportions HH :BH vers des proportions approchant aujourd'hui 55 : 45%. Aucune modification de l'érosion du Haut-Himalaya ne s'est vraisemblablement produite pendant cette période, ce qui implique que l'érosion du Bas-Himalaya a dû s'intensifier fortement d'un facteur $\times 3$ depuis les 7 dernières années. Or, le Népal central a connu un fort accroissement économique depuis la fin de la guerre civile et de la monarchie (2006-2008) qui s'est accompagné du développement important des infrastructures, notamment du réseau routier dans le Terai et le Bas Himalaya. Le développement souvent mal dimensionné des routes de montagnes dans les pays en voie de développement est connu pour provoquer une érosion des versants par glissements de terrain associés [Fort et al., 2010 ; Sidle et al., 2012]. Par hypothèse, nous attribuons ce « pulse » d'érosion physique dans le Bas-Himalaya à la construction galopante de centaines de km de route.

Ces résultats démontrent l'impact majeur que les activités anthropiques ont sur les équilibres fragiles des environnements montagneux. De même, on le répète encore, ils mettent en garde face aux risques accrus pour les populations exposées et les infrastructures en aval, notamment les barrages hydroélectriques installés sur le cours des rivières himalayennes du Népal, et ceux destinés à l'irrigation et installés sur les rivières de la plaine gangétique en Inde.

Limites et perspectives

L'interprétation complète de ces résultats montre encore certaines limites. Nous nous proposons d'exposer plusieurs axes de recherche potentiels qui permettraient de les compléter :

1. La première limite est issue de la calibration chronostratigraphique encore très partielle des forages. Cette calibration apparaît comme l'axe prioritaire des compléments à apporter à ces résultats. Les pistes de datation évoquées dans le manuscrit sont : la datation par OSL en collaboration avec Pierre Valla et Frédéric Herman de l'Université de Lausanne, et par ^{14}C des fractions du Corg par « dirt-burner » en collaboration avec Valier Galy du WHOI. Une série d'extractions complémentaires d'échantillons de GR2 et GR3 a été effectuée au WHOI par Thomas Rigaudier et

sera analysée prochainement par Maarten Lupker à l'ETH Zürich. Ces résultats apporteront peut-être un ensemble plus cohérent pour l'interprétation des âges produits par cette approche. De plus, elle pourra aussi renseigner sur une problématique plus « géochimique » liée aux problématiques du cycle du carbone et de l'échange dans les plaines du carbone d'origine biosphérique associé aux sédiments détritiques (e.g. [Galy et al., 2008 ; 2008 ; 2012 ; 2015]). Une collaboration avec l'équipe de Lausanne permettrait aussi de préciser les apports potentiellement importants de la méthode de datation OSL de type *single-grain* aux datations des archives détritiques issues de systèmes fluviatiles observant des taux d'érosion importants induisant un mauvais *bleaching* des sédiments lors du transport, et les difficultés d'interprétation auxquelles nous avons dû faire face lors de ce travail.

2. L'évaluation de l'altération chimique des archives sédimentaires par les compositions en éléments majeurs et hydratation sur sédiments totaux s'est révélée assez peu diagnostique car les forages sont essentiellement constitués par des sédiments grossiers. Or, on sait que les sédiments grossiers ne comportent que des proportions très limitées de phases minérales susceptibles de documenter le degré d'altération chimique (micas, argiles). Afin de documenter plus finement les signaux d'altération que les forages contiennent potentiellement, nous proposons deux axes potentiels de recherche : l'analyse des rapports $^{7}Li/^{6}Li$ des sédiments et forages qui ont récemment démontré leurs capacités « diagnostiques » des degrés d'altération chimique des sédiments de rivières actuelles associés aux intrants climatiques [Dellinger et al., 2014 ; 2015] ; l'analyse plus fine des cortèges argileux qui a déjà été appliquée avec succès aux interprétations climatiques passées en Himalaya [Huyghe et al., 2005 ; 2011 ; Derry et France-Lanord et Derry, 1997]. Une autre approche pourrait porter sur l'analyse des taux de dénudation par [^{10}Be] cosmogéniques mesurées dans des minéraux sensibles à l'altération comme les feldspaths. Une série d'échantillons de feldspaths a déjà été produite avec succès par méthode de séparation par flottation non-présentée dans ce manuscrit et « ne demande qu'à être analysée ».
3. Un cadre interprétatif permettant le calcul des proportions des processus érosifs à partir des sédiments de rivière a été établi en Himalaya. Il allie modèle de transport sédimentaire, analyse des éléments majeurs et traceurs environnementaux (compositions D/H). Appliqué à d'autres orogènes actifs du globe comme les Alpes euro-

péennes, les Alpes néo-zélandaises ou encore les Andes et par analyse comparée au système Himalayen, il peut potentiellement aider à l'interprétation de la dynamique des intéractions érosion-climat dans d'autres contextes climatiques. Ces approches pourraient se révéler complémentaires d'autres méthodes d'étude de la dénudation et de la production des sols en milieux montagneux, comme par exemple celles des isotopes cosmogéniques [Heimsath et al., 2012 ; Larsen et al., 2014b].

Annexes

« La connaissance est une navigation dans un Océan d'incertitudes, à travers des archipels de certitude. »"

(Edgard Morin, 1999.)

Article : « Shallow subsurface stratigraphy and alluvial architecture of the Kosi and Gandak megafans in the Himalayan foreland basin, India » Sinha et al., 2014.

Sedimentary Geology 301 (2014) 133–149

Contents lists available at ScienceDirect

Sedimentary Geology

journal homepage: www.elsevier.com/locate/sedgeo

Shallow subsurface stratigraphy and alluvial architecture of the Kosi and Gandak megafans in the Himalayan foreland basin, India

Rajiv Sinha [a,*], Jawed Ahmad [a,b], Kumar Gaurav [a,c], Guillaume Morin [d]

[a] Engineering Geosciences Group, Indian Institute of Technology Kanpur, Kanpur 208016, India
[b] Geological Survey of India, Jaipur, India
[c] Institut de Physique du globe de Paris, 1 Rue Jussieu, 75238 Paris Cedex 05, France
[d] CRPG CNRS — UPR2300, 15 rue Notre Dame des Pauvres, 54501 Vandoeuvre-Les-Nancy, France

ARTICLE INFO

Article history:
Received 4 February 2013
Received in revised form 8 June 2013
Accepted 27 June 2013
Available online 5 July 2013

Keywords:
Fluvial megafans
Avulsive deposits
Alluvial stratigraphy
Sediment flux
Ganga plains

ABSTRACT

The Kosi and the Gandak are two major Himalayan tributaries of the Ganga River in the north Bihar plains India. With a large hinterland in the Nepal Himalaya, both these rivers have generated megafans in the plains over the Quaternary time scale. Both these rivers are known to be highly dynamic and sediment-charged. A few conceptual models and limited field data suggested that these megafans have produced thick sand sheets over Late Quaternary period but these ideas have remained speculative and there is no data on the size and dimension of these sand bodies. This paper attempts to reconstruct the subsurface stratigraphy and alluvial architecture for the upper ~100 m of the megafans based on electrical resistivity soundings, borehole data and drill cores. Alluvial architecture of the Kosi megafan shows significant variability from proximal to medial parts of the fan in terms of sediment grain size and layer thicknesses. While the medial part shows ~20–30 m thick medium to coarse sand sheets which are laterally stacked, the proximal part of the fan has a dominantly gravel unit below ~15 m depth that is underlain and overlain by medium to coarse sand units. Further, the medial fan also shows significant vertical and lateral variability in alluvial stratigraphy. The near-surface (<20 m depth) deposits from the Kosi megafan have pockets of clay and silt within large amalgamated sand bodies whereas the shallow sub-surface (50–100 m depth) sediments are largely sandy and devoid of clay and silt pockets. Alluvial architecture of the Gandak megafan shows two major lithounits; the upper fan succession has a higher stacking density of smaller sand bodies perhaps reflecting the migratory behavior of the river whereas the lower succession shows narrow but thick sand fills reflecting incised channels. The western part of the Gandak megafan has more abundant sand bodies compared to the eastern side of the river along both transects. There are no significant differences between proximal and medial transects across the Gandak megafan. The absence of gravel deposits in the shallow subsurface of the Gandak megafan may be attributed to the presence of a prominent intermontane valley in the hinterland of the Gandak river which has acted as a 'sediment filter' thereby trapping most of the coarser fraction. On the other hand, the Kosi river exits directly through the mountain front, and therefore, has been able to transport gravels into the plains in pre-historic times. Our study thus suggests significant variability in subsurface stratigraphy of the Kosi and the Gandak megafans even though they are located in similar geographic region. Such differences are attributed to the geomorphic diversity of the mountain exits of these megafans and their sediment transport history.

1. Introduction

Fluvial megafans are distinct landforms on the earth's surface and are localized in specific climatic, geomorphic and hydrologic regimes. A 'megafan' has been defined as "a large (10^3–10^5 km^2), fan-shaped (in plan view) mass of clastic sediment deposited by a *laterally mobile river system* that emanates from the outer point of a large mountainous drainage network" (Goudie, 2004). A characteristic geomorphic aspect of megafans is the recognition of expansion of flow downstream of a drainage outlet through a branching distributary pattern of channels. In terms of geologic and geomorphic setting, the megafans generally form in areas of orogenic belt, aggrading river basins with high sediment flux, moderate to extreme seasonal discharge fluctuations (producing channel instability and fan shaped sediment lobes), adequate spacing between river exits from mountains to provide accommodation space (Gupta, 1997) and to allow channel shifting (Leier et al., 2005). In total, Leier et al. (2005) identified 33 megafans worldwide based on their specific characteristics

* Corresponding author.
E-mail address: rsinha@iitk.ac.in (R. Sinha).

0037-0738/$ – see front matter © 2013 Elsevier B.V. All rights reserved.
http://dx.doi.org/10.1016/j.sedgeo.2013.06.008

such as a large sediment body, abandoned channels on the fan, and low slope etc. The authors also documented that the megafans are mainly localized between 15° to 35° latitude in both northern and southern hemispheres i.e. tropical zone and several workers have documented the morphological and hydrological characteristics of the rivers draining these fans (summarized in Latrubesse et al., 2005). Due to their unique geomorphic setting, climatic conditions, and complex sedimentary processes, the megafans have drawn enormous attention of researchers from all over the world. The avulsive shifts of rivers on the megafans have often caused severe floods (Assine, 2005; Sinha et al., 2008; Sinha, 2009; Bernal et al., 2011). Stratigraphic studies of the exposures of ancient megafans have also been carried out by several workers to understand their geological evolution and for comparison with modern megafans as their ancient analogs (e.g. DeCelles and Cavazza, 1999; Horton and DeCelles, 2001; Latrubesse et al., 2010). In a recent compilation of global database on geometries of fluvial channels and valley fills in the geological record, Gibling (2006) identified the megafan deposits as a distinct class on the basis of their geomorphic setting, geometry and internal structure and noted the lack of data on 3D geometry from modern settings. Gibling (2006) documented that the channel belts of the major river building the megafan such as the Kosi are characterized by extensive sand sheets typical of braided rivers exiting from active orogenic belt. On the other hand, the megafan surfaces are marked by avulsive and aggradational distributary systems, also of braided style, generating ribbons and narrow sheets. However, there are several other megafans such as the Chaco and Okavango in South America where braided systems and sand sheets are not typical or dominant (McCarthy et al., 1991; Assine, 2005; Latrubesse et al., 2010).

The Indo-Gangetic plains in the Himalayan foreland basin host several megafans namely, the Tista megafan in West Bengal (Chakraborty and Ghosh, 2010), the Kosi and Gandak megafans in north Bihar (Geddes, 1960; Gohain and Prakash, 1990; Mohindra et al., 1992; Sinha and Friend, 1994; Chakraborty et al., 2010) and the Sone megafan in south Bihar (Sahu et al., 2010). The Kosi and Gandak are two important megafans that have attracted global attention due to their large dimensions. The Kosi and Gandak rivers draining through these two megafans are characterized by very high suspended sediment fluxes (43 and 79 Mt/yr respectively), low stream power (6.4–20 W/m^2), low slope (0.01–0.05°), hyperavulsive behavior, and frequent flooding (Sinha and Friend, 1994; Sinha and Jain, 1998; Sinha et al., 2005; Sinha, 2009). It has been speculated that the avulsive shift of the rivers may have generated a distinctive stratigraphy below the fan surface (Wells and Dorr, 1987; Mohindra et al., 1992; Jain and Sinha, 2003). However, there is very little systematic data available on the sub-surface stratigraphy of these megafans due to the lack of exposures and sub-surface data.

This paper aims to reconstruct the subsurface stratigraphy of the Kosi and Gandak megafans in the Himalayan foreland basin to understand the spatial variability and inhomogeneity in the alluvial architecture developing below and the controlling factors. In particular, we attempt to answer two fundamental questions: (a) What are the spatial and temporal variability in alluvial architecture below the megafans, (b) What are the implications and causal factors for such variability in terms of sub-surface stratigraphic development e.g. mountain front setting, sediment flux, river dynamics? We have used, for the first time, an integrated approach of resistivity surveys coupled with the groundwater well data and drill cores across the fan surface for this study.

2. Study area description

2.1. General geography and climate

The Kosi River originates at an elevation of 5500 m in Tibet (Fig. 1) and has a very large upland area compared to the plains area (u/p = 5.3, Sinha and Friend, 1994). The river enters the plains at Chatra in Nepal and then flows for a distance of ~40 km to the barrage at Bhimnagar and another 40 km along the India–Nepal boundary before entering the north Bihar plains in India. The river follows a curved path from Bhimnagar to Mansi–Koparia railway line further downstream and then takes an easterly turn and runs parallel to the Ganga river for a distance of about 160 km before joining the into Ganga river near Kursela. The Kosi River drains the total area of 69,300 sq km with 29,400 sq km in China, 30,700 sq km in Nepal and 9200 sq km in India (Virgo and Subba, 1994).

The Gandak megafan is formed by the Gandak River which starts at an altitude of 6268 m from the Nhubine Himal glacier in Nepal close to the Tibetan border. It forms a confluence called Triveni Sangam with the river Pachnad and Sonha at a point close to the Indo-Nepal border. The river enters India in west Champaran district of north Bihar, builds a large megafan spanning into the plains of north Bihar and Uttar Pradesh and then joins the Ganga River near Hajipur.

The plains of north Bihar and Uttar Pradesh where both the megafans are located experience moderate to fairly high monsoonal rainfall of about 1000–1600 mm annually of which ~85% occurs in the monsoon season (June–September) itself. The upstream basin area of the megafans in the foothills receives higher rainfall (>2000 mm annually) (Sinha and Friend, 1994) and the main rains start earlier in this region than on the plains. The high mountainous catchments of both the Gandak and the Kosi megafans have distinctly drier climate and are covered by snow and ice all year.

2.2. Geomorphology of megafans

One of the early systematic geomorphic descriptions of the megafans in the Gangetic plains was provided by Geddes (1960) who showed, using closely spaced contours, that megafans have a positive topography. He used the term ‘cone’ to describe these features. Gole and Chitale (1966) described the Kosi megafan as ‘inland delta’ built by large sediment flux from the Himalayan orogen. The term ‘megafan’ was first used by Gohain and Prakash (1990). The average annual discharge of the Kosi at the most downstream station (Baltara) is 2236 m^3/s. Although a large part of the upper catchments of the Kosi is glaciated and a large proportion of sediment flux is intercepted upstream of the Kosi barrage, the average annual suspended sediment flux for the Kosi at Baltara (43 Mt/year; Sinha and Friend, 1994) is still quite high which results in rapid and extensive aggradation within the channel as well as the floodplains. For a total catchment area of ~88, 500 km^2 up to Baltara, modern sediment (suspended) flux of the Kosi is 0.43 Mt/km^2/yr. Such high sediment flux and rapid aggradation within the embankment have been considered as one of the primary reasons for avulsion and flooding in this region (Sinha, 2009; Chakraborty et al., 2010; Kale, 2011).

The vast plain, on which the Kosi megafan has formed, has a general slope from north to south and west to east, being steeper in the north (55–75 cm/km) and flatter in the south (6 cm/km). Thus, the entire fan surface is nearly flat, which is dissected by numerous ‘dhars’ (small channels) representing paleochannels of the Kosi river. Some of the paleochannels are vegetated and muddy due to monsoon water and dry season discharges. There are undulations and innumerable depressions called “chaurs” on the megafan surface, where water remains accumulated for most parts of the year. Some of these waterlogged patches in the lower reaches and close to the embankments are very large which may be related to seepage along the embankment but may partly represent accumulation of floodwater after overbank flooding.

Available historical records of last two centuries report that there has been a net (but not systematic) westward shift of the Kosi river by ~150 km across its fan surface during the last 200 years (Wells and Dorr, 1987; Mishra, 2008); however, several eastward shifts

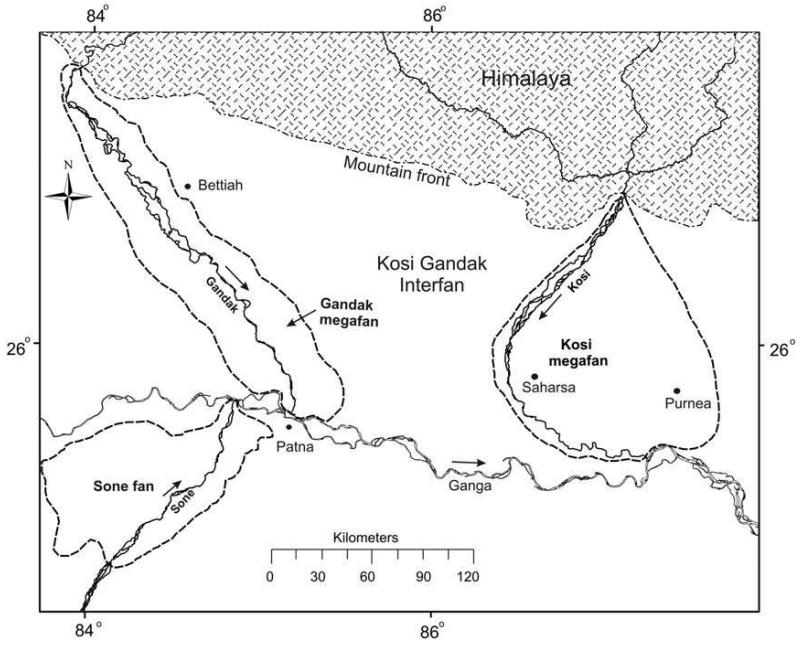

Fig. 1. Landsat TM image showing the Gandak and Kosi megafans in the Himalayan foreland basin. The Ganga is the axial river and both the Gandak and the Kosi rivers join the Ganga. A southern tributary of the Ganga, the Sone River, also forms a large fan and the area further east of the Kosi falls in the Tista megafan region (not see in the figure).

have also been documented including the recent avulsion in August 2008 (Sinha, 2009; Sinha et al., in press). The avulsive movements of the Kosi river have been described as autocyclic and stochastic (Mackey and Bridge, 1995; Stouthamer and Berendsen, 2007), which is typical of most alluvial fans across the world. However, the average avulsion frequency of 24 years for the Kosi is among the lowest in the world compared to 1400 years for the Mississippi river.

The Gandak River, one of the important rivers of Nepal and India, is also characterized by a high ratio of upland source area to plains ($u/p = 3.3$) and high discharge (1555 m^3/s at Dumariaghat) (Sinha and Friend, 1994). The Gandak river is braided throughout its alluvial course with braid channel ratios ranging from 1.33 to 5.38 (Sinha and Friend, 1994). Compared to the Kosi, the Gandak carries a much higher sediment load of 79 Mt/year and with a catchment area of only ~43,000 km^2, modern sediment flux (suspended) of the Gandak river works out to be 0.82 $Mt/km^2/yr$ (Sinha and Friend, 1994). Mohindra et al. (1992) mapped various geomorphological units on the Gandak megafan and the adjoining areas and argued that the development of these geomorphological units was controlled by the climatic change, channel shifting and tectonics in the area over the last 10,000 years. It has also been documented that the Gandak has migrated over its megafan from west to east over a distance of about 80 km in 5000 years (Mohindra and Parkash, 1994) as evidenced from large number of abandoned, highly sinuous, meander loops and waterlogged patches in the lower part of the fan.

The interfan area between the Gandak and the Kosi megafans are drained by the Burhi Gandak, Baghmati, Kamla and Balan rivers that are flowing along south-eastward direction ultimately joining the Ganga in downstream (Sinha and Friend, 1994). Although much smaller in size, the interfan rivers have also been described to be very dynamic (Sinha, 1996; Jain and Sinha, 2003, 2004).

3. Approach and methodology

This study mainly relies on field investigations that include vertical electrical sounding (VES) and drilling of sediment cores. Apart from field data, the study also uses the remotely sensed satellite imagery and the groundwater borehole data as secondary dataset. Borehole data obtained from the Central Ground Water Board (CGWB) and State Groundwater Board (Fig. 2) were analyzed to obtain the first order assessment of the sub-surface stratigraphy of the fans. There are around 100 borehole data points for the Kosi region and 6 points from the Gandak area. The depth of boreholes for both Kosi and Gandak region varies from 15 m to more than 100 m. The main objectives of the borehole data analysis were to record (a) the variation in sub-surface lithology from proximal to medial/distal parts of the megafan, (b) the order of thickness of sand bodies and intermediate clay layers, and (c) the depth of gravely layer and presence of carbonate concretions (locally called 'kankar'). Although limited use of the borehole logs could be made for reconstructing alluvial stratigraphy as the data points were distributed all across the fan, this data was very useful to build a first order stratigraphy, to select transects for resistivity surveys and to calibrate the resistivity data.

For resistivity surveys, two transects were planned for the Kosi region, (a) proximal transect (Kus–Kus'), 6 km long having 4 VES points, and (b) medial transect (Kds–Kds'), 140 km long with a total of 33 points, and (Fig. 2). Similarly, two transects were planned on the Gandak megafan, one in the proximal part (near Bettiah) and another in the medial part (near Motihari). The length of each transect was ~20 km (~10 km on both sides of the main river) and the VES points were selected at ~2 km interval along both transects. A resistivity meter (Aquameter, CRM 500, ANVIC systems) was used for the survey in Schlumberger configuration with a maximum current electrode separation of 400 m in order to get shallow subsurface information as per the previous studies in similar settings (Yadav et al., 2010; Sinha et al., 2012). Yadav et al. (2010) have discussed the detailed methodology and techniques used for interpretation of resistivity data. One of the basic assumptions in most of the interpretation techniques is that the resistivity layers extend horizontally to infinity and are isotropic, homogeneous entities with distinct electrical resistivity contrast and thicknesses. Though all these conditions are seldom satisfied, these techniques are useful for inferring broad scale subsurface hydrogeological conditions.

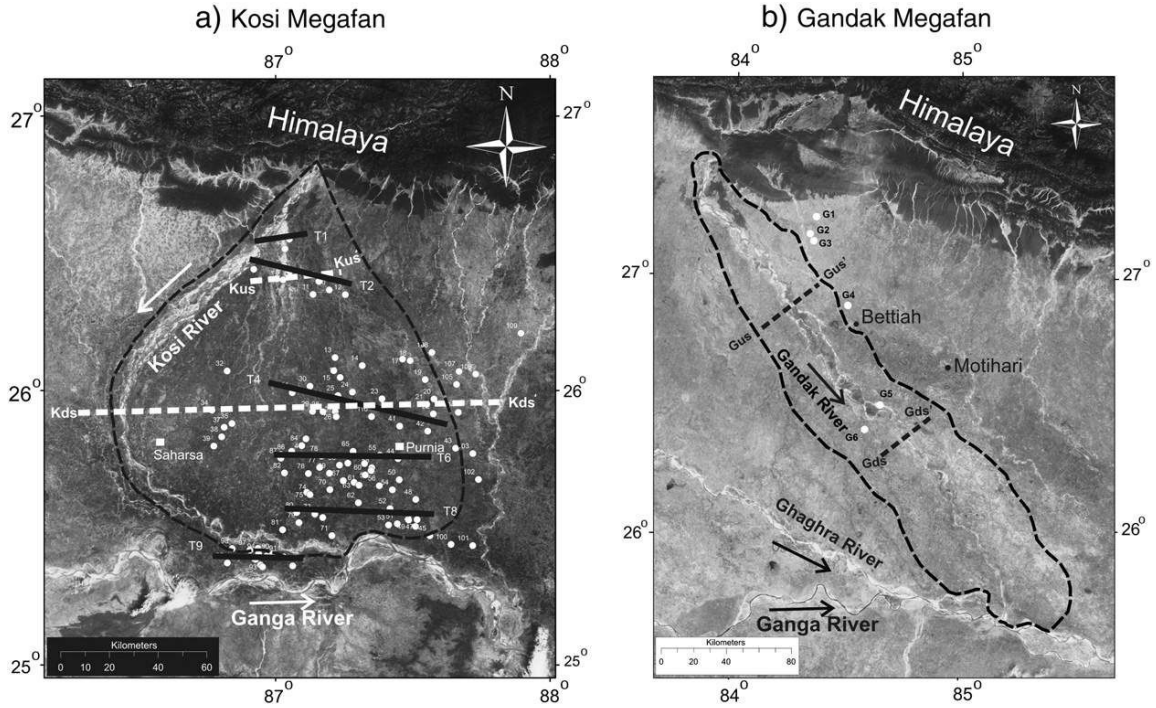

Fig. 2. Locations of groundwater borehole data analyzed from the (a) Kosi and (b) Gandak megafan region. Data for a few selected transects (T1, T2, T4, T6, T8 and T9) have been presented in this paper. Also shown are the proximal (Kus–Kus') and distal (Kds–Kds') transects for resistivity surveys.

Field data was first processed to generate a field curve which was matched with standard master curves for known layer parameters of 2-, 3- and 4-layers (Orellana and Mooney, 1966; Rijkswaterstaat, 1969). This was followed by computer-aided interpretation using 1X1D software developed by the Interprex Limited USA which primarily involved generation of a basic geoelectrical model at each site. Finally, the interpreted results were calibrated with the available lithological information (borehole data and drill cores) to determine resistivity ranges for different lithological units. In alluvial terrain, the stratigraphic boundaries are not always marked by sharp lithological variation and a good correlation may sometimes be difficult due to a variety of reasons viz. thin layers embedded in a thick layer of different material, variations in groundwater salinity. On the other hand, a single lithological unit may include a number of geoelectrical interfaces without any significant variation in its character. Finally, we have integrated all data to generate detailed alluvial architecture below both megafans along pre-defined transects.

4. Borehole data analysis for Kosi and Gandak megafans

4.1. Kosi megafan

Data for more than 100 boreholes for the Kosi megafan (Fig. 2) have been analyzed in different transects from upstream to downstream. Although all data was processed to understand the general distribution of lithology, we present here our analysis of a few selected transects from the proximal, medial and distal regions. Two proximal transects, T1, T2, have been characterized by three and seven boreholes respectively. The K1 and K5 boreholes along T1 transect show the presence of >50 m thick gravel layer starting at 7 m below the surface (Fig. 3a). The K4 borehole shows a coarse sand layer in the upper 30 m and gravels start below 30 m from the surface. There are 7 boreholes along the *T2* transect (Fig. 3a) and several of these boreholes show a mixture of coarse sand and pebbles/gravels at shallow depths (5–10 m). The upper few meters of lithology consists of fine sand and mud.

The boreholes along the medial fan transect, T4, provide information down to 10–20 m and only a few boreholes extend to ~50 m (Fig. 3b). The upper ~5 m of sediments along this transect primarily consist of mud and fine sand which is underlain by a mixture of coarse sand and some gravels/pebbles. Most of the boreholes show a fining upward sequence.

Fig. 3c and d shows two transects (T6 and T8) from the distal fan area and there are 10–12 borehole points of variable depth along each of them. Most of the boreholes along transect T6 provide information for the upper ~30 m out of which the top ~15 m consist of a mixture of silty sand and mud except a few (e.g. K85 and K40) which show 10–15 m thick fine to medium sand with a thin muddy cap. A majority of the boreholes show a fining upward succession with coarse sand layer at the bottom starting at variable depths (8–20 m) which seems to continue to deeper levels. Transect T8 has 10 borehole points and several of them go down to ~75 m depth (Fig. 3c). These boreholes show variable lithology and the only common point is the presence of a coarse sand layer at depth as shallow as 10 m (K79) and as deep as ~50 m (K81). The upper 5–10 m of sediments are invariably muddy or fine sand or a mixture of the two that is comparable to the modern sediment load of the Kosi River in this reach.

Apart from transects discussed above, there are several boreholes available from the confluence zone of the Kosi and the Ganga rivers and they provide information for the upper ~100 m of the stratigraphy and almost all logs are clearly divisible into two distinct units (Fig. 3e). The upper 30–40 m of the succession primarily consist of fine sand with a muddy cap. A sharp change in lithology is noted below 30–40 m depth and the lower unit consists of a coarser unit made up of fine gravels and carbonate nodules in a matrix of coarse sand. In some of the boreholes, this lithology continues down to ~100 m depth intervened by find sand layers.

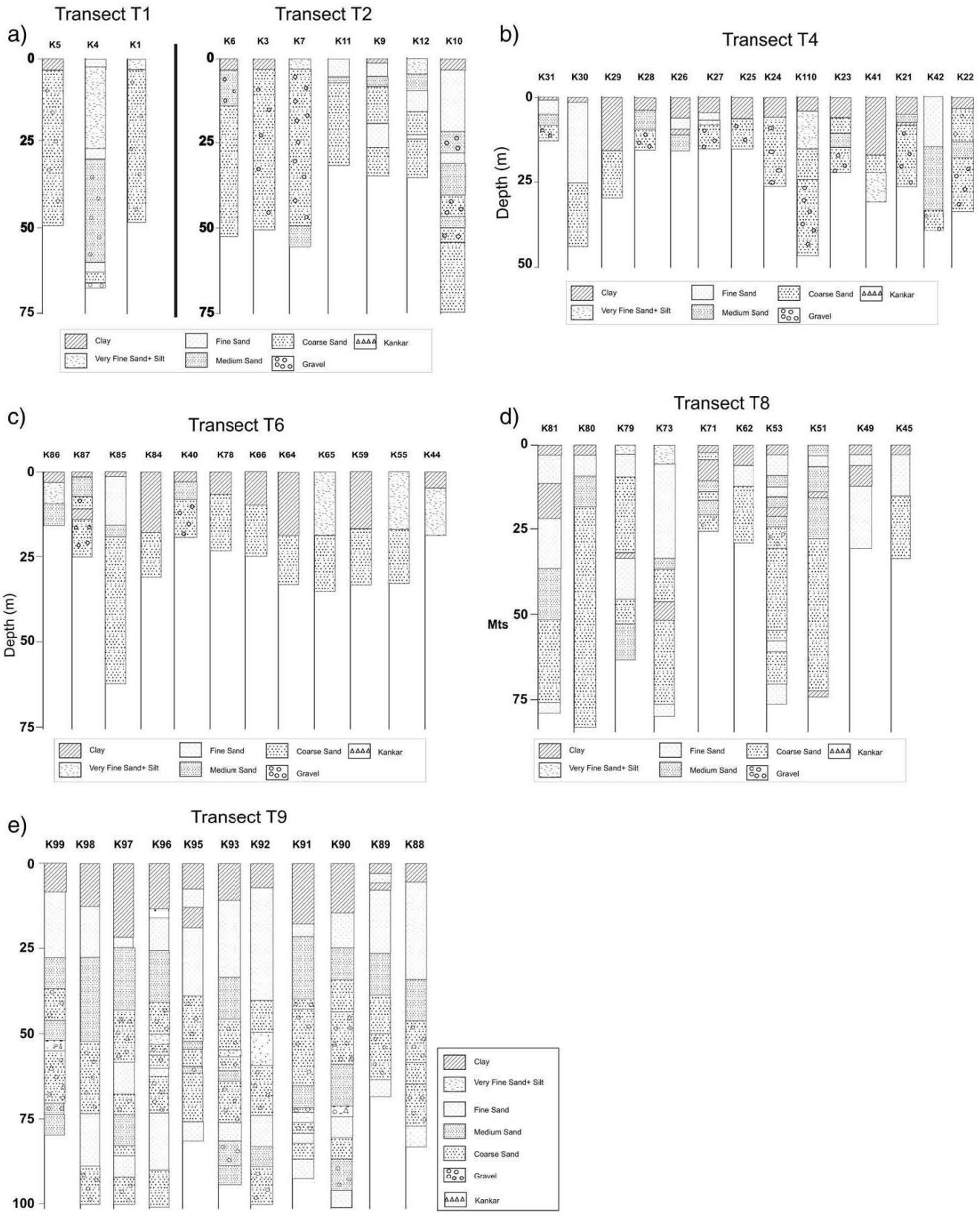

Fig. 3. Groundwater borehole lithologs along selected transects on the Kosi megafan (a) T1 and T2 transects are from the proximal parts and they show the presence of gravels at shallow depths, (b–d) T4, T6 and T8 transects from the medial part of the Kosi megafan where fining upward succession dominates in most of the boreholes starting with coarse sand mixed with gravels and ending with fine sand and mud, (d) T9 transect covering a few boreholes in the confluence zone of the Kosi and the Ganga shows interfingering of coarser and fine sediments possibly reflecting the influence of the southern tributaries of the Ganga (See Fig. 2a for locations).

Borehole data reveal first order stratigraphic variability from the proximal to distal parts of the Kosi megafan and our major interpretations are as follows:

(a) In the proximal transects (Fig. 3a), the presence of gravels at shallow depths (7–30 m) reflects high energy conditions in this region in the past. This is an important finding keeping in view that the gravelly reaches in the Kosi River are currently located upstream of Chatra (~40 km upstream of this transect).
(b) In the medial transect (Fig. 3b), fining upward succession dominates in most of the boreholes starting with coarse sand mixed with gravels and ending with fine sand and mud. These successions suggest several episodes of deposition with a gradual decrease in energy conditions in each. It is also important to note that the present-day sediments of the Kosi River primarily consist of fine sand only and no coarse sand is observed downstream of Chatra. Therefore, sand bodies in the surface represented by these boreholes suggest that the river was able to transport coarser sediments much further downstream in the past.
(c) The boreholes from the distal parts of the fan (Fig. 3c, d) show variable lithology; while some of these are characterized by fining upward succession as in medial parts, several boreboles do not show any definite trend. In distal fan sequences, such variable lithology is generally explained due to distributary channel systems typically of meandering type (Gohain and Prakash, 1990; Singh et al., 1993; Assine, 2005; Gibling, 2006). In such settings, flow becomes poorly channelized and periodic avulsions results in filling by coarser sediments overlain by fine-grained meandering river deposits.
(d) Borehole data from transect T9 in the confluence zone of the Kosi and the Ganga (Fig. 3e) is interpreted to represent interfingering of sediments from two different sources. The upper, finer succession could have formed by the Kosi as most of the boreholes are quite close to its paleochannels. However, the deeper and coarser succession could be related to an older phase of sedimentation related to the southern tributaries of the Ganga. The southern bank of the Ganga in this reach presently flows very close to the cratonic margin due to its southward migration at historical time scale (Phillip et al., 1989). It is likely that older sediments were mainly fed by the smaller cratonic tributaries and were onlapped by the recent sediments brought by the Kosi. Our earlier study in the Yamuna floodplain in the western Ganga plains also recorded a similar event established on the basis of detailed petrographic studies (Sinha et al., 2009). However, more detailed investigations may be necessary to confirm this interpretation in the study area.

4.2. Gandak megafan

Borehole data from only six points are available from the Gandak megafan (Fig. 2). The G1–G4 boreholes are located close to the eastern margin of the present-day fan. The G1 and G2 boreholes show very fine sediments throughout (Fig. 4). The G3 borehole shows coarse sand with gravel below 70 m depth. The G4 borehole shows medium sand, fine sand and mostly finer deposits (clay and silt) down to 200 m. The G5 and G6 boreholes lie close to the medial VES transect and on opposite sides of the Gandak river. The G5 borehole on the eastern side is muddy in the top 50 m underlain by

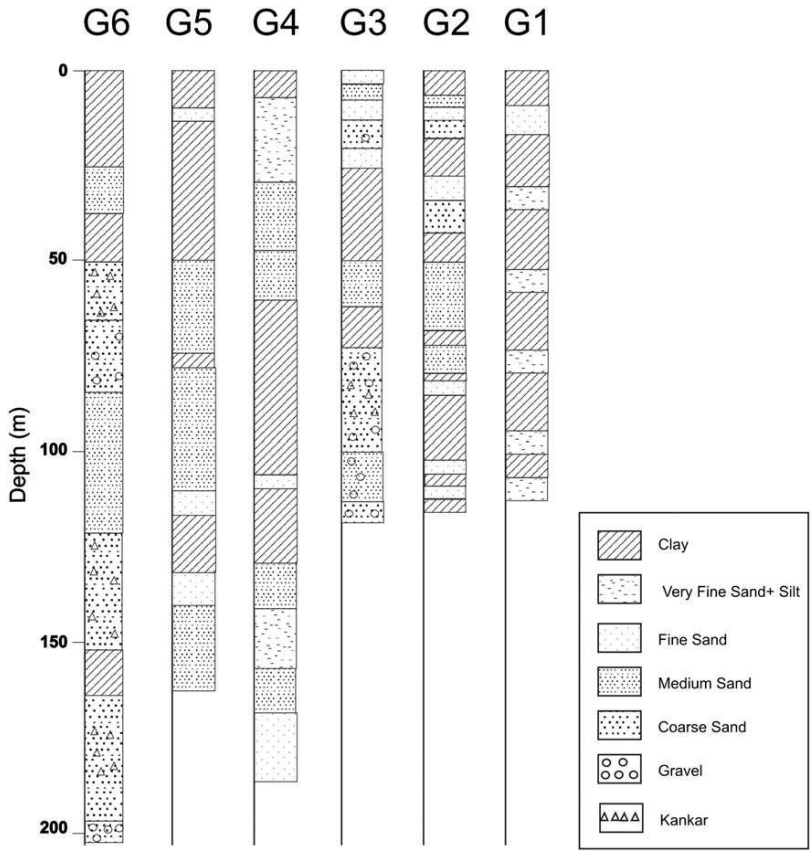

Fig. 4. Groundwater borehole lithologs along selected transects on the Gandak megafan (See Fig. 2b for locations). Only a few boreholes fall within the present boundary of the Gandak megafan and most of them are dominated by fine-grained sediments possibly due to their locations close to the megafan boundary.

several layers of fine to medium sand interleaved by muddy layers. The G6 borehole also shows muddy and fine sand sediments in the top 50 m but is underlain by medium to coarse sand down to ~200 m which contain carbonate nodules and fine gravels between 50 and 83 m and a clay layer between ~150 and 160 m.

In summary, limited borehole data from the Gandak megafan show fine-grained sediments throughout in a few boreholes just outside the fan margin reflecting low energy floodplain environments. Unlike the Kosi megafan, we do not record any gravels at shallow depth in the borehole data from the Gandak. One of the boreholes (G3) records gravel below 70 m depth and this may be associated with a small mountainous stream flowing close to this site.

5. Resistivity data analysis: VES data and layer parameters

5.1. Kosi megafan

The proximal transect (Kus-Kus') has four VES points (Fig. 5). Field curves are not smooth due to large variability in resistivity values. Resistivity data from this transect shows that the upper layers (surface to 25 m depth) have resistivity values between 100 and 300 Ω-m (Fig. 6a) intervened by layers of lower resistivity values (<100 Ω-m). Between 25–30 m and ~50–70 m depth, there is a zone of high resistivity layers (>500 Ω-m) except for an intervening layer of lower resistivity at Kus3. The high resistivity layer is underlain by the layers of moderate resistivity values (<300 Ω-m) in most soundings.

The medial transect (Kds-Kds', Fig. 5) has resistivity values between 100 and 200 Ω-m except for a few layers which have values greater than 1000 Ω-m. Data from the western part of megafan (Kds1–Kds16, Fig. 6b) shows a 20–40 m thick layer of high resistivity (100–500 Ω-m) at depths varying from 25 m to 40 m. This layer is overlain and underlain, at most places, by layers with resistivity values of 10–50 Ω-m and we interpreted this as sharp lithological changes. In the upper 25 m also, there are several thin layers of resistivity 100–300 Ω m. Below 50 m depth, we note large spatial variability in resistivity values; while some profiles show thick (>30 m, base not reached) layers of moderately high resistivity (100–350 Ω-m), others show equally thick layers of lower resistivity (<50 Ω-m) values. Resistivity values of different layers in the eastern part of the Kosi megafan (Kds17–Kds33) generally lie between 100 and 200 Ω-m (Fig. 6c) except for few layers of very high resistivity at different depths e.g. a layer of 4994 Ω-m at Kds19 at ~40 m, 998 Ω-m at Kds24 at ~30 m, and >8000 Ω-m at Kds29 and Kds30 at depths of more than 50 m. Unlike the western part, layers of moderate resistivity (100–500 Ω-m) are exceptionally thick at certain locations (e.g. >90 m thick at Kd23) or occur at multiple depths separated by layers of lower resistivity (<50 Ω-m).

5.2. Gandak megafan

Two transects, each of 10 sounding points, across the Gandak river are located in the proximal and medial parts of the megafan (Fig. 7). The proximal transect on the Gandak megafan is located near Bettiah in West Champaran (Fig. 7). Most of the layers along this transect have resistivity values between 20 and 100 Ω-m (Fig. 8a) except for a few high resistivity (>200 Ω-m) layers at >40 m depth. The western and eastern parts of the megafans have different resistivity values. The sounding points in the western megafan (Gus16–Gus20) have resistivity values ranging from 50 to 100 Ω-m, and there are frequent high resistivity layers at different depths. The eastern megafan

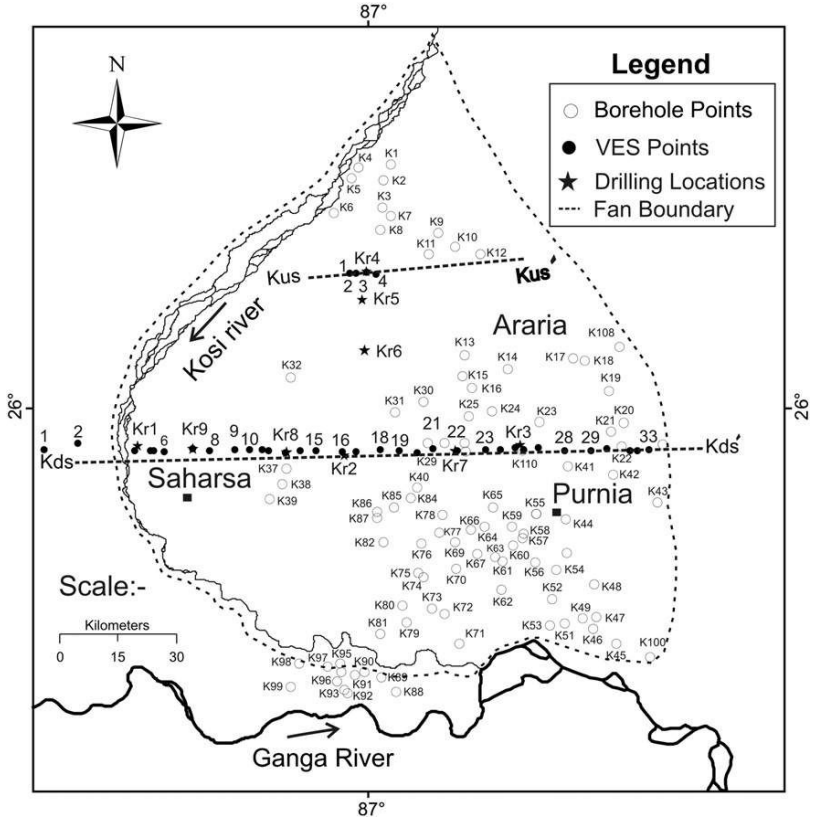

Fig. 5. Location of resistivity sounding points along the proximal and distal transects on the Kosi megafan. A total of 4 soundings were done along the proximal transect whereas 33 soundings were carried out along the medial transect covering the entire stretch of the megafan.

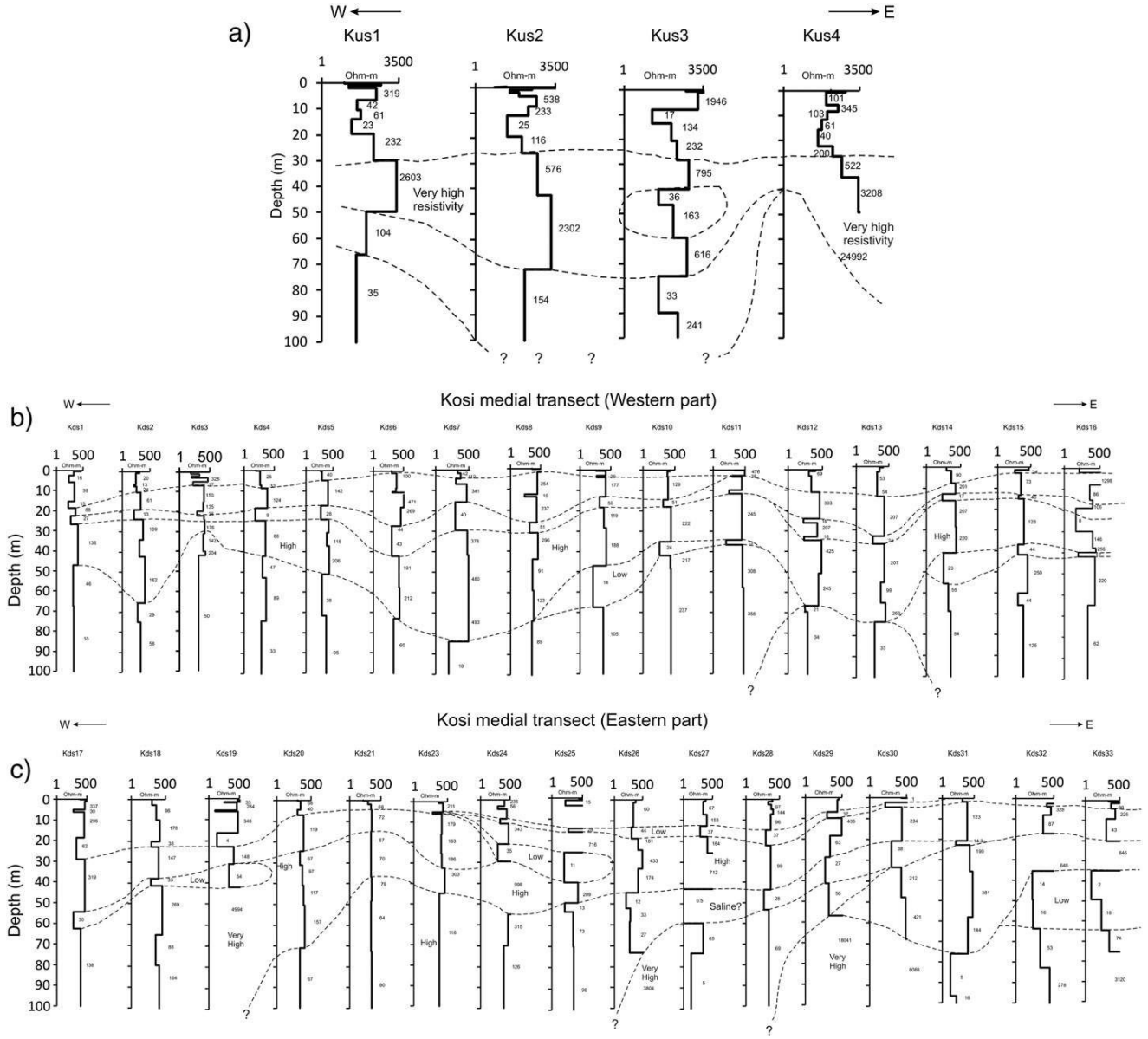

Fig. 6. Resistivity profiles along the (a) proximal and (b, c) medial transects on the Kosi megafan. The proximal transect confirms the presence of gravels at shallow depth as reflected in very high values of resistivity. In the medial transect, the dominance of sandy layers is reflected from the most dominant range of resistivity lying between 100 and 500 Ω-m.

(Gus11–Gus15) has most of the layers showing resistivity values between 20 and 50 Ω-m and once again high resistivity layers at different depths are common.

Data from the medial transect (Fig. 8b) show that most of the layers have resistivity values ranging from 20 to 50 Ω-m. Interestingly, soundings from opposite sides of the river show different resistivity values. Most of the layers from the western part of the megafan (Gds6–Gds10) have two distinct resistivity layers, one with values ranging from 20 to 50 Ω-m and another from 100 to 300 Ω-m (Fig. 8a) except for a few layers with resistivity values in excess of 4000 Ω-m at depths below ~50 m. In contrast, the eastern part of the Gandak megafan (Gds1–Gds5) has most of the layers of resistivity values less than 100 Ω-m (Fig. 8a) intervened by high resistivity layers of 100–300 Ω-m. Two sites, Gds2 and Gds3 show a very high resistivity layer below ~70 m depth.

6. Calibration of resistivity data with boreholes and drill cores

The calibration involves the correlation of layer parameter (layer thickness and its resistivity value) with nearest borehole data and/or drill core data. The VES data of Kosi was calibrated first with the available boreholes, and then with the drill cores to improve the final interpretation. The VES data from the Gandak megafan were calibrated only with drill core data as there were not enough boreholes from this region.

Fig. 9a shows the calibration of the resistivity profile at Kds3 with a drill core at Kr1 (see Fig. 5 for location). The Kr1 is a 44 m deep drill core located in the Saharsa district in the vicinity of the present day Kosi River. This core primarily consists of coarse to medium sand layers interleaved by thin mud layers and sand layers correspond very well with the moderate resistivity layers (150–204 Ω-m) whereas the

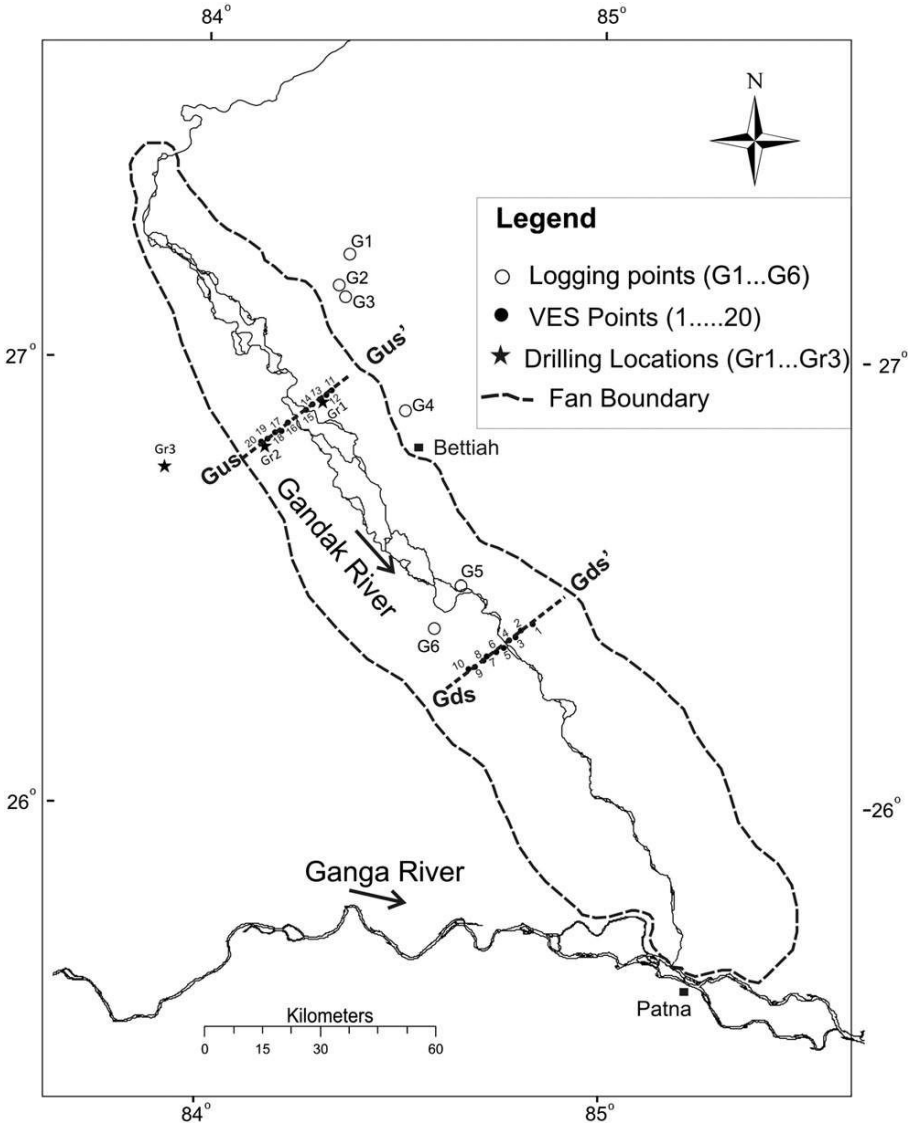

Fig. 7. Location of resistivity sounding points on the Gandak megafan. A total of 10 soundings were carried out for both proximal (Gus11–Gus20) and medial (Gds1–Gds10) transects. Borehole data points (G1–G6) and drill core locations (Gr1–Gr3) are also shown.

muddy layers correspond to low resistivity layers (13–50 Ω-m) (Fig. 9a). At a few sites, some layers show very high resistivity values at depth (>50 m) which has been interpreted as dry sand with kankars as described by Yadav et al. (2010). Similarly, Kds-16, Kds-25, and Kus3 profiles were calibrated with drill cores Kr-3, Kr-3 and Kr-4 (see Fig. 5 for location). Fig. 9b shows the calibration of the Gus-13 resistivity profile with drill core Gr-1. The Gr-1 drill core is dominated by medium sand and most of these layers have resistivity values higher than 100 Ω-m (Fig. 9b). Thin layers of gravel in a sandy matrix were recorded in the core at ~35 m depths and a high resistivity value of 229 Ω-m was measured around this depth. Similarly, Gus20 resistivity profile was calibrated drill core Gr2. Table 1 shows the final calibration results relating the resistivity values with lithology in the Kosi and Gandak megafan region.

Fig. 10 shows that the relative distribution of resistivity classes (interpreted as different lithologies) in the Kosi and Gandak megafans are strikingly different. In the Kosi medial transect, ~50% of resistivity values fall in medium to coarse sand range and only ~5% in the clay range (<20 Ω-m). The proximal transect on the Kosi megafan shows a very different distribution with 28% gravel and <1% clay; medium to coarse sand drops down to ~30% (Fig. 10a). The proximal and medial transects on the Gandak fan also show difference in sediment distribution but there is an overall dominance of silty fraction which decreases slightly from proximal to medial (Fig. 10b). Clay percentage increases downstream and small fractions of kankars are observed in both proximal and medial transects. We also note that the western side is more sandy compared to the eastern side of the fan along both transects.

7. Shallow subsurface alluvial stratigraphy of megafans

Shallow subsurface stratigraphy was reconstructed with the help of resistivity ranges for different lithologies (Table 1) for both the Kosi and Gandak megafans based on the following assumptions and guidelines: (1) the layer has infinite extension, (2) thin, high resistivity layers at surface were ignored for lithological interpretation, and (3) VES data from two consecutive points were correlated when they have similar layer parameters.

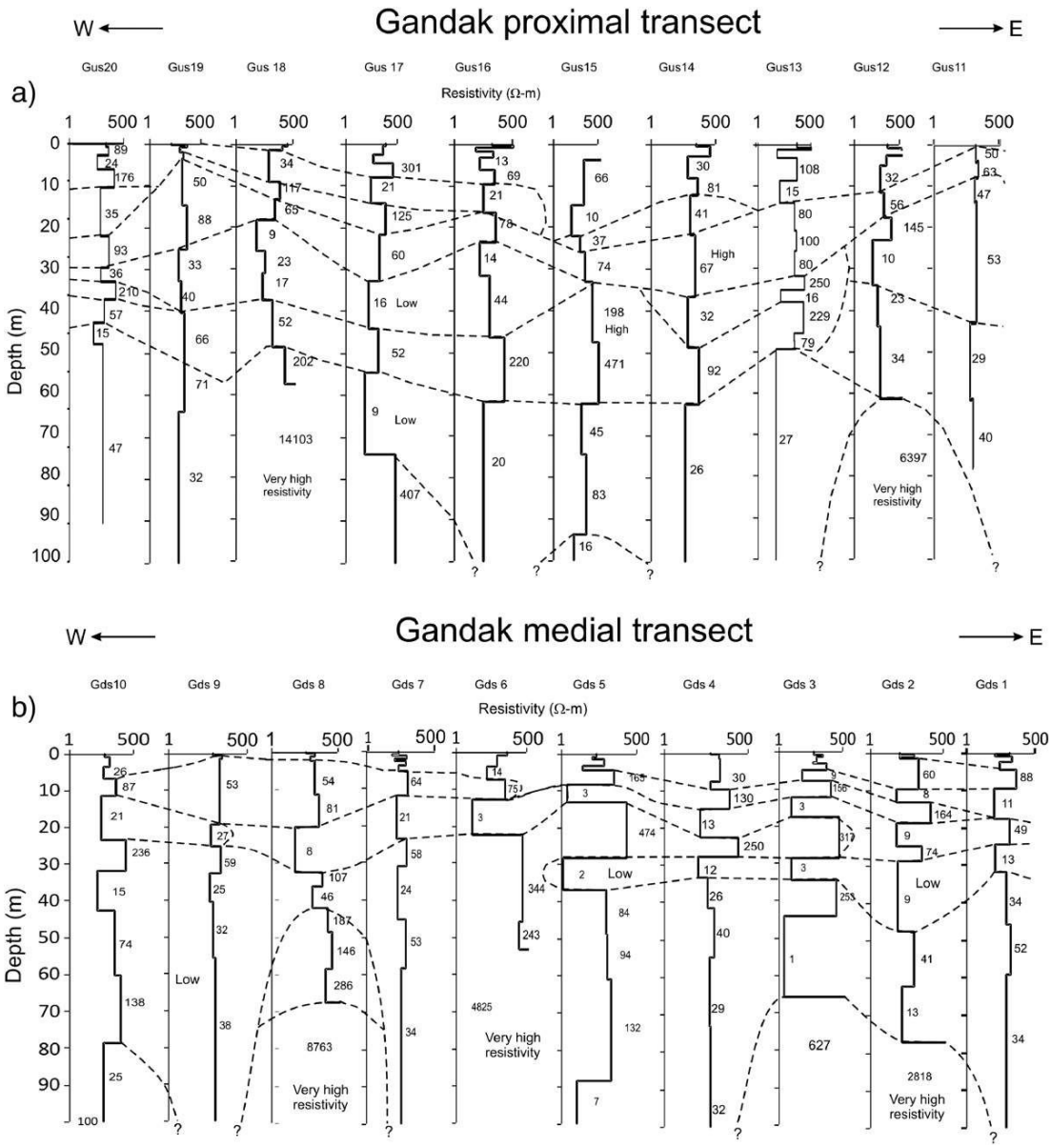

Fig. 8. Resistivity profiles along the (a) proximal and (b) distal transects on the Gandak megafan. Resistivity values along both transects are much lower than those for the Kosi transects suggesting finer sediments below the Gandak megafan.

7.1. Kosi megafan

The subsurface stratigraphy of the proximal transect, ~23 km long, was reconstructed from four resistivity soundings, several boreholes and two shallow drill cores. Panel diagram for this transect shows that the upper 15–20 m of the strata is composed of medium to coarse sand along with thin layers of fine sand and pockets of clay. Below 15–20 m depth, a mix of gravel and coarse sand occurs which continues down to ~30 m. A distinct change is resistivity value around this depth suggests that a gravel-dominated layer occurs below ~30 m depth. Pockets of sand occur within the gravel layer which might represent channel-fill deposits. The resistivity data suggests that the gravel layer is underlain by at least 30 m of medium to coarse sand and pockets of fine sand in the western part of the transect (Fig. 11).

The 140-km long medial fan transect covers almost the entire fan from the western to the eastern margin. The panel diagram presented in Fig. 12 summarizes the alluvial stratigraphy along this transect. The dominant component in the stratigraphy is the sand sheet consisting of medium to coarse sand for most of the upper 100 m of strata penetrated by resistivity soundings. Our drill cores penetrating down to ~40–45 m also confirm the presence of thick sand bodies. We interpret this to be deposits of the Kosi River. The individual sand sheets are 20–30 m thick and the unusual thickness of these sand bodies is due to stacking of multiple sand bodies corresponding to different time periods. Frequent silty layers intervening thick sand bodies both at near surface as well as at deeper levels possibly represent the interchannel areas which were later reoccupied by channels.

7.2. Gandak megafan

We have studied two VES transects across the Gandak megafan in the proximal and medial parts (see Fig. 7 for location of transects).

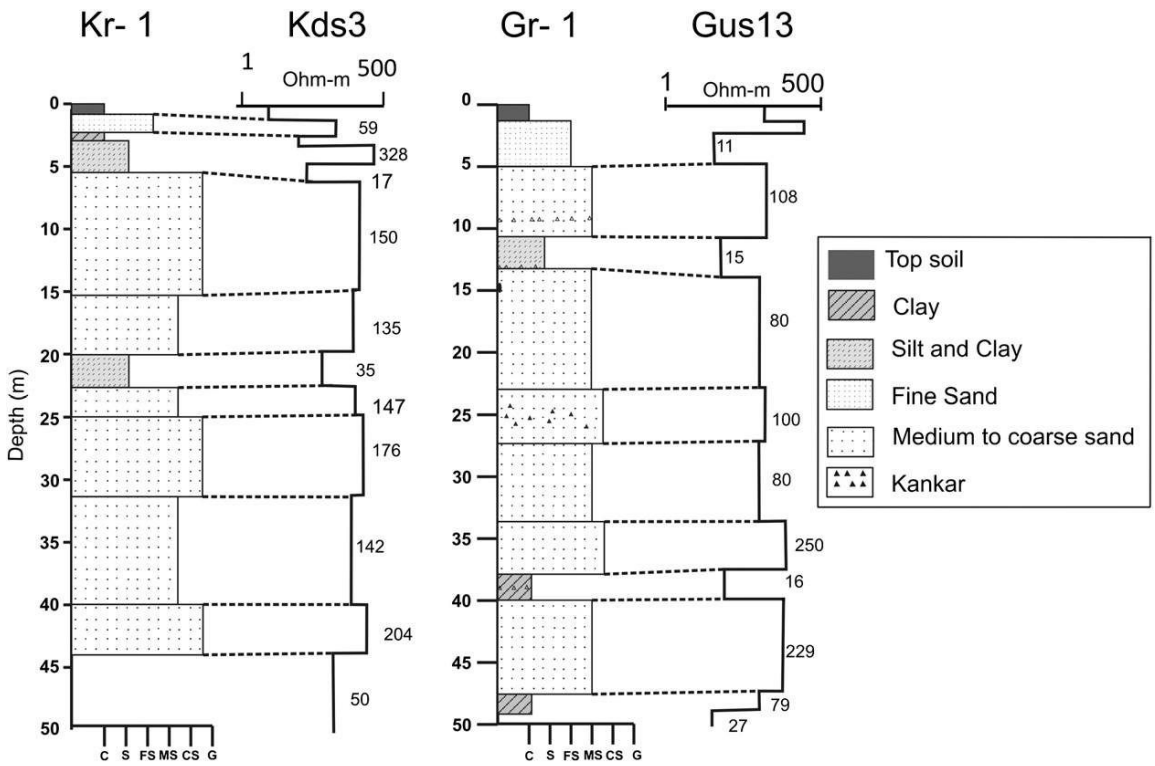

Fig. 9. Calibration of resistivity data with drill core logs (a) Kosi megafan — Kds3 sounding point was calibrated against Kr1 drill core (see Fig. 5 for locations); similar calibrations were done using Kr2, Kr3 and Kr4 drill cores for Kds16, Kds25 and Kus3 sounding points. (b) Gandak megafan — Gus13 sounding point was calibrated against Gr1 drill core and the same process was repeated for Gr2 core and Gus20 (see Fig. 8 for locations). All data was integrated to map the range of resistivity values against lithology as shown in Table 1.

The presence of ~10 to 15 m thick sand is confirmed from drill cores. Resistivity values show finer deposits below 50 m depth and the same is validated from drill cores. Along both transects, the VES data shows significant lateral variability in resistivity values suggesting differences in lithology across the river. Fig. 13 shows the overall alluvial architecture along the proximal transect and unlike the Kosi transect, we record narrow and thick sand bodies instead of sand sheets. The dimensions of these sand bodies are quite variable in the upper (5–20 m thick) and lower (10–30 m thick) parts of the fan succession and these are interpreted as buried channel fills. Thick muddy layers are mapped in the lower part of the succession and interpreted as floodplain deposits. Thin muddy layers in the upper part represent interchannel areas and levees. Drill cores show the presence of kankar (carbonate nodules) at several depths and these layers have high resistivity values in the sounding data. Fig. 14 shows the resistivity-based alluvial architecture for the medial transect. Like the proximal transect, sand bodies in the lower part of the fan succession are relatively thicker (15–25 m). Thick muddy layers and widespread occurrences of carbonate concretions (kankar) are noted in the lower part. The upper part shows significant lateral variation on both sides of the river. While the western part has several smaller (10–20 m thick), laterally stacked sand bodies, mostly fine sand, the eastern part is more muddy and has even smaller sand bodies (5–10 m thick).

Table 1
Range of resistivity values for different lithologies in the Kosi and Gandak megafan region after calibration with drill cores.

Resistivity Range (Ω-m)	Interpreted lithology
<20	Clay
20–50	Silt and clay
50–100	Fine sand
100–500	Medium to coarse sand
500–900	Coarse sand with gravel/Kankar
≥ 2000	Gravel or Kankar rich layer

8. Discussion

8.1. Alluvial architecture of megafan succession

Megafan successions interpreted through resistivity data and borehole records reveal significant variability in alluvial architecture in space and time. The topmost layer (2–4 m thick) in all transects represents the top soil and includes one to three thin layers of variable resistivity — a function of surface moisture and lithology. The Kosi proximal transect shows four distinct litho-units in the upper 100 m (Fig. 11). The lowermost unit 1 of medium to coarse sand (base not reached) is overlain by a gravel-dominated unit 2 (base not reached) and then by ~10 to 20 m thick coarse sand with minor gravels (unit 3). Lithounits 2 and 3 form a major channel fill succession. The uppermost unit consists of medium to coarse sand, ~5 to 10 m thick, immediately below the modern soil. Such marked variation in lithological distribution should reflect a sharp change in energy condition which in turn is a function of sub-environments within the fan system. The presence of gravel at depth in the proximal transect suggests high-energy floods during the monsoon season in the past. We do not have any dates on these cores at this stage and hence it is not possible to constrain the timing of these events. It is important to note here that the modern Kosi river does not carry any gravel downstream of Chatra (~40 km upstream of transect).

Panel diagram along the medial transect on the Kosi megafan shows two major litho-units – lower fan and upper fan – but with significant lateral variability in terms of lithology, depth and thickness of sand bodies. The western edge of the transect falls outside the modern limit of the Kosi megafan; however, we do not record any major change in lithology, except for a thick muddy layer at the surface,

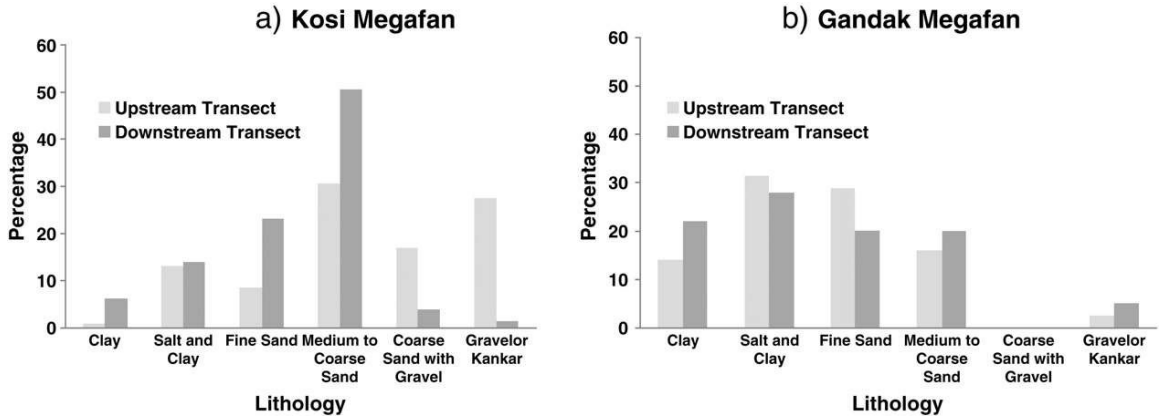

Fig. 10. Histogram distribution of major resistivity classes (interpreted into different lithologies) for (a) Kosi and (b) Gandak megafans. A marked distinction is noted between the Kosi and Gandak megafan in terms of dominant lithology. While the Kosi megafan is dominated by medium to coarse sand and has a marked presence of gravels in the upstream transect, the Gandak megafan is characterized by fine sand and muddy lithologies.

suggesting a continuation of similar deposits westward in the subsurface. The lower unit below 50–70 m depth consists of fine sand (>30 m thick) overlain by ~20 to 30 m thick medium to coarse sand with clay and silt pockets. We interpret this as a major channel fill sequence. The central part of the fan shows a lower unit made up of medium to coarse sand sheet and a number of smaller channel fills consisting of finer sediments. We interpret these as abandoned channel belts that were later filled by flood flows or gradual silting by finer sediments. Some of these fills are 20–30 m thick that might represent stacking of multiple channel fills due to reoccupation of channels. The upper unit, ~40 m thick, is also composed of coarse to medium sand sheet but has much smaller channel fills compared to the lower fan succession (Fig. 12). A major channel fill consisting of fine sand is recorded close to the surface that should correspond to the near-central, prolonged course of the Kosi river in historical time scale (Chakraborty et al., 2010). The eastern part of the megafan has

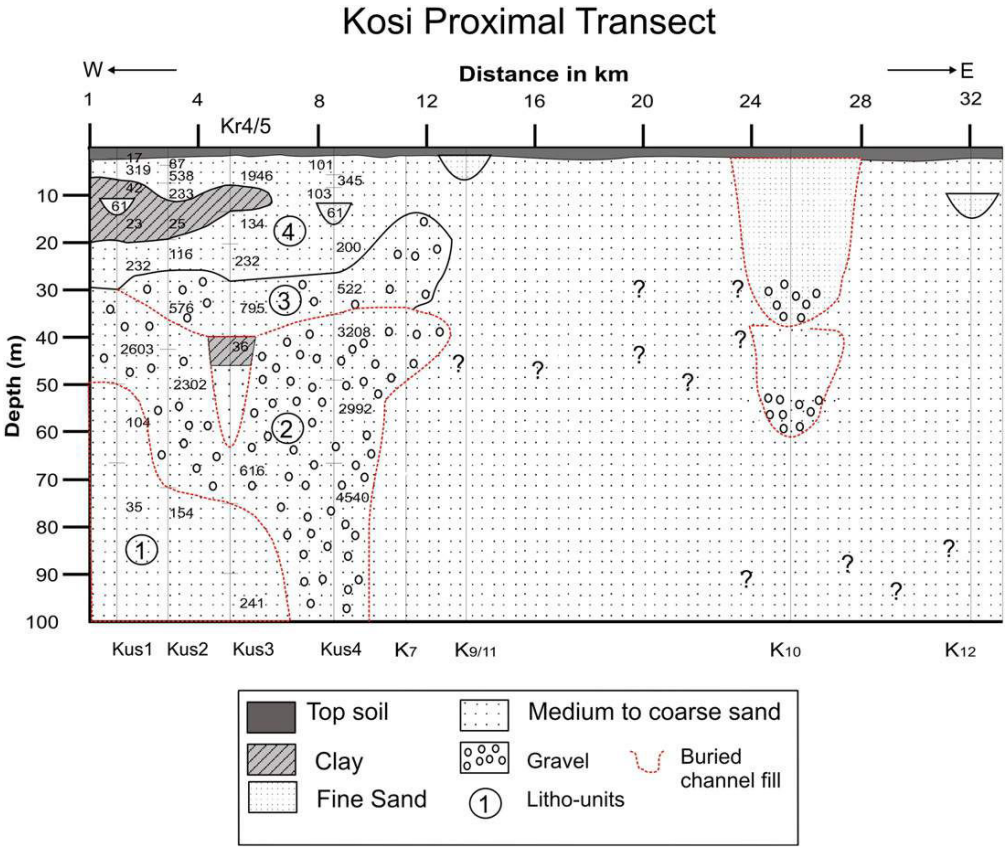

Fig. 11. Alluvial stratigraphy of the proximal part of the Kosi megafan as interpreted from resistivity data, borehole lithologs and drill cores; the most striking feature is the presence of gravels at shallow depths and an overall dominance of medium to coarse sand lithology. There is a data gap for a large part of the section and therefore the interpretations are tentative (shown as ? in the figure).

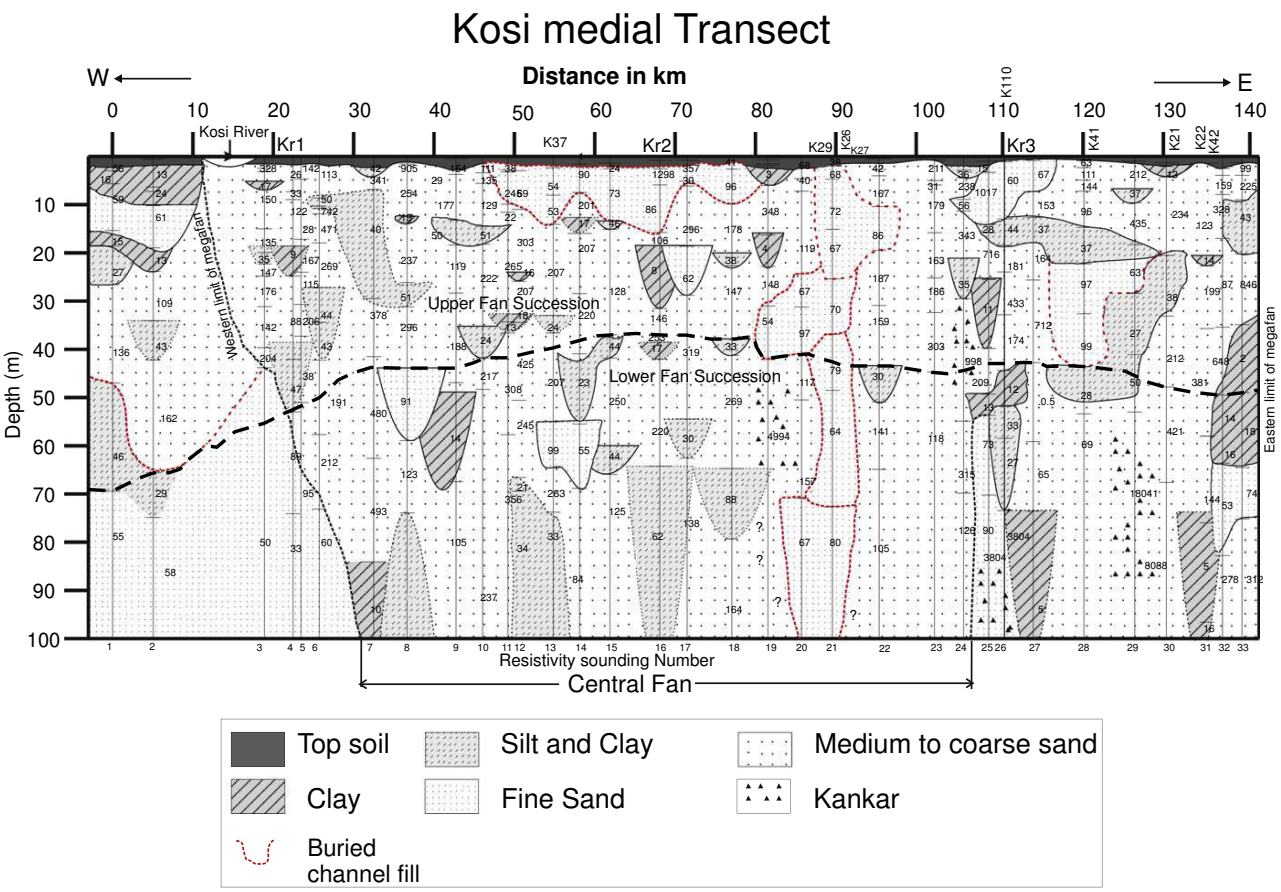

Fig. 12. Alluvial stratigraphy of the medial part of the Kosi megafan as interpreted from resistivity data, borehole lithologs and drill cores. Extensive sand sheets characterize the medial fan succession; upper and lower fan successions (separated by thick black line) are distinguished on the basis of sand body geometry and dimensions which also show significant lateral variability. Both western and eastern limits of the modern megafan surface have also been shown. Major buried channels have been marked in red and uncertainties in the interpretation (?) are also indicated.

medium to coarse sand sheet with intervening clay pockets in the lower part and channel fills of fine sand and thick muddy layers in the upper part.

These large sand bodies primarily represent former channel belts of the river and the unusual width and thickness of these bodies is attributed to lateral as well as vertical stacking of channel deposits resulting in multistoried bodies (Bridge and Mackey, 1993). Typically, such multistoried sand bodies are separated by erosional surfaces as in geological records (Hampson et al., 1999) but it is often difficult to recognize such boundaries in unconsolidated deposits in the absence of a marked lithological contrast. Silt and clay pockets within the sand represent the interchannel areas, channel fills or backswamps (Horton and DeCelles, 2001). The Kosi is primarily a multi-channel system and even though the river is presently confined by the embankments on both sides, it has a ~10 km wide channel belt with wide, muddy interchannel areas some of which have formed large vegetated islands. Outside the channel belt, several paleochannels on the megafan surface primarily transport mud when they flow during the monsoon season. The sub-surface stratigraphy reconstructed in this paper is therefore consistent with the present-day geomorphic set up in this region.

Panel diagram shows that the major sand body is located between Kds7 to Kds24 and, the eastern and western margins of the fan are characterized by relatively finer deposits (Fig. 12). This suggests that the Kosi river has occupied the central part of the fan for a major part of the time represented by the upper ~100 m of the succession. Singh et al. (1993) suggested two different phases of deposition for the Kosi megafan; the upper 8 to 10 m of medium sand associated with historical shifting of river on the megafan and the lower 40 to 80 m of coarse sand with gravel corresponding to the Late Holocene glaciations melting. Chakraborty et al. (2010) have questioned this interpretation and argued that 8 to 10 m of deposition during historical shifting would require a sedimentation rate of ~50 mm/yr which is unrealistic in a fluvial environment. It is difficult to test any of these hypotheses at this stage in the absence of chronology of these sand bodies.

The sub-surface stratigraphy of the Kosi megafan reveals that the multistoried sand bodies are ~8 to 10 km wide and 20–30 m thick. These values are comparable to those of the modern channel of the Kosi which is about 500 to 1000 m wide and the channel belt width varies from 2 to 11 km. Chakraborty et al. (2010) have documented the width of paleochannels on the Kosi megafan to vary from 0.6 to 3.45 km with a mean width of 1.5 km. In the geological record, multistoried sandstones of the Siwaliks in NW Himalaya have been documented to be 300–1000 m wide and 10s of meters thick with lenses of fine grained sediments which represent abandoned channel fills and floodplain deposits (Kumar, 1993; Willis, 1993; Khan et al., 1997; Zaleha, 1997; Jain and Sinha, 2003). Such dimensions of sand bodies are typical of the braided and low-sinuosity rivers as reflected from the compilation of rock record across the globe (Gibling, 2006). It has also been suggested that thick and extensive channel deposits reflect repeated avulsions and lateral amalgamation of sand bodies (Gibling, 2006). The megafan deposits in the ancient record generally comprise of channel deposits, ribbons and narrow sheets (Friend et

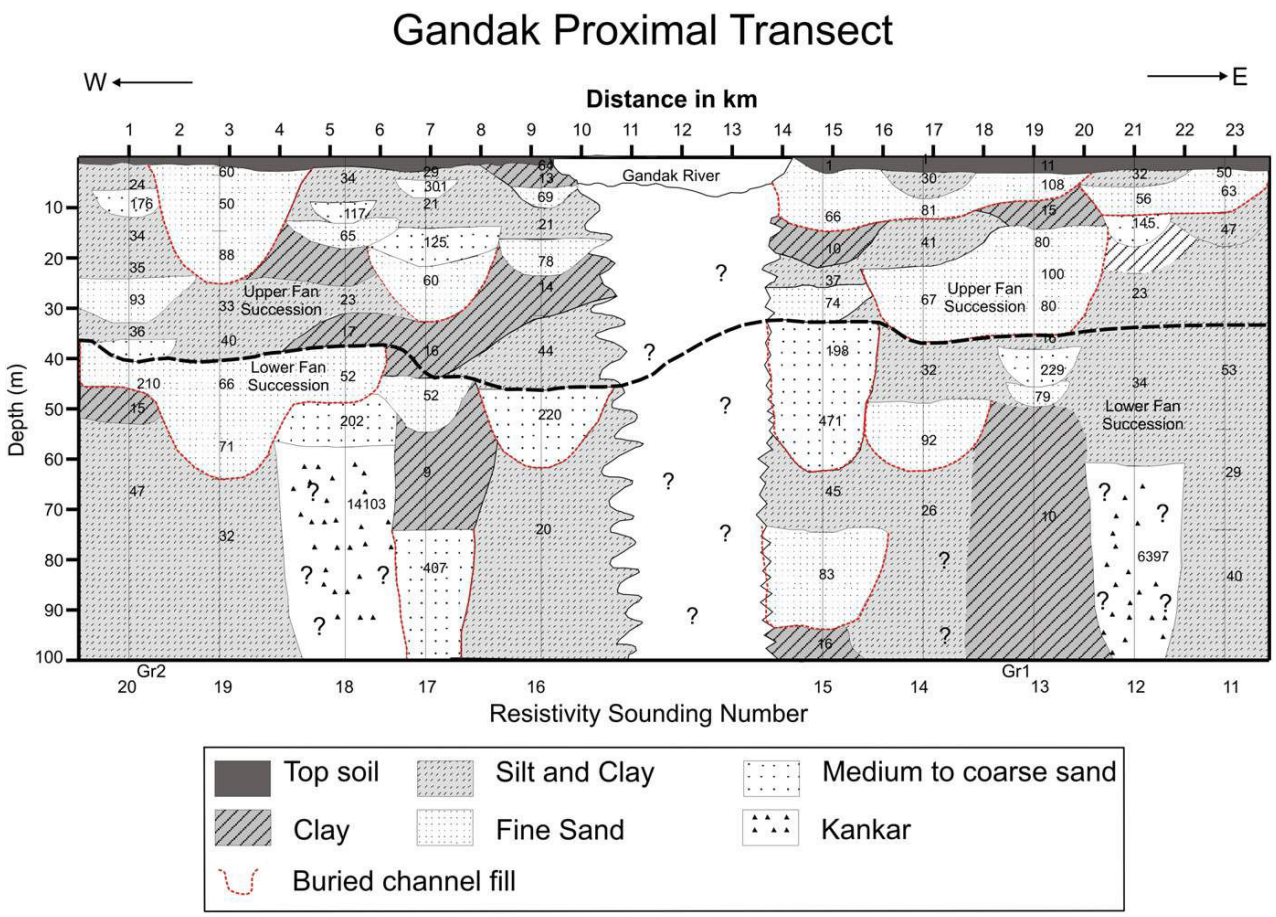

Fig. 13. Alluvial stratigraphy of the proximal part of the Gandak megafan as interpreted from resistivity data, borehole lithologs and drill cores. Unlike the Kosi megafan, narrow sand bodies characterize the Gandak megafan succession. Major buried channels have been marked in red and uncertainties in the interpretation (?) are also indicated. The upper and lower fan succession (separated by thick black line) show some difference in architecture and stacking of sand bodies which is likely to be related to change in avulsion frequency and sedimentation rate.

al., 1979) with only modest evidence of any lateral accretion. Some of these sheets are thicker, typically of braided style and the channel bodies reflect an avulsion and aggradation. The Kosi megafan has often been cited as a modern analog for generating such extensive channel bodies due to rapid lateral sweeping by the Kosi river across the fan over historical time scales (Wells and Dorr, 1987; Friend et al., 2001). Our reconstruction of subsurface stratigraphy of the Kosi megafan has confirmed most of these speculations and has provided the much needed field data.

Alluvial architecture of the upper 100 m of the Gandak megafan shows at least two major litho-units for both proximal and medial transects (Figs. 13, 14). The lower unit (below ~40 to 50 m depth) shows narrow but thick (>40 m) channel fills. The upper unit (above ~40 m) has sand bodies of ~10 to 15 m thickness but several kilometers wide. It is interpreted that the lower and upper units represent two different fluvial processes. The upper unit probably represents frequent migration of the Gandak River on the megafan from west to east (Mohindra et al., 1992) thereby generating laterally stacked sand bodies. This may imply a relatively limited residence time for channels that is in turn related to avulsion frequency and sedimentation rate as demonstrated by recent experiments by Bryant et al. (1995) and Heller and Paola (1996). On the other hand, the lower unit of the Gandak megafan succession represents an incised river system when active channel cutting was followed by rapid vertical accretion. In the ancient record, such 'fixed' river systems are characterized by sand ribbons (Friend et al., 1979; Friend, 1983). Such marked change in the alluvial architecture of the Gandak megafan through time must be related to sharp changes in hydrologic regime and sediment transport characteristics of the Gandak River. It is also important to note that the Gandak megafan is much narrower compared to the Kosi and hence the sediment storage below the Gandak megafan is also smaller. Therefore, a marked variation in sediment flux through time would be sharply reflected in alluvial architecture through adjustments in fluvial style.

Experiments by Bryant et al. (1995) and Heller and Paola (1996) also suggested that an increase in density of stacking pattern of sand bodies depends upon the relative rate of increase in avulsion frequency compared to that of sedimentation rate; however, both increasing and decreasing sedimentation rate can result in a high density of stacking. We do not have sufficient data at this stage in terms of chronology and paleoclimatic reconstruction to constrain the timing and causal factors for such change e.g. increase or decrease in sedimentation rate through time but our ongoing analysis of sediment geochemistry and OSL dating should provide further insights.

8.2. Proximal to distal variability in stratigraphy: implications for sediment flux

The Kosi megafan shows significant variability in alluvial stratigraphy along the proximal and distal transects. Firstly, there is a marked reduction in the overall grain size of sediments from proximal to distal parts of the fan as observed in resistivity data, drill cores and borehole

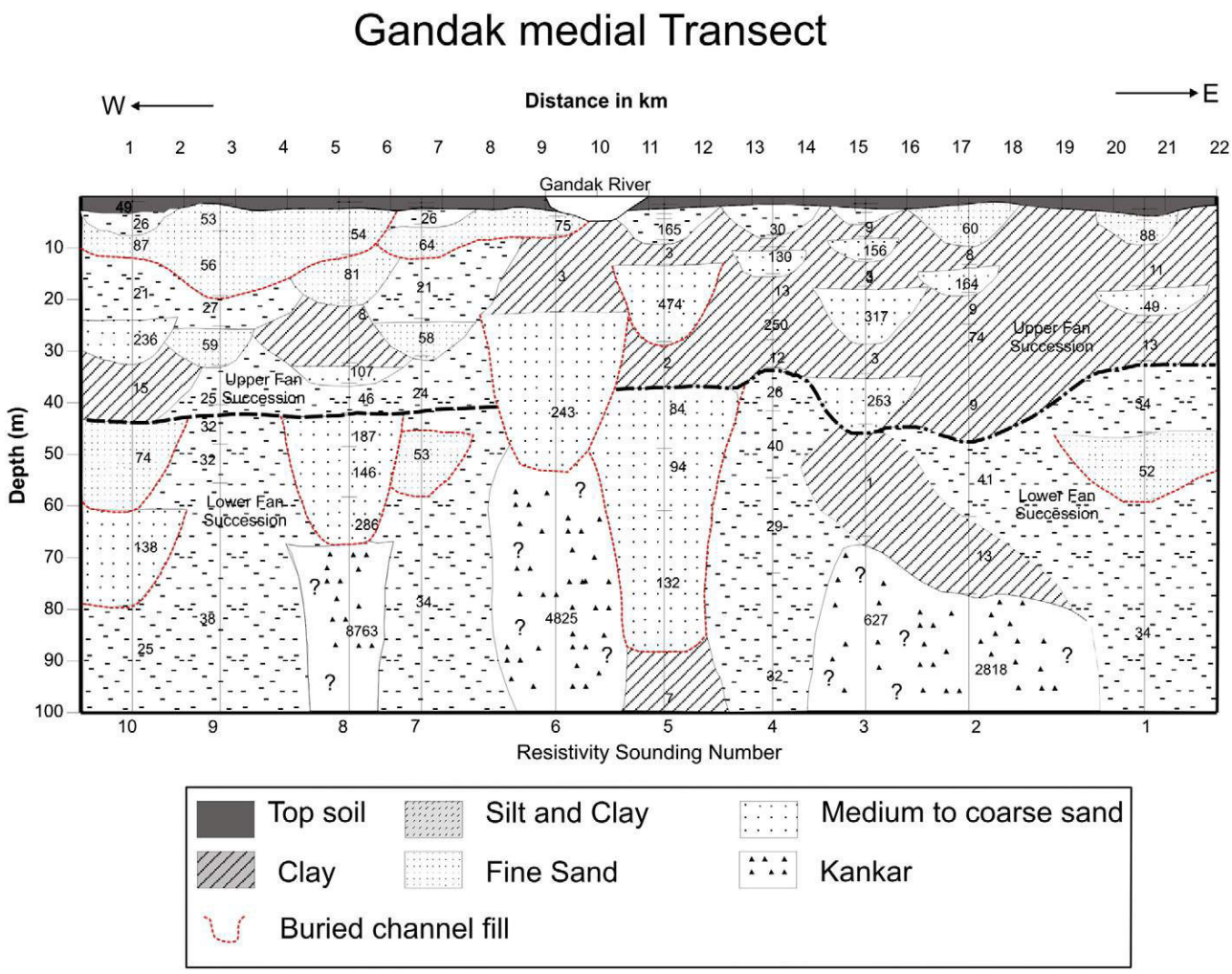

Fig. 14. Alluvial stratigraphy of the, medial part of the Gandak megafan as interpreted from resistivity data, borehole lithologs and drill cores. Major buried channels have been marked in red and uncertainties in the interpretation (?) are also indicated. No major difference is recorded between the proximal and medial transect except for a dominance of muddy sediments in the upper fan succession in the medial transect. Dimensions of the sand bodies and their stacking patterns are comparable in both transects.

logs. The proximal part shows medium to coarse sand layers and gravels, the medial part shows mainly medium to coarse sand and the distal fan is dominantly composed of fine to medium sand and clay. Proximal to distal variability on Kosi fan is very prominent and also has been observed by the previous workers as well (Wells and Dorr, 1987; Singh et al., 1993). The modern Kosi shows distinct downstream change in channel pattern from gravel-braided and sandy-braided to straight and meandering channel as identified by Gohain and Prakash (1990) and Singh et al. (1993). Such sediment grain size reduction is very common on the alluvial fans (Wells and Dorr, 1987; Jain and Sinha, 2003) and is mainly associated with the sediment carrying capacity of the river which decreases from upstream to downstream. However, the present transition from gravel-braided to sandy-braided river occurs 5 km downstream of Chatra, at least 35 km upstream of our proximal resistivity transect (Kus–Kus', Fig. 5). The presence of gravels at shallow depths (<15 m) at this point suggests a much more dynamic regime of the Kosi in the past when the gravel could be transported much downstream. We do not have any chronological data on the cores at this stage, and therefore, we cannot constrain the timing of this change in the hydrologic regime. Although the Gandak fan also shows some reduction in grain size from proximal to medial transects but no gravels are recorded in the subsurface of the Gandak megafan in any of these transects and it appears that the gravel front is much upstream in the case of the Gandak.

Further, thickness of sand bodies decreases and that of the muddy layers increases from proximal to medial transects on the Kosi megafan. The Gandak megafan however does not show a marked variation in thickness of sand bodies from proximal to medial transect. There are high resistivity layers at depth along the medial transect across the Gandak megafan and this is attributed to the presences of kankar (concretions) as in other parts of the Ganga plains (Yadav et al., 2010). Mohindra et al. (1992) have also reported high carbonate content for the Gandak sediments and the borehole data from this region also shows abundant concretions.

An important distinction between the sub-surface stratigraphy of the Kosi and the Gandak megafans is the presence of gravel layers at <15 m depth in the proximal transect of the Kosi whereas the Gandak transect in the proximal part does not show any gravels down to 40 m depth. Although the proximal transects for the Gandak and Kosi are located at different distances from the mountain front, 80–115 km and 50–85 km respectively, this difference is still striking. We suggest that the absence of gravels in the Gandak stratigraphy in the plains may be attributed to the mountain front setting, most importantly the presence or absence of intermontane basin (dun). The Kosi river exits

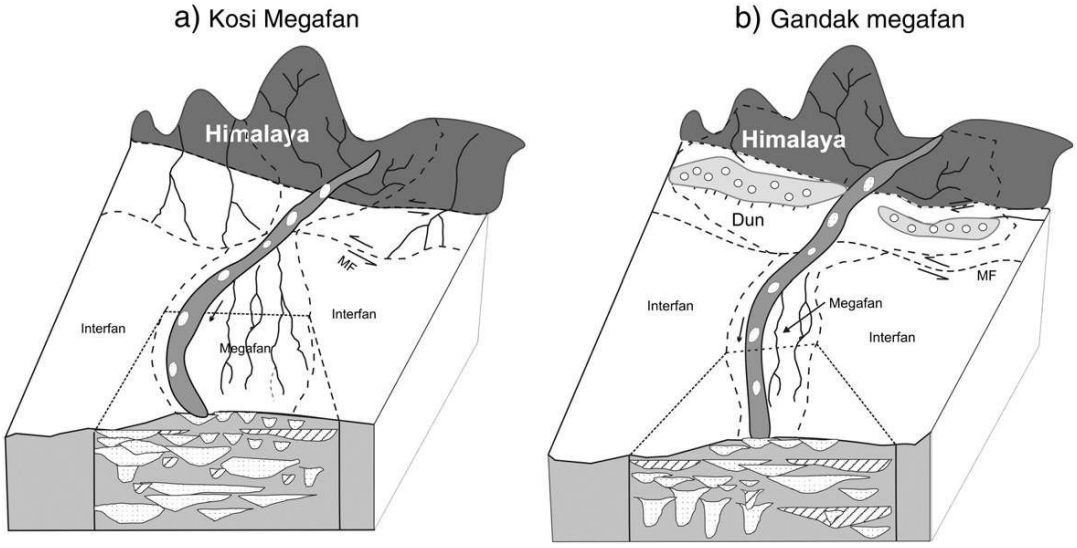

Fig. 15. Conceptual depositional model for spatial variability of alluvial stratigraphy of (a) the Kosi and (b) the Gandak megafans. The Kosi emerges directly from the mountain exit and has therefore carried coarser sediments to much farther parts of the megafan in the past. In contrast, the Gandak has a major intermontane basin ('Dun') before it exits in the plains; the intermontane basin has acted as a 'filter' particularly for the coarse grained sediments. Further, sand body geometries in the sub-surface of the two megafans are strikingly different; while the Kosi shows extensive sand sheets, the Gandak shows narrow ribbons near surface and incised valley fills at depth.

directly from the mountain front (Fig. 15a), and has provided a more efficient conduit for sediments (also due to higher discharge) allowing the coarser fragments to travel into the plains in the past. With gradual reduction in stream capacity of the river due to changes in hydrological regime, the Kosi no longer transports gravels downstream of Chatra as also evidenced in the field. The gravel dominated succession in the proximal part of the megafan is therefore onlapped by sandy sediments. On the other hand, the Gandak has a fairly large intermontane basin in the hinterland (Fig. 15b) which has provided significant storage for the coarse grained sediments originating in the hinterlands. Field observations in the Gandak hinterland in Nepal showed widespread gravel bed streams feeding the dun but very little of them are transported downstream. Due to such 'filtering' of sediments, only finer fraction (sands) were transported downstream, and therefore, the megafan sediments in the plains are devoid of gravels at depth. Apart from generation of distinctive alluvial stratigraphy, filtering of sediments through 'duns' also has implications in terms of documenting stratigraphic response to climate change in the alluvial plains and our ongoing work on sediment cores from both the megafans will provide further insights.

9. Conclusions

Three-dimensional geometry of modern megafans has not received much attention from sedimentologists compared to significant literature available on the geomorphology and process models of megafan evolution. The primary reason for this has been the lack of subsurface data and enough surface exposures to document alluvial architecture. We have documented the subsurface stratigraphy of two well-known megafans from the Himalayan foreland basin, the Kosi and the Gandak, based on an integrated dataset. Our results not only provide the first hand estimates of the dimensions of the sand body geometry below these fans but also demonstrate significant variability in space and time in terms of fluvial style which are in turn related to hydrologic regime and sediment flux from the hinterland. The Kosi megafan is characterized by thick, laterally extensive sand sheet in the medial fan region whereas the proximal part has a prominent gravel layer at shallow depth contrary to the fact that the gravel transport ceases in the modern Kosi at least 40 km upstream. In contrast, the stratigraphy of the Gandak megafan in both proximal and medial transects is characterized by laterally stacked sand sheets in near surface layers — representing migratory behavior and thicker, narrow sand ribbons at depth representing incised channel fills. We suggest that such spatial variability in megafan stratigraphy is a manifestation of mountain front setting (presence or absence of intermontane valleys), sediment flux and variable hydrological regime through time. Our ongoing investigations on the sediment cores from both the megafans would further constrain the chronology and paleohydrological variability which have played a significant role in alluvial stratigraphic development and long-term evolution of these megafans.

Acknowledgments

The authors are thankful to the Ministry of Earth Sciences (MOES) and Indo-French Centre for Promotion of Advanced Research (IFCPAR) for funding this research. We are grateful to Prof. G.S. Yadav at Banaras Hindu University, India for his help in processing the resistivity data. We thank Mrs Shikha Sinha and Ms. Maninee Dash for their valuable help in drawing the figures for this paper. We thankfully acknowledge the help of all local organizations and individuals who helped us in conducting the resistivity surveys.

References

Assine, M.L., 2005. River avulsions on the Taquari megafan, Pantanal wetland, Brazil. Geomorphology 70, 357–371.
Bernal, C., Christophoul, F., Darrozes, J., Soula, J., Baby, P., Burgo, J., 2011. Late Glacial and Holocene avulsions of the Rio Pastaza Megafan (Ecuador–Peru): frequency and controlling factors. International Journal of Earth Sciences 100, 1759–1782.
Bridge, J.S., Mackey, S.D., 1993. A revised alluvial stratigraphy model. In: Marzo, M., Puigdefabregas, C. (Eds.), Alluvial Sedimentation: International Association of Sedimentologists Special Publication, 17, pp. 319–336.
Bryant, M., Falk, P., Paola, C., 1995. Experimental study of avulsion frequency and rate of deposition. Geology 23, 365–368.
Chakraborty, T., Ghosh, P., 2010. The geomorphology and sedimentology of the Tista megafan, Darjeeling Himalaya: implications for megafan building processes. Geomorphology 115, 252–266.
Chakraborty, T., Kar, R., Ghosh, P., Basu, S., 2010. Kosi megafan: Historical records, geomorphology and the recent avulsion of the Kosi River. Quaternary International 227, 143–160.
DeCelles, P.G., Cavazza, W., 1999. A comparison of fluvial megafans in the Cordilleran (Upper Cretaceous) and modern Himalayan foreland basin systems. Geological Society of America Bulletin 111, 1315–1334.

Friend, P.F., 1983. Towards the field classification of alluvial architecture or sequence. In: Collinson, J.D., Lewin, J. (Eds.), Modern and Ancient Fluvial Systems. International Association of Sedimentologists, Special vol. 6, pp. 345–354.
Friend, P.F., Slater, M.J., Williams, R.C., 1979. Vertical and lateral building of river sandstone bodies, Ebro Basin, Spain. Journal of the Geological Society of London 136, 39–46.
Friend, P.F., Raza, S.M., Geehan, G., Sheikh, K.A., 2001. Intermediate-scale architectural features of the fluvial Chinji Formation (Miocene), Siwalik Group, northern Pakistan. Journal of the Geological Society of London 158, 163–177.
Geddes, A., 1960. The alluvial morphology of the Indo-Gangetic plain: its mapping and geographical significance: Institute of British Geographers. Transactions and Papers 28, 253–276.
Gibling, M.R., 2006. Width and thickness of fluvial channel bodies and valley fills in the geological record: a literature compilation and classification. Journal of Sedimentary Research 76, 731–770.
Gohain, K., Prakash, B., 1990. Morphlogy of the Kosi Megafan. In: Rackchoki, A.H., Church, M. (Eds.), Alluvial Fans: A field Approach. John Wiley and Sons Ltd, pp. 151–178.
Gole, V.C., Chitale, V.S., 1966. Inland delta building activity of Kosi River. Journal of Hydraulics Division, ASCE 92, 111–126.
Goudie, A.S. (Ed.), 2004. Encyclopedia of Geomorphology. Routledge Publishers, New York (1156 pp.).
Gupta, S., 1997. Himalayan drainage patterns and the origin of fluvial megafans in the Ganges foreland basin. Geology 25, 11–14.
Hampson, G., Stollhofen, H., Flint, S., 1999. A sequence stratigraphic model for the Lower Coal Measures (Upper Carboniferous) of the Ruhr district, north-west Germany. Sedimentology 46, 1199–1231.
Heller, P.L., Paola, C., 1996. Downstream change sin alluvialo architecture: an exploration of controls on channel stacking patterns. Journal of Sedimentary Research 66, 297–306.
Horton, B.K., DeCelles, P.G., 2001. Modern and ancient fluvial megafans in the foreland basin system of the central Andes, southern Bolivia: Implications for drainage network evolution in fold–thrust belts. Basin Research 13, 43–61.
Jain, V., Sinha, R., 2003. River systems in the Gangetic plains and their comparison with the Siwaliks: a review. Current Science 84 (8), 1025–1033.
Jain, V., Sinha, R., 2004. Fluvial dynamics of and anabranching river system in Himalayan foreland basin, Baghmati River, north Bihar plains, India. Geomorphology 60, 147–170.
Kale, V.S., 2011. Himalayan catastrophe that engulfed North Bihar. Journal of Geological Society of India 72, 713–719.
Khan, I.A., Bridge, J.S., Kappelman, J., Wilson, R., 1997. Evolution of Miocene fluvial environments, eastern Potwar plateau, northern Pakistan. Sedimentology 44, 221–251.
Kumar, R., 1993. Coalescence megafan: multistorey sandstone complex of the late-orogenic (Mio-Pliocene) sub-Himalayan belt, Dehra Dun, India. Sedimentary Geology 85, 327–337.
Latrubesse, E.M., Stevaux, J.C., Sinha, R., 2005. Tropical rivers. Geomorphology 70, 187–206.
Latrubesse, E.M., Cozzuol, M., da Silva-Caminha, Silane A.F., Rigsby, Catherine A., Absy, M.L., Carlos, J., 2010. The Late Miocene paleogeography of the Amazon Basin and the evolution of the Amazon River system. Earth-Science Reviews 99, 99–124.
Leier, A.L., Decelles, P.G., Pelletier, J.D., 2005. Mountains, monsoons, and megafans. Geology 33, 289–292.
Mackey, S.D., Bridge, J.S., 1995. Three-dimensional model of alluvial stratigraphy: theory and application. Journal of Sedimentary Research 65, 7–31.
McCarthy, T.S., Stanistreet, I.G., Cairncroos, B., 1991. The sedimentary dynamics of active fluvial channels on the Okavango fan, Botswana. Sedimentology 38, 471–487.
Mishra, D.K., 2008. Trapped! Between the Devil and Deep Waters. Peoples' Science Institute, SANDRP, New Delhi.
Mohindra, R., Parkash, B., 1994. Geomorphology and neotectonic activity of the Gandak megafan and adjoining areas, middle Gangetic plains. Journal of the Geological Society of India 43, 149–157.
Mohindra, R., Parkash, B., Prasad, J., 1992. Historical geomorphology and pedology of the Gandak megafan, Middle Gangetic plains, India. Earth Surface Processes and Landforms 17, 643–662.
Orellana, E., Mooney, H.M., 1966. Master Tables for Vertical Electrical Soundings over Layered Structures. Interciencia, Madrid.
Phillip, G., Gupta, R.P., Bhattacharya, A.B., 1989. Channel migration studies in the middle Ganga basin, India using remote sensing. International Journal of Remote Sensing 10 (6), 1141–1149.
Rijkswaterstaat, 1969. Standard Graphs for Resistivity Prospecting. European Association of Exploration Geophysicists, The Hague.
Sahu, S., Raju, N.J., Saha, D., 2010. Active tectonics and geomorphology in the Sone-Ganga alluvial tract in mid-Ganga Basin, India. Quaternary International 227, 116–126.
Singh, H., Parkash, B., Gohain, K., 1993. Facies analysis of the Kosi megafan deposits. Sedimentary Geology 85, 87–113.
Sinha, R., 1996. Channel avulsion and floodplain structure in the Gandak-Kosi interfan, north Bihar plains, India. Zeitschrift fur Geomorphologie, Neue Folge, Supplementband 103, 249–268.
Sinha, R., 2009. The great avulsion of Kosi on 18 August 2008. Current Science 97, 429–433.
Sinha, R., Friend, P.F., 1994. River systems and their sediment flux, Indo-Gangetic plains, northern Bihar, India. Sedimentology 41, 825–845.
Sinha, R., Jain, V., 1998. Flood Hazards of North Bihar Rivers, Indo-Gangetic Plains. Memoir Geological Society of India 41, 27–52.
Sinha, R., Jain, V., Prasad, Babu G., Ghosh, S., 2005. Geomorphic characterization and diversity of the fluvial systems of the Gangetic plains. Geomorphology 70, 207–225.
Sinha, R., Bapalu, G.V., Singh, L.K., Rath, B., 2008. Flood risk analysis in the Kosi river basin, north Bihar using multi-parametric approach of Analytical Hierarchy Process (AHP). Indian Journal of Remote Sensing 36, 293–307.
Sinha, R., Gibling, M.R., Kettanah, Y., Tandon, S.K., Bhattacharjee, P.S., Dasgupta, A.S., Ghazanfari, P., 2009. Craton-derived alluvium as a major sediment source in the Himalayan Foreland Basin of India. GSA Bulletin 121, 1596–1610.
Sinha, R., Yadav, G.S., Gupta, S., Singh, Ajit, Lahiri, S.K., 2012. Geo-electric resistivity evidence for subsurface palaeochannel systems adjacent to Harappan sites in northwest India. Quaternary International. http://dx.doi.org/10.1016/j.quaint.2012.08.002.
Sinha, R., Gaurav, K., Chandra, S., Tandon, S.K., 2013. Exploring the channel channel connectivity structure of the August 2008 avulsion belt of the Kosi river: application to flood risk assessment. Geology. http://dx.doi.org/10.1130/G34539.1 (in press).
Stouthamer, E., Berendsen, H.J.A., 2007. Avulsion: the relative roles of autogenic and allogenic processes. Sedimentary Geology 198, 309–325.
Virgo, K.J., Subba, K.J., 1994. Land-use change between 1978 and 1990 in Dhankuta District, Koshi Hills, Eastern Nepal. Mountain Research and Development 14, 2.
Wells, N.A., Dorr, J.A., 1987. Shifting of the Kosi River, Northern India. Geology 15, 204–207.
Willis, B.J., 1993. Ancient river systems in the Himalayan foredeep, Chinji Village area, northern Pakistan. Sedimentary Geology 88, 1–76.
Yadav, G.S., Dasgupta, A.S., Sinha, R., Lal, T., Srivastava, K.M., Singh, S.K., 2010. Shallow sub-surface stratigraphy of interfluves inferred from vertical electric soundings in western Ganga plains, India. Quaternary International 227, 104–115.
Zaleha, M.J., 1997. Siwalik paleosols (Miocene, Northern Pakistan): genesis and controls on their formation. Journal of Sedimentary Research 67 (5), 821–839.

Article : « Enhanced dissolution of basaltic glass in brackish waters : Impact on biogeochemical cycles » Morin et al., 2015.

Earth and Planetary Science Letters 417 (2015) 1–8

Contents lists available at ScienceDirect

Earth and Planetary Science Letters

www.elsevier.com/locate/epsl

Enhanced dissolution of basaltic glass in brackish waters: Impact on biogeochemical cycles

Guillaume P. Morin [a,*], Nathalie Vigier [b], Aurélie Verney-Carron [c]

[a] Centre de Recherche Pétrographique et Géochimique (CRPG), CNRS UMR 7358, Université de Lorraine, 15 rue Notre Dame des Pauvres, F-54500 Vandoeuvre-lès-Nancy, France
[b] Laboratoire d'Océanographie de Villefranche (LOV), CNRS, UPMC, 06230 Villefranche sur Mer, France
[c] Laboratoire Interuniversitaire des Systèmes Atmosphériques, UMR CNRS 7583, UPEC, UPD, IPSL, 61 avenue du Général de Gaulle, 94010 Créteil Cedex, France

ARTICLE INFO

Article history:
Received 30 July 2014
Received in revised form 5 February 2015
Accepted 6 February 2015
Available online xxxx
Editor: J. Lynch-Stieglitz

Keywords:
basaltic glass
salinity
alteration
silicon cycle
estuary

ABSTRACT

In order to better constrain the geochemical budget of Si in the ocean, and potentially other elements released by the dissolution of silicates, the alteration of riverine particulate material in estuaries and seawater needs to be estimated. For this, a series of alteration experiments of basaltic glass were performed at various degrees of salinity (from 0 to 3.5 $g\,L^{-1}$) in far-from-equilibrium conditions. The solution used is a filtered natural seawater standard from the Atlantic Ocean. The forward dissolution rates increase from $2.1 \cdot 10^{-7}$ $mol\,Si\,m^{-2}\,s^{-1}$ ($S = 0\ g\,L^{-1}$) to $7.7 \cdot 10^{-7}$ $mol\,Si\,m^{-2}\,s^{-1}$ ($S = 3.5\ g\,L^{-1}$) at 90 °C and were extrapolated at 16 °C (from $2.9 \cdot 10^{-10}$ $mol\,Si\,m^{-2}\,s^{-1}$ at $S = 0\ g\,L^{-1}$ to $1.1 \cdot 10^{-9}$ $mol\,Si\,m^{-2}\,s^{-1}$ at $S = 3.5\ g\,L^{-1}$). This positive relationship between glass dissolution rate and salinity degree is consistent with published investigations concerning the role of specific cations and ligands present in seawater, which can promote dissolution at the glass surface. These results illustrate the potential of river basaltic glass particles to dissolve quickly in the water column after entering into the brackish waters of estuaries, and before sinking on continental margins. Based on these dissolution rates and on assumptions on the particulate solid flux of fresh basaltic glass exported by rivers towards the ocean, the corresponding flux of dissolved Si is estimated to range between 2 and $8 \cdot 10^{12}$ $mol\,Si\,yr^{-1}$. This is of the same order of magnitude as the estimated river dissolved Si flux, which represents therefore a significant input of Si into the ocean. Additionally, if the glass dissolution process remains congruent during the residence time of suspended particles into the water column, the K flux to the ocean could also be significantly affected.

1. Introduction

The ocean chemistry results mainly from riverine and atmospheric inputs, hydrothermal exchange with oceanic crust, sedimentation processes and biological cycles. However, present-day disequilibrium for a majority of dissolved elements has been highlighted (e.g. Vance et al., 2009 and references therein). This was shown for example for Ca (Gislason et al., 2006), Mg (Holland, 2005; Tipper et al., 2006), Sr (Hodell et al., 1989; Davis et al., 2003; Jones et al., 2014), Os (Oxburgh et al., 2007; Paul et al., 2010), U and Mo (Dunk et al., 2002; Rahaman et al., 2010).

These imbalances in marine geochemical budgets are thought to stem from uncertainties on input fluxes, especially on the riverine particulate material. Several authors (Lacan and Jeandel, 2005; Gislason et al., 2006; Arsouze et al., 2009; Oelkers et al., 2011; Jones et al., 2012a, 2012b, 2014; Pearce et al., 2013) have shown an underestimation of elemental fluxes from continents, due to the dissolution of river suspended material in estuaries and seawater. Jones et al. (2014) recently highlighted a strong impact of riverine particulate dissolution on the Sr ocean budget as they estimated the range of Sr flux derived by volcanic particulate dissolution in an Icelandic estuary to be 1.1 to 7.5 times greater than river dissolved Sr. These results show that changes of conditions (salinity, biological activity), that are indeed drastic when river particulate matter passes from river freshwaters to estuarine waters, trigger a series of rapid reactions difficult to monitor but of a first order importance.

The dissolution of riverine particulate material in estuaries may also impact the concentration and fluxes of major nutrients (Si, P, and N) playing a key role for the primary productivity (Falkowski, 1997; Falkowski et al., 1998; Cloern et al., 2014). In particular, Si

* Corresponding author.
E-mail address: gmorin@crpg.cnrs-nancy.fr (G.P. Morin).

http://dx.doi.org/10.1016/j.epsl.2015.02.005
0012-821X/

as a limiting and major nutrient in marine ecosystems (Nelson et al., 1995; Tréguer et al., 1995; Tréguer and De la Rocha, 2013) and in estuaries where the phytoplankton is principally composed of diatoms (Roubeix et al., 2008). This element can be responsible for environmental catastrophes such as harmful algal blooms (Anderson et al., 2002; Berner and Berner, 2012). Tréguer et al. (1995) estimated that around 80% of dissolved Si in the ocean is delivered by rivers.

The major source of dissolved Si is the weathering of continental rocks (Berner et al., 1983), and especially of basalts (either from volcanic islands or large basaltic provinces) as they are easily weathered (e.g. Louvat and Allègre, 1997, 1998; Gaillardet et al., 1999; Dessert et al., 2001, 2003; Rad et al., 2006; Gislason et al., 2009; Allègre et al., 2010). The alteration kinetics of basaltic glass was determined in various controlled conditions (e.g. Crovisier et al., 1987; 2003; Guy and Schott, 1989; Daux et al., 1997; Techer et al., 2000; Oelkers and Gislason, 2001; Gordon and Brady, 2002; Gislason and Oelkers, 2003; Flaathen et al., 2010; Verney-Carron et al., 2011). However, little is known about the influence of salinity on the dissolution rate of basalts and basaltic glass over short timescales, while this parameter may play a key role in the case of a direct input of volcanic material into the ocean (during an intensive volcanic activity), or when river particles enter estuaries. Previous alteration experiments of basaltic glass have been performed using seawater or NaCl solutions (Gislason and Eugster, 1987; Guy and Schott, 1989; Crovisier et al., 1987, 2003; Gislason and Oelkers, 2003), but the impact of increasing salinity on the forward dissolution rate was not investigated. Some studies explored the role of specific element concentrations: NaCl (Gislason and Eugster, 1987), sulphate (Flaathen et al., 2010), carbonate (Stockmann et al., 2011) on dissolution rate. Increasing NaCl concentrations has been shown to enhance amorphous silica dissolution ($\sim$ 20 times in 0.05 M NaCl compared to deionized water, Icenhower and Dove, 2000). This "salt effect" was also seen for quartz with a dependency to the nature of the cation. The dissolution rate increases in the order: $Mg^{2+} < Ca^{2+} \approx Li^{+} \approx Na^{+} \approx K^{+} \approx Ba^{+}$ (Dove, 1994, 1999; Dove and Nix, 1997). The correlation between the dissolution rate and the exchange rate of the solvent around the aqueous cations suggests that the cations present at the silica–water interface are attracted to the negatively charged surface of silica, thus changing the interfacial environment (Dove and Nix, 1997). Dove (1999) has shown that in presence of only 2 salts the dissolution rate is limited by the cation with the lowest rate-enhancing effect, which highlights a competition between cations at the solid–water interface. These studies allowed the dissolution mechanism to be better understood, but the results are difficult to extrapolate to the natural waters that are complex mixtures of cations. Moreover, there is no study focusing on the effect of several seawater dilutions over very short reaction timescales. The principal difficulty in obtaining these very short timescale rates relies on very low amounts of cations released by leaching in comparison to the ones already present in the initial seawater solutions, as well as the difficulty in analyzing chlorine-rich solutions by conventional methods.

The objective of this study is thus to determine the role of increasing salinity on the dissolution rates of small particles of basaltic glass during very short times of reaction. For this, we performed dissolution experiments of a basaltic glass powder with solutions of various salinities in far-from-equilibrium conditions. We then evaluate the potential of brackish waters present in mixing zones to affect the global input to the ocean of dissolved silicon and other elements.

2. Experimental methods

2.1. Characteristics of the basaltic glass powder

The glass used in the experiments is a synthetic basaltic glass (SBG) (Techer et al., 2000, 2001). It was constituted by melting a mixture of powdered oxides, carbonates, nitrates and phosphates in an alumina crucible for 3 h at 1500 °C in a Saint-Gobain furnace. The melt was poured into a graphite crucible preheated at 700 °C, annealed for 1 h at 670 °C, and quenched by pouring onto a plate at room temperature. The chemical composition of SBG is close to a typical basaltic glass from mid-ocean ridges (MORB), except that it was doped with 1 wt.% Li_2O (Techer et al., 2001). Its chemical composition is (in wt.%) 49.1% SiO_2, 14.8% Al_2O_3, 10.8% Fe_2O_3, 8.2% MgO, 10.7% CaO, 2.7% Na_2O and 1.7% TiO_2.

The glass was ground in an agate mortar and was sieved to isolate the 40–100 µm size fraction. This powder was then washed several times in acetone and the finest particles (<40 µm) were removed according to Stokes' law (settling time used). The absence of remaining finest particles was confirmed by optical microscope observations.

Specific surface area (S_s) was determined using three different methods. First, the geometric specific surface area $S_{geo}(calc)$ was calculated from the radius of particles considered as spheres:

$$S_{geo}(calc) = \frac{n \times S_{grain}}{m} = \frac{n \times 4\pi \times r^2}{n \times 4/3\pi \times r^3 \times \rho} = \frac{3}{r \times \rho} \quad (1)$$

with n the number of particles, S the particle surface, r the particle average radius (here, 70 µm), ρ the density of SBG measured by picnometry ($\rho = 2.7 \pm 0.1$ g cm^{-3}, Verney-Carron et al., 2011). Particle-size measurements were also performed using a Laser–Granulometer (Symantec's HELOS/BF with a classic wet disperser SUCELL at LIEC, Nancy, France). Detailed grain-size distribution spectra (on 5 replicates) for each grain-size class gives a $S_{geo}(opt)$ expressed as:

$$S_{geo}(opt) = \sum_{0}^{1}\left(X_r \times \frac{3}{r \times \rho}\right) \quad (2)$$

with X_r, the optical fraction of a given radius r.

This value was also compared to the specific surface area (S_{BET}) measured by gas (Kr) adsorption according to Brunauer, Emmett and Teller method (BET) (GET, Toulouse, France).

2.2. Experimental conditions

The seawater standard used for the leaching experiments is a filtered natural Atlantic Ocean water provided by OSIL, with a guaranteed salinity of 35.0 ± 0.2%. The solutions SW 1‰, SW 1% and SW 10% used in the experiments were prepared by diluting the seawater standard by a factor 1000, 100 and 10, respectively, with Millipore® deionized water (pure water) (see Table 1 for their initial chemical compositions). One leaching experiment was performed using pure water (PW, Table 2). All diluted solutions were stored in the dark at 4 °C and were heat conditioned at 90 °C in 240 mL Savillex® PTFE reactors a few hours before the onset of the experiments.

Glass leaching experiments were carried out in Savillex® PTFE reactors in static conditions, in an oven at 90 °C to accelerate alteration. Solid/fluid (S/V) ratio were set to low value (S/V < 0.027 cm^{-1}), which are high Water/Rock ratios (W/R) between 6200 and 6400 g/g, and the experiments were run for short durations (<8 days) in order to maintain far-from-equilibrium conditions during the duration of experiments and to simulate a diluted medium. A maximum of 3 solution aliquots were removed from

Table 1
Initial elemental concentrations of solutions used for the leaching experiments.

Solution name	Si (ppm)	Al (ppm)	Mg (ppm)	Ca (ppm)	Na (ppm)	K (ppm)	Li (ppb)
SW 1‰ m[a]	<L.D.[c]	<L.D.	1.30	–	10.79	<L.D.	<L.D.
SW 1‰ c[b]	0.003	0	1.29	0.411	10.8	0.39	0
SW 1% m	0.028	< L.D.	13.07	3.97	104.4	3.86	<L.D.
SW 1% c	0.029	0	12.90	4.11	108	3.92	0.002
SW 10% m	<L.D.	<L.D.	129.83	40.61	968.8	38.46	<L.D.
SW 10% c	0.290	0	129.0	41.1	1080.0	39.2	0.017

[a] m: concentrations measured by ICP-AES at SARM, CRPG Nancy.
[b] c: concentrations calculated from the seawater standard chemical composition and dilution factors.
[c] L.D = Limit of Detection: Si < 0.02 ppm, Al < 0.10 ppm, Mg < 0.03 ppm, Ca < 0.15 ppm, Na < 0.03 ppm, K < 0.05 ppm.

Table 2
Si concentrations measured in the various aliquots sampled along the course of each experiment. Amount of Si released by glass leaching is also given (Si_{corr}), as well as pH of and S/V values. The Si normalized loss of mass (NL(Si)) are calculated following Eq. (3).

Exp. name	S/V (cm^{-1})	Time (day)	PH	Si (ppm)	Si_{cor} $(ppm)_r$	NL(Si) ($g\,m^{-2}$)
PW	0.025	0.04	5.6	0.019	0.019	0.033
	0.025	0.13	5.8	0.026	0.026	0.045
	0.025	0.22	6.1	0.046	0.046	0.080
	0.026	0.30	5.8	0.044	0.044	0.074
	0.026	0.68	6.5	0.119	0.119	0.198
	0.027	1.03	5.5	0.103	0.103	0.167
	0.026	4.02	7.2	1.203	1.203	1.985
	0.025	7.01	8.5	2.165	2.165	3.767
SW 1‰	0.025	0.04	5.4	0.013	0.01	0.018
	0.025	0.13	5.3	0.154	0.151	0.263
	0.025	0.21	5.7	0.041	0.038	0.067
	0.026	0.29	5.3	0.049	0.046	0.077
	0.026	0.68	6.2	0.201	0.198	0.328
	0.027	1.02	5.9	0.335	0.332	0.535
	0.026	4.02	8.7	2.010	2.007	4.620
	0.024	7.01	8.7	2.401	2.398	7.357
SW 1%	0.025	0.0	6.22	<L.D.	–	–
	0.025	0.1	6.5	0.021	–	–
	0.025	0.21	6.1	0.063	0.034	0.059
	0.026	0.29	6.7	0.093	0.064	0.106
	0.026	0.69	7.1	0.408	0.379	0.623
	0.027	1.02	7.7	0.625	0.596	0.955
	0.027	4.02	8.8	2.787	2.758	4.534
	0.025	7.00	8.0	4.225	4.196	7.316
SW 10%	0.025	0.04	7.3	<L.D.	–	–
	0.025	0.13	6.7	<L.D.	–	–
	0.026	0.21	6.9	0.126	–	–
	0.027	0.29	6.7	0.236	–	–
	0.025	0.69	7.7	1.334	1.044	1.821
	0.025	1.01	7.8	1.452	1.162	2.031
	0.026	4.00	7.7	4.762	4.472	7.380
	0.025	7.01	7.5	5.239	4.949	8.652

a single batch reactor, such that the sampling never decreased the fluid volume by more than 10%.

Prior to each sampling, the reactor was agitated and temperature was immediately measured. Reactors were open for only a few minutes in order to avoid cooling and evaporation. The pH measurement was done on a specific small aliquot (1.5 mL) after cooling to room temperature (25 °C). Samples aliquots were filtered at 0.45 µm and acidified with concentrated HNO_3 to obtain 0.3 N HNO_3 for ICP-AES measurements.

2.3. Chemical analyses

Si, Ca, Na and Al concentrations were measured in most solutions by ICP-AES (ICAP 6500) at the national facilities SARM (CRPG, Nancy, France). Very diluted leachates obtained during experiments with PW (pure water) and SW 1‰ during the first 24 h of reaction were analyzed using a Spectro ARCOS ICP-AES (at LISA, France) installed in a clean and regulated room (ISO5) and equipped with an autosampler placed under a laminar flow hood (ISO1). Detection limit for Si is lower than 20 ppb and 2σ uncertainties are 10%. These parameters are reported in Table 2 for others elements.

3. Results

3.1. Si release to solution

The amount of Si released by the glass over time was calculated by correcting the measured concentrations from the Si content of the initial solution used for the alteration experiment (see Table 1). Thus, released Si varies between 0.4 days and 7 days from 0.02 to 2.15 $mg\,L^{-1}$ in pure water (PW), from 0.01 to 2.40 $mg\,L^{-1}$ in SW 1‰, from 0.06 to 4.22 $mg\,L^{-1}$ in SW 1% and from 0.13 to 4.76 $mg\,L^{-1}$ (after 4 days) and 4.95 $mg\,L^{-1}$ (after 7 days) for SW 10%. For all other major elements (typically Mg, Na, Ca, K), the amount released is too small compared to the amount already present in the initial solutions, making it difficult to precisely quantify.

3.2. Normalized mass loss

In order to compare the different experiments, Si concentrations was normalized to the fraction of Si in the initial glass (x_{Si}) and to the S/V ratio to calculate the Normalized Loss of mass NL(Si) (expressed in $g\,m^{-2}$):

$$\mathrm{NL(Si)} = \frac{C_{Si} \times V}{S \times x_{Si}} \tag{3}$$

where C_{Si} is the concentration of Si in solution in $g\,L^{-1}$ and x_{Si} is equal to 0.294 $g\,g^{-1}$ for SBG.

In Eq. (3), the surface area is required and was measured by using the 3 methods described in Section 2.1. The calculation of the geometric specific surface area ($S_{geo}(calc)$) from the sieved size fraction and from the grain-size measurements by Laser diffraction sensor gives a geometric surface area of 0.016 $m^2\,g^{-1}$. The BET surface area was estimated to be 0.015 ± 0.002 $m^2\,g^{-1}$. The associated large uncertainty is explained by the low amount of SBG powder available for this measurement (0.5 g). The agreement between the three techniques used in this study is noteworthy, and strongly supports the value estimated for the surface area of the glass powder used in the calculations.

All the leaching experiments exhibit a linear evolution of Si concentrations and NL(Si) as a function of time (Table 2 and Fig. 1). This strongly supports far-from-equilibrium conditions and indicate that the alteration experiments never approached equilibrium. These conditions are the consequence of low level of glass dissolution rates, low S/V ratios and of the lack of formation of secondary minerals. Only the 7th day of the experiment performed in 10% SW clearly shows a stabilization of Si concentration in solution. Si concentrations range between 10 ppb and 5 ppm and are always lower than the solubility of quartz ([Si] = 24 ppm at 90 °C) and of amorphous silica ([Si] = 155 ppm at 90 °C) (Gunnarsson and Arnórsson, 2000).

3.3. Dissolution rates of the basaltic glass

The complete dissolution of glass is considered to be obtained by the breaking of Si–O bonds (Oelkers, 2001). Hence, the release of Si into solution through time reflects the global dissolution rate of the glass. At the first stage of alteration, the silicate network is rapidly broken and the glass network elements (Si, Al) are released into solution following a linear relationship

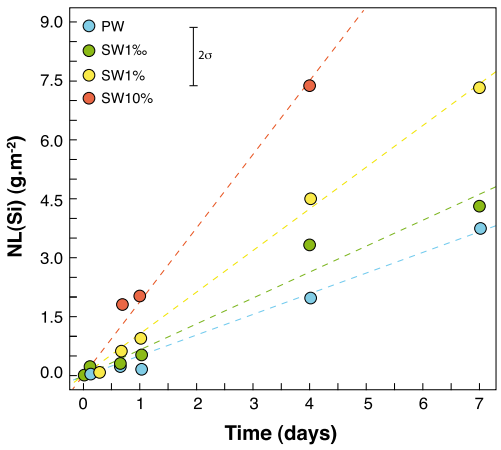

Fig. 1. Evolution of NL(Si) as a function of time for each set of experiment. PW = pure water, 1‰ SW = dilution of 1‰ of natural seawater, 1% SW = dilution of 1% of natural seawater, 10% SW = dilution of 10% of natural seawater. Regressions show systematic linear evolutions with coefficients $r^2 > 0.97$.

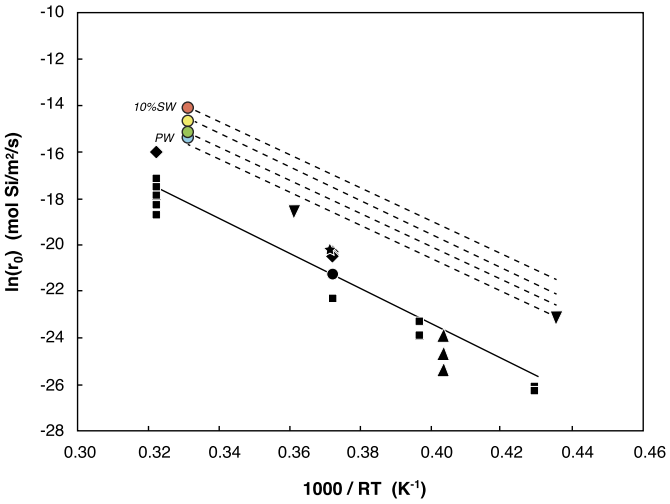

Fig. 2. Forward dissolution rates calculated for each set of experiment (colored circles, same symbols as Fig. 1), expressed as $\ln(r_0)$, calculated by using Eq. (4) and regressions shown in Fig. 1, as a function of $1000/RT$ (T in Kelvin). Published values from literature are also shown for comparison (black symbols). Data correspond to experimental alteration of basaltic glass, either as a powder or as a cube, for temperatures of less than 100 °C and at pH between 6.5 and 8.5 (at the temperature of the experiment). References are: diamonds for Guy and Schott (1989) (0.05 M NaCl); squares: Gislason and Oelkers (2003) (S_{BET} values, 0.01 M NH_4Cl); triangles: Oelkers and Gislason (2001); stars: Flaathen et al. (2010); inverse triangles: Crovisier et al. (1987) (artificial seawater, S/V = 0.08 cm^{-1}); circles: Verney-Carron et al. (2011). Even if all these data cannot be directly compared due to differences in experimental conditions (S/V, pH, solution or glass composition, …), it is interesting to note that the best slope of all considered data (black line) is close to the one used for extrapolating our experimental results to lower temperatures (dashed line) ($E_a = 72$ kJ mol^{-1}). (For interpretation of the references to color in this figure legend, the reader is referred to the web version of this article.)

as a function of time. This dissolution rate is constant and called "initial" or "forward" rate. In the case of far-from-equilibrium condition, there is no retroaction of the solution evolution on the rate. Over longer timescales, the dissolution rate drops as the solution chemical composition approaches equilibrium, due to a decrease of the chemical affinity between the solution and the glass (Aagard and Helgeson, 1982; Grambow, 1985; Berger et al., 1994; Daux et al., 1997; Frugier et al., 2009; Verney-Carron et al., 2010), and to the concomitant formation of a gel layer at the glass surface (e.g. Frugier et al., 2008). This phenomenon is accompanied by secondary phase formation and the dissolution becomes incongruent.

In this study, the linear relationship of Si as a function of time allows a forward dissolution rate (r_0) to be deduced for each series of experiments:

$$r_0 = \frac{d\mathrm{NL(Si)}}{dt} \tag{4}$$

The values for r_0 are calculated by linear regression of NL(Si) with an intercept forced to 0. For PW (pure water), SW 1‰, SW 1%, experiments, regressions are calculated between 0 and 7 days. For the SW 10% experiment, it was calculated between 0 and 4 days because after 4 days, NL(Si) is not linear any more.

The corresponding dissolution rates calculated based on the leaching experiments performed at 90 °C are found to be: 0.52 ± 0.02 g m^{-2} d^{-1} in pure water (PW), 0.66 ± 0.04 g m^{-2} d^{-1} in SW 1‰, 1.06 ± 0.02 g m^{-2} d^{-1} in SW 1% and 1.88 ± 0.09 g m^{-2} d^{-1} in SW 10% (see Table 3). This corresponds to a flux of Si from $2.1 \cdot 10^{-7}$ mol Si m^{-2} s^{-1} to $7.7 \cdot 10^{-7}$ mol Si m^{-2} s^{-1}. The forward dissolution rates are in agreement with published estimations of basaltic glass dissolution rates performed in pure water, in alkaline solutions (NaOH + NaCl) and in seawater at high temperature. Indeed, published values vary between $1.1 \cdot 10^{-8}$ and $3.5 \cdot 10^{-7}$ mol Si m^{-2} s^{-1} at 90–100 °C and pH 7 to 8.6 (given at the experimental temperature) (Guy and Schott, 1989; Daux et al., 1997; Techer et al., 2001; Gislason and Oelkers, 2003; Verney-Carron et al., 2011). The wide range of data highlighted in Fig. 2 is likely to be due to the variety of experimental conditions used (surface area, pH, ionic strength, solution composition, etc.), making difficult a direct comparison difficult.

4. Discussion

4.1. Strong effect of increasing salinity on glass dissolution rates

Results show that the forward dissolution rate increases with the degree of salinity (Fig. 3). A salinity of 3.5 g L^{-1} (SW 10%) increases the glass dissolution rate by a factor of 3.5. The relationship with salinity is visibly not linear, and even a very dilute solution, with a salinity of 0.35 g L^{-1} (SW 1%) increases the dissolution rate by a factor of 2 compared to pure water.

Several lines of evidence show that this positive correlation with the salinity degree is not an indirect effect of pH (see Table 2). First, all experimental solutions display a roughly similar increase of pH that reach values close to 8 after 7 days. At the onset of the experiment, the solution pH of pure water and of SW 1‰ solution (pH ∼ 5.5) are lower than the pH of SW 1% and SW 10% solutions (pH ∼ 6.5). However, this should not induce a significant difference in the alteration rates. Indeed, Guy and Schott (1989) showed that dissolution rates are constant between pH 4

Table 3
Calculated specific forward dissolution rates reported for both the mass of glass (r_0) and for Si (r_0(Si)), at 90 °C and at 16 °C.

Forward rate/Exp.	PW	SW 1‰	SW 1%	SW 10%
r_0 [g m^{-2} d^{-1}] – 90 °C	0.52	0.66	1.06	1.88
r_0 [g m^{-2} d^{-1}][a] – 16 °C	$7.14 \cdot 10^{-4}$	$9.06 \cdot 10^{-4}$	$1.46 \cdot 10^{-3}$	$2.58 \cdot 10^{-3}$
r_0(Si) [mol Si m^{-2} s^{-1}] – 90 °C	$2.14 \cdot 10^{-7}$	$2.72 \cdot 10^{-7}$	$4.37 \cdot 10^{-7}$	$7.73 \cdot 10^{-7}$
r_0(Si) [mol Si m^{-2} s^{-1}][a] – 16 °C	$2.94 \cdot 10^{-10}$	$3.73 \cdot 10^{-10}$	$6.01 \cdot 10^{-10}$	$1.06 \cdot 10^{-9}$

[a] Calculated using Eq. (5) and $E_a = 72$ kJ mol^{-1} (see text for more details).

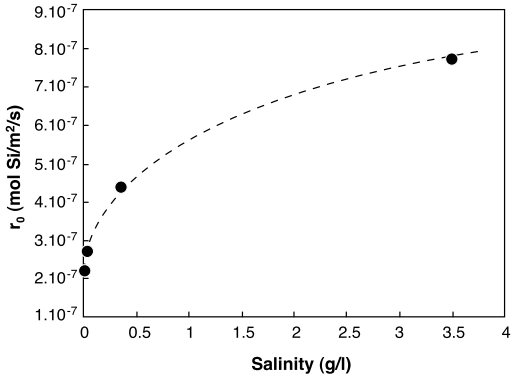

Fig. 3. Glass dissolution rate (r_0) as a function of salinity degree (in $g\,L^{-1}$).

and 8 at 50 °C and between pH 4 and 6 at 100 °C. In addition, except for the experiment with pure water (PW), the increase in pH is non-linear, as pH stabilizes at day 1, 4 or 7, depending on the experiment. These differences in the pH evolution are not reflected in the Si release rate since NL(Si) display a linear increase as a function of time for all experiments (Fig. 1). This strongly suggests that, under these conditions, the slightly different initial pH between experiments have only a minor influence on the Si release degree.

The effect of salinity is caused by the presence of cations in solution. Alkali and alkaline-earth elements at low concentrations in solution increase the dissolution rate of quartz and amorphous silica by factor up to 100 for concentrations around 0.01 or 0.05 M compared to deionized water (Dove and Crerar, 1990; Dove and Nix, 1997; Dove, 1999; Icenhower and Dove, 2000). However, these experiments are performed in single-cation bearing solutions. Dove (1999) shows that addition of Mg in sodium, calcium, barium chloride salts reduces this "salt effect". In diluted seawater, this competitive effect of cations at the basaltic glass–solution interface can explain that the salinity increases significantly but moderately the dissolution rate. The presence of ligands (OH^-, Cl^-, SO_4^{2-}) and the formation of surface complexes could also promote surface dissolution by weakening interatomic bonds in the vicinity of the central metal and by facilitating the detachment of these metals into solution.

4.2. Implications for natural systems

River particles are subject to number of effects upon their arrival in the mixing zones of estuaries (Dagg et al., 2004). Since the ionic strength of seawater is higher than riverine freshwaters, charged surfaces of particles tend to aggregate very rapidly (Sharp et al., 1983; Stumm, 1990), and the resultant is an acceleration of sedimentation velocity (Gibbs, 1986). Because river particles are mainly composed of silicates that are in disequilibrium with ocean waters, they will react at different time-scale depending on their specific reaction kinetics. In the following, we propose an approach to extrapolate our experimental results in order to estimate if the accelerate dissolution of river suspended particles of basaltic glass can represent a significant or a negligible flux for dissolved Si and other soluble elements.

4.2.1. Extrapolation to lower temperatures

While the impact of temperature on alteration rates is difficult to evaluate on the field (White and Blum, 1995; see Millot et al., 2002 for a review), dissolution rate constants in the laboratory is temperature dependent and characterized by Arrhenius' law:

$$\ln(r_0) = \ln(A) - \frac{E_a}{R \times T} \quad (5)$$

where A is the pre-exponential factor, E_a the apparent activation energy in $J\,mol^{-1}$, R the ideal gas constant in $J\,mol^{-1}\,K^{-1}$ and T the temperature in K.

By using Eq. (5), it is possible to extrapolate the forward dissolution rate at temperatures more representative of continental environments. The published range of activation energy for basaltic glass forward dissolution rate is narrow: $E_a = 65\ kJ\,mol^{-1}$ for tholeiitic glass altered by seawater (Crovisier et al., 1987), $72.4\ kJ\,mol^{-1}$ at pH = 8.4 for basaltic glass (Techer et al., 2001) and $76.5 \pm 9.5\ kJ\,mol^{-1}$ in pure water (Verney-Carron et al., 2011). In our calculations, we used the value of $72 \pm 5\ kJ\,mol^{-1}$, which covers the published range, within uncertainties. Dissolution rates were thus determined at lower temperatures (from 5 °C to 90 °C) by resolution of $\ln(A)$ for each salinity using a fixed E_a value (Fig. 2). Results are compared to published values from laboratory experiments performed at temperatures less than 100 °C and at pH between 6.5 and 8.5 (at the temperature of the experiment), the slope of which gives a similar value for E_a (within uncertainties). Even if the data are scarce, our extrapolations give consistent values and are therefore considered to be reliable. We thus estimate glass dissolution rates ranging between $7.14 \cdot 10^{-4}\ g\,m^{-2}\,d^{-1}$ for $S = 0‰$ and $2.58 \cdot 10^{-3}\ g\,m^{-2}\,d^{-1}$ at 16 °C for $S = 3.5‰$ (Table 3).

4.2.2. Impact on Si cycle

Currently, the best-known river-borne Si flux to the coastal ocean (*DSi*) is $6.2 \pm 1.8 \cdot 10^{12}\ mol\,Si\,yr^{-1}$ (i.e. $37110^6\ t\,yr^{-1}$, Dürr et al., 2011; Tréguer and De la Rocha, 2013), based on the re-evaluation of $5.5 \cdot 10^{12}\ mol\,Si\,yr^{-1}$ (i.e. $330 \cdot 10^6\ t\,yr^{-1}$, Meybeck and Ragu, 1996; Milliman and Farnsworth, 2011) (from register of global rivers, GEMS-GLORI). This flux considers a gross input of $7.3 \cdot 10^{12}\ mol\,Si\,yr^{-1}$ (based on measurements carried out upstream the mixing zone), minus Si removal by reverse weathering ($1.5 \cdot 10^{12}\ mol\,Si\,yr^{-1}$) (Laruelle et al., 2009; Tréguer and De la Rocha, 2013). *DSi* derived from river particle interactions with seawater or in estuaries has been little studied thus far. The knowledge of basaltic products associated with chemical weathering is well-known, but very few estimates of the dissolution of basaltic particles and sediments arriving at the mixing zones have been provided (Gislason et al., 2006). Our experiments show that glass alteration may be enhanced as soon as river particles enter estuarine waters having a salinity that is slightly more elevated than the river. The transfer time of river suspended particles from the onset of the mixing zone up to the ocean or down to their deposit at the bottom of the delta therefore plays a key role. Based on our experiments, we propose to estimate the global annual Si flux (Φ_{Si} in $mol\,Si\,yr^{-1}$) resulting from the dissolution of basaltic glass carried by rivers as suspended sediments to a mixing zone, following:

$$\Phi_{Si} = r_0(T) \times \phi_{reacBG} \times S_S \times \tau \quad (6)$$

where $r_0(T)$ is the temperature-dependent glass dissolution rate ($mol\,Si\,m^{-2}\,d^{-1}$), Φ_{reacBG} is the particulate solid flux of fresh basaltic glass ($g\,yr^{-1}$), S_s is the specific surface of the suspended glass particles ($m^2\,g^{-1}$), and τ is the residence time of particulate matter in the mixing zone i.e. the time of reaction (d).

From Eq. (5), and given an average temperature of 16.1 °C, we estimate a dissolution rate of $2.58 \cdot 10^{-3}\ g\,m^{-2}\,d^{-1}$ at a salinity of 3.5‰. Note that this is certainly a minimum value, as the dependence of dissolution rate on salinity does not reach a plateau across the range of salinity evaluated in this study (although the slope is decreasing at high seawater content, Fig. 3). It is therefore expected that higher salinities may be associated with higher dissolution rates, but we will not extrapolate our results to salinity higher than $3.5\ g\,L^{-1}$ since more experimental investigations would be required to better define this dependency at higher salinity. For solving Eq. (6), one difficulty is that, although basaltic

provinces are known to have a dominant role in chemical erosion of continents and in the CO_2 cycle (Dessert et al., 2003; Li and Elderfield, 2013), the corresponding flux of suspended particles and sediments exported to the oceans is less constrained. Worldwide river suspended sediment flux to the ocean has been estimated to be $1.9 \cdot 10^{10}$ t yr^{-1} by Milliman and Farnsworth (2011), and more than 45% of this input is provided by volcanically and tectonically active islands (Milliman and Syvitski, 1992; Gislason et al., 2006). This river particles flux is greater than $8550 \cdot 10^6$ t yr^{-1} but is calculated for islands of Oceania representing a total surface area of $3 \cdot 10^6$ km^2 (Milliman and Syvitski, 1992), where a part of the sediment is not of volcanic origin. We can estimate the total volcanic island derivated sediment flux considering that 1-worldwide island volcanic rock surface area represents $2.02 \cdot 10^6$ km^2 (Allègre et al., 2010) and 2-assuming that the same erosion rates proposed by Milliman and Syvitski (1992) for volcanically and tectonically active islands are applied to that surface area. Therefore, the worldwide island volcanic rock derived sediment particles flux represents $5757 \cdot 10^6$ t yr^{-1}.

Among them, the proportion of fresh basaltic glass in Icelandic river particles was observed to span a large range, from 5% to 65% of the particle flux (Stefánsdóttir and Gíslason, 2005), but the highest values should be excluded for other islands where weathering of basaltic glass is more intense than in Iceland. For the purpose of our estimation, we consider the very low end of these observations: 15 ± 10% of basaltic particles carried by rivers to the ocean are considered to be fresh basaltic glass. This represents flux (Φ_{reacBG}) of $864 \pm 576 \cdot 10^6$ t yr^{-1}.

The specific surface of river particles of basaltic volcanic islands was estimated to be between 11.85 and 22.26 m^2 g^{-1} in Iceland (Stefánsdóttir and Gíslason, 2005). For volcanic ash, the reported range is lower, typically between 0.45 and 2 m^2 g^{-1} (e.g. Delmelle et al., 2004 for 5 eruptions; Gislason et al., 2011 for the Eyjafjallajökull 2010 eruption). Nevertheless the specific surface of explosive ash was estimated to be 4.3 m^2 g^{-1} (Gislason et al., 2011). Based on this published range, even if Oelkers et al. (2011) considered a value of 20 m^2 g^{-1} for their extrapolation, a range of 5 to 15 m^2 g^{-1} was considered for estimating the flux of Si released by the dissolution of fresh glass entering the mixing zone.

The last parameter that plays a key role is the mean residence time of suspended particles in the mixing zone. Estuarine hydrology and sedimentary dynamics are rarely directly monitored and depend on numerous parameters (Dyer, 1997) that can be divided in two categories: (1) hydrological parameters such as the mixed water composition which results from mixing efficiency between river and marine waters and is mainly controlled by water-flow balance between tide and river discharge, and (2) the sedimentary parameters: solid concentration, density, grain-size, specific area, chemical composition, sensitivity to fluid/rock chemical reactions as well as their residence time. The water residence times in estuaries or *flushing times* range from one day to more than 12 months (Dyer, 1997; Berner and Berner, 2012). Accumulation of coarser sediments occurs rapidly (Meade, 1972) as effects of water turbulence and grain-size cause their residence time to vary from minutes to days (Prandle, 2009). Residence time of finer suspended particles is more difficult to determine because these particles can be subject to aggregation and sedimentation (Gibbs, 1986). After particle burial, lower rates of reaction are expected because W/R ratios decrease, leading to rapid over-saturation of connate waters with respect to secondary clays (Oelkers et al., 2011). Nevertheless, the reduced interaction of deposited sediment with water in estuaries or continental shelves is still considered to be significant because residence times are long (Aller, 1998; Jeandel et al., 2011). Therefore, we consider that the time reported in Eq. (6) corresponds to the time during which particles remain in suspension and are still reactive (fresh), and when W/R is high

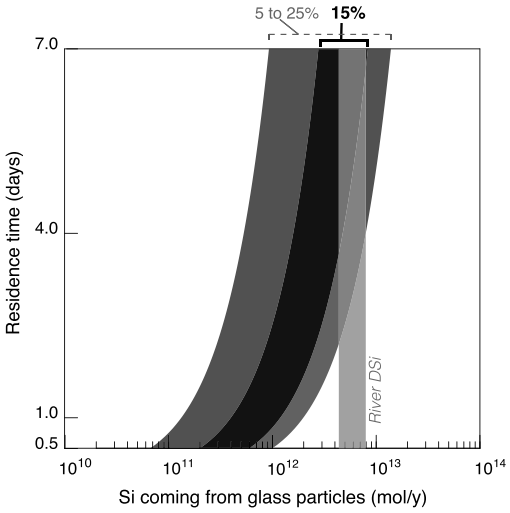

Fig. 4. Estimate of global Si flux coming from the dissolution of river glass particles into estuary (dark grey and black) as a function of their residence time in the water column, assuming the same dissolution rate as the one determined at a salinity 3.5 g L^{-1} (at 16.1 °C, see text for more details). The associated error includes uncertainties on the proportion of fresh basaltic glass into river particles at global scale ($864 \pm 576 \cdot 10^6$ t yr^{-1}) for ratios of fresh basaltic glass in the global volcanic-rock island derived sediment flux of 15% (black), and between 5 to 25% (dark grey), and also uncertainties on the specific area of these particles (5–15 m^2 g^{-1}). For comparison, the flux of dissolved silicon transported to estuaries by rivers (light grey) is also given ($D_{Si} = 6.2 \pm 1.8$ T mol Si/yr; Tréguer and De la Rocha, 2013).

enough to ensure the system is still under-saturated (with respect to secondary phases). For the purpose of our calculation, we thus consider a range of suspended particle residence times from 0.5 to 7 days that correspond to lower estimates.

By using Eq. (6), published ranges for the required parameters, and a very low end of fresh basaltic glass of 15% derived from volcanic-rock islands, the flux of Si released by the dissolution of river basaltic glass particles is found to range between $2 \cdot 10^{12}$ and $8 \cdot 10^{12}$ mol Si yr^{-1} (see Fig. 4). This is of similar magnitude to the river dissolved flux (between 4 and $8 \cdot 10^{12}$ mol Si yr^{-1}) (Dürr et al., 2011; Tréguer and De la Rocha, 2013) and corresponds to a minimal estimation when higher ratios of fresh basaltic glass are considered. As a consequence, we conclude that enhanced dissolution of basalt glassy particles during their entry in brackish waters have the potential to significantly influence the Si input flux to the ocean and needs to be incorporated into the Si cycle.

This phenomenon, which is related to the destruction of the silicate network of basaltic particles carried by rivers, might also influence the release of other elements. By assuming a congruent dissolution, observed in natural systems or in experimental systems characterized by low amounts of secondary phases, flux of other elements can be roughly estimated (e.g. Crovisier et al., 2003; Vigier et al., 2006). Given the differences in saturation state with regards to each element in water, and clear evidence for contemporaneous dissolution and precipitation of secondary phases, these elemental fluxes are likely maximized. The elements that are potentially the most affected by congruent dissolution of river suspended particles after spending only 1 day in the saline zones, are K and Si. For Fe, Ca, Na, and Mg, the order of magnitude is estimated to be lower than river dissolved flux, even considering uncertainties (see Fig. 5). For these elements, and especially for Fe, other phases may play a more crucial role in their transport to the ocean such as oxyhydroxides and colloids.

5. Conclusions

Laboratory experiments demonstrate that dissolution rates of basaltic glass particles are significantly enhanced in presence

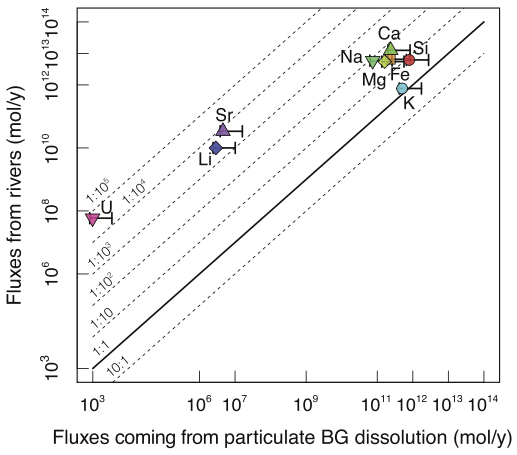

Fig. 5. Estimations for global fluxes of Ca, Mg, Si, K, Na, Fe, Sr, Li, U coming from dissolution of basaltic glass particles into estuarine waters assuming that this process is congruent during their residence time in the water column. Fluxes are compared to published estimations for river fluxes (parameters: specific area = 10 $m g^{-1}$; time of reaction = 1 day; ratio of fresh basaltic glass on basaltic islands driven sediment = 15%, the uncertainties correspond to the range of specific area between 5 and 15 $m g^{-1}$, and the range of ratio of fresh basaltic glass between 5 and 25%).

of seawater, even in diluted waters with relatively low salinity (<3.5 $g L^{-1}$). These results are a complement to previous experimental results performed with seawater where saturation with respect to secondary phases was rapidly obtained. Si concentrations measured in the leachates collected in the very first moments of interaction between water and suspended load allow a robust extrapolation to natural environment. The acceleration of glass particle dissolution in the estuarine mixing environment is investigated along with its impact on the Si cycle. Considering the large ranges of glass particles residence time, specific area, and relative abundances in these environments, we provide a range of values for the Si and the K flux that is of the same order of magnitude as their global river flux (considering the most recent estimates). These results highlight the key role of suspension river-borne particles passing through estuaries before their sink to the continental margins. Suspended matter has a strong influence on the coastal and marine biochemical cycles. The anthropogenic impact on sediment fluxes to the ocean through damming and soil erosion is therefore expected to modify the equilibrium of such transitional environments and modify the primary productivity that is the first link of the oceanic trophic chain.

Acknowledgements

The authors would like to thank SARM team at CRPG (Nancy) for their Si analyses and Elisabeth Bon Nguyen for low Si concentration measurements at LISA (Créteil). Bruno Lartiges from GET (Toulouse) is acknowledged for his help in obtaining the specific area of our tiny residual powder sample. We thank David Doxaran from LOV (Villefranche-sur-mer) for his advice concerning sedimentary processes in estuaries, Céline Caillet from LIEC (Nancy) for her help on granulo-laser, and Laurent Truche from GeoRessources (Nancy) for fruitful discussions. Christian Miller (UH Manoa) is also thanked for English corrections. Furthermore, we thank Morgan T. Jones and an anonymous reviewer for thoughtful and highly appreciated comments. The editor Jean Lynch-Stieglitz is acknowledged for the very efficient handling of the manuscript. This is CRPG contribution number 2358.

References

Aagard, P., Helgeson, H.C., 1982. Thermodynamic and kinetic constraints on reaction rates among minerals and aqueous solutions. I. Theoretical considerations. Am. J. Sci. 282, 237–285.

Allègre, C.J., Louvat, P., Gaillardet, J., Meynadier, L., Rad, S., Capmas, F., 2010. The fundamental role of island arc weathering in the oceanic Sr isotope budget. Earth Planet. Sci. Lett. 292, 51–56.

Aller, R.C., 1998. Mobile deltaic and continental shelf muds as suboxic, fluidized bed reactors. Mar. Chem. 61, 143–155.

Anderson, D.M., Glibert, P.M., Burkholder, J.M., 2002. Harmful algal blooms and eutrophication: nutrient sources, composition, and consequences. Estuaries 25, 704–726.

Arsouze, T., Dutay, J.C., Lacan, F., Jeandel, C., 2009. Reconstructing the Nd oceanic cycle using a coupled dynamical–geochemical model. Biogeosciences 6, 1–18.

Berger, G., Claparols, C., Guy, C., Daux, V., 1994. Dissolution rate of a basalt glass in silica-rich solutions: implications for long-term alteration. Geochim. Cosmochim. Acta 58, 4875–4886.

Berner, E.K., Berner, R.A., 2012. Global Environment: Water, Air, and Geochemical Cycles. Princeton University Press. 464 pp.

Berner, R.A., Lasaga, A.C., Garrels, R.M., 1983. The carbonate–silicate geochemical cycle and its effect on atmospheric carbon-dioxide over the past 100 million years. Am. J. Sci. 283, 641–683.

Cloern, J.E., Foster, S.Q., Kleckner, A.E., 2014. Phytoplankton primary production in the world's estuarine-coastal ecosystems. Biogeosciences 11, 2477–2501.

Crovisier, J., Honnorez, J., Eberhart, J., 1987. Dissolution of basaltic glass in seawater: mechanism and rate. Geochim. Cosmochim. Acta 51, 2977–2990.

Crovisier, J.L., Advocat, T., Dussossoy, J.L., 2003. Nature and role of natural alteration gels formed on the surface of ancient volcanic glasses (natural analogues of waste containment glasses). J. Nucl. Mater. 321, 91–109.

Dagg, M., Benner, R., Lohrenz, S., Lawrence, D., 2004. Transformation of dissolved and particulate materials on continental shelves influenced by large rivers: plume processes. Cont. Shelf Res. 24, 833–858.

Daux, V., Guy, C., Advocat, T., Crovisier, J.L., Stille, P., 1997. Kinetic aspects of basaltic glass dissolution at 90 °C: role of aqueous silicon and aluminium. Chem. Geol. 142, 109–126.

Davis, A.C., Bickle, M.J., Teagle, D.A.H., 2003. Imbalance in the oceanic strontium budget. Earth Planet. Sci. Lett. 211, 173–187.

Delmelle, P., Villiéras, F., Pelletier, M., 2004. Surface area, porosity and water adsorption properties of fine volcanic ash particles. Bull. Volcanol. 67, 160–169.

Dessert, C., Dupré, B., François, L.M., Schott, J., Gaillardet, J., Chakrapani, G., Bajpai, S., 2001. Erosion of Deccan Traps determined by river geochemistry: impact on the global climate and the $^{87}Sr/^{86}Sr$ ratio of seawater. Earth Planet. Sci. Lett. 188, 459–474.

Dessert, C., Dupré, B., Gaillardet, J., François, L.M., Allègre, C.J., 2003. Basalt weathering laws and the impact of basalt weathering on the global carbon cycle. Chem. Geol. 202, 257–273.

Dove, P., Nix, C., 1997. The influence of the alkaline earth cations, magnesium, calcium, and barium on the dissolution kinetics of quartz. Geochim. Cosmochim. Acta 61, 3329–3340.

Dove, P.M., 1994. The dissolution kinetics of quartz in sodium chloride solutions at 25 to 300 °C. Am. J. Sci. 294, 665–712.

Dove, P.M., 1999. The dissolution kinetics of quartz in aqueous mixed cation solutions. Geochim. Cosmochim. Acta 63, 3715–3727.

Dove, P.M., Crerar, D.A., 1990. Kinetics of quartz dissolution in electrolyte solutions using a hydrothermal mixed flow reactor. Geochim. Cosmochim. Acta 54, 955–969.

Dunk, R.M., Mills, R.A., Jenkins, W.J., 2002. A reevaluation of the oceanic uranium budget for the Holocene. Chem. Geol. 190, 45–67.

Dürr, H.H., Meybeck, M., Hartmann, J., Laruelle, G.G., Roubeix, V., 2011. Global spatial distribution of natural riverine silica inputs to the coastal zone. Biogeosciences 8, 597–620.

Dyer, K.R., 1997. Estuaries: A Physical Introduction, 2nd ed. Wiley, New York. 195 pp.

Falkowski, P.G., 1997. Evolution of the nitrogen cycle and its influence on the biological sequestration of CO_2 in the ocean. Nature 387, 287.

Falkowski, P.G., Barber, R., Smetacek, V., 1998. Biogeochemical controls and feedbacks on ocean primary production. Science 281, 200–206.

Flaathen, T.K., Gislason, S.R., Oelkers, E.H., 2010. The effect of aqueous sulphate on basaltic glass dissolution rates. Chem. Geol. 277, 345–354.

Frugier, P., Gin, S., Minet, Y., Chave, T., Bonin, B., Godon, N., Lartigue, J.E., Jollivet, P., Ayral, A., De Windt, L., Santarini, G., 2008. SON68 nuclear glass dissolution kinetics: current state of knowledge and basis of the new GRAAL model. J. Nucl. Mater. 380, 8–21.

Frugier, P., Chave, T., Lartigue, J.E., Gin, S., 2009. Application of the GRAAL model to leaching experiments with SON68 nuclear glass in initially pure water. J. Nucl. Mater. 392, 552–567.

Gaillardet, J., Dupré, B., Louvat, P., Allègre, C.J., 1999. Global silicate weathering and CO_2 consumption rates deduced from the chemistry of large rivers. Chem. Geol. 159, 3–30.

Gibbs, R.J., 1986. Segregation of metals by coagulation in estuaries. Mar. Chem. 18, 149–159.

Gislason, S.R., Eugster, H.P., 1987. Meteoritic water–basalt interactions. I. A laboratory study. Geochim. Cosmochim. Acta 51, 2827–2840.

Gislason, S., Oelkers, E., 2003. Mechanism, rates, and consequences of basaltic glass dissolution. II. An experimental study of the dissolution rates of basaltic glass as a function of pH and temperature. Geochim. Cosmochim. Acta 67, 3817–3832.

Gislason, S.R., Oelkers, E.H., Snorrason, Á., 2006. Role of river-suspended material in the global carbon cycle. Geology 34, 49–52.
Gislason, S.R., Oelkers, E.H., Eiriksdottir, E.S., Kardjilov, M.I., Gisladottir, G., Sigfusson, B., Snorrason, A., Elefsen, S., Hardardottir, J., Torssander, P., Oskarsson, N., 2009. Direct evidence of the feedback between climate and weathering. Earth Planet. Sci. Lett. 277, 213–222.
Gislason, S.R., Hassenkam, T., Nedel, S., Bovet, N., Eiriksdottir, E.S., Alfredsson, H.A., Hem, C.P., Balogh, Z.I., Dideriksen, K., Oskarsson, N., Sigfusson, B., Larsen, G., Stipp, S.L.S., 2011. Characterization of Eyjafjallajokull volcanic ash particles and a protocol for rapid risk assessment. Proc. Natl. Acad. Sci. USA 108, 7307–7312.
Gordon, S.J., Brady, P.V., 2002. In situ determination of long-term basaltic glass dissolution in the unsaturated zone. Chem. Geol. 190, 113–122.
Grambow, B., 1985. A general rate equation for nuclear waste glass corrosion. Mater. Res. Soc. Symp. Proc. 44, 15–27.
Gunnarsson, I., Arnórsson, S., 2000. Amorphous silica solubility and the thermodynamic properties of H_4SiO_4 in the range of 0° to 350 °C at P_{sat}. Geochim. Cosmochim. Acta 64, 2295–2307.
Guy, C., Schott, J., 1989. Multisite surface reaction versus transport control during the hydrolysis of a complex oxide. Chem. Geol. 78, 181–204.
Hodell, D.A., Mueller, P.A., McKenzie, J.A., Mead, G.A., 1989. Strontium isotope stratigraphy and geochemistry of the late Neogene ocean. Earth Planet. Sci. Lett. 92, 165–178.
Holland, H.D., 2005. Sea level, sediments and the composition of seawater. Am. J. Sci. 305, 220–239.
Icenhower, J.P., Dove, P.M., 2000. The dissolution kinetics of amorphous silica into sodium chloride solutions: effects of temperature and ionic strength. Geochim. Cosmochim. Acta 64, 4193–4203.
Jeandel, C., Peucker-Ehrenbrink, B., Jones, M.T., Pearce, C.R., Oelkers, E.H., Godderis, Y., Lacan, F., Aumont, O., Arsouze, T., 2011. Ocean margins: the missing term in oceanic element budgets? Eos Trans. AGU 92, 26–28.
Jones, M.T., Pearce, C.R., Jeandel, C., Gislason, S.R., Eiriksdottir, E.S., Mavromatis, V., Oelkers, E.H., 2012a. Riverine particulate material dissolution as a significant flux of strontium to the oceans. Earth Planet. Sci. Lett. 355–356, 51–59.
Jones, M.T., Pearce, C.R., Oelkers, E.H., 2012b. An experimental study of the interaction of basaltic riverine particulate material and seawater. Geochim. Cosmochim. Acta 77, 108–120.
Jones, M.T., Gislason, S.R., Burton, K.W., Pearce, C.R., Mavromatis, V., Pogge von Strandmann, P.A.E., Oelkers, E.H., 2014. Quantifying the impact of riverine particulate dissolution in seawater on ocean chemistry. Earth Planet. Sci. Lett. 395, 91–100.
Lacan, F., Jeandel, C., 2005. Neodymium isotopes as a new tool for quantifying exchange fluxes at the continent–ocean interface. Earth Planet. Sci. Lett. 232, 245–257.
Laruelle, G.G., Roubeix, V., Sferratore, A., Brodherr, B., Ciuffa, D., Conley, D.J., Dürr, H.H., Garnier, J., Lancelot, C., Le Thi Phuong, Q., Meunier, J.D., Meybeck, M., Michalopoulos, P., Moriceau, B., Ní Longphuirt, S., Loucaides, S., Papush, L., Presti, M., Ragueneau, O., Regnier, P., Saccone, L., Slomp, C.P., Spiteri, C., Van Cappellen, P., 2009. Anthropogenic perturbations of the silicon cycle at the global scale: key role of the land–ocean transition. Glob. Biogeochem. Cycles 23, 17 pp.
Li, G., Elderfield, H., 2013. Evolution of carbon cycle over the past 100 million years. Geochim. Cosmochim. Acta 103, 11–25.
Louvat, P., Allègre, C.J., 1997. Present denudation rates on the island of Réunion determined by river geochemistry: basalt weathering and mass budget between chemical and mechanical erosions. Geochim. Cosmochim. Acta 61, 3645–3669.
Louvat, P., Allègre, C.J., 1998. Riverine erosion rates on Sao Miguel volcanic island, Azores archipelago. Chem. Geol. 148, 177–200.
Meade, R.H., 1972. Transport and deposition of sediments in estuaries. Geol. Soc. Am. Mem. 133, 91–120.
Meybeck, M., Ragu, A., 1996. River discharges to the Oceans: an assessment of suspended solids, major ions and nutrients. Environmental Information and Assessment Rpt. UNEP, Nairobi. 250 pp.
Milliman, J.D., Syvitski, J.P.M., 1992. Geomorphic/tectonic control of sediment discharge to the ocean: the importance of small mountainous rivers. J. Geol., 525–544.
Milliman, J.D., Farnsworth, K.L., 2011. River Discharge to the Coastal Ocean: a Global Synthesis. Cambridge University Press. 392 pp.
Millot, R., Gaillardet, J., Dupré, B., Allègre, C.J., 2002. The global control of silicate weathering rates and the coupling with physical erosion: new insights from rivers of the Canadian Shield. Earth Planet. Sci. Lett. 196, 83–98.
Nelson, D.M., Tréguer, P., Brzezinski, M.A., Leynaert, A., Quéguiner, B., 1995. Production and dissolution of biogenic silica in the ocean: revised global estimates, comparison with regional data and relationship to biogenic sedimentation. Glob. Biogeochem. Cycles 9, 359–372.
Oelkers, E.H., 2001. General kinetic description of multioxide silicate mineral and glass dissolution. Geochim. Cosmochim. Acta 65, 3703–3719.
Oelkers, E.H., Gislason, S.R., 2001. The mechanism, rates and consequences of basaltic glass dissolution: I. An experimental study of the dissolution rates of basaltic glass as a function of aqueous Al, Si and oxalic acid concentration at 25 °C and pH = 3 and 11. Geochim. Cosmochim. Acta 65, 3671–3681.
Oelkers, E.H., Gislason, S.R., Eiriksdottir, E.S., Jones, M., Pearce, C.R., Jeandel, C., 2011. The role of riverine particulate material on the global cycles of the elements. Appl. Geochem. 26, S365–S369.
Oxburgh, R., Pierson-Wickmann, A.C., Reisberg, L., Hemming, S., 2007. Climate-correlated variations in seawater $^{187}Os/^{188}Os$ over the past 200 000 yr: evidence from the Cariaco Basin, Venezuela. Earth Planet. Sci. Lett. 263, 246–258.
Paul, M., Reisberg, L., Vigier, N., 2010. Dissolved osmium in Bengal plain groundwater: implications for the marine Os budget. Geochim. Cosmochim. Acta 74, 3432–3448.
Pearce, C.R., Jones, M.T., Oelkers, E.H., Pradoux, C., Jeandel, C., 2013. The effect of particulate dissolution on the neodymium (Nd) isotope and Rare Earth Element (REE) composition of seawater. Earth Planet. Sci. Lett. 369–370, 138–147.
Prandle, D., 2009. Estuaries: Dynamics, Mixing, Sedimentation and Morphology. Cambridge University Press. 236 pp.
Rad, S., Louvat, P., Gorge, C., Gaillardet, J., Allègre, C.J., 2006. River dissolved and solid loads in the Lesser Antilles: new insight into basalt weathering processes. J. Geochem. Explor. 88, 308–312.
Rahaman, W., Singh, S.K., Raghav, S., 2010. Dissolved Mo and U in rivers and estuaries of India: implications to geochemistry of redox sensitive elements and their marine budgets. Chem. Geol. 278, 160–172.
Roubeix, V., Rousseau, V., Lancelot, C., 2008. Diatom succession and silicon removal from freshwater in estuarine mixing zones: from experiment to modelling. Estuar. Coast. Shelf Sci. 78, 14–26.
Sharp, J., Pennock, J., Church, T., Tramontano, J., Cifuentes, L., 1983. The estuarine interaction of nutrients, organics and metals: a case study in the Delaware estuary. In: Kennedy, V. (Ed.), The Estuary as a Filter. Academic Press, New York, pp. 241–260.
Stefánsdóttir, M.B., Gíslason, S.R., 2005. The erosion and suspended matter/seawater interaction during and after the 1996 outburst flood from the Vatnajökull Glacier, Iceland. Earth Planet. Sci. Lett. 237, 433–452.
Stockmann, G.J., Wolff-Boenisch, D., Gislason, S.R., Oelkers, E.H., 2011. Do carbonate precipitates affect dissolution kinetics? 1: basaltic glass. Chem. Geol. 284, 306–316.
Stumm, W., 1990. Aquatic Chemical Kinetics: Reaction Rates of Processes in Natural Waters. Wiley/Interscience, New York. 545 pp.
Techer, I., Advocat, T., Lancelot, J., Liotard, J.M., 2000. Basaltic glass: alteration mechanisms and analogy with nuclear waste glasses. J. Nucl. Mater. 282, 40–46.
Techer, I., Advocat, T., Lancelot, J., Liotard, J.M., 2001. Dissolution kinetics of basaltic glasses: control by solution chemistry and protective effect of the alteration film. Chem. Geol. 176, 235–263.
Tipper, E.T., Galy, A., Gaillardet, J., Bickle, M.J., Elderfield, H., Carder, E.A., 2006. The magnesium isotope budget of the modern ocean: constraints from riverine magnesium isotope ratios. Earth Planet. Sci. Lett. 312–313, 80–92.
Tréguer, P., Nelson, D.M., Van Bennekom, A.J., Demaster, D.J., Leynaert, A., Quéguiner, B., 1995. The silica balance in the world ocean: a reestimate. Science 268, 375–379.
Tréguer, P.J., De La Rocha, C.L., 2013. The world ocean silica cycle. Ann. Rev. Mar. Sci. 5, 477–501.
Vance, D., Teagle, D.A.H., Foster, G.L., 2009. Variable Quaternary chemical weathering fluxes and imbalances in marine geochemical budgets. Nature 458, 493–496.
Verney-Carron, A., Gin, S., Frugier, P., Libourel, G., 2010. Long-term modeling of alteration-transport coupling: application to a fractured Roman glass. Geochim. Cosmochim. Acta 74, 2291–2315.
Verney-Carron, A., Vigier, N., Millot, R., 2011. Experimental determination of the role of diffusion on Li isotope fractionation during basaltic glass weathering. Geochim. Cosmochim. Acta 75, 3452–3468.
Vigier, N., Burton, K.W., Gislason, S.R., Rogers, N.W., Duchene, S., Thomas, L., Hodge, E., Schaefer, B., 2006. The relationship between riverine U-series disequilibria and erosion rates in a basaltic terrain. Earth Planet. Sci. Lett. 249, 258–273.
White, A., Blum, A., 1995. Effects of climate on chemical weathering in watersheds. Geochim. Cosmochim. Acta 59, 1729–1747.

Bibliographie

[Adler 01] M. Adler & U. Nicodemus. *A new computer model for the evaluation of data from acoustic Doppler current profilers (ADCP).* Physics and Chemistry of the Earth, Part C : Solar, Terrestrial & Planetary Science, vol. 26, no. 10-12, pages 711–715, January 2001. www

[Agrawal 14] Shailesh Agrawal, Prasanta Sanyal, Srinivasan Balakrishnan & Jitendra K. Dash. *Climate induced temporal change in Sr-Nd isotope ratios in the valley-fill deposits of the Ganga river.* GEOCHEMICAL JOURNAL, vol. 48, no. 5, pages 451–462, 2014. www

[Aller 04] Robert C Aller & Neal E Blair. *Early diagenetic remineralization of sedimentary organic C in the Gulf of Papua deltaic complex (Papua New Guinea) : Net loss of terrestrial C and diagenetic fractionation of C isotopes.* Geochimica et Cosmochimica Acta, vol. 68, no. 8, pages 1815–1825, 2004. www

[Aller 08] Robert C. Aller, Neal E. Blair & Gregg J. Brunskill. *Early diagenetic cycling, incineration, and burial of sedimentary organic carbon in the central Gulf of Papua (Papua New Guinea).* Journal of Geophysical Research, vol. 113, no. F1, page F01S09, January 2008. www

[Andermann 11] C. Andermann, S. Bonnet & R. Gloaguen. *Evaluation of precipitation data sets along the Himalayan front.* Geochemistry Geophysics Geosystems, vol. 12, no. 7, page Q07023, 2011. www

[Andermann 12a] Christoff Andermann, Stéphane Bonnet, Alain Crave, Philippe Davy, Laurent Longuevergne & Richard Gloaguen. *Sediment transfer and the hydrological cycle of Himalayan rivers in Nepal*. Comptes Rendus Geoscience, vol. 344, pages 627–635, November 2012. www

[Andermann 12b] Christoff Andermann, Alain Crave, Richard Gloaguen, Philippe Davy & Stéphane Bonnet. *Connecting source and transport : Suspended sediments in the Nepal Himalayas*. Earth and Planetary Science Letters, vol. 351-352, pages 158–170, October 2012. www

[Andermann 12c] Christoff Andermann, Laurent Longuevergne, Stéphane Bonnet, Alain Crave, Philippe Davy & Richard Gloaguen. *Impact of transient groundwater storage on the discharge of Himalayan rivers*. Nature Geoscience, vol. 5, no. 2, pages 127–132, January 2012. www

[Anders 06] Alison M AM Anders, Gerard H GH Roe, David R Montgomery & Noah J Finnegan. *Spatial patterns of precipitation and topography in the Himalaya*. Geological Society of America Special Paper, vol. 398, no. 03, pages 39–53, 2006. www

[Anderson 06] Robert S Anderson, Peter Molnar & Mark A Kessler. *Features of glacial valley profiles simply explained*. Journal of Geophysical Research, vol. 111, no. F1, 2006.

[Anderson 10] Robert S Anderson & Suzanne P Anderson. Geomorphology : the mechanics and chemistry of landscapes. Cambridge University Press, 2010.

[Attal 06] M Attal & J Lavé. *Changes of bedload characteristics along the Marsyandi River (central Nepal) : Implications for understanding hillslope sediment supply, sediment load evolution along*. Tectonics, climate, and landscape evolution, vol. 2398, no. 09, pages 143–171, 2006. www

[Avouac 96] JP Avouac & EB Burov. *Erosion as a driving mechanism of intracontinental mountain growth.* Journal of Geophysical Research B, vol. 101, no. B8, pages 17747–17769, 1996.

[Avouac 01] Jean-Philippe Avouac, Laurent Bollinger, Jérôme Lavé, Rodolphe Cattin & Mireille Flouzat. *Le cycle sismique en Himalaya.* Comptes Rendus de l'Académie des Sciences-Series IIA-Earth and Planetary Science, vol. 333, no. 9, pages 513–529, 2001.

[Baillie 04] I. C. Baillie, Kado Tshering, Tshering Dorji, H. B. Tamang, Tsheten Dorji, Chencho Norbu, a. a. Hutcheon & R. Baumler. *Regolith and soils in Bhutan, Eastern Himalayas.* European Journal of Soil Science, vol. 55, no. 1, pages 9–27, March 2004. www

[Balco 09] Greg Balco, Jason Briner, Robert C. Finkel, John A. Rayburn, John C. Ridge & Joerg M. Schaefer. *Regional beryllium-10 production rate calibration for late-glacial northeastern North America.* Quaternary Geochronology, vol. 4, no. 2, pages 93–107, April 2009. www

[Balkaya 08] Çağlayan Balkaya, M. Ali Kaya & Gökhan Göktürkler. *Delineation of shallow resistivity structure in the city of Burdur, SW Turkey by vertical electrical sounding measurements.* Environmental Geology, vol. 57, no. 3, pages 571–581, 2008. www

[Banister 81] Judith Banister. The population dynamics of Nepal, volume 78. 1981.

[Barbey 96] P. Barbey, M. Brouand, P. Le Fort & A. Pêcher. *Granite-migmatite genetic link : the example of the Manaslu granite and Tibetan Slab migmatites in central Nepal.* Lithos, vol. 38, no. 1-2, pages 63–79, 1996.

[Barros 00] A. P. Barros, M. Joshi, J. Putkonen & D. W. Burbank. *A study of the 1999 monsoon rainfall in a mountainous region in central Nepal using TRMM products and rain gauge observations.* Geophysical Research Letters, vol. 27, no. 22, pages 3683–3686, November 2000. www

[Barros 03] Ana P. Barros & Timothy J. Lang. *Monitoring the Monsoon in the Himalayas : Observations in Central Nepal, June 2001.* Monthly Weather Review, vol. 131, no. 7, pages 1408–1427, July 2003. www

[Bauer 14] Kerstin K. Bauer & Torsten W. Vennemann. *Analytical methods for the measurement of hydrogen isotope composition and water content in clay minerals by TC/EA.* Chemical Geology, vol. 363, pages 229–240, January 2014. www

[Beaumont 01] C. Beaumont, R. A. Jamieson, M. H. Nguyen & B. Lee. *Himalayan tectonics explained by extrusion of a low-viscosity crustal channel coupled to focused surface denudation.* Nature, vol. 414, no. 6865, pages 738–742, December 2001. www

[Berner 83] R. A. Berner, A. C. Lasaga & R. M. Garrels. *The carbonate-silicate geochemical cycle and its effect on atmospheric carbon dioxide over the past 100 million years.* American Journal of Science, vol. 283, no. 7, pages 641–683, September 1983. www

[Bersezio 07] R. Bersezio, M. Giudici & M. Mele. *Combining sedimentological and geophysical data for high-resolution 3-D mapping of fluvial architectural elements in the Quaternary Po plain (Italy).* Sedimentary Geology, vol. 202, no. 1-2, pages 230–248, November 2007. www

[Bettinelli 08] Pierre Bettinelli, Jean-Philippe Avouac, Mireille Flouzat, Laurent Bollinger, Guillaume Ramillien, Sudhir Rajaure & Som Sapkota. *Seasonal variations of seismicity and geodetic strain in the Himalaya induced by surface hydrology.* Earth and Planetary Science Letters, vol. 266, no. 3-4, pages 332–344, February 2008. www

[Bickle 01] M J Bickle, N B W Harris & J M Bunbury. *Controls on the 87Sr/86Sr ratios of carbonates in the Garhwal Himalaya, Headwaters of the Ganges.* Journal of \ldots, 2001. www

[Bilham 15] Roger Bilham. *Seismology : raising kathmandu.* Nature Geoscience, vol. 8, no. 8, pages 582–584, 2015.

[Blöthe 13] Jan Henrik Blöthe & Oliver Korup. *Millennial lag times in the Himalayan sediment routing system.* Earth and Planetary Science Letters, vol. 382, pages 38–46, November 2013. www

[Blum 98] Joel D. Blum, Carey A. Gazis, Andrew D. Jacobson & C. Page Chamberlain. *Carbonate versus silicate weathering in the Raikhot watershed within the High Himalayan Crystalline Series.* Geology, vol. 26, no. 5, page 411, 1998. www

[Bluth 94] Gregg JS Bluth & Lee R Kump. *Lithologic and climatologic controls of river chemistry.* Geochimica et Cosmochimica Acta, vol. 58, no. 10, pages 2341–2359, 1994.

[Blythe 07] AE Blythe, DW Burbank, A CARTER, K. Schmidt & J PUTKONEN. *Plio-Quaternary exhumation history of the central Nepalese Himalaya : 1. Apatite and zircon fission track and apatite [U-Th]/He analyses.* Tectonics, vol. 26, no. 3, page TC3002, 2007.

[Bollinger 07] L. Bollinger, F. Perrier, J.-P. Avouac, S. Sapkota, U. Gautam & D. R. Tiwari. *Seasonal modulation of seismicity in the Himalaya of Nepal.* Geophysical Research Letters, vol. 34, no. 8, April 2007. www

[Bookhagen 05a] Bodo Bookhagen, Rasmus C. Thiede & Manfred R. Strecker. *Abnormal monsoon years and their control on erosion and sediment flux in the high, arid northwest Himalaya.* Earth and Planetary Science Letters, vol. 231, no. 1-2, pages 131–146, February 2005. www

[Bookhagen 05b] Bodo Bookhagen, Rasmus C Thiede, Manfred R Strecker & P O Box. *Late Quaternary intensified monsoon phases control landscape evolution in the northwest Himalaya.* Geology, vol. 33, no. 2, page 149, 2005. www

[Bookhagen 06] Bodo Bookhagen & Douglas W. Burbank. *Topography, relief, and TRMM-derived rainfall variations along the Himalaya.* Geophysical Research Letters, vol. 33, no. 8, 2006. www

[Bookhagen 10] Bodo Bookhagen & Douglas W. Burbank. *Toward a complete Himalayan hydrological budget : Spatiotemporal distribution of*

snowmelt and rainfall and their impact on river discharge. Journal of Geophysical Research, vol. 115, no. F3, page F03019, 2010. www

[Boos 10] William R Boos & Zhiming Kuang. *Dominant control of the South Asian monsoon by orographic insulation versus plateau heating.* Nature, vol. 463, no. 7278, pages 218–222, 2010. www

[Botter-Jensen 10] L Botter-Jensen, K J Thomsen & M Jain. *Review of optically stimulated luminescence (OSL) instrumental developments for retrospective dosimetry.* Radiation Measurements, vol. 45, no. 3-6, pages 253–257, 2010. www

[Bouchez 11a] J. Bouchez, F. Métivier, M. Lupker, L. Maurice, M. Perez, J. Gaillardet & C. France-Lanord. *Prediction of depth-integrated fluxes of suspended sediment in the Amazon River : particle aggregation as a complicating factor.* Hydrological Processes, vol. 25, no. 5, pages 778–794, 2011. www

[Bouchez 11b] Julien Bouchez, Maarten Lupker, Jerome Gaillardet, Christian France-Lanord & Laurence Maurice. *How important is it to integrate riverine suspended sediment chemical composition with depth ? Clues from Amazon River depth-profiles.* Geochimica et Cosmochimica Acta, vol. 75, no. 22, pages 6955–6970, November 2011. www

[Bouchez 12] Julien Bouchez, Jérôme Gaillardet, Maarten Lupker, Pascale Louvat, Christian France-Lanord, Laurence Maurice, Elisa Armijos & Jean-Sébastien Moquet. *Floodplains of large rivers : Weathering reactors or simple silos ?* Chemical Geology, vol. 332-333, pages 166–184, November 2012. www

[Bouquillon 90] A. Bouquillon, C France-Lanord, A Michard & J.J. Tiercelin. *5. SEDIMENTOLOGY AND ISOTOPIC CHEMISTRY OF THE BENGAL FAN SEDIMENTS : THE DENUDATION OF THE HIMALAYA1, 5.* Proceedings of the Ocean Drilling Program : Scientific results, vol. 116, page 43, 1990.

[Brantley 11] Susan L. Brantley & Marina Lebedeva. *Learning to Read the Chemistry of Regolith to Understand the Critical Zone*. Annual Review of Earth and Planetary Sciences, vol. 39, no. 1, pages 387–416, 2011. www

[Braucher 01] Regis Braucher. *UTILISATION DU 10BE COSMOGENIQUE PRODUIT IN-SITU POUR L'ETUDE DE LA DYNAMIQUE DES LATERITES EN ZONE INTERTROPICALE*. Theses, Université de droit, d'économie et des sciences - Aix-Marseille III, June 2001. www

[Broecker 70] Wallace S. Broecker. *A boundary condition on the evolution of atmospheric oxygen*. Journal of Geophysical Research, vol. 75, no. 18, pages 3553–3557, June 1970. www

[Brouand 89] Marc Brouand. *Pétrogenèse des migmatites de la dalle du Tibet (Himalaya du Népal)*. Thèse de Doctorat, Institut National Polytechnique de Lorraine, 1989. www

[Brown 91] Erik Thorson Brown, John M Edmond, Grant M Raisbeck, Françoise Yiou, Mark D Kurz & Edward J Brook. *Examination of surface exposure ages of Antarctic moraines using in situ produced 10Be and 26Al*. Geochimica et Cosmochimica Acta, vol. 55, no. 8, pages 2269–2283, August 1991. www

[Burbank 92] Douglas W. Burbank. *Causes of recent Himalayan uplift deduced from deposited patterns in the Ganges basin*. Nature, vol. 357, no. 6380, pages 680–683, 1992.

[Burbank 96a] Douglas W. Burbank, John Leland, Eric Fielding, Robert S. Anderson, Nicholas Brozovic, Mary R. Reid & Christopher Duncan. *Bedrock incision, rock uplift and threshold hillslopes in the northwestern Himalayas*. Nature, vol. 379, no. 6565, pages 505–510, February 1996. www

[Burbank 96b] DW Burbank, Richard A Beck & Thomas Mulder. *The Himalayan foreland basin*. World and regional geology, vol. 1, no. 8, pages 149–190, 1996.

[Burbank 03] D. W. Burbank, A. E. Blythe, J. Putkonen, B. Pratt-Sitaula, E. Gabet, M. Oskin, A. Barros & T. P. Ojha. *Decoupling of erosion and precipitation in the Himalayas.* Nature, vol. 426, no. 6967, pages 652–655, December 2003. www

[Cai 10] Y. Cai, H. Cheng, Z. An, R. L. Edwards, X. Wang, L. Tan & J. Wang. *Large variations of oxygen isotopes in precipitation over south-central Tibet during Marine Isotope Stage 5.* Geology, vol. 38, no. 3, pages 243–246, March 2010. www

[Calmels 11] Damien Calmels, Albert Galy, Niels Hovius, Mike Bickle, a. Joshua West, Meng-Chiang Chen & Hazel Chapman. *Contribution of deep groundwater to the weathering budget in a rapidly eroding mountain belt, Taiwan.* Earth and Planetary Science Letters, vol. 303, no. 1-2, pages 48–58, 2011. www

[Carignan 01] Jean Carignan, Pascal Hild, Guy Mevelle, Jacques Morel & Delphine Yeghicheyan. *Routine Analyses of Trace Elements in Geological Samples using Flow Injection and Low Pressure On-Line Liquid Chromatography Coupled to ICP-MS : A Study of Geochemical Reference Materials BR, DR-N, UB-N, AN-G and GH.* Geostandards and Geoanalytical Research, vol. 25, no. 2-3, pages 187–198, 2001. www

[Caspari 06] Thomas Caspari, Rupert Bäumler, Chencho Norbu, Kado Tshering & Ian Baillie. *Geochemical investigation of soils developed in different lithologies in Bhutan, Eastern Himalayas.* Geoderma, vol. 136, no. 1-2, pages 436–458, 2006. www

[Cerling 99] Thure E. Cerling & John M. Harris. *Carbon isotope fractionation between diet and bioapatite in ungulate mammals and implications for ecological and paleoecological studies.* Oecologia, vol. 120, no. 3, pages 347–363, 1999. www

[Chakraborty 10a] Tapan Chakraborty & Parthasarathi Ghosh. *The geomorphology and sedimentology of the Tista megafan, Darjeeling Himalaya : Implications for megafan building processes.* Geomorphology, vol. 115, no. 3-4, pages 252–266, March 2010. www

[Chakraborty 10b] Tapan Chakraborty, Rimpal Kar, Parthasarathi Ghosh & Sounak Basu. *Kosi megafan : Historical records, geomorphology and the recent avulsion of the Kosi River.* Quaternary International, vol. 227, no. 2, pages 143–160, November 2010. www

[Chamberlin 99] Thomas Chrowder Chamberlin. *An attempt to frame a working hypothesis of the cause of glacial periods on an atmospheric basis.* The Journal of Geology, vol. 7, no. 6, pages 545–584, 1899.

[Champagnac 07] J.D. Champagnac, P. Molnar, R.S. Anderson, C. Sue & B. Delacou. *Quaternary erosion-induced isostatic rebound in the western Alps.* Geology, vol. 35, no. 3, page 195, 2007. www

[Champagnac 12] Jean-Daniel Champagnac, Peter Molnar, Christian Sue & Frédéric Herman. *Tectonics, climate, and mountain topography.* Journal of Geophysical Research, vol. 117, no. B2, February 2012. www

[Chandra 07] S. Chandra, E. Rhodes & K. Richards. *Luminescence dating of late Quaternary fluvial sediments in the Rapti Basin, north-central Gangetic plains.* Quaternary International, vol. 159, no. 1, pages 47–56, January 2007. www

[Clift 06] PD Clift. *Controls on the erosion of Cenozoic Asia and the flux of clastic sediment to the ocean.* Earth and Planetary Science Letters, vol. 241, no. 3-4, pages 571–580, 2006. www

[Clift 08] Peter D Clift, Liviu Giosan, Jerzy Blusztajn, Ian H Campbell, Charlotte Allen, Malcolm Pringle, Ali R Tabrez, Mohammed Danish, M M Rabbani, Anwar Alizai, Andrew Carter & Andreas Lückge. *Holocene erosion of the Lesser Himalaya triggered by intensified summer monsoon.* Geology, vol. 36, no. 1, page 79, 2008.

[Colchen 86] M Colchen, P Le Fort & A Pêcher. *Notice explicative de la carte géologique Annapurna-Manaslu-Ganesh (Himalaya du Népal) au 1 : 200.000 e (bilingue : Français-English).* Cent. Natl. de la Rech. Sci., Paris, 1986.

[Costa 75] John E. Costa. *Effects of Agriculture on Erosion and Sedimentation in the Piedmont Province, Maryland.* Geological Society of America Bulletin, vol. 86, no. 9, page 1281, 1975. www

[Crerar 81] D A Crerar, J L Means, R F Yuretich, M P Borcsik, J L Amster, D W Hastings, G W Knox, K E Lyon & R F Quiett. *Hydrogeochemistry of the New Jersey Coastal Plain : 2. Transport and deposition of iron, aluminum, dissolved organic matter, and selected trace elements in stream, ground- and estuary water.* Chemical Geology, vol. 33, no. 1-4, pages 23–44, 1981. www

[Dadson 03] Simon J Dadson, Niels Hovius, Hongey Chen, W Brian Dade, Meng-Long Hsieh, Sean D Willett, Jyr-Ching Hu, Ming-Jame Horng, Meng-Chiang Chen, Colin P Stark, Dimitri Lague & Jiun-Chuan Lin. *Links between erosion, runoff variability and seismicity in the Taiwan orogen.* Nature, vol. 426, no. 6967, pages 648–51, 2003. www

[Dadson 04] Simon J. Dadson, Niels Hovius, Hongey Chen, W. Brian Dade, Jiun-Chuan Lin, Mei-Ling Hsu, Ching-Weei Lin, Ming-Jame Horng, Tien-Chien Chen, John Milliman & Colin P. Stark. *Earthquake-triggered increase in sediment delivery from an active mountain belt.* Geology, vol. 32, no. 8, page 733, 2004. www

[Dahal 08] Ranjan Kumar Dahal & Shuichi Hasegawa. *Representative rainfall thresholds for landslides in the Nepal Himalaya.* Geomorphology, vol. 100, no. 3, pages 429–443, 2008.

[Deeken 11] A. Deeken, R.C. Thiede, E.R. Sobel, J.K. Hourigan & M.R. Strecker. *Exhumational variability within the Himalaya of northwest India.* Earth and Planetary Science Letters, vol. 305, no. 1-2, pages 103–114, May 2011. www

[Delcaillau 92] Bernard Delcaillau. Les Siwalik de l'Himalaya du Népal oriental : fonctionnement et évolution d'un piémont. Editions du Centre national de la recherche scientifique, 1992.

[Dellinger 14] Mathieu Dellinger, Jérôme Gaillardet, Julien Bouchez, Damien Calmels, Valier Galy, Robert G. Hilton, Pascale Louvat & Chris-

tian France-Lanord. *Lithium isotopes in large rivers reveal the cannibalistic nature of modern continental weathering and erosion.* Earth and Planetary Science Letters, vol. 401, pages 359–372, September 2014. www

[Delunel 10] Romain Delunel, Peter A. van der Beek, Julien Carcaillet, Didier L. Bourlès & Pierre G. Valla. *Frost-cracking control on catchment denudation rates : Insights from in situ produced 10Be concentrations in stream sediments (Ecrins–Pelvoux massif, French Western Alps).* Earth and Planetary Science Letters, vol. 293, no. 1-2, pages 72–83, April 2010. www

[Deniel 87] Catherine Deniel, Philippe Vidal, Angel Fernandez, Patrick Le Fort & Jean-Jacques Peucat. *Isotopic study of the Manaslu granite (Himalaya, Nepal) : inferences on the age and source of Himalayan leucogranites.* Contributions to Mineralogy and Petrology, vol. 96, no. 1, pages 78–92, 1987.

[Derry 96] Louis A. Derry & Christian France-Lanord. *Neogene Himalayan weathering history and river87Sr86Sr : impact on the marine Sr record.* Earth and Planetary Science Letters, vol. 142, no. 1-2, pages 59–74, 1996. www

[Devkota 12] Krishna Chandra Devkota, Amar Deep Regmi, Hamid Reza Pourghasemi, Kohki Yoshida, Biswajeet Pradhan, In Chang Ryu, Megh Raj Dhital & Omar F. Althuwaynee. *Landslide susceptibility mapping using certainty factor, index of entropy and logistic regression models in GIS and their comparison at Mugling–Narayanghat road section in Nepal Himalaya.* Natural Hazards, vol. 65, no. 1, pages 135–165, 2012. www

[DHM 03] DHM. *Suspended Sediment Concentration Records.* Rapport technique, Department of Hydrology and Meteorology, His Majesty's Government, Kathmandu, Nepal, 2003.

[DHM/FFS 04] DHM/FFS. *Hydrological Data (2002–2003).* Rapport technique, Department of Hydrologyand Meteorology, Flood Forecasting Section, Kathmandu, Nepal, 2004.

[Dingle 12] Elizabeth Dingle. *The effects of differential uplift and sediment supply on major Himalayan river systems at the mountain front.* PhD thesis, Durham University, 2012. www

[Dixon 09a] J L Dixon, A M Heimsath, J Kaste & R Amundson. *Climate-driven processes of hillslope weathering.* Geology, vol. 37, no. 11, pages 975–978, 2009. www

[Dixon 09b] Jean L Dixon, Arjun M Heimsath & Ronald Amundson. *The critical role of climate and saprolite weathering in landscape evolution.* Earth Surface Processes and Landforms, vol. 34, no. 11, pages 1507–1521, 2009. www

[Dubille 15] Matthieu Dubille & Jérôme Lavé. *Rapid grain size coarsening at sandstone/conglomerate transition : similar expression in Himalayan modern rivers and Pliocene molasse deposits.* Basin Research, vol. 27, no. 1, pages 26–42, February 2015. www

[Duller 08] Geoffrey a. T. Duller. *Single-grain optical dating of Quaternary sediments : why aliquot size matters in luminescence dating.* Boreas, vol. 37, no. 4, pages 589–612, November 2008. www

[Eckhardt 05] K. Eckhardt. *How to construct recursive digital filters for baseflow separation.* Hydrological Processes, vol. 19, no. 2, pages 507–515, February 2005. www

[Eckhardt 08] K. Eckhardt. *A comparison of baseflow indices, which were calculated with seven different baseflow separation methods.* Journal of Hydrology, vol. 352, no. 1-2, pages 168–173, April 2008. www

[Edmond 92] J M Edmond. *Himalayan tectonics, weathering processes, and the strontium isotope record in marine limestones.* Science, 1992. www

[Egholm 09] D L Egholm, S B Nielsen, V K Pedersen & J E Lesemann. *Glacial effects limiting mountain height.* Nature, vol. 460, no. 7257, pages 884–887, 2009. www

[Egholm 13] David L. Egholm, Mads F. Knudsen & Mike Sandiford. *Lifespan of mountain ranges scaled by feedbacks between landsliding and*

erosion by rivers. Nature, vol. 498, no. 7455, pages 475–478, 2013. www

[Enzel 99] Y. Enzel. *High-Resolution Holocene Environmental Changes in the Thar Desert, Northwestern India.* Science, vol. 284, no. 5411, pages 125–128, April 1999. www

[Evans 01] Matthew J. Evans, Louis a. Derry, Suzanne P. Anderson & Christian France-Lanord. *Hydrothermal source of radiogenic Sr to Himalayan rivers.* Geology, vol. 29, no. 9, page 803, 2001. www

[Evans 04] Matthew J Evans. *Geothermal fluxes of alkalinity in the Narayani river system of central Nepal.* Geochemistry Geophysics Geosystems, vol. 5, no. 8, 2004. www

[Fairchild 99] Ian J Fairchild, Jacque A Killawee, Bryn Hubbard & Wolfgang Dreybrodt. *Interactions of calcareous suspended sediment with glacial meltwater : a field test of dissolution behaviour.* Chemical Geology, vol. 155, no. 3, pages 243–263, 1999.

[Fielding 94] Eric Fielding, Bryan Isacks, Muawia Barazangi & Christopher Duncan. *How flat is Tibet ?* Geology, vol. 22, no. 2, page 163, 1994. www

[Filizola 04] Naziano Filizola & Jean Loup Guyot. *The use of Doppler technology for suspended sediment discharge determination in the River Amazon / L'utilisation des techniques Doppler pour la détermination du transport solide de l'Amazone.* Hydrological Sciences Journal, vol. 49, no. 1, pages 143–153, February 2004. www

[Finkel 03] Robert C. Finkel, Lewis A. Owen, Patrick L. Barnard & Marc W. Caffee. *Beryllium-10 dating of Mount Everest moraines indicates a strong monsoon influence and glacial synchroneity throughout the Himalaya.* Geology, vol. 31, no. 6, page 561, 2003. www

[Finnegan 08] N J Finnegan, B Hallet, D R Montgomery, P K Zeitler, J O Stone, A M Anders & L Yuping. *Coupling of rock uplift and river incision in the Namche Barwa-Gyala Peri massif, Tibet.* Geological Society of America Bulletin, vol. 120, no. 1-2, pages 142–155, 2008. www

[Fischer 06] L. Fischer, A. Kääb, C. Huggel & J. Noetzli. *Geology, glacier retreat and permafrost degradation as controlling factors of slope instabilities in a high-mountain rock wall : the Monte Rosa east face.* Natural Hazards and Earth System Science, vol. 6, no. 5, pages 761–772, September 2006. www

[Fort 87a] M Fort. *Sporadic morphogenesis in a continental subduction setting : an example from the Annapurna Range, Nepal Himalaya.* Zeitschrift für Geomorphologie, vol. 63, no. 9, page 36, 1987.

[Fort 87b] M Fort. *Sporadic morphogenesis in a continental subduction setting : an example from the Annapurna Range, Nepal Himalaya.* Zeitschrift für Geomorphologie, vol. 63, no. 9, page 36, 1987.

[Fort 09] Monique Fort, Etienne Cossart, Philip Deline, Marc Dzikowski, Gérard Nicoud, Ludovic Ravanel, Philippe Schoeneich & Patrick Wassmer. Geomorphic impacts of large and rapid mass movements : a review. Numeéro 1/2009. Groupe français de géomorphologie, 2009.

[Fort 10] M. Fort, E. Cossart & G. Arnaud-Fassetta. *Hillslope-channel coupling in the Nepal Himalayas and threat to man-made structures : The middle Kali Gandaki valley.* Geomorphology, vol. 124, no. 3-4, pages 178–199, December 2010. www

[France-Lanord 87] Christian France-Lanord. *Chevauchement, métamorphisme et magmatisme en Himalaya du Népal central étude isotopique H, C, O.* PhD thesis, Institut National Polytechnique de Lorraine, 1987.

[France-Lanord 88] Christian France-Lanord & Patrick Le Fort. *Crustal melting and granite genesis during the Himalayan collision orogenesis.* Transactions of the Royal Society of Edinburgh : Earth Sciences, vol. 79, no. 2-3, pages 183–195, 1988.

[France-Lanord 93] C France-Lanord, L Derry & A Michard. *Evolution of the Himalaya since Miocene time : isotopic and sedimentological evidence from the Bengal Fan.* Geological Society, London, Special Publications, vol. 74, no. 1, pages 603–621, January 1993.

[France-Lanord 97] C France-Lanord & LA Derry. *Organic carbon burial forcing of the carbon cycle from Himalayan erosion.* Nature, vol. 390, no. November, pages 65–68, 1997. www

[France-Lanord 03] Christian France-Lanord, Matthew Evans, Jean-Emmanuel Hurtrez & Jean Riotte. *Annual dissolved fluxes from Central Nepal rivers : budget of chemical erosion in the Himalayas.* Comptes Rendus Geoscience, vol. 335, no. 16, pages 1131–1140, 2003. www

[Froelich 14] Flip Froelich. *Was the Late Paleocene-Early Eocene Hot Because Earth Was Flat ? An Ocean Lithium Isotope View of Mountain Building, Continental Weathering, Carbon Dioxide, and Earth's Cenozoic Clima.* Oceanography, vol. 27, no. 1, pages 36–49, March 2014. www

[Fukushima 87] Yoshihiro Fukushima, K Kawashima, M Suzuki, T Ohta, H Motoyama, H Kubota, T Yamada & OM RATNA BAJRACHARYA. *Runoff characteristics in three glacier-covered watersheds of Langtang Valley, Nepal Himalayas.* Bulletin of glacier research, no. 5, pages 11–18, 1987.

[Fuller 03] Christopher W. Fuller, Sean D. Willett, Niels Hovius & Rudy Slingerland. *Erosion Rates for Taiwan Mountain Basins : New Determinations from Suspended Sediment Records and a Stochastic Model of Their Temporal Variation.* The Journal of Geology, vol. 111, no. 1, pages 71–87, January 2003. www

[Furey 01] Peter R Furey & Vijay K Gupta. *A physically based filter for separating base flow from streamflow time series.* Water Resources Research, vol. 37, no. 11, pages 2709–2722, 2001.

[Gabet 04a] EJ Gabet, DW Burbank & JK Putkonen. *Rainfall thresholds for landsliding in the Himalayas of Nepal.* Geomorphology, vol. 63, no. 3-4, pages 131–143, 2004. www

[Gabet 04b] Emmanuel J. Gabet, Beth a. Pratt-Sitaula & Douglas W. Burbank. *Climatic controls on hillslope angle and relief in the Himalayas.* Geology, vol. 32, no. 7, page 629, 2004. www

[Gabet 07] Emmanuel J Gabet. *A theoretical model coupling chemical weathering and physical erosion in landslide-dominated landscapes.* Earth and Planetary Science Letters, vol. 264, no. 1-2, pages 259–265, 2007. www

[Gabet 08] E Gabet, D Burbank, B Prattsitaula, J Putkonen & B Bookhagen. *Modern erosion rates in the High Himalayas of Nepal.* Earth and Planetary Science Letters, vol. 267, no. 3-4, pages 482–494, March 2008. www

[Gabet 09] E J Gabet & S M Mudd. *A theoretical model coupling chemical weathering rates with denudation rates.* Geology, vol. 37, no. 2, pages 151–154, 2009.

[Gadgil 04] Sulochana Gadgil. *Extremes of the Indian summer monsoon rainfall, ENSO and equatorial Indian Ocean oscillation.* Geophysical Research Letters, vol. 31, no. 12, 2004. www

[Gaillardet 99a] J Gaillardet, B. Dupré & C.J. Allègre. *Geochemistry of large river suspended sediments : silicate weathering or recycling tracer ?* Geochimica et Cosmochimica Acta, vol. 63, no. 23-24, pages 4037–4051, 1999. www

[Gaillardet 99b] J Gaillardet, B DUPRE & P LOUVAT. *Global silicate weathering and CO2 consumption rates deduced from the chemistry of large rivers.* Chemical Geology, 1999. www

[Gajurel 06] Ananta Prasad Gajurel, Christian France-Lanord, Pascale Huyghe, Caroline Guilmette & Damayanti Gurung. *C and O isotope compositions of modern fresh-water mollusc shells and river waters from the Himalaya and Ganga plain.* Chemical Geology, vol. 233, no. 1-2, pages 156–183, September 2006. www

[Gallo 14a] F. Gallo & J. Lavé. *Evolution of a large landslide in the High Himalaya of central Nepal during the last half-century.* Geomorphology, vol. 223, pages 20–32, October 2014. www

[Gallo 14b] Florian Gallo. *Glissements de terrain et érosion des chaînes de montagnes : étude de cas dans l'Himalaya central.* PhD

thesis, 2014. Thèse de doctorat dirigée par Lavé, Jérôme et France-Lanord, Christian Géosciences Université de Lorraine 2014 2014LORR0093. www

[Galy 99a] Albert Galy. *Etude géochimique de l'érosion actuelle de la chaîne himalayenne*. PhD thesis, Institut national polytechnique de Lorraine, Vandoeuvre-lès-Nancy, FRANCE, January 1999.

[Galy 99b] Albert Galy & Christian France-Lanord. *Weathering processes in the Ganges–Brahmaputra basin and the riverine alkalinity budget*. Chemical Geology, 1999. www

[Galy 99c] Albert Galy, Christian France-Lanord & Louis A Derry. *The strontium isotopic budget of Himalayan rivers in Nepal and Bangladesh*. Geochimica et Cosmochimica Acta, vol. 63, no. 13-14, pages 1905–1925, July 1999. www

[Galy 01] A Galy & C France-Lanord. *Higher erosion rates in the Himalaya : Geochemical constraints on riverine fluxes*. Geology, 2001. www

[Galy 07a] Valier Galy. *Source, transport et enfouissement du carbone organique lors de l'érosion continentale : l'exemple du système himalayen*. PhD thesis, 2007. www

[Galy 07b] Valier Galy, Julien Bouchez & Christian France-Lanord. *Determination of Total Organic Content and delta13C in Carbonate-Rich Detrital Sediments*. Geostandards and Geoanalytical Research, vol. 31, no. 3, pages 199–207, September 2007.

[Galy 07c] Valier Galy, Christian France-Lanord, Olivier Beyssac, Pierre Faure, Hermann Kudrass & Fabien Palhol. *Efficient organic carbon burial in the Bengal fan sustained by the Himalayan erosional system.* Nature, vol. 450, no. 7168, pages 407–10, November 2007. www

[Galy 08] Valier Galy, Christian France-Lanord & Bruno Lartiges. *Loading and fate of particulate organic carbon from the Himalaya to the Ganga–Brahmaputra delta*. Geochimica et Cosmochimica Acta, vol. 72, no. 7, pages 1767–1787, April 2008. www

[Galy 10] Valier Galy, Christian France-Lanord, Bernhard Peucker-Ehrenbrink & Pascale Huyghe. *Sr–Nd–Os evidence for a stable erosion regime in the Himalaya during the past 12Myr.* Earth and Planetary Science Letters, vol. 290, no. 3, pages 474–480, 2010.

[Galy 11a] Valier Galy & Timothy Eglinton. *Protracted storage of biospheric carbon in the Ganges-Brahmaputra basin.* Nature Geosci, vol. 4, no. 12, pages 843–847, 2011. www

[Galy 11b] Valier Galy, Timothy Eglinton, Christian France-Lanord & Sean Sylva. *The provenance of vegetation and environmental signatures encoded in vascular plant biomarkers carried by the Ganges–Brahmaputra rivers.* Earth and Planetary Science Letters, vol. 304, no. 1-2, pages 1–12, 2011. www

[Garcia 08] Marcelo H Garcia & others. *Sedimentation transport and morphodynamics.* In Sedimentation Engineering : Processes, Measurements, Modeling, and Practice., volume 110 of *ASCE Manuals and Reports on Engineering Practice*, pages 21 – 164. American Society of Civil Engineering, Reston, Va, 2008.

[Garçon 14] Marion Garçon, Catherine Chauvel, Christian France-Lanord, Mara Limonta & Eduardo Garzanti. *Which minerals control the Nd–Hf–Sr–Pb isotopic compositions of river sediments ?* Chemical Geology, vol. 364, pages 42–55, 2014.

[Gardner 96] R Gardner & N Walsh. *Chemical weathering of metamorphic rocks from low elevations in the southern Himalaya.* Chemical Geology, 1996. www

[Gardner 03] R Gardner. *Runoff and soil erosion on cultivated rainfed terraces in the Middle Hills of Nepal.* Applied Geography, vol. 23, no. 1, pages 23–45, 2003. www

[Garrels 67] ROBERT M Garrels & FRED T Mackenzie. *Origin of the chemical compositions of some springs and lakes.* Equilibrium concepts in natural water systems, vol. 67, pages 222–242, 1967.

[Garzanti 07] Eduardo Garzanti, Giovanni Vezzoli, Sergio Andò & Jérôme Lavé. *Quantifying sand provenance and erosion (Marsyandi River, Nepal Himalaya).* Earth and Planetary \ldots, vol. 258, no. 3-4, pages 500–515, 2007. www

[Garzanti 10] Eduardo Garzanti, Sergio Andò, Christian France-Lanord, Giovanni Vezzoli, Paolo Censi, Valier Galy & Yani Najman. *Mineralogical and chemical variability of fluvial sediments1. Bedload sand (Ganga–Brahmaputra, Bangladesh).* Earth and Planetary Science Letters, vol. 299, no. 3-4, pages 368–381, November 2010. www

[Garzanti 11] Eduardo Garzanti, Sergio Andó, Christian France-Lanord, Paolo Censi, Pietro Vignola, Valier Galy & Maarten Lupker. *Mineralogical and chemical variability of fluvial sediments 2. Suspended-load silt (Ganga–Brahmaputra, Bangladesh).* Earth and Planetary Science Letters, vol. 302, no. 1-2, pages 107–120, 2011. www

[Garzione 00] C N Garzione, J Quade & P G DeCelles. *Predicting paleoelevation of Tibet and the Himalaya from [delta] 18O vs. altitude gradients in meteoric water across the Nepal Himalaya.* Earth and Planetary \ldots, 2000. www

[Garzione 08] Carmala N Garzione, Gregory D Hoke, Julie C Libarkin, Saunia Withers, Bruce MacFadden, John Eiler, Prosenjit Ghosh & Andreas Mulch. *Rise of the Andes.* Science (New York, N.Y.), vol. 320, no. 5881, pages 1304–7, 2008. www

[Gayer 06] E Gayer, J Lavé, R Pik & Christian France-Lanord. *Monsoonal forcing of Holocene glacier fluctuations in Ganesh Himal (Central Nepal) constrained by cosmogenic 3He exposure ages of garnets.* Earth and Planetary Science Letters, vol. 252, no. 3-4, pages 275–288, 2006. www

[Ghimire 90] G. P. S. Ghimire & B. K. Uprety. *Causes and effects of siltation on the environment of Nepal.* The Environmentalist, vol. 10, no. 1, pages 55–65, March 1990. www

[Ghimire 06] Sohan K. Ghimire, Daisuke Higaki & Tara P. Bhattarai. *Gully erosion in the Siwalik Hills, Nepal : estimation of sediment production from active ephemeral gullies.* Earth Surface Processes and Landforms, vol. 31, no. 2, pages 155–165, February 2006. www

[Ghimire 13a] Chandra Prasad Ghimire, Mike Bonell, L. Adrian Bruijnzeel, Neil a. Coles & Maciek W. Lubczynski. *Reforesting severely degraded grassland in the Lesser Himalaya of Nepal : Effects on soil hydraulic conductivity and overland flow production.* Journal of Geophysical Research : Earth Surface, vol. 118, no. 4, pages 2528–2545, 2013. www

[Ghimire 13b] Sohan Ghimire, Daisuke Higaki & Tara Bhattarai. *Estimation of Soil Erosion Rates and Eroded Sediment in a Degraded Catchment of the Siwalik Hills, Nepal.* Land, vol. 2, no. 3, pages 370–391, 2013. www

[Gilg 96] H. Albert Gilg & Simon M.F. Sheppard. *Hydrogen isotope fractionation between kaolinite and water revisited.* Geochimica et Cosmochimica Acta, vol. 60, no. 3, pages 529–533, 1996. www

[Gilg 00] H.Albert Gilg. *D–H evidence for the timing of kaolinization in Northeast Bavaria, Germany.* Chemical Geology, vol. 170, no. 1-4, pages 5–18, October 2000. www

[Girard 96] Jean-Pierre Girard & Samuel M. Savin. *Intracrystalline fractionation of oxygen isotopes between hydroxyl and non-hydroxyl sites in kaolinite measured by thermal dehydroxylation and partial fluorination.* Geochimica et Cosmochimica Acta, vol. 60, no. 3, pages 469–487, 1996. www

[Girard 97] J P Girard & D Razanadranorosoa. *Laser oxygen isotope analysis of weathering goethite from the lateritic profile of Yaou, French Guiana : paleoweathering and paleoclimatic implications.* Applied Geochemistry, 1997. www

[Gislason 06] Sigurdur R. Gislason, Eric H. Oelkers & Árni Snorrason. *Role of river-suspended material in the global carbon cycle.* Geology, vol. 34, no. 1, pages 49–52, 2006. www

[Gislason 09] Sigurdur R Gislason, Eric H Oelkers, Eydis S Eiriksdottir, Marin I Kardjilov, Gudrun Gisladottir, Bergur Sigfusson, Arni Snorrason, Sverrir Elefsen, Jorunn Hardardottir, Peter Torssander & Niels Oskarsson. *Direct evidence of the feedback between climate and weathering.* Earth and Planetary Science Letters, vol. 277, no. 1-2, pages 213–222, January 2009. www

[Godard 06] V. Godard, J. Lave & R. Cattin. *Numerical modelling of erosion processes in the Himalayas of Nepal : effects of spatial variations of rock strength and precipitation.* Geological Society, London, Special Publications, vol. 253, no. 1, pages 341–358, January 2006. www

[Godard 12] V. Godard, D. W. Burbank, D.L. Bourles, B. Bookhagen, R. Braucher, G. B. Fisher & D. L. Bourlès. *Impact of glacial erosion on 10 Be concentrations in fluvial sediments of the Marsyandi catchment, central Nepal.* Journal of Geophysical Research, vol. 117, no. F3, pages 1–17, 2012. www

[Godard 14] V. Godard, D. L. Bourles, F. Spinabella, D. W. Burbank, B. Bookhagen, G. B. Fisher, A. Moulin & L. Leanni. *Dominance of tectonics over climate in Himalayan denudation.* Geology, no. January, January 2014. www

[Gong 07] Bing Gong, Yong-Fei Zheng & Ren-Xu Chen. *TC/EA-MS online determination of hydrogen isotope composition and water concentration in eclogitic garnet.* Physics and Chemistry of Minerals, vol. 34, no. 10, pages 687–698, 2007. www

[Goodbred 00] Steven L. Goodbred & Steven A. Kuehl. *Enormous Ganges-Brahmaputra sediment discharge during strengthened early Holocene monsoon.* Geology, vol. 28, no. 12, pages 1083–1086, 2000. www

[Goodbred 03] Steven L. Goodbred. *Response of the Ganges dispersal system to climate change : a source-to-sink view since the last interstade.* Sedimentary Geology, vol. 162, no. 1-2, pages 83–104, November 2003. www

[Govindaraju 87] Kuppusami ;Mevelle Govindaraju Guy. *Fully automated dissolution and separation methods for inductively coupled plasma atomic emission spectrometry rock analysis. Application to the determination of rare earth elements. Plenary lecture.* Journal of analytical atomic spectrometry, vol. 2, no. 6, page 615, January 1987.

[Granger 96] Darryl E. Granger, James W. Kirchner & Robert Finkel. *Spatially Averaged Long-Term Erosion Rates Measured from in Situ-Produced Cosmogenic Nuclides in Alluvial Sediment.* The Journal of Geology, vol. 104, no. 3, pages pp. 249–257, 1996. www

[Grujic 04] D Grujic, I Coutand & B BOOKHAGEN. *Dissimilar denudation histories along the Himalaya : Climatic causes—tectonic and landscape responses.* Nova, no. 1, pages 123–124, 2004. www

[Grujic 06] Djordje Grujic, Isabelle Coutand, Bodo Bookhagen, Stéphane Bonnet, Ann Blythe & Chris Duncan. *Climatic forcing of erosion, landscape, and tectonics in the Bhutan Himalayas.* Geology, vol. 34, no. 10, page 801, 2006. www

[Gu 93] Zhaoyan Gu, Jiaqi Liu, Baoyin Yuan, Tunsheng Liu, Rongmo Liu, Yu Liu, Gaungyu Zhang & K Yasukawa. *The changes in monsoon influence in the Qinghai-Tibetan Plateau during the past 12, 000 years : geochemical evidence from the lake Selin sediments.* Chinese Science Bulletin, vol. 38, no. 1, pages 61–64, 1993.

[Gupta 97] S Gupta. *Himalayan drainage patterns and the origin of fluvial megafans in the Ganges foreland basin.* Geology, vol. 25, no. 1, page 11, 1997. www

[Gurung 05] JayaK. Gurung, Hiroaki Ishiga & MohanS. Khadka. *Geological and geochemical examination of arsenic contamination in*

groundwater in the Holocene Terai Basin, Nepal. Environmental Geology, vol. 49, no. 1, pages 98–113, 2005. www

[Hallet 96] B Hallet, L Hunter & J Bogen. *Rates of erosion and sediment evacuation by glaciers : A review of field data and their implications*. Global and Planetary Change, vol. 12, no. 1-4, pages 213–235, 1996. www

[Harden 93] Carol P. Harden. *Land Use, Soil Erosion, and Reservoir Sedimentation in an Andean Drainage Basin in Ecuador*. Mountain Research and Development, vol. 13, no. 2, page 177, May 1993. www

[Haritashya 10] Umesh K Haritashya, Amit Kumar & Pratap Singh. *Particle size characteristics of suspended sediment transported in meltwater from the Gangotri Glacier, central Himalaya — An indicator of subglacial sediment evacuation*. Geomorphology, vol. 122, no. 1-2, pages 140–152, 2010. www

[Hasnain 99] S.I. Hasnain & R.J. Thayyen. *Discharge and suspended-sediment concentration of meltwaters, draining from the Dokriani glacier, Garhwal Himalaya, India*. Journal of Hydrology, vol. 218, no. 3-4, pages 191–198, May 1999. www

[Hayes 99] John M. Hayes, Harald Strauss & Alan J. Kaufman. *The abundance of 13C in marine organic matter and isotopic fractionation in the global biogeochemical cycle of carbon during the past 800 Ma*. Chemical Geology, vol. 161, no. 1-3, pages 103–125, September 1999. www

[Hedges 95] John I. Hedges & Richard G. Keil. *Sedimentary organic matter preservation : an assessment and speculative synthesis*. Marine Chemistry, vol. 49, no. 2-3, pages 81–115, 1995. www

[Heimsath 12] Arjun M Heimsath, Roman A DiBiase & Kelin X Whipple. *Soil production limits and the transition to bedrock-dominated landscapes*. Nature Geoscience, vol. 5, no. 3, pages 210–214, 2012. www

[Herman 10] Frédéric Herman, Peter Copeland, Jean-Philippe Avouac, Laurent Bollinger, Gweltaz Mahéo, Patrick Le Fort, Santaman Rai, David Foster, Arnaud Pêcher, Kurt Stüwe & Pierre Henry. *Exhumation, crustal deformation, and thermal structure of the Nepal Himalaya derived from the inversion of thermochronological and thermobarometric data and modeling of the topography.* Journal of Geophysical Research, vol. 115, no. B6, June 2010. www

[Herman 13] Frédéric Herman, Diane Seward, Pierre G. Valla, Andrew Carter, Barry Kohn, Sean D. Willett & Todd A. Ehlers. *Worldwide acceleration of mountain erosion under a cooling climate.* Nature, vol. 504, no. 7480, pages 423–426, December 2013. www

[Herman 15] F. Herman, O. Beyssac, M. Brughelli, S. N. Lane, S. Leprince, T. Adatte, J. Y. Y. Lin, J.-P. Avouac & S. C. Cox. *Erosion by an Alpine glacier.* Science, vol. 350, no. 6257, pages 193–195, October 2015. www

[Hetényi 06] György Hetényi, Rodolphe Cattin, Jérôme Vergne & John L. Nábělek. *The effective elastic thickness of the India Plate from receiver function imaging, gravity anomalies and thermomechanical modelling.* Geophysical Journal International, vol. 167, no. 3, pages 1106–1118, December 2006. www

[Hilley 10] G E Hilley, C P Chamberlain, S Moon, S Porder & S D Willett. *Competition between erosion and reaction kinetics in controlling silicate-weathering rates.* Earth and Planetary Science Letters, vol. 293, no. 1-2, pages 191–199, 2010. www

[Hilton 08] Robert G. Hilton, Albert Galy, Niels Hovius, Meng-Chiang Chen, Ming-Jame Horng & Hongey Chen. *Tropical-cyclone-driven erosion of the terrestrial biosphere from mountains.* Nature Geoscience, vol. 1, no. 11, pages 759–762, October 2008. www

[Hodges 00] K. V. Hodges. *Tectonics of the Himalaya and southern Tibet from two perspectives.* Geological Society of America Bulletin, vol. 112, no. 3, pages 324–350, March 2000. www

[Hovius 97] Niels Hovius, Colin P. Stark & Philip A. Allen. *Sediment flux from a mountain belt derived by landslide mapping.* Geology, vol. 25, no. 3, page 231, 1997. www

[Hovius 00] Niels Hovius, Colin P Stark, Chu Hao-Tsu & Lin Jiun-Chuan. *Supply and removal of sediment in a landslide-dominated mountain belt : Central Range, Taïwan.* The Journal of Geology, vol. 108, no. 1, pages 73–89, 2000. www

[Huyghe 01] Pascale Huyghe, Albert Galy, Jean-Louis Mugnier & Christian France-Lanord. *Propagation of the thrust system and erosion in the Lesser Himalaya : Geochemical and sedimentological evidence.* Geology, vol. 29, no. 11, page 1007, 2001. www

[Huyghe 05] P Huyghe, J L Mugnier, A P Gajurel & B Delcaillau. *Tectonic and climatic control of the changes in the sedimentary record of the Karnali River section (Siwaliks of Western Nepal).* Island Arc, vol. 14, no. 4, pages 311–327, 2005. www

[Immerzeel 10] W. W. Immerzeel, L. P. H. van Beek & M. F. P. Bierkens. *Climate Change Will Affect the Asian Water Towers.* Science, vol. 328, no. 5984, pages 1382–1385, June 2010. www

[Iverson 00] Richard M. Iverson. *Landslide triggering by rain infiltration.* Water Resources Research, vol. 36, no. 7, pages 1897–1910, July 2000. www

[Iverson 12] N. R. Iverson. *A theory of glacial quarrying for landscape evolution models.* Geology, vol. 40, no. 8, pages 679–682, 2012. www

[Ives 89] Jack D Ives & Bruno Messerli. The Himalayan dilemma : reconciling development and conservation. Psychology Press, 1989.

[Jacobsen 80] Stein B. Jacobsen & G. J. Wasserburg. *Sm-Nd isotopic evolution of chondrites.* Earth and Planetary Science Letters, vol. 50, no. 1, pages 139–155, 1980.

[Jain 03] Vikrant Jain & R. Sinha. *River systems in the Gangetic plains and their comparison with the Siwaliks : A review.* Current Science, vol. 84, no. 8, pages 1025–1033, 2003.

[Jones 12] Morgan T. Jones, Christopher R. Pearce, Catherine Jeandel, Sigurður R. Gislason, Eydis S. Eiriksdottir, Vasileios Mavromatis & Eric H. Oelkers. *Riverine particulate material dissolution as a significant flux of strontium to the oceans.* Earth and Planetary Science Letters, vol. 355-356, pages 51–59, November 2012. WWW

[Jones 14] Morgan T. Jones, Sigurður R. Gislason, Kevin W. Burton, Christopher R. Pearce, Vasileios Mavromatis, Philip a.E. Pogge von Strandmann & Eric H. Oelkers. *Quantifying the impact of riverine particulate dissolution in seawater on ocean chemistry.* Earth and Planetary Science Letters, vol. 395, pages 91–100, 2014. WWW

[Kirchner 06] James W Kirchner. *Getting the right answers for the right reasons : Linking measurements, analyses, and models to advance the science of hydrology.* Water Resources Research, vol. 42, no. 3, 2006.

[Kirchner 13] James W. Kirchner & Ken L. Ferrier. *Earth science : Mainly in the plain.* Nature, vol. 495, no. 7441, pages 318–319, March 2013. WWW

[Koons 90] P. O. Koons. *Two-sided orogen : Collision and erosion from the sandbox to the Southern Alps, New Zealand.* Geology, vol. 18, no. 8, page 679, 1990. WWW

[Koppes 09] Michele N Koppes & David R Montgomery. *The relative efficacy of fluvial and glacial erosion over modern to orogenic timescales.* Nature Geoscience, vol. 2, no. 9, pages 644–647, 2009. WWW

[Koppes 15] Michéle Koppes, Bernard Hallet, Eric Rignot, Jérémie Mouginot, Julia Smith Wellner & Katherine Boldt. *Observed latitudinal variations in erosion as a function of glacier dynamics.* Nature, vol. 526, no. 7571, pages 100–103, October 2015. WWW

[Korup 10] Oliver Korup, Alexander L. Densmore & Fritz Schlunegger. *The role of landslides in mountain range evolution.* Geomorphology, vol. 120, no. 1-2, pages 77–90, 2010. WWW

[Krishnaswami 92] S Krishnaswami, JR Trivedi, MM Sarin, R Ramesh & KK Sharma. *Strontium isotopes and rubidium in the Ganga-Brahmaputra river system : Weathering in the Himalaya, fluxes to the Bay of Bengal and contributions to the evolution of oceanic 87 Sr/86 Sr.* Earth and Planetary Science Letters, vol. 109, no. 1, pages 243–253, 1992.

[Kudrass 01] H.R. Kudrass, A. Hofmann, H. Doose, K. Emeis & H. Erlenkeuser. *Modulation and amplification of climatic changes in the Northern Hemisphere by the Indian summer monsoon during the past 80 k.y.* Geology, vol. 29, no. 1, page 63, 2001. www

[Kump 00] L R Kump, S L Brantley & M A Arthur. *Chemical weathering, atmospheric CO2, and climate.* Annual Review of Earth and Planetary Sciences, vol. 28, no. 1, pages 611–667, 2000. www

[Lal 91] D. Lal. *Cosmic ray labeling of erosion surfaces : in situ nuclide production rates and erosion models.* Earth and Planetary Science Letters, vol. 104, no. 2-4, pages 424–439, June 1991. www

[Lambert 89] Larason Lambert & BD Chitrakar. *Variation of potential evapotranspiration with elevation in Nepal.* Mountain Research and Development, pages 145–152, 1989.

[Larsen 97] Matthew C. MC Larsen & John E. JE Parks. *How wide is a road ? The association of roads and mass-wasting in a forested montane environment.* Earth Surface Processes and Landforms, vol. 22, no. 9, pages 835–848, September 1997. www

[Larsen 10] Isaac J. Larsen, David R. Montgomery & Oliver Korup. *Landslide erosion controlled by hillslope material.* Nature Geoscience, vol. 3, no. 4, pages 247–251, April 2010. www

[Larsen 12] Isaac J. Larsen & David R. Montgomery. *Landslide erosion coupled to tectonics and river incision.* Nature Geoscience, vol. 5, no. 7, pages 468–473, 2012. www

[Larsen 14a] I. J. Larsen, D. R. Montgomery & H. M. Greenberg. *The contribution of mountains to global denudation.* Geology, no. April, 2014. www

[Larsen 14b] Isaac J Larsen, Peter C Almond, Andre Eger, John O Stone, David R Montgomery & Brendon Malcolm. *Rapid Soil Production and Weathering in the Western Alps, New Zealand.* Science (New York, N.Y.), vol. 637, January 2014. www

[Larson 99] Kristine M. Larson, Roland Bürgmann, Roger Bilham & Jeffrey T. Freymueller. *Kinematics of the India-Eurasia collision zone from GPS measurements.* Journal of Geophysical Research, vol. 104, no. B1, page 1077, 1999. www

[Lavé 00] J. Lavé & J. P. Avouac. *Active folding of fluvial terraces across the Siwaliks Hills, Himalayas of central Nepal.* Journal of Geophysical Research, vol. 105, no. B3, page 5735, 2000. www

[Lavé 01] J. Lavé & J. P. Avouac. *Fluvial incision and tectonic uplift across the Himalayas of central Nepal.* Journal of Geophysical Research, vol. 106, no. B11, page 26561, 2001. www

[Lavé 04] J. Lavé & D. W. Burbank. *Denudation processes and rates in the Transverse Ranges, southern California : Erosional response of a transitional landscape to external and anthropogenic forcing.* Journal of Geophysical Research, vol. 109, no. F01006, pages 1–31, 2004. www

[Lawrence 72] J.R Lawrence & H.P Taylor. *Hydrogen and oxygen isotope systematics in weathering profiles.* Geochimica et Cosmochimica Acta, vol. 36, no. 12, pages 1377–1393, December 1972. www

[Le Fort 75] Patrick Le Fort. *Himalayas : the collided range. Present knowledge of the continental arc.* American Journal of Science, vol. 275, no. 1, pages 1 – 44, 1975.

[Le Fort 87] P Le Fort, M Cuney, C Deniel, C France-Lanord, S M F Sheppard, B N Upreti & P H Vidal. *Crustal generation of the Himalayan leucogranites.* Tectonophysics, vol. 134, no. 1-3, pages 39–57, 1987. www

[Lebeau 14] Oanez Lebeau, Vincent Busigny, Carine Chaduteau & Magali Ader. *Organic matter removal for the analysis of carbon and oxygen isotope compositions of siderite.* Chemical Geology, vol. 372, pages 54–61, 2014. www

[Licht 14] A. Licht, M. van Cappelle, H. A. Abels, J.-B. Ladant, J. Trabucho-Alexandre, C. France-Lanord, Y. Donnadieu, J. Vandenberghe, T. Rigaudier, C. Lécuyer, D. Terry Jr, R. Adriaens, A. Boura, Z. Guo, Aung Naing Soe, J. Quade, G. Dupont-Nivet & J.-J. Jaeger. *Asian monsoons in a late Eocene greenhouse world.* Nature, vol. 513, no. 7519, pages 501–506, September 2014. www

[Loke 99] M H Loke. *Electrical imaging surveys for environmental and engineering studies.* A practical guide to, vol. 2, no. 1999, 1999. www

[Lorphelin 85] Lénaïck Lorphelin. *Etude d'une séquence altitudinale de sols le long d'un versant-type de l'Himalaya népalais : les sols du versant Salmé = Study of an altitudinal soils sequences along a type basin of Nepal Himalaya : the soils of Salmé basin.* PhD thesis, Université de Poitiers, 1985. www

[Lupker 11a] Maarten Lupker. *Dynamique sédimentaire, érosion physique et altération chimique dans le système himalayen.* Thèse de doctorat en Géosciences, Université de Lorraine, Vandoeuvre-les-Nancy, INPL, 2011.

[Lupker 11b] Maarten Lupker, Christian France-Lanord, Jérôme Lavé, Julien Bouchez, Valier Galy, François Métivier, Jérôme Gaillardet, Bruno Lartiges & Jean-Louis Mugnier. *A Rouse-based method to integrate the chemical composition of river sediments : Application to the Ganga basin.* Journal of Geophysical Research, vol. 116, no. F4, page F04012, November 2011. www

[Lupker 12a] Maarten Lupker, Pierre-Henri Blard, Jérôme Lavé, Christian France-Lanord, Laetitia Leanni, Nicolas Puchol, Julien Charreau & Didier Bourlès. *10Be-derived Himalayan denudation rates*

and sediment budgets in the Ganga basin. Earth and Planetary Science Letters, vol. 333-334, no. C, pages 146–156, 2012.

[Lupker 12b] Maarten Lupker, Christian France-Lanord, Valier Galy, Jérôme Lavé, Jérôme Gaillardet, Ananta Prasad Gajurel, Caroline Guilmette, Mustafizur Rahman, Sunil Kumar Singh & Rajiv Sinha. *Predominant floodplain over mountain weathering of Himalayan sediments (Ganga basin).* Geochimica et Cosmochimica Acta, vol. 84, pages 410–432, 2012. www

[Lupker 13] Maarten Lupker, Christian France-Lanord, Valier Galy, Jérôme Lavé & Hermann Kudrass. *Increasing chemical weathering in the Himalayan system since the Last Glacial Maximum.* Earth and Planetary Science Letters, vol. 365, pages 243–252, March 2013. www

[Lyon-Caen 85] H Lyon-Caen. *Gravity anomalies, flexure of the Indian plate, and the structure, support and evolution of the Himalaya and Ganga basin.* Tectonics, 1985. www

[Macfarlane 93] A. M. Macfarlane. *Chronology of tectonic events in the crystalline core of the Himalaya, langtang National Park, central Nepal.* Tectonics, vol. 12, no. 4, pages 1004–1025, 1993. www

[Melchiorre 11] Erik B. Melchiorre & H. Albert Gilg. *Oxygen stable isotope fractionation behavior of cerussite and hydrocerussite : New results and reconciliation of the recent literature.* Geochimica et Cosmochimica Acta, vol. 75, no. 11, pages 3191–3195, 2011. www

[Meredith 13] Karina Meredith, Takuya Moriguti, Paul Tomascak, Suzanne Hollins & Eizo Nakamura. *The lithium, boron and strontium isotopic systematics of groundwaters from an arid aquifer system : Implications for recharge and weathering processes.* Geochimica et Cosmochimica Acta, vol. 112, pages 20–31, 2013. www

[Métivier 99a] François Métivier & Yves Gaudemer. *Stability of output fluxes of large rivers in South and East Asia during the last 2 million years : implications on floodplain processes.* Basin Research, vol. 11, no. 4, pages 293–303, December 1999. www

[Métivier 99b] François Métivier, Yves Gaudemer, Paul Tapponnier & Michel Klein. *Mass accumulation rates in Asia during the Cenozoic.* Geophysical Journal International, vol. 137, no. 2, pages 280–318, 1999. www

[Meunier 08] Patrick Meunier, Niels Hovius & John Allan Haines. *Topographic site effects and the location of earthquake induced landslides.* Earth and Planetary Science Letters, vol. 275, no. 3-4, pages 221–232, November 2008. www

[Meybeck 96] Michel Meybeck & Alain Ragu. River discharges to the oceans : an assessment of suspended solids, major ions and nutrients, volume 243. Environment Information and Assessment, 1996.

[Mezaki 84] S Mezaki & M Yabiku. *Channel geomorphology of the Kali gandaki and the Narayani rivers in central Nepal.* J. Nepal Geol. Soc, vol. 4, no. Special, pages 161–176, 1984. www

[Mikutta 05] R. Mikutta, M. Kleber, K. Kaiser & R. Jahn. *Review : Organic Matter Removal from Soils using Hydrogen Peroxide, Sodium Hypochlorite, and Disodium Peroxodisulfate.* Soil Science Society of America Journal, vol. 69, no. 1, page 120, 2005. www

[Mikutta 06] Robert Mikutta, Markus Kleber, MargaretS. Torn & Reinhold Jahn. *Stabilization of Soil Organic Matter : Association with Minerals or Chemical Recalcitrance ?* Biogeochemistry, vol. 77, no. 1, pages 25–56, 2006. www

[Mikutta 11] R Mikutta & K Kaiser. *Organic matter bound to mineral surfaces : Resistance to chemical and biological oxidation.* Soil Biology and Biochemistry, 2011. www

[Milliman 83] John D. Milliman & Robert H. Meade. *World-Wide Delivery of River Sediment to the Oceans.* The Journal of Geology, vol. 91, no. 1, pages 1–21, January 1983. www

[Milliman 92] John D. Milliman & James P. M. Syvitski. *Geomorphic/Tectonic Control of Sediment Discharge to the Ocean : The Importance of Small Mountainous Rivers.* The Journal of Geology, vol. 100, no. 5, pages 525–544, September 1992. www

[Milliman 11] J D Milliman & K L Farnsworth. River discharge to the coastal ocean : a global synthesis. Cambridge University Press, 2011.

[Millot 02] Romain Millot, Jérôme Gaillardet, Bernard Dupré & Claude Jean Allègre. *The global control of silicate weathering rates and the coupling with physical erosion : new insights from rivers of the Canadian Shield*. Earth and Planetary Science Letters, vol. 196, no. 1-2, pages 83–98, February 2002. www

[Misra 12] Sambuddha Misra & Philip N Froelich. *Lithium isotope history of Cenozoic seawater : changes in silicate weathering and reverse weathering.* Science (New York, N.Y.), vol. 335, no. 6070, pages 818–23, 2012. www

[Mohindra 92] R. Mohindra, B. Parkash & J. Prasad. *Historical geomorphology and pedology of the Gandak Megafan, Middle Gangetic Plains, India*. Earth Surface Processes and Landforms, vol. 17, no. 7, pages 643–662, November 1992. www

[Molnar 90] Peter Molnar & Philip England. *Late Cenozoic uplift of mountain ranges and global climate change : chicken or egg ?* Nature, vol. 346, no. 6279, pages 29–34, July 1990. www

[Molnar 03] Peter Molnar. *Geomorphology : Nature, nurture and landscape*. Nature, vol. 426, no. 6967, pages 612–614, December 2003. www

[Molnar 04] Peter Molnar. *LATE CENOZOIC INCREASE IN ACCUMULATION RATES OF TERRESTRIAL SEDIMENT : How Might Climate Change Have Affected Erosion Rates ?* Annual Review of Earth and Planetary Sciences, vol. 32, no. 1, pages 67–89, 2004. www

[Molnar 10] Peter Molnar, William R. Boos & David S. Battisti. *Orographic Controls on Climate and Paleoclimate of Asia : Thermal and Mechanical Roles for the Tibetan Plateau*. Annual Review of Earth and Planetary Sciences, vol. 38, no. 1, pages 77–102, April 2010. www

[Morin 14] Guillaume Morin, Christian France-Lanord, Ananta Gajurel, Florian Gallo & Jérôme Lavé. *High K and Ca Chemical Erosion*

Triggered by Physical Erosion in a Watershed of the High Himalaya of Nepal. Procedia Earth and Planetary Science, vol. 10, pages 292–296, 2014. www

[Morin 15] Guillaume P. Morin, Nathalie Vigier & Aurélie Verney-Carron. *Enhanced dissolution of basaltic glass in brackish waters : Impact on biogeochemical cycles.* Earth and Planetary Science Letters, vol. 417, pages 1–8, May 2015. www

[Mueller 13] Erich R. Mueller & John Pitlick. *Sediment supply and channel morphology in mountain river systems : 1. Relative importance of lithology, topography, and climate.* Journal of Geophysical Research : Earth Surface, vol. 118, pages n/a–n/a, November 2013. www

[Muste 04] M. Muste, K. Yu & M. Spasojevic. *Practical aspects of ADCP data use for quantification of mean river flow characteristics ; Part I : moving-vessel measurements.* Flow Measurement and Instrumentation, vol. 15, no. 1, pages 1–16, March 2004. www

[Najman 01] Y Najman, M Pringle, L Godin & G Oliver. *Dating of the oldest continental sediments from the Himalayan foreland basin.* Nature, vol. 410, no. 6825, pages 194–7, March 2001. www

[Najman 05] Y Najman. *The detrital record of orogenesis : A review of approaches and techniques used in the Himalayan sedimentary basins.* Earth-Science Reviews, December 2005. www

[Najman 08] Y. Najman, M. Bickle, M. BouDagher-Fadel, A. Carter, E. Garzanti, M. Paul, J. Wijbrans, E. Willett, G. Oliver, R. Parrish, S.H. Akhter, R. Allen, S. Ando, E. Chisty, L. Reisberg & G. Vezzoli. *The Paleogene record of Himalayan erosion : Bengal Basin, Bangladesh.* Earth and Planetary Science Letters, vol. 273, no. 1-2, pages 1–14, August 2008. www

[Nepal 00] Sanjay K Nepal. *Tourism in protected areas.* Annals of Tourism Research, vol. 27, no. 3, pages 661–681, July 2000. www

[Nepal 14] S Nepal, P Krause, W-A Flügel, M Fink & C Fischer. *Understanding the hydrological system dynamics of a glaciated alpine*

catchment in the Himalayan region using the J2000 hydrological model. Hydrological Processes, vol. 28, no. 3, pages 1329–1344, 2014.

[Niemi 05] Nathan A. Niemi, Michael Oskin, Douglas W. Burbank, Arjun M. Heimsath & Emmanuel J. Gabet. *Effects of bedrock landslides on cosmogenically determined erosion rates*. Earth and Planetary Science Letters, vol. 237, no. 3-4, pages 480–498, September 2005. www

[Nishiizumi 07] Kunihiko Nishiizumi, Mineo Imamura, Marc W. Caffee, John R. Southon, Robert C. Finkel & Jeffrey McAninch. *Absolute calibration of 10Be AMS standards*. Nuclear Instruments and Methods in Physics Research Section B : Beam Interactions with Materials and Atoms, vol. 258, no. 2, pages 403–413, May 2007. www

[Oberg 02] K Oberg. *In Search of Easy-to-Use Methods for Calibrating ADCP's for Velocity and Discharge Measurements*. \ldots ., Hydraulic Measurements & Experimental Methods \ldots, pages 1–11, 2002. www

[Oelkers 11] Eric H. Oelkers, Sigurdur R. Gislason, Eydis Salome Eiriksdottir, Morgan Jones, Christopher R. Pearce & Catherine Jeandel. *The role of riverine particulate material on the global cycles of the elements*. Applied Geochemistry, vol. 26, no. S, pages S365–S369, 2011. www

[Oelkers 12] Eric H. Oelkers, Morgan T. Jones, Christopher R. Pearce, Catherine Jeandel, Eydis Salome Eiriksdottir & Sigurdur R. Gislason. *Riverine particulate material dissolution in seawater and its implications for the global cycles of the elements*. Comptes Rendus Geoscience, vol. 344, no. 11-12, pages 646–651, November 2012. www

[Owen 02] Lewis A. Owen, Robert C. Finkel & Marc W. Caffee. *A note on the extent of glaciation throughout the Himalaya during the global Last Glacial Maximum*. Quaternary Science Reviews, vol. 21, no. 1-3, pages 147–157, January 2002. www

[Owen 09] Lewis a. Owen. *Latest Pleistocene and Holocene glacier fluctuations in the Himalaya and Tibet.* Quaternary Science Reviews, vol. 28, no. 21-22, pages 2150–2164, October 2009. www

[Owen 14] Lewis a. Owen & Jason M. Dortch. *Nature and timing of Quaternary glaciation in the Himalayan–Tibetan orogen.* Quaternary Science Reviews, vol. 88, pages 14–54, March 2014. www

[Pandey 88] MR Pandey & Peter Molnar. *The distribution of intensity of the Bihar-Nepal earthquake of 15 January 1934 and bounds on the extent of the rupture zone.* Journal of Nepal Geological Society, vol. 5, no. 1, pages 22–44, 1988.

[Pandey 95] M. R. Pandey, R. P. Tandukar, J. P. Avouac, J. Lavé & J. P. Massot. *Interseismic strain accumulation on the Himalayan crustal ramp (Nepal).* Geophysical Research Letters, vol. 22, no. 7, pages 751–754, April 1995. www

[Parker 11] Robert N. Parker, Alexander L. Densmore, Nicholas J. Rosser, Marcello de Michele, Yong Li, Runqiu Huang, Siobhan Whadcoat & David N. Petley. *Mass wasting triggered by the 2008 Wenchuan earthquake is greater than orogenic growth.* Nature Geoscience, vol. 4, no. 7, pages 449–452, 2011. www

[Patriat 84] Philippe Patriat & José Achache. *India–Eurasia collision chronology has implications for crustal shortening and driving mechanism of plates.* Nature, vol. 311, no. 5987, pages 615–621, October 1984. www

[Pearce 13] Christopher R. Pearce, Morgan T. Jones, Eric H. Oelkers, Catherine Pradoux & Catherine Jeandel. *The effect of particulate dissolution on the neodymium (Nd) isotope and Rare Earth Element (REE) composition of seawater.* Earth and Planetary Science Letters, vol. 369-370, pages 138–147, 2013. www

[Pecher 78] Arnaud Pecher. *Déformations et métamorphisme associés à une zone de cisaillement. Exemple du grand Chevauchement Central Himalayen (M.C.T.) , transversale des Anapurnas et du Manaslu*

(Népal). Theses, Université Scientifique et Médicale de Grenoble, May 1978. www

[Pedersen 13] Vivi Kathrine Pedersen & David Lundbek Egholm. *Glaciations in response to climate variations preconditioned by evolving topography*. Nature, vol. 493, no. 7431, pages 206–10, January 2013. www

[Peizhen 01] Zhang Peizhen, Peter Molnar & WR R Downs. *Increased sedimentation rates and grain sizes 2–4 Myr ago due to the influence of climate change on erosion rates*. Nature, vol. 410, no. April, pages 891–897, 2001. www

[Petley 07] David N. Petley, Gareth J. Hearn, Andrew Hart, Nicholas J. Rosser, Stuart a. Dunning, Katie Oven & Wishart a. Mitchell. *Trends in landslide occurrence in Nepal*. Natural Hazards, vol. 43, no. 1, pages 23–44, March 2007. www

[Pierson-Wickmann 01] Anne-Catherine Pierson-Wickmann, Laurie Reisberg, Christian France-Lanord & Herman R Kudrass. *Os-Sr-Nd results from sediments in the Bay of Bengal : Implications for sediment transport and the marine Os record*. Paleoceanography, vol. 16, no. 4, pages 435–444, 2001.

[Portenga 11] Eric W Portenga & Paul R Bierman. *Understanding Earth's eroding surface with 10 Be*. GSA Today, vol. 21, no. 8, pages 4–10, 2011.

[Pratt-Sitaula 07] Beth Pratt-Sitaula, Michelle Garde, Douglas W. Burbank, Michael Oskin, Arjun Heimsath & Emmanuel Gabet. *Bedload-to-suspended load ratio and rapid bedrock incision from Himalayan landslide-dam lake record*. Quaternary Research, vol. 68, no. 1, pages 111–120, July 2007. www

[Pratt-Sitaula 11] Beth Pratt-Sitaula, Douglas W. Burbank, Arjun M. Heimsath, Neil F. Humphrey, Michael Oskin & Jaakko Putkonen. *Topographic control of asynchronous glacial advances : A case study from Annapurna, Nepal*. Geophysical Research Letters, vol. 38, no. 24, pages n/a–n/a, 2011. www

[Prescott 97] J R Prescott & G B Robertson. *Sediment dating by luminescence : a review.* Radiation Measurements, vol. 27, no. 5-6, pages 893–922, 1997. www

[Puchol 13] Nicolas Puchol. *Détermination des paléo-taux d'érosion par l'utilisation des isotopes cosmogéniques. Cas de la transition Pliocène-Pleistocène.* PhD thesis, Université de Lorraine, 2013.

[Puchol 14] Nicolas Puchol, Jérôme Lavé, Maarten Lupker, Pierre-Henri Blard, Florian Gallo & Christian France-Lanord. *Grain-size dependent concentration of cosmogenic 10Be and erosion dynamics in a landslide-dominated Himalayan watershed.* Geomorphology, vol. 224, pages 55–68, November 2014. www

[Putkonen 04] JK Putkonen. *Continuous snow and rain data at 500 to 4400 m altitude near Annapurna, Nepal, 1999-2001.* Arctic, Antarctic, and Alpine Research, 2004. www

[Quade 95] J Quade & JML Cater. *Late Miocene environmental change in Nepal and the northern Indian subcontinent : Stable isotopic evidence from paleosols.* \ldots Society of America \ldots, no. 12, pages 1381–1397, 1995. www

[Quade 97] J Quade. *The Late Neogene 87Sr/86Sr Record of Lowland Himalayan Rivers.* Science, vol. 276, no. 5320, pages 1828–1831, 1997. www

[Quade 03] J Quade. *Silicate versus carbonate weathering in the Himalaya : a comparison of the Arun and Seti River watersheds.* Chemical Geology, vol. 202, no. 3-4, pages 275–296, 2003. www

[Rahaman 09] W Rahaman, S K Singh, R Sinha & S K Tandon. *Climate control on erosion distribution over the Himalaya during the past 100 ka.* Geology, vol. 37, no. 6, pages 559–562, 2009. www

[Rahaman 10] W Rahaman, S K Singh, R Sinha & S K Tandon. *Climate control on erosion distribution over the Himalaya during the past 100 ka : REPLY.* Geology, vol. 38, no. 8, pages e217–e217, 2010. www

[RANA 96] Birbal RANA, Yoshihiro Fukushima, Yutaka Ageta & Masayoshi Nakawo. *Runoff modeling of a river basin with a debris-covered*

glacier in Langtang Valley, Nepal Himalaya. Bulletin of glacier research, no. 14, pages 1–6, 1996.

[Rao 01] K.S Rao & Rekha Pant. *Land use dynamics and landscape change pattern in a typical micro watershed in the mid elevation zone of central Himalaya, India.* Agriculture, Ecosystems & Environment, vol. 86, no. 2, pages 113–124, 2001. www

[Raymo 88] Maureen E. Raymo, William F. Ruddiman & Philip N. Froelich. *Influence of late Cenozoic mountain building on ocean geochemical cycles.* Geology, vol. 16, no. 7, page 649, 1988. www

[Raymo 92] M. E. Raymo & W. F. Ruddiman. *Tectonic forcing of late Cenozoic climate.* Nature, vol. 359, no. 6391, pages 117–122, September 1992. www

[Regmi 13] Amar Deep Regmi, Kohki Yoshida, Hidehisa Nagata, Ananta Man Singh Pradhan, Biswajeet Pradhan & Hamid Reza Pourghasemi. *The relationship between geology and rock weathering on the rock instability along Mugling–Narayanghat road corridor, Central Nepal Himalaya.* Natural Hazards, vol. 66, no. 2, pages 501–532, March 2013. www

[Regmi 14] Amar Deep Regmi, Kohki Yoshida, Hidehisa Nagata & Biswajeet Pradhan. *Rock toppling assessment at Mugling–Narayanghat road section : 'A case study from Mauri Khola landslide', Nepal.* Catena, vol. 114, pages 67–77, March 2014. www

[Reimer 13] Paula J Reimer, Edouard Bard, Alex Bayliss, J Warren Beck, Paul G Blackwell, Christopher Bronk Ramsey, Caitlin E Buck, Hai Cheng, R Lawrence Edwards & Michael Friedrich. *IntCal13 and Marine13 radiocarbon age calibration curves 0-50,000 years cal BP.* Radiocarbon, vol. 55, no. 4, pages 1869–1887, 2013. www

[Reiners 03] Peter W. Reiners, Todd A. Ehlers, Sara G. Mitchell & David R. Montgomery. *Coupled spatial variations in precipitation and long-term erosion rates across the Washington Cascades.* Nature, vol. 426, no. 6967, pages 645–647, December 2003. www

[Rhodes 11] Edward J. Rhodes. *Optically Stimulated Luminescence Dating of Sediments over the Past 200,000 Years.* Annual Review of Earth and Planetary Sciences, vol. 39, no. 1, pages 461–488, 2011. www

[Rice 91] James A. Rice & Patrick MacCarthy. *Statistical evaluation of the elemental composition of humic substances.* Organic Geochemistry, vol. 17, no. 5, pages 635–648, January 1991. www

[Riebe 01] Clifford S Riebe, James W Kirchner, Darryl E Granger & Robert C Finkel. *Minimal climatic control on erosion rates in the Sierra Nevada, California.* Geology, vol. 29, no. 5, pages 447–450, 2001.

[Riebe 04a] Clifford S. Riebe, James W. Kirchner & Robert C. Finkel. *Erosional and climatic effects on long-term chemical weathering rates in granitic landscapes spanning diverse climate regimes.* Earth and Planetary Science Letters, vol. 224, no. 3-4, pages 547–562, 2004. www

[Riebe 04b] Clifford S. Riebe, James W. Kirchner & Robert C. Finkel. *Sharp decrease in long-term chemical weathering rates along an altitudinal transect.* Earth and Planetary Science Letters, vol. 218, no. 3-4, pages 421–434, 2004. www

[Right 86] D. Right & L. Lorphelin. *Weathering of silt and clay in soils of a toposequence in the Himalayas, Nepal.* Geoderma, vol. 39, no. 2, pages 141–155, 1986. www

[Robinson 01] Delores M. Robinson, Peter G. DeCelles, P.Jonathan Patchett & Carmala N. Garzione. *The kinematic evolution of the Nepalese Himalaya interpreted from Nd isotopes.* Earth and Planetary Science Letters, vol. 192, no. 4, pages 507–521, November 2001. www

[Rosenheim 12] Brad E. Rosenheim & Valier Galy. *Direct measurement of riverine particulate organic carbon age structure.* Geophysical Research Letters, vol. 39, no. 19, pages n/a–n/a, October 2012. www

[Rouse 50] Hunter Rouse*et al. Engineering hydraulics*. In Hydraulics Conference 1949 : Iowa Institute of Hydraulic Research). Wiley, 1950.

[Rowley 96] David B. Rowley. *Age of initiation of collision between India and Asia : A review of stratigraphic data*. Earth and Planetary Science Letters, vol. 145, no. 1-4, pages 1–13, 1996. www

[RSP 96] RSP. *River Survey Project, Flood Action Plan (FAP) final report.* Rapport technique, Delft Hydraulics and DHI, 1996.

[Sapkota 12] S. N. Sapkota, L. Bollinger, Y. Klinger, P. Tapponnier, Y. Gaudemer & D. Tiwari. *Primary surface ruptures of the great Himalayan earthquakes in 1934 and 1255*. Nature Geoscience, vol. 6, no. 1, pages 71–76, 2012. www

[Savin 70] Samuel M Savin & Samuel Epstein. *The oxygen and hydrogen isotope geochemistry of clay minerals*. Geochimica et Cosmochimica Acta, vol. 34, no. 1, pages 25–42, January 1970. www

[Savin 98] Samuel M Savin & Jean C.C Hsieh. *The hydrogen and oxygen isotope geochemistry of pedogenic clay minerals : principles and theoretical background*. Geoderma, vol. 82, no. 1-3, pages 227–253, 1998. www

[Scheingross 14] J. S. Scheingross, F. Brun, D. Y. Lo, K. Omerdin & M. P. Lamb. *Experimental evidence for fluvial bedrock incision by suspended and bedload sediment*. Geology, no. April, 2014. www

[Scherler 11] Dirk Scherler, Bodo Bookhagen & Manfred R Strecker. *Hillslope-glacier coupling : The interplay of topography and glacial dynamics in High Asia*. Journal of Geophysical Research : Earth Surface (2003–2012), vol. 116, no. F2, 2011.

[Scherler 14] Dirk Scherler, Bodo Bookhagen & Manfred R. Strecker. *Tectonic control on 10 Be-derived erosion rates in the Garhwal Himalaya, India*. Journal of Geophysical Research : Earth Surface, vol. 119, no. August 2013, pages n/a–n/a, January 2014. www

[Semwal 04] R.L Semwal, S Nautiyal, K.K Sen, U Rana, R.K Maikhuri, K.S Rao & K.G Saxena. *Patterns and ecological implications of agricultural land-use changes : a case study from central Himalaya,*

India. Agriculture, Ecosystems & Environment, vol. 102, no. 1, pages 81–92, March 2004. www

[Shackleton 85] N. J. Shackleton. *Oceanic carbon isotope constraints on oxygen and carbon dioxide in the Cenozoic atmosphere*. In E. T. Sundquist & W. S. Broecker, editeurs, Geophysical Monograph Series, volume 32, pages 412–417. American Geophysical Union, Washington, D. C., 1985. www

[Sharp 01] Z.D Sharp, V Atudorei & T Durakiewicz. *A rapid method for determination of hydrogen and oxygen isotope ratios from water and hydrous minerals*. Chemical Geology, vol. 178, no. 1-4, pages 197–210, August 2001. www

[Shea 15] JM Shea, WW Immerzeel, P Wagnon, C Vincent & S Bajracharya. *Modelling glacier change in the Everest region, Nepal Himalaya*. The Cryosphere, vol. 9, no. 3, pages 1105–1128, 2015.

[Sheppard 70] Simon M. F. Sheppard & Henry P. Schwarcz. *Fractionation of carbon and oxygen isotopes and magnesium between coexisting metamorphic calcite and dolomite*. Contributions to Mineralogy and Petrology, vol. 26, no. 3, pages 161–198, April 1970. www

[Shrestha 00] M. L. Shrestha. *Interannual variation of summer monsoon rainfall over Nepal and its relation to Southern Oscillation Index*. Meteorology and Atmospheric Physics, vol. 75, no. 1-2, pages 21–28, November 2000. www

[Shroder 98a] John F Shroder. *Slope failure and denudation in the western Himalaya*. Geomorphology, vol. 26, no. 1-3, pages 81–105, December 1998. www

[Shroder 98b] John F Shroder & Michael P Bishop. *Mass movement in the Himalaya : new insights and research directions*. Geomorphology, vol. 26, no. 1-3, pages 13–35, December 1998. www

[Sidle 06] Roy C. Sidle, Alan D. Ziegler, Junjiro N. Negishi, Abdul Rahim Nik, Ruyan Siew & Francis Turkelboom. *Erosion processes in steep terrain—Truths, myths, and uncertainties related to forest*

management in Southeast Asia. Forest Ecology and Management, vol. 224, no. 1-2, pages 199–225, March 2006. www

[Sidle 11] Roy C. Sidle, Takahisa Furuichi & Yasuyuki Kono. *Unprecedented rates of landslide and surface erosion along a newly constructed road in Yunnan, China.* Natural Hazards, vol. 57, no. 2, pages 313–326, May 2011. www

[Sidle 12] Roy C. Sidle & Alan D. Ziegler. *The dilemma of mountain roads.* Nature Geoscience, vol. 5, no. 7, pages 437–438, June 2012. www

[Sime 07] Louise C Sime, Robert I Ferguson & Michael Church. *Estimating shear stress from moving boat acoustic Doppler velocity measurements in a large gravel bed river.* Water Resources Research, vol. 43, no. 3, 2007. www

[Simpson 90] Michael R Simpson & Richard N Oltmann. *An acoustic Doppler discharge-measurement system.* In Hydraulic Engineering (1990), pages 903–908. ASCE, 1990.

[Singh 91] Adal Singh & B.D. Bhardwaj. *Fluvial facies model of the Ganga River sediments, India.* Sedimentary Geology, vol. 72, no. 1-2, pages 135–146, June 1991. www

[Singh 02] Sunil K Singh & Christian France-Lanord. *Tracing the distribution of erosion in the Brahmaputra watershed from isotopic compositions of stream sediments.* Earth and Planetary Science Letters, vol. 202, no. 3-4, pages 645–662, September 2002. www

[Singh 08a] Omvir Singh, Milap C Sharma, A Sarangi & Pratap Singh. *Spatial and temporal variability of sediment and dissolved loads from two alpine watersheds of the Lesser Himalayas.* Catena, vol. 76, no. 1, pages 27–35, 2008. www

[Singh 08b] Sunil K Singh, Santosh K Rai & S Krishnaswami. *Sr and Nd isotopes in river sediments from the Ganga Basin : Sediment provenance and spatial variability in physical erosion.* Journal of Geophysical Research, vol. 113, no. F3, 2008. www

[Sinha 94] Rajiv Sinha & Peter F. Friend. *River systems and their sediment flux, Indo-Gangetic plains, Northern Bihar, India.* Sedimentology, vol. 41, no. 4, pages 825–845, August 1994. www

[Sinha 96] R Sinha. *Channel avulsion and floodplain structure in the Gandak-Kosi interfan, north Bihar plains, India.* 1996. www

[Sinha 05] R Sinha. *Why do Gangetic rivers aggrade or degrade ?* Current Science, 2005. www

[Sinha 09] Rajiv Sinha. *The great avulsion of Kosi on 18 August 2008.* Current Science, vol. 97, no. 03, pages 429–432, 2009.

[Sinha 10] R Sinha, S K Tandon & M R Gibling. *Shallow sub-surface stratigraphy of the Ganga basin, Himalayan foreland : Present status and future perspectives.* Quaternary International, vol. 227, no. 2, pages 81–86, 2010. www

[Sinha 12] Rajiv Sinha, Edgardo M. Latrubesse & Gerald C. Nanson. *Quaternary fluvial systems of tropics : Major issues and status of research.* Palaeogeography, Palaeoclimatology, Palaeoecology, vol. 356-357, pages 1–15, October 2012. www

[Sinha 13a] R. Sinha, K. Gaurav, S. Chandra & S. K. Tandon. *Exploring the channel connectivity structure of the August 2008 avulsion belt of the Kosi River, India : Application to flood risk assessment.* Geology, vol. 41, no. 10, pages 1099–1102, 2013. www

[Sinha 13b] Rajiv Sinha, G.S. Yadav, Sanjeev Gupta, Ajit Singh & S.K. Lahiri. *Geo-electric resistivity evidence for subsurface palaeochannel systems adjacent to Harappan sites in northwest India.* Quaternary International, vol. 308-309, pages 66–75, October 2013. www

[Sinha 14] Rajiv Sinha, Jawed Ahmad, Kumar Gaurav & Guillaume Morin. *Shallow subsurface stratigraphy and alluvial architecture of the Kosi and Gandak megafans in the Himalayan foreland basin, India.* Sedimentary Geology, vol. 301, pages 133–149, March 2014. www

[Smadja 92] Joelle Smadja. *Studies of Climatic and Human Impacts and Their Relationship on a Mountain Slope above Salme in the Himalayan Middle Mountains, Nepal.* Mountain Research and Development, vol. 12, no. 1, page 1, February 1992. www

[Srivastava 10] P. Srivastava & U. K. Shukla. *Climate control on erosion distribution over the Himalaya during past 100 ka : COMMENT.* Geology, vol. 38, no. 8, pages e216–e216, August 2010. www

[Sternai 13] Pietro Sternai, Frédéric Herman, Pierre G. Valla & Jean-Daniel Champagnac. *Spatial and temporal variations of glacial erosion in the Rhône valley (Swiss Alps) : Insights from numerical modeling.* Earth and Planetary Science Letters, vol. 368, pages 119–131, 2013. www

[Stewart 01] Brian W Stewart, Rosemary C Capo & Oliver A Chadwick. *Effects of rainfall on weathering rate, base cation provenance, and Sr isotope composition of Hawaiian soils.* Geochimica et Cosmochimica Acta, vol. 65, no. 7, pages 1087–1099, 2001.

[Stone 00] John O. Stone. *Air pressure and cosmogenic isotope production.* Journal of Geophysical Research, vol. 105, no. B10, page 23753, 2000. www

[Struck 15] Martin Struck, Christoff Andermann, Niels Hovius, Oliver Korup, Jens M. Turowski, Raj Bista, Hari P. Pandit & Ranjan K. Dahal. *Monsoonal hillslope processes determine grain size-specific suspended sediment fluxes in a trans-Himalayan river : Mass wasting determines sediment caliber.* Geophysical Research Letters, vol. 42, no. 7, pages 2302–2308, April 2015. www

[Syvitski 03] James P.M Syvitski, Scott D Peckham, Rachael Hilberman & Thierry Mulder. *Predicting the terrestrial flux of sediment to the global ocean : a planetary perspective.* Sedimentary Geology, vol. 162, no. 1-2, pages 5–24, November 2003. www

[Syvitski 05] James P M Syvitski, Charles J Vörösmarty, Albert J Kettner & Pamela Green. *Impact of humans on the flux of terrestrial*

sediment to the global coastal ocean. Science (New York, N.Y.), vol. 308, no. 5720, pages 376–80, 2005. www

[Syvitski 07] James P M Syvitski & John D. Milliman. *Geology, Geography, and Humans Battle for Dominance over the Delivery of Fluvial Sediment to the Coastal Ocean.* The Journal of Geology, vol. 115, no. 1, pages 1–19, January 2007. www

[Szulc 06] A. G. Szulc, Y. Najman, H. D. Sinclair, M. Pringle, M. Bickle, H. Chapman, E. Garzanti, S. Andò, P. Huyghe, J-L. Mugnier, T. Ojha & P. DeCelles. *Tectonic evolution of the Himalaya constrained by detrital 40Ar-39Ar, Sm-Nd and petrographic data from the Siwalik foreland basin succession, SW Nepal : Tectonic evolution of the Himalaya.* Basin Research, vol. 18, no. 4, pages 375–391, December 2006. www

[Tapponnier 82] P. Tapponnier, G. Peltzer, A. Y. Le Dain, R. Armijo & P. Cobbold. *Propagating extrusion tectonics in Asia : New insights from simple experiments with plasticine.* Geology, vol. 10, no. 12, page 611, 1982. www

[Teledyne 14] RD Instruments Teledyne. *WinRiver II ; software user's guide*, 2014.

[Thapa 13] Arjun Jung Thapa. *Status Paper on Road Safety in Nepal 2013.* Rapport technique, DDG, Department of Roads, 2013.

[Thayyen 99] R.J. Thayyen, J. T. Gergan & D. P. Dobhal. *Particle size characteristics of suspended sediments and subglacial hydrology of Dokriani Glacier, Garhwal Himalaya, India.* Hydrological Sciences Journal, vol. 44, no. 1, pages 47–61, 1999.

[Thiede 04] Rasmus C. Thiede, Bodo Bookhagen, J.Ramón Arrowsmith, Edward R. Sobel & Manfred R. Strecker. *Climatic control on rapid exhumation along the Southern Himalayan Front.* Earth and Planetary Science Letters, vol. 222, no. 3-4, pages 791–806, June 2004. www

[Thiel 12] Christine Thiel, Jan-Pieter Buylaert, Andrew S. Murray, Noureddine Elmejdoub & Younes Jedoui. *A comparison of TT-OSL*

and post-IR IRSL dating of coastal deposits on Cap Bon peninsula, north-eastern Tunisia. Quaternary Geochronology, vol. 10, pages 209–217, 2012. www

[Thomson 10] Stuart N Thomson, Mark T Brandon, Jonathan H Tomkin, Peter W Reiners, Cristián Vásquez & Nathaniel J Wilson. *Glaciation as a destructive and constructive control on mountain building.* Nature, vol. 467, no. 7313, pages 313–317, September 2010.

[Tipper 06a] E Tipper, A Galy & M Bickle. *Riverine evidence for a fractionated reservoir of Ca and Mg on the continents : Implications for the oceanic Ca cycle.* Earth and Planetary Science Letters, vol. 247, no. 3-4, pages 267–279, July 2006. www

[Tipper 06b] Edward T Tipper & Mike Bickle. *The isotopic fingerprint of calcium and magnesium : from the alteration of the continental crust to global budgets.* PhD thesis, University of Cambridge, 2006. www

[Tipper 06c] Edward T. Tipper, Mike J. Bickle, Albert Galy, A. Joshua West, Catherine Pomiès & Hazel J. Chapman. *The short term climatic sensitivity of carbonate and silicate weathering fluxes : Insight from seasonal variations in river chemistry.* Geochimica et Cosmochimica Acta, vol. 70, no. 11, pages 2737–2754, June 2006. www

[Tiwari 09] Krishna R. Tiwari, Bishal K. Sitaula, Roshan M. Bajracharya & Trond Borresen. *Runoff and soil loss responses to rainfall, land use, terracing and management practices in the Middle Mountains of Nepal.* Acta Agriculturae Scandinavica, Section B - Plant Soil Science, vol. 59, no. 3, pages 197–207, May 2009. www

[Tolorza 14] Violeta Tolorza, Sébastien Carretier, Christoff Andermann, Francisco Ortega-Culaciati, Luisa Pinto & María Mardones. *Contrasting mountain and piedmont dynamics of sediment discharge associated with groundwater storage variation in the Biobío River.*

Journal of Geophysical Research : Earth Surface, vol. 119, no. 12, pages 2730–2753, December 2014. www

[Tréguer 13] Paul J Tréguer & Christina L De La Rocha. *The world ocean silica cycle.* Annual review of marine science, vol. 5, no. July, pages 477–501, January 2013. www

[Turowski 10] Jens M. Turowski, Dieter Rickenmann & Simon J. Dadson. *The partitioning of the total sediment load of a river into suspended load and bedload : a review of empirical data : The partitioning of sediment load.* Sedimentology, vol. 57, no. 4, pages 1126–1146, February 2010. www

[Valla 10] Pierre G. Valla, Frédéric Herman, Peter A. van der Beek & Jean Braun. *Inversion of thermochronological age-elevation profiles to extract independent estimates of denudation and relief history — I : Theory and conceptual model.* Earth and Planetary Science Letters, vol. 295, no. 3-4, pages 511–522, July 2010. www

[van Hinsbergen 12] Douwe J J van Hinsbergen, Peter C Lippert, Guillaume Dupont-Nivet, Nadine McQuarrie, Pavel V Doubrovine, Wim Spakman & Trond H Torsvik. *Greater India Basin hypothesis and a two-stage Cenozoic collision between India and Asia.* Proceedings of the National Academy of Sciences of the United States of America, vol. 109, no. 20, pages 7659–64, 2012. www

[Vance 03] Derek Vance, Mike Bickle, Susan Ivy-Ochs & Peter W. Kubik. *Erosion and exhumation in the Himalaya from cosmogenic isotope inventories of river sediments.* Earth and Planetary Science Letters, vol. 206, no. 3-4, pages 273–288, February 2003. www

[Vance 09] Derek Vance, Damon A H Teagle & Gavin L Foster. *Variable Quaternary chemical weathering fluxes and imbalances in marine geochemical budgets.* Nature, vol. 458, no. 7237, pages 493–496, 2009. www

[Viers 09] Jérôme Viers, Bernard Dupré & Jérôme Gaillardet. *Chemical composition of suspended sediments in World Rivers : New in-*

sights from a new database. The Science of the total environment, vol. 407, no. 2, pages 853–68, January 2009. www

[Vigier 15] N. Vigier & Y. Goddéris. *A new approach for modeling Cenozoic oceanic lithium isotope paleo-variations : the key role of climate.* Climate of the Past, vol. 11, no. 4, pages 635–645, April 2015. www

[von Blanckenburg 05] Friedhelm von Blanckenburg. *The control mechanisms of erosion and weathering at basin scale from cosmogenic nuclides in river sediment.* Earth and Planetary Science Letters, vol. 237, no. 3-4, pages 462–479, September 2005. www

[Walling 06] D.E. E. Walling. *Human impact on land–ocean sediment transfer by the world's rivers.* Geomorphology, vol. 79, no. 3-4, pages 192–216, September 2006. www

[Wallinga 02] J Wallinga. *Optically stimulated luminescence dating of fluvial deposits : a review.* Boreas, vol. 31, no. 4, pages 303–322, 2002. www

[Wang 01] Q. Wang. *Present-Day Crustal Deformation in China Constrained by Global Positioning System Measurements.* Science, vol. 294, no. 5542, pages 574–577, October 2001. www

[Warrick 14] J. A. Warrick, J. D. Milliman, D. E. Walling, R. J. Wasson, J. P. M. Syvitski & R. E. Aalto. *Earth is (mostly) flat : Apportionment of the flux of continental sediment over millennial time scales : COMMENT.* Geology, vol. 42, no. 1, pages e316–e316, January 2014. www

[Weidinger 06] Johannes T Weidinger. *Predesign, failure and displacement mechanisms of large rockslides in the Annapurna Himalayas, Nepal.* Engineering Geology, vol. 83, no. 1, pages 201–216, 2006.

[West 02] A. Joshua West, Mike J. Bickle, Rob Collins & James Brasington. *Small-catchment perspective on Himalayan weathering fluxes.* Geology, vol. 30, no. 4, page 355, 2002. www

[West 05] A. J. West, A. Galy & M. J. Bickle. *Tectonic and climatic controls on silicate weathering.* Earth and Planetary Science Letters, vol. 235, no. 1-2, pages 211–228, 2005. www

[Whipp 07] David M. Whipp, Todd a. Ehlers, Ann E. Blythe, Katharine W. Huntington, Kip V. Hodges & Douglas W. Burbank. *Plio-Quaternary exhumation history of the central Nepalese Himalaya : 2. Thermokinematic and thermochronometer age prediction model.* Tectonics, vol. 26, no. 3, pages n/a–n/a, 2007. www

[Whipple 99a] Kelin X Whipple, Eric Kirby & Simon H Brocklehurst. *Geomorphic limits to climate-induced increases in topographic relief.* Nature, vol. 401, no. 6748, pages 39–43, 1999. www

[Whipple 99b] Kelin X. Whipple & Gregory E. Tucker. *Dynamics of the stream-power river incision model : Implications for height limits of mountain ranges, landscape response timescales, and research needs.* Journal of Geophysical Research, vol. 104, no. B8, page 17661, 1999. www

[Whipple 09] Kelin X. Whipple. *The influence of climate on the tectonic evolution of mountain belts.* Nature Geoscience, vol. 2, no. 2, pages 97–104, January 2009. www

[White 95] Art F. White & Alex E. Blum. *Effects of climate on chemical weathering in watersheds.* Geochimica et Cosmochimica Acta, vol. 59, no. 9, pages 1729–1747, 1995. www

[White 99] Art F. White, Alex E. Blum, Thomas D. Bullen, Davison V. Vivit, Marjorie Schulz & John Fitzpatrick. *The effect of temperature on experimental and natural chemical weathering rates of granitoid rocks.* Geochimica et Cosmochimica Acta, vol. 63, no. 19-20, pages 3277–3291, October 1999. www

[White 14] A.F. White & H.L. Buss. *Natural Weathering Rates of Silicate Minerals.* In Treatise on Geochemistry, pages 115–155. Elsevier, 2014. www

[Wilcock 96] Peter R. Wilcock. *Estimating Local Bed Shear Stress from Velocity Observations.* Water Resources Research, vol. 32, no. 11, pages 3361–3366, November 1996. www

[Willenbring 10] Jane K. Willenbring & Friedhelm von Blanckenburg. *Long-term stability of global erosion rates and weathering during late-Cenozoic cooling.* Nature, vol. 465, no. 7295, pages 211–214, May 2010. www

[Willenbring 13] J. K. Willenbring, a. T. Codilean & B. McElroy. *Earth is (mostly) flat : Apportionment of the flux of continental sediment over millennial time scales.* Geology, no. January, January 2013. www

[Willenbring 14] J. K. Willenbring, A. T. Codilean & B. McElroy. *Earth is (mostly) flat : Apportionment of the flux of continental sediment over millennial time scales : REPLY.* Geology, vol. 42, no. 1, pages e317–e317, January 2014. www

[Willett 99] Sean D Willett. *Orogeny and orography : The effects of erosion on the structure of mountain belts.* Journal of Geophysical Research : Solid Earth (1978–2012), vol. 104, no. B12, pages 28957–28981, 1999.

[Williams 06] M.A.J. Williams, J.N. Pal, M. Jaiswal & A.K. Singhvi. *River response to Quaternary climatic fluctuations : evidence from the Son and Belan valleys, north-central India.* Quaternary Science Reviews, vol. 25, no. 19-20, pages 2619–2631, October 2006. www

[Wolff-Boenisch 09] Domenik Wolff-Boenisch, Emmanuel J Gabet, Douglas W Burbank, Heiko Langner & Jaakko Putkonen. *Spatial variations in chemical weathering and CO2 consumption in Nepalese High Himalayan catchments during the monsoon season.* Geochimica et Cosmochimica Acta, vol. 73, no. 11, pages 3148–3170, 2009.

[Wolman 60] M. Gordon Wolman & John P. Miller. *Magnitude and Frequency of Forces in Geomorphic Processes.* The Journal of Geology, vol. 68, no. 1, pages 54–74, January 1960. www

[Wulf 10] Hendrik Wulf, Bodo Bookhagen & Dirk Scherler. *Seasonal precipitation gradients and their impact on fluvial sediment flux in*

the Northwest Himalaya. Geomorphology, vol. 118, no. 1-2, pages 13–21, May 2010. www

[Wulf 12] H. Wulf, B. Bookhagen & D. Scherler. *Climatic and geologic controls on suspended sediment flux in the Sutlej River Valley, western Himalaya*. Hydrology and Earth System Sciences, vol. 16, no. 7, pages 2193–2217, July 2012. www

[Yadav 10] G.S. S Yadav, a.S. S Dasgupta, R. Sinha, T. Lal, K.M. M Srivastava & S.K. K Singh. *Shallow sub-surface stratigraphy of interfluves inferred from vertical electric soundings in western Ganga plains, India*. Quaternary International, vol. 227, no. 2, pages 104–115, November 2010. www

[Yapp 97] C J Yapp. *An assessment of isotopic equilibrium in goethites from a bog iron deposit and a lateritic regolith*. Chemical Geology, 1997. www

[Yeh 76] Hsueh-Wen Yeh & Samuel M. Savin. *The extent of oxygen isotope exchange between clay minerals and sea water*. Geochimica et Cosmochimica Acta, vol. 40, no. 7, pages 743–748, July 1976. www

[Yeh 80] Hsueh-Wen Yeh. *Ratios and late-stage dehydration of shales during burial*. Geochimica et Cosmochimica Acta, vol. 44, no. 2, pages 341–352, February 1980. www

[Yin 00] An Yin & T. Mark Harrison. *Geologic Evolution of the Himalayan-Tibetan Orogen*. Annual Review of Earth and Planetary Sciences, vol. 28, no. 1, pages 211–280, May 2000. www

[Zachos 01] J Zachos, M Pagani, L Sloan, E Thomas & K Billups. *Trends, rhythms, and aberrations in global climate 65 Ma to present.* Science (New York, N.Y.), vol. 292, no. 5517, pages 686–93, 2001. www

[Zeitler 01] P. K. Zeitler, A. S. Meltzer, P. O. Koons, D. Craw, B. Hallet, C. P. Chamberlain, W. S. F. Kidd, S. K. Park, L. Seeber, M. Bishop & J. Shroder. *Erosion, Himalayan geodynamics, and the geomor-*

phology of metamorphism. GSA Today, vol. 11, pages 4–9, 2001.
WWW

L’altération chimique et l’érosion physique de la croûte continentale mobilisent de grandes quantités de matière sous formes solide et dissoute. Première productrice de sédiments sur le globe, la chaîne Himalayenne délivre ~1 Gt/a de sédiments aux océans. L'importance des différents facteurs qui contrôlent les flux érodés et celle des processus d’érosion (glaciers, glissements de terrain, sols) sont pourtant encore mal définies. Il en va ainsi des facteurs climatiques, en particulier de leur impact au cours des transitions climatiques. Afin de répondre à ces questions, ce travail s’attache à comparer la composition géochimique des produits de l’érosion à celles des sédiments actuels de rivière et des archives sédimentaires de la plaine du Gange.

Un premier bilan des processus d’érosion a été établi petite échelle dans le bassin Haut-Himalayan de la Khudi. L’érosion actuelle conséquente de ce bassin de ~3 mm/a se produit lors de la mousson, correspond pour l'essentiel à l’érosion des sols et surtout à l'intense activité d'une zone de glissement de terrain. Grâce au développement d'une nouvelle méthode de destruction de la matière organique, la mesure de l’hydratation des silicates a pu être utilisée comme traceur inédit des sols. Sur cette base, l’inversion des compositions des sédiments de la rivière démontre que l’érosion physique est dominée à ~80% par le glissement de terrain, l’érosion de sols étant mineure et comparable aux taux d’érosion des autres bassins alentours. L’érosion chimique qui conduit à un flux d'éléments dissous de 7.9 kt/a (soit une érosion équivalente de 0.02 mm/a) semble dériver de l’altération profonde du substrat rocheux. Néanmoins les flux d'éléments dissous dessinent également une relation marquée avec les flux particulaires durant la mousson, suggérant une altération additionnelle des sédiments au cours du transport fluvial.

Une approche similaire a ensuite été menée à l’échelle plus vaste du bassin de la Narayani drainant l’ensemble du Népal central. Grâce à des mesures de courant par ADCP combinées à l’échantillonnage de sédiments en profondeur, un modèle de transport sédimentaire a été utilisé pour intégrer les flux sédimentaires en profondeur et ainsi réviser le taux d’érosion moyen sur le bassin versant à une valeur de ~1.7 mm/a, proche des taux d'érosion long-terme. Un système géochimique associant la mesure du δD des silicates associée aux concentrations en carbonate s’est révélé un traceur diagnostique de l’érosion glaciaire dans le Nord du bassin, tandis que la teneur en matière organique du sédiment a pu être utilisée comme traceur des sols. L’analyse temporelle des flux de sédiments, de leur composition et du signal granulométrique, a ainsi permis d’établir que seule une faible fraction des sédiments (<20%) provenait de l’érosion par les glaciers et les sols. À l'échelle du Népal central, l’érosion physique semble donc également dominée par les glissements déclenchés lors de la période de mousson.

Le grand cône alluvial de la Narayani-Gandak, situé au débouché de cette rivière dans la plaine du Ganges, a enregistré l’histoire récente de l’érosion du Népal central. Trois forages réalisés dans ce méga-cône permettent ainsi d'étudier l'évolution de l'altération et de l'érosion en Himalaya au cours du tardi-Pléistocène. Ces dépôts sédimentaires révèlent une étonnante stabilité depuis ~45 ka de la géochimie, des provenances et du degré d’altération des sédiments. Seule l’intensité de l’érosion mesurée par isotopes cosmogéniques semble augmenter au cours de l’Holocène.

Par contraste, l’évolution très récente de la distribution de l’érosion dans la chaîne est marquée par un accroissement (x3) de la proportion de matériel des régions basses et plus peuplées de l'Himalaya, montrant que les activités anthropiques, via notamment une forte croissance du réseau routier durant la dernière décennie, ont eu un impact beaucoup plus marqué sur l’érosion que la dernière transition climatique Pléisto-Holocène.